PETROCHEMISTRY OF THE NORTHERN RIFT ZONE, NE ICELAND: PLUMBING DYNAMICS AND SOURCE VARIATIONS

John François Pernet-Fisher

Royal Holloway, University of London

Thesis submitted for the degree of Doctor of Philosophy,

September 2012

Declaration of Authorship

I John Pernet-Fisher, hereby declare that this thesis and the work presented in it is entirely my own. Where I have consulted the work of other, this is always clearly stated.

Signed: …….

Date: …….

ABSTRACT

In this study 156 post, inter- and intra- glacial basalts sampled from the Northern Rift Zone (NRZ), Iceland, have been shown to exhibit a wide range of chemical and isotopic compositions.

In the majority of cases fractional crystallisation has been shown to be the dominant process in controlling major and trace element variations. In addition crystallisation pressures have been estimated resolving location and depth of the main bodies of crystallisation under individual rift systems. The pressures calculated from these samples and their relationships with eruption ages has indicated that whist multiple stacked chambers exist under all central volcanos, only one chamber is responsible for generating the majority of basaltic lava flows during individual eruptive episodes. This precludes the need for complex polybaric crystallisation models during rifting episodes and suggests that a simple one chamber model of magma evolution may be valid.

$\delta^{18}O$ values were determined by laser fluorination on a small number olivine phenocrysts, all showing values below normal mantle. Crystallisation depths indicate that most magma chambers are situated in the lower crust, as such it is difficult to reproduce these light $\delta^{18}O$ values by assimilation of lower crustal cumulates. Large proportions of gabbroic assimilation are required (>60%), inconsistent with the primitive nature of the samples analysed. The light $\delta^{18}O$ values from this study therefore support the hypothesis that Iceland has lower than normal mantle $\delta^{18}O$ (Thirlwall et al, 2006).

Radiogenic isotopes indicate that a mixture of depleted and enriched sections of recycled crust as well as a recycled sediment component is present in the mantle source of NRZ lavas. Double spike corrected Pb isotope ratios shows that the recycled crust is ~450 Ma, consistent with observations from other Icelandic rift zones (Thirlwall et al, 2004). Within individual rift segments lavas form very tight correlations suggesting these mantle components are able to fully homogenise in order to form the tight 'pseudo-binary' mixing trends observed. Overall the influence of the sediment components increase towards the plume centre, coupled with higher Dy/Yb_N and Na_2O/TiO_2 ratios in these samples imply that that these components are tapped by a deep fusible component within the mantle. Based on similar observations from other OIBs these recycled crustal components are expected to be present in the mantle as olivine free pyroxenites, however Ni, Ca and Fe/Mn values of olivines phenocryst from across the rift zone show little evidence for such a pyroxenite evolvement.

TABLE OF CONTENTS

LIST OF FIGURES

LIST OF TABLES

LIST OF ABBREVIATIONS

AFC	Combined assimilation and fractional crystallisation
BSE	Bulk silicate earth
BP	Before present
cpx	clinopyroxene
$\Delta^{207}Pb$, $\Delta^{208}Pb$	vertical deviation of $^{207}Pb/^{204}Pb$ and $^{208}Pb/^{204}Pb$ from the NHRL (Hart, 1984)
D	mineral-melt distribution coefficient
DMM	Depleted MORB mantle
EM1	Enriched mantle 1
EM2	Enriched mantle 2
ERZ	Easter Rift Zone
E	Younger Modulus
Ga	Billions of years
GPa	Giga-pascals
gt	garnet
HIMU	High μ mantle
HREE	Hevey rare earth elements
MC-ICP-MS	multi collector, inductively coupled plasma mass spectrometry
ID	Isotope dilution
km^2	square kilometres
ka	kilo-years
kbar	kilo-bars
LA-ICP-MS	Laser ablation, inductively coupled plasma mass spectrometry
LF	Laser fluorinated
LILE	large ion lithophile elements
LOI	Loss of ignition
LREE	Light rare earth elements
Ma	Million years
MPa	Mega- pascals
MIB	Mid Iceland Belt

MICE	Moderately incompatible elements
MORB	mid ocean ridge basalt
μ	$^{238}U/^{204}Pb$
NHRL	Northern hemisphere reference line
NRZ	Northern Rift Zone
OIB	ocean island basalt
ol	olivine
PM	Primitive mantle
ppm	parts per million
REE	rare earth elements
ROC	recycled oceanic crust
RP	Reykjanes Peninsular
sd	standard deviation
se	standard error
sp	spinel
SISZ	South Iceland Seismic Zone
Σr^2	Sum of squared residuals
TIMS	Thermal ionisation mass spectrometry
VICE	Very incompatible elements
WRZ	Western Rift Zone
XRF	X-ray fluorescence

ACKNOWLEGMENTS

Firstly I would like thank my supervisor Prof. Matthew Thirlwall for the opportunity to conduct this research as well as the continued supervision and training in the lab over the past four years.

I am particularly gratefully for the Department Research Fund, the University of London Research Fund and the Radiogenic Isotope Laboratory who helped in funding two field seasons as well as enabling me to attend the VMSG meeting at Cambridge and the Goldschmit meeting in Prague in 2011. I would like to thank Neil Holloway for the preparation of my thin sections and Kevin D'Souza for help in taking photographs of these said thin sections. In addition I would like to thank Dr. Christina Manning for all her help and advice in the lab as well as Matthews various students over the past few years whose company in the labs were much appreciated. I would also like to thank Kristján Jónasson who very kindly let me analyse a number of his samples from Heiðarsporður.

I especially would like to thank Lorin Davies, without his help in the field as well as ferrying me from outcrop to outcrop this project would have been severely hampered, not to mention for making a very enjoyable two field seasons! Finally I would like to thank Dr. Frasier Crane whose wit helped see me through the final few months of writing up.

During my time at Royal Holloway (all 7 years!) there have been many people who have made my time here a pleasure. All my housemates past and present, particularly the 'ToD' gang (Alex, Dan, Ellis, Raph, Simon, Stephan and Tom) who's continued tour of the pubs of minor towns in the South East has been a necessary distraction. In addition the company of all the postgrads past and present have made 202b (and then 263) a wonderful office to work in.

I would like to dedicate this thesis to Mum and Dad, I couldn´t have done this with your continual encouragement and support over the last four years. Finally thank you to Vicky, I literally could not have gotten through this without your love and support as well as the numerous pizzas bought!

CHAPTER 1: INTRODUCTION

1.1 General Geology

1.1.1 History of the NE Atlantic: The formation of Iceland

Iceland, situated on the Mid Atlantic ridge is unique in being the only mid-ocean ridge centred hotspot active today and forms part of one the large igneous provinces of the world. Continental flood basalts located in north Canada have suggested that this hotspot may have been active since at least 130 Ma (Johnston and Thorkelsen, 2000; Trønnes, 2002). However, the formation of Iceland is linked with the breakup of Pangaea and subsequent rifting of the North Atlantic around 58-62 Ma (Lawver and Muller, 1994; Saunders et al., 1997; Mjelde et al., 2008). At this time thick seaward-dipping reflector sequences were erupted along the Greenland and NW European margins (Saunders et al., 1997). In particular very Forsteritic olivines (up to Fo_{93}) were reported in the West Greenland and Baffin Island sequences strongly implying that the hotspot was centred here at this time (Larsen and Pedersen, 2000). Initial early sea floor spreading was confined to the now extinct Ægir Ridge, whilst continental thinning was occurring to the west, under the hotspot, as Greenland drifted NW. This culminated in oceanic rifting around 25 Ma with the initiation of the Kolbeinsey Ridge. The onset of rifting at this time is thought to mark the start of plume-ridge interaction (Mjelde et al., 2008).

Over the last 25 Ma plume-ridge interaction has created the large elevated basaltic plateau of Iceland. During this time the rift zones located within Iceland have migrated stepwise eastward in order to keep their positions near the surface expression of the hotspot which is currently thought to be located near the Vatnajökull ice cap (Ward, 1971; Darbyshire et al., 2000; Shen et al., 2002; Li and Detrick, 2006; Shorttle et al., 2010).

1.1.2 Plume or no plume?

The Iceland hotspot is often considered to be the surface expression of a convection plume of anomalously hot material rising from the deep mantle (e.g. Morgan 1971; White et al., 1995; Allen et al., 1999), however recently this hypothesis has been questioned (e.g. Foulger et al., 2005).

Several lines of evidence have been used to argue for the presence of a plume. Initially the observation of anomalously thick crust at Iceland (~40 km at the centre, Darbyshire et al, 2000)

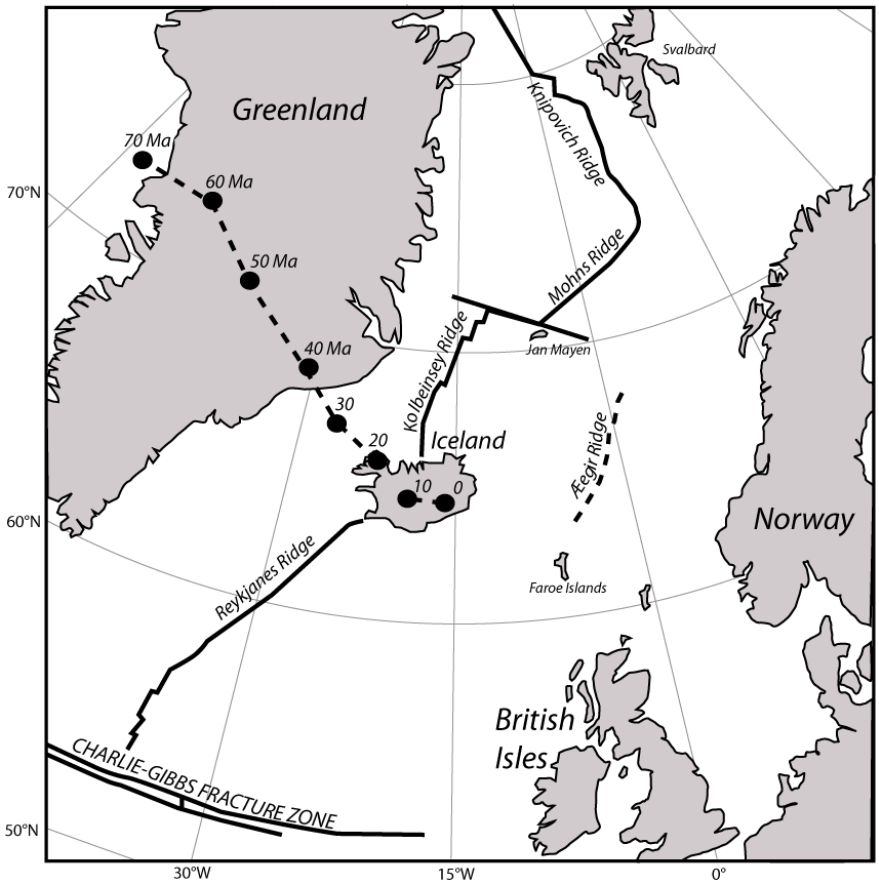

Figure 1.1: *Location of Iceland within the North Atlantic (modified from Saunders et al., 1997). Black dash line with black dot shows the Iceland plume track over the past 70 Ma.*

was linked to increased melt production and therefore elevated mantle temperatures (White et al., 1995; Bjarnson et al., 1996; Allen et al., 1999). In addition geochemical evidence of a deep reservoir was supported by elevated $^{3}He/^{4}He$ ratios (e.g. Kurz et al., 1985; Breddem et al., 2000) as well as olivine-melt thermobarometry indicating that this structure may be up to 200-300 K hotter than the surrounding mantle (Putrika, 2005). More recently seismic tomographic modelling revealed the presences of a deep rooted, hot, 100-200 km cylindrical low velocity anomaly beneath Iceland (e.g. Tryggvason et al., 1983; Wolfe et al., 1997; Bijwaard and Spakman, 1999).

A minority, however, have argued against the presence of plumes and dispute the presence of a temperature anomaly under Iceland. Menke and Levin, (1994) interpreted their seismic data to suggest that mantle temperatures beneath Iceland are in fact lower than spreading ridges in the Pacific Ocean, whilst Gudfinnsson et al. (2003) found no evidence for higher mantle temperatures in their suite of olivine phenocrysts.

Recently Foulger and co-workers put forward a mechanism to explain the increased crustal thickness without the need for a temperature anomaly. The presence of more fertile material beneath Iceland such as a fragment of subducted Iapetus crust was argued to be able to generate greater volumes of melt then the pure peridotite mantle of the surrounding MORB (Foulger et al., 2005; Foulger and Anderson, 2005). Alternatively some workers have suggested that small scale convection, restricted to the upper mantle, would cause a greater mantle flow in the melting region enabling the generation of thicker crust (e.g. Mutter et al., 1988).

Critics have been fast to point out that these models often lack sufficient geodynamic calculations (Bjarnason, 2008) nonetheless, it is difficult to reconcile these plume-less models with the strong combined geochemical and geophysical evidence that Icelandic lavas are able to tap a deep, primitive source.

1.1.3 Icelandic Rift Products

Rift Zones are typically comprised of a number of individual rift segments, each consisting of dyke fed faults and fissures swarms. Typically central volcanoes are built up within these swarms as stable magma chambers develop over time. These start as large shield volcanoes which may undergo caldera collapse in more mature systems (Gudmundosson, 1998). Tholeiites are generally erupted from the dyke-fed fissures, however the development of stable, long lived magma chambers allow the formation of more evolved magmas (Jakobsson, 1979) typically only seen at the mature centres.

The presence of ice sheets across Iceland during glacial periods have led to phreato-magmatic eruptions. During such a magmatic event pillow lavas are initially formed under the high hydrostatic pressure of water and ice over the fissure. As the water escapes hydrostatic pressure decreases, resulting in pillow breccias and pyroclastic glass, which is subsequently altered to hyaloclastite tuffs. These eruptions can form large (>100 km) ridges along rift zones (Gudmundsson et al., 1997). In some cases where the tuff builds above the level of the ice and water, capping lavas are able to form, creating table-mountains (Gudmundsson, 2000).

1.1.4 The Northern Rift Zone

The northern rift zone (NRZ) of Iceland is dominated by five active volcanic systems that are spread 30-40 km apart on a broad N-S trend (Sigurdsson and Sparks, 1978). Each system consists of a series of eruptive and non-eruptive fissures and an associated central volcano (Figure 1.2). K-Ar ages of Tertiary lavas suggest that the Northern Zone became active ~6-7 Ma ago as the location of rifting shifted eastward from Langjökull-Skagi volcanic zone (Cotman,

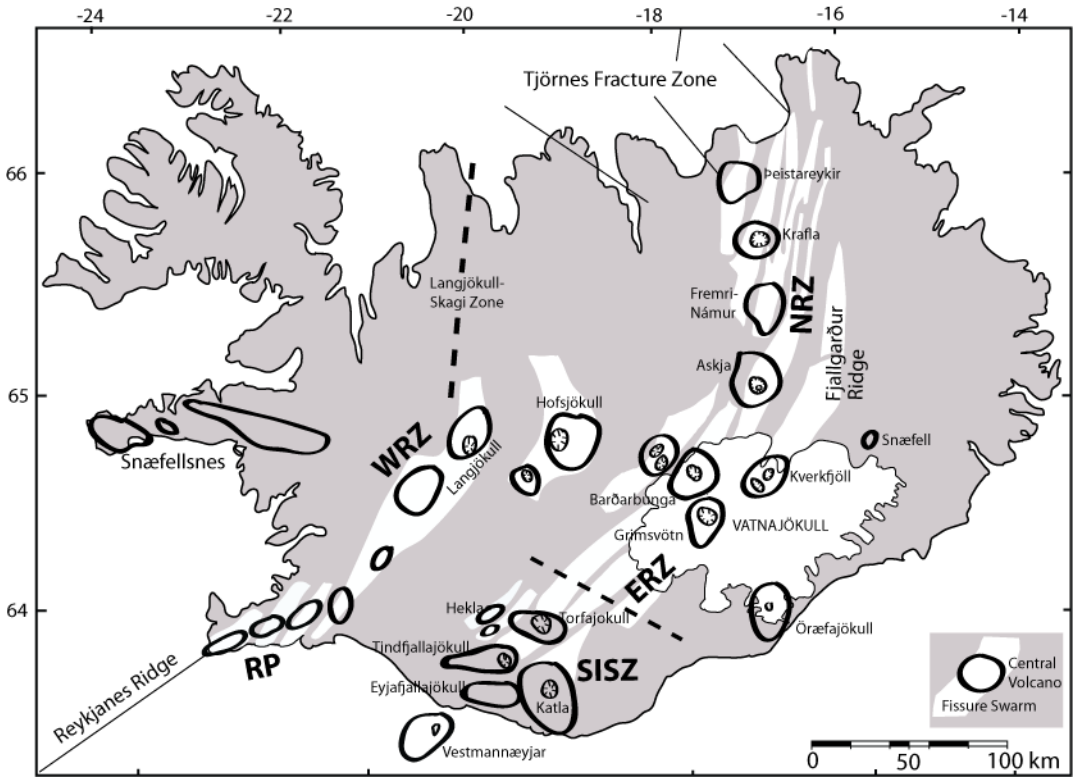

Figure 1.2: *Volcanic zone and Rift systems of Iceland (modified from Sigmundsson, 2006). RP, Reykjanes Peninsula; WRZ, Western Rift Zone; ERZ, Eastern Rift Zone; NRZ, Northern Rift Zone; SISZ, South Iceland Seismic Zone.*

1979; Jancin et al., 1985; Young, 1985). Today rifting episodes occur episodically every 100-200 years (Sigurdsson and Sparks, 1978) with typically only one fissure system active during a rifting episode. primitive

At least four glacial/Interglacial periods have been inferred over the history of the NRZ, however precise ages and stratigraphy are poorly constrained (Thorarinsson, 1979). Ice cores have provided estimates for the end of the last glacial and interglacial at around 10 ka and 70 ka respectively (Nicholson, 1991). The end of the last glacial maximum (~12-10 ka) has been associated with increased melt production linked with to isotactic rebound. Eruption rates calculations based on estimated flow volumes by Maclennan et al. (2002) suggest that melt production at Þeistareykir and Krafla may have been up to 50 time greater than today (12.1 $km^3\ kyr^{-1}$ and 1.3 $km^3\ kyr^{-1}$ between 12.5-10.0 ka cf. 0.26 $km^3\ kyr^{-1}$ and 0.03 $km^3\ kyr^{-1}$ > 10ka for at Þeistareykir and Krafla respectively) whilst similar calculations by Sigvaldason et al (1992) for the Askja area suggest that eruption rates may have been up to 20-30 times higher than today (9.39-5.98 $km^3\ kyr^{-1}$ between 10-4 ka cf. 0.32 $km^3\ kyr^{-1}$ >2.9 ka).

1.1.4.1 Krafla

Krafla is located to the north of the NRZ and is dominated by large swarms of faults and fissures and an associated, well developed central volcano with a large caldera. The caldera is poorly defined, forming the remnants of an old shield volcano dating from the last interglacial period (Sigurdsson and Sparks, 1978). The fissure zone is approximately 80 km long and 40 km wide trending broadly NE-SW. The area has been active for at least the last 300 ka (Nicholson and Latin, 1992) most recently erupting in the 1975 -1984 event (Bjornsson, 1985). Since the last glacial maxium a number of eruptive episodes have been identified, the absolute ages of these periods having been constrained using Hekla tephra marker horizons (Thorarinsson, 1979). In a review of post-glacial volcanic activity in area Thorarinsson (1979) divided eruptive cycles into three main periods:

The Lúdent Cycle: This cycle is comprised of two main eruptive events. Firstly a number of small flows from the fissures at Lúdent and Námafjall were emplaced which, based on correlations with Hekla tephra layer H_5, is around 6000 years old. A period of quiescence followed which lasted around 3500 years during which Hekla tephra layer H_4 was deposited. About 200 years later a large flow, the older Laxárhraun was emplaced from the shield volcano of Ketilárhraun (part of the Fremri Námur volcanic system). This flow covered most of the Mývatn area damming depressions in the area creating lake Mývatn.

The Hverfjall Cycle: The next major cycle started ~2800 BP with a series of small fissure flows and the emplacement of a basaltic tephra ring at Hverfjall. This was followed by the emplacement of the younger Laxárhraun from the Þrengslaborgir-Lúdentsborgir crater row, covering most of the older Laxárhraun and reaching the Skjálfandi Bay.

The Víti Cycle: This is the most recent eruptive cycle occurring after the settlement of Iceland. The first period, known as the 'Mývatn Fires', lasted from 1724-1792 during which series of non-eruptive fissures, earthquakes and lava flows took place. The largest flow, Leirhnjúkshraun, erupted from 1725-1729. The second period, known as the 'Krafla Fires', lasted from 1975-1984. The main flow stretched northward covering Leirhnjúkshraun. Strong geothermal and seismic activity is still present today.

1.1.4.2 Heiðarsporður

Heiðarsporður is a 15 km long ridge to the south of the Krafla central volcano which has produced chemically distinct lavas (Jónasson, 2005). It is particularly unusual as evolved rocks are present in place of a central volcano. There is no recent activity from this ridge; all lavas

were thought to have been emplaced in a relatively short amount of time ~1000 years after onset of the current interglacial (Jónasson, 2005). It is likely that this episode is linked with the high volcanic production associated with the end of the last glacial maximum (Sigvaldason, 2002).

1.1.4.3 Fremri-Námur

This volcanic system, located to the east of Krafla, is made up of a swarm of fissures ~160 km long, ~17 km wide trending broadly NE-SW. Its shield volcano is characterised by a strong geothermal field. Overall, little is known about Fremri-Námur's eruptive history. Tentler and Mazzoli (2005) described three main magmatic fissures associated with this centre: Kræduborgir which is 2500-3000 years old, Raudholar-1 which was formed in the early Holocene and Rauduborgir-Randarholar which is 6000-8000 years old. Associated with the Rauduborgir-Randarholar fissure is the Sveinar graben. During the 1875 Askja eruption this graben saw deepening, propagation as well some magmatism (Tentler and Mazzoli, 2005). A number of large intra-glacial table mounts span this rift system however their relationship with Fremri-Námur is unclear.

1.1.4.4 Dyngjufjöll

Dyngjufjöll, commonly referred to as Askja, is near the Vatnajokull ice sheet. It consists of a fissure swarm ~200 km long and ~20 km wide and its associated central volcano contains the Askja and Öskjuvatn calderas. The northern part of the fissure is well expressed and consists of crater rows, fractures and faults including the Sveingjá and Veggir grabens (Tentler and Mazzoli, 2005). This system derives its name from the shield volcano that existed before the Askja caldera collapse and has been active since the Pleistocene (Sigvaldason, 2002). Dyngjufjöll is located in a tectonically complex area where transform fissures cut the main fissure swarm at near right angles. This has split the centre into a number of crustal blocks that have been uplifted and rotated during rifting (Sigvaldason, 2002). Tephra evidence of a Plinian type eruption at ~10 ka has been found throughout east Iceland and is thought to have formed the Askja caldera. There is some debate as to the exact formation of Askja (Brown et al., 1991), however it is clear that following formation, the caldera was filled by a number of large basaltic flows from fissures situated underneath (Sigvaldason, 2002).

The most recent major rifting event to affect this system occurred in 1872-1875. Lateral movement of high level basaltic magma triggered a caldera collapse at Askja, creating the Öskjuvatn caldera. This lateral movement is thought to have fed the flows that erupted in the Sveingjá graben known as the Nýjahraun. Following this eruption explosive rhyolitic activity

occurred at Askja, thought to be caused by a fresh pulse of magma into a stagnant body of acidic magma (Sigurdsson and Sparks, 1978).

There have been a number of small rifting episodes recently with small basaltic eruptions occurring in 1922-1926, 1929 and 1961 (Sigurdsson and Sparks, 1981). Askja is currently in a 'quiet' period with no eruptions or significant earthquakes or dike injections reported. The main Askja caldera, however, is continuing to subside, with a total amount of at least 0.75 m, as a result of magma solidification in the crust (Sturkell and Sigmundsson, 2000).

A number of inter-glacial and post-glacial shield volcanoes are distributed along the rift zone their relationship with the main volcanic centre of Dyngjufjöll is however unclear.

1.1.4.5 Kverkfjöll and Fjallgarðar

The Kverkfjöll rift system, which is partly buried under the Vatnajökull ice sheet is the most southerly rift segment of the NRZ, extending for 60 km northward from Vatnajökull. Pillow lava and hyaloclastite formation are common along this system as Kverkfjöll was close to the centre of the Quaternary Ice sheet (Einarsson, 1995). Most of the hyaloclastite mounds along this rift system, such as Upptyppingar and Lindafjöll, were formed toward the end of the last glacial period ~ 10 ka (Sigurbjarnarson, 1988; Sigurbjarnarson, 1993). Post-glacial lava flows are generally restricted to near to the main volcanic centre. The exact ages of these eruptions is not well defined; however tephra markers suggest they are likely to have erupted near the start of the post glacial ~7000 BP (Sigbjarnarson, 1988).

A small volume of magmatic activity was last reported at Kverkfjöll in 1968 (Global Volcanism Program). However, recent micro seismic activity has been reported under the Upptyppingar hyaloclastite ridge. This has been widely interpreted as current melt migration through the crust (Jakobsdottir et al., 2008; White et al., 2011).

Located to the north of the Kverkfjöll system is the Fjallgarðar ridge. This is a predominantly sub-glacial ridge around 190 km in length, older than 0.8 Ma (Helgason, 1989). The relationship between Kverkfjöll and Fjallgarðar is not entirely clear. Helgason (1989) reported slight chemical differences together with the observation that the Kverkfjöll fissure swarm intersects the Fjallgarðar ridge at an angle of ~15° lead to the suggestion that this ridge constitutes a separate system to Kverkfjöll.

1.2 Previous work on the NRZ

Previous geochemical investigations of the NRZ have either focused on individual rift segments or form part of wider, pan-Icelandic studies. Due to the recent magmatic activity at Krafla and Askja studies have generally focused on these centres whilst central volcanoes that are not as assessable such as Fremri-Námur are often neglected. The earliest studies that focused on specific centres mainly reported major and trace element chemistry with limited to no isotopic analyses (e.g. Nicholson et al., 1991; Sigurdsson and Sparks, 1981). As accuracy and precision improved for determining radiogenic and stable isotopes, broad regional studies were often conducted, generally including only small numbers of samples from the NRZ (i.e. Thirlwall et al., 2004; Kokfelt et al., 2006; Peate et al., 2010).

Studies have shown that fractional crystallisation accounts for the vast majority of the major and trace element variation in the most primitive suites (Nicholson et al., 1991; Sigurdsson and Sparks, 1981). There has been some debate, however, as to the origin of silicic magmas. Some workers argue that fractional crystallisation is able to generate such lavas (e.g. Carmichael, 1964; Macdonald et al., 1990; Furman et al., 1992; Prestvik et al., 2001), whilst other workers argue that re-melting of altered crust is responsible (Sigvaldason, 1974; Sigmarsson et al., 1991; Jónasson, 1994; Jónasson, 2007). The partial crustal melting models have been partially developed at Krafla. Enrichment in incompatible elements beyond the scope of fractional crystallisation coupled with very light $\delta^{18}O$ values in the most evolved rocks has been cited as evidence for the contamination of altered crust in the generation of silicic magmas (e.g. Nicholson et al., 1991; Jónasson, 1994).

The origin of the altered, $\delta^{18}O$ light crust in the Icelandic lava pile has been widely attributed in the literature as the result of Iceland's unique position as a high latitude island, where meteoric waters are depleted in ^{18}O (e.g. Hattori and Muehenbachs, 1982; Oskarsson et al., 1985; Gautason and Muehenbachs, 1998). Large scale hydrothermal circulation of this $\delta^{18}O$ light water, often to great depths, results in alteration of the country rock. Drill holes at Krafla have shown that at 3 km depth the basaltic lavas found are extremely altered with $\delta^{18}O$ values up to -10‰ (Hattori and Muehlenbachs, 1982).

The presence of light $\delta^{18}O$ in rift zone lavas has been widely reported at other volcanic centres along the NRZ and across Iceland, however significant debate exists as to whether this is solely the consequence of hydrothermally altered contaminants interacting with mantle derived magma with normal $\delta^{18}O$ or whether the Icelandic mantle contains a $\delta^{18}O$ light reservoir (e.g.

Hemond et al., 1998; Nicholson et al., 1991; Gee et al., 1998; Eiler et al., Macpherson et al., Bindeman et al., 2006; Thirlwall et al., 2006)

Due to the primitive nature of lavas, Þeistareykir has largely been at the centre of debate for this argument in the NRZ. Eiler et al. (2000) argued that no 'uncontaminated' lavas are present at Þeistareykir and demonstrated that correlations of $\delta^{18}O$ with trace and major elements can be explained by the assimilation of an enriched andesite. Stracke et al. (2003) was critical of this model arguing that the andesitic assimilant used by Eiler et al. (2000) is not appropriate assimilant. Instead Stracke et al. (2003) attempted to model combined fractionation of lavas with assimilation (assimilation fractional crystallisation; AFC) using an 'average' quartz tholeiite. Assimilation of such material was unable to generate the positive Sr anomaly present in Þeistareykir lavas, as well as unable to explain the isotopic variation. Stracke et al. (2003) concluded, therefore, that whilst small amounts of assimilation cannot be categorically ruled out, the lavas from Þeistareykir are primary melts and as such preserve mantle features. Combined O-Os isotope values reported by Skovgaard et al. (2001) and combined O-Pb-Nd-Sr reported by Thirlwall et al. (2006) for Þeistareykir appeared to support this conclusion. Macpherson et al. (2005) extended the $\delta^{18}O$ data set for the NRZ and reported a number of combined O-He isotope values for primitive lavas from Fremri-Namur, Askja and Kverkfjöll. Whilst Macpherson et al. (2005) did not rule out crustal interaction in the most depleted lavas, the enriched lavas were thought to be produced by primary melts with a $\delta^{18}O$ light mantle source of ~4‰ and MORB like $^{3}He/^{4}He$. This Icelandic mantle $\delta^{18}O$ is consistent with the estimations of Thirlwall et al. (2006) who showed that the enriched source of the Reykjanes Peninsula is likely to have a $\delta^{18}O \sim +4.3‰$.

Early Sr-Nd isotopic studies have shown that NRZ lavas form broad correlations along with other Icelandic lavas (Zindler et al., 1979; Nicholson et al., 1991; Hemond et al., 1993). Ocean Island Basalts (OIBs) have long been noted to show such isotopic correlations and are widely accepted to be the result of mixing as least two distinct mantle components. Increases in the number and quality of analyses, in particular measurements of Pb isotopes, have led to the identification of at least 5 different components within the mantle worldwide (Figure 1.3) (Zindler et al., 1986). Icelandic lavas appear to lie largely on a trend between DMM and HIMU with some possible minor evolvement from an EM type component. The potential involvement of a HIMU component, characterised by elevated Ce/Pb and low K/Nb (Chauvel, 1992) has led many authors to suggest the presence of a recycled component within the Iceland plume mixing with either surrounding north Atlantic asthenosphere (Schilling, 1973; Hart et al., 1973;

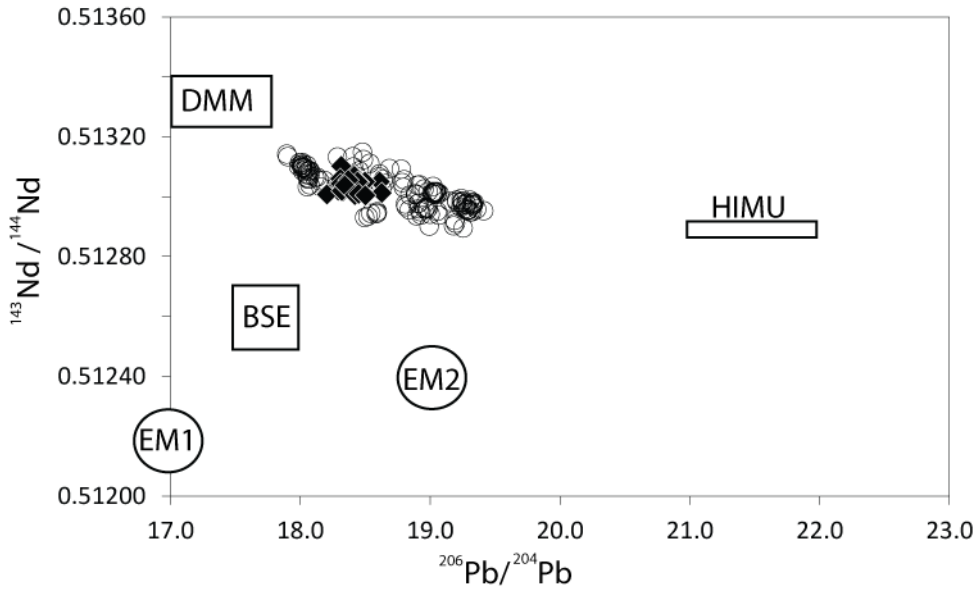

Figure 1.3: *$^{143}Nd/^{144}Nd$ vs. $^{206}Pb/^{204}Pb$ of Icelandic lavas within the mantle Zoo of Zindler et al. (1986). Open circled shows all Iceland (Thirlwall et al., 2004 and Thirlwall, unpublished) variations whilst the black diamonds are NRZ samples. DMM (depleted MORB mantle); HIMU high μ lavas thought to be generated by subducted oceanic lithosphere >1700 Ma old; EM1 is thought to be generated by recycling of lower continental crust; EM2 is thought to be generated by recycling of terrignous sediments; BSE (bulk silicate Earth).*

Sun and Jahn, 1975) or a depleted component intrinsic to the plume (Kerr et al., 1995; Fitton et al., 1997; Kempton et al., 2000; Thirlwall et al., 2004).

Some of the simplest models only argue for the involvement of two source components. Chauvel and Hémond (2000) for instance developed a model which saw the generation of depleted and enriched lavas through recycling a complete section of oceanic crust. The isotopically enriched lavas were thought to tap the upper basaltic crust, characterised by low Sr/Nd, Sm/Hf and high Ce/Pb whilst the isotopically depleted lavas such as reported at Þeistareykir are tapping the lower gabbroic crust, characterised by high Sr/Nd and low Ce/Pb. Kokfelt et al. (2006) supported this hypothesis, reporting Eu/Eu* correlations with isotopes as evidence of recycled gabbro in the source of the most depleted lavas.

As accuracy and precision of isotopic measurements, in particular Pb isotopes have improved more complex regional models have been put forward, resulting in a plethora of proposed source components and mantle end members (Figure 1.4).

An additional EM-type component has been invoked within the Iceland plume, widely accepted to be at the source of the anomalously enriched Öræfajökull lavas. There is some

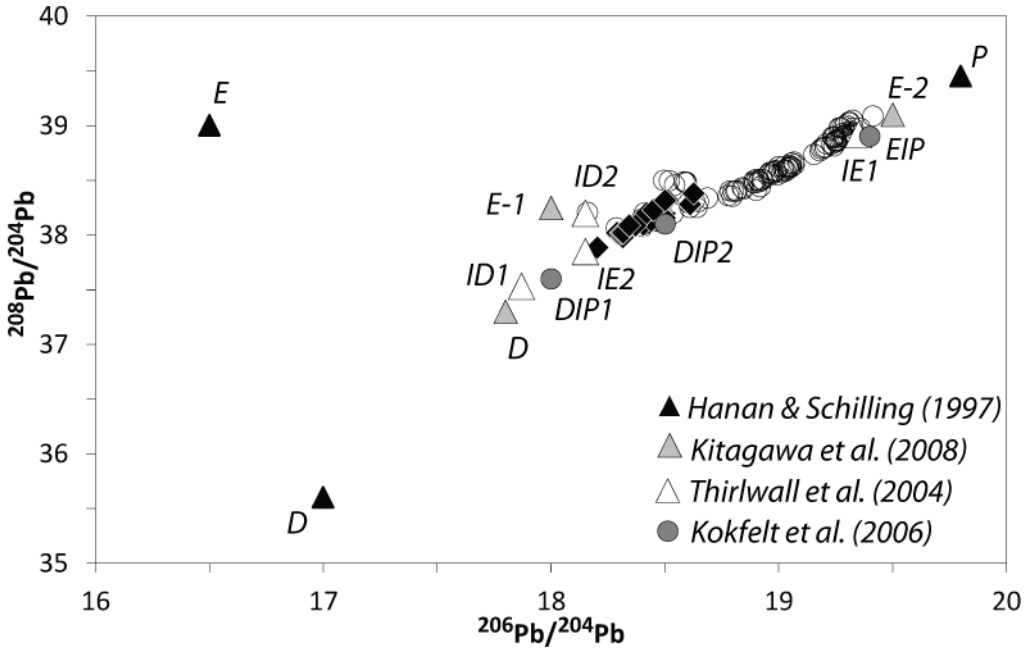

Figure 1.4: *$^{206}Pb/^{204}Pb$ vs. $^{208}Pb/^{204}Pb$ plots showing the range of proposed mantle end-members within the Icelandic plume. Open circled shows all Iceland (Thirlwall et al., 2004 and Thirlwall, unpublished) variations whilst the black diamonds are NRZ samples from this study.*

debate in the literature whether the EM signature has more EM-1 type flavour (e.g. Sigmaarsson et al., 1992; Hanan and Schilling, 1997; Thirlwall et al., 2004) or an EM-2 type flavour (e.g. Prestvik et al., 2001; Kokfelt et al., 2006). It has been argued that this component is only seen in the off-rift segment of Öræfajökull and Snæfell, however recent mixing models have argued that sediment influences are also present at the source of the ERZ (the southern continuation of the NRZ) (Manning and Thirlwall, 2012).

Not all authors have agreed on the nature of the recycled crustal component, some authors argue for C or FOZO, a chemically distinct 'flavour' of recycled material different to 'classic' HIMU, at the source of Icelandic lavas (Hanan and Graham, 1996; Hanan and Schilling, 1997; Stracke et al., 2005; Blichert-Toft et al., 2005; Kitagawa et al., 2008). Whilst within the HIMU supporters there is debate as to the age of the recycled crust. Chauvel and Hémond (2000) argue that correlations in Pb-Pb space represent mixing a complete crustal section; this correlation will also have age significance. Kokfelt et al. (2006) also used such correlations to infer the age of the crust; both studies yielded an Archean age. Such an old age appears to be supported by O-Os isotope correlations. Skovgaard et al. (2001) demonstrated that mixing a basaltic layer ~3 Ga with a depleted mantle of the same age created a high $\delta^{18}O$, $^{187}Os/^{188}Os$ component whilst mixing between the gabbroic section and depleted mantle will form the low $\delta^{18}O$, $^{187}Os/^{188}Os$ component. Brandon et al. (2007) also reported Os-He isotopes consistent with an old age. They suggest that enrichment in $^{187}Os/^{188}Os$ with no related enrichment seen

in $^{186}Os/^{188}Os$ could reflect 1-2 Ga crust that was enriched in Re but not Pt during its formation.

In contrast, Thirlwall et al. (2004); Manning (2010) and Peate et al (2010) argue for a young crust. It has been noted that Iceland lacks the very radiogenic $^{206}Pb/^{204}Pb$ values that are typically associated with HIMU basalts (<19.3 vs. >20-22), together with the almost universal negative deviation of $^{207}Pb/^{204}Pb$ below the Northern Hemisphere Reference Line (expressed as $\Delta^{207}Pb$) led Thirlwall et al. (2004) to suggest that the recycling of a young 450 Ma crust could account for these characteristics. In addition, Thirlwall et al. (2004) found no evidence for the involvement of recycled gabbroic crust in the most depleted lavas, arguing that isotopic variation reflects the sampling of heterogeneity within the upper crust. In support of this Manning (2010) presented Sm/Nd and Lu/Hf isochrons for the most enriched lavas, the recycling process is not likely to have fractionated these ratios, as such if an old crustal age is valid, then lavas should lie on an Archean isochron. All data, however, was found to lie on ~450Ma isochrons. Thirlwall et al. (2004) additionally illustrated that the Os isotope data of Skovgaard et al. (2001) can also be consistent with the incorporation of 11-32% of 450Ma crust into a depleted mantle.

Overall, whilst most of the conclusions reached by these studies are applicable to Iceland as a whole; some differences have been noted between rift zones (e.g. Peate et al., 2010; Manning 2010). As such the small numbers of lavas analysed from the NRZ so far makes it hard to fully evaluate the mantle sources and their arrangement along the NRZ.

1.3 Thesis structure and project aims

The broad aim of this project is to use geochemical and petrological techniques to describe and quantify the magmatic evolution of the NRZ. This process may be divided simply by depth: Chapter 3 discusses shallow level crustal processes, Chapter 4 attempts to resolved magmatic plumbing dynamics whilst Chapter 5 discusses deep level, mantle processes. In Chapter 2 all geochemical and petrological data that has been collected for this project is presented. In addition to the broad aim of this project a number of specific objectives will try to be resolved and are as follows:

1.3.1 Plumbing arrangement and dynamics.

Recent models of magmatic plumbing (e.g. Kelly and Barton, 2008) have proposed that complex arrangements of multiple stacked magma chambers are present under some volcanic

centres in Iceland. The wide number of Holocene lava flows studied provides an excellent opportunity to resolve the magmatic plumbing of the NRZ. A thorough understanding of crustal structure and magmatic plumbing is critical when attempting to accurately model processes such crustal assimilation and magma mixing.

1.3.2 Investigating mantle source heterogeneity along the NRZ

Detailed studies of the western and eastern rift zones clearly show differences in the mantle source arrangement as well as subtle heterogeneities of the mixing components proposed (Thirlwall et al., 2004; Manning, 2010). Within the literature only a limited number of the high precision isotopic analysis needed in order to resolve local mantle source arrangements has been reported for the NRZ (Thirlwall et al, 2004; Peate et al 2010). Comprehensive isotopic and elemental analysis from each rift segment along the NRZ will help resolve source relationships along the rift zone.

1.3.3 Investigating the role of sediment at the source of NRZ lavas.

It has been argued that recycled pelagic sediment is responsible for the anomalously enriched nature of Öræfajökull lavas (Prestvik et al., 2001; Kokfelt et al., 2006; Manning, 2010). So far, outside of this centre, the influence of recycled sediment has only been reported in the two closest central volcanoes in the ERZ (Manning, 2010). Whilst relationships with lavas from Þeistareykir appear to suggest that no direct sediment contribution is present to the north of the NRZ. Comparison of NRZ samples from this study and the samples from Öræfajökull and the ERZ reported by Manning (2010) and Peate et al. (2010) will help identify the potential extent of sediment influence along this rift zone.

1.3.4 The role of pyroxenite beneath Iceland

Pyroxenite is widely accepted to be the physical manifestation of recycled crust within the mantle. The involvement of such pyroxenite material in the Icelandic plume however is still a matter of debate (Sobolev et al., 2007; Stracke and Bourdon, 2009; Shorttle and Maclennan 2011). The presence of high Ni and low Ca and Fe/Mn in olivine phenocrysts has been used to successfully identify pyroxenite at other OIBs (e.g. Sobolev et al., 2007; Gurenko et al., 2009; Herzberg, 2011). The development of a quick method of analysing major and trace elements in olivine phenocrysts by LA-ICP-MS (Thirlwall et al., 2012) has enabled large populations of crystals to be analysed spanning the full range of whole rock chemical heterogeneities observed, in order to assess the potential role of pyroxenite in the Icelandic mantle.

CHAPTER 2: PETROCHEMISTRY OF THE NORTHERN RIFT ZONE

2.1 Geological Sampling

New samples from the NRZ were collected over three summer field seasons in Iceland between 2008 and 2010, this amount of field work was necessary in order to provide the quantity and range of samples for chemical and isotopic analysis, supported by sufficient field data to allow relationships along the rift zone to be confidently identified. The geological map of NE-Iceland, (Sheet 7, Sæmundsson, 1977) as well as the 1: 500 000 geological map of Iceland (Jóhannesson and Sæmundsson, 1998) was the basis for planning the field work Sample locations for reference have been plotted on a digitised copy of these maps (Appendix 6).

In total 102 samples of post-glacial volcanic rocks were collected, 39 from Krafla; 17 from Fremri-Námur; 17 from Askja; 12 from Kverkfjöll. Twenty five inter-glacial volcanic rock samples were collected in total; 6 from Krafla; 10 from Fremri-Námur; 6 from Askja; 3 from Kverkfjöll. Fourteen intra-glacial samples were collected, 6 from Krafla; 3 from Fremri-Námur; 2 from Kverkfjöll and 3 from Fjallgarðar. In addition to this 15 samples from Heiðarsporður were kindly provided by Kristján Jónasson.

No samples were collected from Þeistareykir due to the abundance of high quality chemical analysis available in the literature (e.g. Eiler et al., 2000; Stracke et al., 2003; Peate et al. 2010).

2.2 Classification

All samples have been plotted on a total alkali-silica classification diagram (TAS, Figure 2.1). The majority of samples lie within the basaltic field with the exception of 2 intra glacial samples and 1 inter glacial sample (DL034, DL048 and DL055 respectively) from Krafla as well as 4 lavas from Heiðarsporður. All basalts plot in the sub-alkaline field forming a broad positive array. Within this array the different rift segments lie on largely overlapping sub parallel trends. Kverkfjöll, to the south of the rift zone, shows the highest total alkali contents for a given SiO_2 whilst Krafla and Heiðarsporður, to the north of the rift zone, show the lowest, within the range of Þeistareykir samples. All other NRZ other vocanic centers lie on trends largly intermediant to the Kverkfjöll and Krafla.

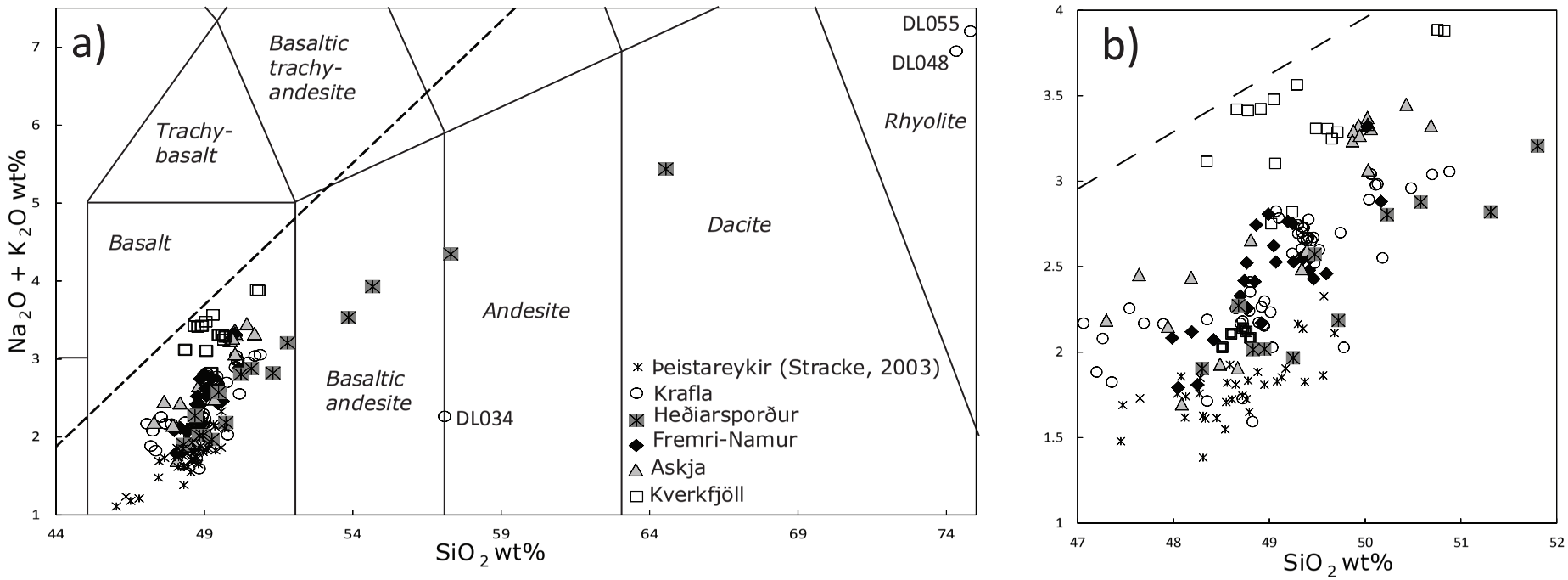

Figure 2.1: *a) Total Alkali-Silica classification plot for NRZ samples of all ages. b) Total Alkali-Silica classification plot for basalts in the NRZ. Dashed line represents division between alkaline and sub-alkaline rocks (MacDonald et al, 1964).*

2.3 Petrography

The numbers in brackets refer to the photomicrographs in plates 1-5. These images show examples of the features described in the following section.

All lavas analysed for this study bar 7 samples are basalts and as such have a restricted mineralogy. Olivine, plagioclase and clinopyroxene are the main phases that crystallise, and are present in varying in combinations and proportions. Approximately 10% of samples are aphyric. Postglacial lavas tend to be highly vesicular with a fine grained groundmass sometimes containing phenocrysts which are typically only seen in thin section. The Inter and Intra glacial lavas are generally much coarser grained with phenocrysts that are clearly seen in hand specimen.

Post glacial lavas range from highly vesicular (1.E) to poorly vesicular and in some cases show several populations of vesicles within a single flow (1.A). Two samples from Kverkfjöll show evidence of flow alignment (1.F; 1.G), where plagioclase crystals are clearly uniformly aligned in one direction; in addition JPF1019 shows glassy streaks that are also aligned in the same direction as the plagioclase (1.F).

Some samples show areas of lighter or darker coloured groundmass either as 'patches' (1.D) or in bands (1.A, 1.B, 1.D). Groundmass typically ranges from fine grained to medium grain intergranular crystals of olivine, plagioclase, clinopyroxene and opaques whereas the highly vesicular samples generally have a glassy groundmass. Where clinopyroxene is more abundant in the groundmass it typically has an ophitic to sub-ophitic texture.

Two populations of phenocrysts are commonly seen in these samples. Firstly large megacrysts (typically 1-50 mm) can be present often in clusters forming glomerocrysts (e.g. 5.F). A second much smaller population of crystals (typically <1 mm) often not much larger than the groundmass is more commonly seen (e.g. 2.A). Plagioclase crystals in this population tend to be tabular in shape showing no zoning and little alteration; on occasion radial clusters of these crystals which have nucleated around a single point can be seen (2.B). When clinopyroxene is present in the groundmass, ophitic textures are common; elongate ophitic clinopyroxene laths can be distinguished in the coarser samples (2.D). When olivine is present it tends to be fairly fresh with only minor amounts of iddingsite alteration. The inter-glacial sample DL046 shows the highest degree of olivine alteration (3.D). On the whole crystals are anhedral to sub euhedral with only a few samples showing well-formed crystals (3.C; 3.A,B). Lavas with a glassy

PLATE 1:

A: DL035 in PPL; Band of darker groundmass, light grey area show large vesicles whilst the darker area shows smaller vesicles.

B: DL035 in XPL; XPL shows the darker area of groundmass to glassy in nature.

C: JPF0949 in XPL; Irregular 'patch' of glassy groundmass within sample.

D: DL046 in XPL; Band of fine grained groundmass intersecting this coarse grained lava.

E: DL041 in PPL; Highly vesicular lavas with glassy groundmass.

F: JPF1019 in XPL; Glassy streaks and plagioclase aligned in the same direction.

G: JPF1020 in XPL; Plagioclase and clinopyroxene aligned in the same direction

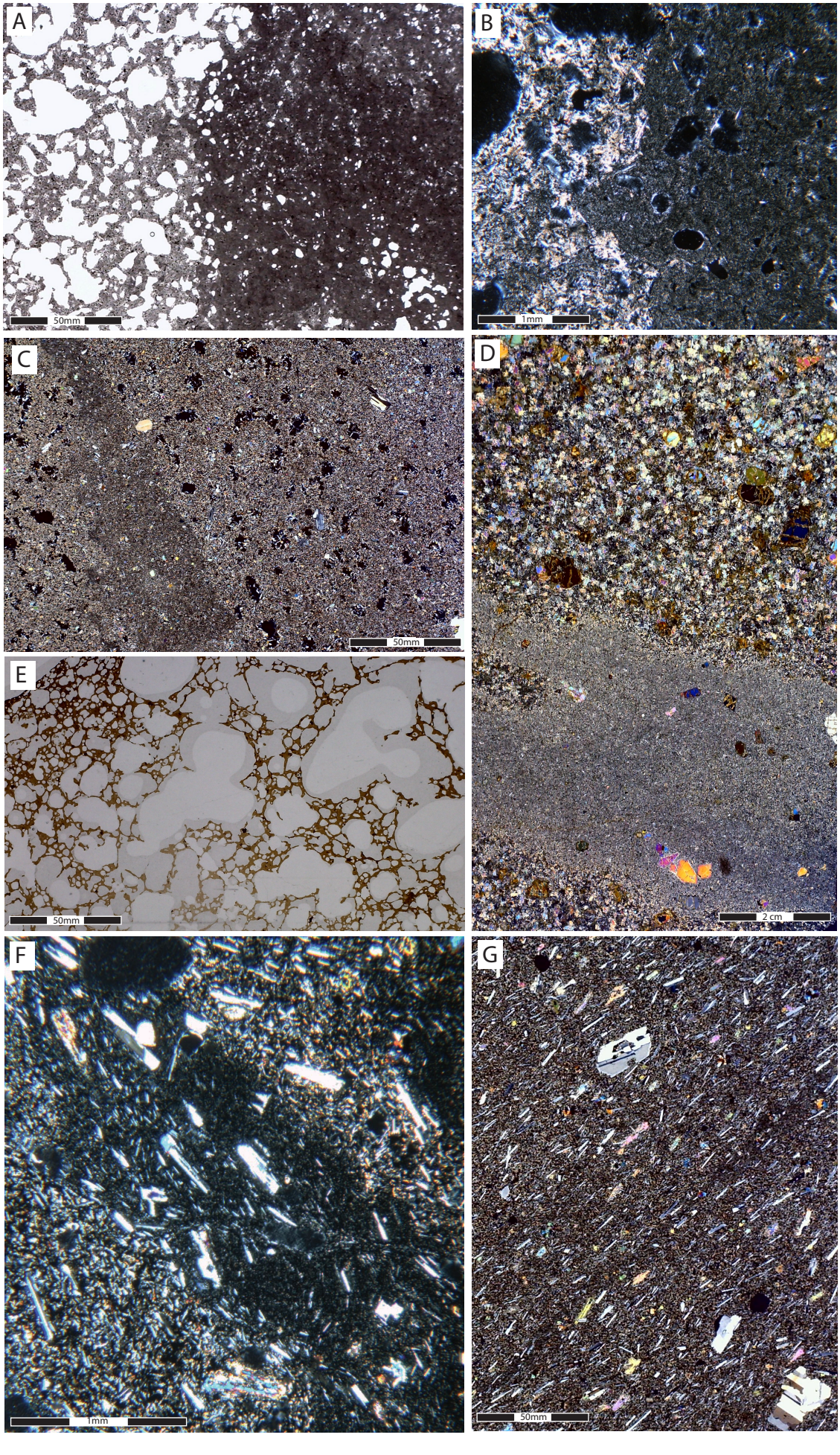
A
50mm
B
1mm
C
50mm
D
2 cm
E
50mm
F
1mm
G
50mm

PLATE 2:

A: DL061 in XPL; Population of small plagioclase and olivine crystals within a medium grained groundmass.

B: DL074 in XPL; radial plagioclase crystals.

C: JPF0909 in XPL; Sub-Ophitic clinopyroxene and plagioclase.

D: DL013 in XPL; coarse grained rock with large olivine phenocryst, elongate clinopyroxene crystals seen with ophitic plagioclase.

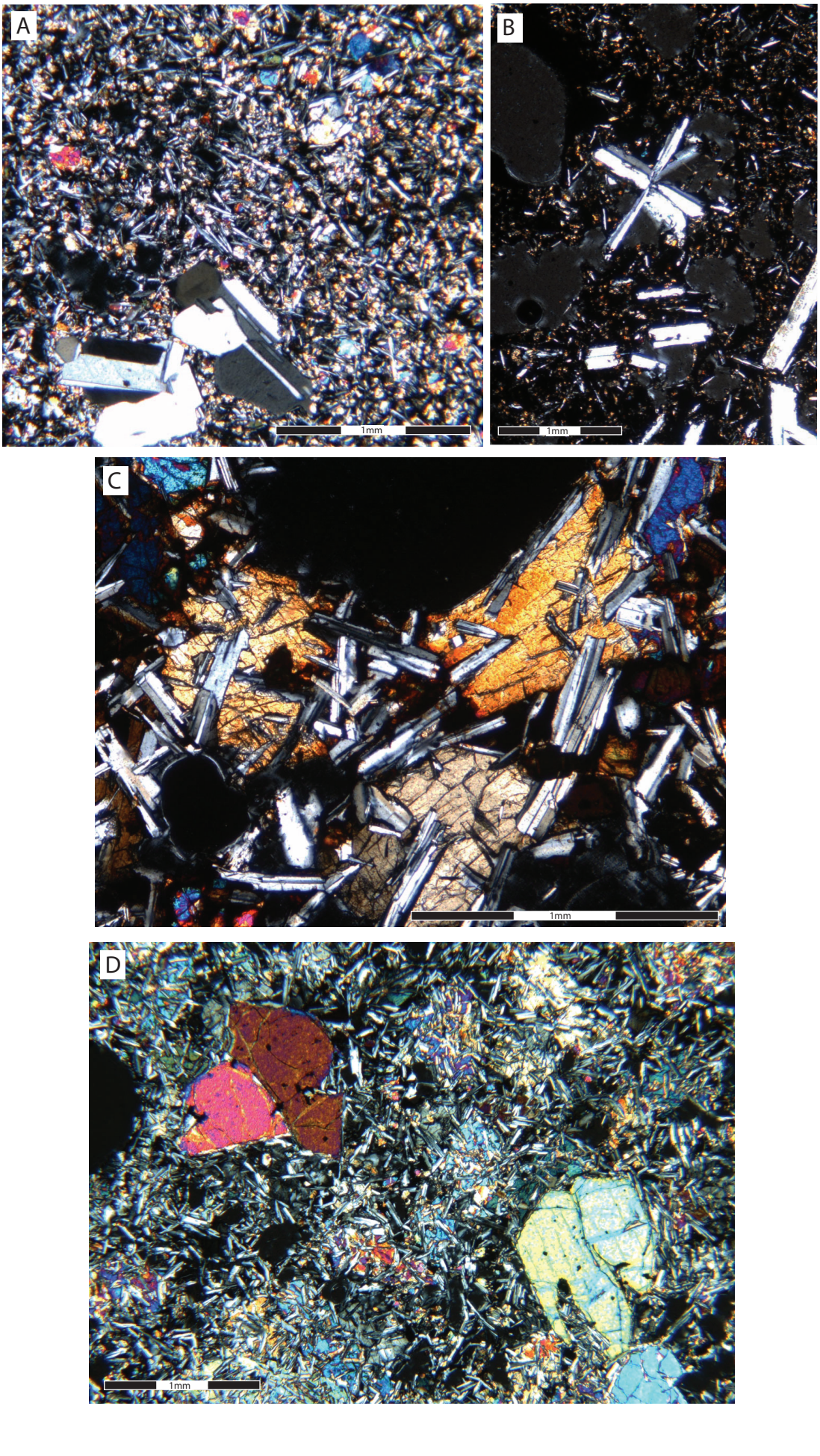
A
1mm
B
1mm
C
1mm
D
1mm

PLATE 3:

A: DL009 in PPL; rare well formed clinopyroxene crystal.

B: DL009 in XPL; same view as A in XPL.

C: JPF0922 XPL; Euhedral olivine crystal.

D: DL046 in PPL; Euhedral olivine crystal showing iddingsite alteration.

E: DL065 in XPL: Euhedral plagioclase crystal showing strong reabsorption textures on the edges of the crystal.

F: DL007 in XPL; Skeletal olivine.

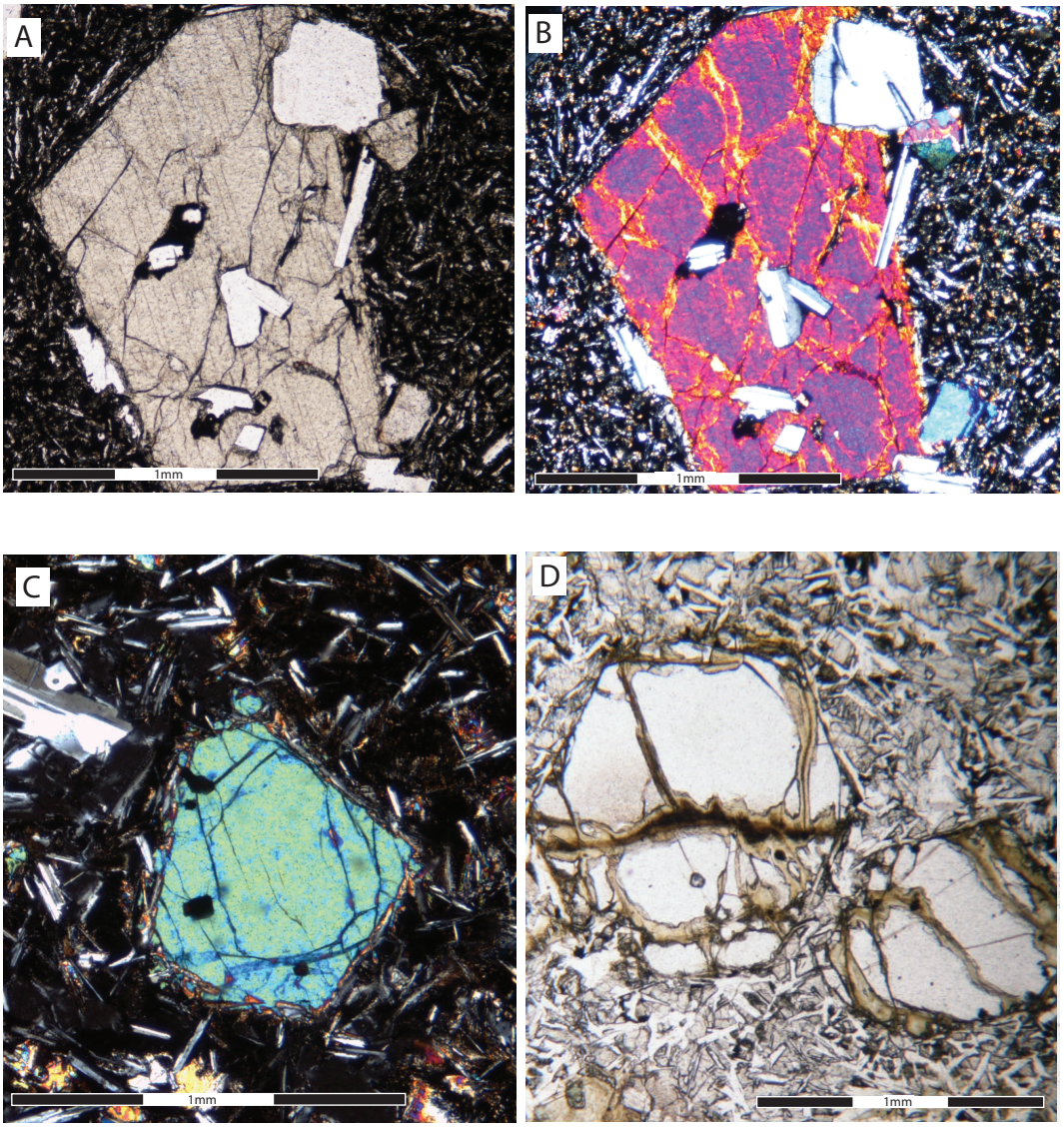
A
1mm
B
1mm
C
1mm
D
1mm
E
1mm
F
500 µm

PLATE 4:

A: DL023 in XPL; Skeletal olivine.

B: DL074 in XPL; Clinopyroxene with reabsorption pits and sector zoning.

C: JPF1023 in XPL; Clinopyroxene with reabsorption pits.

D: Euhedral plagioclases crystals with concentric zoning.

E: JPF0936 in PPL; fine grain lavas with very large plagioclase megacrysts and glomerocrysts.

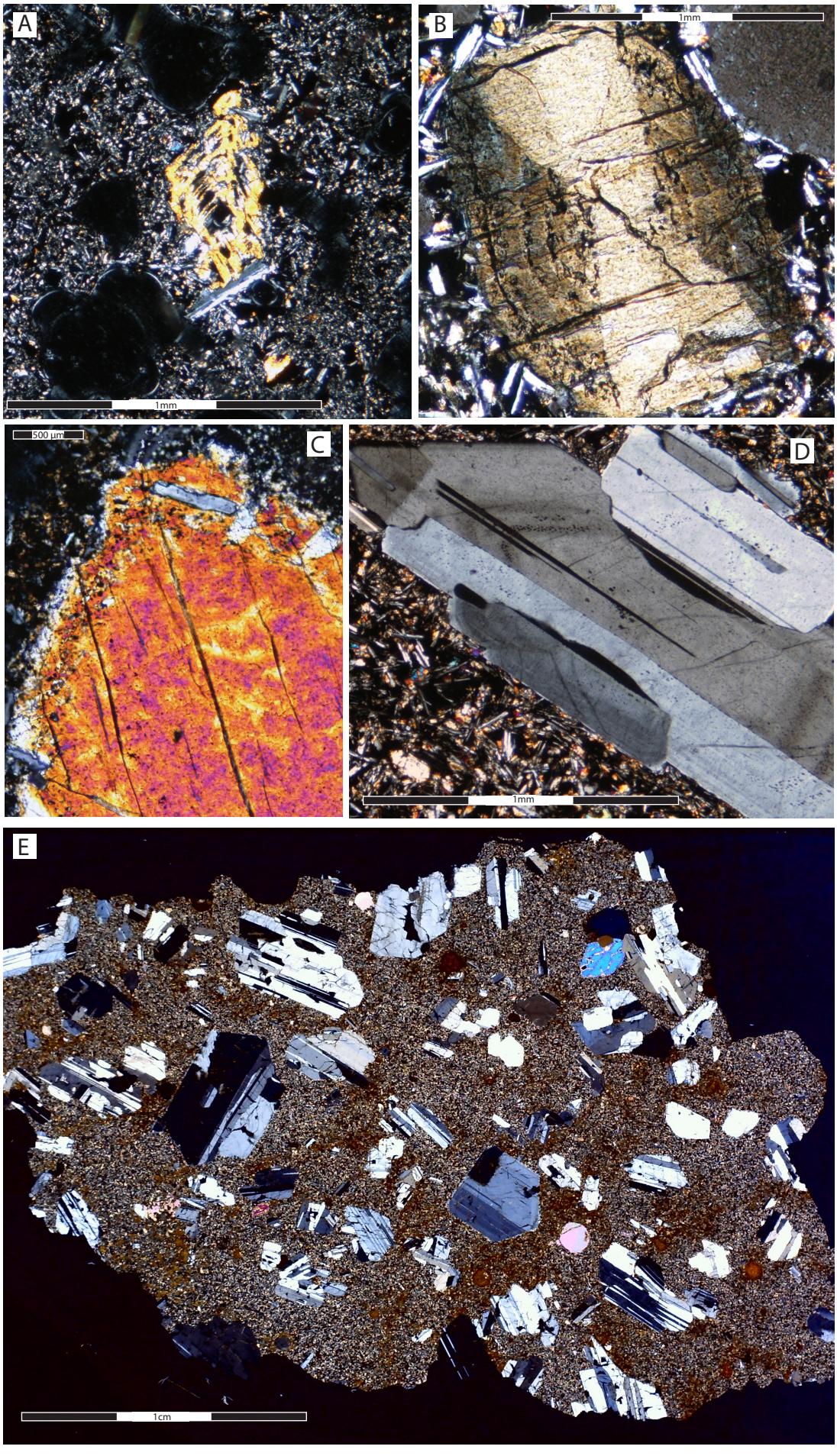
A
1mm
B
1mm
500 µm
C
D
1mm
E
1cm

PLATE 5:

A: DL067 in XPL; medium grained lava with large, elongate gabbroic nodule.

B: DL067 in XPL; Close up of gabbroic nodule, plagioclase crystals show strong reabsorption textures.

C: JPF0950 in XPL; Gabbroic nodule that has undergone some disaggregation.

D: JPF1008 in XPL; Gabbroic nodule with a finer grained size.

E: JPF0957 in XPL; Gabbroic nodule with a larger proportion of clinopyroxene and olivine.

F: DL002 in XPL; Large plagioclase megacrysts.

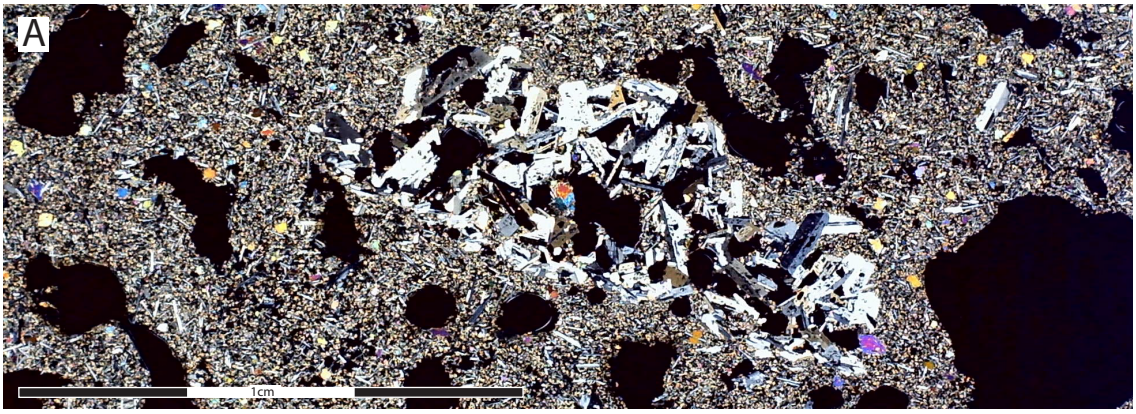
A
1cm

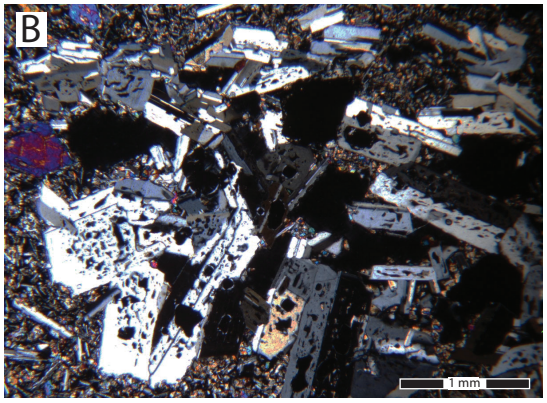
B
1 mm

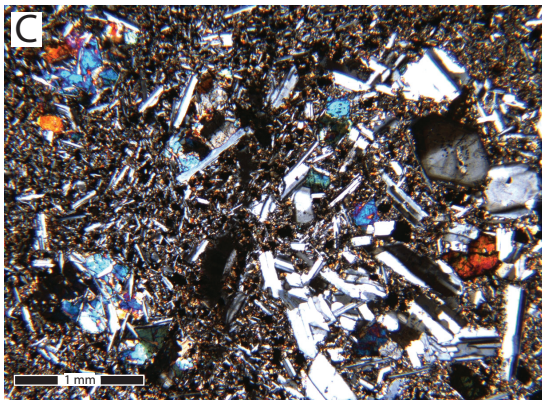
C
1 mm

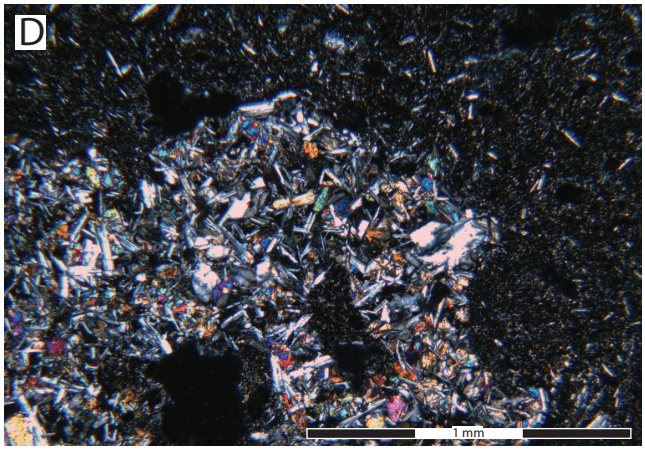
D
1 mm

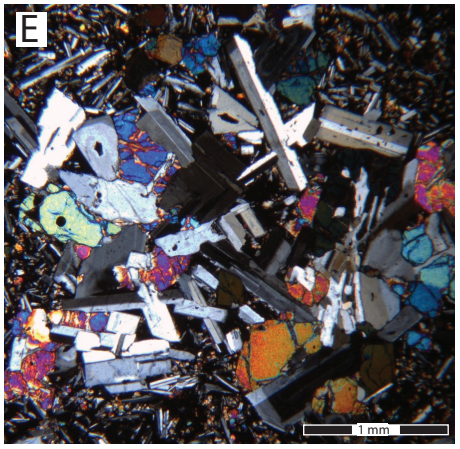
E
1 mm

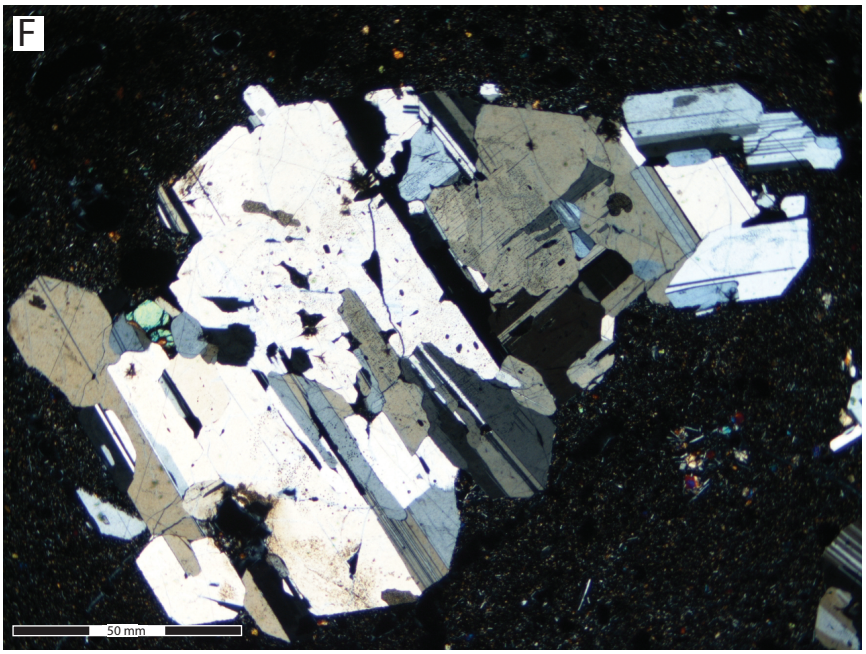
F
50 mm

groundmass typically show phenocryst populations that are much more altered or only contain crystal fragments.

Point counting was undertaken on a large number of thin sections from this study. Typical phenocryst proportions are based on 1500 counts per slide. In samples with glomerocrysts present, relatively high proportions of phenocrysts are seen; 4-33% plagioclase, 3-7.5% olivine and up to 2% clinopyroxene. Lavas with the populations of smaller phenocrysts typically have much lower proportions; ~2-3% plagioclase, 1-2% olivine and <2% clinopyroxene. In the vesicular samples vesicles took up ~8-14% of the sample.

Resorption textures in megacrysts such as sieve textures in the olivines and plagioclase are sometimes seen (3.E; 4.C) commonly associated with sector zoning in the clinopyroxenes (4.B). Skeletal textures are also present in some of the olivines (3.F; 4.A).

Within the largest phenocryst population, plagioclase is the most common mineral, often forming megacrysts up to ~5 mm in length. (4.E) On the whole these crystals show strong zoning and sieve textures (4.D). These megacrysts are commonly grouped in large clusters making up plagioclase glomerocrysts (5.F) or with large olivines and clinopyroxenes making up gabbroic nodules. These nodules can be very large, up to ~1cm in length (5.A) and show a large range in mineral proportions and grain size (5.D; 5.E). In addition these nodules can be seen in different states of disaggregation (c.f. 5.B; 5.C).

2.4 Mineral Chemistry

Phenocrysts chosen for major and trace element analysis were selected from a wide range of samples from all rift segments along the NRZ such that the full range of whole rock chemical heterogeneity is represented. In addition all samples with oxygen isotopes analyses were selected. In the early stages of this study phenocrysts were analysed for major element chemistry by electron microprobe (EMP) on the cores of typically 2 or 3 grains per sample. Subsequently, Thirlwall at et. (2012) developed a method for the simultaneous determination of major and trace elements for olivine, plagioclase and clinopyroxene phenocrysts by LA-ICP-MS (methods in Appendix 1). This has allowed many more grains per sample to be analysed with relative ease. For olivines typically around 20 grains were analysed per sample, whilst for plagioclase and clinopyroxene around 6 gains were analysed per sample. The major and trace element data for olivines are presented in Appendix 3, Table 3.1, the major and trace element data for plagioclase are presented in Appendix 3 Table3.2 and the major and trace element

data for clinopyroxenes are presented in Appendix 3 Table3.3. Grains were picked by hand from the 100-500 micron size fraction.

2.4.1 Olivine

In order to help interpret olivine major element chemistry it is useful to determine whether the mineral compositions observed are in equilibrium with their respective host lavas. This can be done by looking at calculated equilibrium olivine compositions based on bulk rock values. Roeder and Emslie (1970) were the first to show that the equilibrium constant ($K_D(Fe\text{-}Mg)^{ol\text{-}liq}$ = $[Fe^{2+}/Mg]^{ol}/[Fe^{2+}/Mg]^{liq}$) for the following reaction:

$$MgO^{ol} + FeO^{liq} = MgO^{liq} + FeO^{ol}$$

is nearly constant at 0.30 ± 0.03 and is independent of temperature and pressure. Therefore if the K_D value is known and the Fe^{2+}/Mg ratio of the host lava is known it can be calculated whether an olivine is indeed in equilibrium or not. Since this work there has been much debate whether the use of a K_D at 0.30 ± 0.03 regardless of pressure and temperature can be used reliably in order to calculate equilibrium olivine compositions.

A recent review of olivine geo-thermometers (Falloon et al., 2007) compiled evidence that K_D values can be affected by increased pressures. (e.g. Takahashi and Kushiro, 1983; Sobolev and Danyushevsky, 1994). Despite this, in a similar review of olivine geo-thermometers by Putirka (2008) showed experimentally that for basaltic systems at P < 2-3 GPa a K_D =0.30 ± 0.03 is still valid. Crystallisation under the NRZ has been suggested to occur at pressures <~1.5 GPa (Maclennan et al., 2001, Kuratani et al., 2011) therefore a K_D of 0.30 ± 0.03 is clearly still valid.

Most studies used whole rock Fe^{2+}/Mg in calculating K_D, however Falloon et al. (2007), criticised this on the basis that 1) bulk rock values do not necessarily represent the true melt values 2) K_D values are dependent on the FeO/Fe_2O_3 in the melt which is not possible to derive from whole rock data in an unequivocal way. Instead they recommend using experimentally derived values for the correct pressure in order to estimate equilibrium. Throughout the Fallon et al. (2007) review however it has been show experimentally that between 0.1MPa-1 GPa K_D lie within Roeder and Emslie's (1970) 0.30 ± 0.03 value, therefore samples with calculated K_D values within this error have been judged to be in equilibrium.

2.4.1.1 Fo contents:

Overall the majority of olivines analysed have calculated K_D values that lie within error of equilibrium (Figure 2.2). In addition most flows contain small populations of crystals that lie

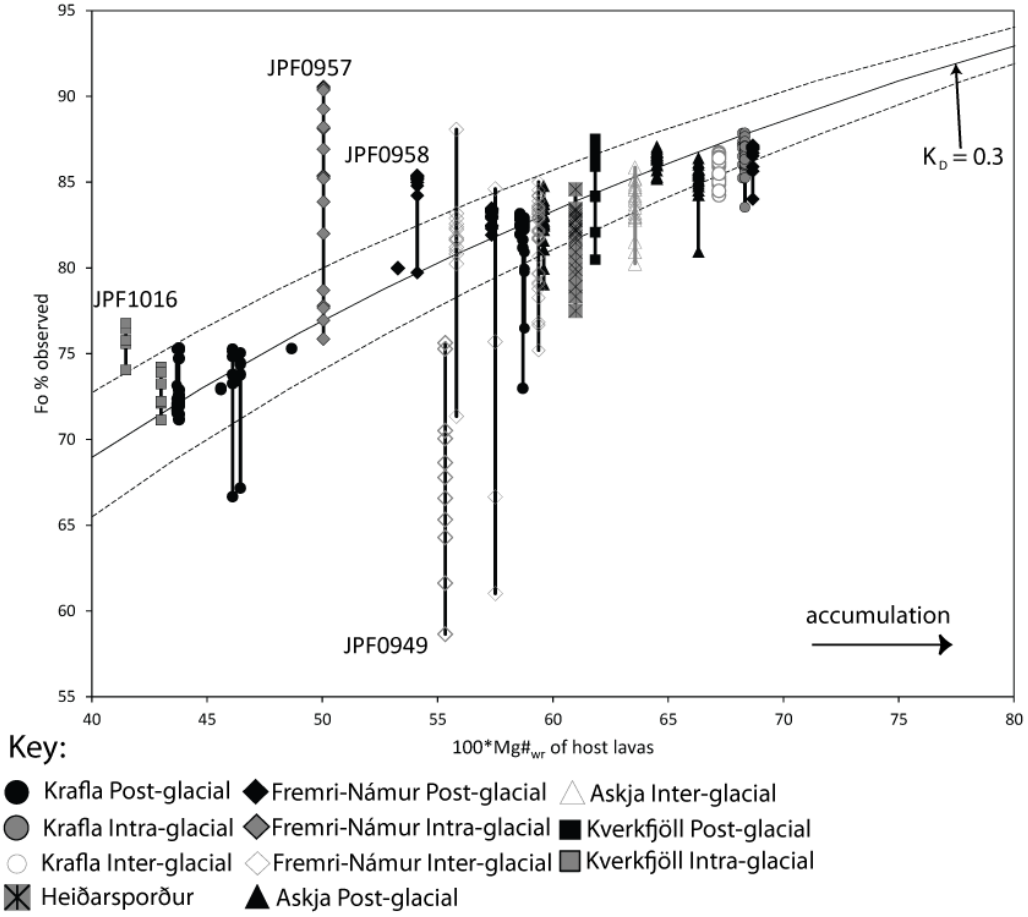

Figure 2.2*: Plot of Fo% of observed versus 100*Mg#$_{WR}$ calculated using a Fe^{3+}/Fe^{2+} of 0.111. Area between dashed lines represent calculated equilibrium Fo% using a K_D values of 0.30 ± 0.03 suggested by Roeder and Emslie (1970). Symbols represent individual olivine compositions while vertical lines indicate the range observed in the flow.*

outside the calculated equilibrium value. In some cases the majority of crystals from a single flow lie outside the error field. For instance JPF1016, JPF0957 and JPF0958 all show populations with higher Fo% than calculated equilibrium values whilst all JPF0949 olivines have lower Fo% than calculated equilibrium value. Typically however, olivines in most post-glacial samples show a moderately limited range of Fo% values (<5 Fo%), with larger variations present in intra and inter glacial samples (up to 17 Fo%). Fo% distributions are presented as histograms in Figure 2.3. Three different types of distribution have been identified from these samples, they are as follows:

1) Equilibrium peaks: Samples where the majority of olivine Fo% values (>80% of the total number of olivines per sample) coincide with the equilibrium field. Typically this distribution is seen mostly in post-glacial samples (e.g. DL009, DL046).

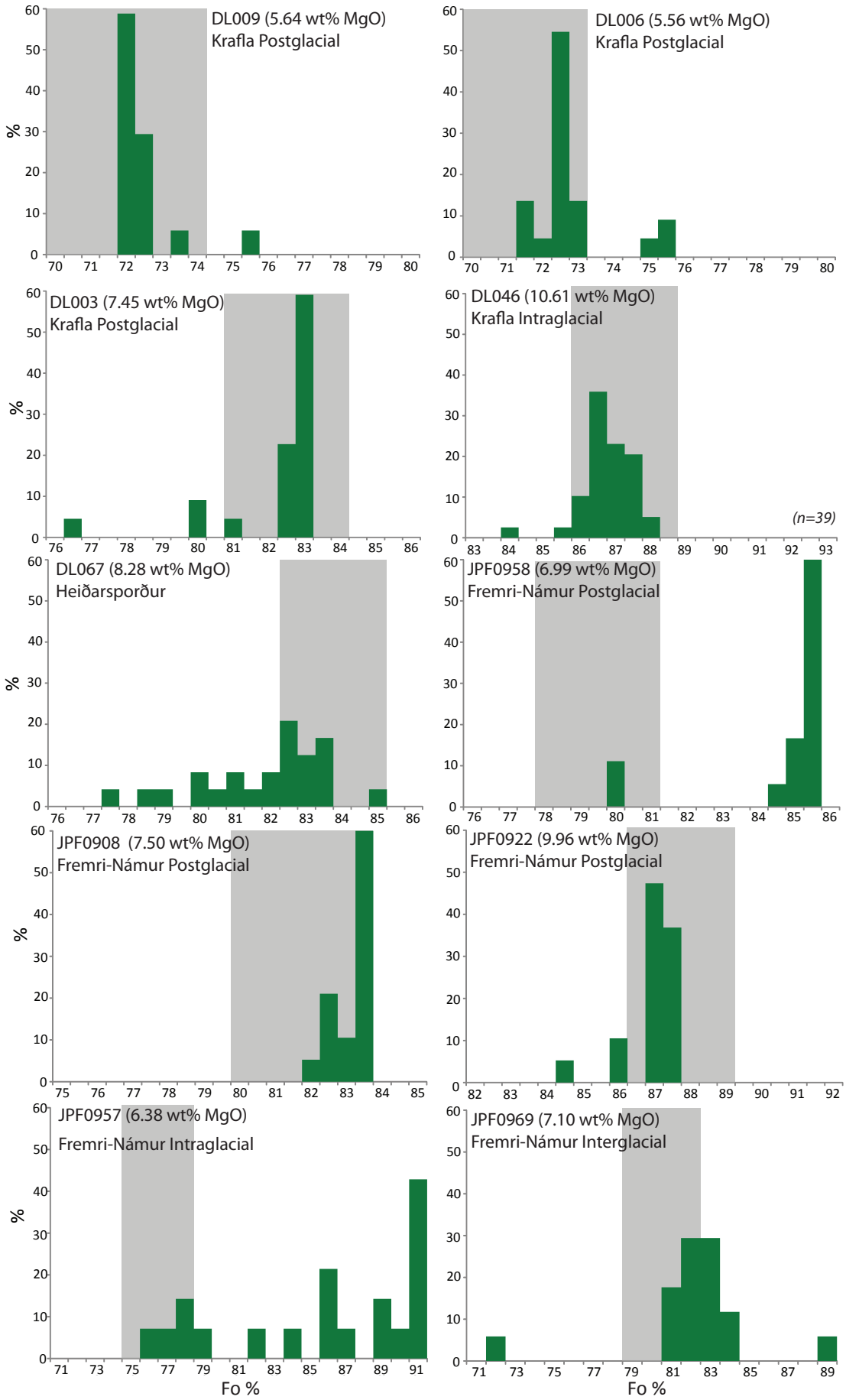

Figure 2.3: *Histograms illustrating the distribution of individual flows. Grey boxes represent the field of equilibrium olivines assuming K_D values of 0.30 ± 0.03. Two different sets of 20 phenocrysts were picked for DL046 in order to assess how representative the distributions presented here These are labelled DL046a and DL046b.*

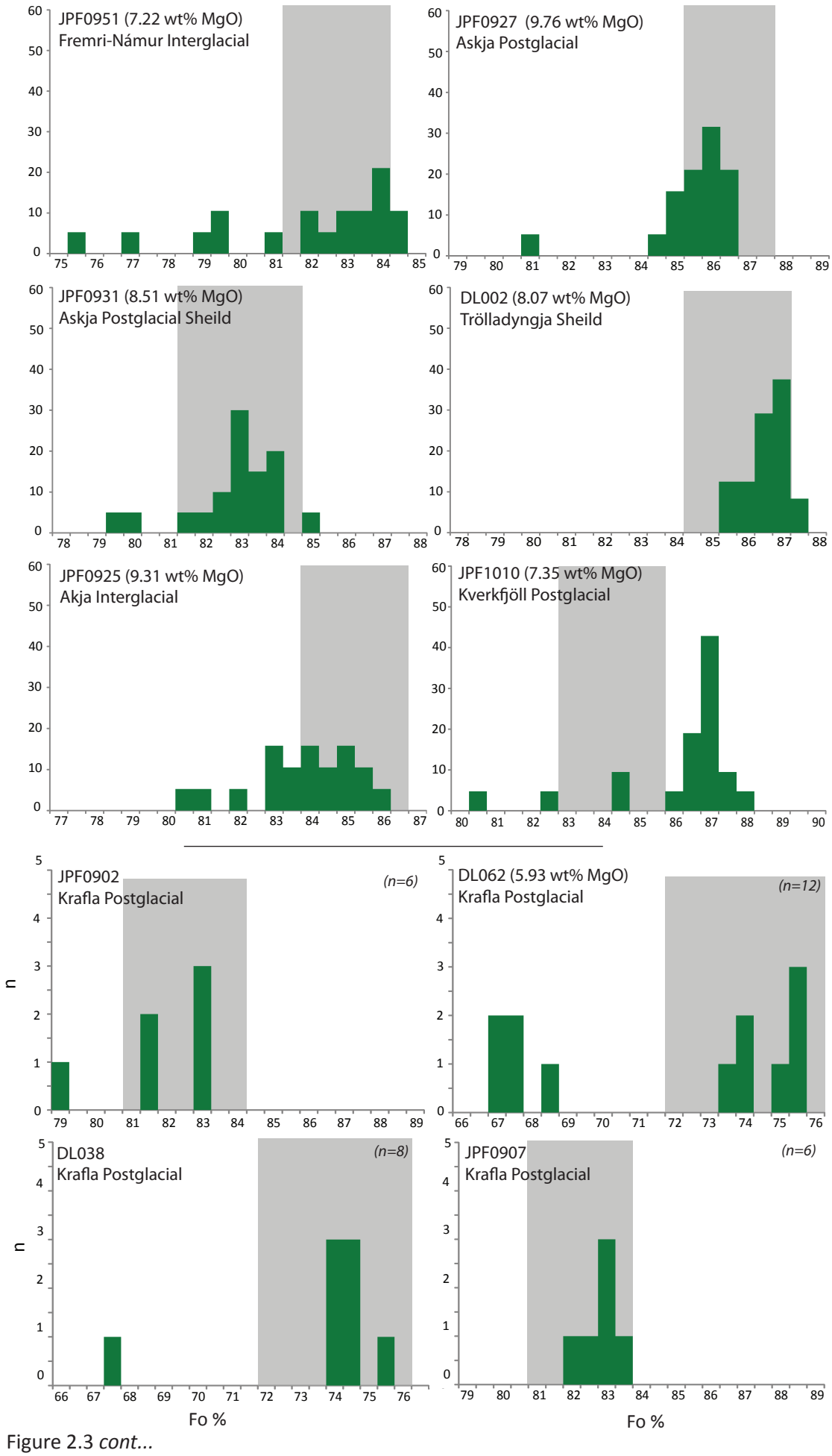

Figure 2.3 *cont...*

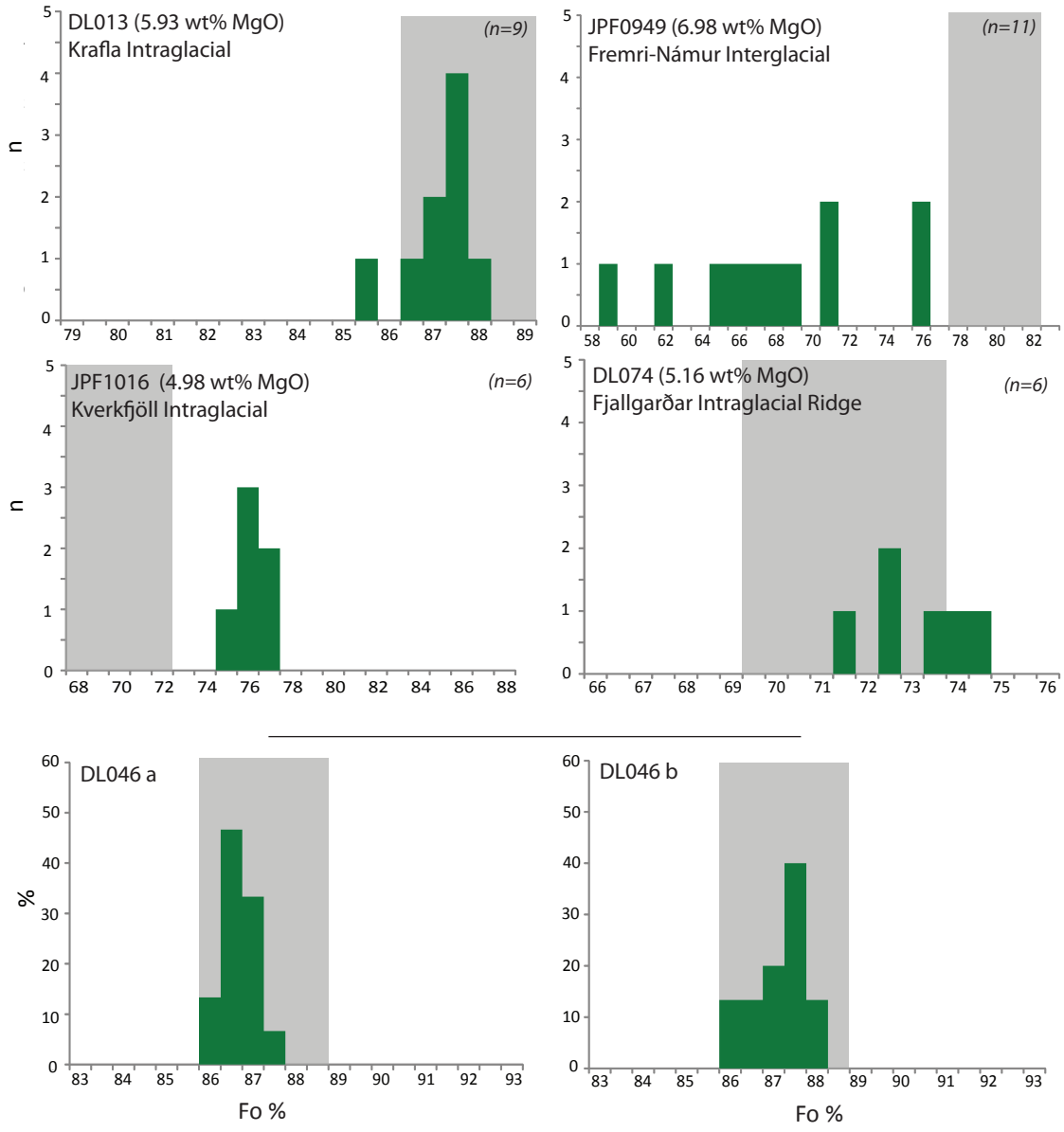

Figure 2.3 *cont...*

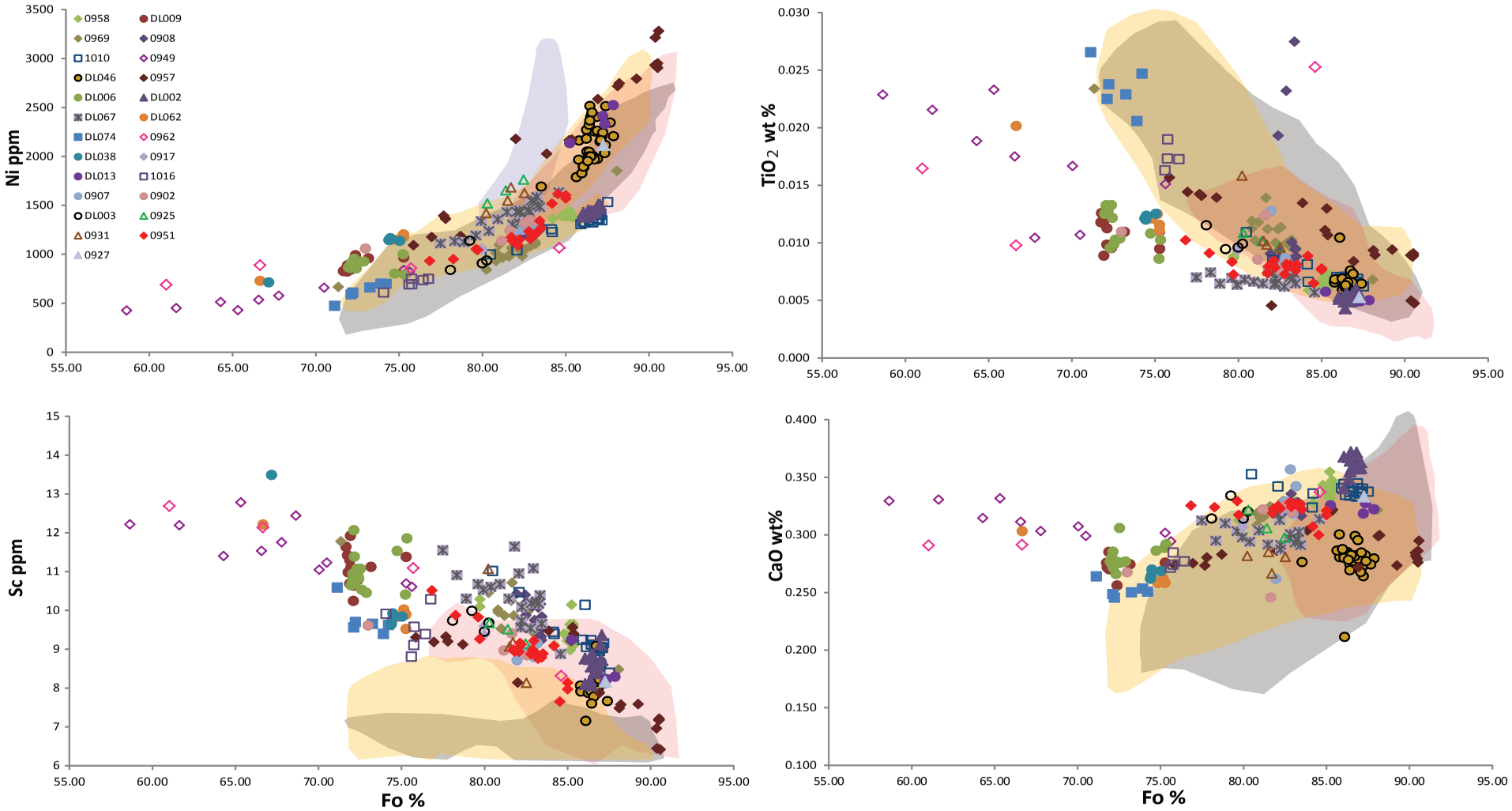

Figure 2.4: *Ni ppm, Sc ppm, TiO2 w.t. % and CaO w.t. % vs. Fo%. Red field show range of values from the Reykjanes Peninsula (data from Thirlwall, unpublished); Yellow field from the SISZ central volcanoes (data from Thirlwall, unpublished); Grey field from Snæfellsnes Peninsular (data from Thirlwall, unpublished) and blue field from Kistufell and Þeistareykir (data from Maclennan et al., 2001 and Breddam, 2002).*

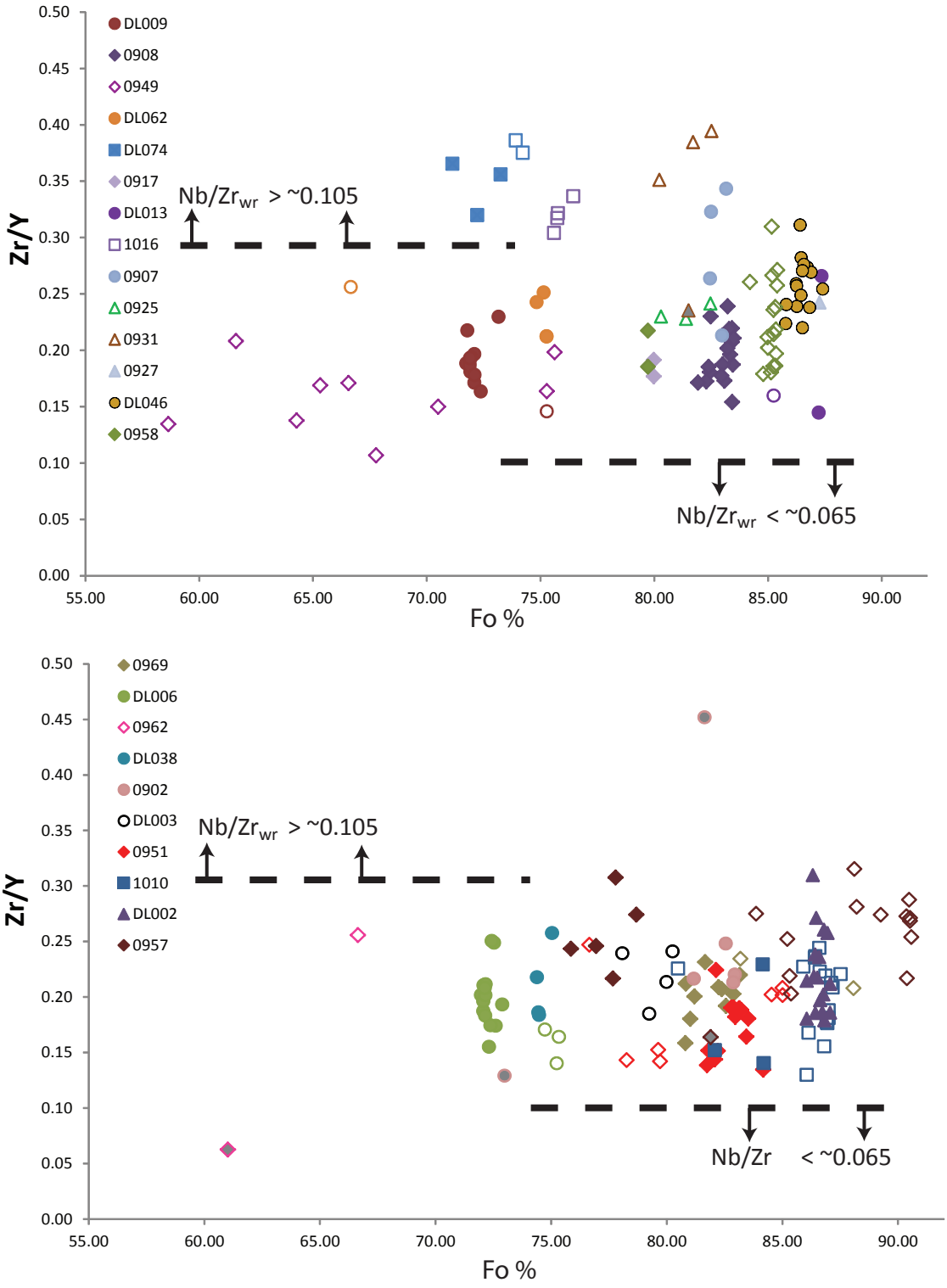

Figure 2.5: *Zr/Y_{ol} vs. Fo% for NRZ lavas. Disequilibrium olivines have open symbols. Olivine populations for a given flow tend to show similar Zr/Y values. Symbols filled in grey highlight olivines with significantly different Zr/Y to the rest of their population suggesting a non-comagmatic origin to these crystals.*

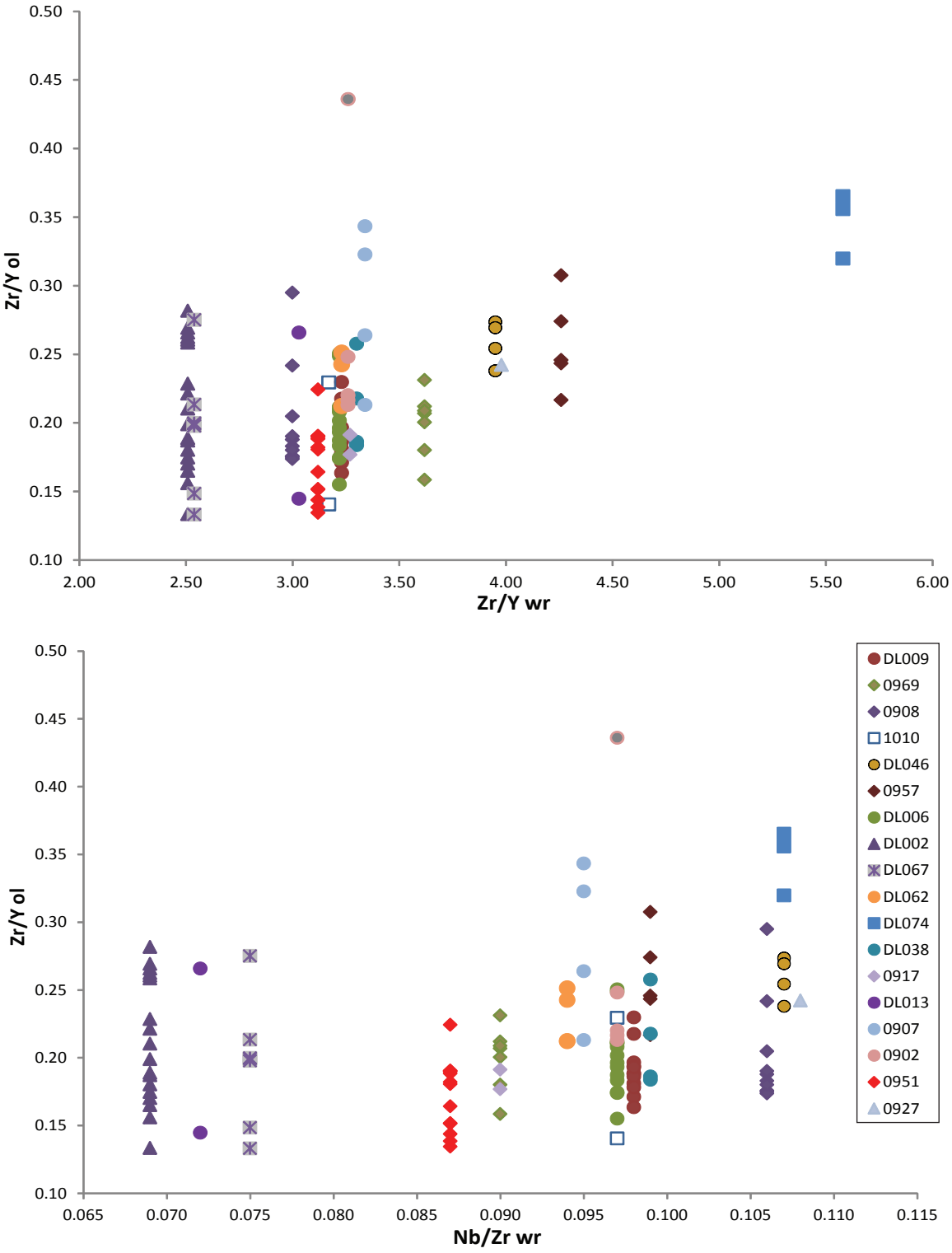

Figure 2.6: *Zr/Y_{ol} vs Z/Y_{wr} and Zr/Y_{ol} vs. Nb/Zr_{wr}. Only equilibrium olivines are plotted. Xenocrysts identified in Figure 2.5 are grey.*

2) Disequilibrium peaks: Some samples show peaks of Fo% higher than equilibrium (e.g. 0958, 1010). This may be a remnant population from a more primitive stage of the host magma (antecrysts) (i.e. Maclennen, 2008) or a population of xenocrysts.

3) No peaks: Basalts, particularly from the inter and intra glacial that have no peak in Fo% and contains a large number of disequilibrium olivines (>40% of the total number of olivines per sample), often from more evolved melts (e.g. 0925, 0951, DL067). This could potentially reflect smaller amounts of crystallisation in these flows combined with mixing or entrainment of crystals from more evolved magmas or slight accumulation of crystals.

2.4.1.2 Minor elements:

Figure 2.4 shows plots of selected minor elements in NRZ olivines. For comparison, data from Snæfellsnes, SISZ central volcanoes and rift zone lavas from the Reykjanes Peninsula, Kistufell and Þeistareykir (where available) have been included on these plots. NRZ samples plot largely within the Reykjanes lava field forming tight sub-parallel trends. This makes it potentially easy to identify non-comagmatic xenocrysts that were incorporated from older magma chamber wallrock or mantle xenocrysts. Studies have suggested that olivine crystallisation may start below the MOHO (e.g. Slater et al., 2001; Maclennan et al., 2001) however CaO values of olivines from this data set does not support either crystallisation in the mantle or the entrainment of mantle xenocrysts (assuming mantle olivine have CaO <0.1 wt. % Simkin and Smith, 1980; Sobolev and Danyushevsky, 1994 cf. >0.25 wt. %, olivines from this study). Despite the large number of disequilibrium olivines in some samples, few crystals lie clearly outside their respective trends. These olivines are best seen in plots of incompatible element ratios such as Zr/Y (Figure 2.5) where fractionation affects are not seen and instead reflect source differences (Figure 2.6). Disequilibrium olivines (open symbols) generally lie in the same range of Zr/Y values as the equilibrium olivines suggesting these might be antecrystal in origin. Only 3 olivines show significantly different Zr/Y values to the rest their population (Symbols filled in grey) implying crystallisation from more enriched/depleted source magmas. The fact few obvious non-comagmatic crystals have been identified in Figure 2.5 would suggest that these crystals have been sporadically entrained from the gabbroic crust into lavas rather than due to the mixing of melts or wholesale crustal contamination, which would generate a trend of increasing or decreasing Zr/Y_{ol} with decreasing Fo%. The correlations present between Zr/Y_{ol}, Zr/Y_{wr} and Nb/Zr_{wr} indicate that variations of Zr/Y_{ol} between flows are related to the extent of enrichment of the host melt (Figure 2.6). Only the equilibrium olivines have been plotted in this figure consequently only one of the non-comagmatic crystals identified above is present.

The relationship seen in Figure 2.6 clearly indicates that this crystal must have derived from a much more enriched melt than its host lava.

Thin sections of the lavas containing these non-comagmatic crystals all contain large megacryts or gabbroic nodules, further indicating that these crystals may have been entrained from the Icelandic crust. Some samples show significant scatter of Zr/Y at similar Fo% (e.g. DL002) making it difficult to confidently identify potential non-comagmatic crystals. It is worth noting that it is possible that crustal xenocrysts could have the same Zr/Y as magmatic olivine, but it is unlikely that such non-comagmatic crystals would have both similar Fo% and Zr/Y, and lie on the same Fo-Ni trend as magmatic olivines. Thin sections may provide clues as to whether some of these crystals were entrain from the crust. In the case of DL002 two populations of crystals are present, a large population which are often associated with large plagioclase glomercrysts and a smaller population in the groundmass. Therefore there is some evidence that some of the scatter could be due to the presences of crustal xenocrysts.

2.4.2 Plagioclase

In assessing plagioclase equilibrium it is important to note that K_D ($Na\text{-}Ca^{plag\text{-}liq}$) values for plagioclases crystals are poorly constrained and water dependant. As a result it is difficult to fully assess the extent of equilibrium in flows due to the large range of K_D values reported in the literature (Breddam, 2002).

Based on phenocrysts from the NRZ Breddam (2002) suggested that K_D may lie between 1.0 and 1.3. In order to assess the reliability of these values a compilation of plagioclase phenocrysts from across Iceland have been added to than those of Breddam (2002) dataset. On a An% vs $Ca\#_{wr}$ (were $Ca\#_{wr} = 100*[Ca/Ca+Na^{2+}]$) graph (Figure 2.8) it appears that most Icelandic plagioclase have higher An% for a given $Ca\#_{wr}$ than defined by Breddam (2002). If a linear regression is fitted to these data then most crystals appear to lie on a K_D of ~0.6. Work carried out by Niu and Batiza (1994) on MORB plagioclase phenocrysts, have suggested that K_D = 0.63-1.11. It should be noted that role of water in the magma may play a part in this large range of values. Feig et al. (2006) have shown that An% of a plagioclase increases significantly if water is present in the crystallising magma, which will lead to a higher K_D value.

The phenocrysts that lie between the 0.6-1.3 K_D line on Figure 2.8 are the most likely to be in equilibrium with their host lavas, however due to the large uncertainties with assessing equilibrium by this method only large deviations can be interpreted as significant.

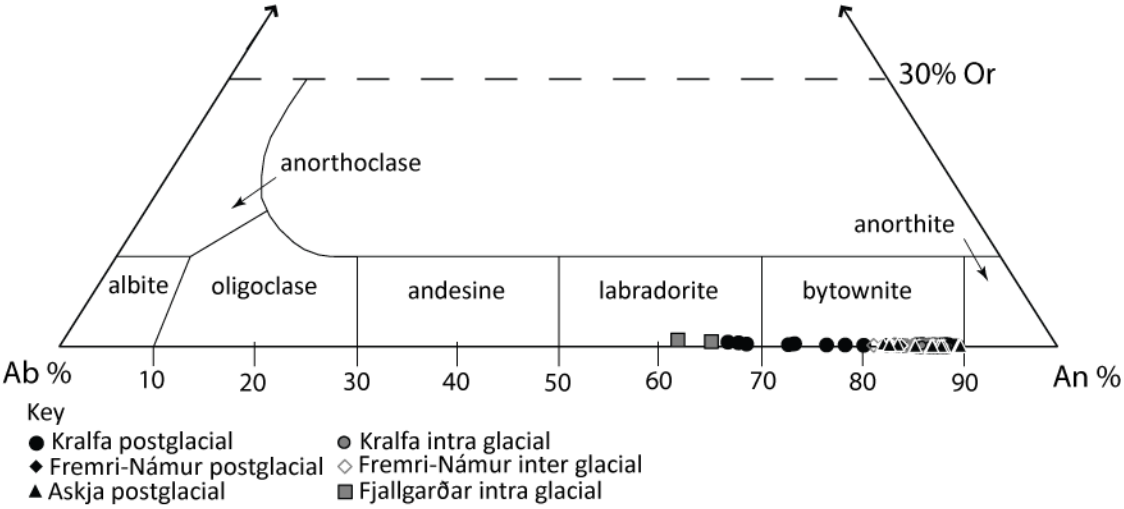

Figure 2.7*: An-Ab-Or triangle plot.*

2.4.2.1 Major and Trace elements

The majority of plagioclase phenocryst lie between 90-70 An% in the bytownite field. Four plagioclase crystals from Krafla and 2 from Fjallgarðar however are labradorites (Figure 2.7). The more evolved lavas generally show a larger range of An% than the more primitive samples and plot generally within the range of An% reported for other rift zone lavas (Figure 2.8b).

Trace element spidergrams (Figure 2.9) show narrow ranges within each rift segment with the exception of Askja. For example JPF0931 shows higher Ba and K than other plagioclase crystals from Askja. Compared to other Icelandic rift zone lavas the NRZ samples have lower trace element concentrations.

All crystals have a sloped REE pattern with very low concentrations of M/HREE and mild LREE enrichment. It is worth noting that often the concentrations are close to the detection limits of the LA-ICP-MS. Selected trace element variations are shown in Figure 2.10 a-c. On the whole phenocrysts from each flow show a relatively small range in trace elements apart from MgO wt. % which shows significant scatter often at a narrow range of An%. DL033 is an exception showing large ranges of concentrations for all trace elements. Figure 2.10d shows a broad positive correlation between the plagioclase VICE/MICE ratio K_2O/TiO_2 vs. Nb/Zr_{wr} indicating that $K_2O/TiO_{2\ plag}$ ratios are related to source enrichment. DL009 appears to show higher $K_2O/TiO_{2\ plag}$ ratios for its Nb/Zr_{wr} possibly suggesting that some of these plagioclase crystals may have derived from a more enriched source implying a possible non-comagmatic origin for these crystals.

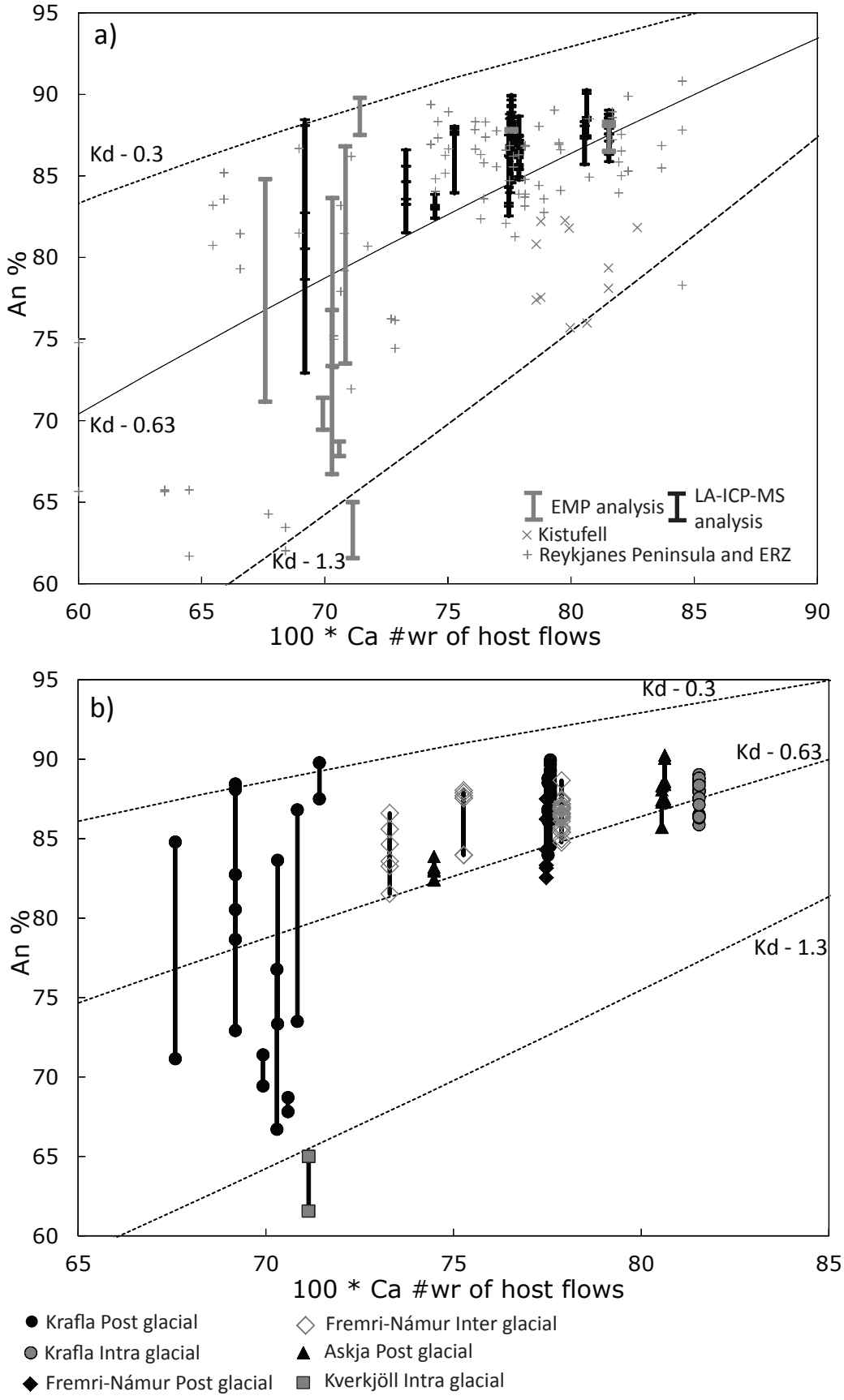

Figure 2.8: a) *100*Ca#wr vs. plagioclase An% from Iceland. Verital bars show the range of An% seen within flows. Kistufell data from Breddam (2002), ERZ data from Manning (2010) and Reykjanes Peninsula from Thirlwall (unpublished).* b) *100* Ca#wr vs. plagioclase An% for flows separated by age.*

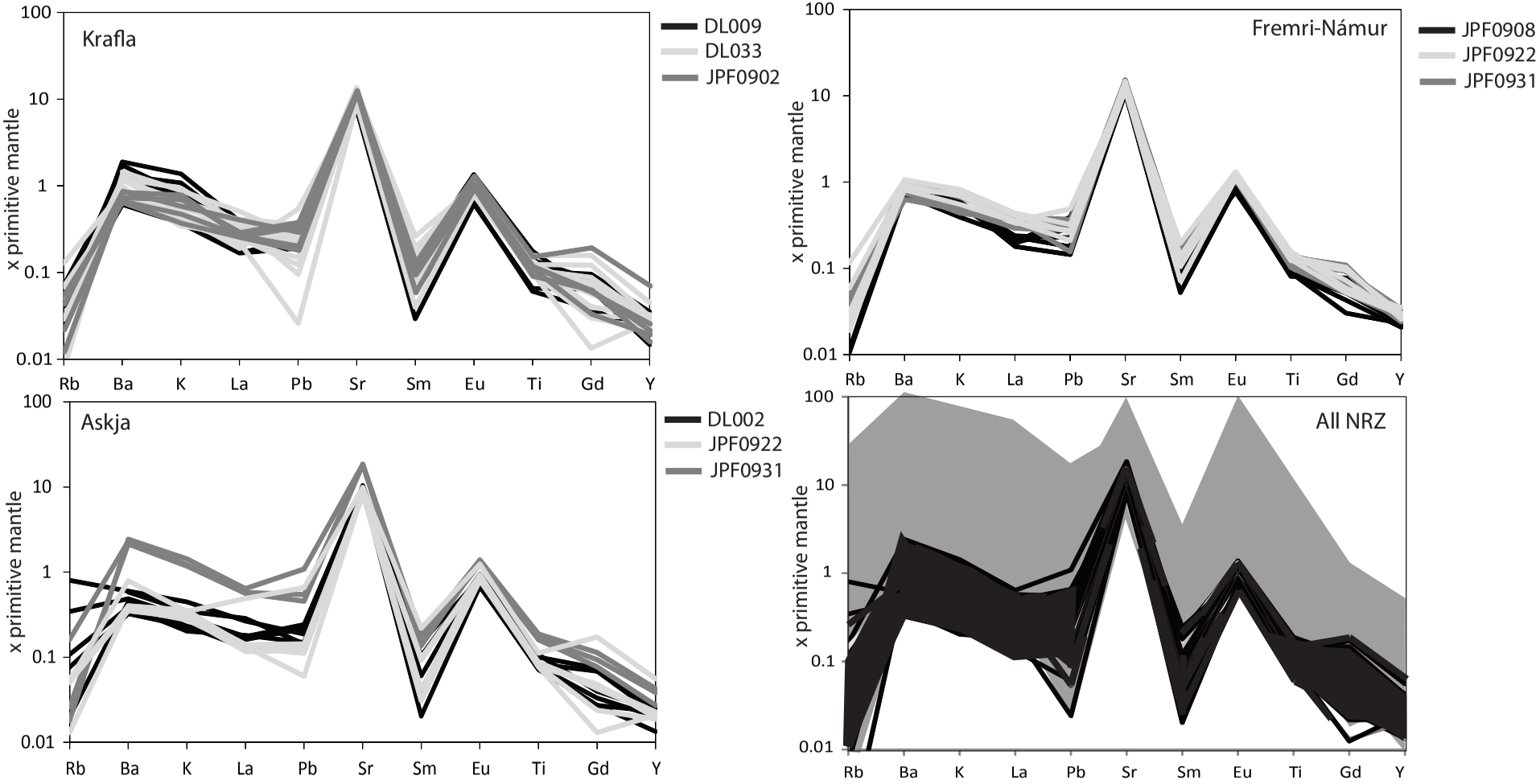

Figure 2.9: *Primitive normalised multi element diagrams of plagioclase crystals normalisation values from Sun McDonough (1989). Grey field in All NRZ diagram shows analyses from other rift zone lava plagioclase (data from Thirlwall, unpublished).*

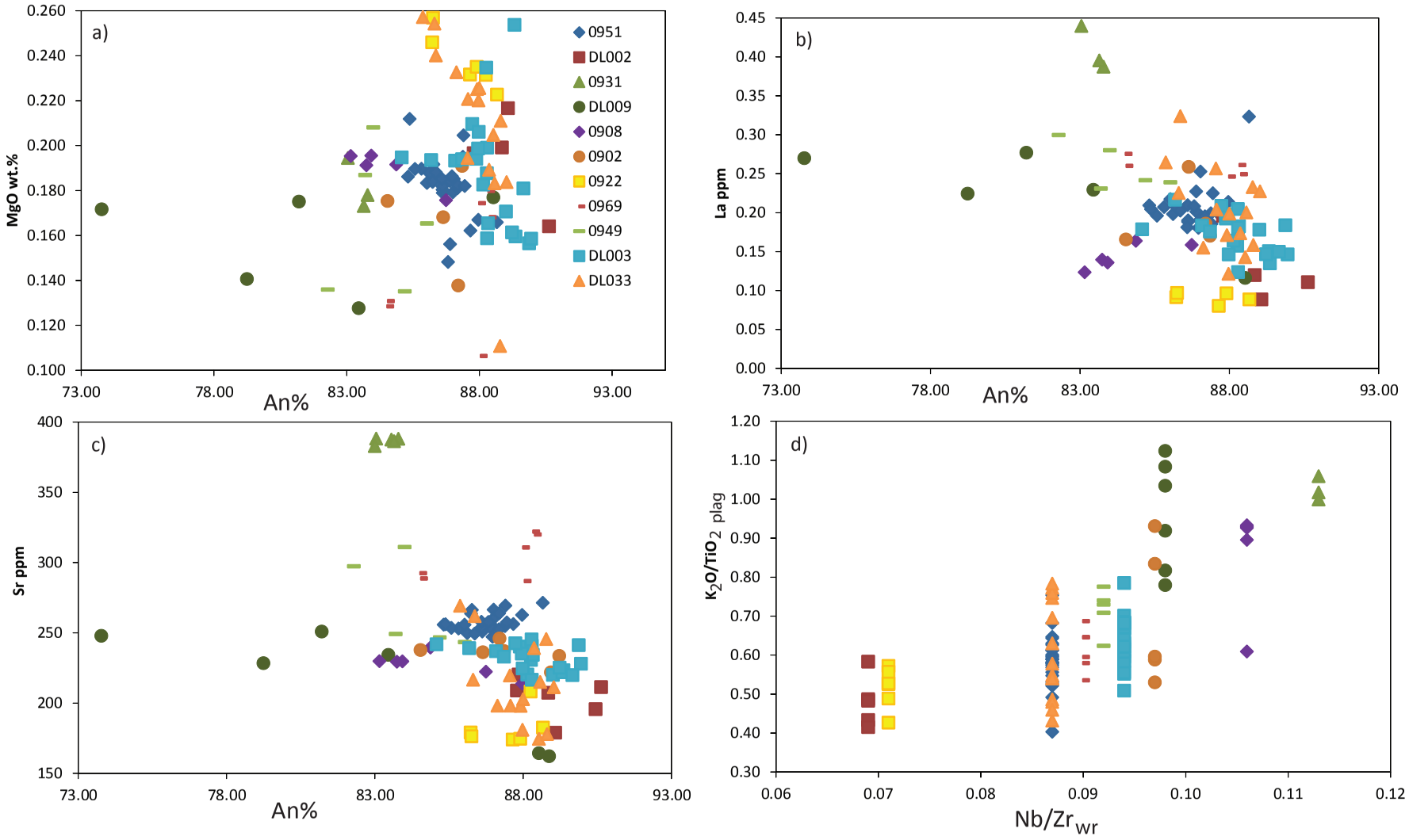

2.10: *Selected trace element variations vs. An% and $K_2O/TiO_{2\ plag}$ vs. Nb/Zr_{wr} for NRZ plagioclase.*

	MgO	TiO_2	Ba	La	K	Sr
x	26.1	41.3	38.2	38	19	26
y	-24.2	-14.2	10.2	-7	-9.8	26.8

Table 2.1: *x and y parameters used to calculate D_i.*

2.4.2.2 Melt Reconstruction

Over the past several decades there has been considerable work on determining mineral-melt partition coefficients (D_i) for plagioclase major and trace elements, were i represents the element in question (e.g. Wood and Blundy, 1991; Tepley et al., 2010). Partition coefficients have been particularly used by studies to attempt to reconstruct the concentration of the melt required to crystallise the plagioclase in question based on this relationship:

(1) $$D_i = \frac{X_i^{plag}}{X_i^{liquid}}$$

Were X_i^{plag} is the concentration of a given element in the plagioclase and X_i^{liquid} is the concentration of a given element in the crystallising melt. Comparing the calculated melt values with the actual concentrations of the host lavas provides an alternative way to crudely assess whether a plagioclase has crystallised in equilibrium with the host lava.

Wood and Blundy (1991) were the first to show that D_i is linearly dependent on An% content for Sr and Ba with the general equation:

(2) $$RT\ln D_i = y - x \cdot X_{An}$$

Where R is the gas constant, 8.314 JK^{-1}; X_{An} is the anorthite mole fraction; T is the temperature in K; x is the slope and y is the intercept. Bindeman et al. (1998), Bédard (2006), Aigner-Torres (2007), Tepley et al. (2010) and many other works have subsequently demonstrated that the same relationship is also present for a wide range of trace and major elements. This therefore provides an opportunity to robustly assess whether the often large ranges of An% observed in NRZ plagioclases are in equilibrium with their host lavas.

Bindeman et al. (2008) found that *T* has a linear dependence on An%:

(3) $$\frac{1}{T} = m\,X_{An} + n$$

Where m = -2.04 x 10^{-4} and n = 7.92 x 10^{-4}. Temperatures calculated by this method were found to agree with temperatures calculated by clinopyroxene thermometry for similar samples from Krafla and Askja (Maclennan, 2001; Kuritani et al., 2011) and were subsequently used in D_i calculations.

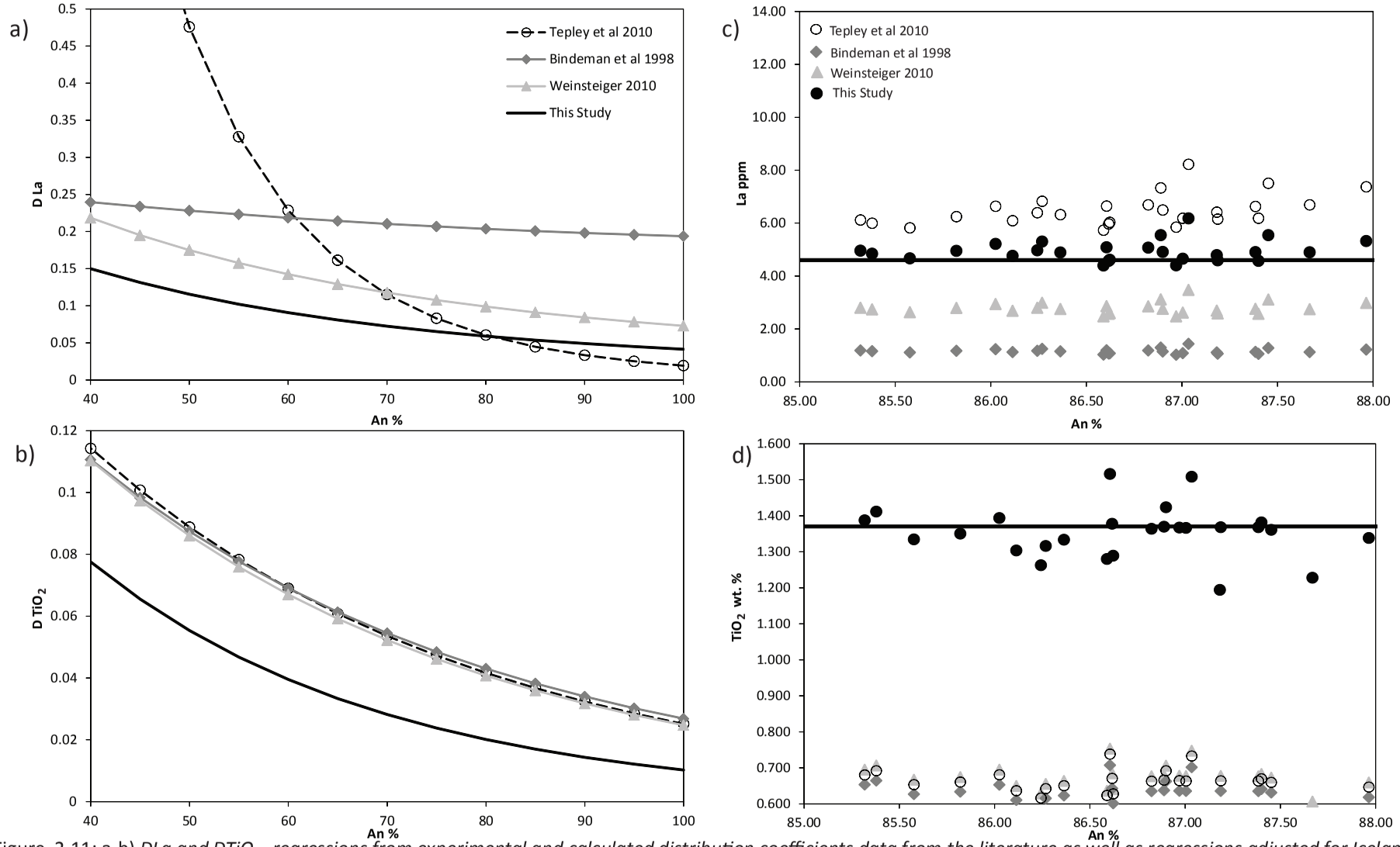

Figure 2.11: a-b) *DLa and DTiO$_2$ regressions from experimental and calculated distribution coefficients data from the literature as well as regressions adjusted for Icelandic populations* c-d) *Equilibrium melt reconstruction for a suite of NRZ phenocrysts using the range of D values from a-b) solid black line shows the whole rock value.*

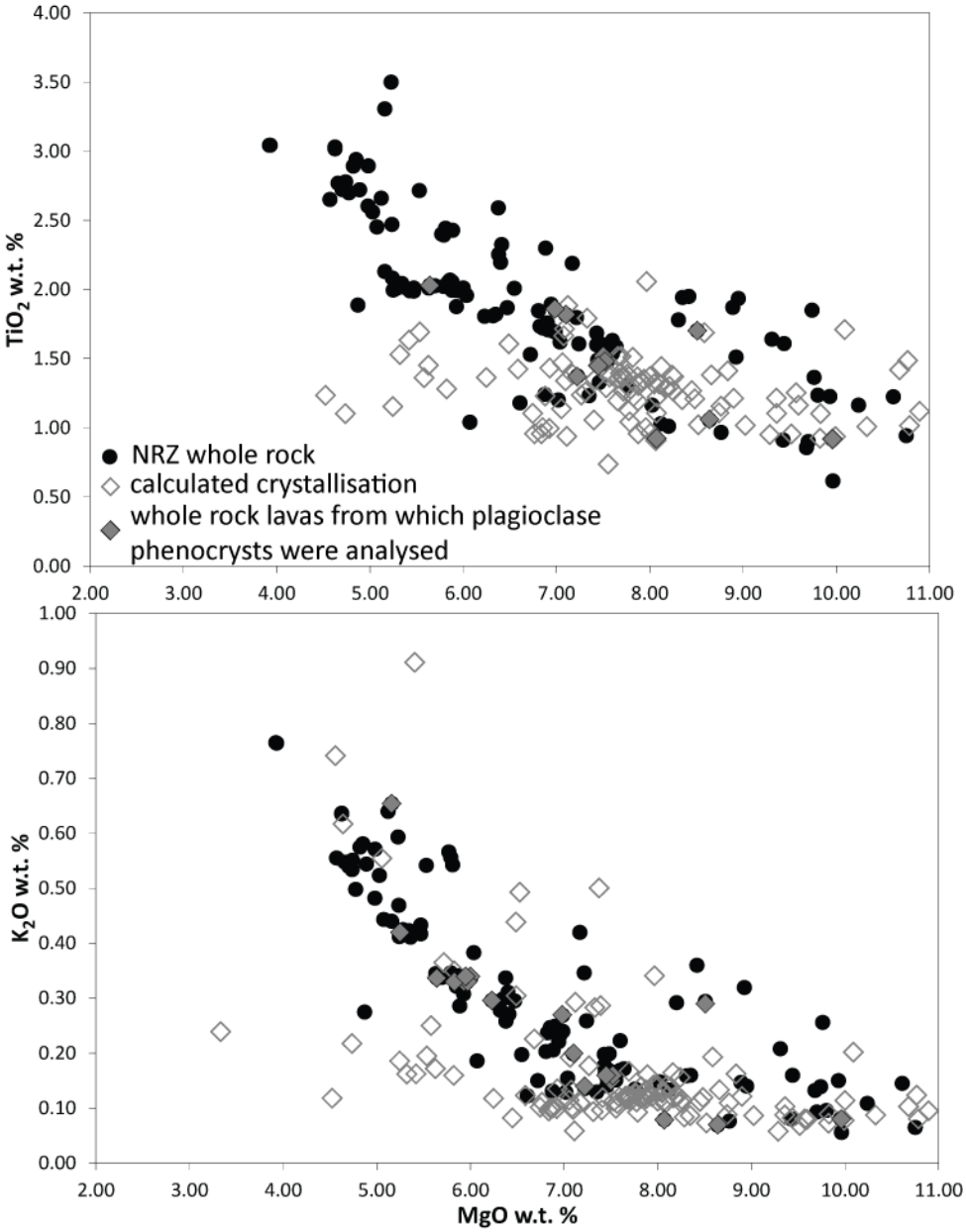

Figure 2.12: *Calculated and measured whole rock MgO vs. TiO_2 and K_2O.*

Depending on the quality and size of the data sets, the *x* and *y* parameters reported from linear regressions using equation (2) vary significantly in the literature resulting in a large range of calculated D_i values (c.f. Bindeman et al., 1998; Weinsteiger, 2010). Consequently, the reported regressions were tested on a number of Icelandic plagioclase crystals that span a range of An% that are thought likely to be in equilibrium with their respective host melts (Crystals from Thirlwall, pers. coms.). These crystals were from relatively aphyric samples were glass analyses agree closely to bulk rock values. The Wood and Blundy (1991) regressions for Sr and Ba generally gave D_i (and therefore predicted melt concentrations) that are in agreement with the host melts however most other elements gave D_i values which are too high, resulting

in significantly low melt concentrations (Figure 2.11). The regressions were consequently adjusted so that the correct calculated melt values for these equilibrium crystals were returned and that sensible values were yielded at low An % (<40%). Figure 2.11 illustrates the range of *D* values from the literature and subsequent concentrations calculated from these values. Table 2.1 shows the *x* and *y* parameters for the regressions used in this study.

Due to the very large scatter in the experimental and calculated data sets a regression has been more difficult to define when considering D_{MgO} values. This is in part due to the strong partitioning of MgO in the host melt into other crystal phases such as olivine and clinopyroxene which will lead to an apparent increase in plagioclase D_{MgO} independent of An% (Weinsteiger, 2010; Miller et al., 2006), resulting in lower calculated MgO values. Figure 2.12 shows calculated MgO wt. % vs. calculated TiO_2 and K_2O. On the whole the calculated melt concentrations lie within the typical range of whole rock values seen for the NRZ and show correlations consistent with fractionation trends. A small number of samples however show much lower MgO for their calculated incompatible element concentrations. These values are likely to have been underestimated, reflecting the issue in calculated accurate D_{MgO} values as highlighted above. Despite this, calculated MgO concentrations still have some use. For instance Figure 2.13 illustrates that populations of high An% plagioclase crystals that are found in relatively evolved basalts from Krafla must have crystallised in more primitive melts than the host lava as the actual MgO concentrations can only be higher than these calculated values.

On the whole, calculated trace element concentrations form positive correlations often lying on trends with the whole rock values (Figure 2.14). This implies that these crystals may have been derived from melts that are either more fractionated or more primitive than the host lava. Phenocrysts of lavas that show populations of more primitive crystals perhaps reflect remnants of the early crystallising history of the host magma whilst the populations of more evolved crystals might be xenocrystal in origin. Plagioclase crystals that show calculated concentrations the same as the whole rock values are uncommon. JPF0922 (and potentially JPF0908) is the only example of a sample containing a homogenous population of plagioclase that shows the same calculated values at their host lava. The case for JPF0908 is not as clear as the whole rock value appears to be slightly higher than the calculated values. This perhaps indicates the presence of plagioclase that derived from a more depleted magma.

Weinsteiger (2010) highlighted that diffusion re-equilibration was an important factor to consider in assessing the validity of such calculated concentrations in plagioclase. Based on

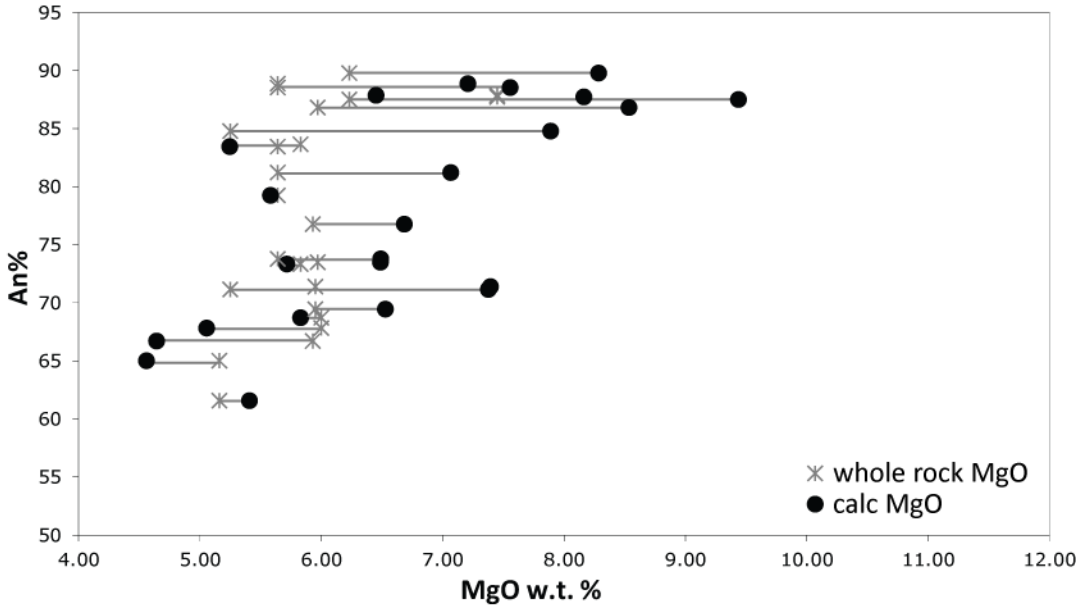

Figure 2.13: *An% vs. whole rock MgO wt. % and predicted equilibrium MgO wt. % from populations of plagioclase phenocrysts from Krafla. Horizontal grey line matched whole rock and calculated MgO. The high An% plagioclase appears to have crystallised in more primitive lavas then the host rock.*

work by Cottrell et al. (2002), Weinsteiger (2010) showed that re-equilibration would be seen more strongly in some element than others; in particular Mg, Sr and Ba are thought to diffuse much more rapidly than more incompatible elements such as Ti or Fe. In the case of Figure 2.14 re-equilibration would result in homogenous calculated Ba values whilst still showing variation in TiO_2 and La. The positive trends seen, then, in this data set (with the possible exception of JPF0908 and JPF0922) suggests that these crystals have not experienced diffusive re-equilibration and that their trace elements concentrations are likely to have remained unchanged since their initial period of crystallisation.

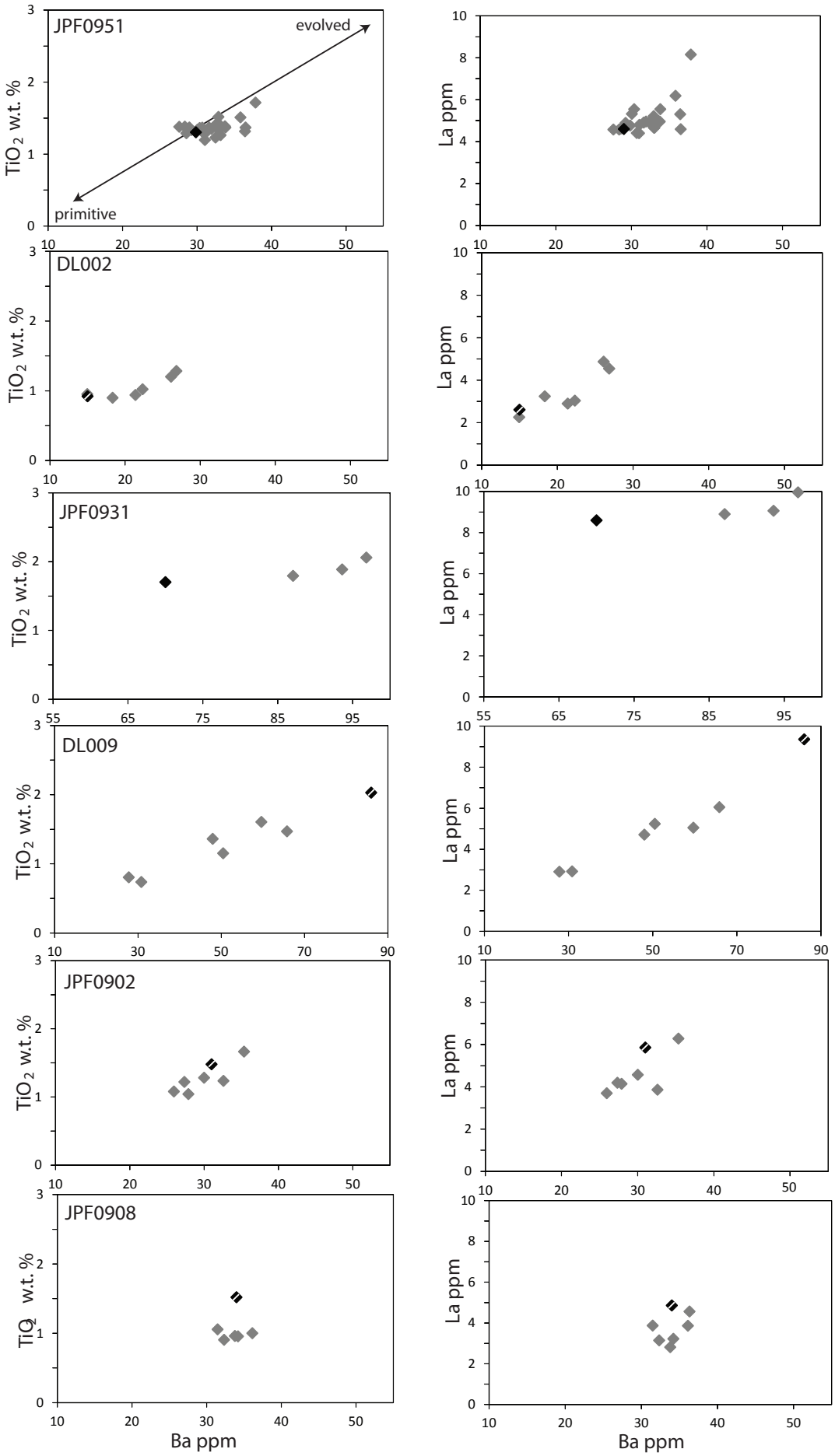

Figure 2.14: *TiO_2 wt. % and La ppm vs Ba ppm grey symbols are calculated crystallisation concentrations. Black symbols are whole rock host lava values. White line thought whole rock symbol denotes concentrations determined by ID.*

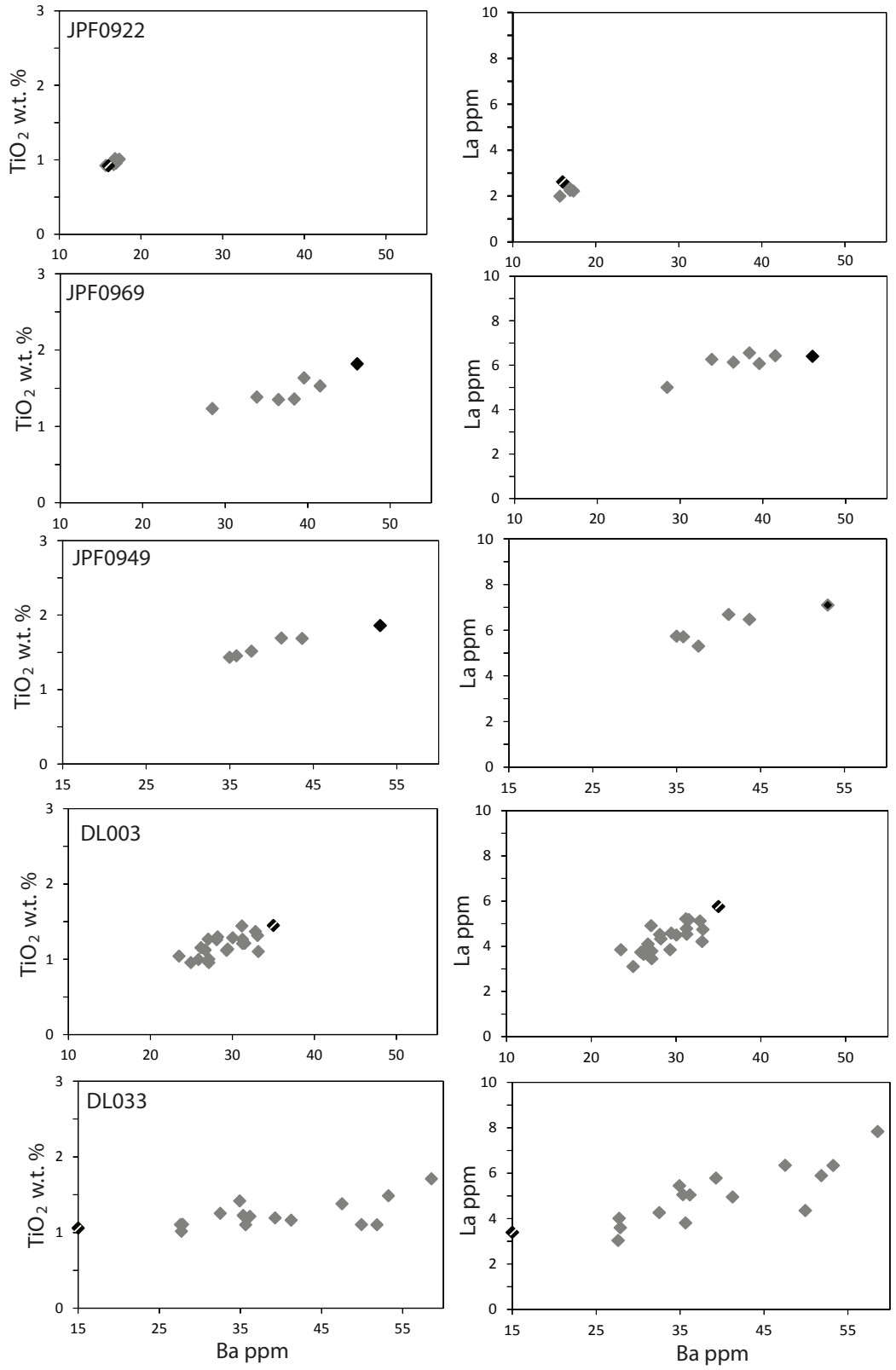

Figure 2.14 *cont...*

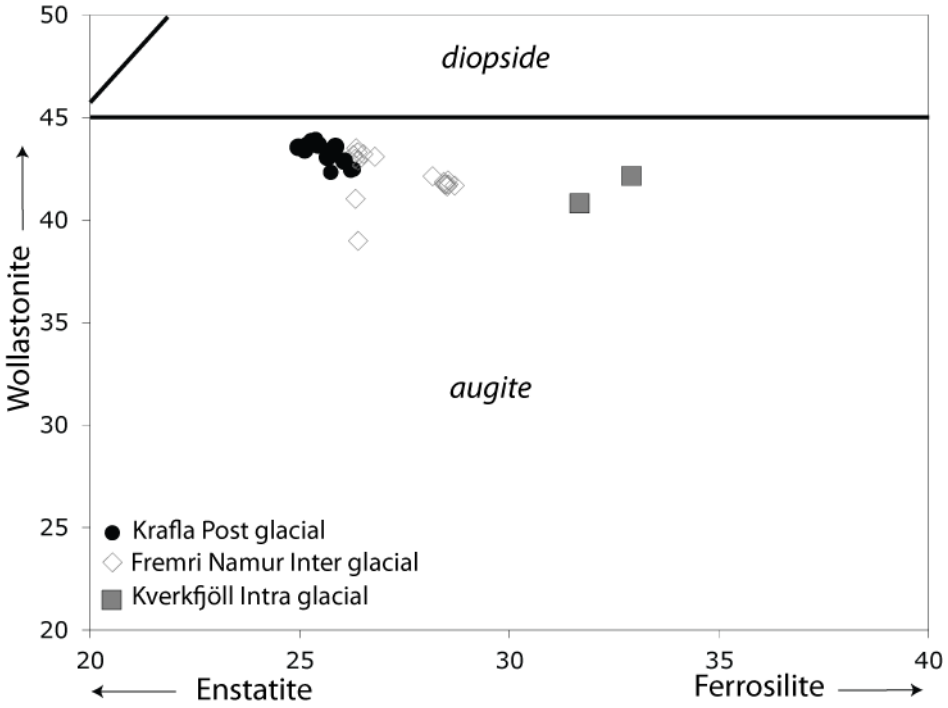

Figure 2.15: *Clinopyroxene quadrilateral diagram.*

2.4.3 Clinopyroxene

2.4.3.1 Major elements.

Overall relatively few clinopyroxene have been analysed for this study. Crystals were selected from lavas that show large ranges in olivine Fo%. All clinopyroxenes analysed plot in the Augite field within the pyroxene classification quadrilateral (Figure 2.15). Clinopyroxenes were judged to be in equilibrium using the following equation; (K_D (Fe-Mg)$^{cpx\text{-}liq}$ = [Fe^{2+}/Mg]^{cpx}/[Fe^{2+}/Mg]^{liq}) using a K_D value of 0.275 ± 0.067 as suggested by Putirka (1996). Overall the clinopyroxenes lie largely in error of equilibrium and show smaller ranges in Mg# than the olivines from their respective flows (Figure 2.16). DL003 and JPF0902 are exceptions, the majority of clinopyroxenes in these lavas lie to higher Mg# then expected. O'Neill and Jenner (2012) have recently proposed that magma replenishment may play a more important role in magmatic systems then previously recognised. The presence of more primitive clinopyroxenes in these lava flows potentially reflects the influx of more primitive primary melts into already fractionated melts.

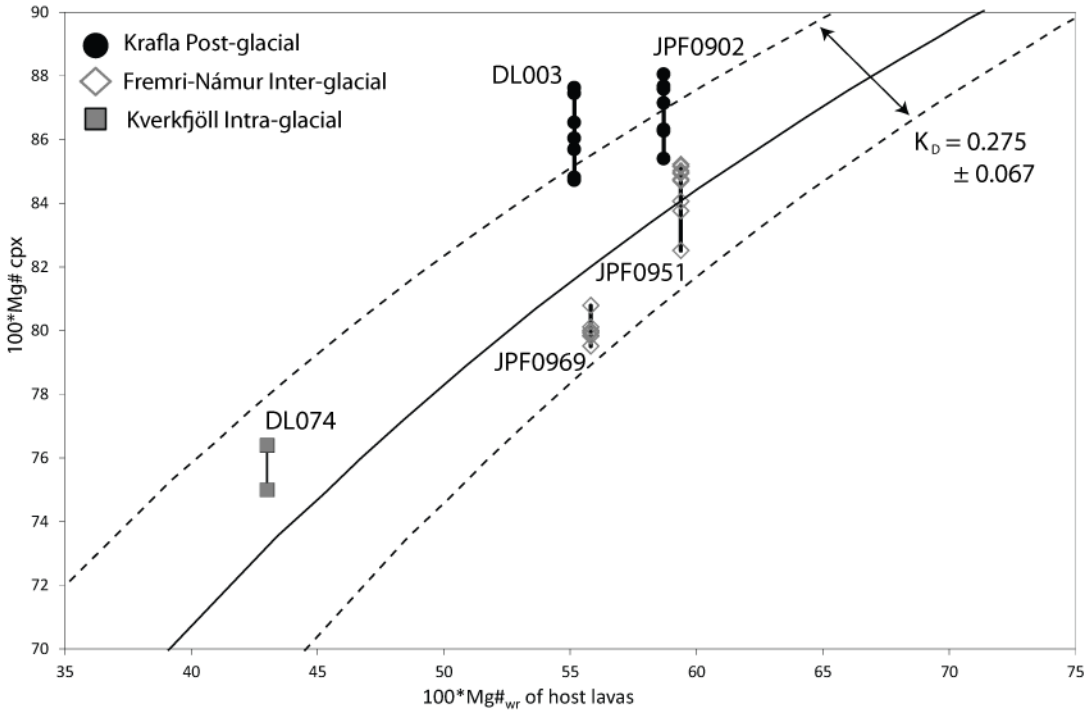

Figure 2.16: *Plot of 100*Mg# cpx vs. 100*Mg# wr of host lavas. The area between dashed lines represent calculated equilibrium using a K_D value of 0.275 ± 0.067 as suggested by Putirka (1996).*

2.4.3.2 Trace elements:

Limited trace element variability is present within each population. In general negative correlations between Mg# and trace element concentrations are present, with the exceptions of Ni and Cr (Figure 2.17).

All clinopyroxenes show concave down REE profiles, with all populations showing LREE and HREE depletion relative to Dy-Gd. All crystals also show negative Sr and Zr anomalies. Patterns in Figure 2.18 are shaded according to Mg# of the crystal, generally concentrations increase with decreasing Mg# due to fractionation however one relatively primitive crystal from JPF0969 show much high concentrations then the rest of its population, this clinopyroxene may be xenocrystal in origin. Incompatible element ratios are able to remove the effects of fractional crystallisation and show little variation within and between lava flows (Figure 2.19).

2.4.3.3 Melt Reconstruction:

Equilibrium melt reconstructions were also calculated for clinopyroxene crystals using equation (1). The partition coefficients needed in this equation was calculated using the method of Wood and Blundy (1997). The crystal-melt barometer and thermometer of Putirka et al. (1996) was used to calculate the pressure and temperature of crystallisation needed in these calculations. These parameters as well as the tetrahedral aluminium content (Al^{IV}) of

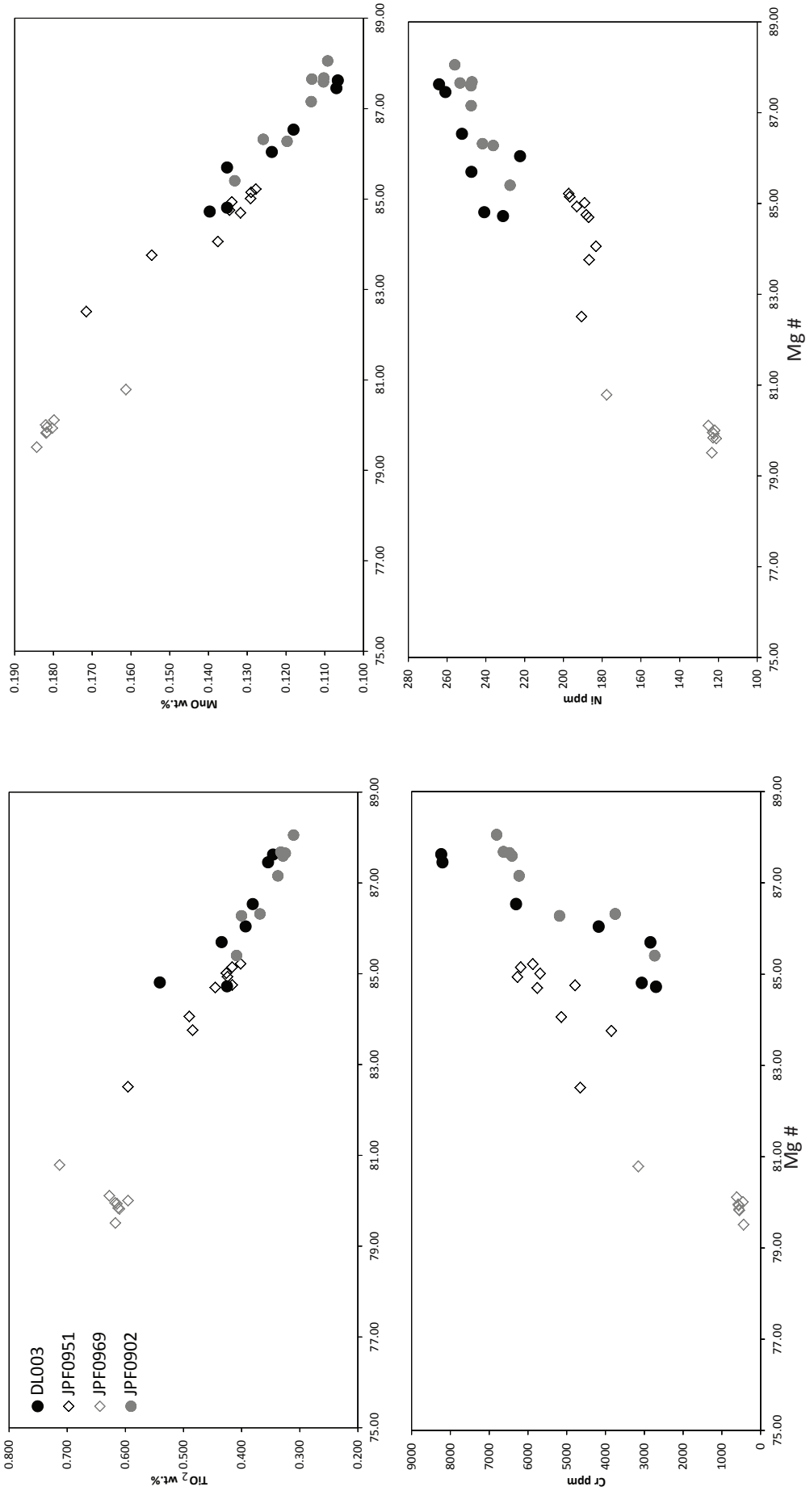

2.17: *Selected trace element variations vs. Mg#*

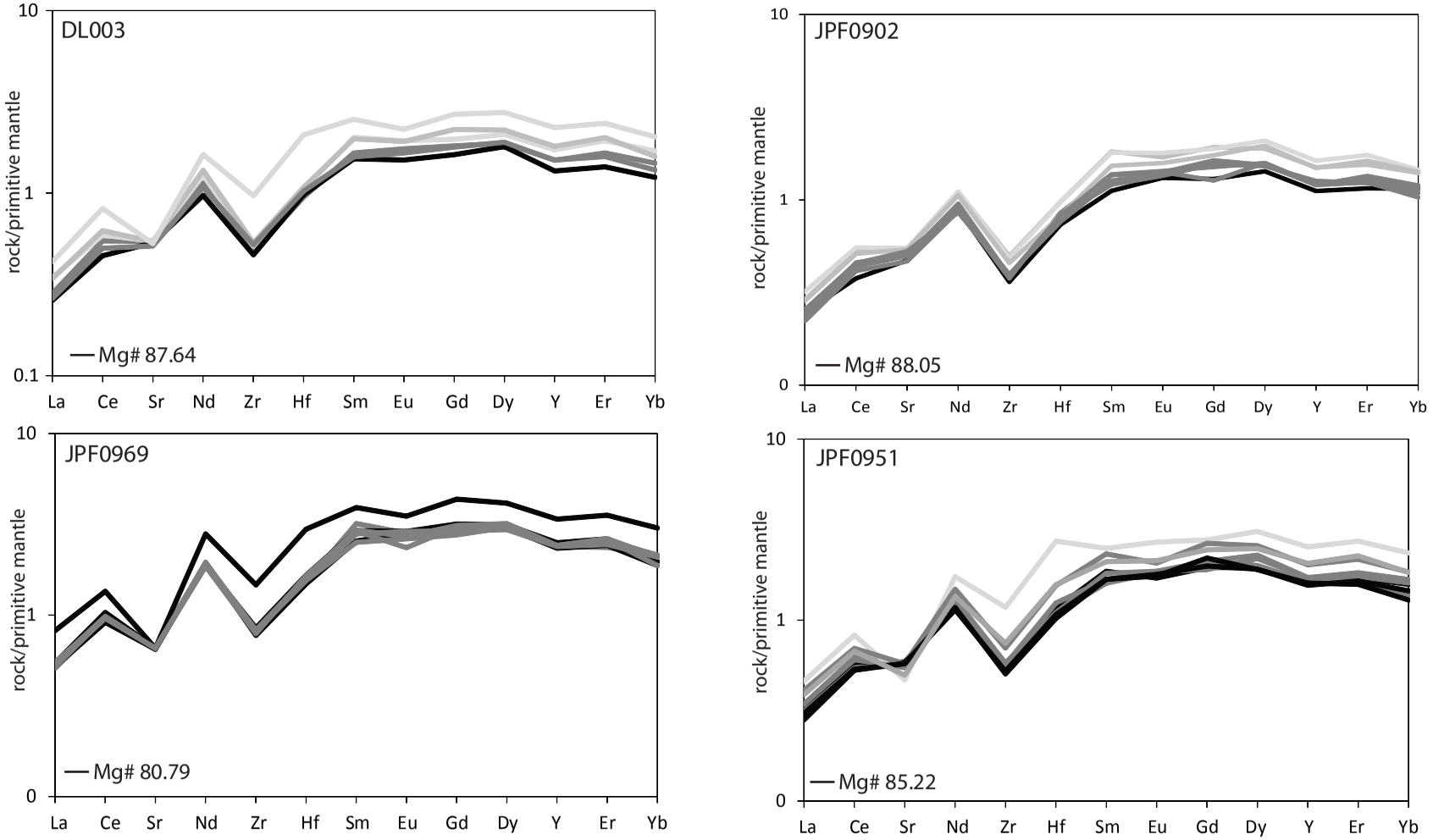

Figure 2.18: *Primitive normalised multi element diagrams of clinopyroxene crystals normalisation values from Sun McDonough (1989). Crystals are shaded by Mg#. Black shows the most primitive crystal present in the population.*

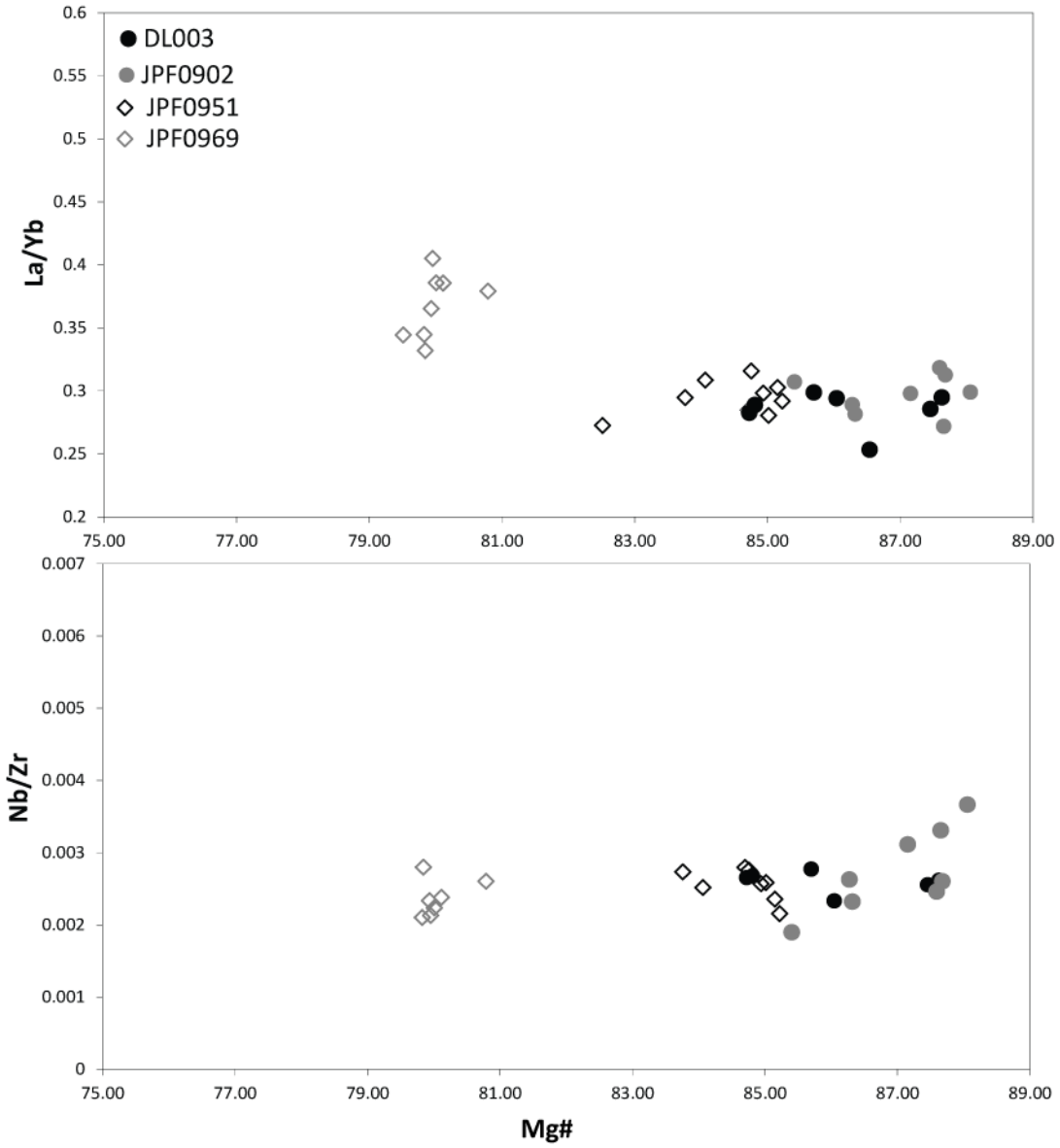

Figure 2.19: *La/Yb and Nb/Zr vs. Mg#$_{cpx}$*

clinopyroxene have been noted to influence partition coefficients calculated (Francis and Minarik, 2008). In an assessment of the Wood and Blundy (1997) method Winpenny and Maclennan (2011) found that these factors did not significantly change the calculated *D* values. Varying the pressure from 5 to 1 kbar at 1260 °C changed the calculated D_{Yb}/D_{Ce} from 3.20 ± 0.2 to 3.26 ± 0.2, whilst varying the temperature from 1210 °C to 1310 °C at 8 kbar caused this value to change from 3.39 ± 0.2 to 3.09 ± 0.18 (Winpenny and Maclennan, 2011). This has enabled *D* values to be calculated from clinopyroxenes that are not in equilibrium with the host basalt.

Whole rock REE ID analysis are only available for two of the lavas from which clinopyroxenes were extracted, thus only comparison with Ce and Y have been made as both these elements

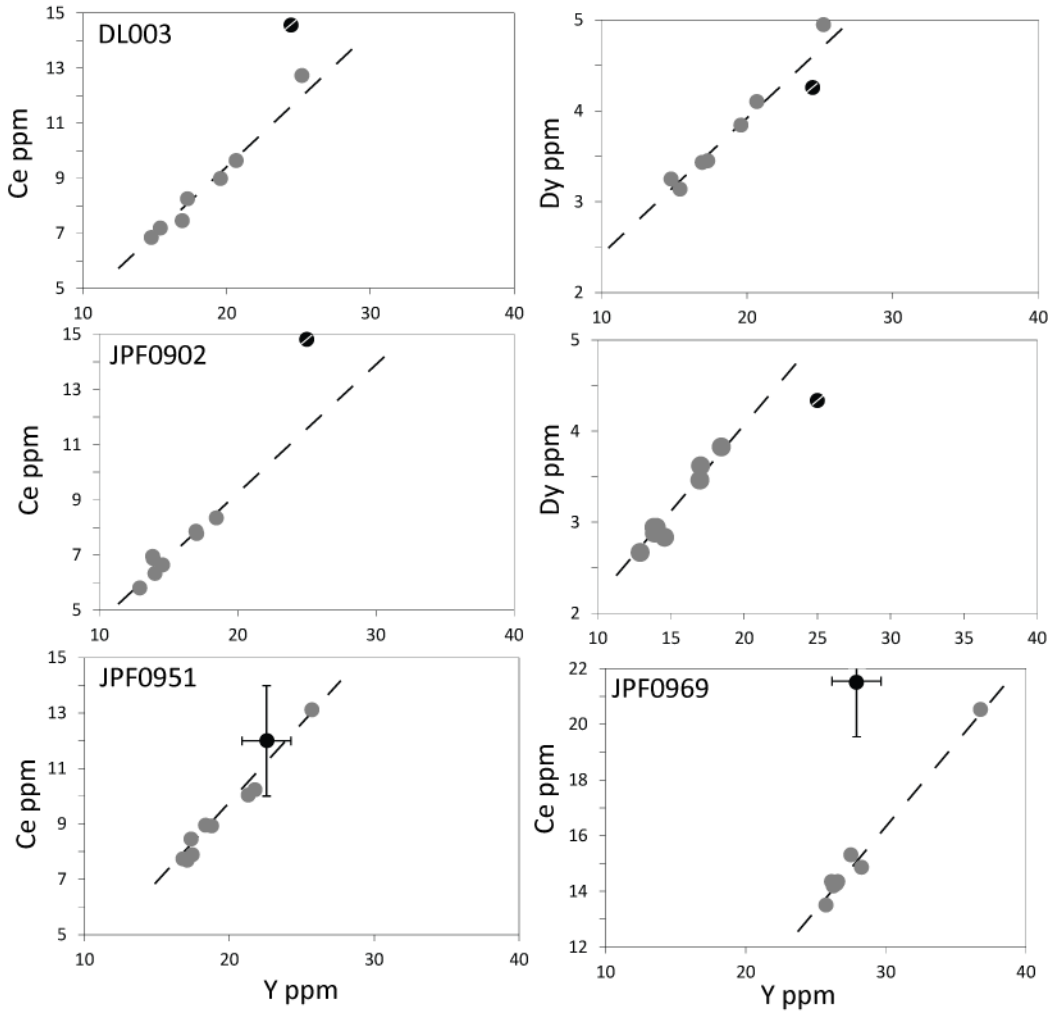

Figure 2.20: *Ce ppm vs. Y ppm and Dy ppm vs. Y ppm grey symbols are calculated crystallisation concentrations whilst black symbols are whole rock host lava values. White line thought whole rock symbol denotes concentrations determined by ID. XRF Whole rock errors are shown for JPF0951 and JPF0969.*

can be reasonably determined by XRF. Like the plagioclase melt reconstructions the clinopyroxene concentration form positive trends (figure 2.20), however the whole rock values, with the exception of JPF0951 do not lie along the same trends. This could indicate that these crystals are not remnants of the early crystallising history of these magmas. It is worth noting that all these lavas show optical evidence of gabbroic nodules in various states of disaggregation. It is likely then that these crystals may have derived from such nodules and did not crystallise from there host lavas.

2.5. Major Element Chemistry

2.5.1 General Comments

Major element chemistry was determined by XRF and together with the mineral chemistry provides the best method in order to assess the extent of shallow level processes such as fractional crystallisation and accumulation. Due to the basaltic nature of the majority of samples MgO has been used as a fractionation index. All major element data from this study has been presented in Appendix 4.

2.5.2 Major element variations

Figure 2.21 shows all major oxides plotted against MgO. The main samples which regularly form outliers on these plots are:

1) DL034; an intra-glacial vesicular, aphyric, glassy sample from Krafla.
2) JPF0936; a post-glacial sample which shows large amounts of plagioclase and is likely to be an accumulate as well as containing a population of glass shards.

The main observations are summarised as follows:

SiO_2 vs. MgO*:* The majority of samples lie within a narrow range of SiO_2 concentrations (47-52 wt. %) which shows a small general increase with falling MgO. All rift segments show similar trends with the exception of a large number of samples from Heiðarsporður and DL034. Heiðarsporður lavas have steeper MgO- SiO_2 trends than other rift segments and overall, with the exception of two samples which are thought to have mixed with typical Krafla tholeiites (Johnanson, 2005), have higher SiO_2 concentrations for a given MgO. DL034 also shows much higher SiO_2 for a given MgO.

Al_2O_3 vs. MgO*:* A general decrease of Al_2O_3 from about 16 to 12 wt. % is observed with decreasing MgO. This correlation is most likely to reflect the crystallisation of plagioclase. Some samples, in particular from Kverkfjöll show scatter to higher Al_2O_3 for a given MgO. The most extreme example of this is JPF0936 which has 19.24 wt. % Al_2O_3. This scatter mostly likely reflects the accumulation of plagioclase. The majority of Heiðarsporður lavas show a very different trend to the rest of NRZ samples; Al_2O_3 concentrations do not vary significantly with MgO, even in the most evolved samples, remaining constant at ~15 wt. %. The two samples thought to be a mix as noted above lie within the main array.

***Fe_2O_3 vs. MgO**:* With the exception of Heiðarsporður lavas define a trend of increasing Fe_2O_3 concentrations with decreasing MgO. Heiðarsporður, like Al_2O_3, remains largely constant at around ~12 wt. %. All samples including those from Heiðarsporður decrease in concentration from ~4 wt. % MgO probably reflecting the crystallisation of FeTi oxides. The same samples that show scatter to higher Al_2O_3 also show scatter to lower Fe_2O_3 reflecting plagioclase accumulation.

***CaO vs. MgO**:* Above 8 wt. % MgO all samples shows little variation in CaO. Below 8 wt. % MgO, CaO concentrations decrease significantly. This is likely to reflect clinopyroxene fractionation. As with to Al_2O_3 some samples show higher CaO for a given MgO again reflecting accumulation of plagioclase.

***Na_2O vs. MgO**:* In all samples Na_2O increases linearly with decreasing MgO behaving like a moderately incompatible element. Both DL034 and JPF0936 show lower Na_2O concentration with respect to the main array for their given MgO contents.

***K_2O vs. MgO**:* K_2O seems to remain constant >8 wt. % MgO, but increases rapidly at lower MgO from ~0.07-3 wt. % K_2O. This change can be explained by the absence of any phase which removes a significant amount of K_2O from the melt. Askja basalts show the highest K_2O concentrations at MgO >8 wt. %. Like Na_2O both DL034 and JPF0936 show lower K_2O concentrations with respect to the main array for their MgO.

***TiO_2 vs. MgO**:* TiO_2 -relationship with MgO is similar to that of Fe_2O_3. There is an overall trend of increasing TiO_2 with decreasing MgO. Like Fe_2O_3 Heiðarsporður lavas do not vary in TiO_2 until ~4 wt. % MgO when concentrations decrease probably reflecting FeTi oxides crystallising. There is much more scatter in TiO_2 than is for Fe_2O_3 in particular for lavas >8 wt. % MgO.

***MnO vs. MgO**:* Like TiO_2, MnO shows a similar trend to Fe_2O_3 with concentrations peaking at ~4 wt. % MgO. Mn can act as a substitute for Fe^{2+} so the decrease in concentration after 4 wt. % MgO is likely to be the result of FeTi oxides crystallising. Unlike TiO_2 however lavas show a much tighter array > 8 wt. % MgO.

***P_2O_5 vs. MgO**:* P_2O_5 also shows similar relationships to that of Fe_2O_3 with peaks in concentrations at ~4 wt% MgO. However, unlike Fe_2O_3 lavas from Heiðarsporður slowly increase in P_2O_5 with decreasing MgO until ~4 wt% MgO.

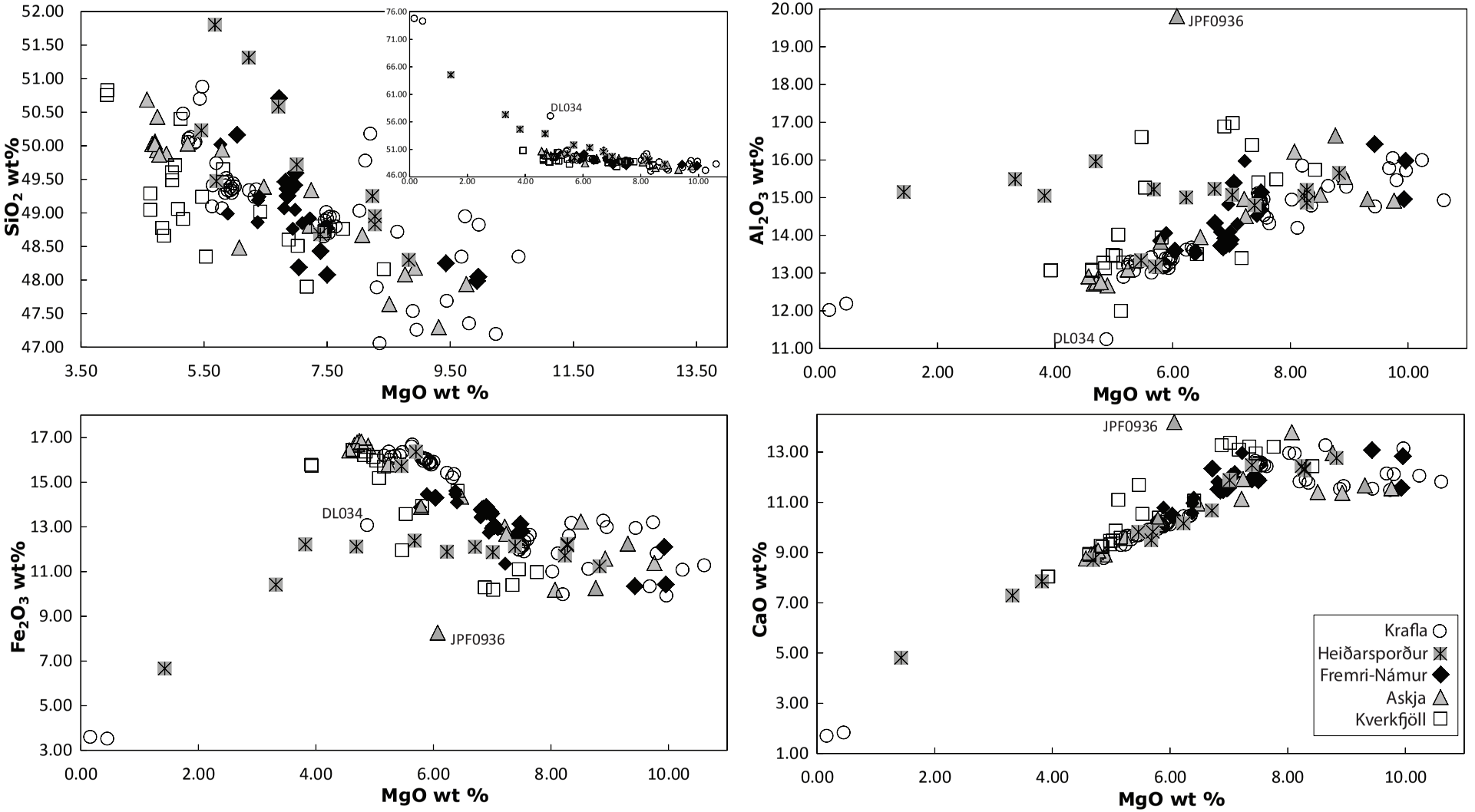

Figure 2.21: *Major element concentrations plotted against MgO wt.%.*

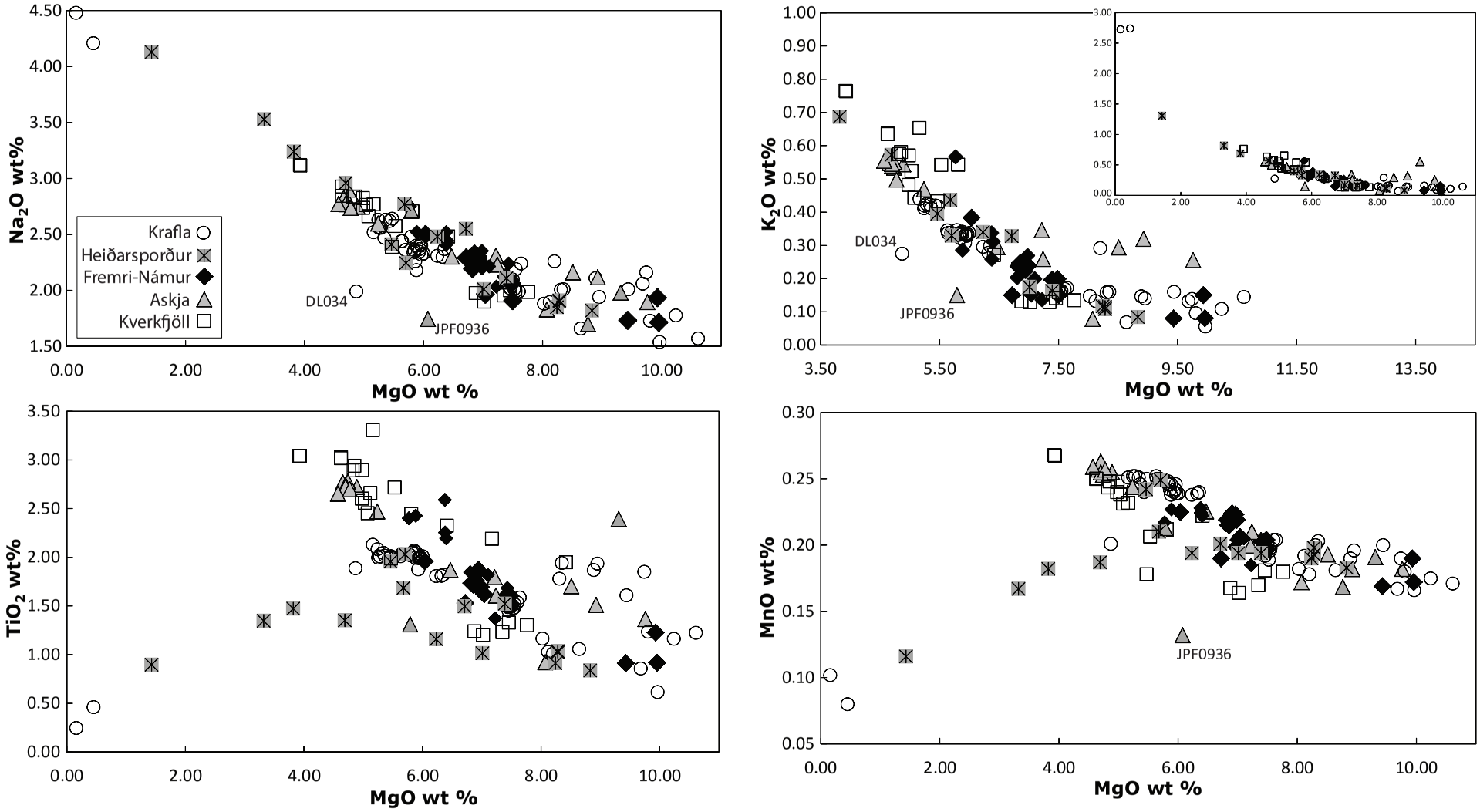

Figure 2.21: *Cont...*

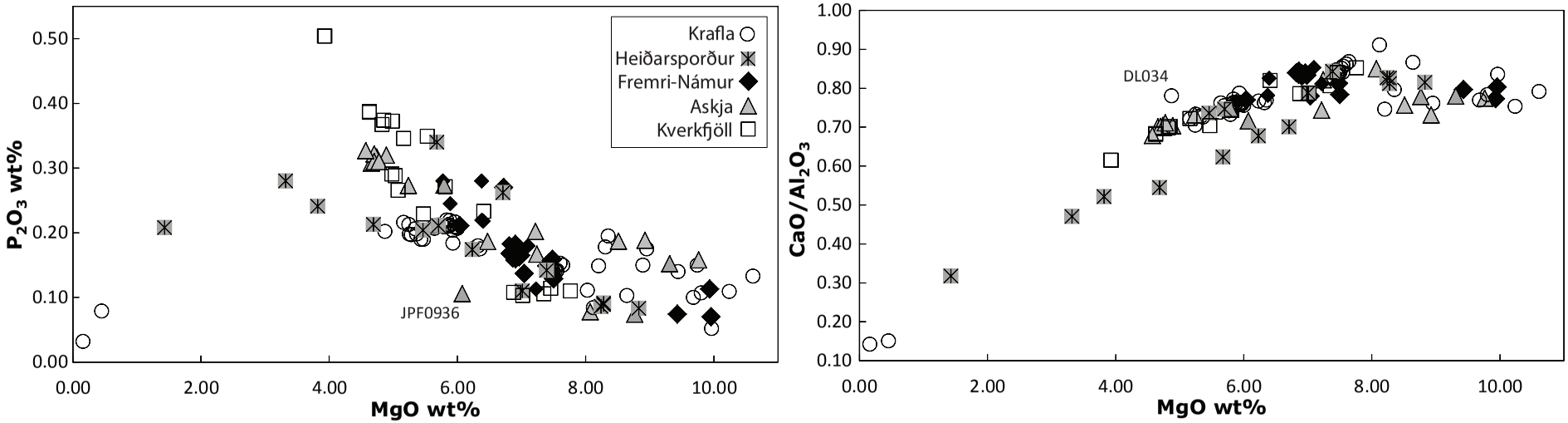

Figure 2.21 *Cont...*

***CaO/A_2O_3 vs. MgO**:* Following a similar trend as CaO and A_2O_3 all samples show little variation of CaO/A_2O_3 ratios above 8 wt% MgO followed by a tight trend of decreasing ratios with decreasing MgO consistent with clinopyroxene fractionation. Due to the differing A_2O_3 contents of Heiðarsporður lavas, these samples form a sub parallel trend to the other rift segments.

2.6. Trace Element Chemistry

2.6.1 General Comments

Trace element variation diagrams like the major elements are plotted against MgO (Figure 2.22). The majority of trace element concentrations presented in this figure were determined by XRF except for Pb, Hf, Yb, U and Th which were determined by Isotope dilution (ID). Trace elements determined by XRF are presented in Appendix 4. Due to the importance of relative trace element concentrations in assessing melting relationships and source differences data from the neighbouring Þeistareykir rift segment has been included in some of the plots (from Stracke, 2003).

The most incompatible trace elements play the most important role in assessing these relationships therefore data from other Icelandic rift zones have also been added (from Gee, 1998; Manning, 2010; Thirlwall, unpublished). Furthermore, to fully assess these relationships all samples have been grouped by age as well as by rift segment.

2.6.2 Trace element variation diagrams

Transition metals + Ga

***Ni and Cr vs. MgO**:* Good correlations are observed in all rift segments, both Ni and Cr decreases with decreasing MgO. This variation is principally controlled by olivine and clinopyroxene crystallisation. Overall Ni forms tighter correlations then Cr.

***V vs. MgO**:* Most NRZ samples show an increase in V with decreasing MgO up to ~5 wt. %, this is due to V behaving like a moderately incomplete element in early fractionating phases. Heiðarsporður like most major element trends show little variation in V. Below 5 wt. % MgO all rift segments shows decreasing V reflecting FeTi oxides crystallisation. Some samples lie to lower V at a given MgO, JPF00936 being the most extreme example, this is likely to reflect plagioclases accumulation as suggested by other major element plots.

***Sc vs. MgO**:* The most primitive samples (>8 wt. %) show lower Sc concentrations then reported for Þeistareykir. Most rift segments then show an increase of Sc with decreasing MgO reflecting the incompatibility of Sc in plagioclase and olivine fractionation. After 7 wt. % MgO concentrations are at first buffered and then decrease due to Sc being very compatible in clinopyroxene. The majority of samples from Heiðarsporður show no increase in Sc >7 wt. % MgO and slowly decreases with decreasing MgO < 7 wt. % MgO. On the whole it would appear that inter and intra glacial lavas show lower Sc for a given MgO then post glacial lavas.

***Cu vs. MgO**:* The relationship with Cu broadly mirrors that of V with a distinct 'Λ' shape. There is however considerable scatter seen within the suite. Unlike V, however, Samples from Heiðarsporður show similar concentration to the rest of the NRZ samples with decreasing MgO.

***Zn vs. MgO**:* Overall concentrations increase with decreasing MgO. At higher MgO (>8 wt. % MgO) there is considerable scatter. The most evolved samples show a large variation in concentrations; the intra-glacial rhyolite from Krafla lies to low Zn (46 ppm) whilst the inter-glacial samples from Krafla shows lie to high Zn (134 ppm). Heiðarsporður lavas also show a general increase in concentrations however <5 wt. % MgO concentrations level out of at ~100 ppm.

***Ga vs. MgO**:* A broad negative correlation with MgO is seen however there is considerable scatter in the data compared to Zn, in particular at high MgO a number of samples show very high Ga. Like Zn there is considerable variation in concentrations in the most evolved samples and Heiðarsporður lavas seems to level of < 5 wt. % MgO. On the whole inter glacial samples show marginally higher concentrations the post and intra glacial lavas.

Large Ion Lithophile Elements (LILE)

***Sr vs. MgO**:* Above 8 wt. % MgO there is an overall increase of Sr concentrations with decreasing MgO. Below 8 wt. % MgO Sr levels out as plagioclase dominates that fractionating assemblage. At a given MgO different rift segments have very different Sr concentrations. Krafla and Fremri-Námur have the lowest concentrations ~150 ppm, Askja forms an array ~175 ppm whilst Kverkfjöll forms an array ~225 ppm. Accumulation of plagioclase will lead to samples having high Sr concentrations; this is the case for the one Askja sample seen within the Kverkfjöll array (JPF0936) and the several Fremri-Námur samples seen within the Askja array. On the whole samples from Heiðarsporður slowly increase in Sr as MgO decreases.

Rb and Ba vs. MgO*:* Rb and Ba show good correlations, increasing strongly with decreasing MgO. Above 7 wt. % MgO the post-glacial lavas from Askja have generally higher Rb and Ba then all the other rift segments. DL034 in both plots shows much lower concentrations with respect to the main array.

Pb ID vs. MgO*:* There is a dramatically reduced data set for Pb ID concentrations however when plotted against MgO a general increase in Pb is observed with decreasing MgO. In the most primitive samples, Pb is generally higher then Þeistareykir for a given MgO but within the range reported for the WRZ. Like Rb and Ba DL034 shows lower Pb with respect to the main array.

High Field Strength Elements (HFSE)

Zr, Nb and Hf ID vs. MgO*:* All these elements increase in concentrations with decreasing MgO. Above 7 wt. % MgO there is a large amount of scatter On the whole for a given MgO concentrations of these elements are higher than Þeistareykir but as above within the range of values reported for the WRZ. In addition DL034 shows lower concentrations with respect to the main array in all plots.

Rare Earth Elements (REE), Y and Actinides (Th and U)

The majority of REEs Y, U and Th are highly incompatible and show sharp increases of concentration with decreasing MgO. All samples fall within the range of values seen at other rift zones. The LREE shows a larger spread of concentrations above 8 wt. % MgO between Þeistareykir and WRZ were as the HREE and Y concentrations from all rift zones tend to plot in a similar field. Furthermore samples identified as plagioclase accumulative tend to show the lowest Y concentrations. U and Th show concentrations between Þeistareykir and the WRZ above 8 wt. % MgO. As above in all these plots DL034 shows much lower concentrations with respect to the main array.

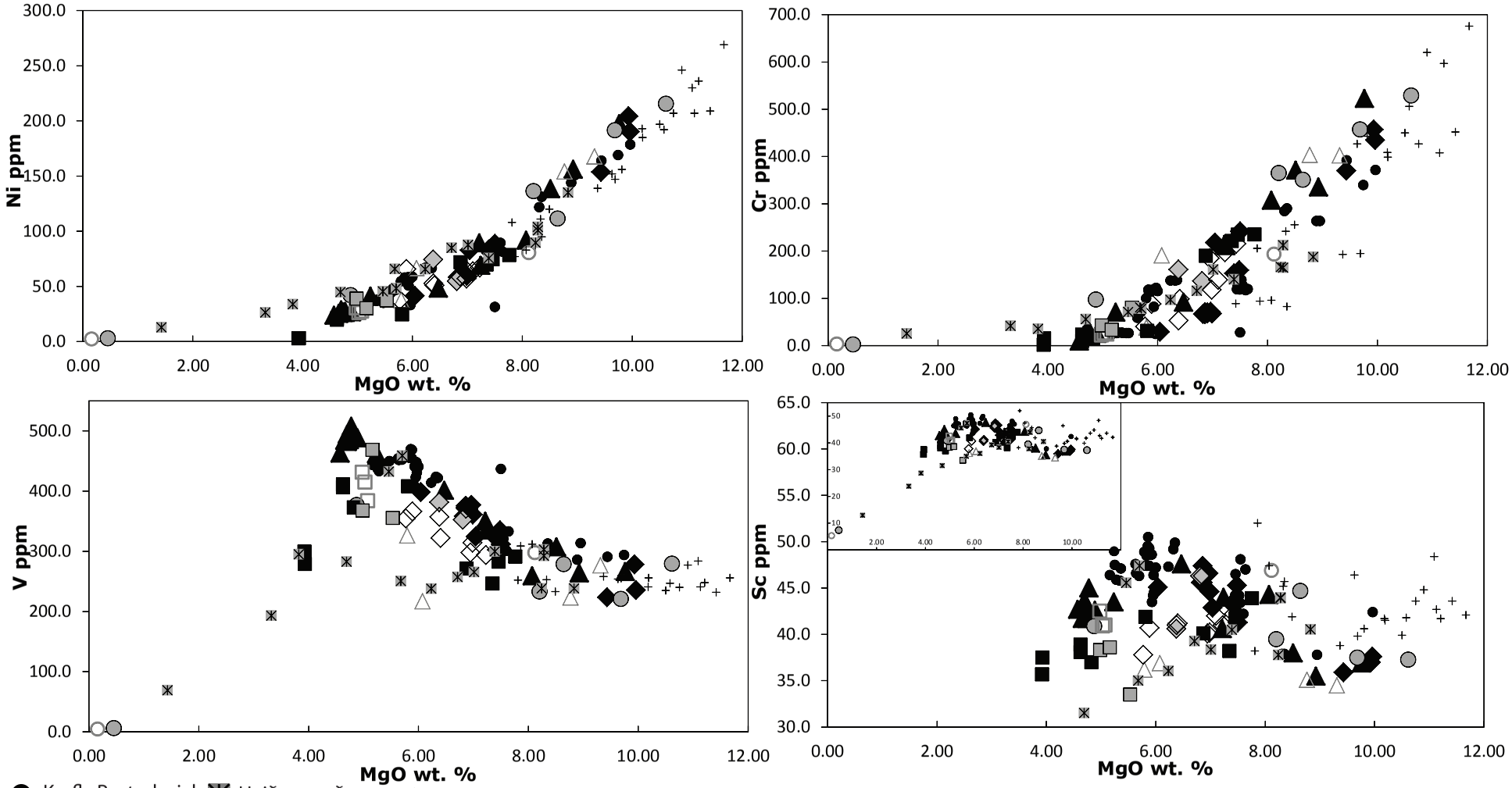

Figure 2.22: *Selected trace element concentrations versus MgO wt.%*

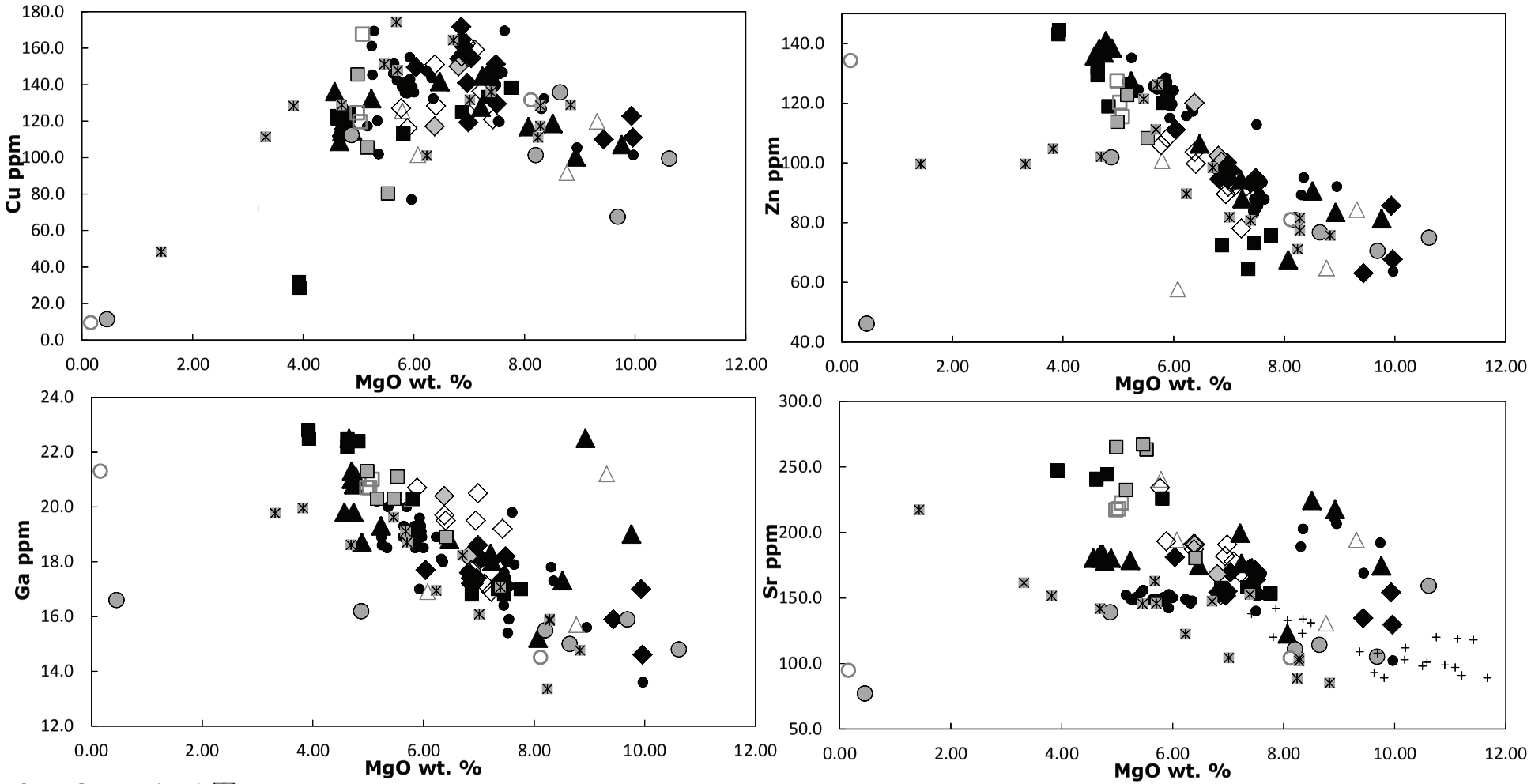

Figure 2.22 *Cont...*

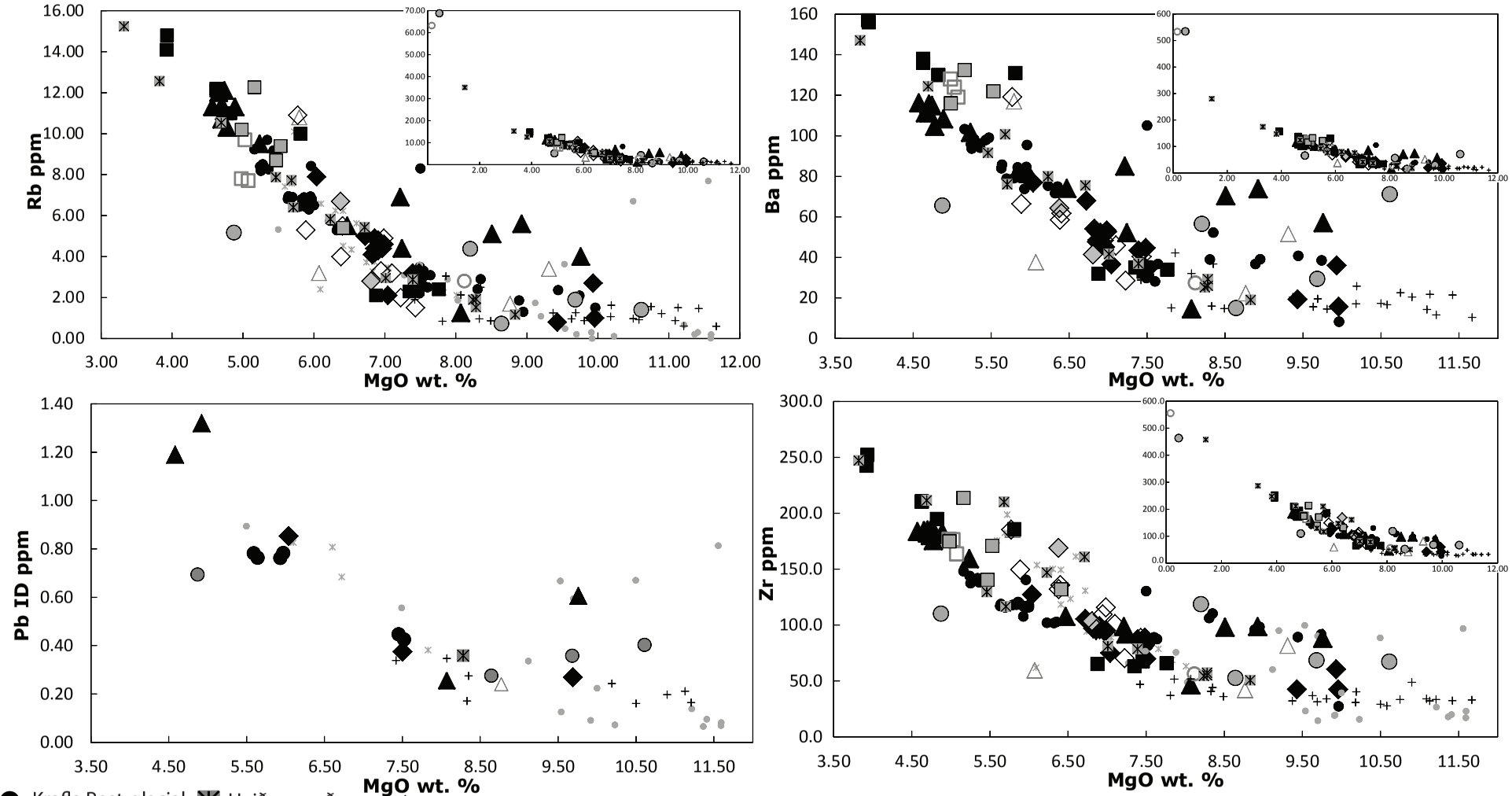

Figure 2.22 *cont...*

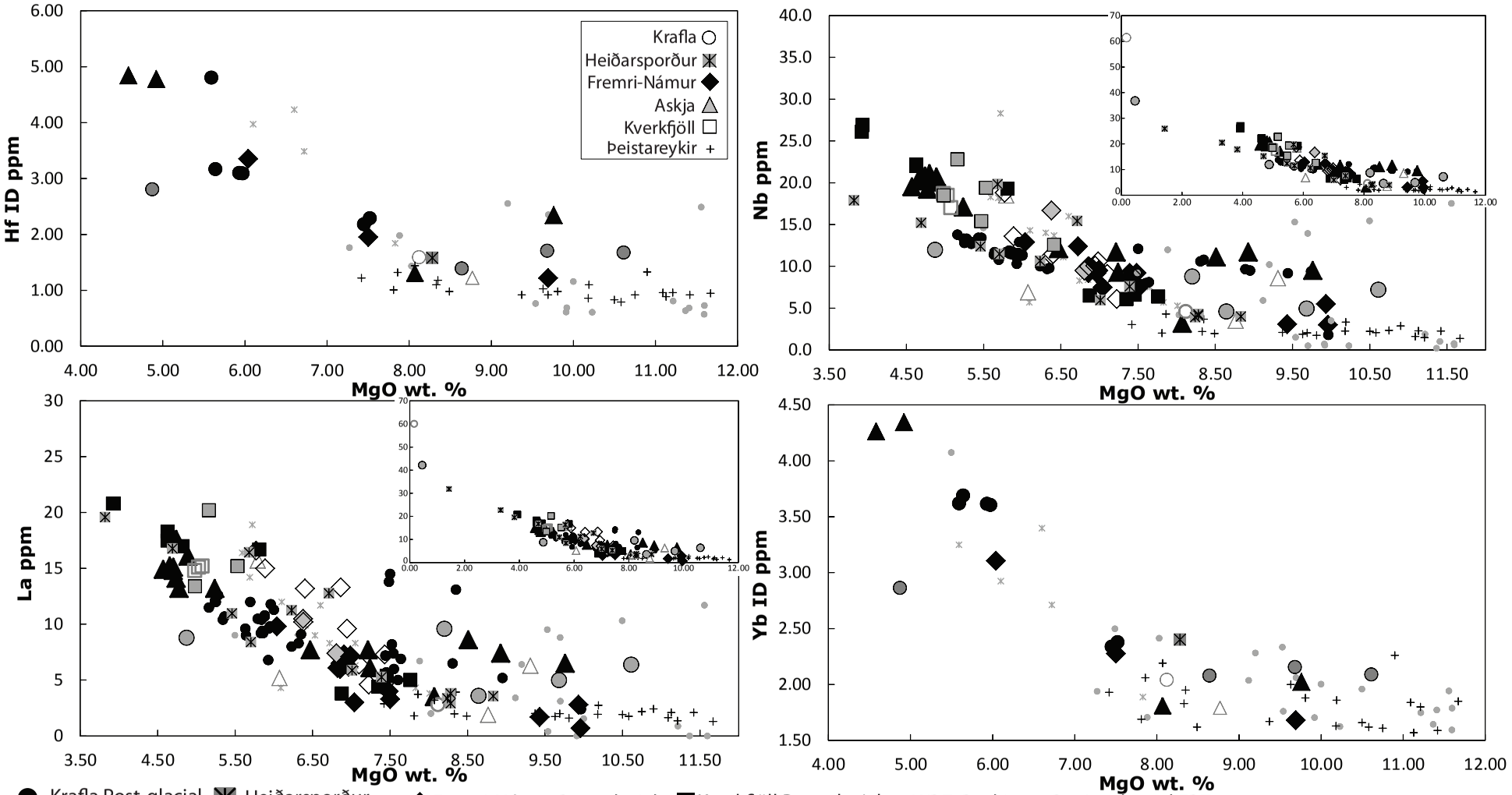

Figure 2.22 *Cont...*

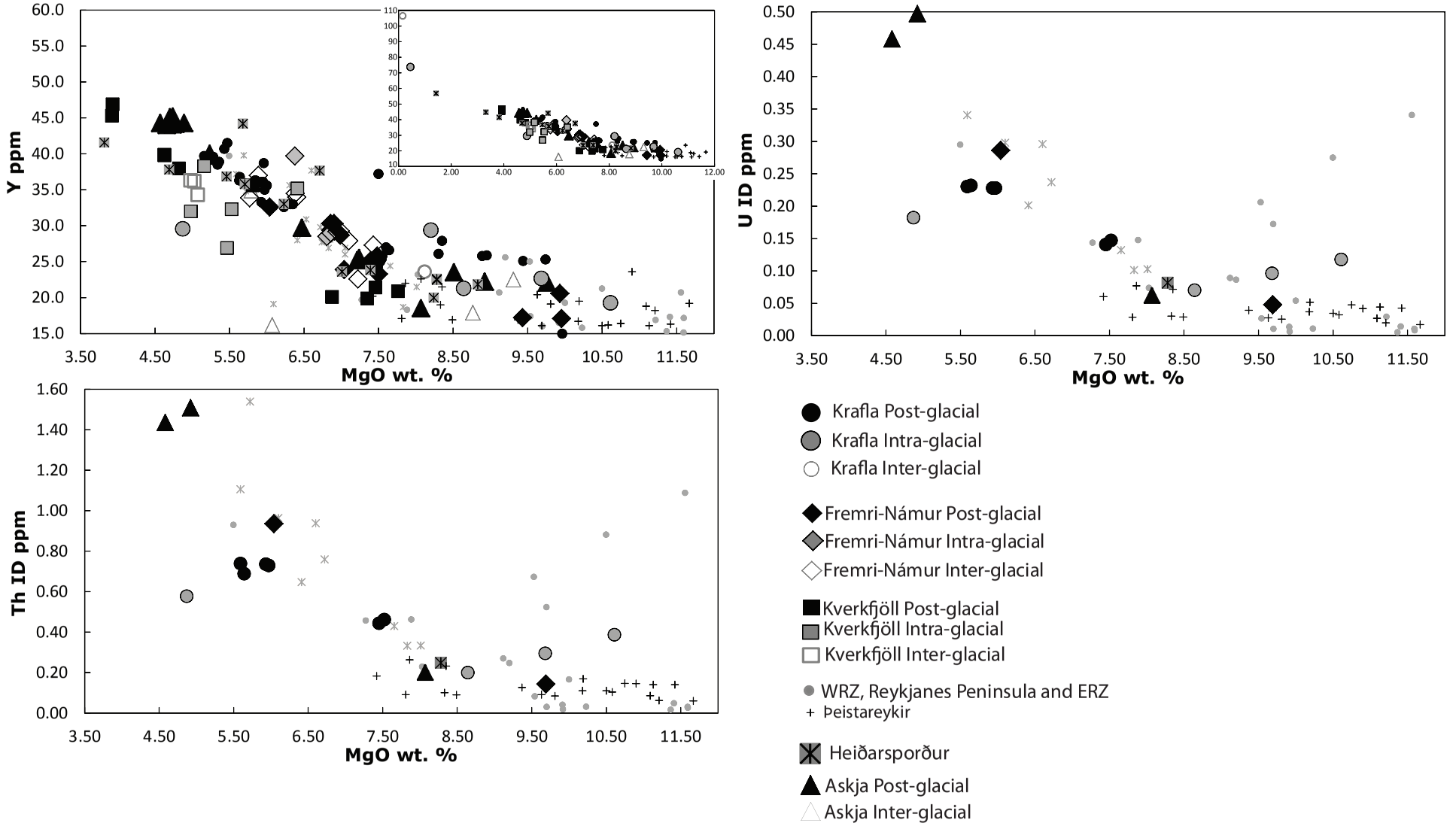

Figure 2.22 *cont...*

2.6.3 Multi-element diagrams

2.6.3.1 Chondrite normalised REE diagrams.

Chondrite normalised diagrams are presented in Figure 2.23. Rare earth element data analysed by isotope dilution for the NRZ are presented in Appendix 4. Samples selected show full range of Nb/Zr observed in each rift segment in order to fully represent the extent of enrichment in NRZ lavas.

Krafla: Despite differences in overall concentrations due to fractionation, post glacial lavas show broadly similar trends. All samples are moderately LREE enriched with La/Sm_N of ~1.15 for the more primitive samples and ~1.30 for the more evolved samples. MREE-HREE slops also show similar slopes with Dy/Yb_N of ~1.17 for the more primitive samples and ~1.09 for the more evolved samples. No Eu anomaly is seen in the more primitive samples whilst the evolved samples show a slight negative anomaly (Eu/Eu* = 0.96). The intra-glacial lavas show the most variation in REE patterns with broadly sub parallel trends. LREE enrichments range from moderately LREE depleted to moderately LREE enriched (La/Sm_N of 0.97 and 1.31 for DL033 and DL034 respectively) all converging to similar HREE concentrations. As a result, steep MREE-HREE trends are observed for the more LREE enriched samples (Dy/Yb_N of 1.17 for DL034) and shallower MREE-HREE trends are observed for the more LREE depleted samples (Dy/Yb_N of 1.07 for DL033). All samples show very limited Eu anomalies, ranging from slightly negative to slightly positive (Eu/Eu* of 0.98 and 1.02 for DL034 and DL033 respectively). One inter-glacial sample was analysed (JPF0971) and shows a fairly flat pattern with virtually no LREE enrichment (La/Sm_N = 1.02) with HREE concentrations converging to similar concentrations as the intra-glacial samples. No Eu anomaly is seen. One sample from the Heiðarsporður rift segments was also included (DL067) this also show a fairly flat pattern with very limited LREE enrichment (La/Sm_N = 1.04) and a flat MREE-HREE slope (Dy/Yb_N = 1.01). No Eu anomaly is also seen.

Fremri-Námur: Three post-glacial lavas were analysed for Fremri-Námur, they show a range of LREE slopes from moderately LREE depleted to moderately LREE enriched (La/Sm_N ratios of 0.88 and 1.44 for JPF0922 and JPF0945 respectively); like lavas from Krafla the most LREE enriched samples shows a steeper MREE-HREE slope (Dy/Yb_N of 1.17 for JPF0945 in contrast to Dy/Yb_N of 1.10 for JPF0945). The two most primitive samples show small positive Eu anomalies

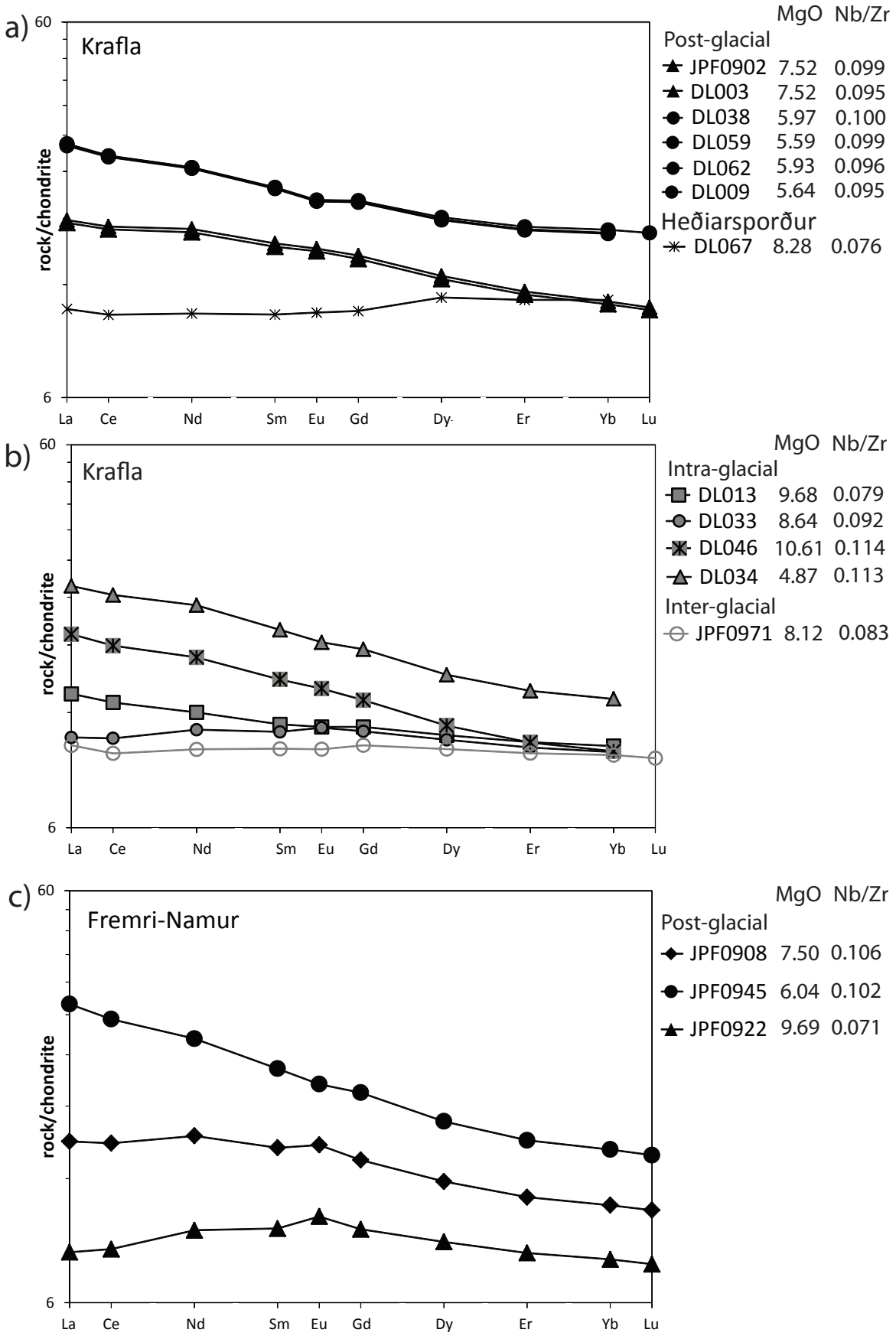

Figure 2.23: *Chondrite normalised REE profiles, normalisation values for are from Nakamura (1974). Grey fields in e) and f) show extent profiles for the Reykjanes Peninsular (data from Gee et al, 1998; Thirlwall, unpublished), ERZ (data from Manning, 2010) and Þeistareykir (data from Stracke et al, 2003).*

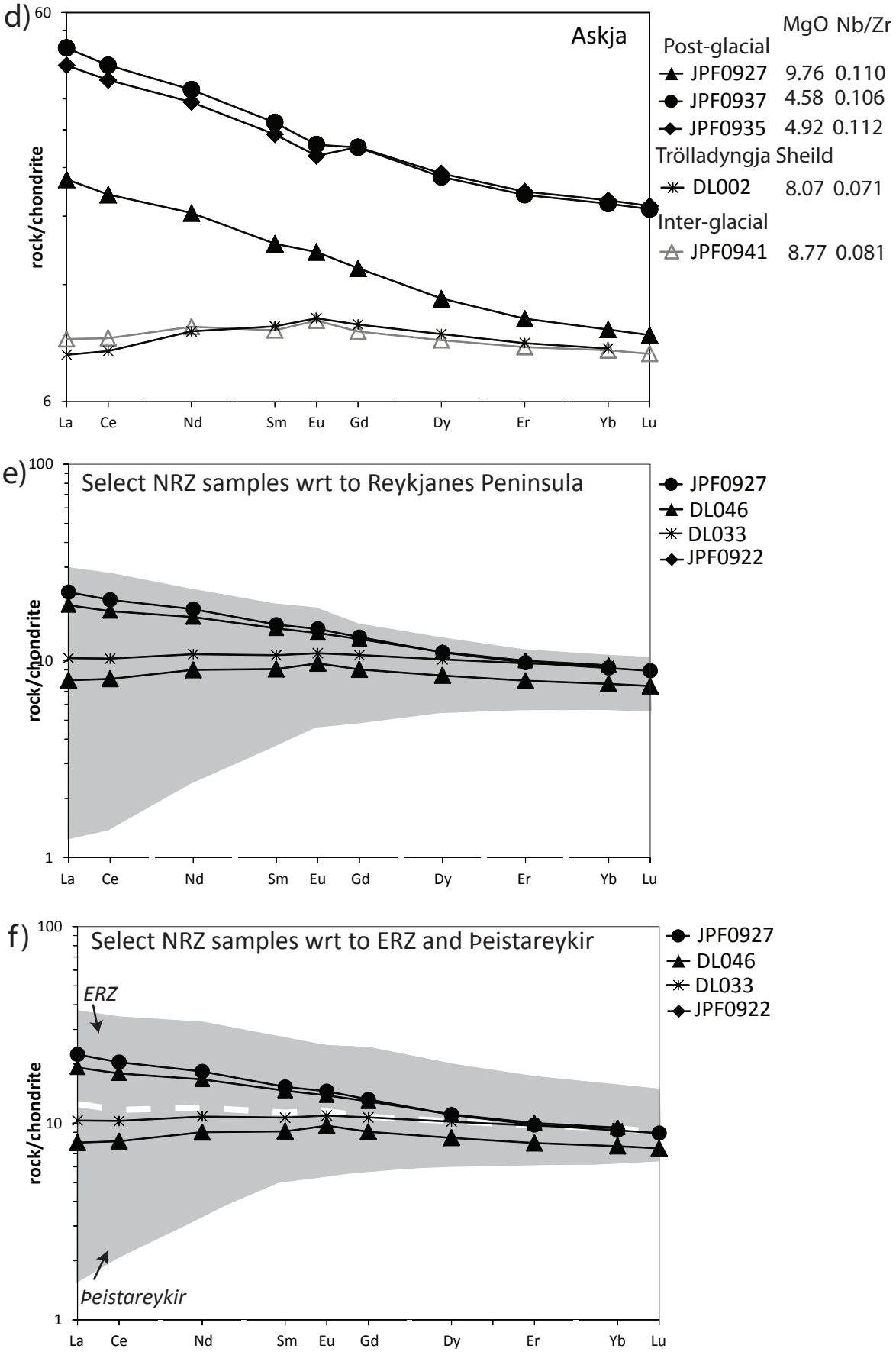

Figure 2.23 *Cont...*

whilst the more evolved lavas show a very small negative anomaly (Eu/Eu* of 1.05 and 1.07 for the more primitive samples and Eu/Eu* of 0.98 for the more evolved sample).

Askja:

Post-glacial samples show broadly parallel trends. All samples have similar LREE enrichments (La/Sm_N of 1.46-1.55) and similar MREE-HREE slopes (Dy/Yb_N of ~1.19). The most primitive sample shows a slight positive Eu anomaly (Eu/Eu* of 1.02) whilst the more evolved samples show a small negative anomaly (Eu/Eu* of 0.91-0.94). One lava from the nearby post-glacial shield volcano of Trölladyngja was analysed; this sample is moderately LREE depleted (La/Sm_N of 0.85) with a flatter MREE-HREE slope (Dy/Yb_N of 1.14) as well as a more positive Eu anomaly (Eu/Eu* of 1.04). The one inter-glacial lava analysed shows the lowest Nb/Zr for all Askja lavas collected. This sample has a very similar pattern to DL002, showing a LREE depletion (La/Sm_N of 0.95) but has a flatter MREE-HREE slope (Dy/Yb_N of 1.06) and a larger Eu anomaly (Eu/Eu* of 1.06).

Figure 2.23e and 2.23f shows the range of REE patterns from this study with respect to other rift zone lavas. NRZ lavas clearly plots within the field defined by these lavas however only moderate enrichments and depletions are seen.

2.6.3.2 Primitive-mantle normalised diagrams.

Primitive mantle normalised diagrams presented for Krafla, Fremri-Námur and Askja in figure 2.24.

Krafla: Post-glacial samples show largely parallel trends with negative Ba, Th, U, K, Pb and Sr anomalies; in contrast Nb shows a significant positive anomaly, whilst Zr and Hf show slight negative anomalies. Intra-glacial trends show also show negative K, Th, U Ba and Pb anomalies with the exception of DL046 which show a significant Ba enrichment. All intra-glacial samples show negative Sr, Zr and Hf anomalies apart from DL033 which shows a sight positive Sr anomaly and DL013 which show a slight positive Zr and Hf anomalies as well as a pronounced negative Ti anomaly. The one inter-glacial sample shows a broadly flat pattern with a very weak Ba and K anomalies and a positive, Sr, Zr and Hf anomaly. DL067 shows a very similar pattern to the inter-glacial samples but shows stronger Ba and K anomalies.

Fremri-Námur: All post-glacial flows show broadly parallel patterns showing negative Rb, Ba, Th, U, K and Pb anomalies as well as positive Nb and Sr anomalies with the exception of JPF0908 which shows a negative Sr anomaly. In particular the Sr anomaly is much more pronounced in JPF0922. In addition JPF0945 and JPF0922 show slight negative Zr, Hf anomalies.

Askja: The post-glacial pattern shows similar trends to that of the Fremri-Námur lavas showing negative Rb, Ba, Th, K, Pb and Sr anomalies and a positive Zr, Hf and Nb anomalies. The inter-glacial lava and DL002 both show similar flatter patterns. As above these lavas show negative Rb, Ba, Th and K and positive Nb anomalies are. In contrast however these flows show a positive Sr and a negative Zr, Hf anomaly.

Like the chondrite normalised diagrams, Figure 2.24e and 2.24f shows spidergrams from this study with respect to other rift zone lavas. NRZ lavas clearly plot within the field defined by these lavas however only moderate enrichments and depletions are seen.

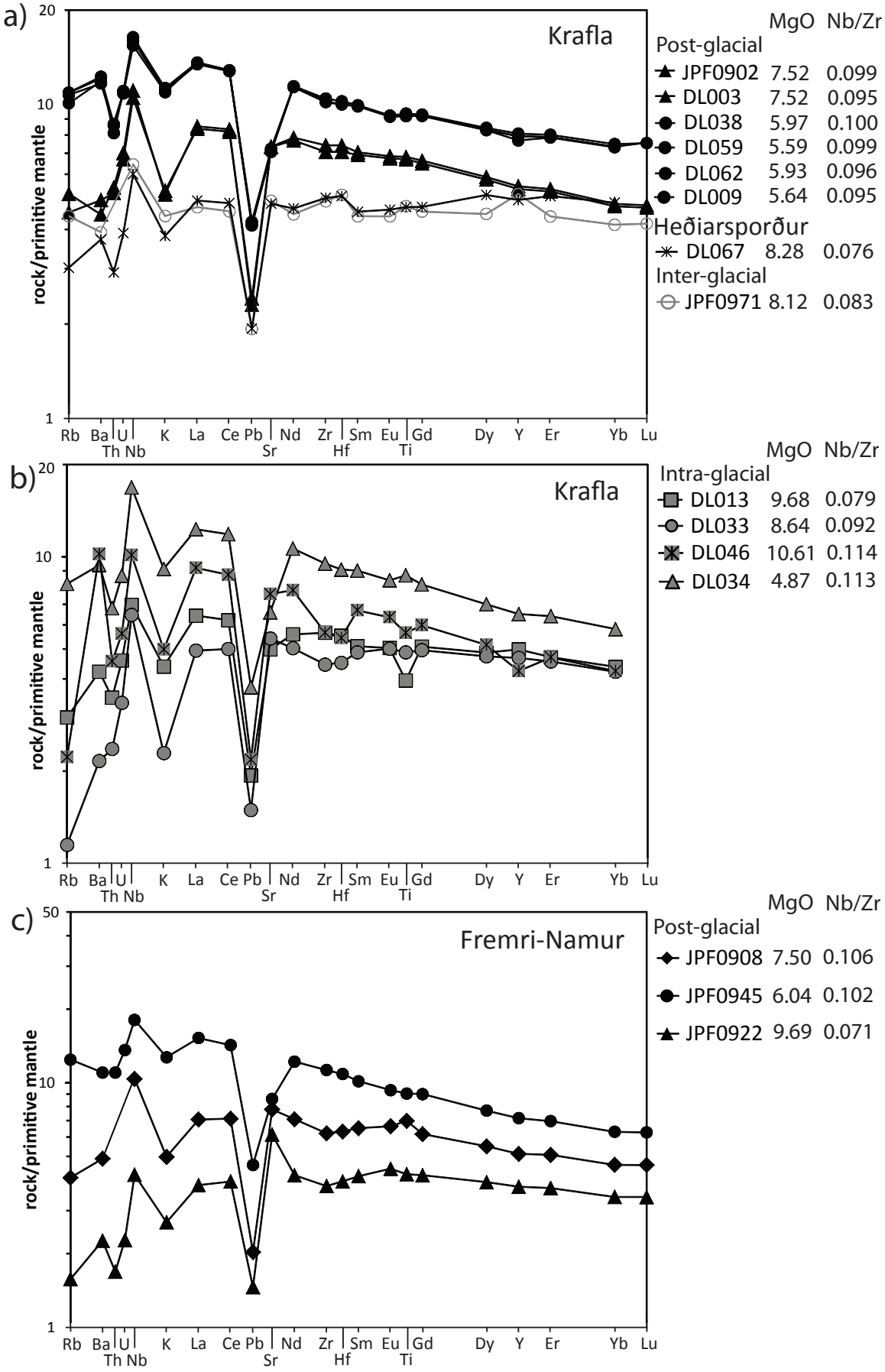

Figure 2.24: *Primitive normalised multi element diagrams, normalisation values from Sun McDonough (1989) except for Pb which is from Hoffmann (1988). Ce/Pb = 25 for Sun McDonough (1989) vaules, this is too high to be primitive mantle. Data from grey field as figure 2.20.*

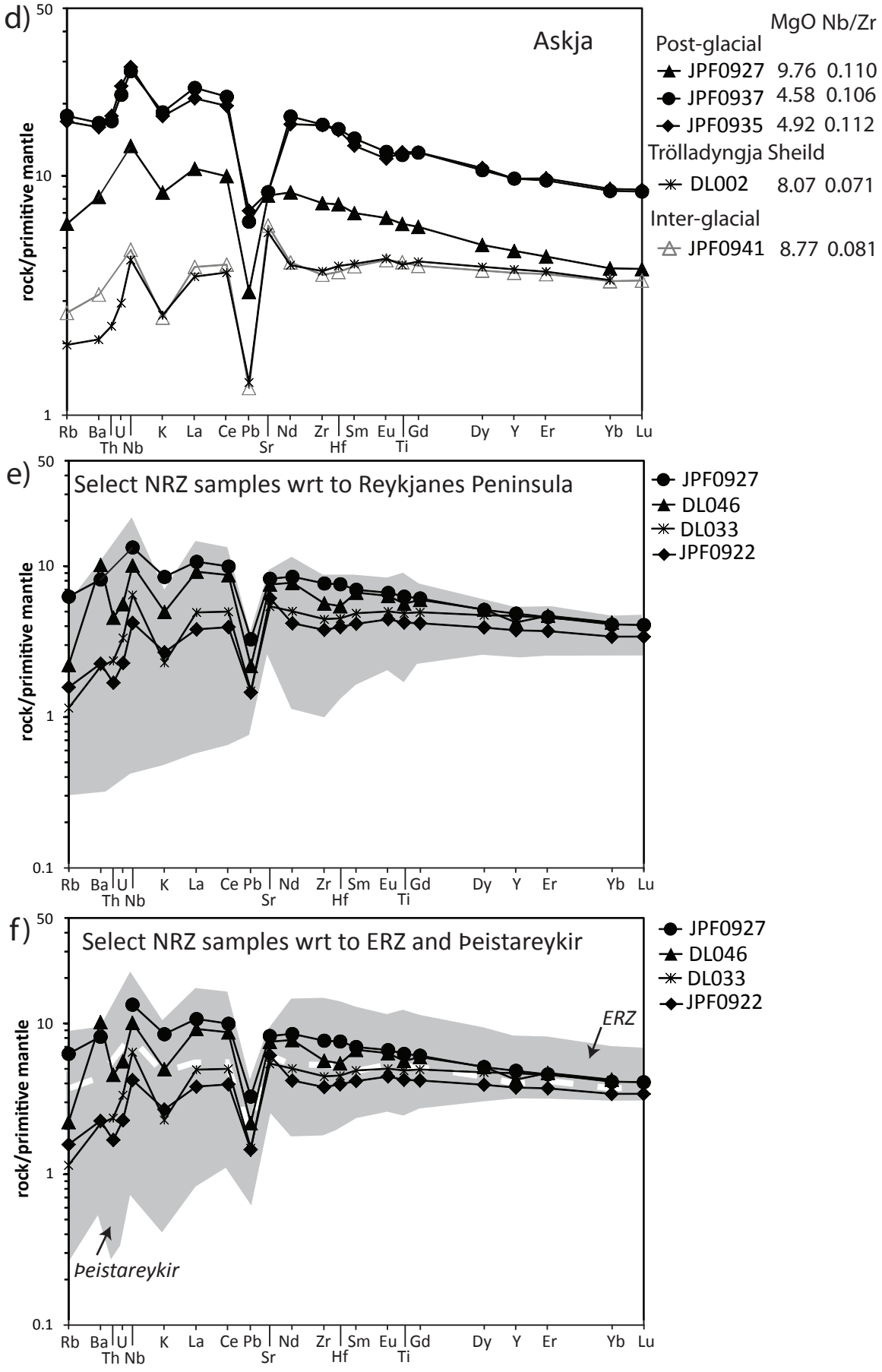

Figure 2.21 *Cont...*

2.7 Radiogenic Isotope Chemistry

2.7.1 General Comments

Previous literature has shown that Icelandic basalts are heterogeneous in terms of their isotope compositions (i.e. Hemond et al., 1993). It has been suggested that these variations can be attributed to mixing of several isotopically distinct sources (Thirlwall et al., 2004). Manning (2010) showed that lavas from the ERZ lie on different trends to the WRZ variations observed by Thirlwall et al. (2004). Manning (2010) concluded that a different mantle arrangement was needed with different mantle components, suggesting that the addition of a recycled oceanic crustal component as well as sediment is needed in order to explain the variations. Given that these components appear to be absent from lavas at Þeistareykir (Stracke et al., 2003) and the WRZ it could be argued that these components only affect rift tholeiites locally in the ERZ. In light of limited isotopic data along the NRZ a wide range of lavas and basaltic hyaloclastite clasts from the length of the rift have been analysed for Sr-Nd-Hf-Pb isotopic ratios in order to determine the extent of influence of these components along the NRZ. All isotope data are presented in Appendix 5. All diagrams within this section contain comparative data from Þeistareykir from Stracke et al. (2003) and Peate et al. (2010), WRZ and Reykjanes Peninsula lavas from Thirlwall et al. (2004, 2006) and Thirlwall (unpublished), as well as ERZ and Öræfajökull lavas from Manning (2010). Samples analysed by Thirlwall and Manning (2012) were prepared and analysed using the sample analytical methods as this study and so are directly comparable. Uncertainties quoted throughout are ±2 sd based on the external precision of standards.

2.7.2 Sr- Nd isotope chemistry

All samples form a good negative correlation (Figure 2.25). NRZ data overlap the ERZ data, whilst Reykjanes Peninsula, WRZ and Þeistareykir lavas lie on a shallower trend (Figure 2.25). Samples from Heiðarsporður lie largly within the main NRZ array apart from one sample that has lower $^{87}Sr/^{86}Sr$ for a given $^{143}Nd/^{144}Nd$. Lavas from Askja show the largest range in $^{87}Sr/^{86}Sr$ and $^{143}Nd/^{144}Nd$ (0.703041-0.70323 and 0.513016-0.513102 respectively), whilst lavas from Krafla show the smallest range (0.703202-0.703237 and 0.513026-0.513041 respectively).

2.7.3 Pb isotopic composition

Lavas from the NRZ show a relatively restricted range of $^{206}Pb/^{204}Pb$ ratios from 18.290-18.626 (figure 2.26). Like most Icelandic rift zone lavas the NRZ has negative $\Delta^{207}Pb$ values, with the

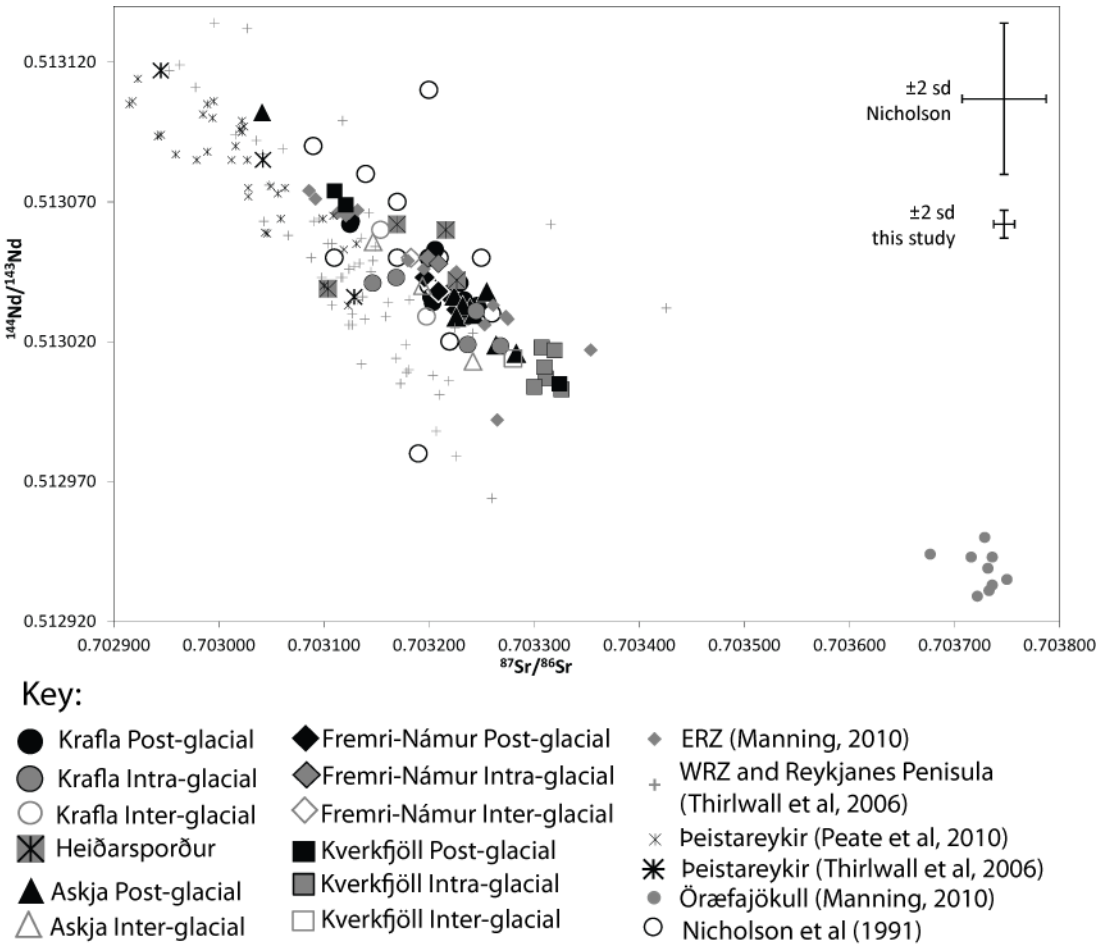

Figure 2.25: *Sr-Nd array for NRZ samples Krafla with comparative data. R^2 values for this study's array is 0.922 (Critical R^2 values show this correlation to be greater than 99% significant) compared to R^2 of 0.178 for Nicholson et al. (1991) array.*

exception of one post glacial lava from Fremri-Námur which is very mildly positive (0.241). The NRZ also displays some of the most negative Δ^{207}Pb double spike corrected values measured in Icelandic rift zone lavas (-3.64 in JPF0962, an intra-glacial Fremri-Námur lava). As with the Sr-Nd plot, NRZ lavas overlap the ERZ field. Individual rift segments (except Kverkfjöll) form negative correlations that are broadly sub parallel to the Öræfajökull trend. More scatter is present in the intra and inter glacial lavas. Due to the smaller number of samples analysed from these ages it is difficult to fully assess the extent of correlations of these samples. Despite analysis of only 3 intra glacial samples from Kverkfjöll they appear to lie on the same 'Öræfajökull' like trend similar to other rift segments, however the post glacial samples appear to form a different trend pointing towards the Öræfajökull.

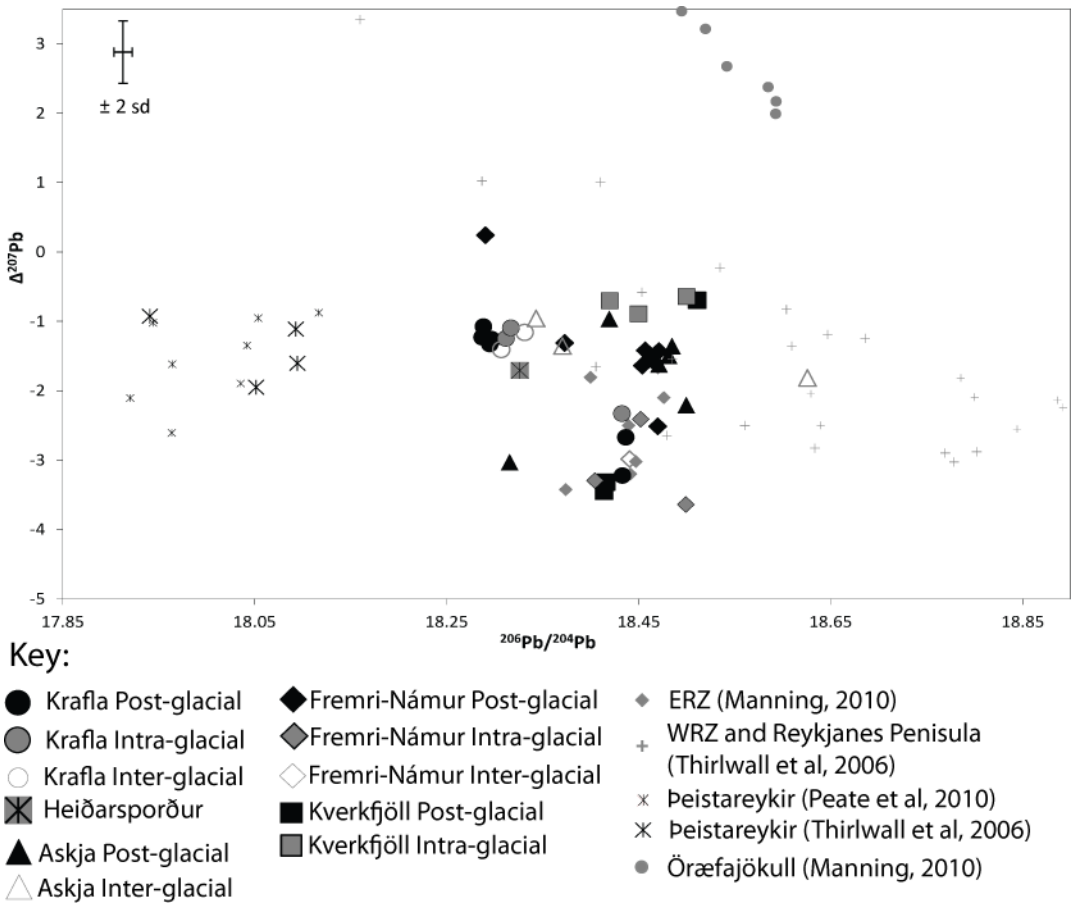

Figure 2.26: *$\Delta^{207}Pb$ vs $^{206}Pb/^{204}Pb$ plot with comparative data.*

2.7.4 Hf isotopic composition

The range of Hf isotopes reported falls within the range of isotopes seen for other rift zone lavas. Figure 2.27a shows a broad positive correlation between Hf-Nd. DL002, the most depleted sample from this suite a has much lower $^{176}Hf/^{177}Hf$ for its $^{143}Nd/^{144}Nd$ than all other rift zone lavas.

2.7.5 Correlations between radiogenic isotopic compositions

Unlike other rift zones no broad rift zone wide correlations are present in Nd-Pb or Sr-Pb isotope space (Figure 2.27b,c). For a given $^{206}Pb/^{204}Pb$, NRZ samples generally lie to lower $^{143}Nd/^{144}Nd$ and higher $^{87}Sr/^{86}Sr$ than Reykjanes Peninsula lavas whilst ERZ lavas fall within the NRZ range. Between individual rift segments sub parallel 'Öræfajökull' like trends are also seen, except for Kverkfjöll which trends towards the Öræfajökull array. The correlations within these rift segments could suggest that local binary mixing is occurring along this rift zone, the extent of this will be assessed in chapter 5.

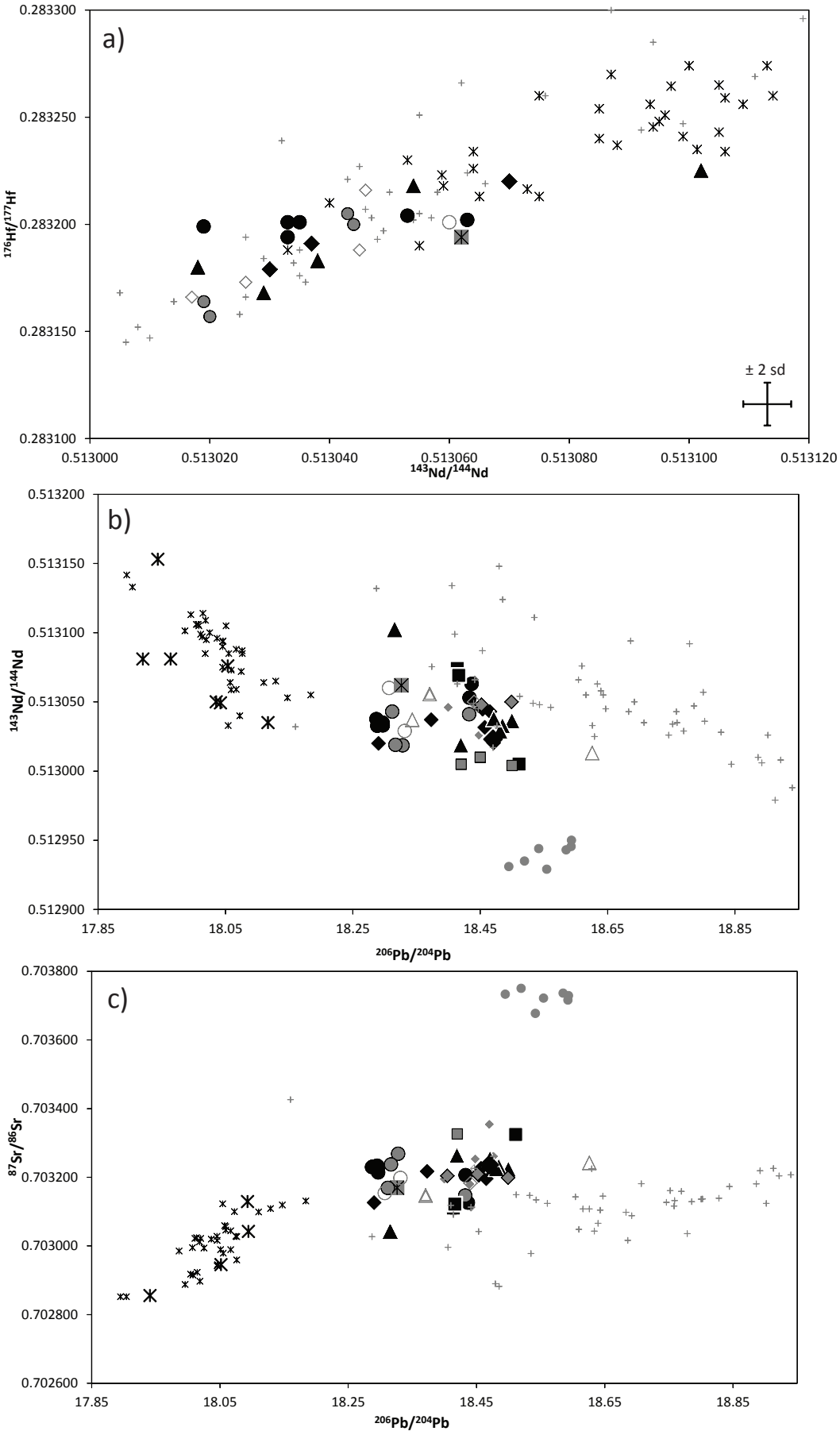

Figure 2.27: *$^{176}Hf/^{177}Hf$ vs. $^{143}Nd/^{144}Nd$; $^{143}Nd/^{144}Nd$ vs. $^{206}Pb/^{204}Pb$ and $^{87}Sr/^{86}Sr$ vs. $^{206}Pb/^{204}Pb$ plots with comparative data. Where no error bar shown the 2 sd is small than the symbol size. Key as figure 2.26.*

2.8. Oxygen isotope chemistry

2.8.1 General comments

Mattey et al. (1994) has shown in a study of 76 mantle xenoliths that the lithospheric mantle is homogeneous in $\delta^{18}O$ with a value of +5.18 ± 0.28 2sd. Similarly MORB glasses have been shown to have a limited range of $\delta^{18}O$ near to mantle values +5.50 ± 0.29 (Eiler et al., 2000b). In contrast Icelandic lavas have been shown to have significantly lower values, with reported $\delta^{18}O$ in whole rocks ranging down to -0.2 and $\delta^{18}O$ in olivine down to +3.2 (Muehlenbachs et al., 1974; Hemond et al., 1988; Nicholson et al., 1991; Hemond et al, 1993; Gee et al., 1998a Eiler et al., 2000a; Skovgaard et al., 2001; Macpherson et al., 2005; Thirlwall et al., 2006). The majority of published oxygen isotope data for the NRZ was analysed using conventional fluorination on whole rock powders (Muehlenbachs et al., 1974; Hemond et al., 1988; Nicholson et al., 1991; Hemond et al, 1993). Several studies have highlighted that there can be large discrepancies between whole rock and phenocryst/glass data (Davidson and Harmon, 1989; Thirlwall et al., 1996; Downes et al., 2001; Thirlwall et al., 2006) as whole rock powders are very susceptible to surficial alteration, in particular secondary hydration of samples by local meteoric waters. In addition Mattey et al., (1994) importantly noted that the heterogeneity reported in whole rock conventionally fluorinated studies is the result of low O yields. It is therefore important to ascertain real $\delta^{18}O$ values in order to test crustal contamination models.

Fresh Olivine separates from 4 post-glacial lavas, 1 inter-glacial lava and 2 intra-glacial basaltic hyaloclastite clasts from Krafla were analysed for oxygen isotopes by laser fluorination and are presented in Appendix 5.

Unfortunately it is currently not possible to determine the Fo% of olivines analysed by laser fluorination therefore it is not possible to ascertain directly whether the olivines analysed are in equilibrium with their respective host magmas or whether they are xenocrysts. The Fo% distributions presented in Figure 2.3 gives an idea whether it is likely that the olivines picked for laser fluorination are in equilibrium or not. With the exception of DL067, all distributions show that these lavas contain large numbers of equilibrium crystals suggesting that it is unlikely that the olivines picked are xenocrysts. However, the $\delta^{18}O$ value for DL067 should be treated with caution. Despite the large number of equilibrium crystals in the majority of lavas it is however important to keep in mind that all these samples do all contain a small number of

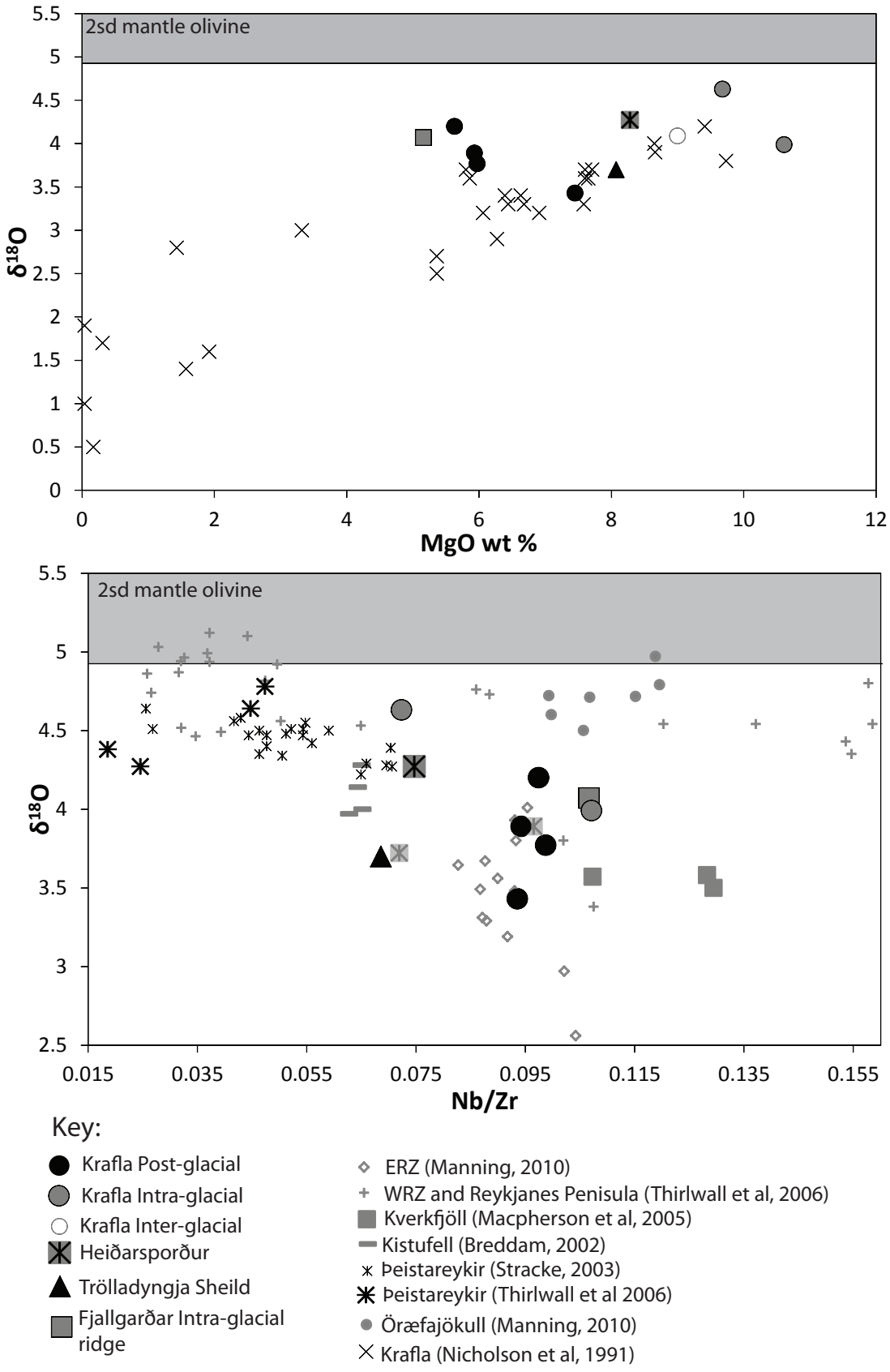

Figure 2.28: *$\delta^{18}O$ vs MgO w.t. % and ^{18}O vs. Nb/Zr. Nicholson et al (1991) samples have been adjusted to ol values using a whole rock-olivine fractionation of 0.5%.*

disequilibrium crystals, therefore it is entirely possible that some of the crystals analysed for $\delta^{18}O$ may not have necessarily crystallised from their host magmas.

2.8.2 Correlations between oxygen and elemental data

The olivines show a range of below mantle values from +4.63‰ to +3.43 ‰. All samples show a weak positive correlation with MgO. In comparison to published whole rock data for Krafla from Nicholson et al. (1991) a shallower trend is observed. No strong correlations are observed within individual rift segments with Nb/Zr. The moderately enriched samples (> 0.095 Nb/Zr) fall within the range of values reported for the ERZ whilst the more depleted samples show a greater range of values than reported $\delta^{18}O$ of similarly depleted lavas.

2.8.4 Correlations between oxygen and radiogenic isotopic ratios

Post-glacial lavas show no correlation between $\delta^{18}O_{ol}$ and $^{87}Sr/^{86}Sr$, all the samples lie within a very small range of $^{87}Sr/^{86}Sr$ and display large variations in $\delta^{18}O_{ol}$. In general the Krafla samples lie within the ERZ range with the exception of DL013 which has much higher $\delta^{18}O_{ol}$. A similar relationship is observed with $^{143}Nd/^{144}Nd$, the post-glacial lavas and DL046 lie within the ERZ field with DL013 lying to higher $\delta^{18}O_{ol}$. As with other isotope-isotope plots Krafla lies to less radiogenic $^{206}Pb/^{204}Pb$ than the ERZ, however both intra and post-glacial samples seem to lie on a vaguely positive correlation.

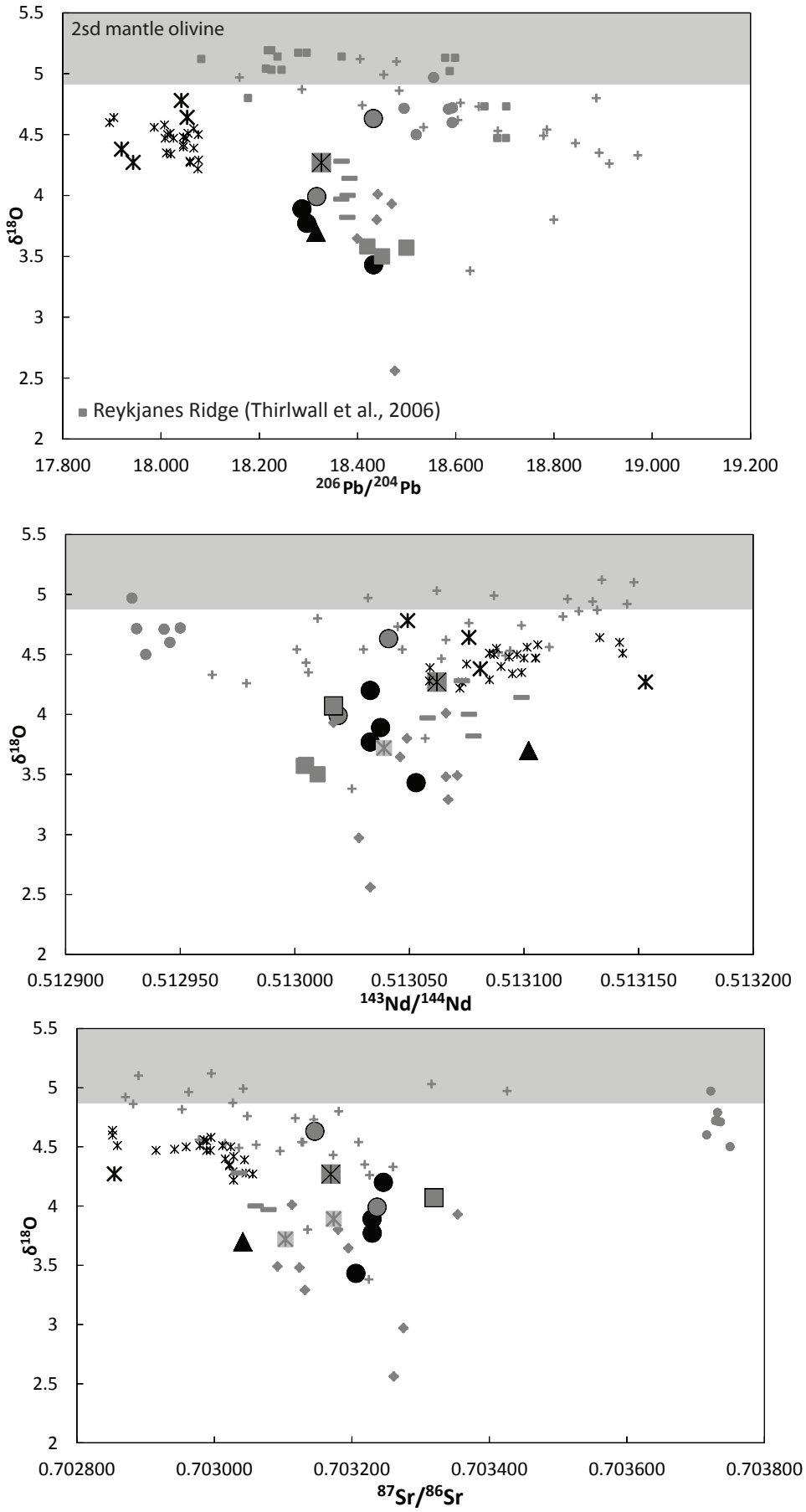

Figure 2.29: δ ^{18}O vs.^{206}Pb /^{204} Pb, ^{143}Nd/ ^{144}Nd and ^{87} Sr/ ^{86} Sr Key as figure 2.28.

CHAPTER 3: THE ROLE OF SHALLOW LEVEL PROCESSES

3.1. General Comments

Before assessing the role of deep processes on the chemistry of NRZ lavas it is important to recognise the effect of shallow crustal processes. In particular mechanisms such as fractional crystallisation and crustal contamination can lead to a systematic change in chemistry from its primary melt composition. Fractional crystallisation has been widely evoked to play a dominant role in Icelandic lavas (e.g. Wood, 1977; Meyer et al., 1985; Nicholson, 1991; Furman et al., 1992) however the importance of contamination by crustal material into a crystallising body of magma has been thoroughly debate in the literature (e.g. Nicholson et al., 1991; Gee et al., 1998a; Eiler et al., 2000; Macpherson et al., 2005; Bindeman et al., 2006). The knowledge of crystallisation depths for individual samples will help in refining contamination models and in particular help assess the origin of $\delta^{18}O$ light olivines. The following sections will attempt to differentiate between mechanisms can affect compositional variations at shallow levels (i.e. fractional crystallisation) and those that occur at deeper levels (ie source variation).

3.2 Alteration and Crystal Accumulation

3.2.1 Introduction

The suites of rocks described in this chapter include intra and inter-glacial samples which may have undergone surface alteration. This needs to be assessed before considering shallow level processes such as fractional crystallisation and crustal contamination. In addition several lavas have been shown to contain high proportions of phenocrysts possibly as a function of accumulation. It is important to identify what phases have accumulated and what the effect on the chemistry might be.

3.2.2 Alteration

The relatively old age of intra and inter glacial lavas collected in this study means that it they are more likely that they have undergone surface or hydrothermal alteration and weathering. It is therefore important to recognise the effects on the chemistry by these processes before considering other shallow level mechanisms. It is expected that fresh basalts give negative loss on ignition (LOI) values due to the oxidations of Fe^{2+} to Fe^{3+} during ignition. Most of the samples analysed indeed show negative LOI values apart from a small number of samples from

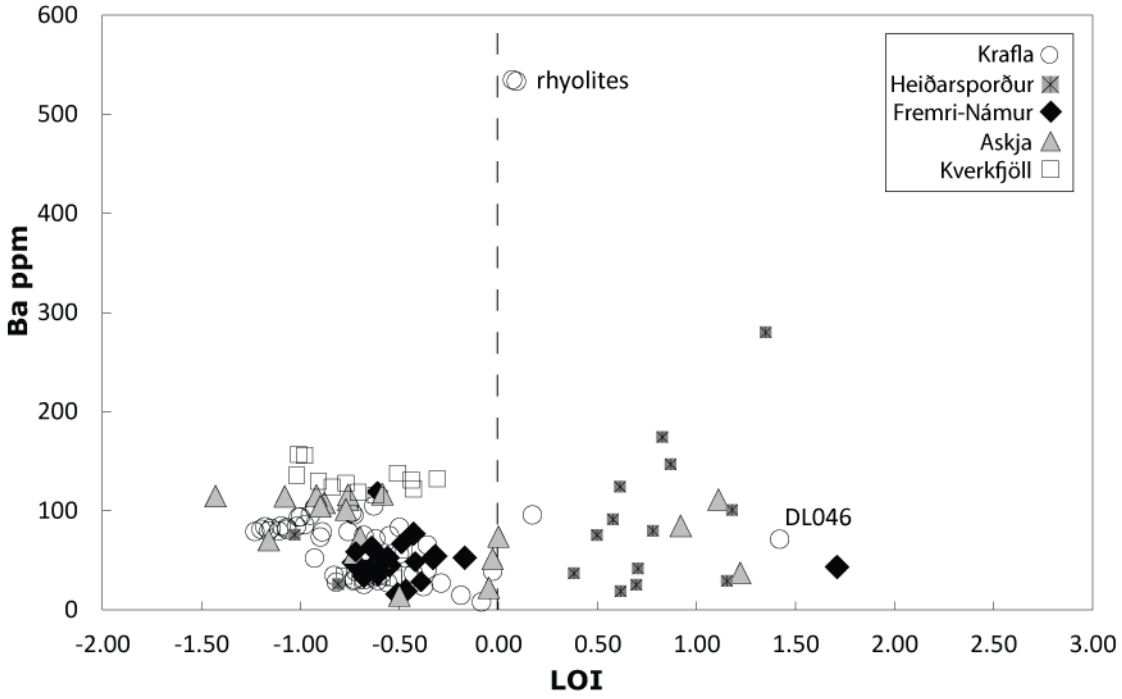

Figure 3.1: *Ba ppm vs. LOI. Majority of samples clearly lie to negative LOI values.*

Krafla, Fremri-Námur and Askja as well as the majority of samples from Heiðarsporður (figure 3.1). Plots of mobile LILE elements (such as Ba) versus immobile elements (such as Nb) show very tight trends within individual rift segments, therefore any significant alteration would shift the high LOI samples of this trend (figure 3.2). Of these samples only DL046 shows an elevated Ba concentration suggesting that the other high LOI samples may not have undergone significant alteration. Plots of other LILE element such as Rb vs. Nb (not shown) and K_2O vs. Nb do not show DL046 to lie significantly off trend, therefore if the high LOI value of DL046 is the result of alteration; it is not likely to have significantly affected the chemistry of this sample. All high LOI samples from Heiðarsporður were analysed for major elements from powder recovered from pellets. Consequently residual organic compounds from the pellet binding solution present in the initial dry weight of the sample before ignition has led to elevated LOI values. The two samples analysed using fresh powder gave negative LOIs.

3.2.3 Accumulation

Accumulation of crystals, whether due to the settling of phenocrysts or by entrainment and disaggregation of large numbers of xenocrysts within a lava can give rise to changes in bulk rock chemistry. It is therefore important to recognise samples that have an abundance of one or more crystal phases in order to omit them from modelling processes such as fractional crystallisation or the calculation of crystallisation pressures.

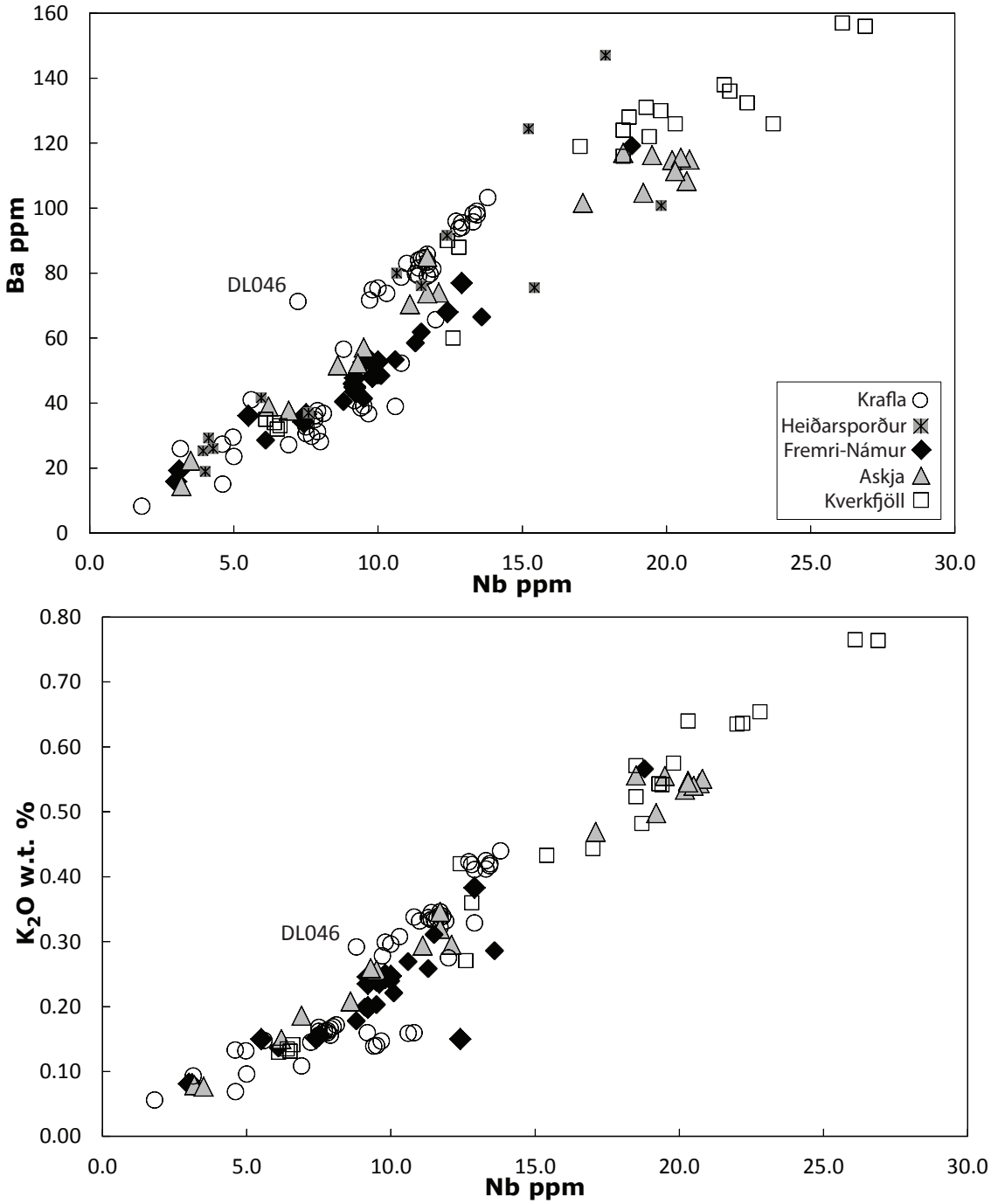

Figure 3.2: *Ba ppm and K_2O w.t. % vs. Nb ppm.*

Olivine: The accumulation of olivine crystals within a magma can elevate the whole rock MgO wt. %. Lavas with up to 30 wt. % MgO have been reported in some Reykjanes Peninsula picrites (Gee et al., 1998a). This would give the appearance on a Rhodes diagram of a population of olivines crystals that are not sufficiently Forsteritic to have crystallised for their host magma.

No such extremely high MgO lavas have been observed in samples collected for this study however JPF0949, JPF0962 or DL067 all contain large numbers of olivines that Fo% that are not in equilibrium with their whole rock values. These samples could have potentially accumulated olivine. Point counting shows these samples to have ~1-3 % olivine present making it unlikely that significant accumulation has taken place in these samples.

Section 2.4.1.2 has highlighted that the Zr/Y of olivines reflects the Zr/Y of the host melt. All olivines from JPF0949 show similar Zr/Y values suggesting they are likely to have crystallised from a chemically similar melt. The presence of gabbroic nodules at different stages of disaggregation in this sample might imply that the population of low Fo% olivines was introduced by crustal contamination of these nodules rather than small amounts of crystal settling. This is also likely to be the case for DL067 and JPF0962 where gabbroic nodules are also present.

Plagioclase: Accumulation of plagioclase can give rise to significantly elevated Al_2O_3 wt. % and Sr/Zr ratios as well as lower Fe_2O_3, TiO_2 and MnO wt. % values. It can, however, sometimes be difficult to confidently assess the extent of accumulation by chemical difference alone as this requires a good estimation of the original magma composition. This is often done by using the trend seen in the rest of the basalt suite. However above 8 wt. % MgO there is significant scatter making it difficult to estimate the true liquid line of decent. It is only when combined with point counted plagioclase abundances can the extent of plagioclase accumulation be more robustly estimated.

Figure 3.3 clearly shows that samples that lay to higher Sr/Zr and Al_2O_3 wt. % than the main trend typically have elevated plagioclase proportions. Three post glacial lavas from Fremri–Námur (highlighted in grey) show the chemical properties of accumulation but have a low plagioclase abundance.

Of the samples with high plagioclase abundance the mineral chemistry was determined in only DL022 and JPF0921. Melt reconstruction of these crystals reveal that the population from DL002 must have derived from more evolved melts then the host magma. This is consistent

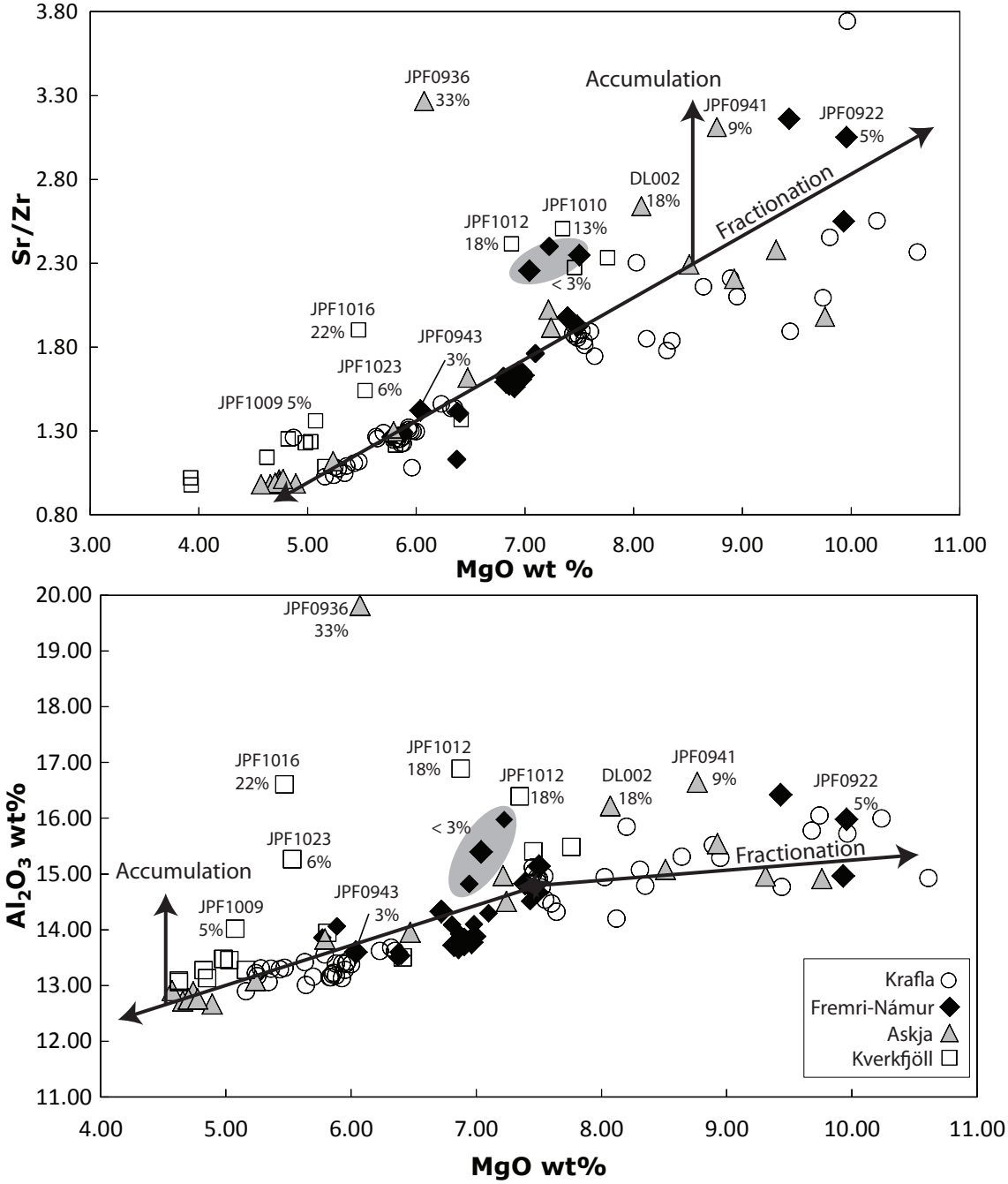

Figure 3.3: *Sr/Zr and Al_2O_3 w.t. % vs MgO w.t. %. A number of samples clearly lie above the main fractionation trend. These samples have abundance % of plagioclase marked next to the symbols. The 3 sample from Fremri-Námur in the grey field lie off the main trend but do not show evidence of abundant plagioclase with in these samples (< 3%).*

with the Zr/Y observations for olivine which suggest a xenocrystal origin of some of these phenocrysts rather than settling. In contrast the plagioclase population of JPF0922 have crystallised from similar melts to the host magma, and as such this sample is a strong candidate for accumulation by settling.

Clinopyroxene: Accumulation would typical elevate CaO/A_2O_3, overall CaO/A_2O_3 ratios form tight trends with decreasing MgO wt. %, only one sample shows higher values from this trend (DL034) potently suggesting accumulation, however no clinopyroxene is present in this sample

3.3 Fractional Crystallisation

Nicholson et al. (1991) first suggested that fractional crystallisation was largely responsible for the major and minor element trends observed at Krafla. The basic assumptions of these models however have been questioned by Jónasson (1994) who pointed out that Nicholson et al. (1991) did not discriminate between lavas from Krafla and Heiðarsporður which have since been shown to be unrelated (Jónasson, 2005). With these samples removed, Maclennan et al. (2001) reassessed the role of fractional crystallisation using the Nicholson et al. (1991) data set and concluded that the large scatter seen in the major elements cannot be easily explained by a single liquid line of descent. Tighter trends are observed in this new data set and strongly suggest that in fact samples from Krafla may be related by a single liquid line of descent. In this section the role of fractional crystallisation will be re-assessed at Krafla and Heiðarsporður and considered at Fremri-Námur, Askja and Kverkfjöll qualitatively and quantitatively.

3.3.1 Qualitative observations

In general the tight trends observed within the major and trace element chemistry are consistent with fractional crystallisation. Decreases in MgO with decreasing Ni and Cr (figure 2.19) are seen in all rift segments and is typical of olivine fractionation. Below 8 wt. % MgO most rift segments show a decrease of Al_2O_3 and CaO wt. % (figure 2.18) along with buffered Sr concentrations and decreasing Sr/Zr ratios, consistent with plagioclase removal. Heiðarsporður however shows no variation in Al_2O_3 suggesting that plagioclase removal maybe not play an important role in these lavas. Below 5 wt. % MgO the decrease in Fe_2O_3, TiO_2 and V all suggest that FeTi oxides are being removed.

All suites show a tight decreasing CaO/Al_2O_3 trend from ~8 wt. % MgO (Figure 2.18), typical of clinopyroxene fractionation. However very few clinopyroxene phenocrysts are present. This 'pyroxene paradox' has been observed by many workers and is common in MORB sample sets (e.g. Francis, 1986; Grove et al., 1992; Maclennan et al., 2001; Herzberg, 2004; Kelly and

Barton, 2008). Several possible explanations for this paradox has been put forward including high pressure clinopyroxene crystallisation followed by dissolution; segregation of clinopyroxene during crystallisation or magma chamber replenishment causing a halt in clinopyroxene crystallisation whilst keeping its chemical signature due to a shift from the ol-plag-cpx cotectic to the ol-plag cotectic (Michael and Cornell, 1998; Coogan et al., 2000; Herzburge, 2004; Gurenko and Sobolev, 2006; O'Neill and Jenner, 2012).

3.3.1 Quantitative modelling

Quantitative modelling of major elements was conducted by applying a least-squares fitting method using the SOLVER addin function in Excel written by M.F. Thirlwall. Olivine and clinopyroxene compositions used in the modelling were calculated from expected equilibrium values, whilst plagioclase compositions were calculated from typical An % seen in the parental lavas.

The aim of this method was to produce model daughters to within analytical error of the real daughter used in the models. Good models typically gave Σr^2 of <1 for 1 phase; <0.5 for 2 phases and <0.2 for 3 phases. Accompanying trace element models were calculated based on the mineral proportions from the major element models. Partition coefficients used in this modelling were taken from Rollinson (1993). Trends calculated from the modelling are presented for selected major and trace element variation diagrams for all rift segments in Figures 3.4 – 3.8 together with summary tables of the stages calculated in Tables 3.1 and 3.2.

Krafla:

Significant scatter is present in high MgO samples (>8 % wt. MgO) suggesting that lavas from Krafla may have derived from a number of different parental magmas. The only high MgO post glacial lavas are from the Ásbyrgi ridge, north of the Krafla caldera. These lavas show lower SiO_2 and higher incompatable element concentrations then other primitive lavas. Beween these samples good crytallisation models can be produced (see Table 3.1) however, due the differing chemistryit is clear that these lavas do not share a common parental magma with the other post glacial lavas, this is reflectedin the modelling by poor Σr^2 values (>1 for JPF0954-DL061).

Inter glacial lavas can be divided in to two groups. Lavas to the north of the Krafla Caldera (DL053, JPF1006) have higher SiO_2 and generally lower incompatible element concentrations whilst lavas to the south of the Krafla Caldera (JPF1010, JPF1009) have lower SiO_2 and higher incompatible element concentrations. Within these two groups good fractionation models

were fitted. However attempts to model crystallisation between groups was unsuccessful (e.g. JPF1010-JPF1006 gave Σr^2 >2); therefore these two groups are likely to have derived from different parental magmas.

A lot of scatter is seen in the high MgO Intra glacial lavas even between samples that are geographically close (DL046 and DL033); as such good fractionation models were difficult to produce. Alteration is a potential factor for some of this scatter, the previous section highlighted that DL046 potentially showed some minor alteration. Consequently Ba has been excluded from modelling however; despite this, good models were difficult to produce. Given that scatter is also seen in the immobile incompatible elements it is likely that alteration is not significant and that intra glacial samples have derived from a number of differing parental magmas.

Despite slightly lower K_2O, Nb and Zr in the model daughter only the southern inter glacial lavas give good fits to the main post-glacial trend (0909-DL061, Σr^2 0.409) suggesting they share a similar parental magma. Overall the major elements of the lower MgO post glacial lavas form a tight trend which modelling was able to successfully reproduce. Clinopyroxene joins the crystallising assemblage at ~7.5 wt. % MgO and magnetite crystallises at ~5.5 wt. % MgO. The model between DL061-DL023 is not able to reproduce high enough K_2O and incompatible trace elements in the model daughter, perhaps suggesting a slight difference in the parental magma between these groups of samples.

Attempts to model crystallisation to the Intra glacial sample DL034, which lies to much higher SiO_2 was unsuccessful. It is clear that the whole rock chemistry of this sample cannot be explained by fractional crystallisation. Furthermore attempts to generate models to the two rhyolites were unsuccessful, models gave large Σr^2 (>2) however this could reflect the large jump in chemistry the model must reproduce.

Heiðarsporður:

The unusual whole rock chemistry of this rift segment was first reported by Jónasson (2005). The fractional crystallisation modelling conducted here agrees with their findings. Above ~7.5 wt. % MgO, whole rock chemistry is consistent with fractional crystallisation, modelling suggests that these lavas were derived from similar parental magmas as Krafla. Good fits between KR88, DL067 and KK77 and the northern Krafla inter glacial lavas were modelled; whilst a good fit between KK55 and the southerly Krafla inter glacial lavas was modelled.

Two samples, JPF0914 and KK79 lie within the main post glacial trend for Krafla. Models from DL023 and between JPF0914 and KK79 show that crystallisation of a similar magma to DL023 can account for these samples. However it is clear that the majority of lavas with <~7.5 w.t. % MgO cannot be accounted for by fractional crystallisation. (The dash line on figure 3.5 illustrates the trend that the crystallisation of olivine, plagioclase and clinopyroxene would take from KK55.) Jónasson (2005) concluded that near-solidus differentiation (i.e. crystallisation of small partial melts in nearly solidified magmas or partially molten magmas) with strong pyroxene and limited or no plagioclase control is required to account for the variations observed. At ~4 wt. % Fe_2O_3 and TiO_2 concentrations decrease, indicating that magnetite crystallisation is taking place. Such a situation for near-solidus differentiation has been proposed by Jónasson (2005) to arise if a body of ol-tholeiite ponds within the upper crust. Heating of adjacent country rock is able to form evolved icelandititc and dacitic melts. Local crustal deformation possibly linked to extension from nearby Krafla caused eruptive activity to resume leading to the segregation of the evolved melts from the country rock and eruption of the ol-tholeiite possibly combined with mixing of the evolved melts generating some of the intermediate compositions.

Fremri-Námur:

The major element variations observed in this suite appear to be consistent with fractional crystallisation. A small number of plagioclase accumulates have been identified from this suite (see 3.2.3), these samples have been excluded from modelling due to the effect on whole rock chemistry accumulation has.

From JPF0919, good models with low Σr^2 values have been fitted to lower MgO samples of all ages. Modelling between an Older Laxárhraun sample, JPF0908 and JPF0919 gave a slightly worse Σr^2 then other models at similar MgO (Σr^2 = 0.35 to JPF0908, c.f. Σr^2 = 0.13 to JPF0916), this is due to JPF0908 having slightly lower SiO_2 and incompatible elements concentrations, perhaps indicating the Older Laxárhraun has a different parent then other Fremri-Námur samples. Despite good Σr^2 for models to post glacial lava JPF0945 most incompatible element concentrations are too low in the model daughters indicating possibly slight differences in the parental magma of this sample. Models from JPF0962 to inter and intra glacial sample also gave good Σr^2 however some of the samples show scatter in some incompatible elements, again, perhaps indicating slight difference in parental magmas. JPF0957 from the Núpar table mountain shows much higher incompatible element concentrations then all other Fremri-

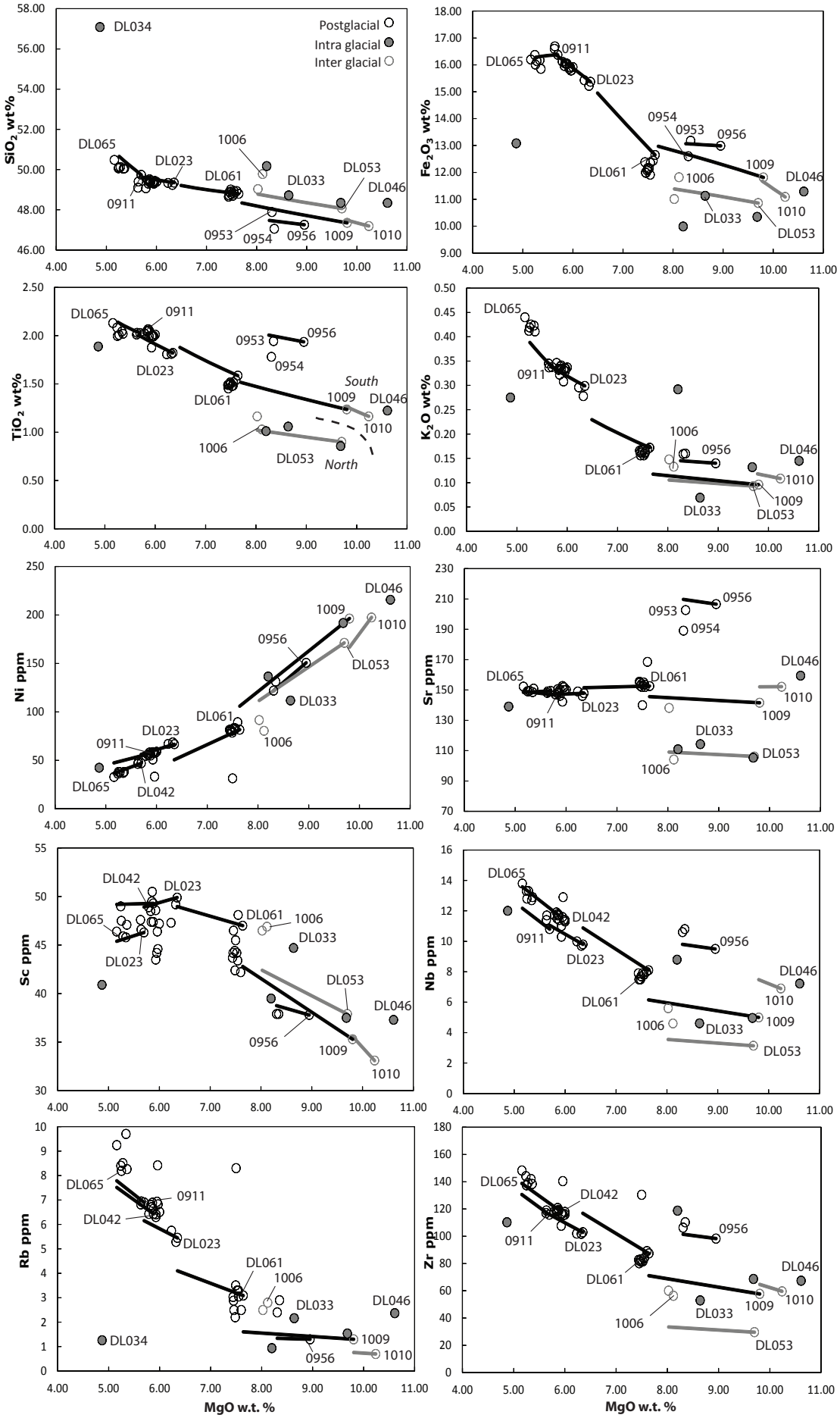

Figure 3.4: *Calculated fractionation trends for selected major and trace element variation diagrams from Krafla. Accumulates are not shown in these plots.*

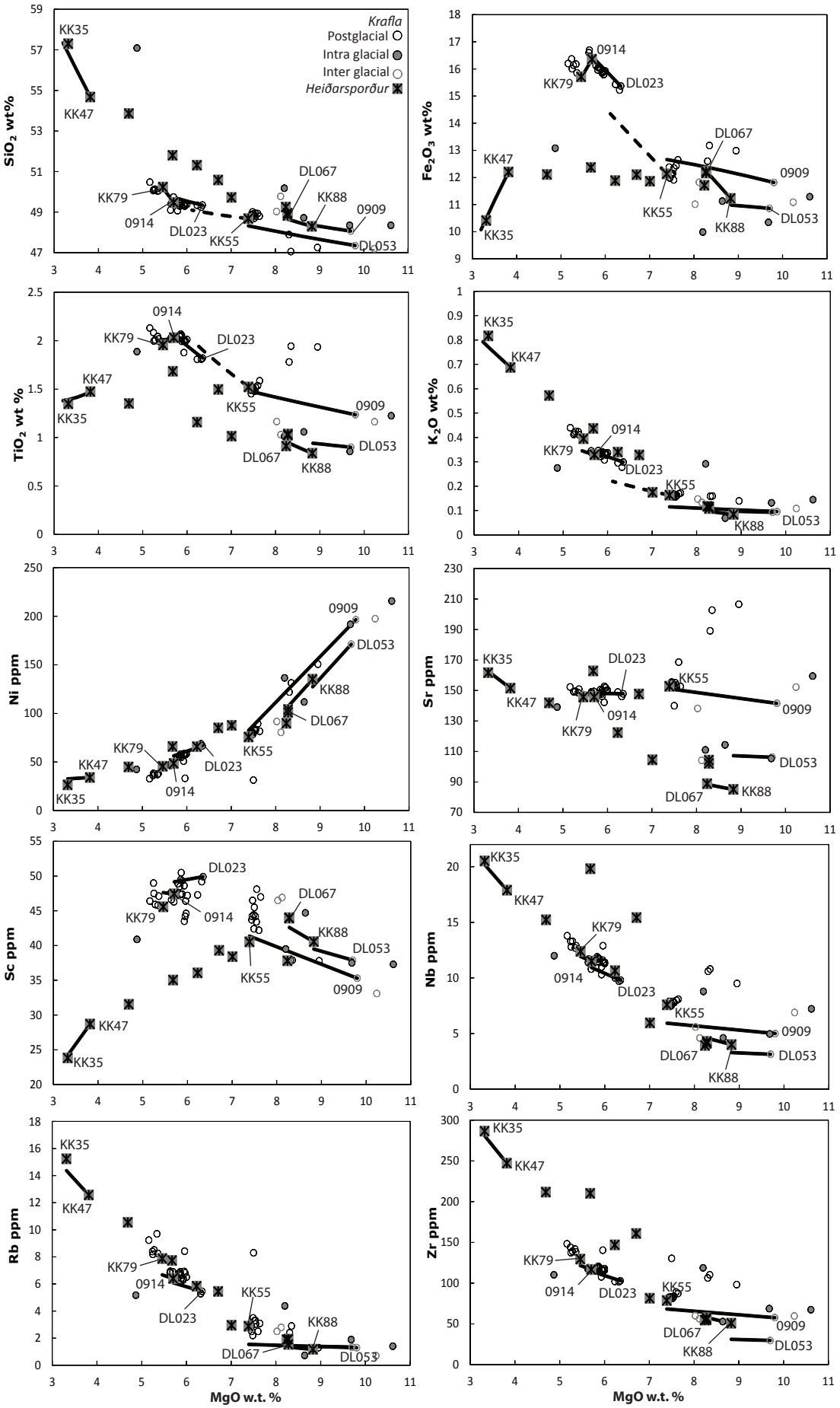

Figure 3.5: *Calculated fractionation trends for selected major and trace element variation diagrams from Heiðarsporður. Accumulates are not shown in these plots.*

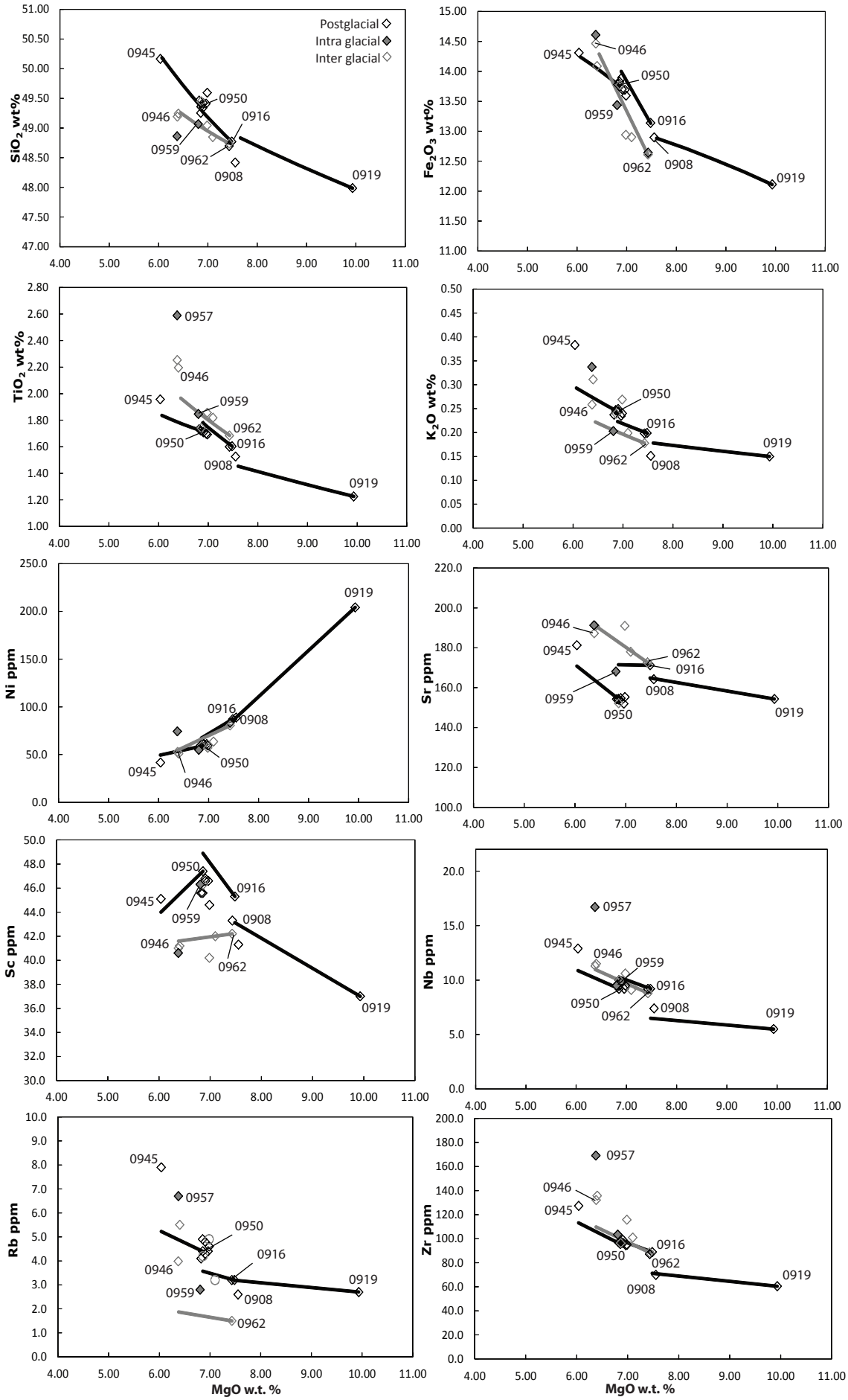

Figure 3.6: *Calculated fractionation trends for selected major and trace element variation diagrams from Fremri-Námur. Accumulates are not shown in these plots.*

	Parent An %	*ol*	*plag*	*cpx*	*mt*	total FC %	Σr^2
		Krafla					
Ásbergí ridge							
JPF0956 - JPF0954	88	65.5	34.5			3.3	0.562
8.95 - 8.31							
JPF0956 - JPF0953	88	40.5	59.5			4.9	0.276
8.85 - 8.35 (not shown)							
Interglacial low SiO_2 group							
JPF0910 - JPF0909	89	33.8	66.2			7.7	0.067
10.24 - 9.80							
Interglacial high SiO_2 group							
DL053 - JP1006	88	49.6	50.4			11.5	0.323
9.70 - 8.02							
Postglacial parents							
JPF0910 - DL061	89	40.4	59.6			24.3	0.293
10.24 - 7.64							
JPF0909 - DL061	89	43.4	56.6			18.4	0.409
9.80 - 7.64							
Main trend of Postglacial lavas							
DL061 - DL023	86	12.9	45.2	41.9		25.7	0.066
7.64 - 6.35							
DL023 - JPF0911	75	21.7	51.5	26.8		11.4	0.034
6.35 - 6.95							
JPF0911 - DL065	65	11.7	42.6	34.1	11.6	12.6	0.074
6.95 - 5.16							
		Heiðarsporður					
High MgO lavas (> 7 w.t % MgO)							
DL053 - KK88	89	61.3	38.7			4.1	0.123
8.95 - 8.83							
KK88 - DL067	87	22.0	58.8	19.1		12.3	0.071
8.83 - 8.26							
JPF0909-KK55	89	49.5	50.5			16.1	0.536
9.80 - 7.39							
Low MgO lavas (< 7 w.t % MgO)							
DL023 - JPF0914	84	17.6	47.9	34.5		10.0	0.034
6.35 - 5.70							
JPF0914 -KK79	82	21.3	26.4	24.6	27.7	4.2	0.074
5.70 - 5.43							
KK47 - KK35	72	10.7	37.0	29.4	42.0	12.6	0.034
3.82 - 3.32							

Table 3.1: *Summary of fractionation models calculated for Krafla and Heiðarsporður.*

Námur samples as such models to this sample were unsuccessful, indicating this sample must have crystallised from a much more enriched magma then seen at Fremri-Námur.

Askja:

Like Fremri-Námur a number of plagioclase accumulates are present in this suite and have been excluding from modelling.

Broadly, samples from Askja can be divided into two groups, a lower and higher SiO_2 group that span the full range of MgO observed. The most primitive sample from these two groups, inter glacial sample JPF0925, shows the lowest SiO_2 and incompatible element concentrations observed within this suite, models from this sample to lower MgO were not successful. Despite the large MgO difference between JPF0931 and JPF0932 models fit remarkably well (Σr^2 0.83), strongly suggesting that all the low SiO_2 samples were derived from a similar parental magma. From JPF0932 fractionation was successfully modelled across the small range of MgO values reaming.

The higher SiO_2 samples can further be divided into lower and higher incompatible element groups. JPF0927, JPF0928 and JPF0940 all show lower incompatible element concentrations, major element models fit these samples well, all giving good Σr^2, however trace element models do give as good a fit. This is also the case for the higher incompatible element samples (JPF0926 and JPF0924), suggesting slight variations in there parental magmas. Models to JPF0942 give better fits from the higher incompatible element samples and as such are likely to be parents to the lower MgO, higher SiO_2 lavas (JPF0924-JPF0942, Σr^2 = 0.312 c.f. JPF0940-JPF0942 Σr^2 = >1). Within these lavas fractionation trends were successfully reproduced with magnetite joining the crystallising assemblage at ~4.5 w.t. % MgO. worce

Kverkfjöll/ Fjallgarðar:

Fractional crystallisation trends are also present in Kverkfjöll lavas, as with other rift segments, accumulates have been excluded. The intra glacial samples from this suite were sampled from the Fjallgarðar intra glacial ridge, north of the main Kverfjöll rift segment.

In a study of the Fjallgarðar ridge, Helgason (1989) reported that samples could be grouped into high K_2O basalts and low K_2O basalts, reflecting different parental magmas. This grouping is also present in this suite, not only in Fjallgarðar samples but in lavas from the main Kverkfjöll

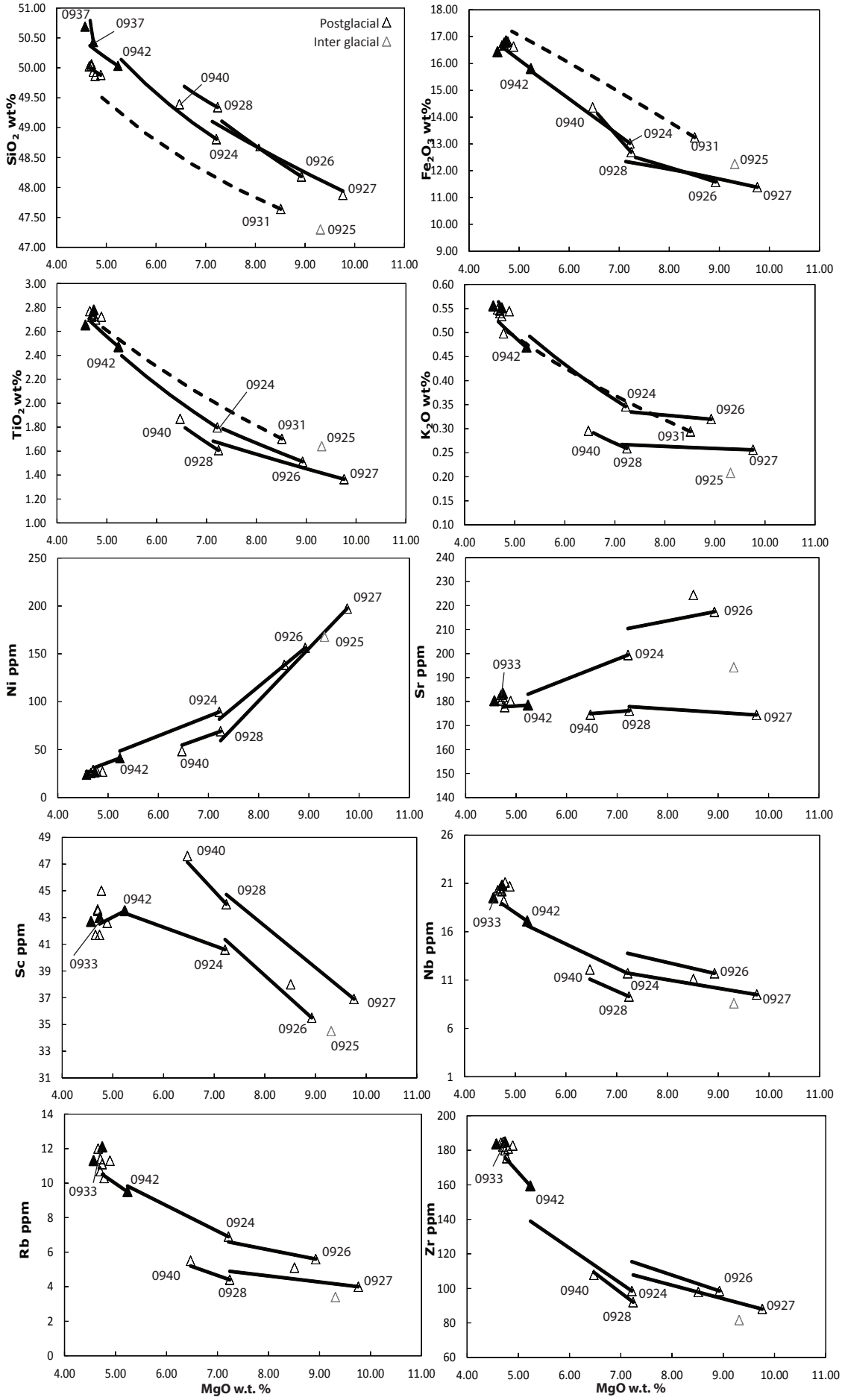

Figure 3.7: *Calculated fractionation trends for selected major and trace element variation diagrams from Askja. Black triangle denote high SiO_2 group. Accumulates are not shown in these plots.*

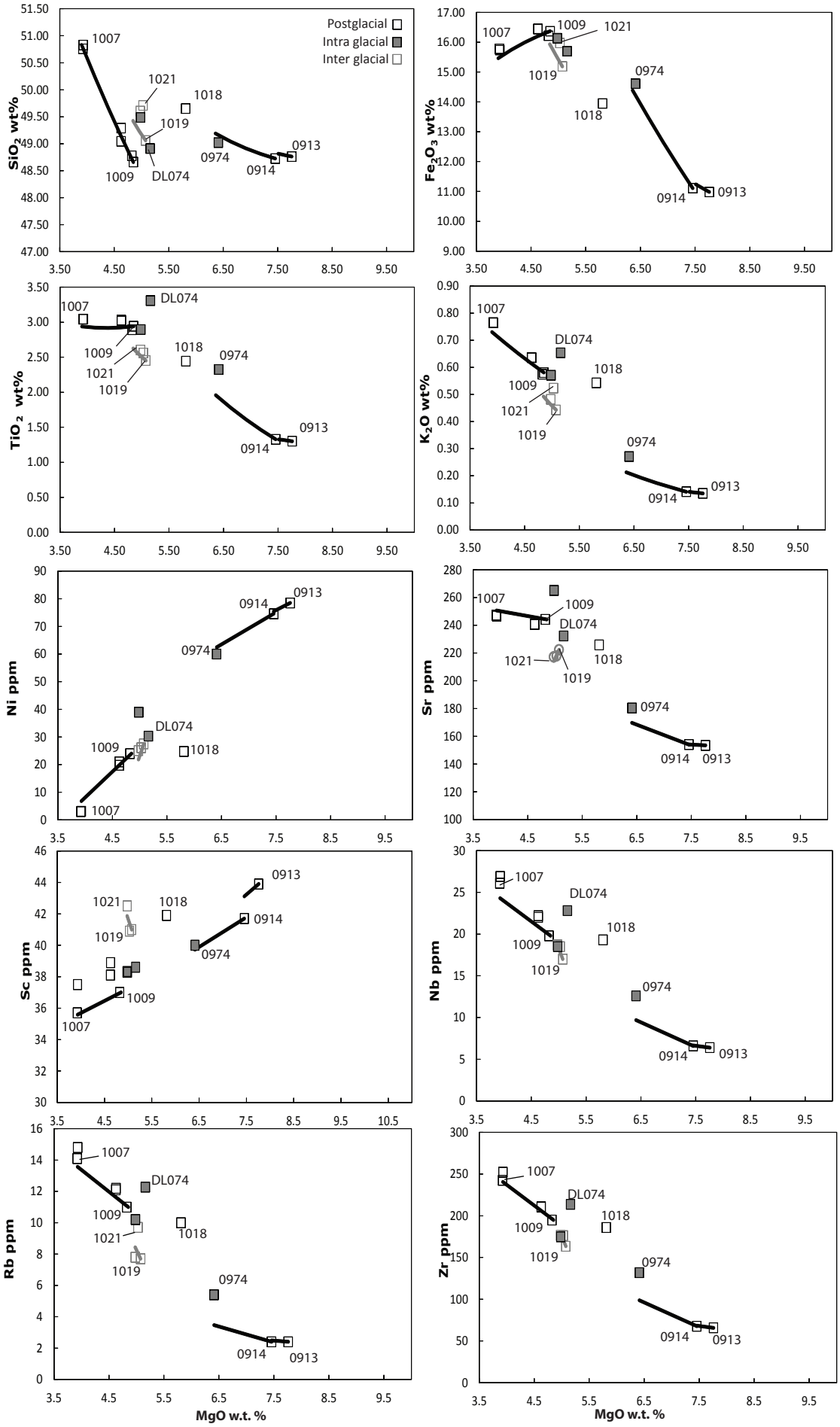

Figure 3.8: *Calculated fractionation trends for selected major and trace element variation diagrams from Kverkfjöll. Accumulates are not shown in these plots.*

	Parent An %	*ol*	*plag*	*cpx*	*mt*	total FC %	Σr^2
			Fremri-Námur				
Post glacial trend							
JPF0919 - JPF0916 *9.93 - 7.48*	89	51.3	48.7			15.4	0.126
JPF0919 - JPF0908 *9.93 - 7.55*	89	60.0	40.0			11.8	0.350
JPF0916 - JPF0950 *7.48 - 6.86*	87	27.6	64.3	8.1		10.4	0.144
JPF0950 - JP0945 *6.85 - 6.03*	85	12.4	38.2	43.8	5.6	15.9	0.045
Inter and Intra glacial trends							
JPF0919 - JPF0962 *9.93 - 7.43*	89	53.4	46.6			14.6	0.250
JPF0962 - JPF0946 *7.43 - 6.38*	87	17.1	50.8	32.1		19.9	0.096
JPF0962 - JPF0959 *7.43 - 6.80*	86	23.5	52.7	23.8		10.1	0.016
			Askja				
Main post glacial trend							
JPF0926 - JPF0924 *8.93 - 7.21*	89	40.9	59.1			15.1	0.510
JPF0924 - JPF0942 *7.21 - 5.24*	86	22.5	55.2	22.3		31.1	0.158
JPF0942 - JPF0933 *5.24 - 4.74*	79	16.8	46.2	37.1		9.9	0.144
JPF0933 - JPF0937 *4.74 - 4.57*	79	2.0	18.0	51.3	28.7	2.1	0.096
Low SiO_2 group							
JPF0931-JPF0932 *8.51 - 4.74*	88	27.5	51.5	21.1		46.3	0.830
JPF0932 - JPF0934 *4.89 - 4.74*	79	47.6	30.1	22.3		1.8	0.005
Low Incompatible element group							
JPF0927 - JPF0928 *9.73 - 7.24*	87	47.9	52.1			18.9	0.290
JPF0928 - JPF0940 *7.24 - 6.47*	85	12.7	48.2	39.1		16.3	0.184
			Kverkfjöll				
Low K Group							
JPF0913- JPF0914 *7.76 - 7.46*	87	16.4	41.5	42.1		3.8	0.420
JPF0914 - JPF0974 *7.46 - 6.41*	82	12.0	55.1	32.9		31.2	0.312
High K Group							
JPF1019 - JPF1021 *4.85 - 3.93*	78	13.1	38.4	33.6	14.9	19.8	0.091
JPF1009 - JPF1007 *5.07 - 4.98*	79	12.4	61.6	22.7	3.2	9.3	0.176

Table 3.2: *Summary of fractionation models calculated for Fremri-Námur, Askja and Kverkfjöll.*

rift segment. Within the low K_2O basalts crystalisation models have been succesfully fitted. The model bewteen JPF1014 and intra glacial sample JPF0974 gave a reflecting Σr^2 (0.312) in particular incompatible elements were too low in the model daughter suggesting differences in the source of the Fjallgarðar and Kverkfjöll low K_2O basalts.

At lower MgO post glacial lavas have lower SiO_2 contents for a given MgO than the intra and inter lavas (with the expetion of JPF1018). Good models were fitted to lower MgO bewteen these post glacial lavas with magnatie joining the crytalising assemblage at ~4.8 wt. % MgO. Models between the higher SiO_2 Inter and Intra glacial lavas fitted relatively well, some scatter of incompatible elements is seen; in particular DL074 lies to higher incompatible element concentration indicating differences within the parental magmas of these samples. Models to and from JPF1018 were unsuccessful, mainly due to much higher SiO_2 of this sample.

3.4 Crustal Contamination

It has long been recognised that Icelandic lavas have light $\delta^{18}O$ values relative to convecting upper mantel. Samples from the NRZ are no exception (figure 2.25, figure 2.26). Low $\delta^{18}O$ of meteoric waters is typical of high latitudes and the presence of extensive hydrothermal systems in Iceland has led many workers to the conclusion that combined assimilation of hydrothermally altered crust and crystallisation (AFC) is responsible for the low $\delta^{18}O$ (e.g. Hémond et al., 1988; Nicholson et al., 1991; Gee et al., 1998; Eiler et al., 2000). In particular Nicholson et al. (1991) proposed that extensive assimilation of light $\delta^{18}O$ silicic melts occurred under Krafla. More recently such assimilation models have been refined (e.g. Macpherson et al., 2005; Bindeman et al., 2006), suggesting that the assimilation of silicic melts is not consistent with the major element chemistry trends observed. Instead, in a study of lavas from the ERZ, Bindeman et al., (2008) proposed that 'bulk digestion' of altered hyaloclastite material was able to produce the range of light $\delta^{18}O$ values observed. The role and extent of contamination by altered crustal material will now be assessed for the NRZ. Due to the small number of $\delta^{18}O$ analyses from this study $\delta^{18}O$ values from Askja and Kverkfjöll analysed by Macpherson et al. (2005) are also considered.

3.4.1 Role of crustal contamination in generating light $\delta^{18}O$ lavas

Hydrothermal fluids are typically enriched in mobile elements such as Sr, Rb, Ba and U whilst having very low $\delta^{18}O$ values (Olafsson and Riley, 1978; Hattori and Muehlenbachs, 1982). As a result, hydrothermal alteration of rocks by such fluids will generate elevated concentrations of

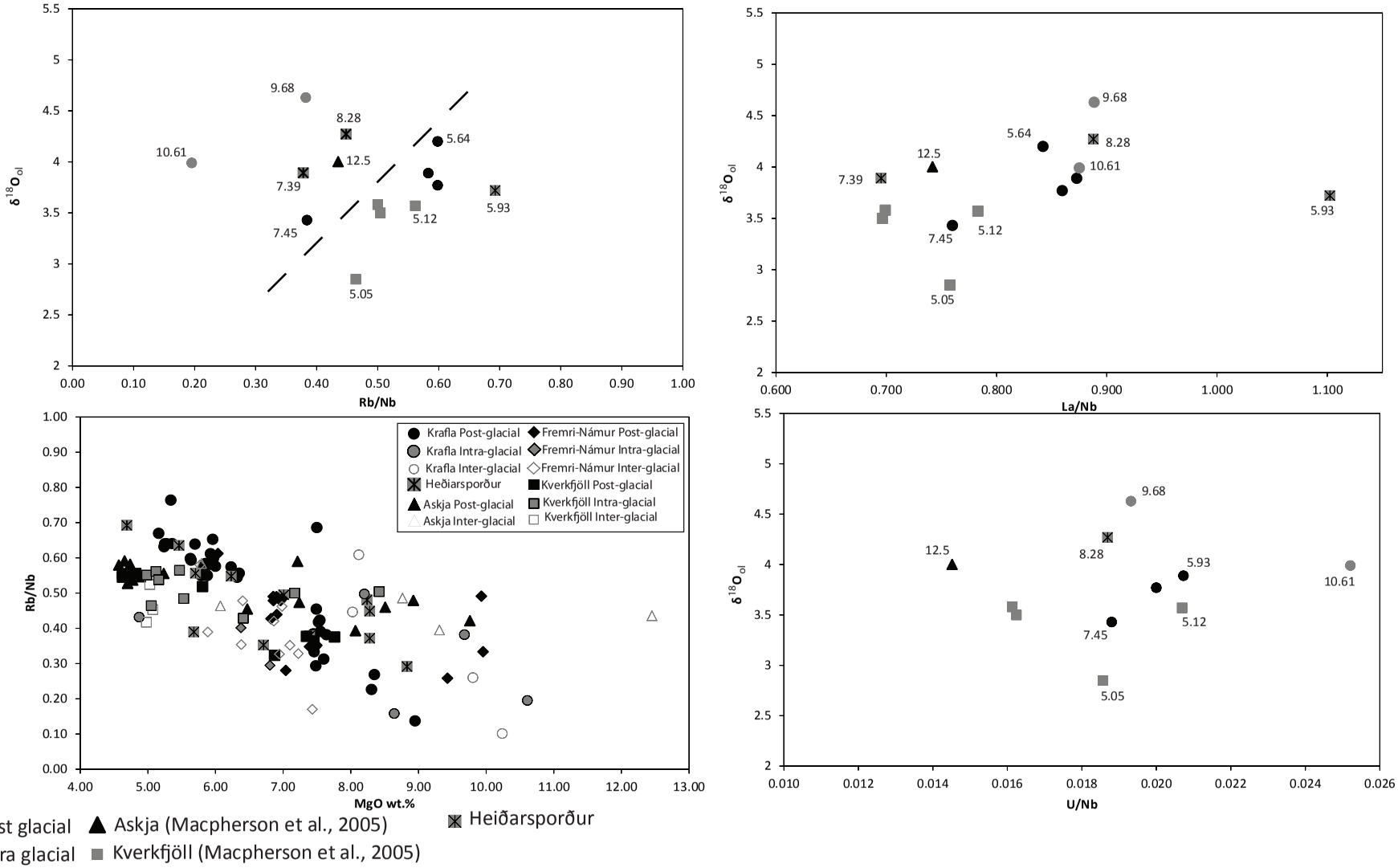

Figure 3.9: *Rb/Nb, U/Nb and La/Nb vs. $\delta^{18}O_{ol}$ and Rb/Nb vs. MgO wt.%. The number beside samples denotes MgO wt. %.*

these trace elements at low $\delta^{18}O$ values whilst immobile elements such as La, Nb, Th etc. will not be significantly affected. Therefore ratios such as Rb/Nb can potentially be used as tracers for the extent of assimilation of hydrothermally altered material. Figure 3.9 shows the relationship between Rb/Nb, La/Nb and U/Nb versus $\delta^{18}O$ as well as Rb/Nb vs. MgO wt. %. Rb/Zr values show a very weak correlation with $\delta^{18}O$ (correlation is less than 90% significant r^2 = 0.02), however on the whole samples that lie to higher $\delta^{18}O$ and lower Rb/Nb tend to be more primitive whilst sample that lie to lower $\delta^{18}O$ and higher Rb/Nb tend to be more evolved. This is in contrast with ratios such as La/Nb where no such relationship is seen, this could be interpreted as evidence for contamination.

Contamination by the lower crust

As chapter 4 will demonstrate a large number of basalts along the NRZ have crystallised in lower crustal magma chambers (>15 km). It is therefore unlikely that these lavas could have directly assimilated low $\delta^{18}O$ upper crustal material (*cf*. Nicholson et al., 1991; Bindeman et al., 2006). Instead the assimilation of lower crustal cumulates is far more likely and should be considered for these deep crystallising lavas. When attempting to model such processes it is important to bear in mind that there are several parameters that are not well-defined. Firstly the $\delta^{18}O$ value for the lower crust under Iceland is uncertain. Several attempts have been made to estimate this, most notably Maclennan et al. (2003) reported a number of $\delta^{18}O$ values from a suite of 40 gabbroic and wehrlitic nodules that are thought to have originated from near the MOHO. These crystals yield a range of values from 3.3-5.2‰ with an average $\delta^{18}O_{ol}$ of 4.5‰. In contrast, Thirlwall et al. (2006) attempted to estimate a value for the lower crust under the Reykjanes Ridge by defining an average value by compiling a range of published $\delta^{18}O$ values for the lower crust from ophiolites and xenoliths found around the world. The lowest mean value found for an individual location was 4.2‰, whilst the world-wide average has a $\delta^{18}O$ of 5.3 ‰. Although the lowest value reported by Maclennan et al. (2003) is lower than the lowest mean found worldwide the average value of 4.5 ‰ appears to be consistent with average values seen around the world. In addition, it is unclear how hydrothermal fluids might affect the $\delta^{18}O$ of the lower crust. Bindeman et al. (2008) suggested that the dehydration of fluids from digesting altered hyaloclastite blocks was a good mechanism to introduce low $\delta^{18}O$ fluids to depth. However it has been suggested by several authors that at depth $\delta^{18}O$ will increase. Values of +4-5 ‰ have been suggested by Hemond et al. (1993) and Breddam (2002) to be reasonable estimates of $\delta^{18}O$ for fluids at these depths. If this is the

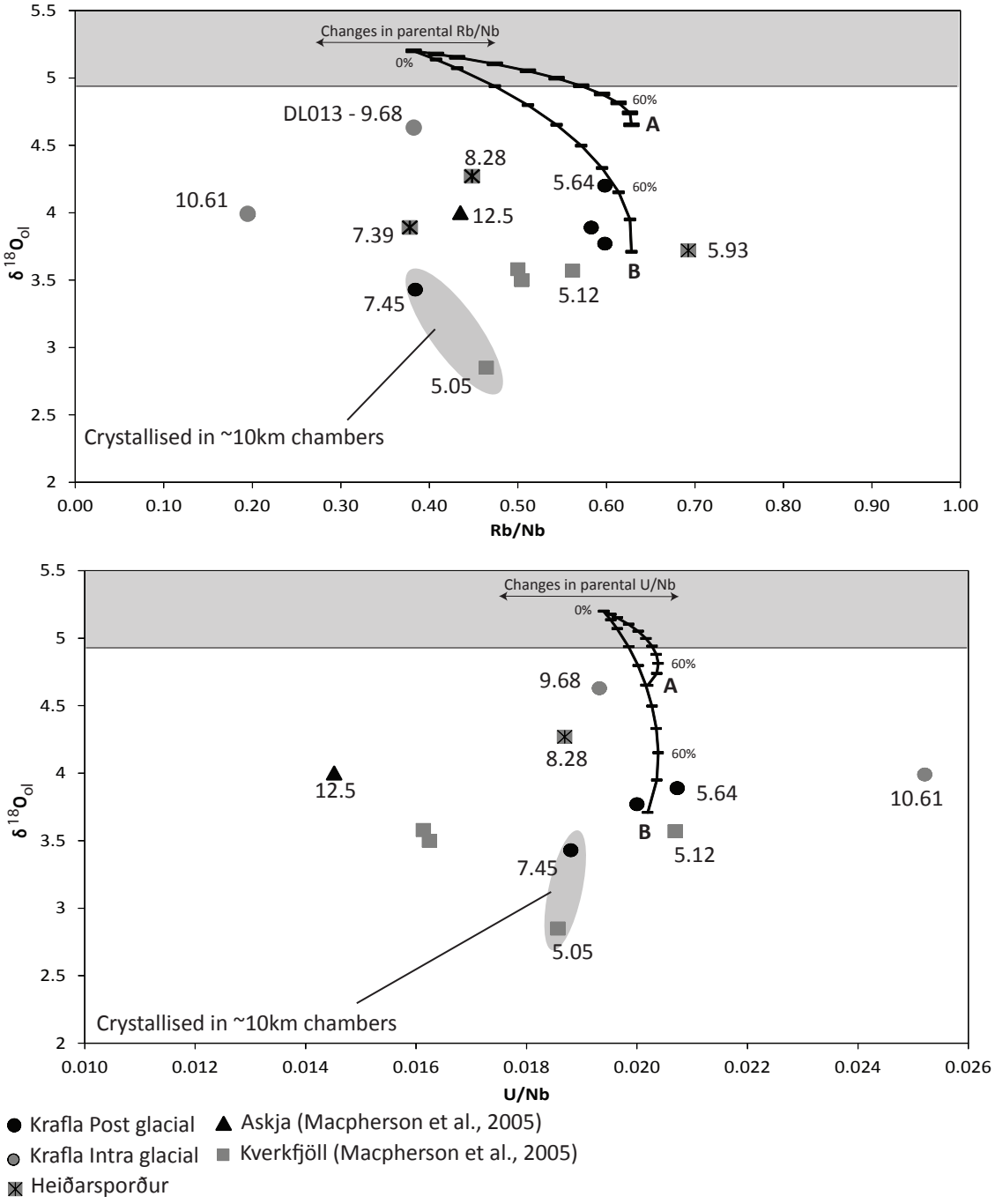

Figure 3.10 : *Bulk digestion trends for typical lower crust. Line A shows digestion trends for gabbro with $\delta^{18}O$ of 4.5‰ and Line B shows digestion trends for a $\delta^{18}O_{ol}$ of 3.3‰. Rb/Nb and U/Nb values for assimilant based on typical values found in Iceland gabbros from Thorarinsson and Tegner (2009) (Rb 6ppm; U 0.1 ppm; Nb 5 ppm). Parental source magmas taken to be similar to DL013 for these trends, however digestion curves will shift left or right reflecting variable enrichment in the Iceland source.*

case, then the interaction of fluids with lower crustal gabbros will not significantly change the mean $\delta^{18}O$ value.

The average value of $4.5_{(ol)}$ ‰ (Maclennan et al., 2003) appears to be a reasonable estimate of the mean $\delta^{18}O$ value of the lower crust, with values potentially ~1‰ lower where gabbros might have interacted with hydrothermal fluids.

If lower crustal material with a $\delta^{18}O$ of 4.5 ‰ was assimilated into magma with normal mantle $\delta^{18}O$, it would not be possible to generate trends that encompass the range of $\delta^{18}O$ values seen in NRZ lavas (Figure 3.10, line A). In order to generate such trends lavas need to assimilate gabbros with much lower $\delta^{18}O$. If a gabbro was assimilated that had the lowest $\delta^{18}O$ observed of 3.3 ‰ then the trends generated can reproduce the full range of values seen (Figure 3.10, line B), however large amounts of assimilation is needed (>60%); this is clearly inconsistent with the primitive nature of these samples. In addition, Trønnes (1990) highlighted that large amounts of lower crustal assimilation would led to high CaO/Al_2O_3 and Sr/Nd due to high proportions of cpx and plagioclase respectively in lower crustal assemblages; such high values are not observed in these samples.

3.4.2 Mixing with low $\delta^{18}O$ magmas at depth

It seems unlikely then that the assimilation of lower crustal material plays a significant role in the evolution of these lavas if normal mantle $\delta^{18}O$ is present under Iceland. However could contaminated lavas that crystallised near the upper crust be mixing at depth with normal mantle $\delta^{18}O$ magma to generate the range in values seen?

It is clear from recent seismic studies at Krafla that after eruptive episodes magma is able to drain downward to deep levels (e.g. Zeeuw-van Dalfsen et al. 2006). If this magma had undergone bulk digestion of hydrothermally altered material then this shallow low $\delta^{18}O$ magma could have the opportunity to mix with magmas in the lowest magma chambers. High MgO lavas have been demonstrated by Maclennan et al. (2008) to be not very well mixed, reflected by chemically heterogeneous olivine melt inclusions. Clearly then, if magmas are draining downwards only the effects of small amounts of mixing (~<15%) should be considered when modelling trends to most primitive, lower $\delta^{18}O$ lavas.

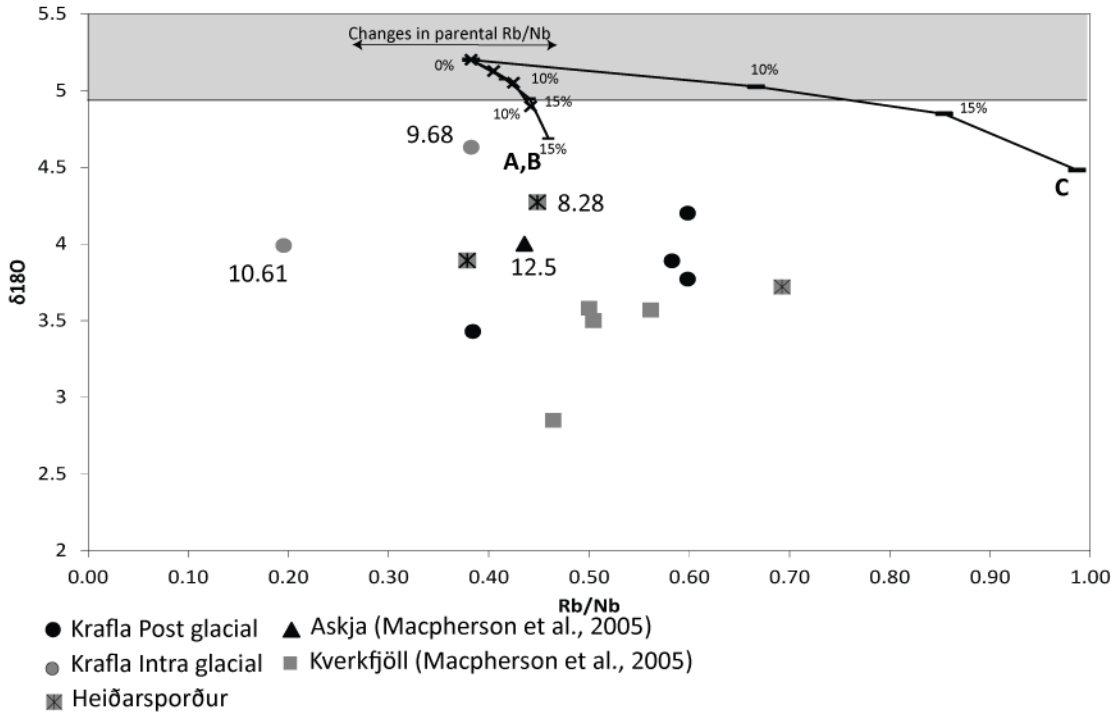

Figure 3.11: *Lines A, B and C represent a range of possible contaminants mixing into normal mantle $\delta^{18}O$. Line A (crosses for maker symbols) represents bulk digestion of altered basaltic hyaloclastite material with a $\delta^{18}O$ of 3‰. Line B (flat marker symbols) and C shows the assimilation of evolved contaminated lava (a dacite and a rhyolite respectively) with $\delta^{18}O$ of 2‰ and 0‰ respectively.*

Figure 3.11 shows the trends that a small amount of mixing would generate from a number of possible contaminated lavas into magma with normal mantle $\delta^{18}O$ magma. What is clear is that whether contaminated basaltic or more evolved lavas (lines A and C respectively) are mixed in small amounts, it is not possible to generate the low $\delta^{18}O$ seen in the most primitive samples.

This would therefore suggest that the range of $\delta^{18}O$ in the most primitive lavas record mantle values. If the higher Rb/Nb observed in the more evolved basalts reflects a contribution from contaminated magmas, it is difficult to generate a mixing or assimilation trend that encompasses both the low parental Rb/Nb, high MgO lavas and the more evolved basalts without evoking a low $\delta^{18}O$ mantle source. Indeed figure 3.12 demonstrates that if the mantle were allowed to have a $\delta^{18}O$ value of 4.5 ‰ and assuming the parental magma is no more depleted then DL013, then a maximum of ~60% AFC is needed to generate the more evolved lavas in this suit. This is consistent with the amount of fractionation required to produce a lava with ~5 wt% MgO.

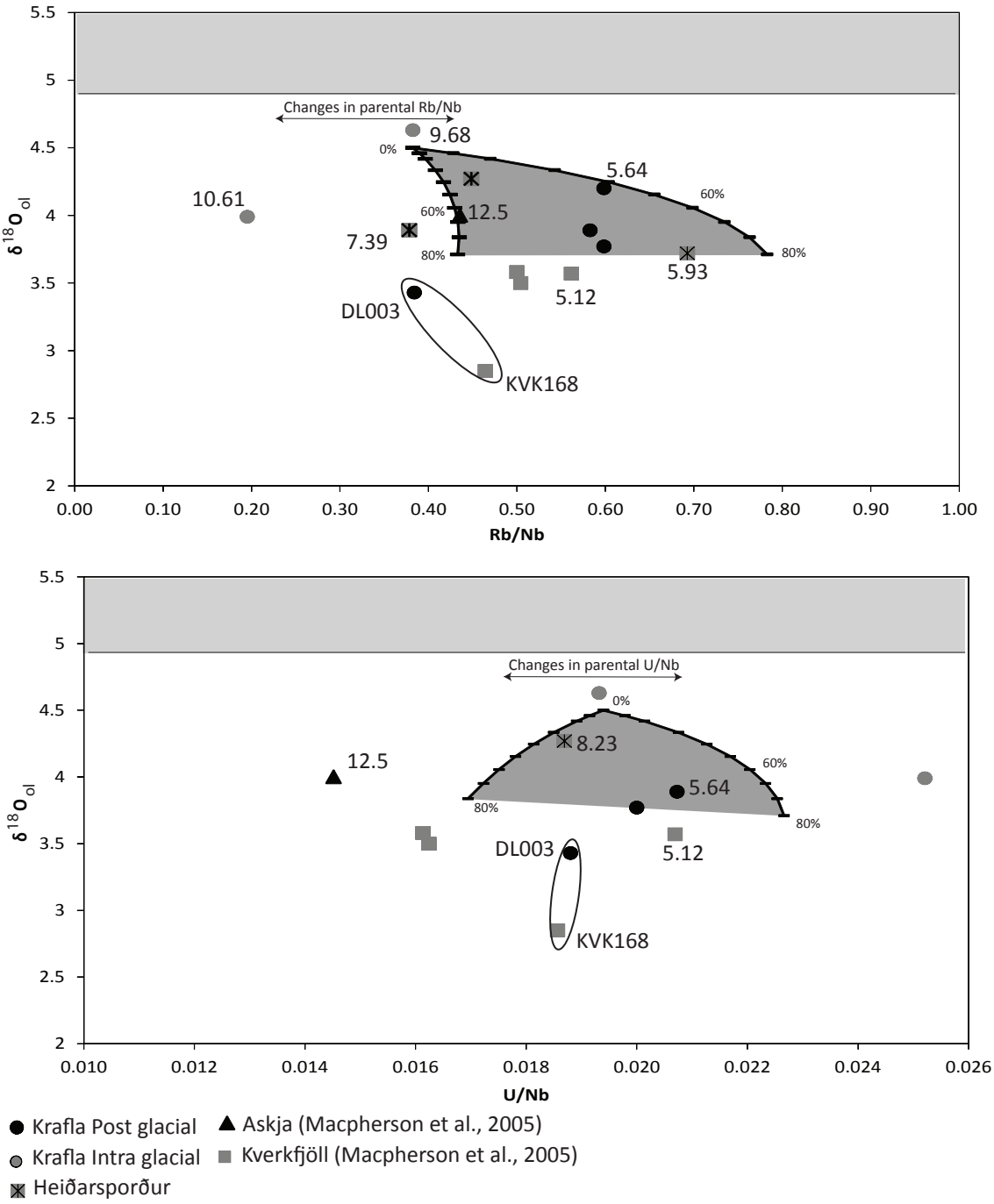

Figure 3.12: *Assimilation of gabbroic material with a $\delta^{18}O$ = 3.3‰ into a parental magma with a $\delta^{18}O$ of 4.5‰. The grey field shows the range of potential enrichment of the gabbroic assimilant. Encircled samples denote crystallisation in ~10km chambers.*

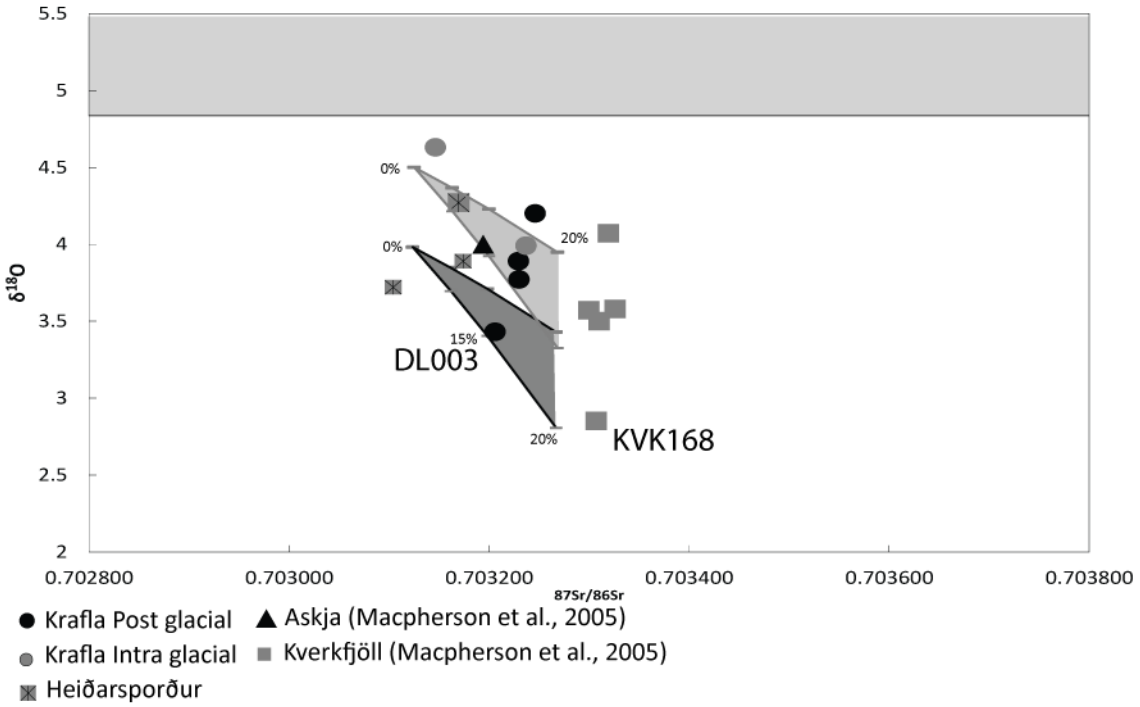

Figure 3.13: *AFC trends for assimilation of contaminated upper crustal material into a parental magma similar to the Younger Laxáhraun. Grey field show potential range of $\delta^{18}O$ in assimilants (upper line has a $\delta^{18}O$ of 0.5‰; lower line has δ18O of -4‰). Assimilant assumed to have an average crustal Nb/Zr ratio of 0.1 and a $^{87}Sr/^{86}Sr$ ratio of 0.7036 as suggested by Gee et al. (1998a).*

3.4.3 Extent of crustal contamination in upper crustal chambers

Assuming a low $\delta^{18}O$ mantle source figure 3.12 illustrates that contamination in the lower most crustal chambers cannot be entirely ruled out. However it is difficult to generate the lower $\delta^{18}O$ values seen in the shallowest chambers in the crust by the assimilation of gabbroic material without assimilating very large amounts (>80 %). DL003 and KVK168 in particular (from Krafla and Kverkfjöll respectfully) show the lowest $\delta^{18}O$ values in the NRZ and both have crystallised in chambers at ~10 km depth (section 4.3.3); at these depths magma is more likely to interact directly with hydrothermal altered upper crustal materials.

It is notable that DL003 (from the Younger Laxáhraun) shows elevated $^{87}Sr/^{86}Sr$ compared to other lavas analysed from the same eruptive unit (0.703206 compared to 0.703125 and 0.703126 for JPF0901 and JPF0902 respectively) whilst all having similar $^{143}Nd/^{144}Nd$ and Nb/Zr ratios. As noted previously by Macpherson et al. (2005) and Bindeman et al. (2006) the assimilation of evolved crustal melts would lead to elevated SiO_2 in magmas which is not observed in NRZ lavas. It was subsequently suggested that a basaltic assimilant with low $\delta^{18}O$ is required in order to fit major element trends. In particular Bindeman et al. (2006) suggested that hydrothermally altered hyaloclastite was the most likely assimilant due to higher

permeability and the often more disaggregated nature of hyaloclastite over lava flows; they further suggested that this material could have a range of $\delta^{18}O$ values between -4 ‰ and +0.5 ‰. Figure 3.13 shows the effects of assimilating material with this range of $\delta^{18}O$ values with the range of parental $\delta^{18}O$ values seen in the most primitive lavas. A maximum of 20% AFC is needed assuming a parental $\delta^{18}O$ of 4.63 ‰ (maximum $\delta^{18}O$ values seen) and with an assimilant having $\delta^{18}O$ = -4 ‰. The 20% estimate is significantly lowered if the parental $\delta^{18}O$ is lowered.

Whilst in principle the low $\delta^{18}O$ of KVK168 can be reproduced by the relatively small amount of assimilation of hydrothermally altered basalt (figure 5.13) this sample does not show the expected elevated $^{87}Sr/^{86}Sr$ ratios with respect to other the other Kverkfjöll samples, casting some doubt whether this particular mechanism is responsible for generating the $\delta^{18}O$ of this sample.

3.4.4 Effect on phenocryst populations

The preceding modelling illustrates that contamination by the lower crust as well as the draining of contaminated magmas downward cannot be entirely ruled out. Bindeman et al. (2006) highlighted that large scale digestion of material would lead to the 'liberation' of crystals into magma reservoirs. It might be expected that this would generate a population of disequilibrium phenocrysts in the contaminated lavas potentially showing strong disequilibrium textures (e.g. Trønnes, 1990). As figure 2.3 shows, large populations of such phenocrysts are not commonly seen. In particular it was suggested previously that the $\delta^{18}O$ and $^{87}Sr/^{86}Sr$ values of DL003 might have be generated by contamination. This sample however does not show a large populations of disequilibrium phenocrysts and consequently casts some doubt on role of hyaloclastite digestion in this sample.

Large populations of disequilibrium phenocrysts are seen in some samples, in particular from the Fremri-Námur volcanic system. Gabbroic nodules that are likely to have been entrained from the lower crust are present in various states of disaggregation in these lavas. This illustrates that contamination from the lower crust does occur however such samples are not associated with elevated $^{87}Sr/^{86}Sr$ or Rb/Nb indicating that the material that is being entrained may not have been significantly altered by hydrothermal fluids (figure 3.14). In addition, the assimilation of large proportions of gabbro might lead to elevated Sr/Nd ratios in these samples; however with the exception of one sample from Fremri-Namur these samples do not

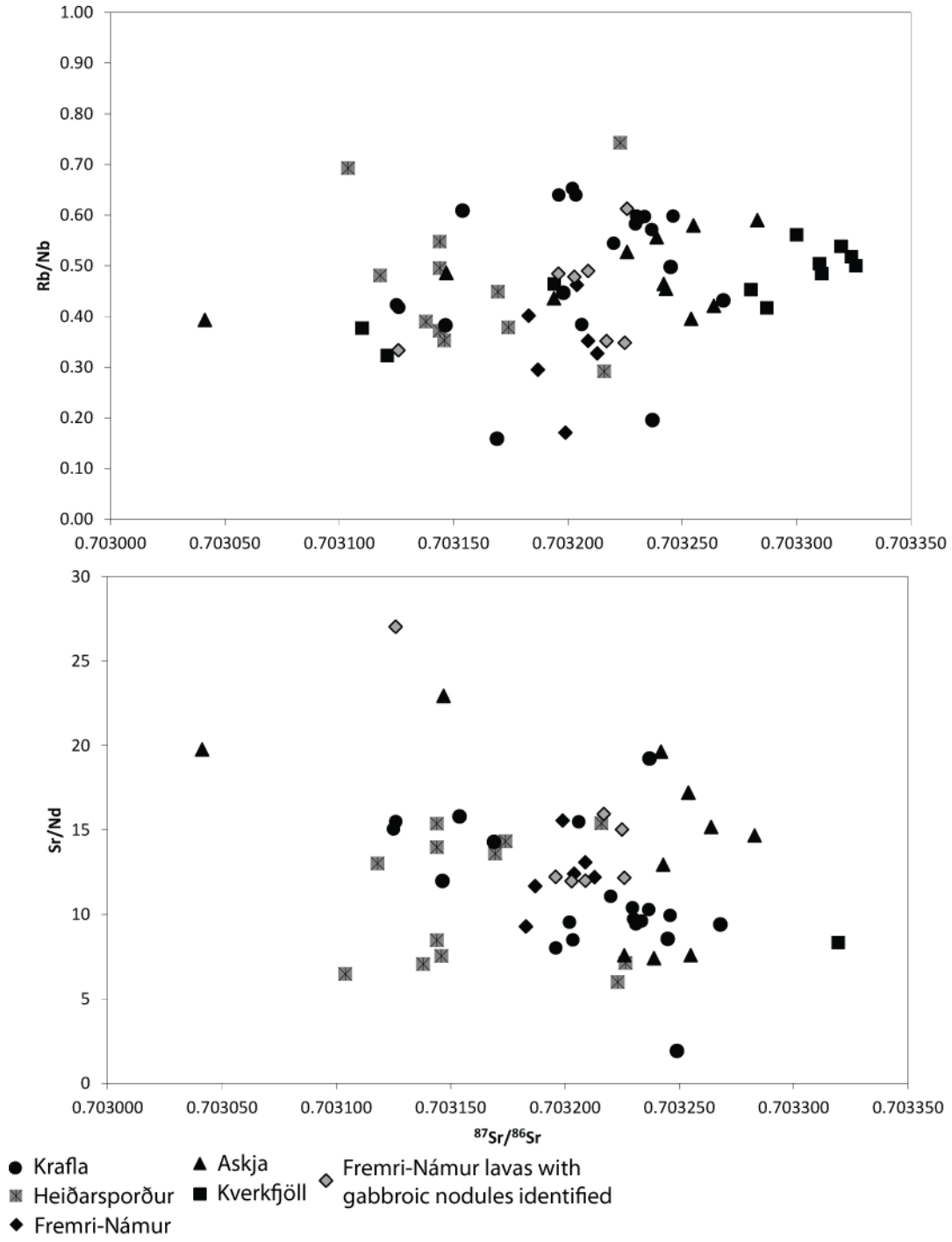

Figure 3.14: *Rb/Nb and Sr/Nd vs. $^{87}Sr/^{86}Sr$ for NRZ lavas. Samples with gabbroic nodules are shaded in grey and do not exhibit extreme chemical signatures.*

show evidence for elevated Sr/Nd ratios, perhaps indicating that generally only small proportions are entrained from the lower crust.

3.4.4 Heiðarsporður

Contamination may play a more significant role in the generation of lavas from Heiðarsporður. Near solidus differentiation has often been argued to take place in the generation of the most evolved lavas from this volcanic system (e.g. Jónasson, 1994) which are the most likely to have

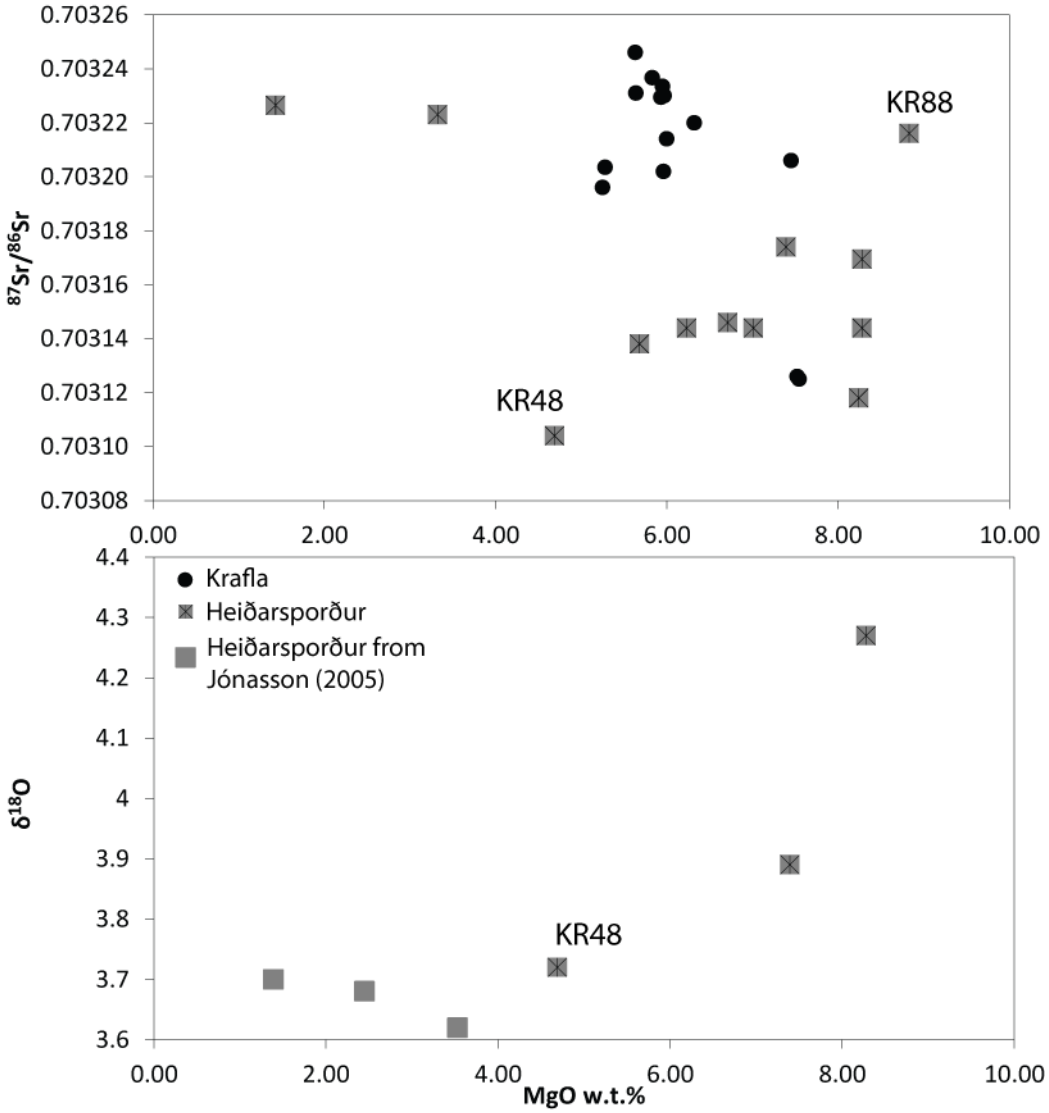

Figure 3.15: *$^{87}Sr/^{86}Sr$ and $\delta^{18}O$ vs. MgO w.t %.*

been contaminated by hydrothermally altered crust, often showing light $\delta^{18}O$ values (e.g. Nicholson et al., 1991) and crystallising in shallow upper crustal chambers (see chapter 4).

At first glance variations of $^{87}Sr/^{86}Sr$ and $\delta^{18}O$ vs. MgO wt. % (figure 3.15) appears to support a contamination model due to the presence of relatively high $^{87}Sr/^{86}Sr$ ratios and associated low $\delta^{18}O$ in the most evolved lavas from Heiðarsporður, however on closer inspection there are a number of problems with this suggestion.

Firstly the low $\delta^{18}O$ seen in the more evolved samples may not be entirely related to hydrothermal contamination. KR48 has a $\delta^{18}O$ value as low as the most evolved samples however this sample has very low $^{87}Sr/^{86}Sr$ for its $^{143}Nd/^{144}Nd$. If then the low $\delta^{18}O$ of this sample was a function of contamination it is likely the $^{87}Sr/^{86}Sr$ ratios will have increased. It is, however, not possible to fit an assimilation trend from a more depleted source to produce a sample with the Nd-Sr ratios of KR48 (figure 3.16). This indicates that the low $\delta^{18}O$ seen in

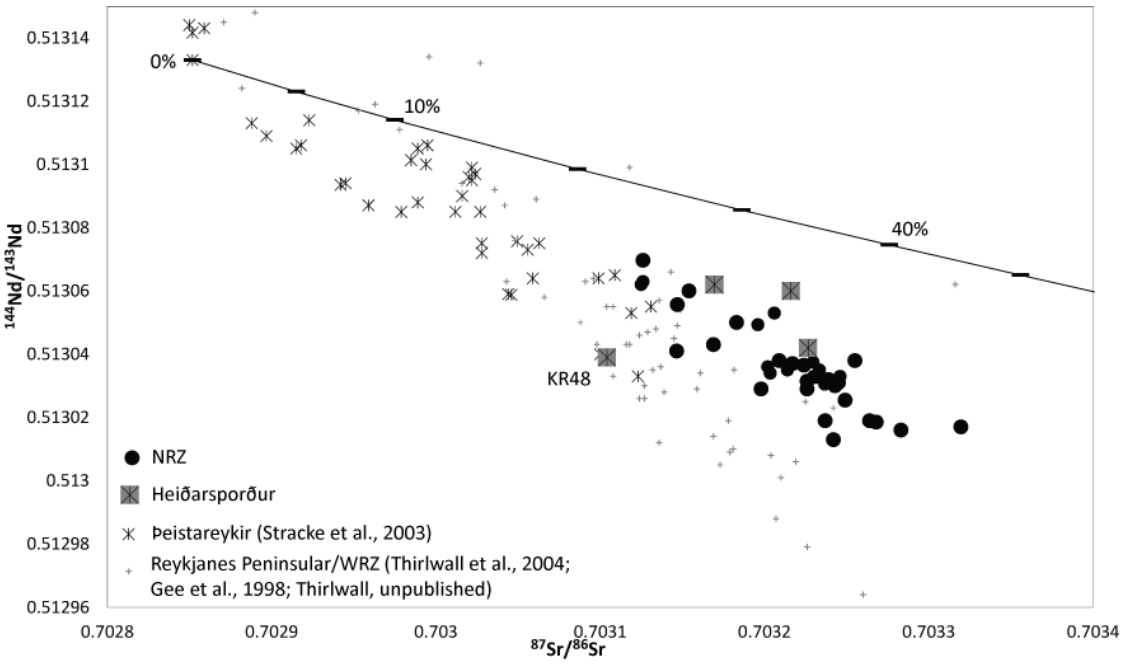

Figure 3.16: *$^{143}Nd/^{144}Nd$ vs. $^{87}Sr/^{86}Sr$. It is not possible to reproduce the Nd-Sr ratios of KR48 by assimilation. KR48 is a moderately evolved lava, therefore in order to reproduce similar $^{87}Sr/^{86}Sr$ values a very depleted source is needed in order to allow for sufficient fractionation. The steepness of the assimilation curve is controlled by the $^{143}Nd/^{144}Nd$ value of the assimilant. This curve has a $^{143}Nd/^{144}Nd$ of 0.51296, the lowest ratio reported for an Icelandic lava. A $^{87}Sr/^{86}Sr$ of 0.7036 was used in the assimilant as suggested by Gee et al. (1998a).*

these lavas may be a primary signature. In addition the high $^{87}Sr/^{86}Sr$ ratios in the low MgO samples are within the range of typical Krafla values as well as the most primitive Heiðarsporður lavas, KK88. Due to the primitive nature of KR88 it is unlikely this sample will have undergone a significant amount of contamination as such it is likely that the high $^{87}Sr/^{86}Sr$ ratios seen at Heiðarsporður also reflects a primary signature.

Petrographic evidence reported by Jónasson (2005), as well as DL067 from this study, shows evidence of gabbroic nodules present in theses lava. As with the Fremri-Námur system, this clearly indicates crustal material is indeed contaminating these lavas, however as with Fremri-Námur it is likely that this material is relatively fresh due to the absence of the extreme geochemical signatures expected from assimilation of hydrothermally altered material (figure 3.14).

3.5 Summary

- Alteration and accumulation clearly does not play a major role in systemically affecting the major and trace element chemistry of this data set.

- There is no evidence for significant accumulation of olivine however a few clear examples of plagioclase accumulation are present, seen clearly seen in Sr/Zr and Al_2O_3 vs. MgO plots. Optical inspections reveal that these lavas contain large gabbroic nodules that are likely to have been entrained from the crust. This would indicate that the accumulation of plagioclase in these samples is the result of extensive entrainment of crystals from the crust and not by the settling of crystals.

- Fractional crystallisation can explain the vast majority of major and trace element trends. Despite the tighter trends seen in this data set modelling confirms the observations of Maclennan et al. (2001) that different liquid lines of decent are present, not just at Krafla but at all other rift segments. These differences between parental magmas are mostly seen between post and inter/intra glacial samples, indicating shifts of parental magma composition over time.

- Trace element fractional crystallisation models have however not always been successful in reproducing trends seen with concentrations often too high to be explained by closed system fractionation models. Resent proposals for MORB sample sets by O'Neill and Jenner (2012) have revisited magma replenishment models similar to those first proposed by O'Hara (1977) and Albarede (1985). In these models continual replenishment of magma chambers by more primitive melts leads to systematic increases of incompatible element concentration that cannot be accounted for by fractional crystallisation whilst major elements remain on ol-plag-cpx cotectics. Such a model provides a potential explanation for the failure of closed systems fractionation to account for some of the elevated trace element concentrations from this data set. Together with evidence of populations of primitive phenocrysts found in relatively evolved basalts indicated that simple closed system fractional crystallisation may be too simplistic and that open system models such as magma replenishment may be more appropriate.

- Helgason (1989) reported that lavas from Fjallgarðar could be split into high and low K_2O lavas. Such a division can be seen in this data set as well as in lavas from Kverkfjöll.

Postglacial lavas from Askja can also be divided, samples clearly show low and high SiO_2 groups.

- Lavas from Heiðarsporður are anomalous in that fractional crystallisation trends do not dominate these lavas. Fractionation models were successful in modelling trends up to ~7.5 MgO wt. % however more evolved samples show higher SiO_2 for a given MgO then other rift segments as well flat Fe_2O_3 and Al_2O_3 patterns, inconsistent with fractionation of ol-plag-cpx.

- Jónasson (2005) suggested that near-solidus differentiation, whereby segregation of partial melts from either cooling bodies of magma or heating of hydrothermally altered crust by deformation, probably during a rift event, can account for these trends. Evidence of such an event can be seen in DL067 were large gabbroic nodules that show strong reabsorption textures are present.

- Jónasson (2005) argued that this is also reflected by the evolved lavas showing lower $\delta^{18}O$ then the most primitive samples. Sr-Nd isotopic analyses show however that it is difficult to generate assimilation trends that reproduces these low $\delta^{18}O$ coupled with the unradiogenic $^{87}Sr/^{86}Sr$ ratios seen in these lavas. sorry to bother you, I used to live here and accidently an amazon package sent here! when it arrives would it be ok you gave me a quick text and I can come and pick it up! inconvenience

- Constraints on depths of crystallisation (presented in the next chapter) have enabled more accurate crustal contamination models to be assessed. It is clear that the majority of lavas crystallise at depths >15 km, therefore the most likely assimilant will be the gabbroic lower crust. Whilst is it not possible to categorically rule out assimilation it is not possible to generate trends that encompasses the range of $\delta^{18}O$ seen in this dataset without evoking a mantle with a $\delta^{18}O$ of ~4.5‰.

CHAPTER 4: CRUSTAL STRUCTURE AND MAGMATIC PLUMBING ALONG THE NORTHERN RIFT ZONE

4.1. General Comments

Over the past several decades there has been considerable interest in the depth and location of magma chambers beneath active volcanic systems in Iceland (e.g. Tryggvasson 1986; Strukell et al., 2006; Kelley and Barton, 2008). This of importance for several reasons including the interpretation of precursory volcanic activity, placing constraints on magma evolution, understanding thermal gradients and developing models of crustal accretion (Kelley, 2009). With increasing precision and larger data sets, recent studies have shown that the magmatic plumbing dynamics may be more complicated than previously thought (e.g. Kelley and Barton, 2008; c.f. Sigurdsson and Sparks, 1981; Jónasson, 1994; Brandsdóttir et al., 1997) The large number of lavas collected over age range in this study provides a good opportunity to investigate the extent to which this is the case along the NRZ. In addition, this information combined with the current understanding of crustal structure and the large suite of mineral data presented in Chapter 2 provides an opportunity to investigate typical magmatic processes that occurs along the rift zone.

4.2. Current Understanding of Structure and Plumbing

Over the past several decades there have been many methods used in order to assess the structure and magmatic plumbing of the Icelandic crust. In particular Krafla and Askja have been the subject of close scrutiny as they are the only two volcanic centres along the NRZ that has seen recent magmatic events. Table 4.1 summarises the crystallisation depths determined by both geophysical and geochemical methods.

4.2.1 Geophysical Methods

Since the respective 1975-1984 and 1961 rifting episodes at Krafla and Askja, these two volcanic centres have been the focus of numerous geophysical studies. The resolution and precision of these techniques have improved greatly over the past 50 years enabling a detailed picture of magma movement and crustal structure to be formed.

Early seismic and geodesic studies have shown clearly that both Krafla and Askja have shallow magma chambers at ~3 km depth (Einarsson, 1978; Tryggvasson 1986; Rymer and Tryggvasson 1993, Brandsdóttir et al., 1997), however the presences of deeper bodies has been harder to

constrain. Tryggvason (1986) first suggested that multiple stacked magma chambers might be present under Krafla but was unable to ascertain the depths of these bodies. It was only until more recent geodesic and gravity studies by de Zeeuw-van Dalfsen et al. (2004, 2006) that showed that magma is currently draining from the shallow chamber at Krafla to depths of around 21 km. Similarly a number of workers showed that a similar process was occurring at Askja after the 1961 eruptive event where magma was draining to depths greater than 16 km (Pagli et al., 2006, Strukell et al., 2006, de Zeeuw-van Dalfsen et al., 2005). Further evidence that melt is present at these depths has been put forward by the recent observations of micro earthquakes at depths between 14-26 km under Askja and Upptyppingar (a Hyaloclastite ridge associated with the Kverkfjöll rift system). Soosalu et al. (2010) and Jakosdottir et al. (2008) have interpreted these earthquakes as the recent active migration of melt through these parts of the crust.

As well as these local studies there are also a number of regional seismic refraction profiles (Figure 4.1) which have shed light on the thickness and structure of the crust. In the context of these studies the terms 'upper crust' and 'lower crust' are used slightly differently from petrological definitions. The upper crust is characterised by P-wave velocities of typically less than 6.5 km s^{-1} and velocity gradients in excess of 0.2 s^{-1} (Flovenz, 1980; Darbshire et al., 2000). These low velocities are thought to signify the presences of fresh porous basaltic flows and hyaloclastite material (Flovenz 1991, Maclennan et al., 2001). In contrast the lower crust is characterised by P-wave velocities of ~6.5-7.4 km s^{-1} with velocity gradients <0.02 s^{-1}. The 6.5 km s^{-1} isovelocity surface is usually taken to define the top of petroglogical lower crust (Kaban et al., 2002). Based on the velocity structures observed workers have interpreted the nature of the crust in two very different ways. The first model proposed has a hot thin crust (10-15 km) underlain by a partially molten upper mantle (e.g. Palmason 1971, Beblo and Bjornsson 1978, 1980, Gebrande et al., 1980); whereas the second model consists of a cooler, 20-40 km thick crust (Bath 1960, Zverev et al., 1976, Staples et al., 1997, Darbyshire et al., 1998, 2000, Kaban et al., 2002). The latter of these two models is currently more widely accepted due to the identification of strong wide angle reflections at 15-40 km depth that have been interpreted as the Moho (Båth 1960; Bjarnason et al., 1993; Darbyshire et al., 1998).

The three main refraction profiles that have sectioned the NRZ (FIRE, ICEMELT and B96) have shown an overall thickening of the crust towards Vatnajökull. At the top of the NRZ the crust is ~25 km thick and reaches a maximum thickness of ~40 km thick under the Bárðarbunga rift system (Darbyshire et al., 2000). This greatly increased thickness is thought to be due to higher melt productivity at the plume head, outstripping the effects of crustal thinning at the plate

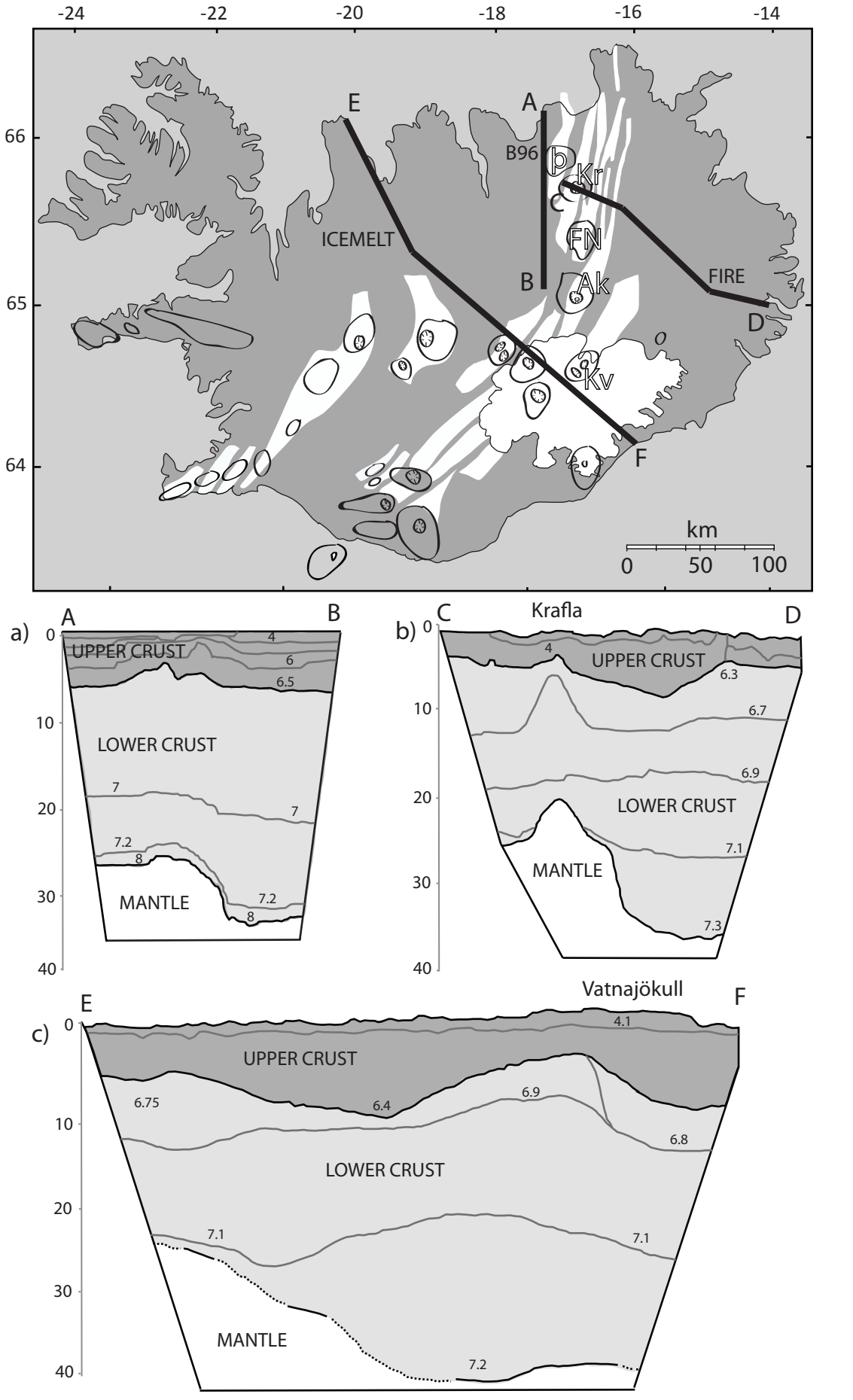

Figure 4.1: *Summary of seismic refraction profiles along the NRZ. Data from Menke et al., (1998), Staples et al., (1997) and Darbyshire et al., (2000) for B96, FIRE and ICEMELT respectively. Numbers in sections denote seismic velocities in km s^{-1}.*

boundary (White and McKenzie, 1995). The effect of crustal thinning is seen most prominently under Krafla were crustal thickness reaches a maximum of ~19 km (Brandsdóttir et al 1997). The upper crust is typically ~4 km thick under the spreading axis and becomes ~10 km thick off rift (Staples et al., 1997; Darbshire et al., 1998). Staples et al. (1997) and Brandsdóttir et al. (1997) located a high velocity dome under Krafla in the lower crust. This zone extends downward from Krafla's shallow 3 km magma chamber to a depth of ~10 km. This feature is hinted at in the ICEMELT profile under the rift zone however the traverse does not pass directly under a central volcano, unlike the FIRE profile. Brandsdóttir et al. (1997) interpreted this dome as the presence of olivine rich cumulates that form at the bottom of the shallow magma chamber which then subsided downward during rifting. These features were used by Menke et al (1998) to locate the roots of extinct central volcanoes along the B96 profile which traversed the western flank of the NRZ.

Darbyshire et al. (2000) re-evaluated the structure of the Icelandic crust determined by the refraction profiles using receiver function modelling based purely on the changes in velocity gradient. Overall an upper crustal thickness of ~4km and total crustal thickness of ~19 km broadly agree with the FIRE refraction profile under Krafla, however a strong low velocity zone (LVZ) was observed at 10-16 km depth. This LVZ has been interpreted by Darbyshire et al. (2000) to be the presence of melt at this depth, perhaps signalling the presents of partially molten sills.

4.2.2 Petrology

Geophysical studies have shown that both Krafla and Askja have shallow magma chambers present at around 3-5 km, although the exact depths of deeper chambers has proved more difficult to detect (e.g. Tryggvasson, 1986). Geochemical techniques provide an independent method to assess depths of proposed deep chambers as well as to investigate the plumbing of volcanic centres in areas were geophysical information is absent. The geobarometer of Putirka et al. (1996) has been generally accepted to give reliable pressures from liquid-clinopyroxene pairs and has been used in a number of studies of central volcanoes within the NRZ (e.g. Slater et al., 2001; Maclennan et al., 2001; Kuritani et al., 2011; Winpenny and Maclennan, 2011). Often these studies have been supplemented by crystallisation pressure calculations on whole rock or glass analyses in order to locate areas of significant crystallisation (i.e. magma chambers). A summary of current understanding of crystallisation depths from the NRZ follows.

Krafla

Maclennan et al. (2001) reported crystallisation pressures using both clinopyroxene thermobarometry and whole rock barometry according to the methods of Putirka et al. (1996) and Yang et al. (1996) respectively. Both methods revealed crystallisation depths between 10-21 km. Schiellerup (1995) reported crystallisation pressures from a number of glasses from the intra-glacial Blafjall hyaloclastite ridge (situated between the Krafla and Fremri Námur rift segments) using the method of Elthon (1984). He identified two areas of crystallisation: 7-10 km depth and 12-17 km depth. With respect to seismic observations, both these studies appear to be consistent with magma draining to ~ 21 km depth, furthermore the samples that show shallower crystallisation pressure estimates appear to agree with the Darbishire et al. (2000) interpretation of the LVZ.

Askja

Crystallisation pressures estimates from Askja have only been calculated on a small number of samples all from the 1875 eruption. Kuritani et al. (2011) calculated the crystallisation pressures for 13 clinopyroxenes from an icelandite the results of which gave an average pressure of 128 MPa (4.5 km). Kelley and Barton (2008) calculated the pressures from 8 glasses (analysed for major elements by Sigurdsson and Sparks, 1981) which largely agree with Kuritani et al. (2011) estimate of ~4-5 km; one sample yielded a much deeper pressure of 520 MPa (18 km). These results are consistent with seismic observations that a shallow magma chamber is present, however there is limited evidence that a lower chamber exists.

Kverkfjöll

Kelley and Barton (2008) complied 6 intra-glacial glass analyses from Hoskuldasson et al. (2006) and Hansen and Gronvold (2000). They observed two main depths of crystallisation, one at ~10-17 km deep and another at ~30km deep. The shallower crystallisation depths are consistent with the micro earthquake observations of Jakobsdottir et al. (2008) showing that melt is present at these depths, furthermore the deeper crystallisation estimates are consistent with the inferred crustal thickness under Kverkfjoll based on available seismic refraction profiles.

4.3. Crystallisation Pressures

4.3.1 Method

Crystallisation Pressures were calculated using algorithms written by Kelley and Barton (2008) using the equations derived by Yang et al. (1996). A series of predicted liquid compositions are

calculated using the equations of Yang et al. (1996) that lie along the *liquid-ol-plag-cpx* cotectic at 100 MPa increments from 100-1200 MPa. These liquid compositions are then converted to normative mineral components and projected from *plag* onto the *ol-cpx-qtz* pseudoternary plane and from *ol* onto the *plag-cpx-qtz* plane. The normative mineral composition calculated for each pressure increment is then regressed to generate an equation; this equation can then be used to find the pressures of crystallisation for the sample of interest. By doing this for each normative mineral projected from *plag* and *ol* six pressures are calculated in total. These values are then averaged to give a final crystallisation pressure with the 1σ reproducibility of these six values giving the associated uncertainty.

Kelley and Barton (2008) tested the accuracy of this method on two sets of glass compositions, one from experiments on natural samples and the other of purely experimental compositions. The first data set calculated pressures that agreed within ± 120MPa of experimental pressures whilst the second set calculated pressures that agreed within ± 90 MPa of experimental pressures. Kelley and Barton (2008) suggested that the pressures calculated with this method are accurate to within ~110 MPa. Yang et al. (1996) assessed the uncertainty of the individual pressure estimates calculated from the standard deviation of the mean of replicate electron microprobe analyses, which yielded a value of ± 50 MPa (2σ) whilst the uncertainties of the final averaged pressures from the Kelley and Barton (2008) experimental glass data set gave a larger value of ± 60-80 MPa (1σ). Subsequently samples with calculated uncertainties larger than 80 MPa were discarded.

Furthermore, in order to independently assess the accuracy of this method a number of crystallisation pressures from Krafla and the ERZ have been compared with pressures calculated from cpx thermobarometry the results of which show that overall both pressures are in agreement within error (Figure 4.2).

Other workers have devised similar methods to calculated crystallisation pressures (e.g. Langmuir et al., 1992; Danyushevsky et al., 1996; Herzberg, 2004) however the method used in this study has been selected as it has been widely used by workers on the NRZ. This enables a direct comparison of the results from this study.

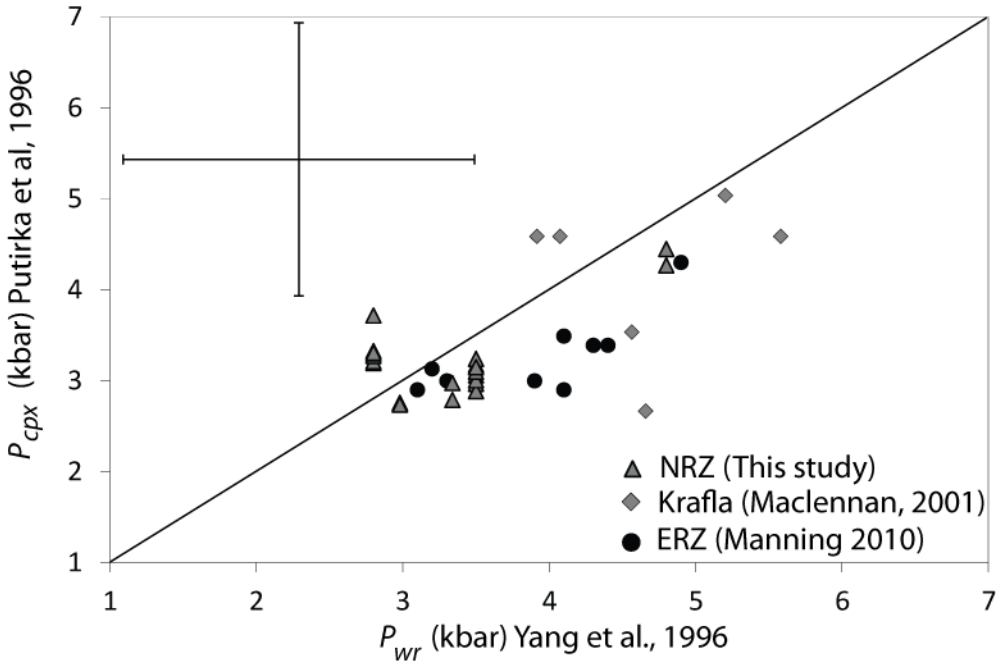

Figure 4.2: *Comparison of pressures calculated by whole rock (Yang et al, 1996) and clinopyroxene methods (Putirka et al., 1996).Solid back line is 1:1 line. Error quoted is the accuracy of each method to 1σ.*

4.3.2 Sample selection

As stated above the pressures of crystallisation are calculated using whole rock analyses that lie along the *liquid-plag-ol-cpx* cotectic, it is therefore important to filter the data set for samples that only crystallise *ol-plag-cpx* and samples that may have had its chemistry altered, which would lead to erroneous pressures.

Firstly the accumulation of phenocryst will affect the whole rock composition of lavas, these samples (which were identified in the previous chapter i.e. figure 3.3) have therefore been excluded from the pressure calculations. Furthermore mixing and assimilation can alter whole rock compositions; however identifying such samples can be difficult. The role of mixing and assimilation on the pressures calculated will be discussed in section 4.4.1.

High MgO samples were included in the calculation of pressures despite only showing evidence for *ol-plag* crystallisation, as whilst these do not accurately reflect the pressure of crystallisation these values can be used to define a minimum pressure at which these high MgO lavas could have crystallised at.

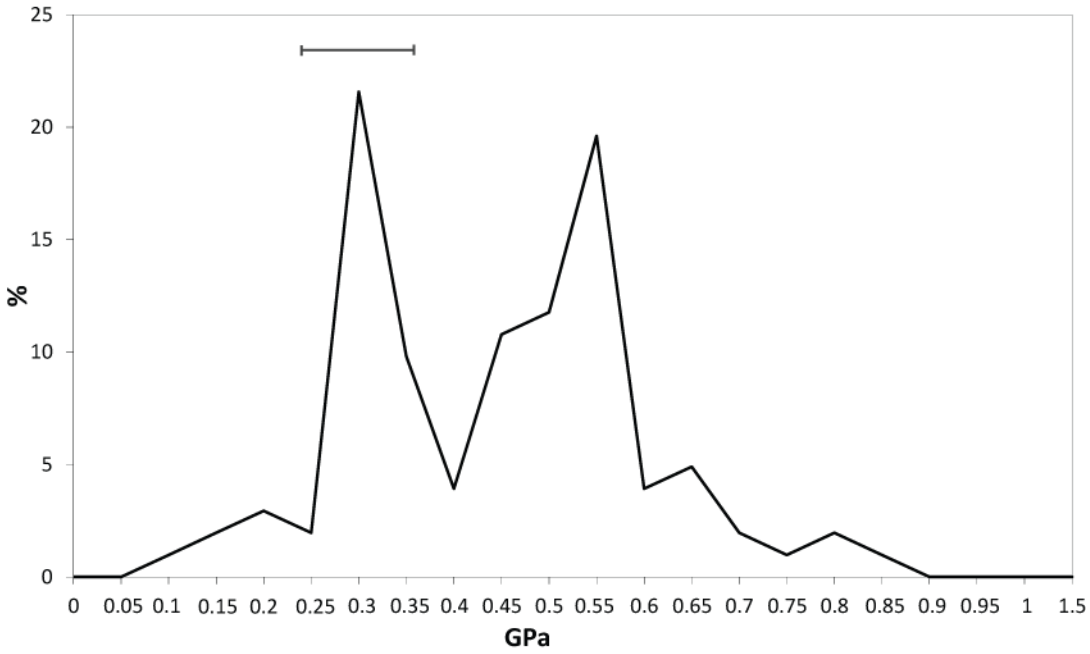

Figure 4.3: *Calculated crystallisation pressure for all filtered NRZ samples (n=102). Two pressure peaks are seen at ~ 0.3 GPa and ~ 0.55 GPa. Horizontal bar shows uncertainty of the calculated pressures.*

4.3.3 Results

All filtered pressure results for the NRZ are plotted in figure 4.3. Depths calculated assuming a crustal density of 2900 kg m^{-3}, roughly the density of basaltic surface rocks in Iceland (Maclennan et al., 2001; Kelley, 2009). Results are presented in Appendix 4.

4.3.3.1 Pressures versus MgO

Michael and Cornell (1998) were the first to identify similar relationships in a selection of MORB samples from around the globe. At high MgO they observed that lavas show decreasing pressures with decreasing MgO due to the fact that more evolved magmas had more opportunity to evolve toward a lower pressure cotectic. Below ~7-8 wt% MgO lavas tended to level out forming horizontal pressure arrays. Michael and Cornell (1998) described these arrays as 'the best estimate of where final crystallization took place'. Kelley and Barton (2008) reported that most of their samples plotted along such pressure arrays and suggested that these areas of significant crystallisation best represented the depth of magma chambers under central volcanoes. Figure 4.4 shows crystallisation pressures calculated for all samples separated by rift segment as well as showing CaO/Al_2O_3 vs MgO plots to help identify what samples are in equilibrium with *ol-plag-cpx*. All pressure graphs show crustal and mantle boundaries extrapolated from seismic reflectance work for reference.

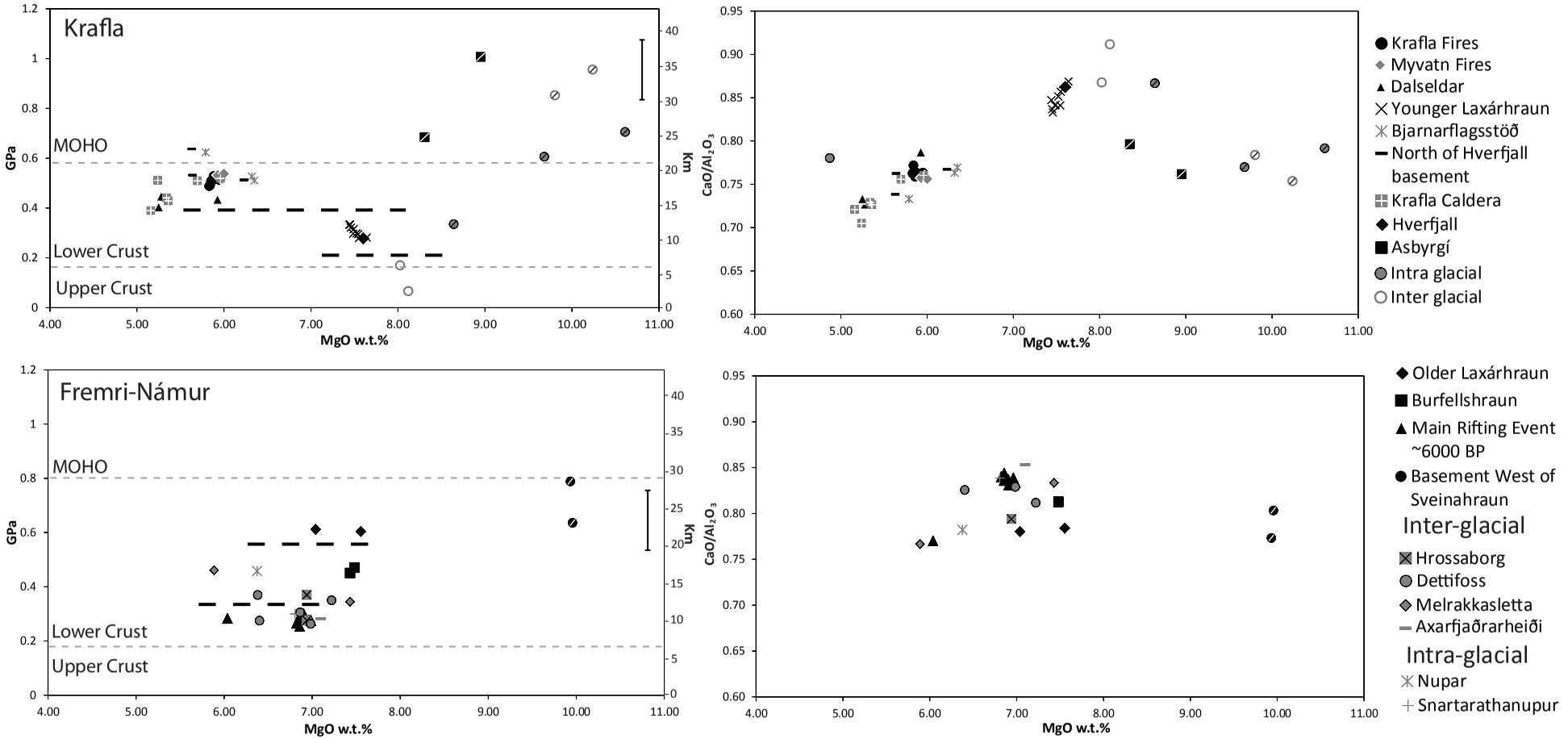

Figure 4.4: *Crystallisation pressures vs. MgO w.t. %, CaO/Al_2O_3 vs. MgO w.t. %. Samples have been grouped by eruptive event. The key is listed in age order (youngest at the top). Samples with black/white bars indicate samples that are in equilibrium with olivine and plagioclase. Dashed black lines delimit arrays identified whilst dashed grey line show relative positions within the crust (Data extrapolated from Staples et al., 1997; Menke et al., 1998; Darbyshire et al., 2000).*

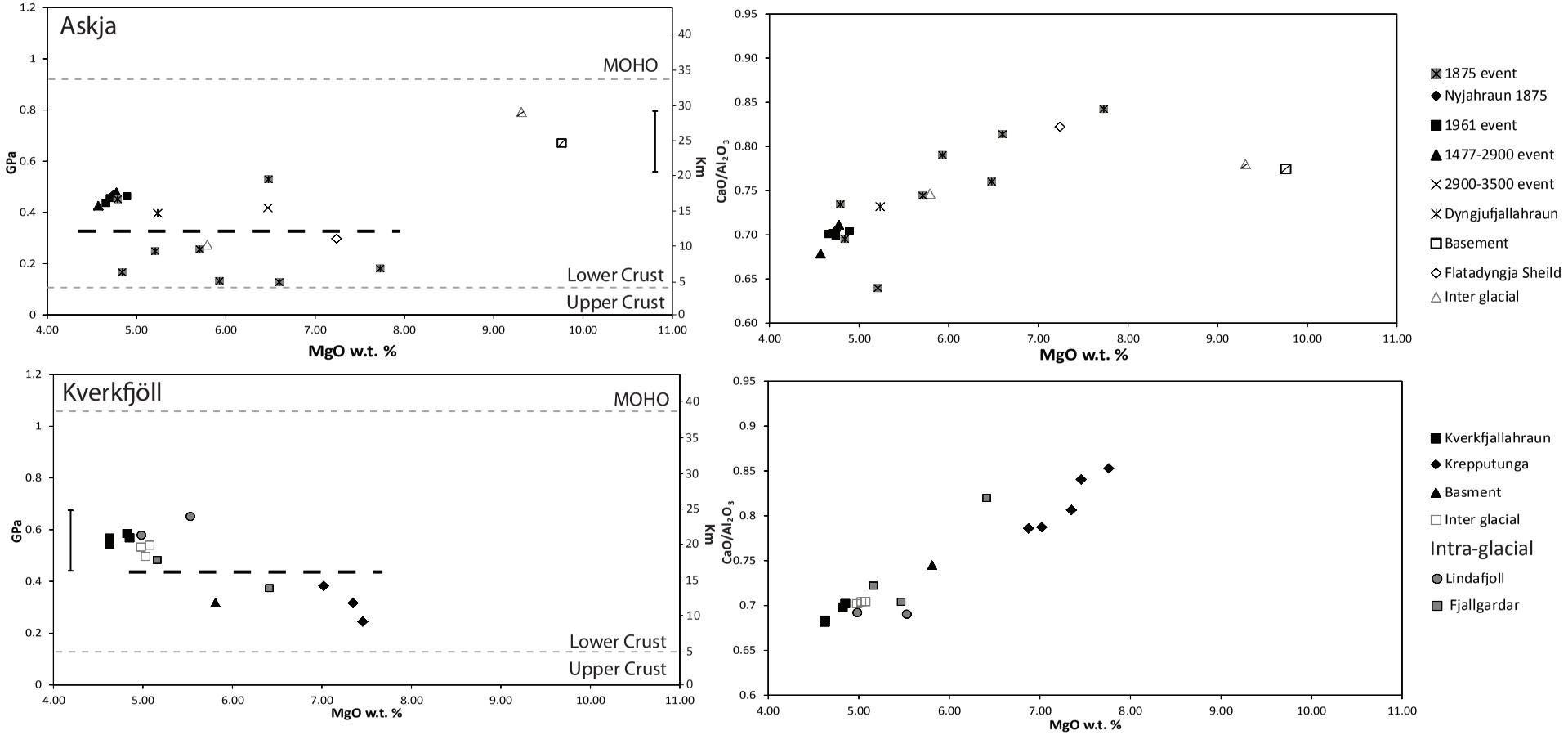

Figure 4.4 *cont.*

Krafla: CaO/ Al_2O_3 vs MgO plots and petrological observations show that the majority of post glacial samples are in equilibrium with *ol-plag-cpx*. Within these samples three potential horizontal pressure arrays are present. There is slight scatter within each group, however the range in pressures is about equal to the expected precision of the results therefore an average was taken to define each array. The majority of the samples appear to originate in a magma chamber at ~18km depth. A smaller number of samples show that crystallisation also occurs at ~11km depth. Based on seismic reflectance work both arrays appear to be located in the lower crust. In contrast, the two interglacial samples that are in equilibrium with *ol-plag-cpx* have crystallisation pressures of ~4 km providing evidence for crystallisation in shallow upper crustal chambers similar to those identified by seismic studies.

Despite significant scatter within the Intra-glacial suite in fractionation trends, these samples, along with 3 post glacial samples from Asbergí and 2 inter glacial lavas from the shield volcano Grænavatnsoruni are not in equilibrium with *ol-plag-cpx*. These pressures, as stated above, only reflect an upper limit of crystallisation; therefore whist the exact figures calculated should be treated with caution these samples are likely to have crystallised toward the base of the crust or at the top of the mantle. All suites show good correlations of pressure with MgO, the Intra-glacial samples in particular seeming to level out at ~11 km.

Fremri-Námur: Due to the smaller sample numbers from the Fremri-Námur suite, the identification of distinct pressure arrays and therefore the presence of magma chambers have been more difficult to establish. The post glacial samples show good evidence for a shallow array ~10 km deep with samples spanning a range from 6-7 MgO wt. %. A further two groups tentatively suggest crystallisation from ~16km and ~22km depth however the lack of a significant range of MgO and small numbers of samples makes it difficult to establish whether this reflects stable magma chambers at these levels or mechanisms such as sill/dyke fed eruptions. Taken as a whole, the interglacial samples show more scatter however appear to lie largely along the ~10 km array. Due to the undeveloped nature of the Fremri-Námur system, this scatter could reflect the lack of a developed magma chamber and the presence of closely space sills at this time. Only two intra glacial samples were collected from this system and yield crystallisation pressures of 16 km and 10 km; however it is unclear whether these samples fit in to the arrays suggested for the post glacial samples. Only two samples are in equilibrium with only *ol-plag*, like Krafla the pressures calculated suggest that these samples are likely to have crystallised at the base of the crust or in the upper mantle.

Askja: One group of samples can be identified from the Askja suite as originating at ~16 km depth. This consists of the majority of the post glacial samples, suggesting that a magma chamber could be present at this depth. One post glacial sample as well as an interglacial sample show slightly lower pressure. In light of the little scatter within the ~16 km array, these samples could represent crystallisation in a shallower chamber. To better constrain the array present at Askja samples were added from the 1887 eruption analysed by Sigurdsson and Sparks (1981). These glasses alongside the two samples with lower pressures from this study clearly show a grouping at ~8 km depth (the other two glasses from Sigurdsson and Sparks (1981) plot within the 16 km array). This shows the value of having large data sets to accurately identify the location of potential magma chambers. As with Krafla and Fremri-Námur the samples that have only crystallised olivine and plagioclase yield pressures suggesting crystallisation at the base of the crust.

Kverkfjöll/ Fjallgarðar: Two distinct arrays can be seen from the Kverkfjöll suite, a shallow array at ~12 km depth, consisting of mostly post glacial lavas and a deeper array at ~20km consisting of samples from all ages. Only two samples were collected from the Fjallgarðar ridge and appear to plot in both arrays identified for Kverkfjöll. Both samples however, are within uncertainly of each other; therefore together with the very small number of samples it is unclear whether plumbing under this ridge is the same as under Kverkfjöll.

Table 4.1 shows a summary of the average depths of arrays identified compared with estimates from the literature.

4.3.3.2 Pressure variation over geography and time

Figure 4.5 shows pressures calculated for samples that underwent cotectic crystallisation of ol-plag-cpx versus time whilst Figure 4.6 (See also CD appendix A7.1 for rotating model) shows pressures calculated versus point of eruption. Together these two figures can create a 3D model which shows the likely positions of magma chambers along the NRZ whilst also assessing their relationship over time. Ages assigned and point of eruption locations are based on field observations and published work (see figure 4.5 caption for references). It is therefore important to note that the confidence of the ages and locations decreases with increasing age, for this reason Inter glacial samples have been omitted from figures 4.5 and 4.6.

Whilst the sub-section above appears to confirm observations by Kelley and Barton (2008) that multiple stacked magma chambers are a common feature under central volcanoes, a closer look at samples from individual eruptive episodes appear to show the majority of lavas only

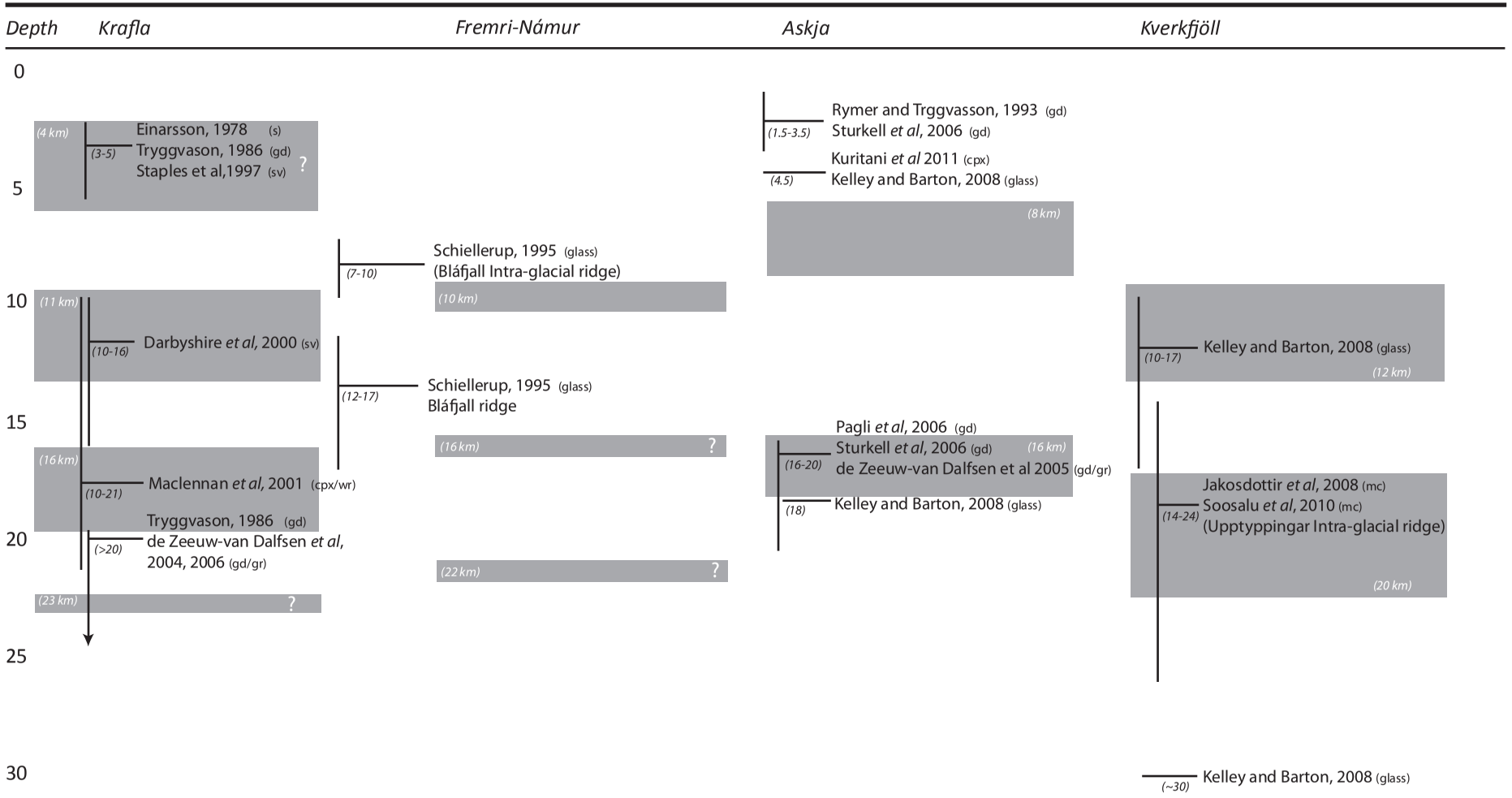

Table 4.1: Summary of crystallisation locations along the NRZ from literature. Grey boxes represent the of pressures calculated for the arrays identified from this study whist the white numbers within the boxes give the average depths of the arrays. Black italic numbers denote range of values reported in the literature. gd- Geodesy; sv- Seismic Velocities; s - seismology; gr - gravity; mc- micro-earthquake; glass - major element glass analyses; wr - major element whole rock analyses; cpx - clinopyroxene barometry.

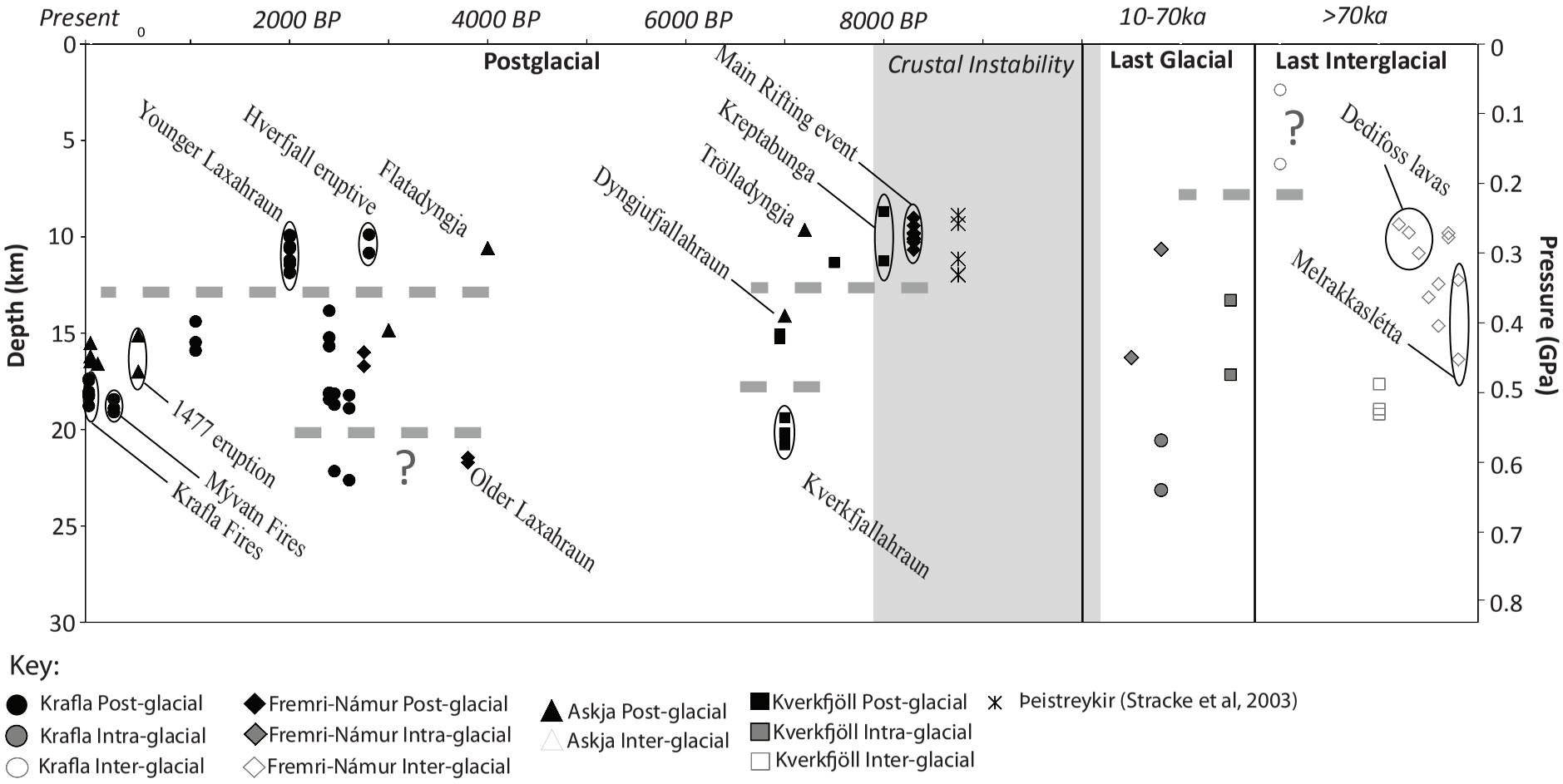

Figure 4.5: *Crystallisation pressures vs. Time. Ages of samples have been assigned based on field observations; Global Volcanism Program www.volcano.si.edu; Hjartarson, (2008); Tentler and Mazzoli, (2005); Jóhannesson and Sæmundsson (1999); Sigvaldason et al., (1992); Nicholson, (1990); Helgason, (1989); Sigbjarnarson (1988); Sigurdsson and Sparks, (1981); Thorarinsson (1979); Sæmundsson, (1977). Confidence of the ages decreases with increasing age. Crustal Instability period defined by Gee et al., (1998b). Dashed grey line delimits arrays identified from figure 4.4.*

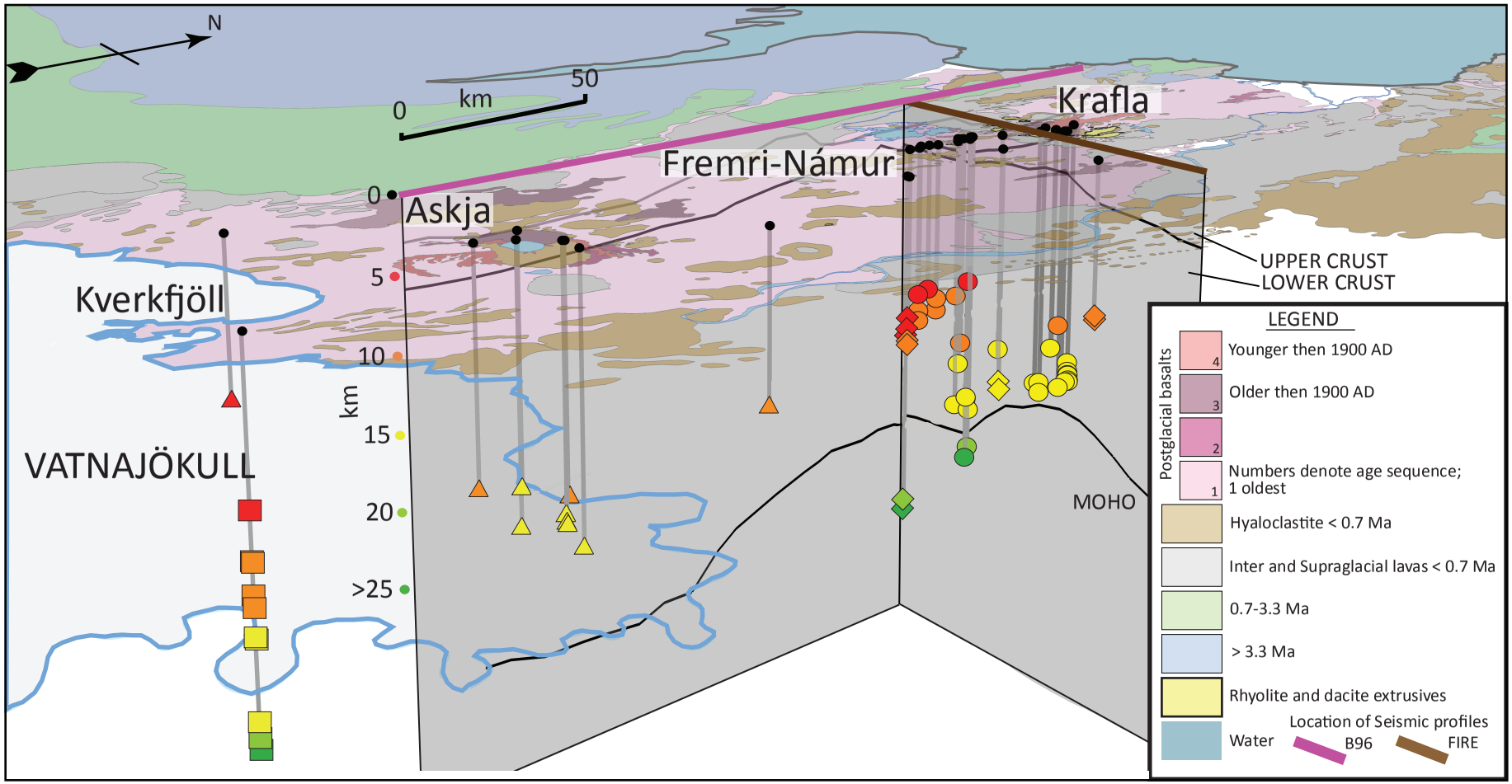

○ Krafla ◇ Fremri-Námur △ Askja □ Kverkfjöll

Figure 4.6: *Crystallisation depth vs. Geography. Samples were traced back to their point of eruption. Only post and intra glacial samples are shown due to the large errors in judging the points of eruptions of inter glacial samples. Data for the B96 and FIRE seismic sections from Menke et al., 1998; Staples et al., 1997 respectively, base map from Jóhannesson and Sæmundsson (1999).*

make use of one chamber per eruptive episode. For instance, lavas collected from the recent Krafla Fires and Mývatn Fires eruptive episodes only show crystallisation occurring in the deeper 18 km chamber, whilst lavas from the significantly older Younger Laxáhraun eruption at Krafla appears to have only crystallised lavas in the shallower 11 km chamber. This relationship can be seen at all other rift segments. Figure 4.5 has a number of major and well documented eruptions labelled in order to help demonstrate this relationship.

The earliest postglacial samples appear to show no evidence for eruptions from chambers deeper than 15 km. These samples erupted during a time of crustal rebound after the last glaciation (Gee et al., 1998b) and the possibility that this had an effect on crystallisation pressures will be assessed in the next section. It is important to note however that the apparent lack of deep crystallisation events during this time could reflect sampling bias as the youngest eruptions will have largely overlain older lavas, making these lavas harder to sample.

Whether such relationships are present in intra and inter glacial lavas is more difficult to identify due to the large uncertainties associated with tracing the eruption locations and assigning an age. As mentioned above the two inter glacial samples from Krafla are unusual in showing evidence of crystallisation in a shallow upper crustal chamber. In contrast interglacial samples from Kverkfjöll appear to have crystallised at a fairly deep level within the lower crust around 20 km depth. When inter glacial lavas are grouped by geography at Fremri-Námur samples still show scatter suggesting that lavas from all locations crystallised at a range of mid crustal depths.

4.3.3.3 Pressure variation with Radiogenic and Stable Isotopes and Trace elements

Figure 4.7 shows Nb/Zr, $^{86}Sr/^{86}Sr$, $^{143}Nd/^{144}Nd$, $\delta^{18}O$ and variation versus pressures for all samples that underwent cotectic crystallisation of ol-plag-cpx. Due to the small number of $\delta^{18}O$ analyses from this study (n=6) oxygen isotope data from the Reykjanes Ridge, ERZ, Kverkfjöll and Fremri-Námur analysed by Thirlwall et al., (2006), Manning (2010) and Macpherson et al. (2005) have been added in order to assess whether a relationship is present. An average $\delta^{18}O$ value of ~ +4‰ is present at all depths however the lowest $\delta^{18}O$ values seen at Iceland appear to be from the shallowest magma chambers; this is consistent with the idea that lavas crystallising at shallower levels have more chance of interacting with hydrothermally altered $\delta^{18}O$ light material. If this was the case samples might be expected to trend to higher $^{87}Sr/^{86}Sr$ with decreasing pressure. Overall a very weak negative correlation with $^{87}Sr/^{86}Sr$ is present, inconsistent with assimilation. Overall there is a very weak correlation with

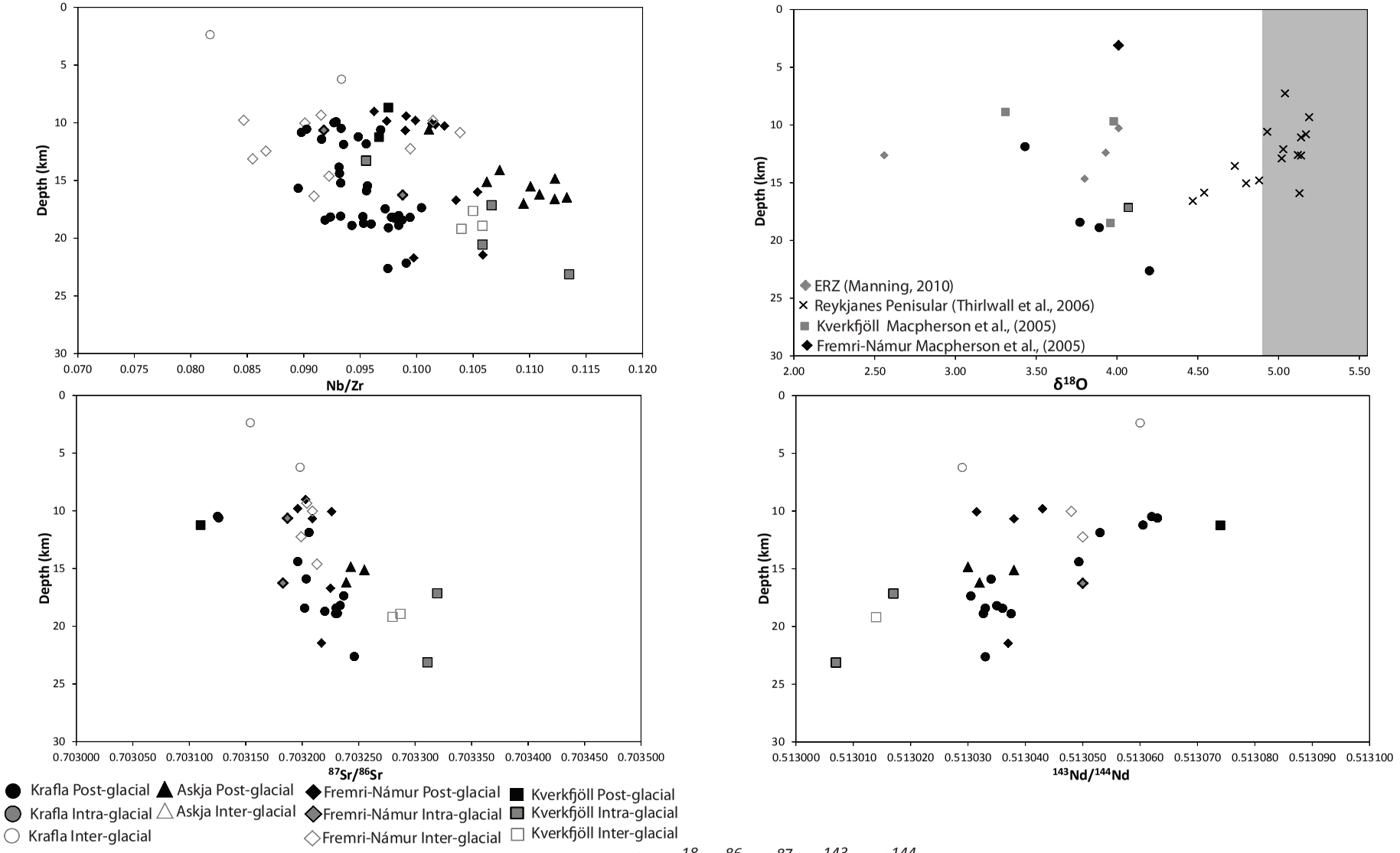

Figure 4.7: *Nb/Zr, δ ^{18}O, ^{86}Sr/ ^{87}Sr, ^{143} Nd/ ^{144}Nd vs. depth*

$^{143}Nd/^{144}Nd$ and Nb/Zr. Krafla seems to show a relatively steep correlation with Nb/Zr whilst the other volcanic systems seem to show a shallower correlation.

4.4. Discussion

4.4.1 Role of crustal rebound in controlling pressures

At the start of the post glacial there was a period of rapid fluctuations in local isostacy which resulted in a period of crustal instability from 9-13 kyr (Gee et al., 1998b). During this period large volumes of primitive, incompatible element depleted (Nb/Zr <0.09) lavas were erupted associated with a significant increase in magmatisim (Gee et al., 1998b). It has been suggested that during this period melt production at Þeistareykir and Krafla may have been up to 50 times greater than today whilst at Askja melt production may up to 20-30 times greater (Sigvadason et al., 1992; Maclennan et al., 2002).

What followed was a slow shift in chemistry back to 'normal' values (low Mg# and high Nb/Zr) seen during glacial periods and the most recent eruptions, (figure 4.8). Andrew and Gudmundsson (2007) suggested that the change to lower Mg# lavas could only occur after ice had been completely removed. Stresses would relax such that the tapping of evolved magma chambers that had accumulated in the crust during the glacial period would be possible. The gradual shift in chemistry seen in this data set and identified by Gee et al. (1998b) in the WRZ would seem to suggest that this relaxation of stress could take in the order of ~8 ka (figure 4.8).

Andrew and Gudmundsson (2007) further suggested that only as these stresses slowly relax, deeper magma reservoirs that accumulated during glacial periods are tapped. This provides a potential mechanism to explain the observed shift from eruptions originating in predominantly shallow chambers at the start of this relaxation period to eruptions originating in deeper chambers.

4.4.2 Effect of mixing and AFC on pressures calculated

Many authors have suggested that magma mixing can play an important role within crustal magma chambers (e.g. Sparks et al., 1977; McGarvie et al., 1990). If magmas that have derived from different crustal chambers mix, this could potentially yield erroneous pressures (Figure 4.9). Mixing magmas with significantly different wt. % MgO will produce major element trends that are not observed within this data set however mixing magmas that are chemically similar would not only introduce a population of xenocrystal olivines but would generate mixing lines that are indistinguishable from fractionation trends.

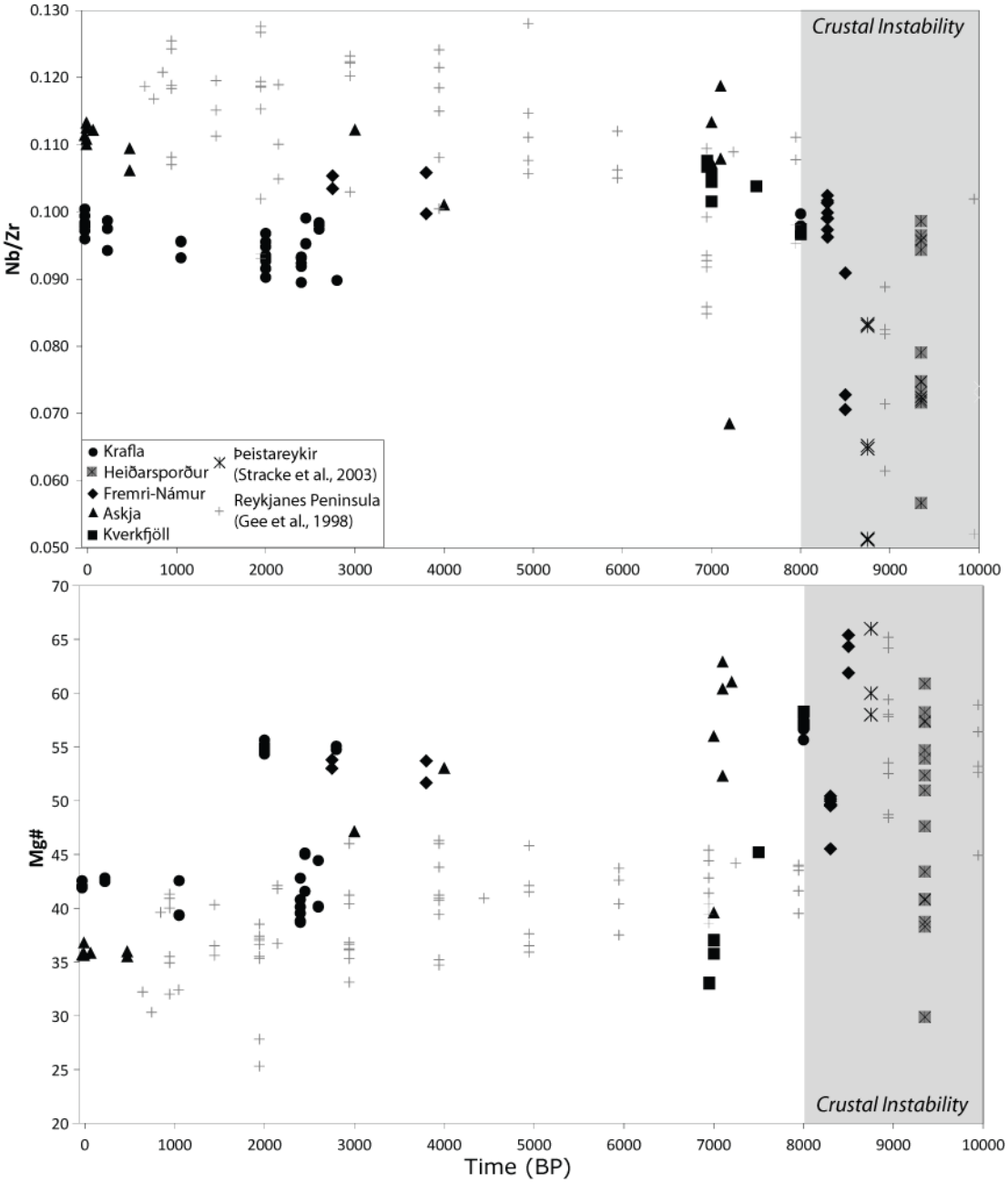

Figure 4.8: *Nb/Zr and Mg# vs. age of eruption. Grey box indicates period of glacioisostatic adjustment at the end of the last glacial as described by Gee et al ., (1998b).*

Mixing, either by fresh pulses of magma from depth into a chamber or by magma draining from a higher level has been suggested to act as a potential eruptive trigger (e.g. Sparks et al., 1977); in such as case magmas would have little time to homogenise prior to eruption, this will have the effect of producing scatter within the pressure estimates though out the course of a eruptive episode. Despite the small numbers of samples from some eruptive events, tight pressure arrays are often seen (figure 4.4). This relationship can be strongly demonstrated in the recent 1977-1984 Krafla eruptive episode, where pressures calculated in this study along with pressures calculated from lavas reported by Maclennan et al. (2001) show that over the

course of this event crystallisation pressure estimates do not vary significantly (figure 4.10). Where significant scatter is present, this tends to be from the oldest events, where there is less certainty as to whether the lavas grouped are from the same event. This is particularly hard to assess for the older inter glacial lavas where it is not always possible to pick out different eruptive events. It is perhaps worth noting that some of the scatter in the inter and intra glacial of Fremri-Námur could in principal, reflect this style of mixing.

AFC will also yield erroneous in pressure estimates; in particular this will generate correlations within eruptive episodes to shallower depths if upper crustal assimilants are considered. DL003 from the Younger Laxárhraun was suggested in chapter 3 to have under gone some contamination based on its low $\delta^{18}O$ value. If significant AFC had taken place then the calculated pressure of this sample might be expected to be much higher than other samples from its eruptive unit, however, this is not the case. The calculated pressure for DL003 gives a nearly identical pressure as the other samples from the Younger Laxárhraun suggesting that assimilation may not have played significant role in the formation of this sample.

Figure 4.9: *Large arrows show the crystallisation paths of a melt. A melt from a-b will crystallise ol-plag and from b to c will crystallise ol-plag-cpx. The dash line shows the effect of mixing the two lavas (Modified from Kelley and Barton, 2008).*

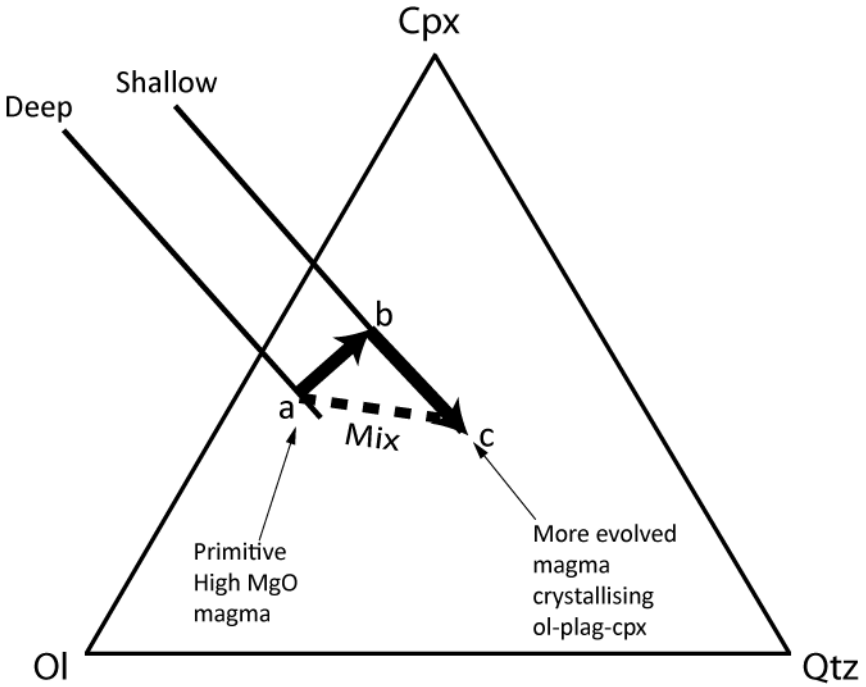

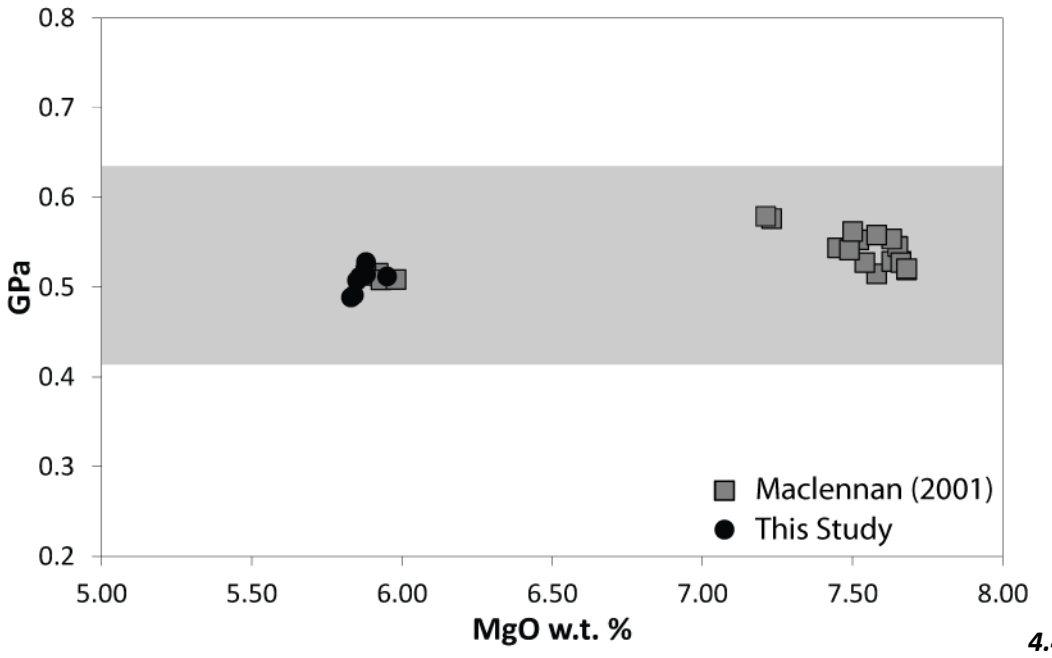

Figure 4.10: *Crystallisation pressure estimates for lavas from the 1977-1984 Krafla eruptive episode. Grey box shows the expected accuracy of pressure estimates.*

4.4.3 Petrological Implications

It has previously been noted that Icelandic lavas have complex crystal cargos (e.g. Maclennan et al., 2001; Maclennan, 2008), in particular over the past decade a small number of lava flows from Þeistareykir and Krafla have been extensively studied (e.g. Nicholson et al., 1991; Maclennan et al., 2001; Slater et al., 2001; Maclennan, 2008; Winpenny and Maclennan, 2011). By combining information on the depth and location of magma chambers as well as the extensive suite of mineral data gathered by this study, this provides an opportunity to give a broad insight into typical magmatic processes that occur across the rift zone as a whole (figure 4.11).

As noted above, generally, only one magma chamber is responsible for generating the majority of basaltic flows per eruptive episode. This would therefore appear to preclude the need for complex polybaric crystallisation models during rifting episodes (e.g. Kelley and Barton, 2008) and would suggest that a simple one chamber model of magma evolution may valid. It can also be noted that, with the exception of two inter glacial lavas from Krafla there is no evidence for basaltic crystallisation in the shallowest, upper crustal chambers identified by seismic studies. This would suggest that only the most evolved lavas crystallise in these chambers.

Recently Maclennan (2008) undertook an extensive study of the primitive Borgarhaun and Gæsafjöll lavas from Þeistareykir and Krafla respectively. These flows were found to contain large populations of disequilibrium olivines that are too primitive to be in equilibrium with the

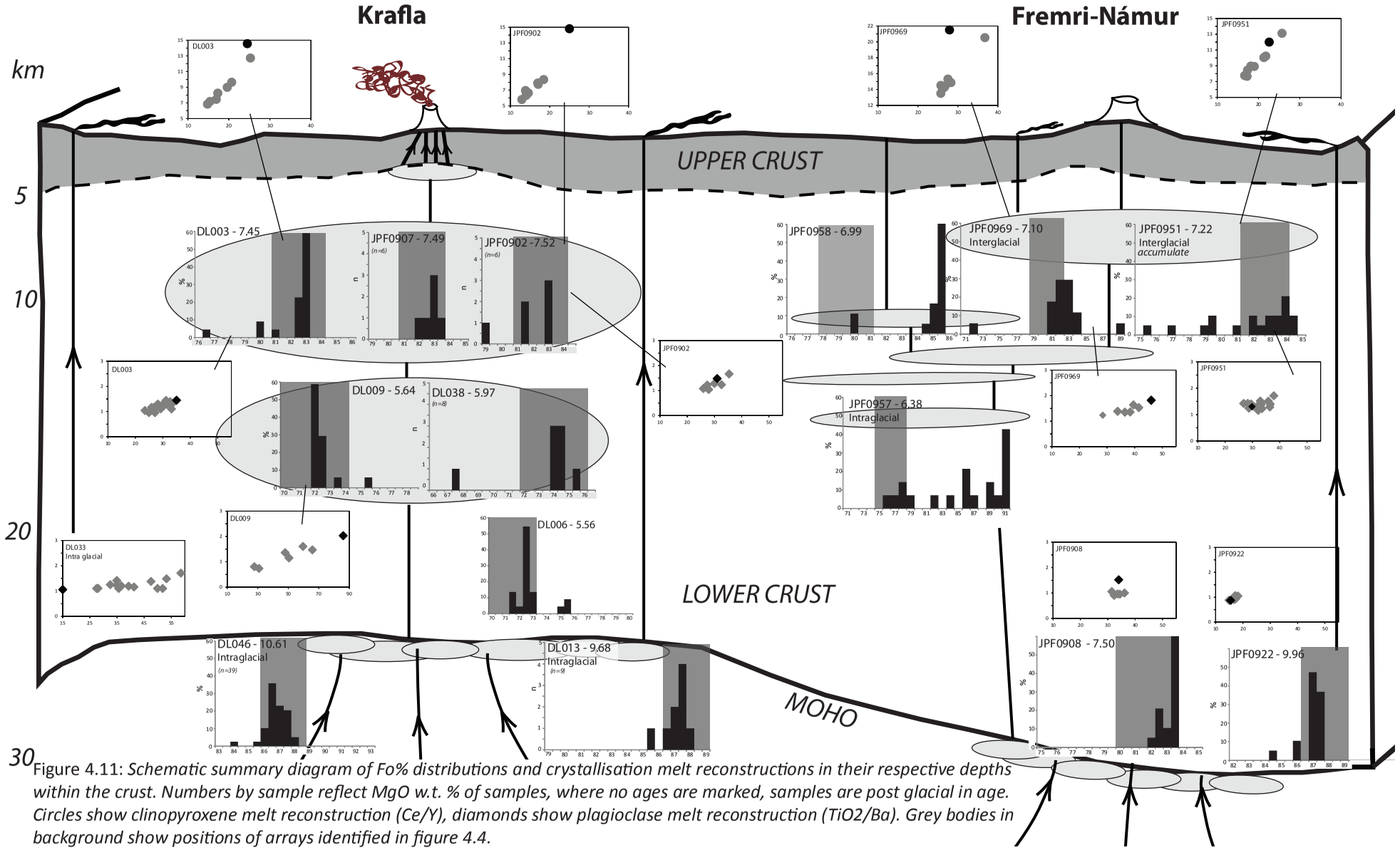

Figure 4.11: *Schematic summary diagram of Fo% distributions and crystallisation melt reconstructions in their respective depths within the crust. Numbers by sample reflect MgO w.t. % of samples, where no ages are marked, samples are post glacial in age. Circles show clinopyroxene melt reconstruction (Ce/Y), diamonds show plagioclase melt reconstruction (TiO2/Ba). Grey bodies in background show positions of arrays identified in figure 4.4.*

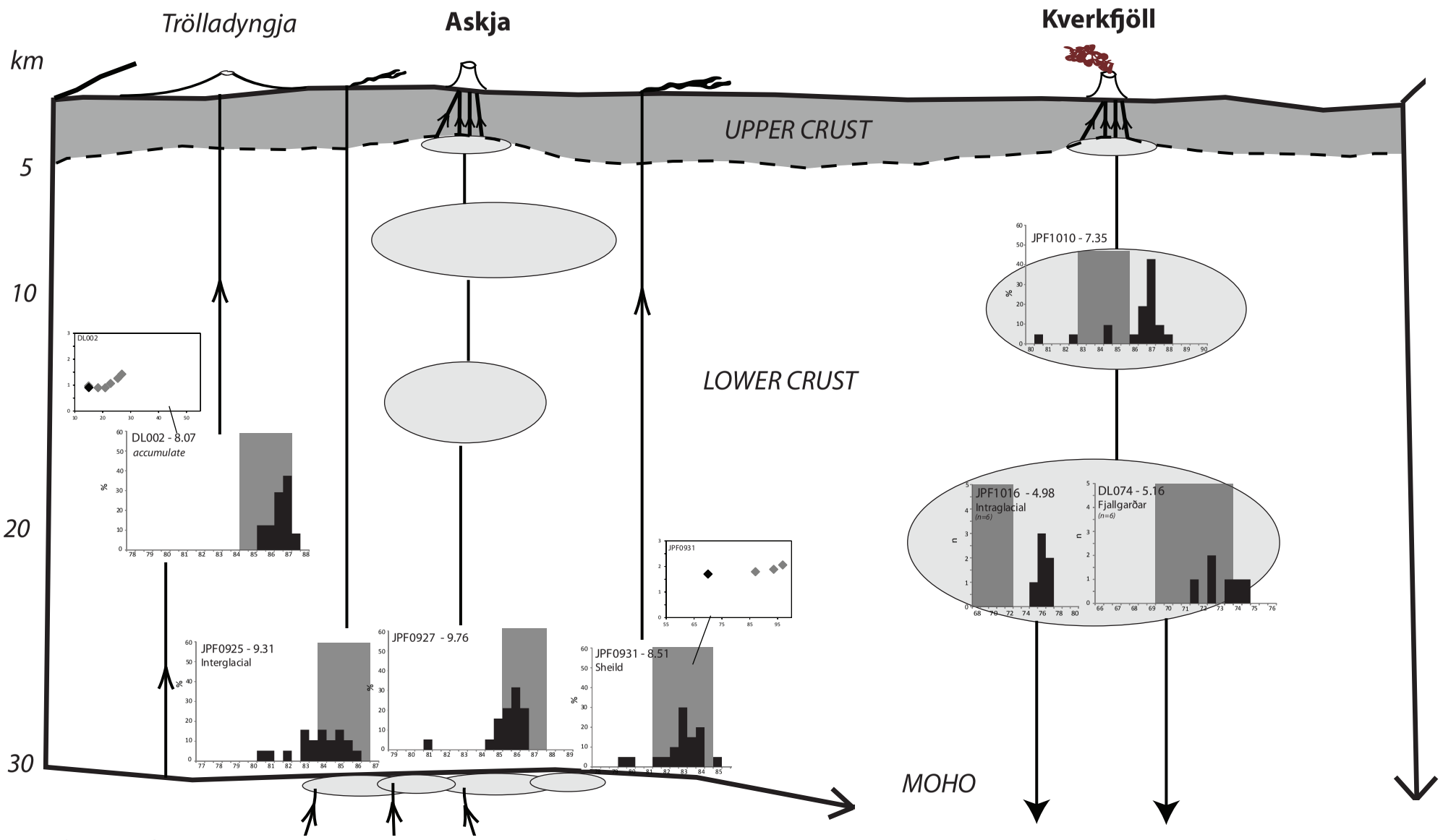

Figure 4.11 *Cont...*

host flow, Melt inclusion analyses from these olivines reveal that these phenocrysts are not accidental xenocrysts, but are remnants from the early crystallisation history of these flows (loosely termed antecrysts; Davidson et al., 2007). Continued crystallisation and homogenisation of these flows then resulted in the crystallisation of a small number of equilibrium olivines prior to eruption.

In contrast to these findings populations of more primitive olivines are not commonly seen in the high MgO lavas of this data set. These lavas tend to have crystallised in magma chambers at the base of the crust and with the exception an inter glacial lava from Askja, these lavas have large numbers of equilibrium olivines only occasionally showing either small numbers of more primitive or more evolved crystals. The absence of phenocrysts from the early crystallisation history of these flows is also reflected by the plagioclase populations of these lavas. Crystallisation melt reconstructions show that plagioclase populations from JPF0908 and JPF0922 crystallised from melts identical to the host magma whist all other high MgO show populations of plagioclase that must have crystallised from more evolved melts.

Only two lavas from Kverkfjöll and two lavas from Fremri-Námur show similar olivine patterns to those described by Maclennan (2008). These lavas are significantly more fractionated then the Borgarhaun and Gæsafjöll flows and appear to have crystallised in mid crustal chambers. Such numbers of disequilibrium olivines will only be preserved if the crystals are held in the host melt for a timescale that is short compared with the timescale required for diffusional equilibration of olivine (Maclennan, 2008). The fact then that four lavas generally show large populations of equilibrium olivines would suggest that these lavas may have had very short crustal residence times. This is potentially reflected by skeletal textures observed in the Kverkfjöll lavas indicating that these phenocrysts may has grown very rapidly.

This however may not be the case for the two lavas from Fremri-Námur. These lavas both contain gabbroic nodules in various states of disaggregation (See Plate 5 chapter 2) as well as showing much larger ranges of Fo% then the Kverkfjöll lavas. This is a feature also seen in other Fremri-Námur lavas, JPF0925 and DL067 from Heiðarsporður. These nodules are often coarse grained, and as such are likely to have been preferentially picked during the mounting of crystals onto stubs during preparation for analysis. The large range of olivine Fo% as well as large numbers of disequilibrium plagioclase and clinopyroxene crystals could therefore reflect the analysis of these gabbroic nodules.

The presence of these nodules may cause the whole rock analyses to not accurately reflect the true liquid composition of the lava; in turn this has the potential to yield erroneous crystallisation pressures for these samples. This could give a possible alternative explanation as to why scatter is present in the pressure calculations of the Fremri-Námur system.

In many cases the presence of gabbroic nodules can be hard to identify, particularly when they have fully disaggregated within a lava. Crustal accretion models argue that accretion takes place via crystallisation in sills and melt lenses throughout the crust (e.g. Kelemen et al., 1997; Korenaga and Kelemen, 1997). Due to the overall general chemical heterogeneity seen between lavas of the same volcanic system, the surrounding crust of a crystallising body is likely to be chemically similar to magmas actively crystallising in a chamber or sill. As such entrainment of crustal gabbroic nodules into a melt will generate a population of phenocryst that may have similar trace element signatures to population of phenocrysts crystallising in the host melt. This chemical similarity is potentially reflected by the fact only 3 xenocrystal olivines that are clearly and not related to the host flow have been identified. These olivines show very different trace element chemistry to the rest of the population (figures 2.5 and 2.6), the origin of such crystals however is unclear. The lack of such crystals could perhaps indicate that accretion of crustal materials does not advect significantly along the crust.

All other mid crustal bodies show large peaks of equilibrium olivines however the plagioclase and clinopyroxenes show populations of more primitive crystals. The plagioclase populations lie on trends with the whole rock values and are likely to reflect early crystallised products that have not had time to re-equilibrate with the host lavas, however the clinopyroxenes do not lie on tends with the whole rock. These sample all show very large plagioclase glomercrysts or gabbrioic nodules. This is likely that these clinopyroxene crystals are xenocrystal to the host melts and were entrained from the lower crust.

4.4.4 Controls on magma chamber depth

Dyke to sill transition is thought to be the principal way in which magmas pond, and ultimately lead to the formation of magma chambers (e.g. Gudmundsson, 1990; Gudmundsson, 2011; Menand, 2011). The factors that control this transition however are currently a matter of debate within the literature. Menand (2011) in a review of magma chamber formation highlighted several of the main controls:

Firstly, it has long been suggested that bodies of magma will pond at depths were magma becomes neutrally buoyant within the crust (e.g. Corry, 1988; Taisne and Jaupart, 2009). This

***E* (GPa)** *(ol:cpx)*	**Gabbro**	**Dunite**	**Peridotite 1** *0.59:0.41*	**Peridotite 2** *0.73:0.27*
Christensen (1966)	-	178-194	108-170	117-183
Vutukuri et al. (1983)	98.9	-	-	-
Kou and Rustan (1992)	108.2	-	-	-
Gupta and Bergstrom (1997)	92	150	-	-
Raffery (2011)	80-90	150-170	-	-

Table 4.2: *Range of Young's modulus values (E) for lower crustal lithologies in the literature.*

mechanism in particular, has been widely used to argue for the formation of magma chambers during glacial periods, were a high overpressure due to ice loading promotes the arresting of dykes (e.g. Andrew and Gudmundsson, 2007). Rheology/Rigidity-contrast has also been more recently cited as an important control, in particular in the formation of shallow chambers. Depending on the material stiffness (Young's modulus, *E*) at a contact a dyke may either continue to propagate (i.e. propagating through layers of basaltic flow) or deflect to form a sill (i.e defection when a dyke reaches a contact with a lower *E* value such as a layer of softer pyroclastic deposits (e.g. Gudmundsson, 2009; Gudmundsson, 2011)).

In an attempt to understand the potential controls on Icelandic crustal density and seismic profiles Kelley (2009) noted a number of potential changes that occur at ~10 km depth that could explain the common presence of chambers at this depth. In considering the effects of metamorphism of the Icelandic crust Kelley (2009) predicted the mineralogical, and hence density changes that will occur at a constant crustal composition. These predictions show that at 10 km depth there is likely to be a strong density change as the mineral assemblage changes from amphibolite facies rocks to granulite facies rock. This change in density was suggested to be sufficient to halt buoyant magma from rising causing it to pond at these depths. In addition geotherms calculated based on this model predicted temperatures of ~700 °C at these depths, this temperature marks the approximate depth of the brittle ductile transition further aiding sill formation.

Kelley (2009) found that whilst the predicted metamorphic changes replicated Icelandic density and seismic profiles reasonably well, changing the chemical compositions of the crust with depth gave the best fit. This model is based on the compositional changes detailed by Farnetani et al. (1996). Modelling from this study suggests the lowermost crust is likely to comprise of olivine and clinopyroxene rich cumulates due to the fractionation of picritic primary melts at the base of the crust. Could this transition have implications for the formation of the deeper 16-20km chambers? As highlighted above dykes may arrest or continue to

propagate depending on the material toughness. In a compilation of *E* values for gabbros and dunites (Table 4.2) despite the wide range of values reported, all studies appear to suggest that gabbros have lower *E* values than dunites tentatively indicating that in principle conditions may be favourable for dykes to arrest at this lithological transition. The lower most crust is unlikely to be a pure dunite, however very few experiment studies have focused on accurately determining material toughness values for lower crustal lithologies. Consequently this suggestion should be treated with caution, however highlights that there is a clear need for a more detailed understanding on the lithological structure and mechanics of the lower crust in order to help resolve issues surrounding magma chamber depths.

4.5. Conclusions

- Crystallisation pressures were calculated from an extensive suite of lavas spanning the length of the NRZ and spanning a large age range. This has enabled the location and depth of significant bodies of crystallisation to be identified under the NRZ.

- Results indicate that that multiple stacked chambers are present under the volcanic systems of the NRZ, consistent with other volcanic centres around Iceland (e.g. Kelley and Barton, 2008).

- In contrast to early volcanic plumbing models there is little evidence for basaltic crystallisation in chambers located in or at the base of the upper crust. This would suggest that these shallow chambers are responsible for the development of the most evolved products associated with central volcanoes.

- The deeper chambers responsible for basaltic eruptions are located at relatively consistent depths within the crust. An upper, lower crustal chambers is typically present at ~10 km depth in addition to a second deeper chamber at ~16-20 km.

- When crystallisation pressures are considered over time it is clear that generally only one body is responsible for crystallising the majority of basaltic lavas during individual eruptive episodes.

- Broadly, eruptive episodes appear to only be able to tap magma from shallow chambers at the start of the post glacial. Crustal readjustment after the unloading of ice may be responsible of this observation. Andrew and Gudmundsson (2007) have described that only as stress slowly relax after such an event can volcanic systems start

to tap deeper magma bodies. Based on observations from the WRZ and this data set this relaxation period may take up to 8 ka for the crust to fully readjust.

- The pressure relationship with time is less clear for the older intra and inter glacial lavas, were the ages assigned are significantly less confident.

- The combination of mineral data and crystallisation pressures show that fractional crystallisation is a dominant mechanism and generating the majority of phenocryst populations within the chambers identified. In addition few lavas preserve primitive populations of phenocrysts suggesting that crustal residence times, even in dyke fed eruptions may be generally longer then implied by the Maclennan (2008) data set.

- The nature of the plumbing dynamics at Fremri-Námur is less clear from these results.

- A chamber at ~10km depth can be confidently identified however the few postglacial samples that yield deeper pressures and the slight scatter seen in the intra and inter glacial samples make the identification of deeper chambers more difficult.

- The cause of the scatter at Fremri-Námur is not clear with a number of potential explanations available:

- Fremri-Námur is a relatively undeveloped volcanic system. The scatter present in the older samples could reflect the lack of a well-developed magma chamber at this time and instead reflect a series of closely spaced sills that would eventually combine to form the 10 km deep body identified in the postglacial suite.

- This scatter could also be explained by mixing. Mixing has been recognised as a potential eruptive trigger during rifting episodes. However this will have the effect of generating scatter throughout the course of an eruptive event.

- In addition, optical inspection of lavas from Fremri-Námur shows that this system has a high proportion of gabbroic nodules present compared with other centres. In many cases these nodules may have fully disaggregated in the lava, consequently these nodules can be difficult to confidently identify. In cases were lavas contain significant proportions of nodules the true liquid composition of the sample will be affected,

leading to erroneous pressures. Therefore the scatter seen could also be a consequence of the presence of large proportions gabbroic nodules.

- In reality a combination of the above is probably in operation. This highlights that in addition to filtering results for processes such as accumulation, through optical examination and a good understanding of the relative stratigraphy of samples is vital when attempting to interpret crystallisation pressure results.

- Over the past few years studies have been conducted to explain why chambers consistently form at similar depths, particularly focusing on the formation of the shallowest chambers (e.g. Kelley, 2009; Gudmundsson, 2011). The formation of the deepest 16-20 km chambers however is currently not fully understood. Limited experimental work on the mechanics of crustal lithologies tentatively indicates that a change from olivine and clinopyroxene rich cumulates to gabbros near the base of the crust may be a factor in the ponding of magma. Clearly however further work is needed to help explain why chambers form at these depths.

CHAPTER 5: THE ROLE OF DEEP LEVEL PROCESSES

5.1 General Comments

Much work has been done to understand the nature of the isotopic heterogeneity of Icelandic lavas and, as alluded to in chapter 1 and in section 2.7.1, many workers have attributed the heterogeneity observed to the mixing of a number of distinct enriched and depleted mantle components beneath Iceland (Schilling, 1973; Hémond, 1993; Chauvel and Hémond, 2000; Thirlwall et al., 2004; Kokfelt et al., 2006; Koornneef et al., 2012). The number and nature of these components is still widely debated. Binary mixing generally forms tight correlations between isotopic systems, the scatter seen in samples from the NRZ suggests that at least 3 different endmembers are required, including a significant proportion of recycled oceanic crust, the arrangement of which can vary locally. Such crust during recycling will be transformed into a variety of predominantly olivine free, garnet and perovskite bearing assemblages generally termed in the literature pyroxenites (e.g. Stracke and Bourdon, 2009). The lack of olivine in the residue of such lithologies will strongly affect the chemistry of partial melts; as such melts are generally enriched in Ni but depleted in Ca and Mn in comparison to melts from host peridotites (Kelemen et al., 1998; Humayun et al., 2004; Sobolev et al., 2005; Herzberg, 2006). The observation of such characteristics has been used to illustrate clearly the presence of pyroxenite within the Hawaiian plume (e.g. Sobolev et al., 2005); however its presence under Iceland remains a point of debate (Sobolev et al., 2007; Stracke and Bourdon, 2009; Shorttle and Maclennan 2011). It is hoped that further light can be shed on this issue by a combination of olivine and whole rock chemistry from lavas analysed in this study.

5.2 Source variation and mixing

As discussed in chapter 1, recent models have argued that enriched and depleted rift zone lavas could be generated by melts derived from recycled oceanic crust which was subducted and entrained into the Iceland plume. Chauvel and Hémond (2000) and Kokfelt et al (2006) used correlations between trace elements and isotopic ratios to argue for the recycling of a complete section of oceanic crust. The enriched end member, best seen in alkali basalts, is thought by these authors to represent the sampling of upper basaltic crust whilst the depleted end-member, best seen in the Icelandic picrites, is thought to represent sampling of the lower gabbroic crust. Chauvel and Hémond (2000) and Kokfelt et al (2006) go on to suggest that mixing between these two endmembers can account for the full range of isotopic and trace

element variation seen in Icelandic lavas. In contrast, Thirlwall et al (2004) and Manning (2010) showed through modelling of high precision double spike corrected Pb isotope ratios from a wide selection of Icelandic lavas, that the full range of isotopic variation can alternatively be accounted for by the sampling of heterogeneities within the basaltic part of the recycled crust and that correlations between trace element and isotopic ratios in part reflect this heterogeneity, and in part reflect variable mixing between recycled crust and mantle.

5.2.1 Gabbro vs. Basaltic crust recycling

One of the main assumptions with the upper and lower crustal recycling model is that the lower crustal cumulates will retain their trace element characteristics during the recycling process (i.e. during subduction and deep storage within the mantle). Consequently, authors have cited the presence of positive Sr and Ba anomalies in depleted primitive lavas, typically associated with the melting of gabbros (as these have a high proportion of plagioclase), as the result of melting such a source. (Chauvel and Hémond, 2000; Breddam, 2002; Kokfelt et al, 2006; Waight and Baker, 2012). It seems unwise to assume that mobile elements such as Sr and Ba will not undergo some fractionation during subduction (e.g. Kogiso et al, 1997; Geldmacher and Hoerle, 2000 Spandler et al 2004); nonetheless positive Sr anomalies are observed in some of the most primitive lavas from this study. The lavas with the highest anomalies from the NRZ can be attributed to the accumulation of plagioclase (shown in figure 5.1 as empty diamonds), excluding these samples Sr/Nd ratios plot generally to lower Sr/Nd for a given $^{206}Pb/^{204}Pb$ and Nb/Zr than the lavas reported by Chauvel and Hémond (2000) and plot within the range of values reported for Atlantic MORB (Murton et al, 2002); whilst samples from Þeistareykir have generaly higher Sr/Nd values that the rest of the NRZ. Overall, in contrast to the Chauvel and Hémond (2000) data set no correlations of Sr/Nd with degrees of enrichment are seen within the NRZ lavas from this study.

The uniformly high Sr/Nd ratios of the Þeistareykir lavas would suggest that the evolvement of such crust cannot be categorically ruled out if gabbros are able to retain elevated Sr with respect to the basaltic upper crust during subduction; however the lack of correlations and the generally lower Sr/Nd values from the rest of the NRZ would suggest that the depleted component is not solely tapping a lower crustal source.

5.2.2 Age of the recycled component

Proponents of the recycled upper and lower crustal model typically expand this hypothesis to argue that the U-Pb system will not have been significantly disturbed since the formation and subduction of the recycled crust. Therefore if melts from the basaltic upper crust mix with

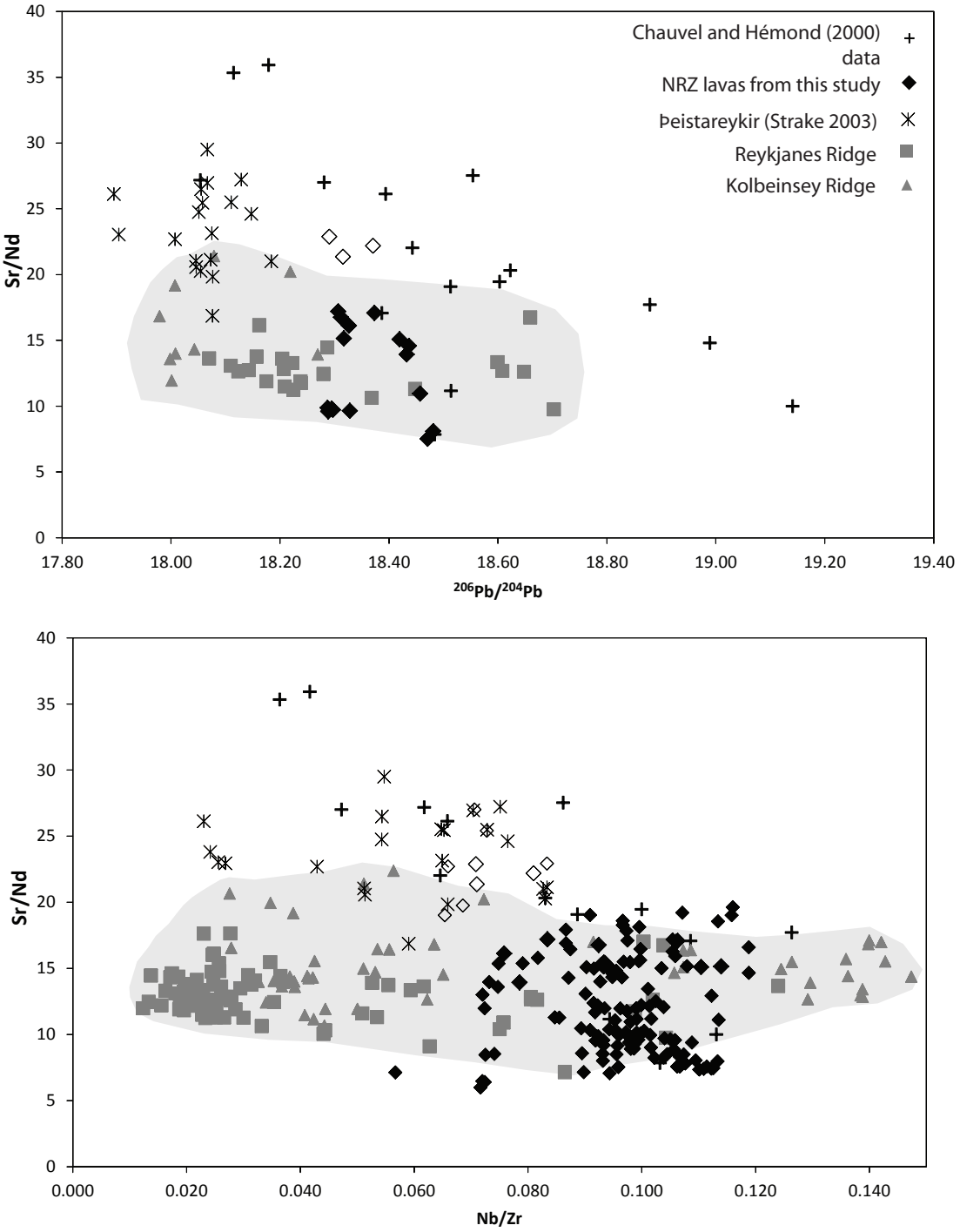

Figure 5.1: *Sr/Nd vs.* $^{206}Pb/^{204}Pb$ *and Sr/Nd vs. Nb/Zr. NRZ lavas do not show correlations with Sr/Nd unlike data from Chauvel and Hémond (2000) and plot within the range of MORB values (grey field). Empty dimonds are plagioclase cumulates.*

melts from the lower gabbroic crust, the resulting mixing array should have age significance on a Pb-Pb diagram (Chauvel and Hémond, 2000; Kokfelt et al 2006). Ages calculated by this method suggests that the recycling process was Archean. There are, however a number of problems with this suggestion:

- Large heterogeneities are present in modern MORB (up to ~0.7 units of $^{206}Pb/^{204}Pb$). It is likely that such variation was also present in ancient MORB, in addition it is unlikely that μ increase during subduction is uniform throughout the entire section of crust which could lead to large errors in the ages calculated from these relationships.

- Sm/Nd, $^{143}Nd/^{144}Nd$ and Lu/Hf $^{176}Hf/^{177}Hf$ ratios are far less likely to be affected by subduction. Thus if the recycled crust was Archean then such ages should be present in Nd-Hf isotopic relationships. This is not the case. Sm-Nd and Lu-Hf pseudo-isochrons for Icelandic lavas yield significantly *younger* ages <450 Ma (Zindler et al 1979; Kempton et al 2000; Manning, 2010). Thirlwall et al (2004) highlighted that LREE enrichment during melting could increase these ages, however to give an Archean age the enriched source would have to have Sm/Nd and Lu/Hf ratios almost as high as the depleted source. Figure 5.2 shows that, excluding the depleted picrites found at Þeistareykir and the Reykjanes Peninsula that potential have had their trace element ratios significantly fractionated during formation and melting of a very young residue (Thirlwall et al, 2004), Icelandic samples clearly form an array along a 450 Ma isochron.

- The ages generated from the Nd-Hf pseudo-isochron are consistent with the age of the recycled component suggested by Thirlwall et al (2004) based on $^{207}Pb/^{206}Pb$ systematics. In order to generate negative $\Delta^{207}Pb$ coupled with relatively unradiogenic $^{206}Pb/^{204}Pb$ values (<19) seen in the majority of Icelandic lavas, a young (<550 Ma) HIMU source is required. This is therefore inconsistent with an Archean recycled component which would generate high $^{206}Pb/^{204}Pb$ (>20) (Thirlwall et al, 1997).

5.2.3 Source mixing end-members

As reported in section 2.7.3 all samples from this study have $^{207}Pb/^{204}Pb$ ratios that plot below the NHRL (with the exception of one lava from Fremri-Námur which plot just above it) whilst showing relatively low $^{206}Pb/^{204}Pb$ values (<18.6). On a $^{206}Pb/^{204}Pb$ vs. Nb/Zr (figure 5.3a) plot, for a given Nb/Zr ratio NRZ lavas lie intermediate between Þeistareykir and Reykjanes Peninsula lavas lying on a broad positive trend showing that lavas with lower $^{206}Pb/^{204}Pb$ are

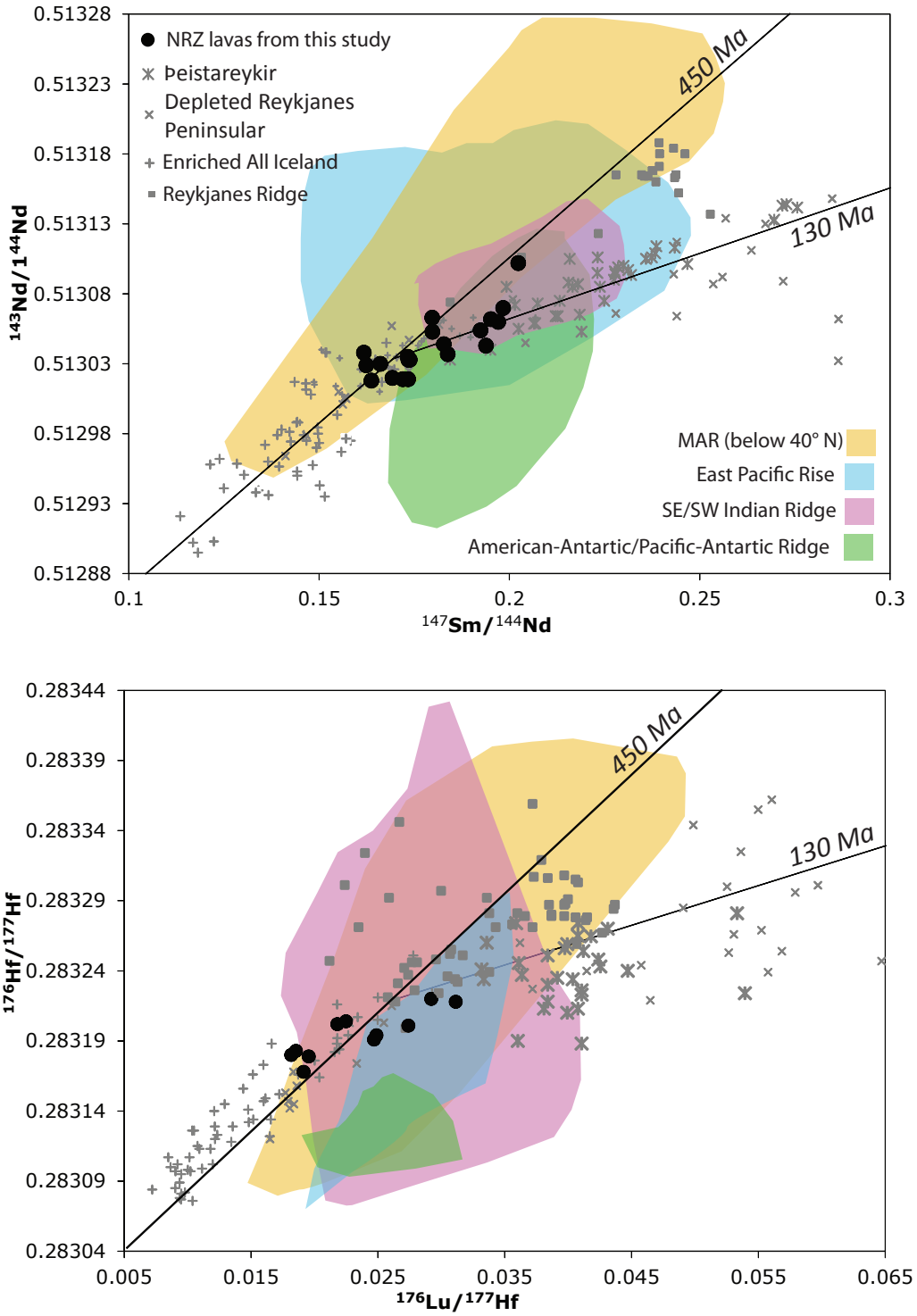

Figure 5.2: *Sm-Nd and Lu-Hf pseudo-isochrons for all Iceland data. Þeistareykir data from Stracke et al, (2003); all other Iceland data from Thirlwall et al., (2004), Gee et al., (1998), Thirlwall, unpublished; Reykjanes Ridge data from Murton et al., (2002), Thirlwall et al., (2004), Blichert-Toft et al., (2005). With the exception of Þeistareykir and the depleted Reykjanes Peninsular lavas, all samples appear to lie on an isochron no older than 450Ma. For comparison MORB from around the globe has been added. Data compiled from the PETDB database.*

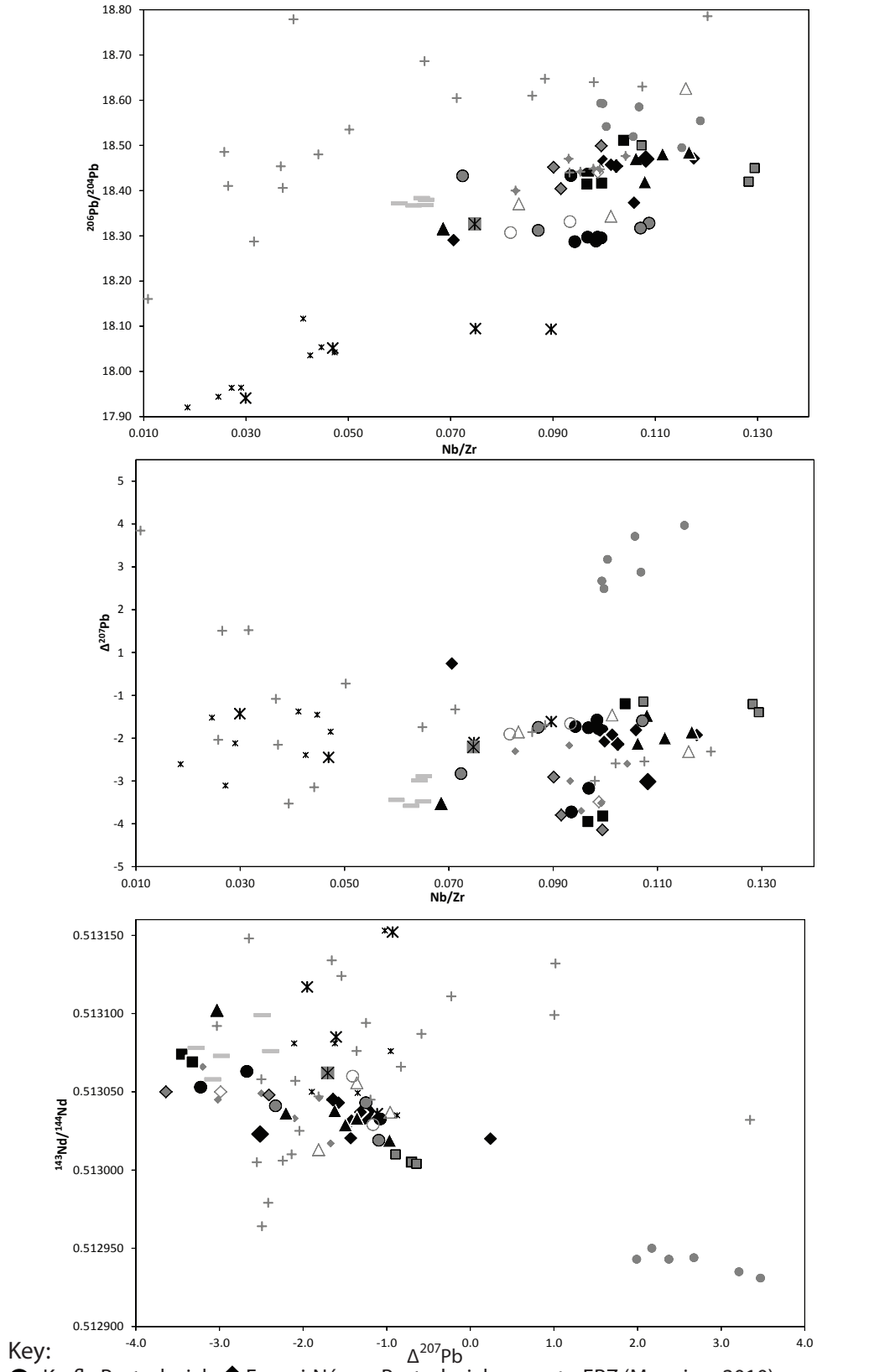

Figure 5.3: *$^{206}Pb/^{204}Pb$ vs. Nb/Zr, $\Delta^{207}Pb$ vs. Nb/Zr and $^{143}Nd/^{144}Nd$ vs. $\Delta^{207}Pb$.*

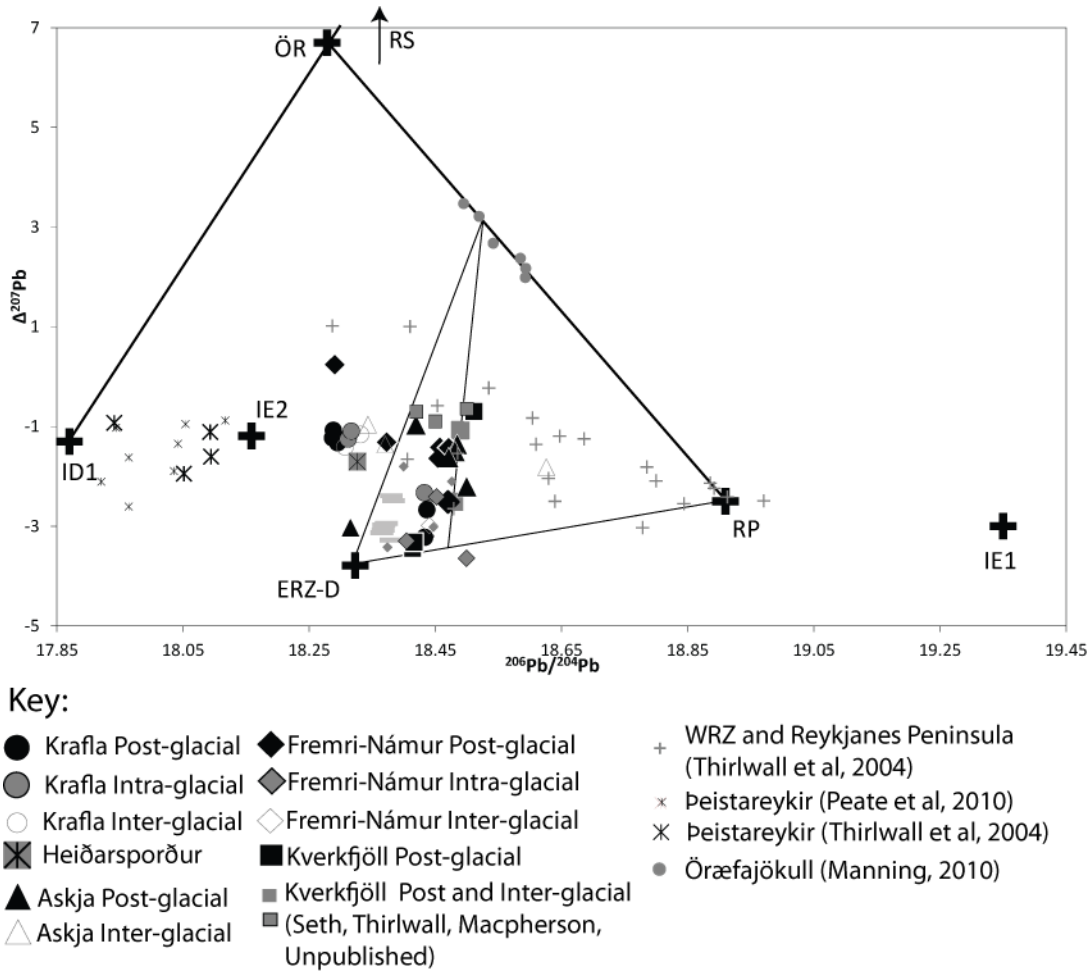

Figure 5.4: *Large crosses show endmembers suggested by Thirlwall et al, (2004) and Manning and Thirlwall (2012). Straight lines show mixing between endmembers. NRZ lavas from this study do not fit within the mixing model proposed by Manning and Thirlwall (2012) that encompass ERZ lavas.*

generally more incompatible element depleted. Relationships with $\Delta^{207}Pb$ are less clear, more scatter is present in plots of Nb/Zr (figure 5.3b). For a given Nb/Zr ratio each rift segment shows a similar range of $\Delta^{207}Pb$. $^{143}Nd/^{144}Nd$- $\Delta^{207}Pb$ (figure 5.3c) correlations are seen with NRZ lavas. High $\Delta^{207}Pb$ values generally have less radiogenic Nd isotope compositions.

Overall, however the DS Pb isotopes are consistent with the presence of a young recycled component in the Iceland plume. Thirlwall et al. (2004) and Manning and Thirlwall (2012) have identified a number of local and regional end-members for WRZ and ERZ lavas. In particular, Manning and Thirlwall (2012) proposed that most rift zone lava variations can be accounted for by mixing varying amounts of recycled enriched and depleted sections of upper oceanic crust (RP/IE1 and ERZ-D respectively) with a component that has a sediment signature seen most strongly at Öræfajökull. Figure 5.4 illustrates that it is difficult to fit all of NRZ lavas within this potential 'mixing triangle'. The following will attempt to see whether similar components can still be invoked to account for the Pb isotope variation seen of the NRZ lavas. To help

achieve this, Δ^{207}Pb and Δ^{208}Pb values after a 450Ma recycling event will be modelled using the same equations as presented by Thirlwall et al. (2004) (Equation 5.1 and 5.2). For this modelling it is assumed that the MORB source has a μ of 10 (Thirlwall et al., 1997).

Equation 5.1:

$$\Delta^{207}Pb = 100 \cdot \left[\frac{(\mu_H - \mu_M) \cdot (e^{\lambda^{235}t} - 1)}{137.88 - 0.1084 \cdot (\mu_H - \mu_M) \cdot (e^{\lambda^{238}t} - 1)}\right]$$

Equation 5.2:

$$\Delta^{208}Pb = 100 \cdot \left[\begin{matrix}(\kappa_H\mu_H - \kappa_M\mu_M) \cdot \left(e^{\lambda^{232}t} - 1\right) - 1.209 \cdot (\mu_H - \mu_M) \\ \cdot \left(e^{\lambda^{238}t} - 1\right)\end{matrix}\right]$$

Where: μ_H ^{238}U/^{204}Pb of the HIMU component
μ_M ^{238}U/^{204}Pb of the MORB source
κ_H ^{232}Th/^{238}U of the HIMU component
κ_M ^{232}Th/^{238}U of the MORB source
λ^{232} = decay constant of ^{232}Th
λ^{235} = decay constant of ^{235}U
λ^{238} = decay constant of ^{238}U

Unlike ERZ lavas, individual rift segments of the NRZ (with the exception of Kverkfjöll) form trends that are broadly sub parallel with the Öræfajökull array (best seen in figure 5.5). The most well defined trends are made up by the post glacial samples. The inter and intra glacial samples lie on similar trends but have more scatter. This could reflect slight variations in the source of the different rift segments over time. In addition to the trend that lies between the Krafla and Askja arrays a number of samples from Fremri-Námur also appear to form a second array that over laps the Askja trend. One post-glacial sample from the Trölladyngja Shield volcano, near Askja, appears to lie on a different trend to the main post glacial array. This samples is very is incompatible element depleted and the relatively unradiogenic composition may be the result of an old depletion event. As noted above, the Kverkfjöll samples appear to form different trends, both post and inter glacial sample form arrays similar to ERZ and Kistufell lavas that trend toward the Öræfajökull arrey. These tight trends, particularly in the post glacial samples, strongly suggest that localised pseudo-binary mixing is taking place at

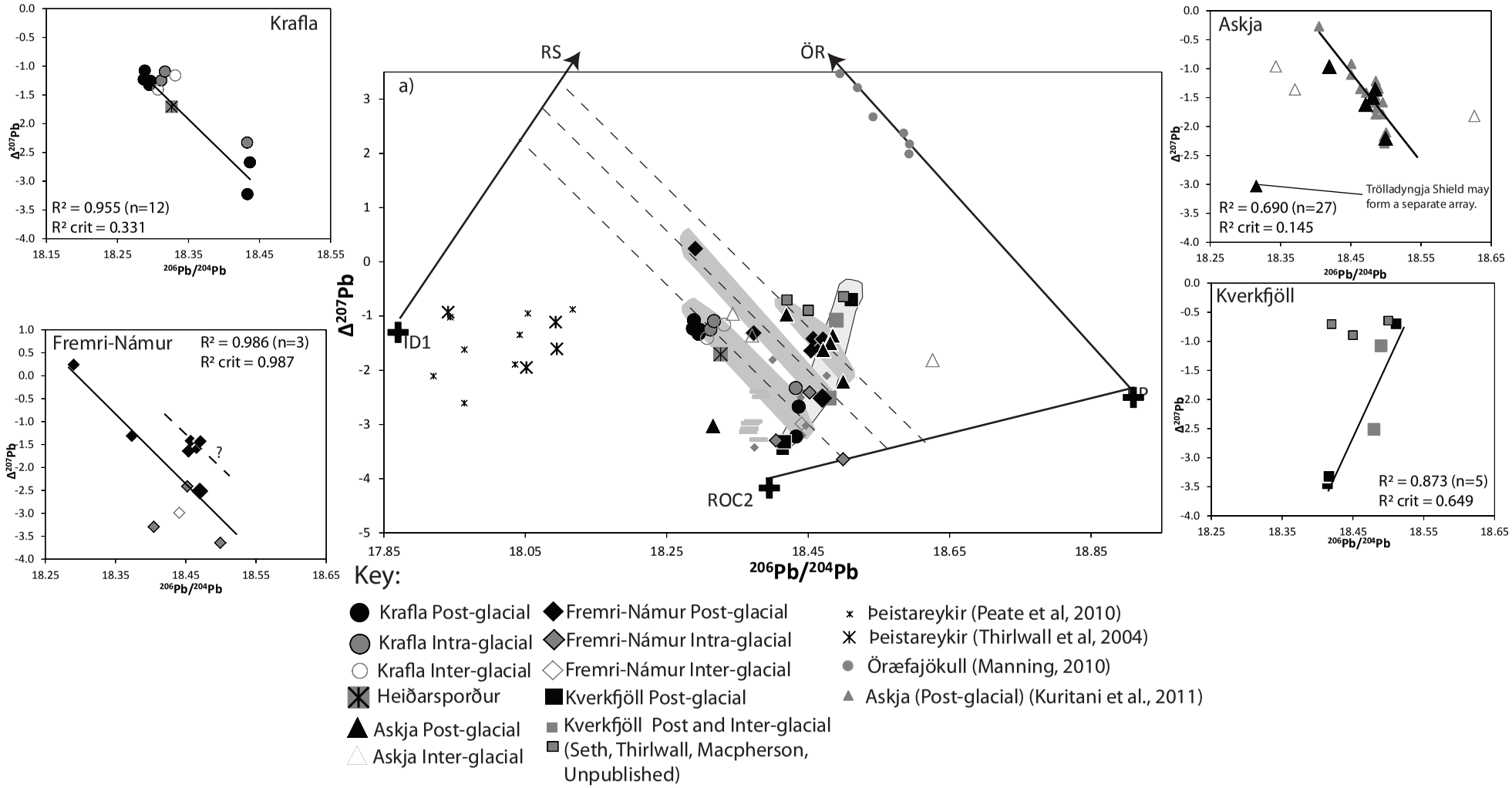

Figure 5.5: a) *Dashed lines and grey fields illustrate the sub parallel pseudo-binary mixing trends observed for Krafla, Fremri-Namur and Askja samples. Light grey field with black outline illustrates the Kverkfjöll trend. Graphs to the side show correlations for each rift segment in more detail. Linear regressions are shown for post glacial samples. R^2 crit values are 95% confidence limits.*

	$^{206}Pb/^{204}Pb$	$\Delta^{207}Pb$	$\Delta^{208}Pb$	$^{87}Sr/^{86}Sr$	$^{144}Nd/^{143}Nd$	$\delta^{18}O_{ol}$
ROC2	18.395	-4.17	15	0.702950	0.513095	3.55
ROC3	17.962	-2.90	18	0.703010	0.513179	
KR	18.280	-1.20	29	0.702765	0.513020	
RÞ	18.113	-2.69	21	-	-	

Table 5.1: *Compositions of the hypothetical end-members used in the mixing models.*

each rift segment along the rift zone.

In order to encompass these trends within the Manning and Thirlwall (2012) mixing model different end-members are needed for the recycled component. A wide range of potential components can be modelled within the scope of potential heterogeneity of the oceanic crust and in the host mantle into which it is subducted into. It is perhaps more appropriate to view the recycled component as a wide array of either specific end members reflecting the full range of heterogeneities within the crust or local well blended mixes of the most extreme depleted and enriched components. This gives rise to a number of possible combinations to fit the pseudo-binary mixing trends observed. These combinations will now be assessed in the following sections.

Manning and Thirlwall (2012) suggested that the low $^{206}Pb/^{204}Pb$, high $\Delta^{207}Pb$ end-member (ÖR) of the Öræfajökull array is a mix between recycled sediment that underwent U loss during subduction and a depleted section of recycled crust (in this case the ID1 component as defined by Thirlwall et al. (2004) figure 5.4). Such a mixture with lower proportions of sediment are likely candidates to be the low $^{206}Pb/^{204}Pb$ end-members of the rift segments that show the sub parallel Öræfajökull trends.

If the high $^{206}Pb/^{204}Pb$ end-members of these pseudo-binary mixing trends are extrapolated these end-members are likely to be, either a well-blended mixture of a component similar to the Manning and Thirlwall (2012) relatively depleted recycled crustal end-member ERZ-D and RP (the common enriched recycled component), or a number of individual recycled components that reflect the sampling of heterogeneities present in the recycled crust.

Figure 5.4 illustrates that the ERZ-D/RP mixing line cannot quite encompass all the NRZ lavas implying that the ERZ and NRZ lavas may not share the same depleted component. Instead a

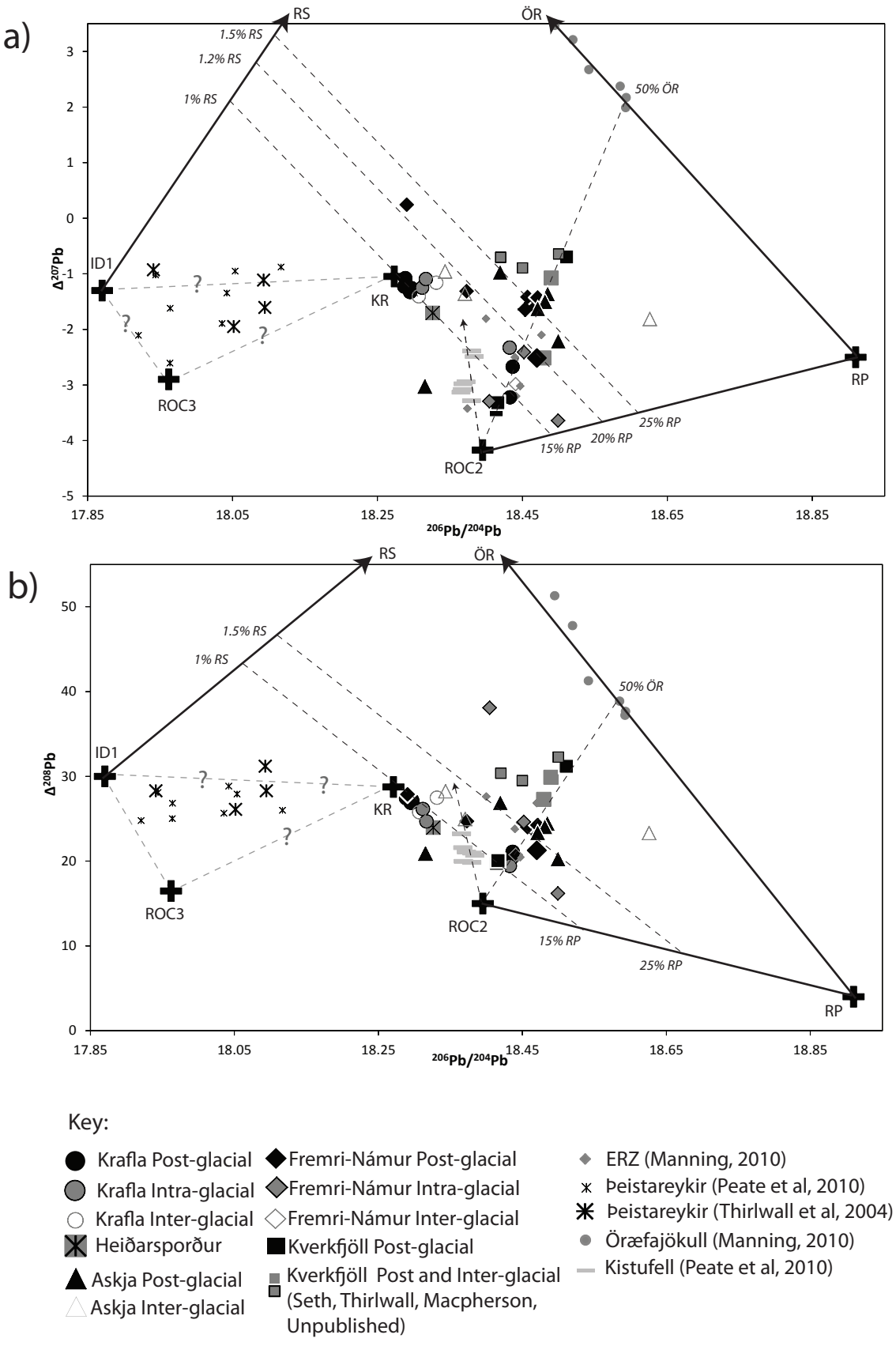

Figure 5.6: *Mixing relationships for NRZ lavas. Large crosses mark the endmembers proposed from this study and by Manning and Thirlwall (2012) and Thirlwall et al (2004). Grey dashed lines indicated the suggested mixing relationship for Þeistareykir lavas (see section 5.2.3).*

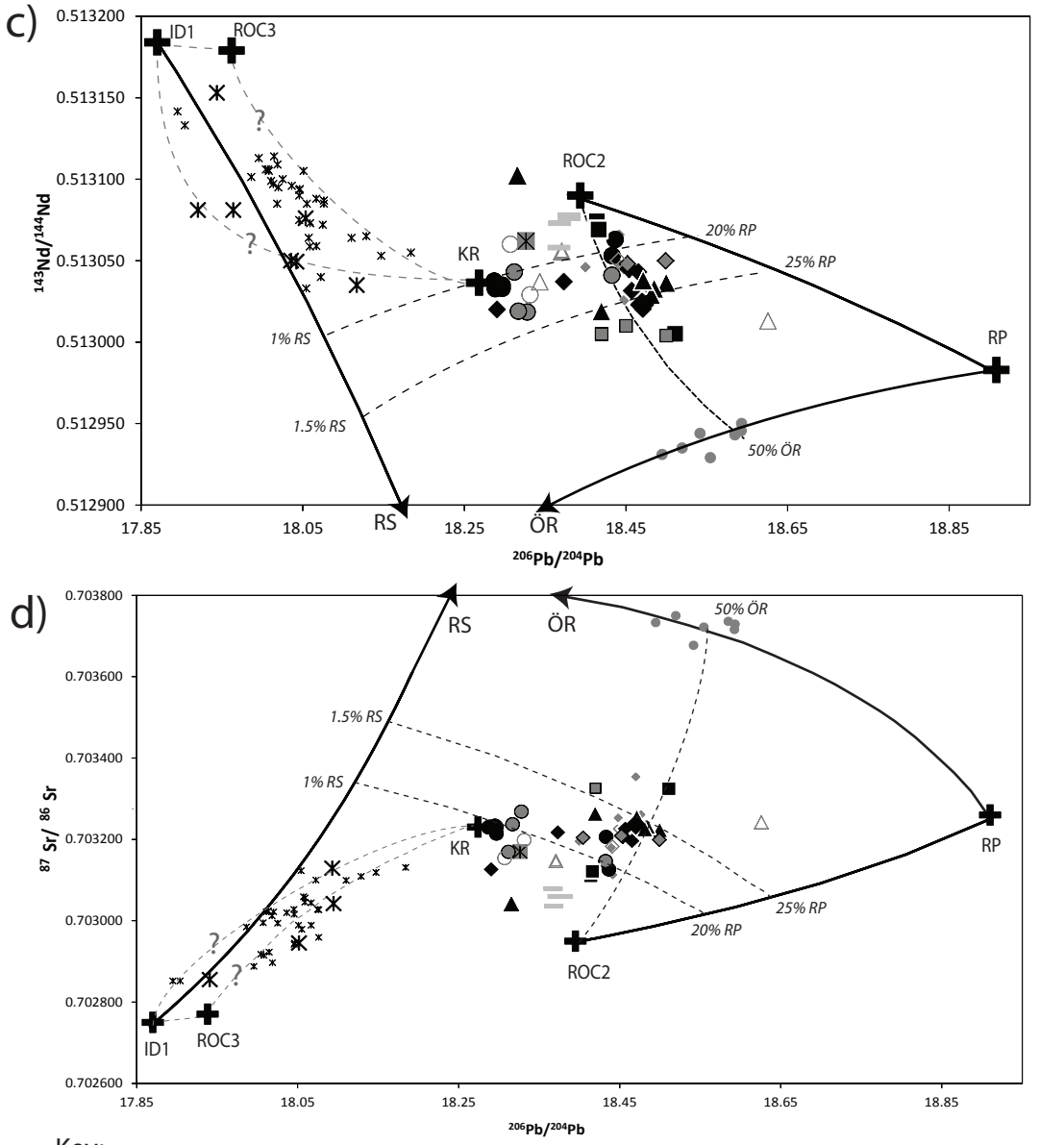

Figure 5.6 *Cont...*

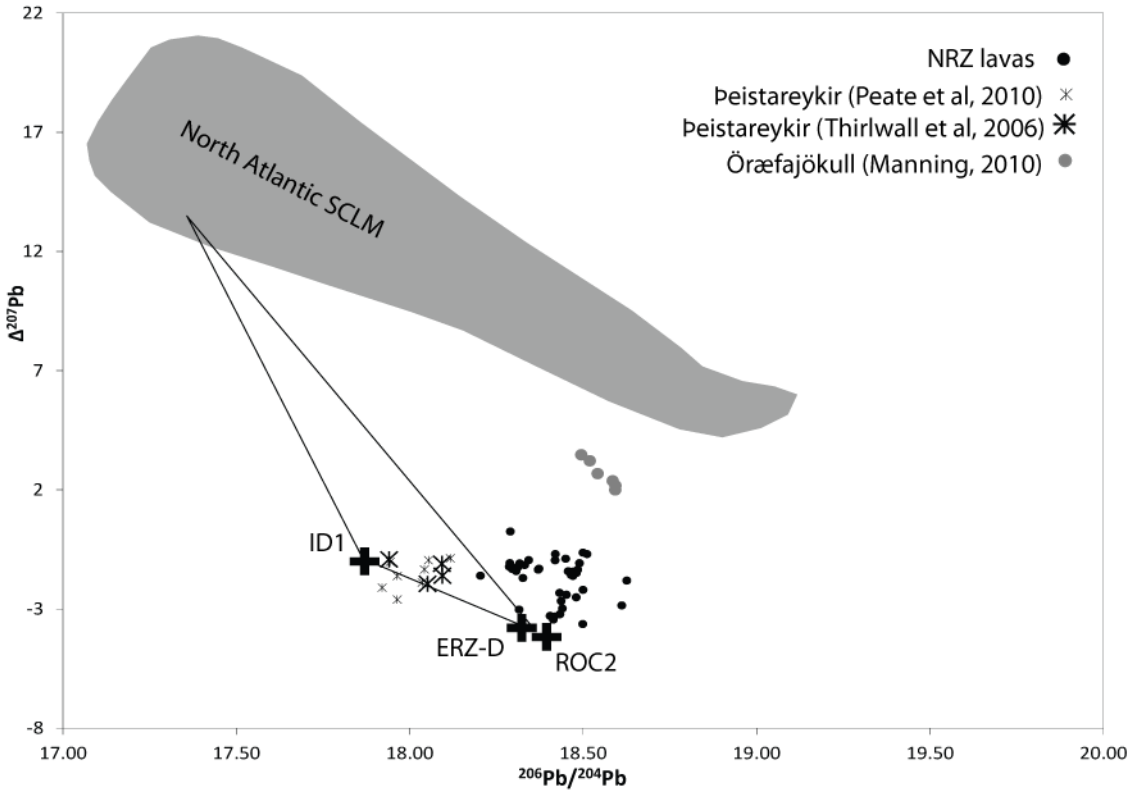

Figure 5.7: *North Atlantic SCLM (data from Long et al. 1992) with respect to NRZ lavas, Despite SCLM extending to low $^{206}Pb/^{204}Pb$, mixing with such a component is unable to reproduce the $^{206}Pb/^{204}Pb$ and negative $\Delta^{207}Pb$ of Þeistareykir.*

recycled component (ROC2) with an overall μ increase to 20 into a 450 Ma MORB source that would give present day $^{206}Pb/^{204}Pb$ values of 17.6 will give a suitable mixing line that encompasses this data set (figure 5.6).

As highlighted above post glacial samples from Kverkfjöll do not lie along similarly orientated mixing trends as the rest of the NRZ basalts, instead the trend seen in this suite indicates a mix between an ROC2 like component and a local Öræfajökull like component. Similar trends are also observed for double spike corrected data reported by Peate et al. (2010) from Kistufell and from the Veiðivötn and Grímsvötn ERZ lavas (Manning, 2010). These 4 central volcanoes are all geographically close together as well as being the nearest centres to Öræfajökull. This change of mixing trends could indicate a local shift in the arrangement of mantle sources at the Vatnajökull end of the rift zone.

5.2.4 Source variations at Þeistareykir

Isotopic variations at Þeistareykir are harder to reconcile with the source end-members proposed in previous section. Thirlwall et al. (2004) initially argued that the isotopic variation at Þeistareykir can also be explained by mixing a very depleted portion of the recycled crust

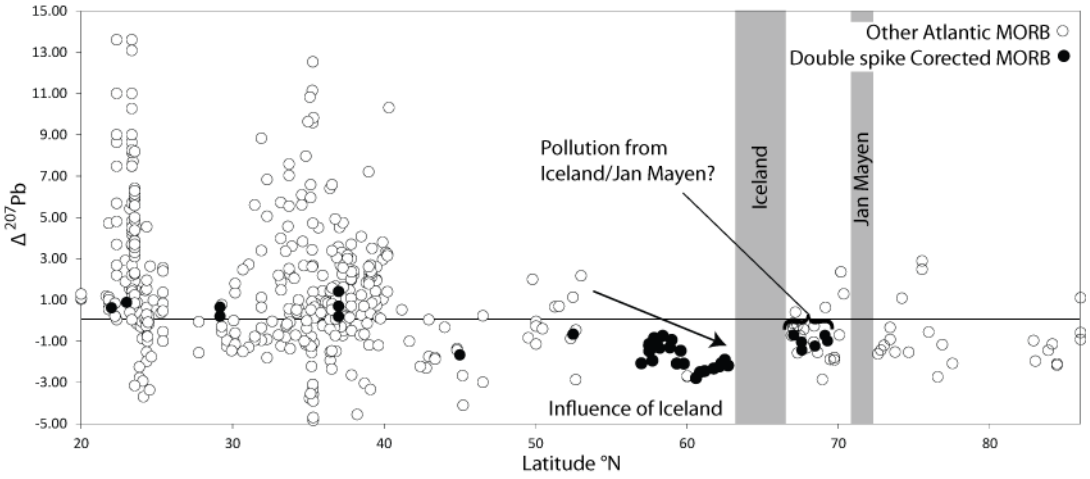

Figure 5.8: *Comparison between $\Delta^{207}Pb$ in sample analysed using double spike from Thirlwall et al. (2004) and published MORB data (compiled from the PETDB database). Despite very few analysis > 73°N most samples have negative $\Delta^{207}Pb$ values.*

(ID1) with a local enriched end-member (IE2). Additional double-spike corrected Pb isotopes analysed by Peate et al. (2010) revealed that Þeistareykir lavas extend to much lower $\Delta^{207}Pb$ (down to -2.6) than reported by Thirlwall et al. (2004) data set. Consequently it is difficult to generate a recycled end member with the low $^{206}Pb/^{204}Pb$ of the Þeistareykir lavas as well as the negative $\Delta^{207}Pb$ values reported. In order to generate a component with such low $^{206}Pb/^{204}Pb$ and negative $\Delta^{207}Pb$ using the equations of Thirlwall et al. (2004) the 450Ma MORB source would need to evolve to a present day MORB value of 17.3.

No such values are seen in modern Atlantic MORB, however very low $^{206}Pb/^{204}Pb$ values have been reported for Indian MORB (Dupre and Allegre, 1983; Gautier et al., 1990; Mahoney et al., 1998; Nauret et al., 2002). These low values have been attributed to pollution by Sub Continental Lithospheric Mantle (SCLM), reflected by elevated $\Delta^{207}Pb$ values (Xu and Castillo, 2004; Hanan et al., 2004), however it is not possible to fit mixing trends between North Atlantic SCLM (values from Long et al., 1992) and the ROC end members to encompasses Þeistareykir lavas (figure 5.7).

Waight and Baker (2012) reported lavas with similarly low $^{206}Pb/^{204}Pb$ and negative $\Delta^{207}Pb$ as Þeistareykir from depleted flood basalts in East Greenland, associated with the proto-Iceland plume during the initial stages of opening of the North Atlantic. The negative $\Delta^{207}Pb$ values of these samples have been attributed to crustal contamination of Archean crust. Whilst this would provide an adequate solution to explain the negative $\Delta^{207}Pb$ values at Þeistareykir, there is no evidence from any Icelandic lavas that segments of Archean crust is present in the

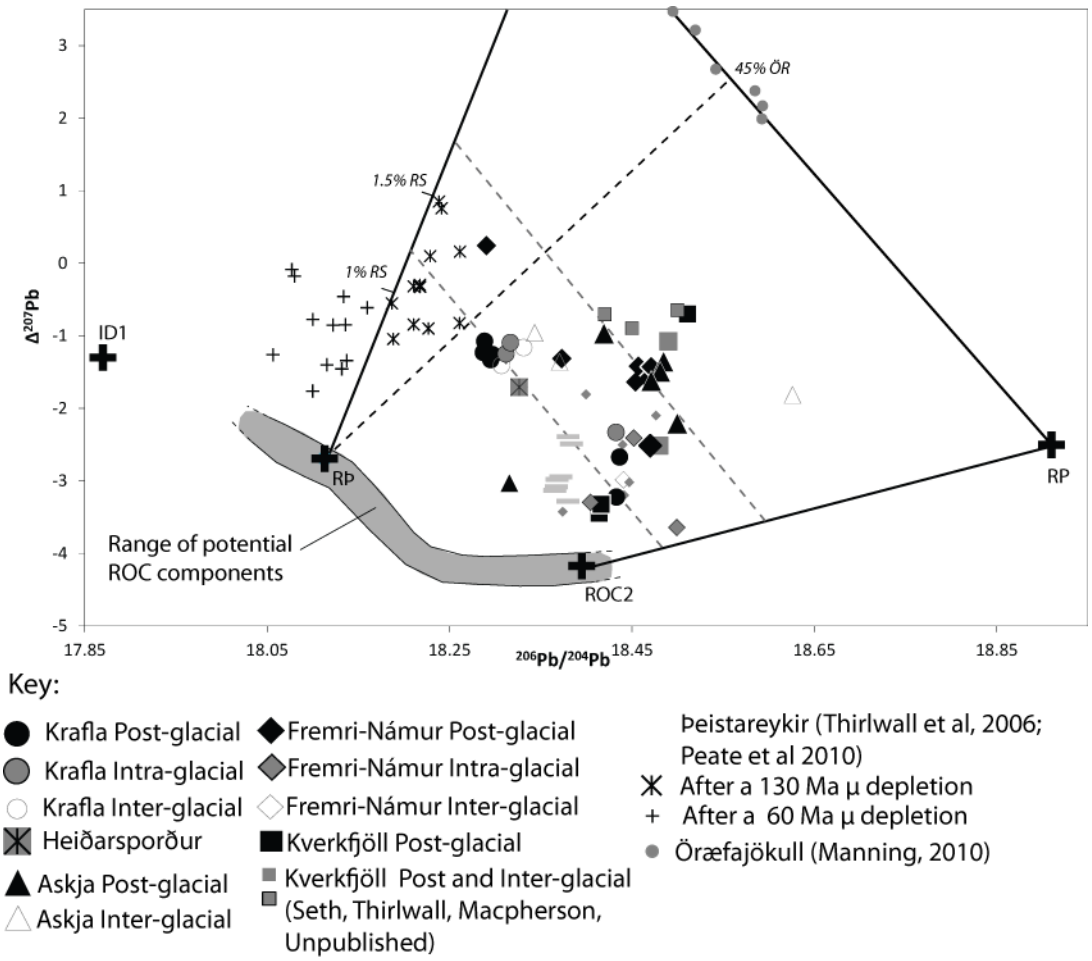

Figure 5.9: *Corrected Pb isotopic ratios from Þeistareykir after a 130 Ma and 60 Ma depletion event, in context with other NRZ samples.*

Icelandic lava pile to generate such values. This is reflected by the fact that NRZ lavas correlations to lower $^{87}Sr/^{86}Sr$ with decreasing $\Delta^{207}Pb$.

One potential solution to encompass the negative $\Delta^{207}Pb$ values of Þeistareykir is by suggesting the NHRL is not accurately describing $\Delta^{207}Pb$ of Atlantic MORB (e.g. Stracke et al., 2005). The equations presented by Thirlwall et al., (2004) to model recycled crust assumes that MORB without a μ increase will evolve to the NHRL and as such will have a present day $\Delta^{207}Pb$ value of 0. This might not necessarily be the case. Thirlwall et al., (2004) reported that double spike corrected low latitude MAR lavas have mildly positive values, (up to +1), whilst despite limited numbers of double spike corrected and conventional Pb data, MORB to the north of Iceland that is likely to be not polluted by Iceland or Jan Mayen appear to be largely mildly negative (up to -2 $\Delta^{207}Pb$) (figure 5.8). If MORB is allowed to evolve to a present day $\Delta^{207}Pb$ value of -1, then resulting calculated recycled components can have sufficiently negative $\Delta^{207}Pb$ at low $^{206}Pb/^{204}Pb$ to encompass Þeistareykir lavas (ROC3). Consequently mixing such a component with the Thirlwall et al., (2004) ID1 endmember and a component similar to the

Thirlwall et al., (2004) IE2 end-member (KR) can encompass the variations observed at Þeistareykir (figure 5.9). The KR component is likely to represent a local well homogenised mix of Krafla melts. In order to fully test this additional double spike corrected analysis of high latitude MORB lavas (in particular north of Jan Mayen) are needed to show that MAR north of Iceland does indeed have negative Δ^{207}Pb values.

The above suggestion assumes that these very depleted lavas were formed by a recent (last few Ma) depletion event (e.g. Thirlwall et al., 2004) however some studies have eluded to the fact that these depleted lavas may have been formed by a much older depletion event (e.g. Manning, 2010), perhaps reflected by the younger isochronous ages that the depleted lavas show in the Nd-Hf isotopic systems (130-170 Ma). Studies have suggested that the Icelandic plume may have been generating large volumes of melt since at least 60 Ma and potentially as far back as 130 Ma (Larsen and Pedersen, 2000; Trønnes, 2002) Taking these dates as maximum potential depletion ages this would substantially slow isotopic growth. In order to correct Pb isotopic ratios to give the ratios that would be observed today if a depletion event had not occurred, combined Pb isotopic ratios and μ values are needed, however no studies report high quality Pb ratios with combined U and Pb concentrations. In order to correct for such an event for the double spike corrected lavas from Þeistareykir, μ values were estimated from ^{206}Pb/^{204}Pb ratios and μ values reported by Stracke (2003). Lavas with ^{206}Pb/^{204}Pb ratios under 18 were assumed to have a μ of 3, under 18.1 to have a μ of 9 and over 18.1 to have a μ of 13. Depletion

Isotopic ratios depleted to these μ values at 130Ma and 60 Ma from a recycled crust that had a μ increase to 17.6 at 450Ma (RÞ) are presented in figure 5.9. Despite the lack of accurate μ values from the samples shown in figure 5.9, the lavas appear lie on a general mixing trend between RÞ and the Öræfajökull array. If then Þeistareykir lavas are the result of an old depletion event then the ID1 end member, which is in part defined by the low ^{206}Pb/^{204}Pb ratios of Þeistareykir may not be accurately describing the extent of depletion of the recycled crust in the Icelandic mantle, instead a component such as RÞ may better reflect the true extent of depletion. Mixing lines between RS to RÞ can still reproduce a component similar to ÖR as well as the other pseudo-binary mixing endmembers needed to reproduce the trends observed without significantly changing the proportion of recycled crust/sediment. It should be made clearly however that RÞ should not be taken to definitively define the most extreme depleted sections of the recycled crust. Whether a 60/130 Ma depletion event of a crust that has a μ slight more or less than 17.6 will not significantly affect the mixing lines proposed in figure 5.9; In this case μ of 17.6 was selected as this is the average μ of Krafla lavas. Due to the

relatively depleted nature of Krafla lava this value is likely to best represent the source μ in this part of Iceland to within a few units.

In summary without further double spike corrected Pb analyses from MORB north of Iceland as well as a lack of combined high quality Pb isotope and μ analyses from Þeistareykir makes it hard to rigorously test these different solutions for the relationships observed. However in light of the isochronous correlations seen in the Nd-Hf isotope systems of the most depleted lavas it is tentatively suggested that the ratios seen at Þeistareykir are the result of an old depletion event ~130 Ma and as such it's present day isotopic ratios are no longer reflecting its original mantle source.

5.2.5 Evidence from O isotopes

In contrast to radiogenic isotopes, tight mixing correlations are not as evident in O isotope plots; this is partially due to small potential shifts in $\delta^{18}O$ in the more evolved lavas due to crustal contamination as well as the limited numbers of combined O-Pb-Nd analyses available for the NRZ. Thirlwall et al. (2006) reported that enriched lavas tap a mantle source with ~+4.6 ‰ (assuming d $\delta^{18}O_{mantle\text{-}ol}$ = 0.3 (Mattey et al., 1994)) whilst depleted lavas have near mantle values. Samples from this study are consistent with oxygen analysis from other central Iceland volcanics (Macpherson et al., 2005) and ERZ lavas (Manning 2010). All of which suggest that the source of these relatively depleted lavas has a significantly lighter mantle $\delta^{18}O$ value than WRZ lavas. In order for mixing relationships to be consistent with radiogenic isotopic trends, the ROC component requires a very low mantle value of ~3.65 ‰. Despite insufficient analyses to confidently identify potential pseudo-binary mixing trends such as identified in section 5.2.3 some relationships in O-Pb space are similar to the relationship repored in radiogenic isotope space. Firstly the lavas from Kistufell reported by Breddam (2002) have $\delta^{18}O$ that extend toward the Öræfajökull array. In addition the NRZ lavas appear to lie on a generally trend toward where a ID1/RS mixing line would lie (figure 5.10). These relationships however are much harder to reconcile in O-Nd space.

The exact mechanism that might introduce light $\delta^{18}O$ values into the Icelandic mantle is currently not fully understood. Significant issues are associated with the introduction of a light $\delta^{18}O$ signature by the subduction of oceanic crust (Thirlwall et al., 2006). Using simple mass balance calculations, Macpherson et al. (2005) argued that ~40% recycled crust with a $\delta^{18}O$ of +2‰ is needed to be introduced into mantle with normal $\delta^{18}O$ of 5.5 ‰ to generate a recycled component with a $\delta^{18}O$ of 4‰. This amount is increases to ~50% to generate a $\delta^{18}O$ of 3.65

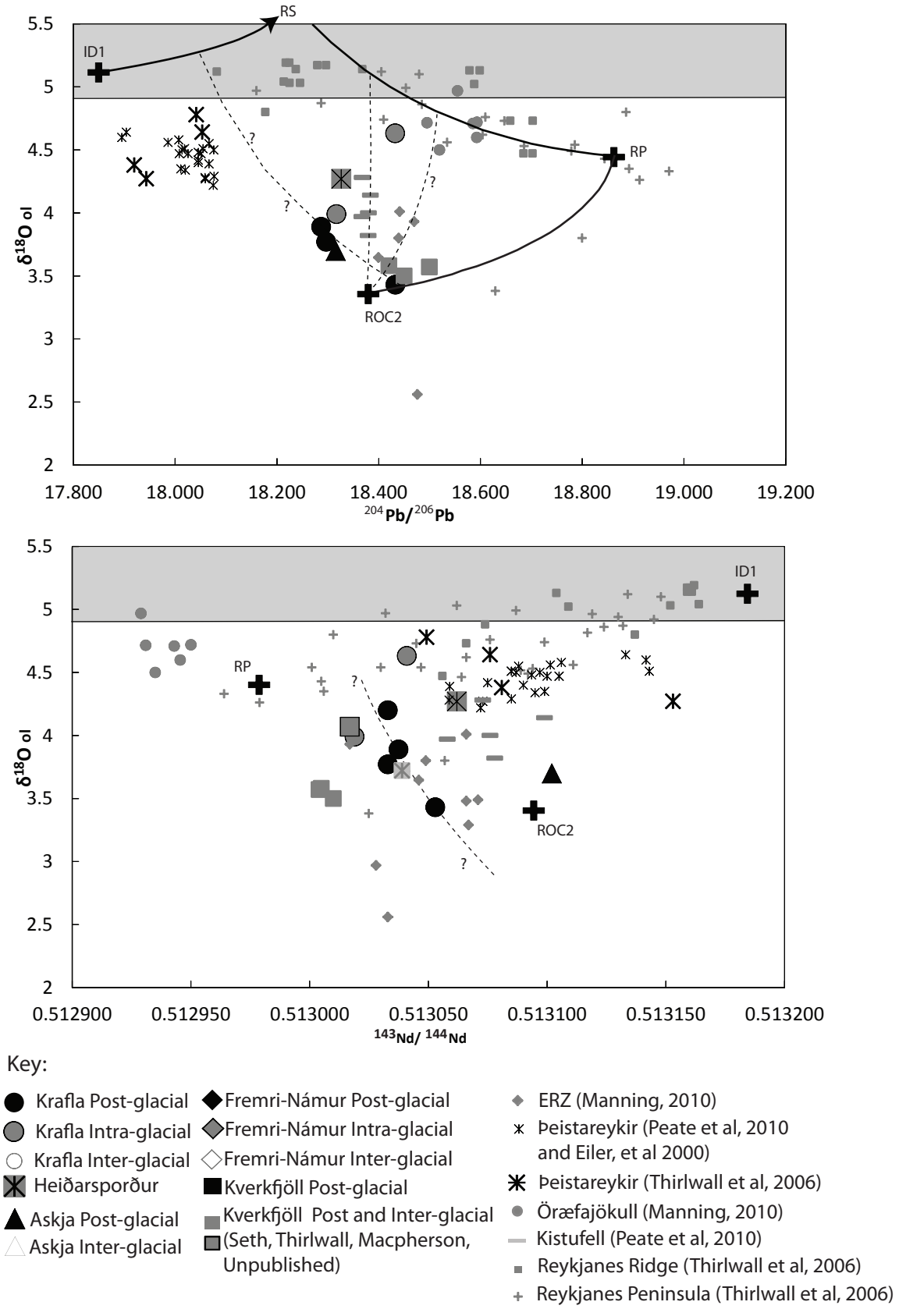

Figure 5.10: *$\delta^{18}O$ vs. $^{206}Pb/^{204}Pb$ and $\delta^{18}O$ vs. $^{143}Nd/^{144}Nd$.*

‰. These figures are inconsistent with the amount of recycling needed based on Os isotopes which Thirlwall et al. (2006) and Brandon et al. (2007) suggested that 11-34% recycling is required to explain the observed Os variation. In addition it is unlikely that a recycled crust will have a $\delta^{18}O$ value of 2‰, Thirlwall et al. (2006) highlighted that values as low as this within the crust has only been reported in very rare ophiolitic gabbros.

5.3 Partial Melting and Source Lithology.

5.3.1 Semi-quantitative melt modelling

At a broad level the melting regime of the NRZ can be established by considering plots of Dy/Yb_N vs. La/Yb_N. For peridotite melting La/Yb_N is a good indicator of the degree of melting whilst Dy/Yb_N is a good indicator of depth. Dy is compatible in garnet, which is only stable at depth, as such the tapping of deep melts where garnet is stable will yield melts with higher Dy/Yb_N. Due to larger proportions of pyroxene and garnet melts from pyroxenite reagdless of depth will always yield melts that have elevated Dy/Yb_N. Plot of Dy/Yb_N vs. La/Yb_N have the additional advantage that both axes share the same denominator; consequently potential mixing between shallow and deep sources can be easy assessed.

Before any melt modelling can be undertaken it is important to assess partition coefficients and melt modal mineralogies that are used during partial melt calculations, as these are potential source of error.

5.3.1.1 Partition Coefficients, Source and Melting modes

Published partition coefficients (*D*) can vary considerably, consequently the use of incorrect or inappropriate *D* values can lead to systematic errors in modelling. In the literature *D* values have either been derived by empirical methods or by mathematically calculated models. For this study the coefficients used were experimentally derived values are which are in agreement with calculated values.

D_{garnet}, $D_{clinopyroxene}$ and $D_{orthopyroxene}$ values are all largely derived from improved or modified versions of the Lattice Strain Model (LSM) first derived by Brice (1975) all with the aim of better constraining r_0-D_o-E (Optimum ionic radius of lattice site, Maximum distribution coefficient, Youngs modulus respectively) which in some previous studies have been 'fudged' to fit experimental data (Bernard, 2007). For Garnet the approach of van Westrenen and Daper (2007) was used whilst for orthopyroxene the approach of Bedard (2007) was used. Pressure and melt polymerisation has been found to have a significant effect on $D_{clinopyroxene}$ values

(Salters and Longie, 1999; Gaetani, 2004); as such two sets of coefficients for spinel facies (12kbar) and Garnet facies (45kbar) melts have been used, using the method of Wood and Blundy (1997) and Gaetani (2004). *D* values for olivine and spinel are based on measured concentrations from Reykjanes Peninsula lavas calculated by Thirlwall (unpublished).

5.3.1.2 Source modes

Melt modes are more difficult to calculate, relying on experimental data. Walter et al. (1995) devised a method for calculating melt modes from mass balance equations using the CaO-MgO-Al_2O_3-SiO_2-Na_2O (CMASN) system at varying pressures and temperatures. Authors have since adapted this method for a range of differing starting lithologies of spinel and garnet lherzolite and garnet pyroxenite, largely these calculated melting modes are in agreement with Walter et al., (1995), as such the values of Walter et al. (1995) have been used for lherzolite partial melt models. Very few melting modes exist in the literature for pyroxenites, the values of Pertermann and Hirschmann (2003) have been selected for modelling in this section.

Workers have highlighted that typical depleted MORB mantle may not be an appropriate source for Icelandic lavas particularly due the low La/Yb_N of the most depleted lavas (Waight and Baker, 2012), instead they suggest that sources that have had small degrees of melt removed previously may be more appropriate (Momme et al., 2006; Stracke and Bourdon, 2009; Waight and Baker, 2012). In this case a depleted DMM modified after Workman and Hart (2005) has been used for the source for the shallow spinel facies melts (values from Stracke and Bourdon, 2009) whilst unmodified DMM values were used (vaules from Workman and Hart, 2005). Stracke and Bourdon (2009) also suggested a composition for a pyroxenite that best represents recycled crust, which has also been used in subsequent models.

Partition Coefficients, Source and Melting modes as well as source compositions used in subsequent modelling are presented in table 5.2. Modelling was conducted using the equation for point average, non-modal fractional melting (McKenzie and O'Nions, 1991):

Equation 5.3:

$$\frac{C^i}{C_o^s} = \left[\frac{1}{F}\right] \cdot \left[1 - (1 - PF/D_o)^{(1/P)}\right]$$

Partition Coefficients:

D	ol	opx	cpx 12kbar	cpx 45kbar	sp	gt
La	0.00001	0.001	0.049	0.029	0.00006	0.008
Dy	0.002	0.05	0.432	0.240	0.002	2.001
Yb	0.014	0.108	0.435	0.242	0.005	6.189

Source modes:

	ol	opx	cpx	sp	gt
Spinel Lherzolite	0.53	0.27	0.17	0.03	-
Garnet Lherzolite	-	0.70	0.23	-	0.09
Pyroxenite	-	-	0.8	-	0.2

Melt modes:

	ol	opx	cpx	sp	gt
Spinel Lherzolite	-	0.30	0.70	0.1	-
Garnet Lherzolite	0.10	-	0.88	-	0.25
Pyroxenite	-	-	0.87	-	0.13

Source Compositions:

	La	Dy	Yb
DMM	0.192	0.505	0.365
Depleted DMM	0.1	0.471	0.348
Pyroxenite	1.74	5	3.2

Table 5.2: *Partition Coefficients, Source modes, Melting modes and Source compositions used in partial melt modelling.*

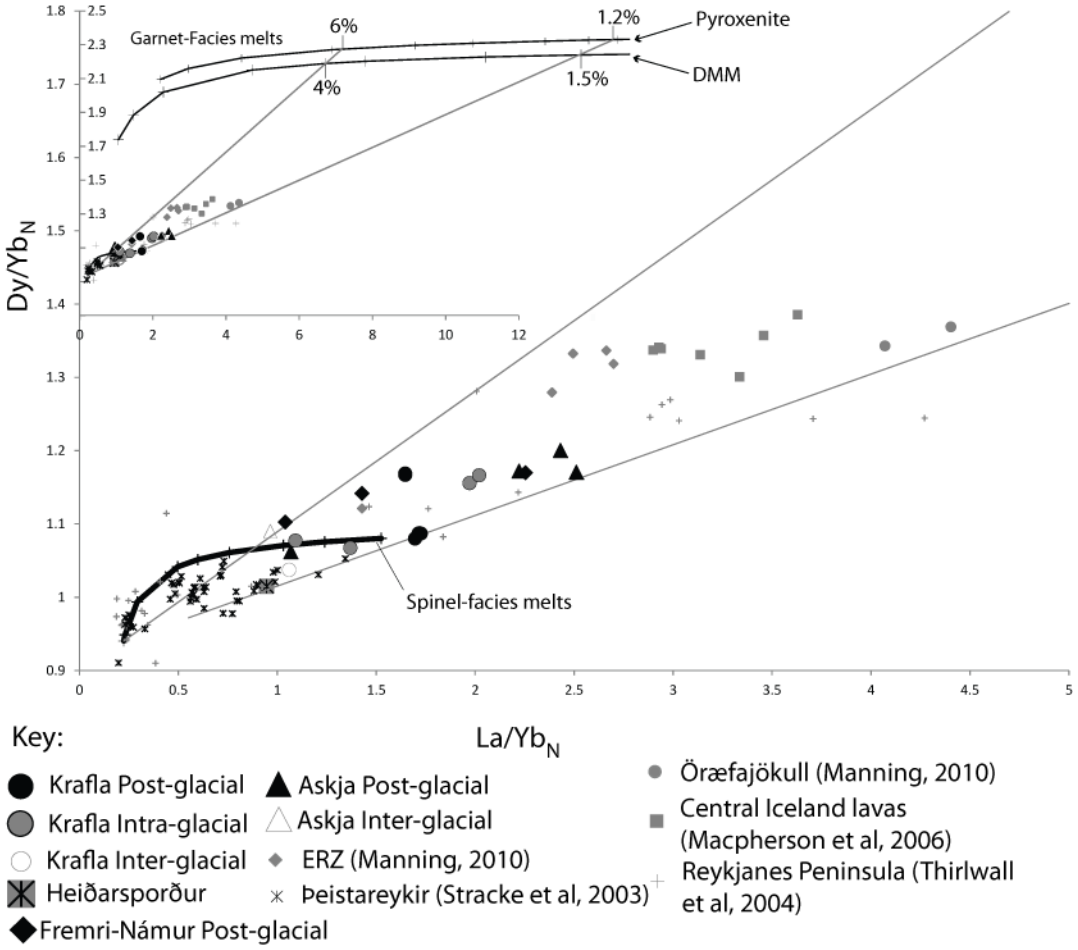

Figure 5.11: *Dy/Yb$_N$ vs. La/Yb$_N$ variation for the NRZ. Mixing with garnet-facies melts is required to generate the elevated Dy/Yb$_N$ values seen.*

Where:

C^i = Concentration of trace element in the partial melt
C^s_o = Initial concentration of the trace element in the source
F = fraction of melt formed
D_o = Bulk distribution coefficient
P = proportion in which mineral enters melt * distribution coefficient

Figure 5.11 clearly shows that NRZ lavas form good correlations between La/Yb$_N$ and Dy/Yb$_N$ ploting within the field of other rift zone lavas, roughly intermediate between the ERZ and WRZ trend. This correlation is consistent with the involvement of garnet facies melts. Melting curves have been generated based on the parameters stated in table 5.2 and indicate that large degree melts in the spinel field (>15%) can mix with small degrees of melts of garnet lherzolite (~1.5-4%) or pyroxenite (~1-6%) in order to reproduce the trends observed. It is important to note however that figure 5.11 cannot differentiate between a pyroxenite and garnet lherzolite melt.

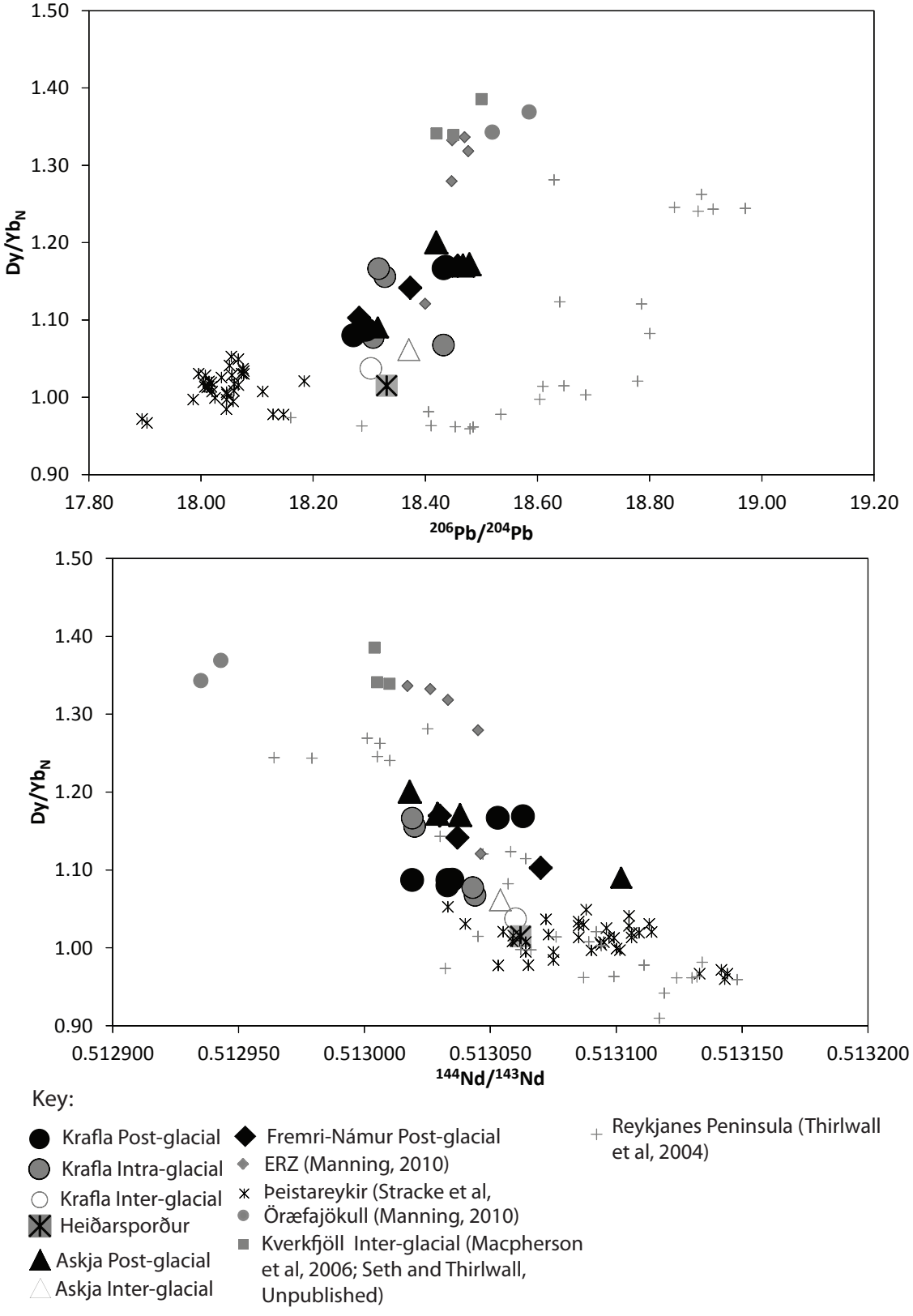

Figure 5.12: *variations between Dy/Yb$_N$ and radiogenic isotopes. Correlations suggest that more enriched samples have greater access to deeper melts.*

High Dy/Yb_N ratios in the enriched lavas have led authors to suggest that enriched mantle sources are preferentially tapped by deeper melts (figure 5.12) (e.g. Thirlwall et al., 1994; Peate et al., 2010; Thirlwall et al., 2011; Manning and Thirlwall, 2012). Therefore mantle components seen strongest in these lavas such as RP, IE1 and RS1, have been inferred to be housed in more fusible enriched 'blebs' (e.g. Manning and Thirlwall, 2012) whilst depleted rift zone lavas lie generally to lower Dy/Yb_N are tapping a more refractory peridotite matrix. Broad correlations seen between depleted and enriched lavas and Dy/Yb_N could be interpreted to represent mixing of melts between the enriched and depleted endmembers, as suggested by figure 5.11.

A more thorough assessment of the arrangement of these mantle components will be conducted in section 5.4.

5.3.2 Pyroxenite involvement

As previously established, the recycled component is likely to be present within the plume as a pyroxenite; partial melt modelling from section 5.3.1 does not preclude this. During adiabatic up-welling pyroxenite is able to start melting at relatively higher pressures (Yasuda et al. 1994; Yaxley, 2000; Kogiso et al., 1998; Hirschmann et al., 2003), this makes it a good candidate for the more fusible garnet bearing packages required for the source of the higher Dy/Yb_N lavas.

A. V. Sobolev, C. Herzberg and associated workers have argued that melts from a pyroxenite and a peridotite will interact in varying proportions to form 'hybrid' melts (e.g. Sobolev et al., 2007; Gurenko et al., 2009; Herzberg, 2011). Consequently correlations between parameters such Ni, Ca and Mn concentrations in olivine crystals have been used to estimate the amount of recycled material in the source of OIBs. It has been suggested that Iceland contains a relatively small proportion of recycled material. Sobolev et al. (2007) indicated that a mix of ~20% pyroxenite melt is required to reproduce the observed correlations (c.f Hawaii ~60% pyroxenite mix). In addition, Sobelev et al. (2008) reported very good correlations between Ni, Mn/Fe and Os isotopes, which appear to confirm that the recycled crustal component is in part present in the mantle as a pyroxenite. Olivine data for the NRZ reported here shows a similar range of Ni and Mn/Fe ratios as Sobelev et al. (2008); if then, the more enriched recycled components are housed as an olivine free source, such as a pyroxenite, then good correlations should also be expected between enrichment indices such as $^{206}Pb/^{204}Pb$ or Dy/Yb_N and olivine chemistry. This is not the case. Overall Ni, Mn and Ca concentrations from NRZ olivines plot largely between expected fields for peridotite and pyroxenite melts (figure 5.13), however as these elements are controlled by the presence of olivine at the source, the lack of correlation

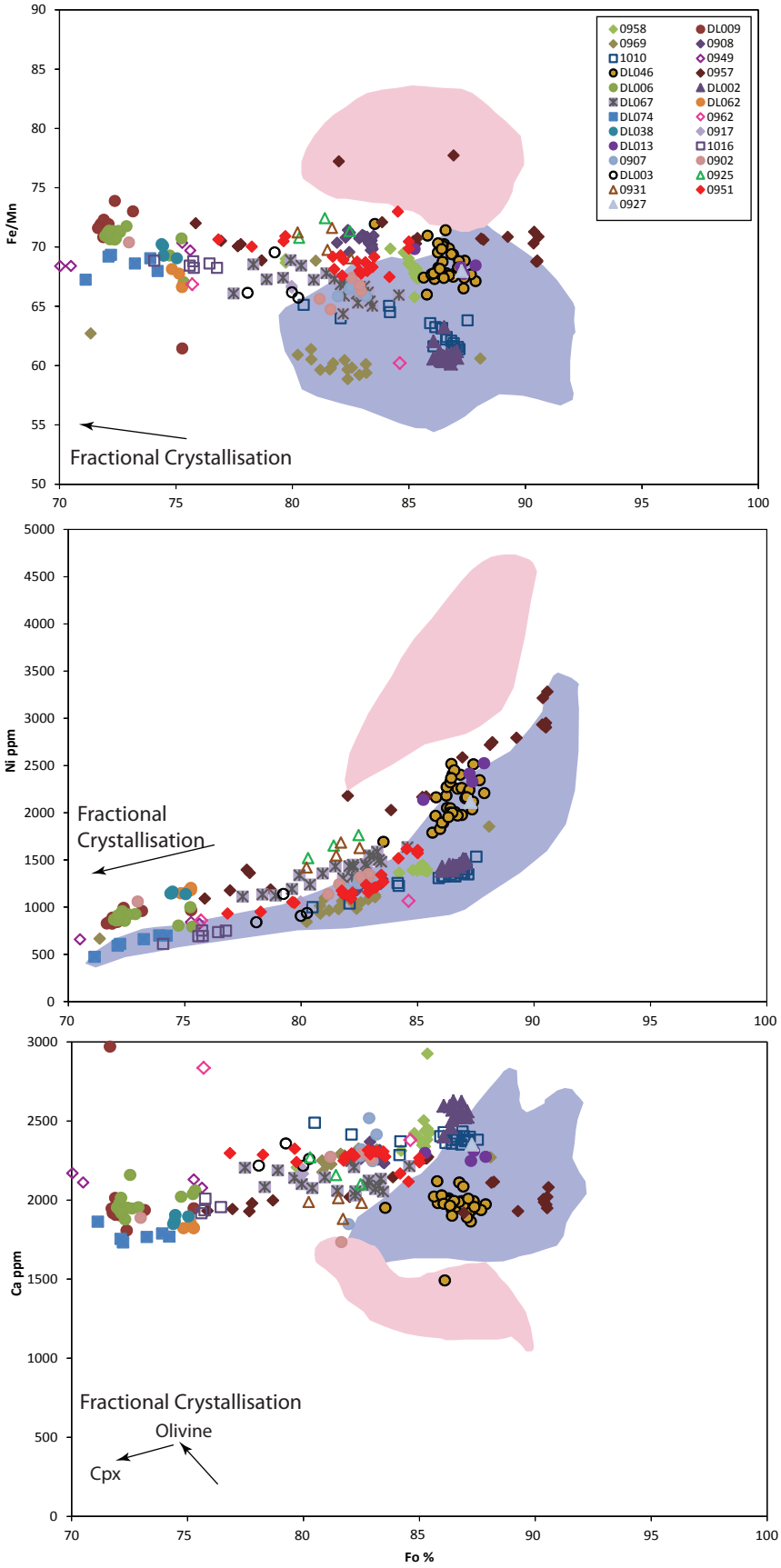

Figure 5.13: *Fe/Mn, Ni ppm and Ca ppm of olivines from the NRZ. Blue field indicates range of MORB values (data from Sobolev et al, 2007). Pink field indicates range of values from Hawaiian lavas that are argued to contain significant pyroxenite at their source (data from Herzberg, 2011).*

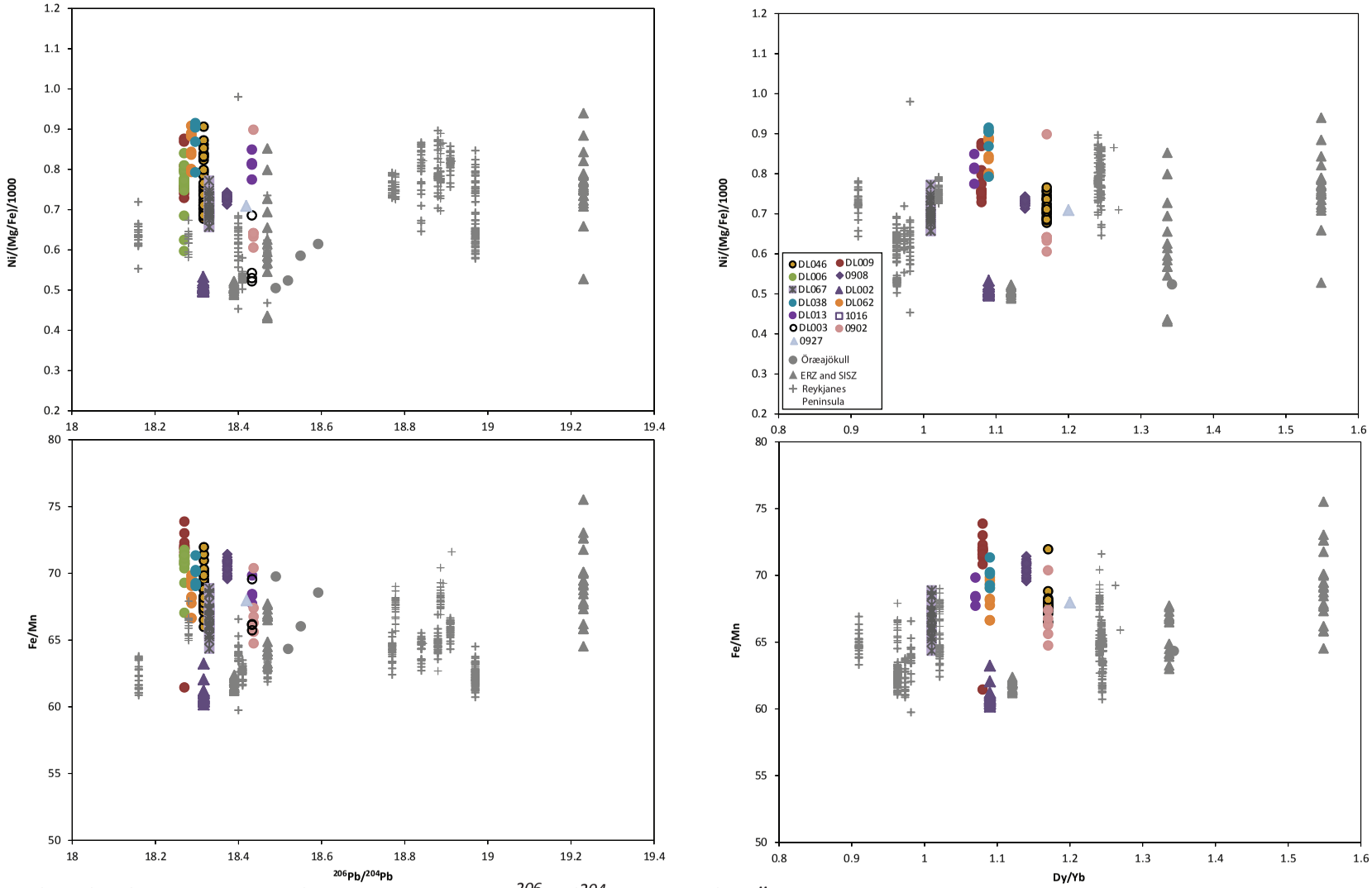

Figure 5.14: *Ni/(Mg/Fe)/1000ppm and Fe/Mn of olivines verses $^{206}Pb/^{204}Pb$ and Dy/Yb. Öræajökull, Reykjanes Peninsula and ERZ and SISZ from Thirlwall unpublished. The Ni/(Mg/Fe)/1000 parameter suggested by Sobolev et al. 2007 removes the effects of fractionation.*

with enrichment and depth of melting would tend to suggest that both the enriched and depleted sources have similar olivine proportions (figure 5.14).

This does not necessarily rule out involvement of a pyroxenite in the Icelandic source. During up-welling, at the contact between the pyroxenite and the host peridotite a SiO_2 poor olivine pyroxenite can form. Such source lithologies have been argued to be present under the Canary Islands due to lower Ni_{ol} (Gurenko et al., 2009; Herzberg, 2011). However, as Herzberg (2011) has importantly noted, due to the presence of olivine at the source, melts from peridotite and olivine pyroxenite can be difficult to distinguish. In experimental studies Yaxley and Green (1998) have shown that in extreme cases the pyroxenite will fully react, leaving a re-fertilised garnet lherzolite. As such the greater proportion of olivine present in the enriched source will remove correlations with Ni, Ca and Mn, consistent with observations in this data set.

It is perhaps interesting to note that Hawaii, which shows the strongest pyroxenite signature, is situated in an intra plate setting, whilst Iceland which do not readily show this signature is located near spreading ridges where decompression and melt productivity is greater.

5.4 Mantle source arrangement.

There has been considerable debate in the literature as to whether the depleted components identified at Iceland are intrinsic to the plume or were they whether entrained from surrounding upper mantle (Fitton et al., 1997; Hanan et al., 2000; Kempton et al., 2000; Stracke et al., 2003; Thirlwall et al., 2004; Brandon et al., 2007). Fitton et al. (1997) was amongst that first to argue against MORB evolvement using the ΔNb parameter; In their study Icelandic lavas were found to have exclusively negative ΔNb values, whist MORB had positive ΔNb values. Recently the suitability of ΔNb to discriminate between MORB and plume components has been questioned by Hanan et al. (2000) and Stracke et al. (2003). These workers presented larger data set which blurred the contrast between the Iceland and MORB fields observed by Fitton et al. (1997) as well as suggesting that the parameter may be affected by variable extents of melting and pressures. In response to this Kempton et al. (2000) and Fitton et al. (2003) showed that MORB and plume components could also be distinguished in Hf-Nd space, where MORB plots below the mantle reference line and Icelandic products fall above the mantle reference line. Figure 5.15 shows that whilst NRZ lavas do not only show positive ΔNb values, the tight correlations present make it very difficult to intersect the MORB field by mixing (figure 5.15), consistent with the proposal that the depleted components is not entrained from surrounding asthenosphere.

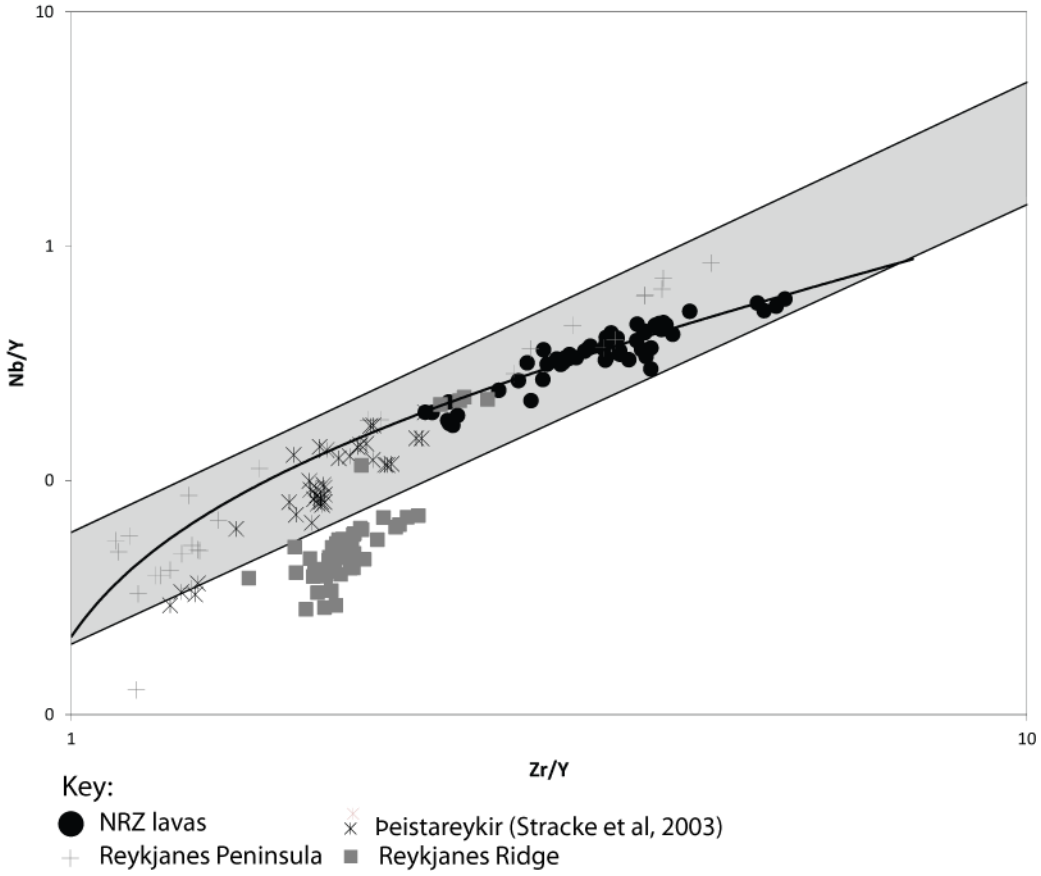

Figure 5.15: *Nb-Zr-Y systematics. NRZ lavas form a tight linear trend, regression through these lavas does not intersect with MORB lavas.*

The distribution of chemical signatures around Iceland has led a number of authors to attempt to describe the spatial arrangement of mantle components within the plume. Early work proposed that the plume is compositionally heterogeneous over scales of 100 kms, forming distinct concentric zones, consisting of an enriched core, surrounded by a depleted 'sheath'. (e.g. Fitton et al., 1997; Kempton et al., 2000; Murton et al., 2002; Thirlwall et al., 2004). At first glance NRZ lavas are consistent with this suggested arrangement; NRZ lavas generally become more incompatible element enriched towards the centre of Iceland (Figure 5.15a).

Recently Shorttle et al. (2010) proposed a simple kinematic model showing that such large scales of heterogeneity are not needed. The model describes the change in trace element and isotopic variation during radial outflow from a plume source that consists of an enriched phase embedded in a more depleted matrix. The greater fusibility of the enriched material will be able to melt at higher pressures due to the stronger decompressive forces at the plume centre, subsequent flow away from such centres will only be able to extract the more depleted, shallower components; consequently melt is progressively more depleted away from the

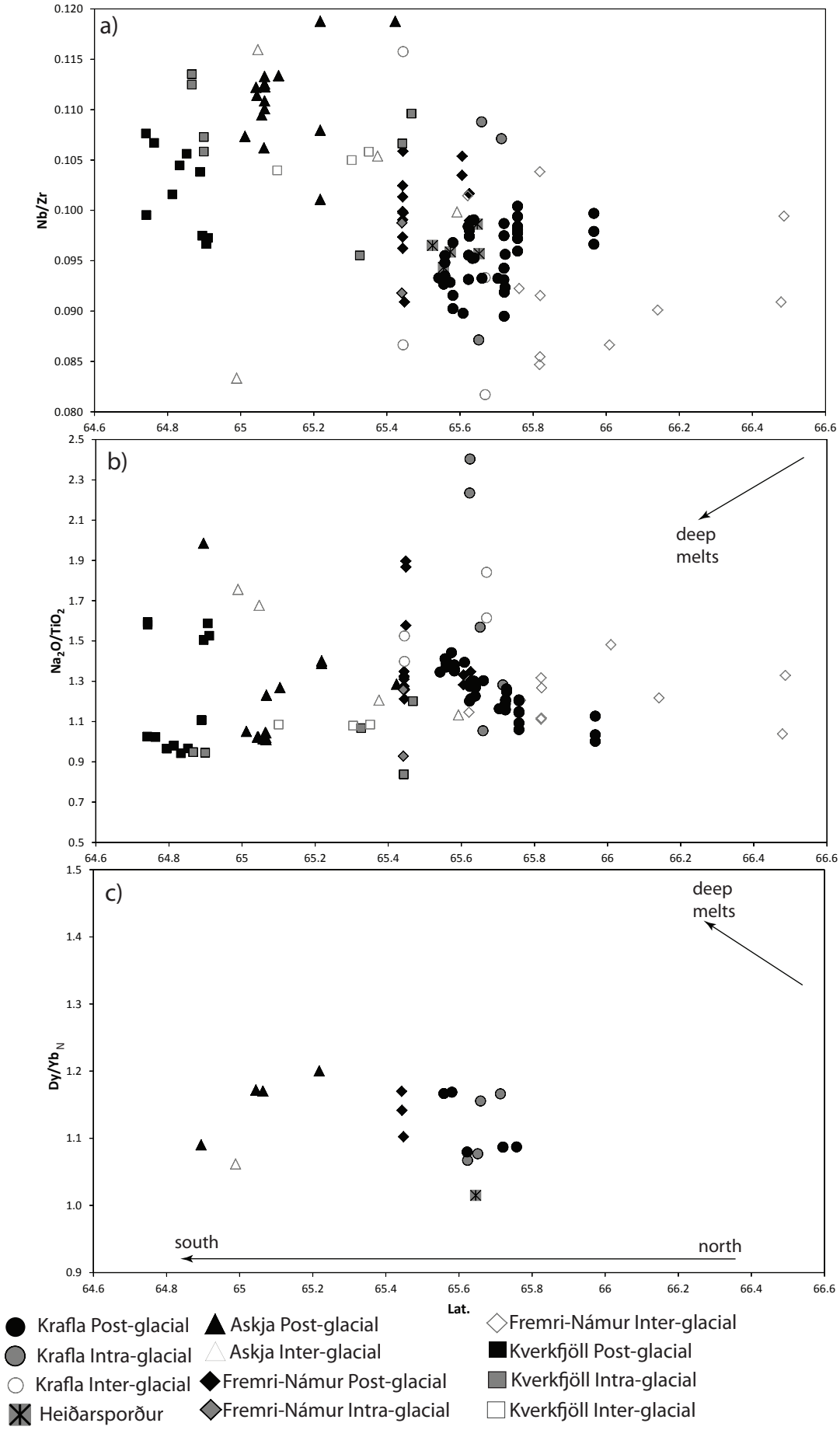

Figure 5.16: *Nb/Zr; Na_2O/TiO_2; Dy/Yb_N variation with latitude. Latitude of samples was traced back to point of eruption.*

plume centre. In such a model a systematic decrease in the contribution from deep sources away from the plume centre is expected; however no such decrease is seen with these lavas (Figure 5.15b,c). Each rift segment shows a similar range of Dy/Yb_N and Na_2O/TiO_2 values; therefore in order to reconcile this with the apparent decrease of sediment influence away from Vatnajökull that is suggested by radiogenic isotope trends (figure 5.6), heterogeneity within the mantle source must be present on a larger regional scale.

The recycled sediment component must be present as very small 'blobs' in order to fully homogenise to generate the individual pseudo-binary mixing ID1/RS endmembers required along the rift zone. Whilst the influence of sediment appears to get weaker to the north, radiogenic isotopes suggest that depleted sections of the recycled crust have a greater influence toward the north. This appears to culminate at Þeistareykir where the most depleted section of crust is tapped (ID1/ROC3 or RÞ). If the $\Delta^{207}Pb$ of modern MORB is allowed to evolve to -1 then Þeistareykir lavas can be encompassed in a mix of depleted sections of recycled crust (ID1/ROC3) and a local homogenised KR melt, this suggestion implies that a direct sediment contribution is absent. Considering the proximity of Þeistareykir to Krafla (~30 km between the main volcanic centres) it is unclear why the mantle arrangement should shift so suddenly.

The Húsavík-Flatey Transform fault is located nearby; whilst the full extent of this fault on land is unclear due to Holocene lava cover, it could potentially intersect the Þeistareykir and Krafla volcanic centres (Gudmundsson et al., 1993). Vogt and Johnson (1975) proposed that transform faults are able to act as a 'barrier' limiting asthenosphere flow, potentially creating a mechanism for the sudden change of mantle arrangement. This barrier however typically creates a ridge of thicker crust along the fault, this is not seen suggesting that the fault does not extent this far.

Alternatively if an old 130 Ma depletion event at the source of the Þeistareykir lavas is considered then corrected isotopic ratios suggest that the Þeistareykir lavas would lie on an RÞ /sediment mixing line with very little to no enriched sections of recycled crust present in the source. This would be consistent with the findings of Stracke (2003) who argued that an enriched component was almost completely absent at Þeistareykir, as well as being consistent with the 130-170 Ma isochronous relationship seen in the most depleted lavas of Iceland.

5.5 Conclusions

- $\Delta^{207}Pb$ and $\Delta^{208}Pb$ modelling as well as Sm-Nd and Lu-Hf pseudo-isochrons are consistent with a young, ~450 Ma recycled crustal component within the Icelandic mantle.

- NRZ lavas are able to tap heterogeneities within in this recycled crust; this is reflected by tight mixing trends seen within radiogenic isotope space of varying proportions of enriched and depleted recycled crust. Most rift segments along the NRZ show sub-parallel trends to Öræfajökull, suggesting that a diluted sediment component is being sampled along this rift zone (figure 5.5).

- The radiogenic isotope mixing relationships suggest that the influence of sediment is not confined to the immediate vicinity of Öræfajökull and decrease steadily away from the plume centre.

- The source variation at Þeistareykir is less clear. If these lavas reflect a recent depletion event then modern MORB in this part of the Atlantic would need to have evolved to a $\Delta^{207}Pb$ of -1 in order to encompass these lavas with recycled crustal endmembers. However if the source at Þeistareykir had undergone an old (130Ma) depletion event then corrected ratios plot these lavas largely within the range of other NRZ lavas and suggest that Þeistareykir may be dominated by depleted sections of recycled crust whilst having similar amounts of sediment is present in the source as Krafla lavas.

- Lavas clearly get progressively more enriched toward the south of the rift zone, however the lack of a systematic northward decrease of Dy/Yb_N seen in lavas from these rift segments suggests that the heterogeneities sampled are present over large wavelengths and not focused at the plume centre and subsequently diluted along the ridge as suggested by Shorttle et al. (2010).

- It has been widely suggested that recycled crust is present in the mantle as an olivine free pyroxenite; however there is little evidence that such a pyroxenite is present beneath Iceland. The lack of correlations between indices of depth of melting or isotopic enrichment with olivine free pyroxenite signatures such as high Ni and low Ca

and Fe/Mn suggests that similar olivine modal proportions must be present in both the enriched and depleted lava sources.

CHAPTER 6: SUMMARY

6.1 Summary of Conclusions

A suite of 156 post, intra and inter glacial samples from the length of the Northern Rift Zone have provided chemical and isotopic data which support many of the established views of Icelandic magmatism as well as permitting new and more detailed models to be constructed.

Fractional crystallisation is common to the vast majority of lavas and the tight trends present in this data set have enabled different liquid lines of descent to be identified and modelled, reflecting variations in the parental magmas within rift systems. In particular differences in parental magmas have been mostly identified between the post and inter/intra glacial samples suggesting shifts of parental magmas over time. Samples from Heiðarsporður however, are anomalous in their major and trace element trends. Below ~7.5 wt. % MgO model fractional crystallisation trends were not able to reproduce the variations seen. These lavas have higher SiO_2 wt. % that other rift zone lavas and have flat Fe_2O_3 and Al_2O_3 patterns as well as relatively low Sc concentrations suggesting a stronger clinopyroxene control on their chemistry rather than plagioclase. Instead of fractional crystallisation (near liquidus differentiation) Jónasson (2005) suggested that near-solidus differentiation, whereby segregation of partial melts from either cooling bodies of magma or the heating of hydrothermally altered crust by deformation, probably during a rifting event, can potentially account for these trends.

On the whole olivine and plagioclase are the dominant phenocrysts present with clinopyroxene only seen in a small number of samples. Despite the large number of lavas from Þeistareykir that are reported to be olivine accumulate, there is no evidence of olivine accumulation in this data set; there is however evidence of plagioclase accumulation in a small number of samples, mostly from Kverkfjöll.

Below 8 wt. % MgO the tight ol-plag-cpx crystallisation trends together with the lack of accumulation and alteration in the majority of samples provided an opportunity to calculate the pressures (and therefore depths) of crystallisation for these samples. Pressures were calculated using a programme devised by Kelley and Barton (2008) using the equations derived by Yang et al. (1996). Overall, multiple bodies of crystallisation have been identified under central volcanoes. Typically basaltic lavas originate from chambers or sills located in the lower

gabbroic crust at around 10 km and 16 km depths, consistent with estimated depths from other Icelandic centres (Kelley and Barton, 2008). This is in contrast to classic models of magmatic plumbing under central volcanoes that describe the presence of one shallow chamber at the source of both basaltic and acidic eruptions.

Krafla, Askja and Kverkfjöll are all relatively well developed central volcanoes and as such two distinct depths of crystallisation are clearly identified. However, the crystallisation depths of lavas from Fremri-Námur have been more difficult to interpret. A chamber at ~10km depth can be confidently identified however only the few postglacial samples that yield deeper pressures as well as the slight scatter seen in the intra and inter glacial sample depths makes the identification of deeper chambers more difficult. The scatter present in the older samples could represent the lack of a well-developed magma chamber at this time reflecting the less developed nature of the Fremri-Námur system. Alternatively, optical inspections of these samples reveal that gabbroic nodules in various states of disaggregation are present, in some cases these nodules are found in lavas that have been identified as plagioclase accumulates. As such the entrainment of large proportions of nodules could have an effect on the true liquid composition of samples which would lead to the calculation of erroneous pressures.

Given the typical depths of magma chambers identified in this study these gabbroic nodules are likely to have been entrained from the lower crust into magmas. Generally such nodules are easily identified in thin section. However if these nodules have fully disaggregated it can be difficult to optically identify these samples. Phenocryst compositions can be used to identify such lavas. Samples with gabbroic nodules often large ranges of Fo%, whilst plagioclase crystals often show populations of more evolved crystals. This is in contrast to phenocryst populations from the majority of lavas, which do not contain nodules. From these samples olivine Fo% generally show peaks in the expected equilibrium field whilst plagioclase generally shows equilibrium to more primitives crystals that their host melt. A minority of lavas show peaks of Fo% that are more primitive than expected, this could indicate that these samples had shorter crustal residences times.

The better constraints on crystallisation depths have enabled better models of crustal assimilation to be constructed. In particular the assimilation of the lower crust clearly plays a more important role (in part reflected by the presence of gabbroic nodules identified in many of the lavas from this study). This is in contrast to classic models of assimilation that describe contamination from hydrothermally altered crust. Assimilation has often been cited as the principle method of generating the light $\delta^{18}O$ signature commonly associated with Icelandic

basalts. Assimilation models based on contamination from the lower crust demonstrates that whilst assimilation cannot be categorically ruled out, it is not possible to recreate the $\delta^{18}O$ values seen within this data set without evoking a mantle that has below normal values. This is perhaps seen most clearly in the suite of lavas from Heiðarsporður. These lavas contain large gabbrioc noudles that show strong resorption textures, whilst also showing some of the lightest $\delta^{18}O$ values in the most evolved samples (Jónasson, 2005). If these light values were a function of contamination then high $^{87}Sr/^{86}Sr$ ratios and high concentrations of mobile elements such as Ba and Rb might be expected. However this is not seen. In addition the range of $^{87}Sr/^{86}Sr$ observed in the more evolved lavas is within the range of the primitive lavas which are unlikely to have undergone significant modification from their source. The presence of gabbroic nodules in these samples as well as in other lavas from this data set shows that contamination from the lower crust is not uncommon; however the absence of extreme geochemical signatures suggests that this material is relatively fresh.

This is little debate as to the heterogeneous nature of the source of Icelandic lavas in particular the tight correlations observed between isotopic systems and ratios of incompatible elements have led workers to suggest that this heterogeneity is accounted for by the mixing of distinct components within the Icelandic mantle. Sr-Nd-Pb isotopic ratios all indicate that a mixture of depleted and enriched sections of a recycled ~450 Ma crust are dominant in the source of NRZ lavas. With the exception of Kverkfjöll, between rift segments tight pseudo-binary sub-parallel trends to Öræfajökull are observed further suggesting that a dilute sediment component is present. This is significant as it may suggest that the sediment component, thought to be only observed at Öræfajökull and its closest neighbouring central volcanoes, may play a more significant role at the source of Icelandic basalts. Generally the more enriched lavas have higher Dy/Yb_N and lower Na_2O/TiO_2 ratios suggesting that the more enriched recycled crustal and sediment mantle components may be housed in fusible 'blebs' whilst the depleted components are present in a more refractory matrix. Each rift segment shows similar ranges of Dy/Yb_N and Na_2O/TiO_2 values suggesting the heterogeneity within the mantle must be present over a large regional scale however these 'blebs' must be relatively small in order to fully homogenise and to generate the pseudo-binary end members for each rift zone. The sub-parallel trends indicate that the sediment contribution is slowly decreasing to the north of the rift zone.

Other studies of OIB have shown that these recycled crustal components are expected to be present in the mantle as garnet bearing, olivine free pyroxenites. Such lithologies are able to

start melting at relatively higher pressures, and are good candidates for housing the more fusible enriched mantle components. However there is little evidence that such a pyroxenite is present within the Icelandic mantle. Typically olivines that crystallise from these pyroxenite melts have a higher Ni and lower Ca and Fe/Mn values. Furthermore, mixing of these melts with olivine bearing lherzolites will produce correlations between Ni/(Mg/Fe)/1000, Ca and Fe/Mn values in olivines and enrichment indices of their respective whole rocks. No such relationships have been identified casting doubt on the presence of an olivine free pyroxenite beneath Iceland however the involvement of a re-fertilised olivine bearing pyroxenite such as identified at the source of the Canary Islands cannot be categorically ruled out.

6.2 Suggested further work

- It was noted in chapter 5 that the lack of a strong pyroxenite signature at Iceland may be linked to the large de-compressive stress due to its ridge location. If this is the case then olivine compositions from flood basalts from Greenland, or the British Tertiary province that were emplaced before the onset of rifting may show stronger pyroxenitic signatures. Major and trace element analysis from populations of olivines from these locations may help to further resolve the debate surrounding the role pyroxenite within the Icelandic plume.

- This work has shown that detailed studies of individual volcanic centres is needed to fully resolve local mantle arrangements, in the case of the NRZ/ERZ revealing that the influence of sediment may be more important along this rift zone than previously thought. Detailed isotopic studies of other rift segments such as the MIB may help to resolve the full extent of sediment contribution between rift zones.

- Finally, continued detailed analysis of phenocryst populations from wide selections of flows and ages together with crystallisation pressure estimates will help to further confidently identify the typical magmatic processes that occur in magma chambers across the NRZ.

REFERENCES CITED

Aigner-Torres, M., Blundy, J., Ulmer, P., and Pettke, T., 2007, Laser Ablation ICPMS study of trace element partitioning between plagioclase and basaltic melts: an experimental approach: Contributions to Mineralogy and Petrology, v. 153, no. 6, p. 647-667.

Albarede, F., 1985, Regime and trace-element evolution of open magma chambers: Nature, v. 318, p. 356-358

Allen, R. M., Nolet, G., Morgan, W. J., Vogfjord, K., Bergsson, B. H., Erlendsson, P., Foulger, G. R., Jakobsdottir, S., Julian, B. R., Pritchard, M., Ragnarsson, S., and Stefansson, R., 1999, The thin hot plume beneath Iceland: Geophysical Journal International, v. 137, no. 1, p. 51-63.

Andrew, R. E. B., and Gudmundsson, A., 2007, Distribution, structure, and formation of Holocene lava shields in Iceland: Journal of Volcanology and Geothermal Research, v. 168, no. 1-4, p. 137-154.

Baker, J., Waight, T., and Ulfbeck, D., 2002, Rapid and highly reproducible analysis of rare earth elements by multiple collector inductively coupled plasma mass spectrometry: Geochimica Et Cosmochimica Acta, v. 66, no. 20, p. 3635-3646.

Båth, M., 1960, Crustal structure of Iceland: Journal of Geophysical Research, v. B65, p. 1793-1807.

Beblo, M., and Bjornsson, A., 1978, Magnetotelluric Investigation of the Lower Crust and Upper Mantle beneath Iceland: Journal of Geophysics-Zeitschrift Fur Geophysik, v. 45, no. 1, p. 1-16.

Bedard, J. H., 2006, Trace element partitioning in plagioclase feldspar: Geochimica Et Cosmochimica Acta, v. 70, no. 14, p. 3717-3742.

Bedard, J. H., 2007, Trace element partitioning coefficients between silicate melts and orthopyroxene: Parameterizations of D variations: Chemical Geology, v. 244, p. 263-303.

Bijwaard, H., and Spakman, W., 1999, Tomographic evidence for a narrow whole mantle plume below Iceland: Earth and Planetary Science Letters, v. 166, no. 3-4, p. 121-126.

Bindeman, I., Gurenko, A., Sigmarsson, O., and Chaussidon, M., 2008, Oxygen isotope heterogeneity and disequilibria of olivine crystals in large volume Holocene basalts from Iceland: Evidence for magmatic digestion and erosion of Pleistocene hyaloclastites: Geochimica Et Cosmochimica Acta, v. 72, no. 17, p. 4397-4420.

Bindeman, I., Sigmarsson, O., and Eiler, J., 2006, Time constraints on the origin of large volume basalts derived from O-isotope and trace element mineral zoning and U-series disequilibria in the Laki and Grímsvötn volcanic system: Earth and Planetary Science Letters, v. 245, no. 1-2, p. 245-259.

Bindeman, I. N., Davis, A. M., and Drake, M. J., 1998, Ion microprobe study of plagioclase-basalt partition experiments at natural concentration levels of trace elements: Geochimica Et Cosmochimica Acta, v. 62, no. 7, p. 1175-1193.

Bjarnason, I. P., 2008, An Iceland hotspot saga: Jokull, v. 58, p. 3-16.

Bjarnason, I. T., Menke, W., Flovenz, O. G., and Caress, D., 1993, Tomographic Image of the Mid-Atlantic Plate Boundary in Southwestern Iceland: Journal of Geophysical Research-Solid Earth, v. 98, no. B4, p. 6607-6622.

Bjarnason, I. Þ. W., C, J Solomon, S. C. Gudmundson, G, 1996, Initial results from the ICEMELT experiment: Body wave delay time and shear wave splitting across Iceland: Geophysical Research Letters, v. 5, p. 459-462.

Bjornsson, A., 1985, Dynamics of Crustal Rifting in Ne Iceland: Journal of Geophysical Research-Solid Earth and Planets, v. 90, no. Nb12, p. 151-162.

Blichert-Toft, J., 2005, Geochemical segmentation of the Mid-Atlantic Ridge north of Iceland and ridge–hot spot interaction in the North Atlantic: Geochemistry Geophysics Geosystems, v. 6, no. 1.

Blundy, J. D., and Wood, B. J., 1991, Crystal-Chemical Controls on the Partitioning of Sr and Ba between Plagioclase Feldspar, Silicate Melts, and Hydrothermal Solutions: Geochimica Et Cosmochimica Acta, v. 55, no. 1, p. 193-209.

Brandon, A. D., Graham, D. W., Waight, T., and Gautason, B., 2007, 186Os and 187Os enrichments and high-3He/4He sources in the Earth's mantle: Evidence from Icelandic picrites: Geochimica et Cosmochimica Acta, v. 71, no. 18, p. 4570-4591.

Brandon, A. D., Graham, D. W., Waight, T., and Gautason, B., 2007, Os-He isotope systematics of Iceland picrites: Evidence for a deep origin of the Iceland plume: Geochimica Et Cosmochimica Acta, v. 71, no. 15, p. A119-A119.

Brandsdottir, B., Menke, W., Einarsson, P., White, R. S., and Staples, R. K., 1997, Faroe-Iceland Ridge Experiment .2. Crustal structure of the Krafla central volcano: Journal of Geophysical Research-Solid Earth, v. 102, no. B4, p. 7867-7886.

Breddam, K., 2002, Kistufell: Primitive melt from the Iceland mantle plume: Journal of Petrology, v. 43, no. 2, p. 345-373.

Brice, J. C., 1975, Some Thermodynamic Aspects of Growth of Strained Crystals: Journal of Crystal Growth, v. 28, no. 2, p. 249-253.

Brown, G. C., Everett, S. P., Rymer, H., Mcgarvie, D. W., and Foster, I., 1991, New Light on Caldera Evolution - Askja, Iceland: Geology, v. 19, no. 4, p. 352-355.

Carmichael, I., S, E., 1964, The petrology of Thingmuli, a Tertiary volcano in eastern Iceland: Journal of Petrology, v. 5, no. 3, p. 435-460.

Chauvel, C., Hofmann, A., H., Vidal, P., 1992, HIMU-EM: The French Polynesian connection: Earth and Planetary Science Letters, v. 110, p.99-119.

Chauvel, C., and Hemond, C., 2000, Melting of a complete section of recycled oceanic crust: Trace element and Pb isotopic evidence from Iceland: Geochemistry Geophysics Geosystems, v. 1.

Christensen, N., 1966, Elasticity of Ultrabasic Rocks: Journal of Geophysical Research, v. 71, p. 5921-5932.

Coogan, L. A., Kempton, P. D., Saunders, A. D., and Norry, M. J., 2000, Melt aggregation within the crust beneath the Mid-Atlantic Ridge: evidence from plagioclase and clinopyroxene major and trace element compositions: Earth and Planetary Science Letters, v. 176, no. 2, p. 245-257.

Corry, C. E., 1988, Laccoliths: mechanics of emplacement and growth.: Geological Society of America Special Paper, v. 220.

Cotman, R. M., 1979, Potassium-Argon evidence for shifting of the axial rift zone in northern Iceland [M.S: Case Western Reserve University.

Cottrell, E., Spiegelman, M., and Langmuir, C. H., 2002, Consequences of diffusive reequilibration for the interpretation of melt inclusions: Geochemistry Geophysics Geosystems, v. 3.

Danyushevsky, L. V., Perfit, M. R., Eggins, S. M., and Falloon, T. J., 2003, Crustal origin for coupled 'ultra-depleted' and 'plagioclase' signatures in MORB olivine-hosted melt inclusions: evidence from the Siqueiros Transform Fault, East Pacific Rise: Contributions to Mineralogy and Petrology, v. 144, no. 5, p. 619-637.

Danyushevsky, L. V., Sobolev, A. V., and Dmitriev, L. V., 1996, Estimation of the pressure of crystallization and H2O content of MORE and BABB glasses: Calibration of an empirical technique: Mineralogy and Petrology, v. 57, no. 3-4, p. 185-204.

Darbyshire, F. A., Bjarnason, I. T., White, R. S., and Flovenz, O. G., 1998, Crustal structure above the Iceland mantle plume imaged by the ICEMELT refraction profile: Geophysical Journal International, v. 135, no. 3, p. 1131-1149.

Darbyshire, F. A., Priestley, K. F., White, R. S., Stefansson, R., Gudmundsson, G. B., and Jakobsdottir, S. S., 2000, Crustal structure of central and northern Iceland from analysis of teleseismic receiver functions: Geophysical Journal International, v. 143, no. 1, p. 163-184.

Davidson, J., P., and Harmon, R., S., 1989, Oxygen isotope constraints on the petrogenesis of volcanic arc magmas from Martinique, Lesser Antilles, Earth and Planetary Science Letters, v. 95, p. 255-270.

Davidson, J. P. M., D. J. Charlier, B. L. A. Harlou, R. Hora, J. M., 2007, Microsampling and isotopic analysis of igneous rock implication for the study of magmatic systems.: Annual Review of Earth and Planetary Sciences, v. 35, p. 273-311.

de Zeeuw-van Dalfsen, E., 2004, Satellite radar interferometry 1993–1999 suggests deep accumulation of magma near the crust-mantle boundary at the Krafla volcanic system, Iceland: Geophysical Research Letters, v. 31, no. 13.

de Zeeuw-Van Dalfsen, E., Rymer, H., Sigmundsson, F., and Sturkell, E., 2005, Net gravity decrease at Askja volcano, Iceland: constraints on processes responsible for continuous caldera deflation, 1988-2003: Journal of Volcanology and Geothermal Research, v. 139, no. 3-4, p. 227-239.

de Zeeuw-van Dalfsen, E. P., R Sigmundsson, F., 2004, Satellite radar interferometry 1993–1999 suggests deep accumulation of magma near the crust-mantle boundary at the Krafla volcanic system, Iceland: Geophysical Research Letters, v. 31, p. L13611.

Debaille, V., Trønnes, R. G., Brandon, A. D., Waight, T. E., Graham, D. W., and Lee, C.-T. A., 2009, Primitive off-rift basalts from Iceland and Jan Mayen: Os-isotopic evidence for a mantle source containing enriched subcontinental lithosphere: Geochimica et Cosmochimica Acta, v. 73, no. 11, p. 3423-3449.

Downes, H., Thirlwall, M., F., Trayhorn, S., C., 2001. Miocene subductionrelated magmatism in southern Sardinia: Sr–Nd- and oxygen isotopic evidence for mantle source enrichment: Journal of Volcanolical and Geothermal Research, v. 106 p. 1-21.

Dupre, B., and Allegre, C. J., 1983, Pb-Sr Isotope Variation in Indian-Ocean Basalts and Mixing Phenomena: Nature, v. 303, no. 5913, p. 142-146.

Eiler, J. M., Gronvold, K., and Kitchen, N., 2000, Oxygen isotope evidence for the origin of chemical variations in lavas from Theistareykir volcano in Iceland's northern volcanic zone: Earth and Planetary Science Letters, v. 184, no. 1, p. 269-286.

Eiler, J. M., Schiano, P., Kitchen, N., and Stolper, E. M., 2000, Oxygen-isotype evidence for recycled crust in the sources of mid-ocean-ridge basalts: Nature, v. 403, no. 6769, p. 530-534.

Einarsson, P., 1978, Seismological evidence for Lateral magma intrusion during the July 1978 deflation of the Krafla volcano in NE-Iceland.: Technical Report University of Iceland, v. UI-79-9-7.

Einarsson, Þ., 1995, Saga bergs og lands, Reykjavik, M´al og Menning.

Elthon, D., 1984, Isomolar and isostructural pseudo-liquidus phase diagrams for oceanic basalts: American Mineralogist, v. 68, p. 506-511.

Falloon, T. J., Danyushevsky, L. V., Ariskin, A., Green, D. H., and Ford, C. E., 2007, The application of olivine geothermometry to infer crystallization temperatures of parental liquids: Implications for the temperature of MORB magmas: Chemical Geology, v. 241, no. 3-4, p. 207-233.

Farnetani, C. G., Richards, M. A., and Ghiorso, M. S., 1996, Petrological models of magma evolution and deep crustal structure beneath hotspots and flood basalt provinces: Earth and Planetary Science Letters, v. 143, no. 1-4, p. 81-94.

Feig, S. T., Koepke, J., and Snow, J. E., 2006, Effect of water on tholeiitic basalt phase equilibria: an experimental study under oxidizing conditions: Contributions to Mineralogy and Petrology, v. 152, no. 5, p. 611-638.

Fitton, J. G., Saunders, A. D., Kempton, P. D., and Hardarson, B. S., 2003, Does depleted mantle form an intrinsic part of the Iceland plume?: Geochemistry Geophysics Geosystems, v. 4.

Fitton, J. G., Saunders, A. D., Norry, M. J., Hardarson, B. S., and Taylor, R. N., 1997, Thermal and chemical structure of the Iceland plume: Earth and Planetary Science Letters, v. 153, no. 3-4, p. 197-208.

Fitton, J. G., 1997, Thermal and chemical structure of the Iceland plume: Earth and Planetary Science Letters, v. 153, no. 3-4, p. 197-208.

Flovenz, O. G., 1980, Seismic Structure of the Icelandic Crust above Layer 3 and the Relation between Body Wave Velocity and the Alteration of the Basaltic Crust: Journal of Geophysics-Zeitschrift Fur Geophysik, v. 47, no. 1-3, p. 211-220.

Flovenz, O. G., and Gunnarsson, K., 1991, Seismic Crustal Structure in Iceland and Surrounding Area: Tectonophysics, v. 189, no. 1-4, p. 1-17.

Foulger, G. R., and Anderson, D. L., 2005, A cool model for the Iceland hotspot: Journal of Volcanology and Geothermal Research, v. 141, no. 1-2, p. 1-22.

Foulger, G. R., Natland, J. H., and Anderson, D. L., 2005, Genesis of the Iceland melt anomaly by plate tectonic processes: Plates, Plumes and Paradigms, v. 388.

Francis, D., 1986, The Pyroxene Paradox in Morb Glasses - a Signature of Picritic Parental Magmas: Nature, v. 319, no. 6054, p. 586-589.

Francis, D., and Minarik, W., 2008, Aluminum-dependent trace element partitioning in clinopyroxene: Contributions to Mineralogy and Petrology, v. 156, no. 4, p. 439-451.

Furman, T., Frey, F. A., and Meyer, P. S., 1992, Petrogenesis of Evolved Basalts and Rhyolites at Austurhorn, Southeastern Iceland - the Role of Fractional Crystallization: Journal of Petrology, v. 33, no. 6, p. 1405-1445.

Gaetani, G. A., 2004, The influence of melt structure on trace element partitioning near the peridotite solidus: Contributions to Mineralogy and Petrology, v. 147, p. 511-527.

Garcia, S., Arnaud, N. O., Angelier, J., Bergerat, F., and Homberg, C., 2003, Rift jump process in Northern Iceland since 10 Ma from 40Ar/39Ar geochronology: Earth and Planetary Science Letters, v. 214, no. 3-4, p. 529-544.

Gautier, I., Weis, D., Mennessier, J. P., Vidal, P., Giret, A., and Loubet, M., 1990, Petrology and Geochemistry of the Kerguelen Archipelago Basalts (South Indian-Ocean) - Evolution of the Mantle Sources from Ridge to Intraplate Position: Earth and Planetary Science Letters, v. 100, no. 1-3, p. 59-76.

Gautason, B., and Muehlenbachs, K., 1998, Oxygen isotopic fluxes associated with high-temperature processes in the rift zones of Iceland: Chemical Geology, v.145, p. 275-286.

Gebrande, H., Miller, H., and Einarsson, P., 1980, Seismic Structure of Iceland Along Rrisp - Profile-I: Journal of Geophysics-Zeitschrift Fur Geophysik, v. 47, no. 1-3, p. 239-249.

Gee, M. A. M., Thirlwall, M. F., Taylor, R. N., Lowry, D., and Murton, B. J., 1998a, Crustal processes: Major controls on Reykjanes Peninsula lava chemistry, SW Iceland: Journal of Petrology, v. 39, no. 5, p. 819-839.

Gee, M. A. M., Taylor, R. N., Thirlwall, M. F., and Murton, B. J., 1998b, Glacioisostacy controls chemical and isotopic characteristics of tholeiites from the Reykjanes peninsula, SW Iceland: Earth and Planetary Science Letters, v. 164, no. 1-2, p. 1-5.

Geldmacher, J., and Hoernle, K., 2000, The 72 Ma geochemical evolution of the Madeira hotspot (eastern North Atlantic): recycling of Paleozoic (<= 500 Ma) oceanic lithosphere: Earth and Planetary Science Letters, v. 183, no. 1-2, p. 73-92.

Global Volcanism Program, www.volcano.si.edu, *Smithsonian Institution*.

Grove, T. L., Kinzler, R. J., and Bryan, W. B., 1992, Fractionation of Midocean Ridge Basalt (Morb): Mantle Flow and Melt Generation at Mid-Ocean Ridges, v. 71, p. 281-310.

Gudfinnsson, G., Presnall, D.C. & Oskarsson, N, 2003, Contrasting origins of the most magnesian glasses from Iceland and Hawaii., Hveragerdi , Iceland, Geological Society of America, Plume IV: Beyond the Plume Hypothesis.

Gudmundsson, A., 1990, Emplacement of Dikes, Sills and Crustal Magma Chambers at Divergent Plate Boundaries: Tectonophysics, v. 176, no. 3-4, p. 257-275.

Gudmundsson, A., 1998, Formation and development of normal-fault calderas and the initiation of large explosive eruptions.: Bulletin of Volcanology, v. 60, p. 160-170.

Gudmundsson, A., 2000, Dynamics of volcanic systems in Iceland: Example of tectonism and volcanism at juxtaposed hot spot and mid-ocean ridge systems: Annual Review of Earth and Planetary Sciences, v. 28, p. 107-140.

Gudmundsson, A., 2009, Toughness and failure of volcanic edifices: Tectonophysics, v. 471, no. 1-2, p. 27-35.

Gudmundsson, A., 2011, Deflection of dykes into sills at discontinuities and magma-chamber formation: Tectonophysics, v. 500, no. 1-4, p. 50-64.

Gudmundsson, A., Brynjolfsson, S., and Jonsson, M. T., 1993, Structural-Analysis of a Transform-Fault Rift-Zone Junction in North Iceland: Tectonophysics, v. 220, no. 1-4, p. 205-221.

Gudmundsson, M. T., Sigmundsson, F., and Bjornsson, H., 1997, Ice-volcano interaction of the 1996 Gjalp subglacial eruption, Vatnajokull, Iceland: Nature, v. 389, no. 6654, p. 954-957.

Gupta, V. B., J. S., 1997, Compressive failure of rocks: International Journal of Rock Mechanics and Mining Sciences & Geomechanics Abstracts, v. 34, no. 3-4, p. 1-23.

Gurenko, A. A., and Sobolev, A. V., 2006, Crust–primitive magma interaction beneath neovolcanic rift zone of Iceland recorded in gabbro xenoliths from Midfell, SW Iceland: Contributions to Mineralogy and Petrology, v. 151, no. 5, p. 495-520.

Gurenko, A. A., Sobolev, A. V., Hoernle, K. A., Hauff, F., and Schmincke, H.-U., 2009, Enriched, HIMU-type peridotite and depleted recycled pyroxenite in the Canary plume: A mixed-up mantle: Earth and Planetary Science Letters, v. 277, no. 3-4, p. 514-524.

Haase, K. M., Devey, C. W., and Wieneke, M., 2003, Magmatic processes and mantle heterogeneity beneath the slow-spreading northern Kolbeinsey Ridge segment, North Atlantic: Contributions to Mineralogy and Petrology, v. 144, no. 4, p. 428-448.

Hanan, B. B., Blichert-Toft, J., Kingsley, R., and Schilling, J. G., 2000, Depleted Iceland mantle plume geochemical signature: Artifact of multicomponent mixing?: Geochemistry Geophysics Geosystems, v. 1, no. 4, p. 1.

Hanan, B. B., Blichert-Toft, J., Pyle, D. G., and Christie, D. M., 2004, Contrasting origins of the upper mantle revealed by hafnium and lead isotopes from the Southeast Indian Ridge (vol 432, pg 91, 2004): Nature, v. 432, no. 7017, p. 653-653.

Hanan, B. B., and Graham, D. W., 1996, Lead and helium isotope evidence from oceanic basalts for a common deep source of mantle plumes (vol 272, pg 991, 1996): Science, v. 272, no. 5268, p. 1573-1573.

Hanan, B. B., and Schilling, J. G., 1997, The dynamic evolution of the Iceland mantle plume: the lead isotope perspective: Earth and Planetary Science Letters, v. 151, no. 1-2, p. 43-60.

Hansen, H., and Gronvold, K., 2000, Plagioclase ultraphyric basalts in Iceland: the mush of the rift: Journal of Volcanology and Geothermal Research, v. 98, no. 1-4, p. 1-32.

Hart, S. R., Schillin.Jg, and Powell, J. L., 1973, Basalts from Iceland and Along Reykjanes Ridge - Sr Isotope Geochemistry: Nature-Physical Science, v. 246, no. 155, p. 104-107.

Hattori, K., and Muehlenbachs, K., 1982, Oxygen Isotope Ratios of the Icelandic Crust: Journal of Geophysical Research, v. 87, no. Nb8, p. 6559-6565.

Helgason, J., 1989, The Fjallgardar volcanic ridge in NE Iceland: an aborted early stage plate boundary or a volcanically dormant zone?, Geological Society Special Publication, Magmatism in the Ocean Basins.

Hemond, C., Arndt, N. T., Lichtenstein, U., Hofmann, A. W., Oskarsson, N., and Steinthorsson, S., 1993, The Heterogeneous Iceland Plume - Nd-Sr-O Isotopes and Trace-Element Constraints: Journal of Geophysical Research-Solid Earth, v. 98, no. B9, p. 15833-15850.

Hemond, C., Condomines, M., Fourcade, S., Allegre, C. J., Oskarsson, N., and Javoy, M., 1988, Thorium, Strontium and Oxygen Isotopic Geochemistry in Recent Tholeiites from Iceland - Crustal Influence on Mantle-Derived Magmas: Earth and Planetary Science Letters, v. 87, no. 3, p. 273-285.

Herzberg, C., 2004, Partial Crystallization of Mid-Ocean Ridge Basalts in the Crust and Mantle: Journal of Petrology, v. 45, no. 12, p. 2389-2405.

Herzberg, C., 2006, Petrology and thermal structure of the Hawaiian plume from Mauna Kea volcano: Nature, v. 444, no. 7119, p. 605-609.

Herzberg, C., 2011, Identification of Source Lithology in the Hawaiian and Canary Islands: Implications for Origins: Journal of Petrology, v. 52, no. 1, p. 113-146.

Hirschmann, M. M., Kogiso, T., Baker, M. B., and Stolper, E. M., 2003, Alkalic magmas generated by partial melting of garnet pyroxenite: Geology, v. 31, no. 6, p. 481-484.

Hjartardóttir, Á. R., and Einarsson, P., 2011, The Kverkfjöll fissure swarm and the eastern boundary of the Northern Volcanic Rift Zone, Iceland: Bulletin of Volcanology, v. 74, no. 1, p. 143-162.

Höskuldsson, A., Sparks, R. S. J., and Carroll, M. R., 2006, Constraints on the dynamics of subglacial basalt eruptions from geological and geochemical observations at Kverkfjöll, NE-Iceland: Bulletin of Volcanology, v. 68, no. 7-8, p. 689-701.

Humayun, M., Qin, L. P., and Norman, M. D., 2004, Geochemical evidence for excess iron in the mantle beneath Hawaii: Science, v. 306, no. 5693, p. 91-94.

Jakobsdottir, S. S., Roberts, M. J., Gudmundsson, G. B., Geirsson, H., and Slunga, R., 2008, Earthquake Swarms at Upptyppingar, North-East Iceland: A Sign of Magma Intrusion?: Studia Geophysica Et Geodaetica, v. 52, no. 4, p. 513-528.

Jakobsson, S. P., 1979, Petrology of recent basalts of the Eastern Volcanic Zone, Iceland, Reykjavik, Icelandic Museum of Natural History.

Jancin, M., Young, K. D., Voight, B., Aronson, J. L., and Saemundsson, K., 1985, Stratigraphy and K/Ar Ages across the West Flank of the Northeast Iceland Axial Rift-Zone, in Relation to the 7-Ma Volcano-Tectonic Reorganization of Iceland: Journal of Geophysical Research-Solid Earth and Planets, v. 90, no. Nb12, p. 9961-9985.

Jóhannesson, H. S., K., 1998, Geological Map 1 500 000, scale 1 500 000.

Johnston, S. T. T., D. J, 2000, Continental flood basalts: episodic magmatism above long-lived hotspots: Earth and Planetary Science Letters, v. 175, p. 247-256.

Jónasson, K., 1994, Rholit volcanism in the Krafla central volcano, north east Iceland: Bulletin of Volcanology, v. 56, p. 516-528.

Jónasson, K., 2005, Magmatic evolution of the Heiðarsporður ridge, NE-Iceland: Journal of Volcanology and Geothermal Research, v. 147, no. 1-2, p. 109-124.

Jónasson, K., 2007, Silicic volcanism in Iceland: Composition and distribution within the active volcanic zones: Journal of Geodynamics, v. 43, no. 1, p. 101-117.

Kaban, M. K., Flovenz, O. G., and Palmason, G., 2002, Nature of the crust-mantle transition zone and the thermal state of the upper mantle beneath Iceland from gravity modelling: Geophysical Journal International, v. 149, no. 2, p. 281-299.

Kamenetsky, V. S., and Gurenko, A. A., 2006, Cryptic crustal contamination of MORB primitive melts recorded in olivine-hosted glass and mineral inclusions: Contributions to Mineralogy and Petrology, v. 153, no. 4, p. 465-481.

Kelemen, P. B., Koga, K., and Shimizu, N., 1997, Geochemistry of gabbro sills in the crust-mantle transition zone of the Oman ophiolite: Implications for the origin of the oceanic lower crust: Earth and Planetary Science Letters, v. 146, no. 3-4, p. 475-488.

Kelley, D. F., 2009, Toward an Integrated Model of the Crust in the Icelandic Rift Zones [PhD: The Ohio State University.

Kelley, D. F., and Barton, M., 2008, Pressures of Crystallization of Icelandic Magmas: Journal of Petrology, v. 49, no. 3, p. 465-492.

Kempton, P. D., Fitton, J. G., Saunders, A. D., Nowell, G. M., Taylor, R. N., Hardarson, B. S., and Pearson, G., 2000, The Iceland plume in space and time: a Sr-Nd-Pb-Hf study of the North Atlantic rifted margin: Earth and Planetary Science Letters, v. 177, no. 3-4, p. 255-271.

Kerr, A. C., Saunders, A. D., Tarney, J., Berry, N. H., and Hards, V. L., 1995, Depleted Mantle-Plume Geochemical Signatures - No Paradox for Plume Theories: Geology, v. 23, no. 9, p. 843-846.

Key, J., White, R. S., Soosalu, H., and Jakobsdottir, S. S., 2011, Multiple melt injection along a spreading segment at Askja, Iceland (vol 38, L05301, 2011): Geophysical Research Letters, v. 38.

Kitagawa, H., Kobayashi, K., Makishima, A., and Nakamura, E., 2008, Multiple Pulses of the Mantle Plume: Evidence from Tertiary Icelandic Lavas: Journal of Petrology, v. 49, no. 7, p. 1365-1396.

Kogiso, T., Tatsumi, Y., and Nakano, S., 1997, Trace element transport during dehydration processes in the subducted oceanic crust .1. Experiments and implications for the origin of ocean island basalts: Earth and Planetary Science Letters, v. 148, no. 1-2, p. 193-205.

Kokfelt, T. F., 2006, Combined Trace Element and Pb-Nd-Sr-O Isotope Evidence for Recycled Oceanic Crust (Upper and Lower) in the Iceland Mantle Plume: Journal of Petrology, v. 47, no. 9, p. 1705-1749.

Koornneef, J. M., Stracke, A., Bourdon, B., Meier, M. A., Jochum, K. P., Stoll, B., and Gronvold, K., 2011, Melting of a Two-component Source beneath Iceland: Journal of Petrology, v. 53, no. 1, p. 127-157.

Korenaga, J., and Kelemen, P. B., 1997, Origin of gabbro sills in the Moho transition zone of the Oman ophiolite: Implications for magma transport in the oceanic lower crust: Journal of Geophysical Research-Solid Earth, v. 102, no. B12, p. 27729-27749.

Kou, S. Q., and Rustan, A., 1992, Burden Related to Blasthole Diameter in Rock Blasting: International Journal of Rock Mechanics and Mining Sciences & Geomechanics Abstracts, v. 29, no. 6, p. 543-553.

Kuritani, T., Yokoyama, T., Kitagawa, H., Kobayashi, K., and Nakamura, E., 2011, Geochemical evolution of historical lavas from Askja Volcano, Iceland: Implications for mechanisms and timescales of magmatic differentiation: Geochimica et Cosmochimica Acta, v. 75, no. 2, p. 570-587.

Kurz, M., D., Meyer, P, S., Sigurdsson, H., 1985, Helium isotopic systematics within the neovocanic zones of Iceland: Earth and Planetary Science Letters, v. 74, p. 291-305.

Langmuir, C. H., Klein, E. M., and Plank, T., 1992, Petrological Systematics of Midocean Ridge Basalts - Constraints on Melt Generation beneath Ocean Ridges: Mantle Flow and Melt Generation at Mid-Ocean Ridges, v. 71, p. 183-280.

Larsen., L., M and Pedersen, A., K., 2000, Processes in high-Mg, high-T magmas: evidence from olivine, chromite and glass in Palaeogene picrites from West Greenland: Jounal of Petrology, v. 7, p. 1071-1098.

Lawver, L. A., and Muller, R. D., 1994, Iceland Hotspot Track: Geology, v. 22, no. 4, p. 311-314.

Li, A. B., and Detrick, R. S., 2006, Seismic structure of Iceland from Rayleigh wave inversions and geodynamic implications: Earth and Planetary Science Letters, v. 241, no. 3-4, p. 901-912.

Macdonald, R., Mcgarvie, D. W., Pinkerton, H., Smith, R. L., and Palacz, Z. A., 1990, Petrogenetic Evolution of the Torfajokull Volcanic Complex, Iceland .1. Relationship between the Magma Types: Journal of Petrology, v. 31, no. 2, p. 429-459.

Maclennan, J., 2002, The link between volcanism and deglaciation in Iceland: Geochemistry Geophysics Geosystems, v. 3, no. 11.

Maclennan, J., 2003, Melt mixing and crystallization under Theistareykir, northeast Iceland: Geochemistry Geophysics Geosystems, v. 4, no. 11.

Maclennan, J., 2008, Concurrent Mixing and Cooling of Melts under Iceland: Journal of Petrology, v. 49, no. 11, p. 1931-1953.

Maclennan, J., McKenzie, D., and Gronvold, K., 2001, Plume-driven upwelling under central Iceland: Earth and Planetary Science Letters, v. 194, no. 1-2, p. 67-82.

Macpherson, C., Hilton, D., Day, J., Lowry, D., and Gronvold, K., 2005, High-3He/4He, depleted mantle and low-δ18O, recycled oceanic lithosphere in the source of central Iceland magmatism: Earth and Planetary Science Letters, v. 233, no. 3-4, p. 411-427.

Mahoney, J. J., Frei, R., Tejada, M. L. G., Mo, X. X., Leat, P. T., and Nagler, T. F., 1998, Tracing the Indian Ocean mantle domain through time: Isotopic results from Old West Indian, East Tethyan, and South Pacific seafloor (vol 39, pg 1285, 1998): Journal of Petrology, v. 39, no. 11-12, p. 2153-2153.

Manning, C. J., 2010, Radiogenic isotopic and o18 O variation in Icelandic basalts [electronic resource] : Source variation versus crustal contamination, Royal Holloway, University of London.

Manning, C. J and Thirlwall. M. F., 2012, Isotopic evidence for interaction between Öræfajökull mantle and the Eastern Rift Zone, Iceland, *In press.*

Mattey, D., Lowry, D., and Macpherson, C., 1994, Oxygen-Isotope Composition of Mantle Peridotite: Earth and Planetary Science Letters, v. 128, no. 3-4, p. 231-241.

Mattey, D., and Macpherson, C., 1993, High-Precision Oxygen Isotope Microanalysis of Ferromagnesian Minerals by Laser-Fluorination: Chemical Geology, v. 105, no. 4, p. 305-318.

Mcgarvie, D. W., Macdonald, R., Pinkerton, H., and Smith, R. L., 1990, Petrogenetic Evolution of the Torfajokull Volcanic Complex, Iceland .2. The Role of Magma Mixing: Journal of Petrology, v. 31, no. 2, p. 461-481.

McKenzie, D. and O'Nions, R. K., 1991, Partial Melt Distributions from Inversion of Rare Earth Element Concentrations. Journal of Petrology, 32, 1021-1091.

Menand, T., 2011, Physical controls and depth of emplacement of igneous bodies: A review: Tectonophysics, v. 500, no. 1-4, p. 11-19.

Menke, W., and Levin, V., 1994, Cold Crust in a Hot-Spot: Geophysical Research Letters, v. 21, no. 18, p. 1967-1970.

Menke, W., West, M., Brandsdottir, B., and Sparks, D., 1998, Compressional and shear velocity structure of the lithosphere in northern Iceland: Bulletin of the Seismological Society of America, v. 88, no. 6, p. 1561-1571.

Meyer, P. S., Sigurdsson, H., and Schilling, J. G., 1985, Petrological and Geochemical Variations Along Iceland Neovolcanic Zones: Journal of Geophysical Research-Solid Earth and Planets, v. 90, no. Nb12, p. 43-72.

Michael, P. J., and Cornell, W. C., 1998, Influence of spreading rate and magma supply on crystallization and assimilation beneath mid-ocean ridges: Evidence from chlorine and major element chemistry of mid-ocean ridge basalts: Journal of Geophysical Research-Solid Earth, v. 103, no. B8, p. 18325-18356.

Miller, S. A., Asimow, P. D., and Burnett, D. S., 2006, Determination of melt influence on divalent element partitioning between anorthite and CMAS melts: Geochimica Et Cosmochimica Acta, v. 70, no. 16, p. 4258-4274.

Mjelde, R., Breivik, A. J., Raum, T., Mittelstaedt, E., Ito, G., and Faleide, J. I., 2008, Magmatic and tectonic evolution of the North Atlantic: Journal of the Geological Society, v. 165, p. 31-42.

Momme, P., Tegner, C., Brooks, C. K., and Keays, R. R., 2006, Two melting regimes during Paleogene flood basalt generation in East Greenland: combined REE and PGE modelling (vol 151, pg 88, 2006): Contributions to Mineralogy and Petrology, v. 151, no. 5, p. 631-632.

Morgan, W. J., 1971, Convection Plumes in Lower Mantle: Nature, v. 230, no. 5288, p. 42-&.

Murton, B. J., Taylor, R. N., and Thirlwall, M. F., 2002, Plume-ridge interaction: A geochemical perspective from the Reykjanes Ridge: Journal of Petrology, v. 43, no. 11, p. 1987-2012.

Mutter, J. C., Buck, W. R., and Zehnder, C. M., 1988, Convective Partial Melting .1. A Model for the Formation of Thick Basaltic Sequences during the Initiation of Spreading: Journal of Geophysical Research-Solid Earth and Planets, v. 93, no. B2, p. 1031-1048.

Nauret, F., Abouchami, W., Galer, S. J. G., Hofmann, A. W., and Hemond, C., 2002, Sr-Pb isotopic evidence for plume-ridge interaction along the Central Indian Ridge: Geochimica Et Cosmochimica Acta, v. 66, no. 15A, p. A547-A547.

Nicholson, H., 1991, The magmatic evolution of Krafla, NE Iceland [electronic resource], University of Edinburgh.

Nicholson, H., Condomines, M., Fitton, J. G., Fallick, A. E., Gronvold, K., and Rogers, G., 1991, Geochemical and Isotopic Evidence for Crustal Assimilation beneath Krafla, Iceland: Journal of Petrology, v. 32, no. 5, p. 1005-1020.

Nicholson, H., and Latin, D., 1992, Olivine Tholeiites from Krafla, Iceland - Evidence for Variations in Melt Fraction within a Plume: Journal of Petrology, v. 33, no. 5, p. 1105-1124.

Niu, Y. L., and Batiza, R., 1994, Magmatic Processes at a Slow-Spreading Ridge Segment - 26-Degrees-S Mid-Atlantic Ridge: Journal of Geophysical Research-Solid Earth, v. 99, no. B10, p. 19719-19740.

O'Hara, M., J., 1977 Geochemical evolution during fractional crystallisation of a periodically refilled magma chamber: Nature, v. 266, p. 503-507.

O' Neill, H., St. C., and Jenner, F., 2012, The global pattern of trace-element distributions in ocean floor basalts: Nature, v. 491, p. 698-705.

Olafsson, J., and Riley, J. P., 1978, Geochemical Studies on Thermal Brine from Reykjanes (Iceland): Chemical Geology, v. 21, no. 3-4, p. 219-237.

Oskarsson, N., Steinthorsson, S., Sigvaldason., G., E., 1985, Iceland Geochemical Anomaly: Origin, Volcanotectonics, Chemical Fraction and Isotope Evolution of the Crust: Journal of Geophysical Research, v. 90, p. 10001-10025.

Pagli, C., Sigmundsson, F., Arnadottir, T., Einarsson, P., and Sturkell, E., 2006, Deflation of the Askja volcanic system: Constraints on the deformation source from combined inversion of satellite radar interferograms and GPS measurements: Journal of Volcanology and Geothermal Research, v. 152, no. 1-2, p. 97-108.

Pagli, C., Sigmundsson, F., Árnadóttir, T., Einarsson, P., and Sturkell, E., 2006, Deflation of the Askja volcanic system: Constraints on the deformation source from combined inversion of satellite radar interferograms and GPS measurements: Journal of Volcanology and Geothermal Research, v. 152, no. 1-2, p. 97-108.

Pálmason, G., 1971, Crustalstructure of Iceland from explosionseismology: Soc. Sci. Iceland, p. 187.

Peate, D. W., Breddam, K., Baker, J. A., Kurz, M. D., Barker, A. K., Prestvik, T., Grassineau, N., and Skovgaard, A. C., 2010, Compositional Characteristics and Spatial Distribution of Enriched Icelandic Mantle Components: Journal of Petrology, v. 51, no. 7, p. 1447-1475.

Pertermann, M., and Hirschmann, M. M., 2003, Anhydrous partial melting experiments on MORB-like eclogite: Phase relations, phase compositions and mineral-melt partitioning of major elements at 2-3 GPa: Journal of Petrology, v. 44, no. 12, p. 2173-2201.

Prestvik, T., Goldberg, S., Karlsson, H., and Gronvold, K., 2001, Anomalous strontium and lead isotope signatures in the off-rift Oraefajokull central volcano in south-east Iceland. Evidence for enriched endmember(s) of the Iceland mantle plume?: Earth and Planetary Science Letters, v. 190, no. 3-4, p. 211-220.

Putirka, K., Johnson, M., Kinzler, R., Longhi, J., and Walker, D., 1996, Thermobarometry of mafic igneous rocks based on clinopyroxene-liquid equilibria, 0-30 kbar: Contributions to Mineralogy and Petrology, v. 123, no. 1, p. 92-108.

Putirka, K. D., 2005, Mantle potential temperatures at Hawaii, Iceland, and the mid-ocean ridge system, as inferred from olivine phenocrysts: Evidence for thermally driven mantle plumes: Geochemistry Geophysics Geosystems, v. 6.

Putirka, K. D, 2008, Thermometers and Barometers for Volcanic Systems: Reviews in Mineralogy and Geochemistry, v. 69, no. 1, p. 61-120.

Putirka, K. D., Perfit, M., Ryerson, F. J., and Jackson, M. G., 2007, Ambient and excess mantle temperatures, olivine thermometry, and active vs. passive upwelling: Chemical Geology, v. 241, no. 3-4, p. 177-206.

Rafferty, J. P., 2011, Rocks, New York, Britannica Educational Publishing.

Roeder, P. L., and Emslie, R. F., 1970, Olivine-Liquid Equilibrium: Contributions to Mineralogy and Petrology, v. 29, no. 4, p. 275-&.

Rollinson, H. R., 1993, Using geochemical data : evaluation, presentation, interpretation, Harlow, Longman Scientific & Technical.

Rymer, H., and Tryggvason, E., 1993, Gravity and Elevation Changes at Askja, Iceland: Bulletin of Volcanology, v. 55, no. 5, p. 362-371.

Sæmundsson, K., 1977, Blað 7 Norðausturland 1 250 000, scale 1 250 000.

Salters, V. J. M., and Longhi, J., 1999, Trace element partitioning during the initial stages of melting beneath mid-ocean ridges: Earth and Planetary Science Letters, v. 166, no. 1-2, p. 15-30.

Saunders, A. D. F., J.G. Kerr, A.C. Norry, M, J Kent R.W, 1997, The North Atlantic Igneous Province, Geophysical Monograph, Large igneous provinces: continental, oceanic and planetary flood volcanism.

Schiellerup, H., 1995, Generation and Equilibration of Olivine Tholeiites in the Northern Rift-Zone of Iceland - a Petrogenetic Study of the Blafjall Table Mountain: Journal of Volcanology and Geothermal Research, v. 65, no. 3-4, p. 161-179.

Schilling, 1973, Iceland Mantle Plume: Nature, v. 246, no. 5429, p. 141-143.

Shaw, D. M., 1970, Trace Element Fractionation during Anatexis: Geochimica Et Cosmochimica Acta, v. 34, no. 2, p. 237-&.

Shen, Y., Solomon, S. C., Bjarnason, I. T., Nolet, G., Morgan, W. J., Allen, R. M., Vogfjord, K., Jakobsdottir, S., Stefansson, R., Julian, B. R., and Foulger, G. R., 2002, Seismic evidence for a tilted mantle plume and north-south mantle flow beneath Iceland: Earth and Planetary Science Letters, v. 197, no. 3-4, p. 261-272.

Shorttle, O., Maclennan, J., and Jones, S. M., 2010, Control of the symmetry of plume-ridge interaction by spreading ridge geometry: Geochemistry Geophysics Geosystems, v. 11.

Shorttle, O. and Maclennan, J., 2011, Constraints on the lithology of the Iceland plume, Volcanic and Magmatic Studies Group Annual: Cambridge.

Sigbjarnarson, G., 1988, Krepputunga og Brúardalir: lýsingar á korteiningumjarðfræðikorts, Reykjavík, Orkustofnun.

Sigbjarnarson, G, 1993, Norðan Vatnajökuls: II Jarðlagaskipan og jarðfræðikort: Náttúrufræðingurinn, v. 63, p. 201-217.

Sigmarsson, O., Hemond, C., Condomines, M., Fourcade, S., and Oskarsson, N., 1991, Origin of Silicic Magma in Iceland Revealed by Th Isotopes: Geology, v. 19, no. 6, p. 621-624.

Sigurdsson, H., and Sparks, R. S. J., 1981, Petrology of Rhyolitic and Mixed Magma Ejecta from the 1875 Eruption of Askja, Iceland: Journal of Petrology, v. 22, no. 1, p. 41-84.

Sigurdsson, H., and Sparks, S. R. J., 1978, Lateral Magma Flow within Rifted Icelandic Crust: Nature, v. 274, no. 5667, p. 126-130.

Sigvaldason, G., x000F, and mundur, 2002, Volcanic and tectonic processes coinciding with glaciation and crustal rebound: an early Holocene rhyolitic eruption in the Dyngjufjöll volcanic centre and the formation of the Askja caldera, north Iceland: Bulletin of Volcanology, v. 64, no. 3-4, p. 192-205.

Sigvaldason, G. E., 2002, Volcanic and tectonic processes coinciding with glaciation and crustal rebound: an early Holocene rhyolitic eruption in the Dyngjufjoll volcanic centre and the formation of the Askja caldera, north Iceland: Bulletin of Volcanology, v. 64, no. 3-4, p. 192-205.

Sigvaldason, G. E., Annertz, K., and Nilsson, M., 1992, Effect of Glacier Loading Deloading on Volcanism - Postglacial Volcanic Production-Rate of the Dyngjufjoll Area, Central Iceland: Bulletin of Volcanology, v. 54, no. 5, p. 385-392.

Sigvaldason, G. E. S. S., 1974, Chemistry of tholeiitic basalts from Iceland and their relation to the Kverkfjöll hot spot, Holland, D. Reidel, Dordrecht, Geodynamics of Iceland and the North Atlantic Area.

Simkin, T., and Smith, J., V., 1970, Minor-element Distribution in Olivine: The Journal of Geology, v. 78, p. 304-325.

Skovgaard, A. C., Storey, M., Baker, J., Blusztajn, J., and Hart, S. R., 2001, Osmium-oxygen isotopic evidence for a recycled and strongly depleted component in the Iceland mantle plume: Earth and Planetary Science Letters, v. 194, no. 1-2, p. 259-275.

Slater, L., McKenzie, D., Gronvold, K., and Shimizu, N., 2001, Melt generation and movement beneath Theistareykir, NE Iceland: Journal of Petrology, v. 42, no. 2, p. 321-354.

Sobolev, A. V., and Danyushevsky, L. V., 1994, Petrology and Geochemistry of Boninites from the North Termination of the Tonga Trench - Constraints on the Generation Conditions of Primary High-Ca Boninite Magmas: Journal of Petrology, v. 35, no. 5, p. 1183-1211.

Sobolev, A. V., Hofmann, A. W., Brugmann, G., Batanova, V. G., and Kuzmin, D. V., 2008, A quantitative link between recycling and osmium isotopes: Science, v. 321, no. 5888, p. 536-536.

Sobolev, A. V., Hofmann, A. W., Kuzmin, D. V., Yaxley, G. M., Arndt, N. T., Chung, S. L., Danyushevsky, L. V., Elliott, T., Frey, F. A., Garcia, M. O., Gurenko, A. A., Kamenetsky, V. S., Kerr, A. C., Krivolutskaya, N. A., Matvienkov, V. V., Nikogosian, I. K., Rocholl, A., Sigurdsson, I. A., Sushchevskaya, N. M., and Teklay, M., 2007, The amount of recycled crust in sources of mantle-derived melts: Science, v. 316, no. 5823, p. 412-417.

Sobolev, A. V., Hofmann, A. W., Sobolev, S. V., and Nikogosian, I. K., 2005, An olivine-free mantle source of Hawaiian shield basalts: Nature, v. 434, no. 7033, p. 590-597.

Soosalu, H., Key, J., White, R. S., Knox, C., Einarsson, P., and Jakobsdóttir, S. S., 2009, Lower-crustal earthquakes caused by magma movement beneath Askja volcano on the north Iceland rift: Bulletin of Volcanology, v. 72, no. 1, p. 55-62.

Spandler, C., Hermann, J., Arculus, R., and Mavrogenes, J., 2004, Geochemical heterogeneity and element mobility in deeply subducted oceanic crust; insights from high-pressure mafic rocks from New Caledonia: Chemical Geology, v. 206, no. 1-2, p. 21-42.

Sparks, S. R. J., Sigurdsson, H., and Wilson, L., 1977, Magma Mixing - Mechanism for Triggering Acid Explosive Eruptions: Nature, v. 267, no. 5609, p. 315-318.

Staples, R. K., White, R. S., Brandsdottir, B., Menke, W., Maguire, P. K. H., and McBride, J. H., 1997, Faroe-Iceland Ridge Experiment .1. Crustal structure of northeastern Iceland: Journal of Geophysical Research-Solid Earth, v. 102, no. B4, p. 7849-7866.

Stracke, A., 2003, Theistareykir revisited: Geochemistry Geophysics Geosystems, v. 4, no. 2.

Stracke, A., 2005, FOZO, HIMU, and the rest of the mantle zoo: Geochemistry Geophysics Geosystems, v. 6, no. 5.

Stracke, A., and Bourdon, B., 2009, The importance of melt extraction for tracing mantle heterogeneity: Geochimica et Cosmochimica Acta, v. 73, no. 1, p. 218-238.

Sturkell, E., and Sigmundsson, F., 2000, Continuous deflation of the Askja caldera, Iceland, during the 1983-1998 noneruptive period: Journal of Geophysical Research-Solid Earth, v. 105, no. B11, p. 25671-25684.

Sturkell, E., Sigmundsson, F., Geirsson, H., Ólafsson, H., and Theodórsson, T., 2008, Multiple volcano deformation sources in a post-rifting period: 1989–2005 behaviour of Krafla, Iceland constrained by levelling, tilt and GPS observations: Journal of Volcanology and Geothermal Research, v. 177, no. 2, p. 405-417.

Sturkell, E., Sigmundsson, F., and Slunga, R., 2006, 1983-2003 decaying rate of deflation at Askja caldera: Pressure decrease in an extensive magma plumbing system at a spreading plate boundary: Bulletin of Volcanology, v. 68, no. 7-8, p. 727-735.

Sun, S. S., and Jahn, B., 1975, Lead and Strontium Isotopes in Postglacial Basalts from Iceland: Nature, v. 255, no. 5509, p. 527-530.

Sun, S. S., and McDonough, W. F., 1989, Chemical and isotopic systematics of oceanic basalts: implications for mantle composition and processes: Geological Society, London, Special Publications, v. 42, no. 1, p. 313-345.

Taisne, B., and Jaupart, C., 2009, Dike propagation through layered rocks: Journal of Geophysical Research-Solid Earth, v. 114.

Takahashi, R. E. K., I., 1983, Melting of a dry peridotite at high pressures and basalt magma genesis: American Mineralogist, v. 68, p. 859-879.

Tentler, T., and Mazzoli, S., 2005, Architecture of normal faults in the rift zone of central north Iceland: Journal of Structural Geology, v. 27, no. 9, p. 1721-1739.

Tepley, F. J., Lundstrom, C. C., McDonough, W. F., and Thompson, A., 2010, Trace element partitioning between high-An plagioclase and basaltic to basaltic andesite melt at 1 atmosphere pressure: Lithos, v. 118, no. 1-2, p. 82-94.

Thirlwall, M.F., 1991a, Long-Term Reproducibility of Multicollector Sr and Nd Isotope Ratio Analysis: Chemical Geology, v. 94, no. 2, p. 85-104.

Thirlwall, M. F., 1991b, High-Precision Multicollector Isotopic Analysis of Low-Levels of Nd as Oxide: Chemical Geology, v. 94, no. 1, p. 13-22.

Thirlwall, M.F., 1997, Pb isotopic and elemental evidence for OIB derivation from young HIMU mantle: Chemical Geology, v. 139, no. 1-4, p. 51-74.

Thirlwall, M. F., and Anczkiewicz, R., 2004, Multidynamic isotope ratio analysis using MC-ICP-MS and the causes of secular drift in Hf, Nd and Pb isotope ratios: International Journal of Mass Spectrometry, v. 235, no. 1, p. 59-81.

Thirlwall, M. F., Gee, M. A. M., Lowry, D., Mattey, D. P., Murton, B. J., and Taylor, R. N., 2006, Low δ18O in the Icelandic mantle and its origins: Evidence from Reykjanes Ridge and Icelandic lavas: Geochimica et Cosmochimica Acta, v. 70, no. 4, p. 993-1019.

Thirlwall, M. F., Gee, M. A. M., Taylor, R. N., and Murton, B. J., 2004, Mantle components in Iceland and adjacent ridges investigated using double-spike Pb isotope ratios: Geochimica et Cosmochimica Acta, v. 68, no. 2, p. 361-386.

Thirlwall, M. F., Manning, C. J., Muller, W., 2012, Simultaneous major and trace element analysis of olivine, plagioclase and clinopyroxene phenocrysts and NMNH standards by LA-ICP-MS, Chemical Geology. *In press.*

Thirlwall, M., F., Graham, A., M., Arculus, R., J., Harmon, R., S., Macperson, C., G., 1996. Resolution of the effects of crustal assimilation, sediment subduction and fluid transport in island arc magmas: Pb-Sr-Nd-O isotope geochemistry of Grenada Lesser Antilles: Geochemica Cosmochemica Actaca. v. 60 p. 4785-4810.

Thirlwall, M. F., Upton, B. G. J., and Jenkins, C., 1994, Interaction between Continental Lithosphere and the Iceland Plume-Sr-Nd-Pb Isotope Geochemistry of Tertiary Basalts, Ne Greenland: Journal of Petrology, v. 35, no. 3, p. 839-879.

Thirlwall, M. F. M., C Lowry, D, 2011, Magma sources at Eyjafjöll and adjacent South Iceland central volcanoes, Goldschmidt Prague

Thorarinsson, S., 1979, Post-Glacial History of the Myvatn Area: Oikos, v. 32, no. 1-2, p. 16-28.

Thorarinsson, S. B., and Tegner, C., 2009, Magma chamber processes in central volcanic systems of Iceland: constraints from layered gabbro of the Austurhorn intrusive complex: Contributions to Mineralogy and Petrology, v. 158, no. 2, p. 223-244.

Toplis, M. J., 2004, The thermodynamics of iron and magnesium partitioning between olivine and liquid: criteria for assessing and predicting equilibrium in natural and experimental systems: Contributions to Mineralogy and Petrology, v. 149, no. 1, p. 22-39.

Tronnes, R. G., 1990, Basaltic Melt Evolution of the Hengill Volcanic System, Sw Iceland, and Evidence for Clinopyroxene Assimilation in Primitive Tholeiitic Magmas: Journal of Geophysical Research-Solid Earth and Planets, v. 95, no. B10, p. 15893-15910.

Trønnes, R. G., Introduction on the geology and geodynamics of Iceland: unpublished field guide.

Tryggvason, E., 1986, Multiple Magma Reservoirs in a Rift-Zone Volcano - Ground Deformation and Magma Transport during the September 1984 Eruption of Krafla, Iceland: Journal of Volcanology and Geothermal Research, v. 28, no. 1-2, p. 1-44.

Tryggvason, K., Husebye, E. S., and Stefansson, R., 1983, Seismic Image of the Hypothesized Icelandic Hot Spot: Tectonophysics, v. 100, no. 1-3, p. 97-118.

van Westrenen, W. D., D. S., 2007, Quantifying garnet melt trace element partitioning using lattice-strain theory new crystal-chemical and thermodynamic constraints: Contributions to Mineralogy and Petrology, v. 154, p. 717-730.

Vogt, P. R., and Johnson, G. L., 1975, Transform Faults and Longitudinal Flow Below Midoceanic Ridge: Journal of Geophysical Research, v. 80, no. 11, p. 1399-1428.

Vutukuri, V. S. R., A. Alm, O, 1983, Influence of physical properties of rock and rock-like material on blastability in crater and slab blasting — a literature and model study: Report GF (Swedish Mining Research Foundation) v. 8221.

Waight, T. E., and Baker, J. A., 2012, Depleted Basaltic Lavas from the Proto-Iceland Plume, Central East Greenland: Journal of Petrology, v. 53, no. 8, p. 1569-1596.

Walter, M. J., Sisson, T. W., and Presnall, D. C., 1995, A Mass Proportion Method for Calculating Melting Reactions and Application to Melting of Model Upper-Mantle Lherzolite: Earth and Planetary Science Letters, v. 135, no. 1-4, p. 77-90.

Ward, P. L., 1971, New Interpretation of Geology of Iceland: Geological Society of America Bulletin, v. 82, no. 11, p. 2991-&.

Weinsteiger, A. B., 2010, The Origin of Mid-Ocean Ridge Basalts: Insights from Trace Element Contents in Anorthite, Anorthite-hosted-melt Inclusions, and Ocean Core Complexes [PhD: Oregon State University.

Westrenen, W., and Draper, D. S., 2007, Quantifying garnet-melt trace element partitioning using lattice-strain theory: new crystal-chemical and thermodynamic constraints: Contributions to Mineralogy and Petrology, v. 154, no. 6, p. 717-730.

White, R. S., Drew, J., Martens, H. R., Key, J., Soosalu, H., and Jakobsdottir, S. S., 2011, Dynamics of dyke intrusion in the mid-crust of Iceland: Earth and Planetary Science Letters, v. 304, no. 3-4, p. 300-312.

White, R. S., Drew, J., Martens, H. R., Key, J., Soosalu, H., and Jakobsdóttir, S. S., 2011, Dynamics of dyke intrusion in the mid-crust of Iceland: Earth and Planetary Science Letters, v. 304, no. 3-4, p. 300-312.

White, R. S., and Mckenzie, D., 1995, Mantle Plumes and Flood Basalts: Journal of Geophysical Research-Solid Earth, v. 100, no. B9, p. 17543-17585.

White, R. S., and Morton, A. C., 1995, The Iceland Plume and Its Influence on the Evolution of the Ne Atlantic: Journal of the Geological Society, v. 152, p. 933-933.

Winpenny, B., and Maclennan, J., 2011, A Partial Record of Mixing of Mantle Melts Preserved in Icelandic Phenocrysts: Journal of Petrology, v. 52, no. 9, p. 1791-1812.

Wolfe, C. J., Bjarnason, I. T., VanDecar, J. C., and Solomon, S. C., 1997, Seismic structure of the Iceland mantle plume: Nature, v. 385, no. 6613, p. 245-247.

Wood, B. J., and Blundy, J. D., 1997, A predictive model for rare earth element partitioning between clinopyroxene and anhydrous silicate melt: Contributions to Mineralogy and Petrology, v. 129, no. 2-3, p. 166-181.

Wood, D. A., 1977, Quantitative Crystal Fractionation Model for Silicic Lavas in Iceland: Transactions-American Geophysical Union, v. 58, no. 6, p. 529-529.

Workman, R. K., and Hart, S. R., 2005, Major and trace element composition of the depleted MORB mantle (DMM): Earth and Planetary Science Letters, v. 231, no. 1-2, p. 53-72.

Xu, J.-F., and Castillo, P. R., 2004, Geochemical and Nd–Pb isotopic characteristics of the Tethyan asthenosphere: implications for the origin of the Indian Ocean mantle domain: Tectonophysics, v. 393, no. 1-4, p. 9-27.

Yang, H. J., Kinzler, R. J., and Grove, T. L., 1996, Experiments and models of anhydrous, basaltic olivine-plagioclase-augite saturated melts from 0.001 to 10 kbar: Contributions to Mineralogy and Petrology, v. 124, no. 1, p. 1-18.

Yasuda, A., Fujii, T., and Kurita, K., 1994, Melting Phase-Relations of an Anhydrous Midocean Ridge Basalt from 3 to 20 Gpa - Implications for the Behavior of Subducted Oceanic-Crust in the Mantle: Journal of Geophysical Research-Solid Earth, v. 99, no. B5, p. 9401-9414.

Yaxley, G. M., 2000, Experimental study of the phase and melting relations of homogeneous basalt plus peridotite mixtures and implications for the petrogenesis of flood basalts: Contributions to Mineralogy and Petrology, v. 139, no. 3, p. 326-338.

Yaxley, G. M., and Green, D. H., 1998, Reactions between eclogite and peridotite: Mantle refertilisation by subduction of oceanic crust: Schweizerische Mineralogische Und Petrographische Mitteilungen, v. 78, no. 2, p. 243-255.

Young, K. D., Jancin, M., Voight, B., and Orkan, N. I., 1985, Transform Deformation of Tertiary Rocks Along the Tjornes Fracture-Zone, North Central Iceland: Journal of Geophysical Research-Solid Earth and Planets, v. 90, no. Nb12, p. 9986-9910.

Zindler, A., Hart, S. R., Frey, F. A., and Jakobsson, S. P., 1979, Nd and Sr Isotope Ratios and Rare-Earth Element Abundances in Reykjanes Peninsula Basalts - Evidence for Mantle Heterogeneity beneath Iceland: Earth and Planetary Science Letters, v. 45, no. 2, p. 249-262.

APPENDIX 1 : ANALYTICAL TECHNIQUES

A1.1. Sampling Methodology

Samples approximately 1kg in size were collected from a wide range of post, intra and inter-glacial flows from the Northern Rift Zone of Iceland. Sample locations were selected in order to ensure a wide range of different flows were collected encompassing the whole rift zone. In the case of Krafla, samples, where possible were collected from the same locations as Nicholson (1990) in order to draw direct comparisons. Care was taken to collect fresh samples, especially important in the more vesicular samples where infill from vesicles would possibly lead to contamination of whole rock analyses. Furthermore care was taken to avoid collection from road side outcrops to avoid Pb contamination from exhaust fumes.

A1.2. Rock crushing and mineral separation

A1.2.1 Rock Crushing

Weathered surfaces were removed from the sample using a hydraulic splitter. Once all such surfaces had been removed the sample was crushed into chips (~1cm^3) using a jaw crusher. Both the jaw crusher and Hydraulic splitter were thoroughly cleaned between samples in order avoid contamination from excess dusk and lodged rock fragments. Approximately ⅓ of the chipped material was retained for Pb analysis and mineral separation whist the rest was ground into a fine powder using a tungsten carbide TEMA mill. The powders were stored in new glass jars cleaned previously with acetone in order to ensure the jar was free from dust. The TEMA was clean with water and acetone between samples.

A1.2.2 Mineral separation

The Chips retained from the jaw crusher were crushed further using a steel percussion mill and sieved retaining the 500 µm-1 mm and 250µm-500µm fractions. The fractions were then rinsed with MQ and put in an ultrasonic bath for 10 minutes followed by further rinsing. This process was repeated until the water was clear. The samples were then dried in an oven before being magnetically separated using a hand magnet. The Magnetic chips were retained for Pb analysis. Further picking of the magnetic fraction using binocular microscope from the 500 µm-1 mm fraction removed further sings of alteration. The non-magnetic fraction was handpicked from both sieved fractions to separate olivine, plagioclase and clinopyroxene for oxygen and major and trace element analysis.

A1.3. X-ray fluorescence spectrometry – Major and Trace element analysis

During the course of this study RHUL acquired a new X-ray fluorescence spectrometer; as such a number of the samples from this study were run on a Phillips PW1480 spectrometer whilst all others were run on a new PANalytical Axios spectrometer.

A1.3.1 Fused glass disc preparation

Prior to fusing the powered samples were dried in the oven over night in order to remove surface moisture. ~0.7g of sample was weight out into platinum crucibles in batches of six. Loss on ignition was then determined by igniting the covered sample in a furnace at 1100°C for 30 minutes. After ignition spectra flux was added to the sample in a ratio of 6:1, flux:sample and returned to the furnace for a further 30 minutes. Once cooled the flux loss on ignition was worked out and more sample was added in order to bring the sample up to the correct weight. Samples were heated over 3 Bunsen burners for 5 minutes to re-melt the sample and the added flux was incorporated into the melt by gently swirling the melt. The fussion disks were cast onto Al platurns using a graphite plunger on a hotplate at 180°C. The disks were left to cool before clipping and were stored in individual plastic bags in a desiccator. Between batches the platinum crucibles were cleaned by boiling in 50% HCl until all remaining melt was dissolved and stored in distilled water until needed. Prior to use they are rinsed in fresh distilled water and dried over a Bunsen burner and the inside checked for any remaining deposits.

A1.3.2 Pressed pellet preparation

For trace element analysis run on the Phillips PW1480 pellets were prepared using ~7g of sample mixed with 8 drops of mowiol binder before being pressed into a disc on a tungsten carbide plate. The disc was then backed with boric acid and pressed under 10 tons/in^2 for 1 minute. The pellets were then pumped in a desiccator for 30 minutes prior to running to remove surface moisture.

Due to higher running temperatures of the PANalytical Axios spectrometer, boric acid backed pellets were unable to be used. Instead approximately 10g of powder was mixed with 0.7 ml of PVP-MC binding solution which was then poured in to an Al cap and pressed using a tungsten carbide plate under 10 tons/in^2 for one minute. The sample was then placed in to an oven at 80°C for at least 4 hours in order to set the binder.

	Kv	mA	Collimator	Crystal	+offs	-offs	Detector	LL	UL
SiO_2	60	45	C	InSb			FL	25	76
Al_2O_3	60	45	C	Pe		5	FL	27	78
Fe_2O_3	60	45	C	LiF200		1.6	FL	14	69
MgO	60	45	F	TlAP	3	4.5	FL	24	70
CaO	60	45	C	LiF200			FL	26	72
Na_2O_3	60	45	F	TlAP	3.3		FL	26	72
K_2O	60	45	F	LiF200	3.5		FL	25	75
TiO_2	60	45	F	LiF200	0		FL	28	75
TiO_2 Rh	95	30	F	LiF200	3.74		FL	27	75
MnO	60	45	F	LiF200		0.9	FL	14	70
P_2O_5	60	45	C	Ge	3.2		FL	35	70
Ni	60	45	F	LiF200			FL	14	71
Cr	60	45	F	LiF220		1.5	FL	13	76
V	60	45	F	LiF220		2.5	FL	32	70
Sc	60	45	F	LiF200		0	FL	28	63
Cu	60	45	F	LiF200	0.6	0.4	FL	15	70
Zn	60	45	F	LiF200	0	0.8	FL	15	68
Cl	60	45	F	Pe	2		FL	36	74
Ga	90	30	F	LiF200	0.6		Scint.	20	70
Pb	90	30	F	LiF200	0.78		Scint.	25	73
Sr	90	30	F	LiF200	0.7		Scint.	25	73
Rb	90	30	F	LiF200			Scint.	25	73
Ba	90	30	F	LiF200	1.8	3	FL	28	73
Zr	90	30	F	LiF200		0.4	Scint.	25	73
Nb	90	30	F	LiF200			Scint.	25	73
Th	90	30	F	LiF200			Scint.	25	73
Y	90	30	F	LiF200	0.56		Scint.	25	73
La	60	45	F	LiF220	4.3	2	FL	27	58
Ce	60	45	F	LiF220		1.68	FL	13	76
Nd	60	45	F	LiF220			FL	13	76

Table A1.1: *Run parameters for the Phillips PW1480. C and F are the coarse and fine collimator respectively. FL and Scint. are the flow and Scintillation counters respectively. For crystal abbreviations see table A1.3*

A1.3.4 Run Parameters

Phillips PW1480:

Fused glass disks were analysed for major element oxides using a tungsten x-ray tube whilst the pressed pellets were run twice using both tungsten and rhodium tubes. The run parameters for this spectrometer are presented in table A1.1 and the count times are shown in table A1.5.

PANalytical Axios:

Both fused glass disks and pressed pellets were analysed using a rhodium x-ray tube. The pressed pellets were run four times. The run parameters are presented in table A1.2 and the count times are shown in table A.1.4.

	Kv	mA	Collimator (µm)	Crystal	+offs	-offs	Detector	LL	UL
Si	30	133	300	LiF 200		7.6	FL	24	76
Al	30	133	300	Pe		8.4	FL	22	76
Fe	60	66	300	LiF200		2.33	FL	13	64
Fe1	30	133	300	PX1			FL	23	72
Mg	30	133	300	TlAP	2.7		FL	25	77
Ca	30	133	300	LiF200		4.1	FL	26	73
Na	30	133	300	TlAP	3.06	1.9	FL	25	78
K	30	133	300	LiF200	3.5		FL	28	74
Ti	45	88	300	LiF200	2		FL	10	68
Mn	60	66	300	LiF200	2.65		FL	12	66
P	30	133	700	Ge	4.6		FL	29	76
Cr	50	80	150	LiF220	3.35	2.65	FL	12	65
Ni	66	66	300	LiF200	1.25		Scint.	20	77
Cr1	40	60	300	LiF200		4.31	FL	40	60
V	45	88	300	LiF220	3.25		FL	10	65
Sc	32	125	300	LiF200		1.9	FL	33	69
Cu	60	66	300	LiF200	1.82		Scint.	20	76
Zn	60	66	300	LiF200	0.73	0.9	Scint.	20	76
Cl	32	125	700	Ge	1.42	1.66	FL	34	70
Ga	60	66	300	LiF200	0.6	0.7	Scint.	20	76
Pb	60	66	300	LiF220	0.75		Scint.	25	70
Sr	60	66	300	LiF220	0.92		Scint.	25	70
Rb	60	66	300	LiF220	0.76		Scint.	25	70
Ba	40	100	300	LiF200	1.8	3	FL	35	61
Zr	60	66	300	LiF220	0.85		Scint.	25	70
Nb	60	66	300	LiF220		0.641	Scint.	25	70
Th	60	66	300	LiF220			Scint.	25	70
La	45	88	700	LiF220	2	3	FL	39	58
Ce	50	80	300	LiF220		1.68	FL	40	60
Nd	50	80	300	LiF220	4.3		FL	40	60
Y	60	66	300	LiF220	0.81		Scint.	25	70
Yb	60	66	300	LiF200			Scint.	20	76
U	60	66	300	LiF200			Scint.	25	70
Ta	60	66	300	LiF200			Scint.	20	76
Co	60	66	300	LiF200			Scint.	18	63

Table A1.2: *Run parameters for the PANalytical Axios . FL and Scint. are the flow and Scintillation counters respectively. For crystal abbreviations see table A1.3.*

Table A1.3: *crystal abbreviations*

LiF 200	Lithium fluoride 200
LiF 220	Lithium fluoride 220
Ge	Germanium
Pe	Pentaeythritol
ThAP	Thallium acid phthalate
InSb	Indium antimonide
PX1	Synthetic Multilayer Pseudocrystal

Element	Count time (s)
Si	20
Si+	10
Al	40
Al+	20
Fe	10
Fe+	4
Fe1	40
Fe1+	200
Mg	60
Mg+	60
Ca	24
Ca+	20
Na	120
Na+	72
Na-	48
K	40
K+	40
Ti	40
Ti+	40
Mn	20
Mn+	20
P	40
P+	40
Cr	20

Element	Count time (s)
Cr+	10
Cr-	10
Ni	10
Ni+	70
Cr1	10
Cr+	40
V	20
V+	20
Sc	50
Sc+	50
Cu	10
Cu+	70
Cu+	70
Zn	10
Zn+	10
Zn-	60
Cl	12
Cl+	6
Cl-	6
Ga	12
Ga+	6
Ga-	6
Pb	80
Pb+	70

Element	Count time (s)
Sr	20
Sr+	70
Rb	40
Rb+	70
Ba	80
Ba+	40
Ba-	60
Zr	20
Zr+	20
Nb	40
Nb+	34
Th	80
La	80
La+	80
Ce	80
Ce+	70
Nd	80
Nd+	40
Y	40
Y+	24
Yb	80
U	80
Ta	80
Co	10

TableA1.4*: Count times for the PANalytical Axios spectrometer. + or – denote background counts.*

Rh traces	
Element	Count time (s)
Pb	50
Pb+	50
Th	50
Rb	30
Sr	20
Sr+	50
Y	40
Y+	50
Nb	100
Nb-	100
Cl	50
Ga	10
Ga+	10
Ti1	10
Ti1+	4

W Traces	
Element	Count time (s)
Ca	4
Sc	50
Sc-	50
Ti	16
Ti+	16
La	50
La+	50
Ba	50
Ba-	50
V	16
V-	16
Ba1+	16
Nd	50
Nd+	50
Ce	50
Ce-	50
Cr	10
Cr-	10
Ni	10
Ni+	10
Cu	16
Cu-	16
Cu+	16
Zn	10
Zn-	10

W Major	
Element	Count time (s)
Fe	4
Fe-	2
Mn	4
Mn-	4
Ti	16
Ti+	16
Ca	4
Ca-	2
K	10
K+	8
P	30
P+	30
Si	20
Si+	6
Mg	40
Mg+	40
Na	40
Na+	40
Al	80
Al-	40

TableA1.5*: Count times the Phillips PW1480 spectrometer. + or – denote background counts.*

	I667	I667	I667	I667	I667	mean	2sd
SiO_2	45.90	46.09	46.15	46.08	46.04	46.04	0.19
Al_2O_3	13.79	13.92	13.81	13.82	13.75	13.81	0.12
Fe_2O_3	12.74	12.82	12.78	12.74	12.67	12.75	0.15
MgO	9.52	9.49	9.55	9.56	9.50	9.51	0.06
CaO	10.54	10.58	10.58	10.57	10.56	10.57	0.03
Na_2O	2.50	2.50	2.50	2.48	2.46	2.49	0.03
K_2O	0.897	0.902	0.908	0.905	0.900	0.903	0.008
TiO_2	2.589	2.594	2.604	2.604	2.595	2.597	0.012
MnO	0.221	0.221	0.224	0.223	0.225	0.223	0.003
P_2O_5	0.727	0.731	0.729	0.730	0.730	0.730	0.003
Cr_2O_3	0.088	0.099	0.093	0.094	0.090	0.0937	0.008
Total	99.58	100.0	99.97	99.87	99.58	99.72	
Ni	120.1	117.2	120.7	120.0	120.5	119.7	2.9
Cr	421.6	438.5	430.2	433.9	437.2	432.3	13.6
V	306.3	307.1	305.4	306.3	308.6	306.7	2.4
Sc	30.9	32.1	31.1	31.3	31.1	31.3	0.9
Cu	54.4	53.8	54.3	54.1	54.5	54.2	0.6
Zn	80.6	80.7	80.4	81.3	81.0	80.8	0.7
Cl	165	166	169	163	177	168	11
Ga	17.9	17.3	18	17.4	18.0	17.7	0.7
Pb	1.7	1.8	1.9	2.0	1.8	1.8	0.2
Sr	480	478.9	480.2	480.3	481.2	480.1	1.6
Rb	23.2	23.2	23.4	23.2	23.4	23.3	0.2
Ba	398.5	397.9	403.3	399.4	403.8	400.6	5.5
Zr	171.1	171.0	171.7	171.8	171.7	171.5	0.8
Nb	49.2	49.2	49.2	49.3	49.6	49.3	0.3
Th	3.2	3.0	3.1	3.0	3.4	3.1	0.3
Y	34.5	35.5	36.7	35.7	34.9	35.5	1.7
La	73.4	73.1	75.4	75.1	74.1	74.2	2.0
Ce	36.4	35.8	38.4	36.8	37.2	36.9	2.0
Nd	26.1	25.9	26.0	25.9	25.8	25.9	0.2
Yb	2.1	2.1	2.5	2.5	2.3	2.3	0.4
U	0.9	1.2	0.8	0.7	0.7	0.9	0.4
Ta	2.7	3.5	3.1	3.0	2.2	2.9	1.0
Co	43.6	42.8	44.1	42.8	42.4	43.1	1.4

Table A1.6: *Major and trace element results from the PANalytical spectrometer for an Icelandic basalt repeated 6 times.*

To assess the reproducibility, Icelandic basalts prepared Thrilwall and Manning (Unpublished) were repeated 6 time during the course of this study for both the PANalytical and Phillips spectrometers, the results of which are presented in table A1.6 and A1.7 respectively.

A1.4. Mineral chemistry – Major and Trace element analysis

A 1.4.1 Sample preparation

Hand-picked phenocrysts were mounted in epoxy resin before being filed down to expose a flat surface of all phenocrysts. This surface was covered in a thin layer of graphite for EMP analysis to dissipate the electrical charges that may be generated by the electron beam. The layer of graphite was ground off before LA-ICP-MS analysis.

	I112	I112	I112	I112	I112	I112	mean	2sd
SiO_2	45.51	45.43	45.59	45.60	45.62	45.62	45.56	0.15
Al_2O_3	13.87	13.82	13.86	13.90	13.86	13.98	13.88	0.11
Fe_2O_3	12.74	12.69	12.73	12.71	12.68	12.57	12.68	0.12
MgO	10.08	9.96	9.98	10.05	10.01	10.09	10.03	0.11
CaO	11.17	11.17	11.17	11.20	11.19	11.14	11.17	0.04
Na_2O	2.25	2.30	2.28	2.29	2.32	2.29	2.29	0.04
K_2O	0.784	0.787	0.783	0.785	0.779	0.782	0.78	0.01
TiO_2	2.642	2.634	2.648	2.654	2.649	2.635	2.64	0.02
MnO	0.203	0.197	0.199	0.194	0.194	0.193	0.20	0.01
P_2O_5	0.443	0.455	0.454	0.457	0.455	0.449	0.45	0.01
Total	99.69	99.44	99.70	99.83	99.75	99.75	99.69	0.27
Ni	172.2	172.8	173.1	172.3	172.2	171.9	172.4	0.89
Cr	482.4	480.9	477.6	478.9	475.5	480.3	479.3	4.95
V	359.7	359.8	360.6	364.4	364.3	363.1	362.0	4.41
Sc	34.3	34.4	34.4	34.2	34.0	33.9	34.2	0.42
Cu	68.8	68.6	67.7	69.0	68.3	69.2	68.6	1.08
Zn	86.7	87.5	85.3	85.8	85.4	85.3	86.0	1.82
Cl	186	163	78	138	71	143	129.6	91.97
Ga	16.8	16.7	16.3	15.7	16.7	15.7	16.3	1.02
Pb	2.6	1.4	2.1	1.8	1.4	1.1	1.7	1.10
Sr	437.0	438.6	437.9	439.0	439.0	438.9	438.4	1.60
Rb	15.3	15.5	15.9	15.8	15.8	15.4	15.6	0.50
Ba	335	334	333	332	334	340	334.7	5.13
Zr	159.4	158.5	159.1	158.6	159.3	159.3	159.0	0.78
Nb	39.0	39.1	39.3	39.2	39.3	39.5	39.2	0.35
Th	1.8	1.6	1.7	1.3	1.3	1.3	1.5	0.46
Y	23.7	24.2	23.8	23.8	24.0	24.4	24	0.54
La	26.8	26.5	26.4	26.8	26.8	26.9	26.7	0.40
Ce	59.6	60.4	59.0	59.5	60.1	62.7	60.2	2.62
Nd	30.0	29.0	29.9	29.9	31.3	30.5	30.1	1.52

Table A1.7: *Major and trace element results from the Phillips spectrometer for an Icelandic basalt repeated 6 times.*

A1.4.2 Major element mineral analyses by electron probe

Major element concentrations of minerals were performed on 2-4 grains from a sample and were analysed on the Cameca SX100 wavelength-dispersive electron microprobe at the Natural History Museum. Points for analysis were programmed in for overnight analyses.

A1.4.3 Simultaneous major and trace element mineral analyses by LA-ICP-MS

The majority of crystals were analyses for both major and trace element concentrations using a RESOlution L50 LPXPRO220 193 nm excimer laser coupled to an Agilent 7500ce quadrupole ICP-MS at RHUL. The method for the simultaneous determination of major and trace element analysis for olivine, plagioclase and clinopyroxene crystals has been fully described by Thirlwall et al., (2012).

Olivine:

For olivine analysis a circular spot size of 74 µm was used with a laser repetition rate of 8Hz. The olivine was ablated for 24s with a 40s washout between crystals.

	Cert. San Carlos values	Mean San Carlos (n=56)	2 sd LA-ICP-MS	2 sd EMP	DL059 LA	DL059 EMP
Fo%	90.22	90.22	0.15	0.08	86.30	85.87
MgO	49.43	49.40	0.44	0.12	46.73	45.55
CaO	0.093	0.091	0.010	0.014	0.293	0.310
TiO_2		0.0041	0.0003			
MnO	0.14	0.134	0.004	0.016		
FeO	9.55	9.55	0.12	0.08	13.31	13.36
Li		1.65	0.66			
Al		0.0344	0.0008			
Sc		5.24	1.86			
V		4.25	0.30			
Cr	96	97	3			
Ni	2907	2912	129	368	2200	2500
Y		0.049	0.005			
Zr		0.009	0.002			
Total	100.00	100.29	0.69	0.33	100.76	99.73

Table A1.8: *Long term mean of the San Carlos standard olivine with 2sd and comparative typical 2sd values obtained by EMP. In addition the compositions of two olivines from this study that have been analysed by both LA-ICP-MS and EMP on the same crystal are also shown.*

^{29}Si was used as the internal standard element used for calibration. Concentrations were calculated from measured ratios of analyte to ^{29}Si in order to reduce the effects of fractionation; however unlike most studies the concentrations of the internal standard element are unknown prior to analysis. The SiO_2 concentrations were derived stoichiometrically using the following equation based on EMP results (Thirlwall et al., 2012):

$$wt.\%\, SiO_2 = 0.0005 \cdot Fo\%^2 + 0.079 \cdot Fo\% + 29.6$$

NIST612 was use as the calibration standard for all elements with the exception of MgO and FeO. The concentrations of these elements are 5000x greater than in the NIST612 glass, consequently accurate quantification of these elements cannot be achieved. Instead a San Carlos standard olivine (NMNH 111312-44) was run at the start and the end of a data file which was used as the calibration standard for these two elements. At regular intervals during a run San Carlos olivines were analysed as unknowns, this has allowed the long term reproducibility of this method to be assessed. The major element reproducibility is similar to or better then EMP values whilst trace element values are significantly better than other LA-IC-MS data (Thirlwall et al., 2012). Table A1.8 reports the long term mean and associated 2sd reproducibility of the San Carlos olivine since 05/03/2010 (n=56) of which 28 crystals were from runs that contain olivines from this study. Also shown for comparison is the typical 2sd

	Cert. values	Mean Great Sitkin (n=56)	2 sd LA-ICP-MS	2 sd EMP	Bytownite LA	Bytownite EMP
An%	95.05	95.19	0.37	0.70	87.69	87.60
SiO_2	44.00	44.14	0.09	0.28	45.93	46.16
Al_2O_3	36.03	34.97	0.06	0.12	33.80	34.04
FeO	0.48	0.47	0.02	0.04	0.50	0.51
MgO		0.048	0.004	0.014	0.144	0.14
CaO	19.41	19.19	0.54	0.30	17.54	17.85
Na_2O	0.65	0.53	0.04	0.07	1.30	1.37
K_2O	0.0100	0.0091	0.0009	0.02	0.038	0.04
TiO_2	0.0100	0.0087	0.0007			
Sr		624	12			
Y		0.06	0.01			
Ba		15.7	1.2			
La		0.14	0.02			
Sm		0.03	0.03			
Eu		0.10	0.02			
Gd		0.02	0.02			
Pb		0.39	0.14			
Total	100.00	99.36	0.54	0.47	99.25	100.11

Table A1.9: *Long term mean of the Great Sitkin standard anorthite with 2sd and comparative typical 2sd values obtained by EMP. In addition the compositions of two Icelandic bytownite crystals reported by Thirlwall et al., (2012) that have been analysed by LA-ICP-MS and EMP on the same crystal are also shown.*

reproducibility values for EMP analysis based on 7 repeats of the Eagle Station pallasite (Fo_{91}) standard olivine analysed during this study.

Plagioclase:

For plagioclase analysis a circular spot size of 57 µm was used with a laser repetition rate of 8Hz. The plagioclase was also ablated for 24s with a 40s washout between crystals.

^{44}Ca and ^{29}Si were used as the internal standard elements used for calibration. Like olivine, concentrations were calculated from measured ratios of analyte to ^{29}Si or ^{44}Ca. SiO_2 was calculated using the following equation (Thirlwall et al., 2012):

$$wt.\%\, SiO_2 = -0.24825 \cdot An\% + 67.77$$

It is not possible to determine accurate Na_2O and CaO concentrations through calibration using NIST612 glass despite high concentrations in the glass due to the extensive laser-induced fractionation of Na_2O/CaO (Thirlwall et al., 2012). As such the matrix-matched Lake County NMNH115900 standard labradorite and the Great Sitkin NMNH137041 standard anorthite were used to quantify the major elements Ca, Na, K, Fe and Mg. All other elements were

	Cert. values	Mean Kakanui augite (n=5)	2 sd LA-ICP-MS	2 sd EMP	I359 LA	I359 EMP
SiO_2	50.73	50.88	0.47	0.18	50.81	50.95
TiO_2	0.740	0.814	0.008	0.020	0.633	0.680
Al_2O_3	8.73	8.32	0.08	0.02	5.52	4.66
FeO	6.45	6.31	0.07	0.05	5.21	5.4
MnO	0.130	0.142	0.002	0.020	0.112	0.120
MgO	16.65	16.19	0.20	0.14	15.54	15.79
CaO	15.82	15.86	0.16	0.18	20.88	21.13
Na_2O	1.27	1.35	0.03	0.03	0.29	0.32
Li		1.69	0.14			
Sc		34	1			
V		303	3			
Cr		1054	17	38	6486	6295
Ni		310	9	179		
Sr		58.8	0.8			
Y		8.93	0.21			
Zr		22.6	0.5			
Nb		0.23	0.02			
La		1.34	0.06			
Ce		5.28	0.42			
Nd		6	0.7			
Sm		2.1	0.21			
Eu		0.72	0.07			
Gd		2.26	0.2			
Dy		2.07	0.11			
Er		0.89	0.09			
Yb		0.67	0.09			
Hf		1.16	0.1			
Total	100.52	99.99	0.24	0.47	100.00	99.05

Table A1.10: *Long term mean of the Kakanui augite standard with 2sd and comparative typical 2sd values obtained by EMP. In addition the compositions of two Icelandic clinopyroxene crystals reported by Thirlwall et al., (2012) that have been analysed by LA-ICP-MS and EMP on the same crystal are also shown.*

quantified using NIST612 using ^{44}Ca (also calculated as an unknown) as the internal standard element due to the lower fractionation differences then if SiO_2 is used.

Testing the reproducibility or accuracy is difficult given the heterogeneity present in the standard plagioclase grains analysed in this study and reported by Thrilwall et al., (2012). The Great Sitkin anorthite was found to be the least heterogeneous and as such should give a 'worst-case' estimation of inaccuracy. Table A.1.9 shows the long term mean of the Great Sitkin anorthite and 2sd reproducibility since 13/12/11 (n=20) of which 2 crystals were from runs that contain plagioclases crystals from this study. For comparison 2sd reproducibility values from EMP data are shown, based on 7 repeats of an An_{81} plagioclase used as a standard during EMP analyses of plagioclase crystals from this study.

Clinopyroxene:

For clinopyroxene analysis a circular spot size of 57 µm was also used with a laser repetition rate of 5Hz. The clinopyroxene was ablated for 20s with a 30s washout between crystals.

Like plagioclase ^{44}Ca and ^{29}Si were used as internal standard elements used for calibration. As clinopyroxene are multicomponent minerals it is not possible to adequately predicted concentrations by stoichiometry. Instead the approach of normalisation to 100% total has been used. SiO_2 was iteratively selected as an internal standard element value that yielded a 100% total. As with olivine low concentrations in the NIST612 glass made it not possible to accurately quantify Mg, Fe, Mn and Ti, as such the Chromium augite NMNH 164905 standard was used to quantify these elements. Trace elements use Ca calculated from Ca/Si ratios as an internal standard element which enhanced internal precision.

Thirlwall et al., (2012) reported 4 grains of the NMNH117733 Kakanui augite during the period of this study analysed as unknowns to assess reproducibility. The inferred SiO_2 values are within the range of published EMP values (Thrilwall et al., 2012) and 2sd reproducibility values for all other elements give similar or better reproducibility than EMP 2sd reproducibility based on the repeat of 5 diopside standards during EMP analysis of crystals from this study (table A1.10).

A1.5 Sr and Nd isotopic analysis

A1.5.1 Sr isotope sample preparation

Sample leaching:

Sr isotope preparation was under taken using savillex beakers that had been cleaned in conc. HCl for >24 hours at 175°C and conc. HNO_3 for > 24 hours at 175°C before being stored in MQ water. Prior to use the beakers were boiled for 20 minutes in MQ water and then rinsed multiple times. Where powder was recovered from pellets for analysis, samples were placed in a furnace for ~1h at ~800°C in order to remove the binding solution. Whole rock powders were then leached in 6M HCL for 1 hour at 180°C to remove any surface alteration and then rinsed multiple times with MQ until the supernate was clear. The samples were dissolved using ~2ml TD conc. HNO_3 and ~3ml TD HF in sealed beakers left overnight at 150°C. The sample was then evaporated to dryness before converting to nitrate by the addition of ~2ml HNO_3 and evaporated to dryness again.

Sr separation chemistry:

Samples were dissolved in 1ml 8M HNO_3 and then centrifuged in plastic centrifuge tubes rinsed with MQ H_2O for ~6 minutes. Columns were prepared by inserting 70µ frits into pipette tips which were then soaked in 10% HNO_3 for a minimum of 24 hours. Columns were given an initial clean with 4M HNO_3 and MQ H_2O, after ~5 drops of eichrom Sr-spec resin was added. The resin was cleaned with 4M HNO3 and MQ H_2O before being pre-treated with 8M HNO_3. 1 ml of sample was loaded onto each column using Pasteur pipettes cleaned in 8M HNO_3, followed by 3 elutions of 8M HNO_3. Prior to collection the digestion savillex beaker were cleaned with a few drops of conc. HNO_3 and put of the hotplate for ~30 minutes before rinsing with MQ H_2O. The Sr fraction was eluted with 3 passes of MQ H_2O and collected in the cleaned beakers. Once collected the sample was evaporated to dryness before adding a few drops of TD conc. HNO_3 and evaporating again.

Bead making and loading procedures:

Sr isotopic analyses were run on single Ta filaments. These were prepared by grinding any old filament material off the bead before spot welding new Ta filament into place. These were then cleaned in MQ H_2O using an ultrasonic bath to remove any loose material and rinsed before boiling for 10-20 minutes in fresh MQ H_2O. After drying the beads were degassed at ~5A for 15 minutes then at ~3A for 15 minutes then at ~2.5A for 15 minutes at a pressure of $<1.10^{-5}$ mbar. The beads were then stored in a bead box for ~24 hours prior to loading to allow the filaments to oxidise. The samples were loaded onto the filaments using H_3PO_4 and once dried at a current of 1.2A. The filament was then raised to ~2A in order to burn off any excess acid.

A1.5.2 Nd isotope sample preparation

Sample dissolution:

Nd isotope preparation was undertaken in savillex beakers prepared as for Sr preparation. However, after boiling in MQ water 1ml HNO_3 and 2-3ml HF were added to the beakers which were sealed and left on a hotplate at 150°C overnight to break down any silica gel that might be left in the beakers. The beakers were then rinsed with MQ before ~0.1g of rock powder was added. The rock powder was then dissolved in 2ml TD conc. HNO_3 and 5ml TD HF, sealed and left on a hotplate at 150°C for >36 hours. The resulting solution was evaporated to dryness at ~120°C before adding 2ml TD conc. HNO_3 and evaporated to dryness.

Nd separation chemistry:

Samples were dissolved in 2ml 10% HNO_3 on a hotplate overnight before centrifuging in centrifuge tubes rinsed in MQ H_2O. First stage Nd separation was performed using columns prepared as for Sr separation. 0.05g of dry TRUspec resin was added to each column and cleaned with 0.05M HNO_3. Prior to loading the sample the resin was conditioned with 10% HNO_3. The sample was loaded in two batches of 1ml 10% HNO_3, using pasture pipettes rinsed in 10% HNO_3, followed by the elution of 10% before collecting 2x1ml 0.05M HNO_3 . Before collection the beakers were rinsed in MQ H_2O and placed, sealed, on the hotplate with 1ml HNO_3 to remove any residue and then rinsed with MQ H_2O. The collected fraction was then evaporated to dryness.

The second stage Nd separation was performed on temperature controlled anion exchange columns. The sample was dissolved in 1ml of orange cocktail using repeated periods in the ultrasonic bath to aid dissolution. The columns were pre-treated with orange cocktail at 25°C before addition of the sample onto the resin using paster pipettes rinsed in orange cocktail and then a further 50ml of orange cocktail eluted. An elution of yellow cocktail was performed at 35°C before collection of the sample in beakers that had been on the hotplate, sealed, with 2-3ml TD conc. HNO_3 for > 3 hours and then rinsed in MQ H_2O. The collected sample was evaporated to dryness and a second pass undertaken. Instead of the 35°C stage 15ml of 10% HNO_3 was collected at room temperature and evaporated to dryness

Bead making and loading procedure:

Nd isotopes were run on single Re filaments made using the same procedure as for single Ta filaments and degassed in the same way. Nd sample were loaded onto filaments using a combination of Si gel and H_3PO_4 (Thirlwall, 1991a).

A1.5.3 Mass Spectrometry

Isotopic analysis:

Beads for both Sr and Nd analyses were loaded into a 16 sample turret and analysed on a VG 354 multi-collector mass spectrometer at RHUL at a pressure of 10^{-6}mbar. All samples were run automatically.

Sr isotopic composition:

Sr isotopic composition was determined using a multi-dynamic programme (SrSQ) which uses all five collectors in the configuration shown in table A1.11. There are several benefits of using

Collector	H2	H1	AX	L1	L2
MD1	87	86	85	84	83
MD2	88	87	86	85	84
MD3	89	88	87	86	85
MD4	89.5	88.5	87.5	86.5	85.5
Zeroes	93.4	92.4	91.4	90.4	89.4

Table A1.11: *SrSQ collector confinguration*

a multi-dynamic procedure; it allows for interference of ^{87}Rb on ^{87}Sr to be corrected for accurately as ^{85}Rb is measured in field positions 1,2 and 3, as well as permitting 2 individual $^{87}Sr/^{86}Sr$ calculations using Ax-H1 and H1-H2. The resulting ratios were then corrected for mass fractionation by exponential normalisation to $^{86}Sr/^{88}Sr$ =0.1194 (Thirlwall, 1991a).

Two standard of SRM 987 were run in each turret normally at positions 5 and 11. Over the period of study these gave a mean value of 0.710249 ± 13 (2sd, N=18) which identical to the mean value for all SRM 987 standard run during the period of study of (N=123) (Figure A1.1)

Nd isotopic composition:

Nd isotope sample were analysed as NdO^+ using a multidynamic procedure as outlined in Thirlwall et al. (1991b) with a collector configuration as shown in table A1.12. Analysis of Nd as an oxide gives 20 times better ionisation and the loading technique outline above inhibits SmO^+ and CeO^+ ionbeams reducing isobaric interferences (Thrilwall, 1991b). $^{143}Nd/^{144}Nd$ measurements were normalised to $^{146}Nd/^{144}Nd$ =1.14187 (Thirlwall, 1991b).

Two standards of dilute Aldrich were run in each turret normally in position 5 and 12. Over the period of study these gave a mean value of 0.511405 ± 6 (2sd, N=17), within error of the long term mean of 0.511406 ± 7 (2sd, N=45) (Figure A1.1).

Table A1.12: *NdO^+ collector configuration*

Collector	H2	H1	AX	L1	L2
MD1	160	159	158	157	156
MD2	161	160	159	158	157
MD3	162	161	160	159	158
MD4	168.4	167.4	166.4	165.4	164.4
Outside cycle	157	156	155	154	153

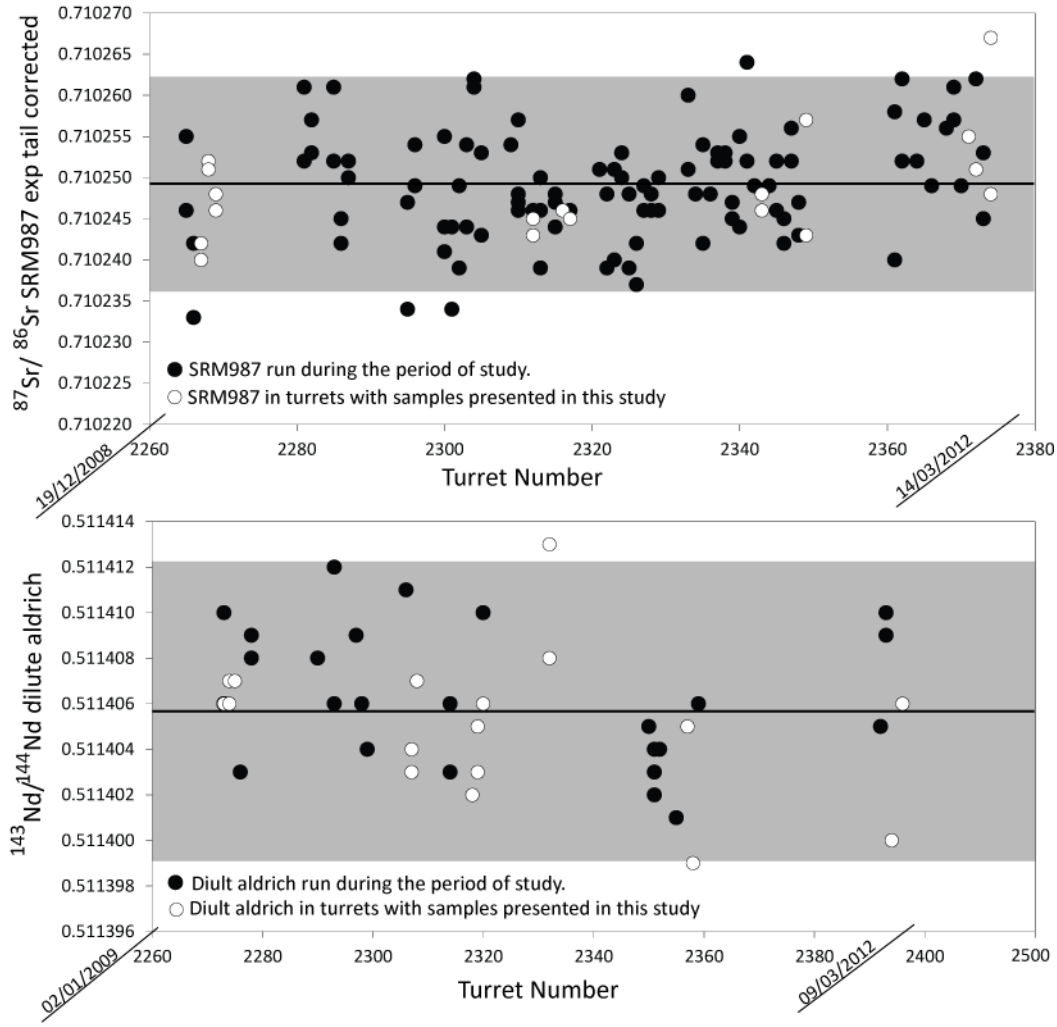

Figure A1.1: *SRM987 and dilute Aldrich ratios over the period of this study. Shaded area indicates the long term means. Dates denote the period in which samples were analysed.*

A1.5 Pb isotopic analysis

A1.5.1 Pb isotope sample preparation

Sample dissolution:

Pb samples were prepared in 3 ml savillex beakers which were previously cleaned in conc. HNO_3 for >48 hours at 130°C and then rinsed with MQ H_2O. Each beaker was half filled with 6M HCl and left on a hotplate at 130°C for 48 hours. TD HNO_3 was added to the 6M HCl and the resulting aqua regia left over night. After rinsing multiple times with MQ water, 20 drops of 2% HNO_3 was added and left on a hotplate overnight before blank testing on the isoprobe. Pb dissolution was performed on ~0.1g handpicked chips which were leached for 1 hour in 6 M HCl at 180°C and rinsed multiple times with MQ H_2O. Two blanks were prepared in each set of 18 samples and were spiked with 1 drop of dilute ^{208}Pb spike. The chips were dissolved in 15

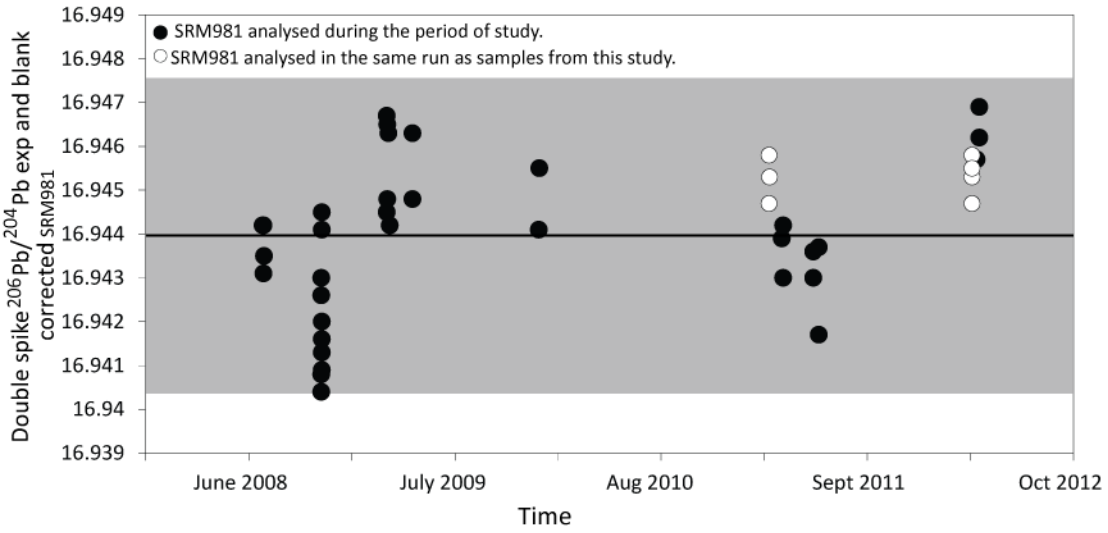

Figure A1.2: *Double spike SRM981 standard data analysed as an unknown.*

drops of TD conc. HNO_3 and TD HF in sealed beakers on a hotplate at 150°C for 48 hours. The remaining solution was evaporated to dryness at 120°C and a further 20 drops of TD conc HNO_3 was added and evaporated to dryness. The sample was then converted to a chloride by adding 6M HCl which was then evaporated before dissolution of the sample in 1M HCl ready for loading onto the columns.

Separation chemistry:

Pb separation chemistry was performed using columns made from Teflon pipette tips cleaned in analar conc. HNO_3 on a hotplate at 130°C for >48 hours. Once the frits were inserted the columns were soaked in SB~7M HCl for ~40 hours. Prior to the addition of resin the columns were cleaned with SB HNO_3 and MQ water. 5 drops of Sr spec resin slurry was added to each column. The resin was cleaned with SB conc. HCl and pre-treated with 1M HCl before sample loading. Samples were centrifuged in plastic centrifuge tubes which had been soaked in SB ~7M HCl for ~24 hours. The sample was then loaded onto the resin using Pasteur pipettes that had also been soaked in SB~7M HCl. Following several elutions of 1 M HCl the sample was collected in 6M HCl in the digestion savillex beakers that had been cleaned with a few drops of conc. HNO_3, sealed on a hotplate for ~30 minutes and then rinsed with MQ H_2O. The collected fraction was evaporated to dryness and dissolved in 1M HCl ready for the second pass through the columns. The collected fraction from the second pass was evaporated to dryness followed by the addition of 2 drops of TD conc. HNO_3 which was also evaporated.

A1.5.2 Mass spectrometry

Pb isotopic analyses were run using the multi-dynamic double spike procedure of Thirlwall (2002) using the micromass IsoProbe MC-ICP-MS at RHUL. ~30 drops of Tl solution was added to samples and ~10 drops to blanks. Samples were run multi-dynamically, in some cases the ^{208}Pb signal was too low to dynamically and in these cases the natural samples were run statically. The blanks were also run statically. Double spike solution ($^{207}Pb/^{204}Pb$) was added to the remaining sample aiming to achieve an optimum $^{204}Pb/^{206}Pb$ of ~0.65, In some cases to achieve this the remaining solution was diluted with Tl solution. All Double spike runs were run dynamically. Throughout the course of analysis natural and double spiked standards SRM981 were analysed as unknowns. (Figure A1.2). Over the period of this study SRM981 gave a $^{206}Pb/^{204}Pb$ mean of 16.9450 ± 9, $^{207}Pb/^{204}Pb$ mean of 15.502 ± 2 and a $^{208}Pb/^{204}Pb$ mean of 36.729 ± 60 (n=7). These values lie with error of the long term mean of 16.944 ± 3, 15.502 ± 3 and 36.727 ± 98 (n= 43) for $^{206}Pb/^{204}Pb$, $^{207}Pb/^{204}Pb$ and $^{208}Pb/^{204}Pb$ respectively.

A1.6 Hf isotopic, REE, Pb, Hf, U and Th ID analysis.

A1.6.1 Sample preparation

Sample dissolution:

Hf isotopic and REE ID, U/Th concentration analyses were performed on a single total dissolution. Sample dissolution was performed in savillex beakers cleaned as for Nd isotope preparation. 0.1g of fresh powder was weighed into the beakers along with with U-Th-Pb, LREE, HREE and Zr-Hf-Ba spikes. The samples were dissolved in TD conc. HNO_3 and TD HF on a hotplate at 150°C for 48 hours and then evaporated to dryness.

Table A1.13: *Summary of column separation chemistry for REE, Hf, Pb, U, Th ID and $^{176}Hf/^{177}Hf$*

Fraction added to column	Resin	Fractions collected	Fraction analysed	IsoProbe programme used
Whole rock dissolutution	Sr spec	REE and Pb	Pb ID	Pb202Ax
Residue from Sr spce colums	Tru spec	LREE, U and Th	U and Th (after a second pass through the same columns)	Th230Ax
LREE fraction	Tru spec	Nd-Eu La-Ce	Nd, Sm, Eu ID La-Ce	SmNdEu LaCeDaly
REE residue from initial columns	Cation	Hf, Zr, Ti; HREE		
Hf, Zr, Ti (after second pass in Cation colmuns)	Eichrom LN	Hf and Zr	$^{176}Hf/^{177}Hf$ Zr and Hf ID	Hfmuilt Hf175Ax
HREE	Eichrom LN	Gd-Dy-Er Yb-Lu	Yb-Lu ID	YbLu

Gd-Dy-Er	Anion	Gd-Dy-Er	Gd, Dy, Er ID	GdDyEr

Separation chemistry:

A series of different columns were used in order to separate different REE fractions for analyses. These are summarised in table A1.13.

A1.6.2 Mass spectrometry

Hf isotopes, REE ID and U/Th analyses were all determined using the micromass IsoProbe at RHUL. The following outlines the collector configurations used.

Th230Ax:

L3	L2	L1	Ax	H1	H2	H3	H4	H5	H6
		229 Th	230 Th	231	232 U	233 U	235 U	236 U	238 U

Standards: TML

Hf isotopes: Hf isotopic ratios were determined multidynamicly.

	L3	L2	L1	Ax	H1	H2	H3	H4	H5	H6
Md1				174	175	176	177	178	179	180
	172	174		175	176	177	178	179	180	182
Md2				176	177	178	179	180	182	

Standard: JMC 475 97ppb

REE and Pb concentrations, these were all determined statically:

Pb202Ax:

L4	L3	L2	L1	Ax	H1	H2	H3	H4	H5	H6
194.5 Hg Wo	198 Hg ReO	201		202	203 Tl ReO	204 Pb ReOH Hg	205 Tl	206 Pb	207 Pb	208 Pb

Standards: SRM 981

SmNdEu:

L3	L2	L1	Ax	H1	H2	H3	H4	H5	H6
143 Nd	145 Nd Spike		146 Nd	147 Sm	148 Nd Sm	149 Sm Spike	151 Eu	153 Eu Spike	154

Standards: Nd-Sm-Eu, 400 Nd

LaCeDaly:

L3	L2	L1	Ax	H1	H2	H3	H4	H5	H6
	135	136	137	138 La Spike Ce Ba	139 La	140 Ce	142 Ce spike Nd	143 Nd	145 Nd spike

Standards: LaNd, CeNd, 0.1Ba 125 Nd

GdDyEr:

L3	L2	L1	Ax	H1	H2	H3	H4	H5	H6
155 Gd Spike	156 Gd Dy		158 Gd Dy	161 Dy spike	163 Dy	164 Dy Er	166 Er	167 Er spike	168 Er Yb

Standards: GdDy 100ppb, DyErYbLu.

YbLu:

L3	L2	L1	Ax	H1	H2	H3	H4	H5	H6
155 Gd	159 Tb	163 Dy		171 Yb Spike	172 Yb	174 Yb	175 Lu	176 Lu spike Yb Hf	177 DyO

Standards: 100 ppb Yb, 86Yb84Lu, Gd400, 180Dy, Tb

Hf ppm ID:

L3	L2	L1	Ax	H1	H2	H3	H4	H5	H6
172	174 Hf		175 Lu	176 Hf Lu Yb	177 Hf	178 Hf	179 Hf	180 Hf Ta W	182 Hf W

Standards: JMC 475 97ppb

The data yielded by the IsoProbe was processed based on the procedure outline by Thirlwall and Anczkiewicz (2004). The measurements were first corrected for the baselines using on peak zeros (OPZ) measured during integrations of the blank solution (typically 2% HNO_3), immediately prior to the analysis of the sample. These OPZ include instrumental memory and amplifier offsets. Corrections for the contribution to peak intensity from adjacent peaks and electronic crosstalk between the Faraday amplifiers are then applied. Instrumental drift, if

present was monitored by running the standards listed above every 6 samples. In assessing reproducibility the reference basalt BHVO-1 was analysed 3 times during the period of

	May 2009	March 2010	March 2011	Mean BHVO-1	Mean from Baker et al (2002)	2sd
La	15.49	15.51	15.49	15.49	15.52	0.02
Ce	38.62	38.25	38.23	38.36	38.23	0.44
Nd	24.80	24.78	24.79	24.79	24.79	0.02
Sm	6.131	6.130	6.133	6.131	6.140	0.003
Eu	2.076	2.076	2.076	2.076	2.067	0.001
Gd	6.282	6.289	6.297	6.289	6.286	0.015
Dy	5.343	5.350	5.370	5.354	5.363	0.027
Er	2.545	2.549	2.558	2.551	2.567	0.013
Yb	1.996	1.999	2.007	2.001	1.978	0.011
Lu	0.2791	0.2790	0.2795	0.2792	0.2739	0.0005

Table A1.14: *Repeat analyses of BHVO-1*

this study. The initial analysis during May 2009 was run on the same days as samples from this study. For comparison the mean of 8 repeated BHVO-1 analyses also measured by Isotope dilution reported by Baker et al (2002) has been include in table A1.14. Figure A1.3 shows the long term $^{176}Hf/^{177}Hf$ mean achieved for JMC475 by the IsoProbe with the samples analysed with this study highlighted.

A1.7 Oxygen isotopic analysis

A1.7.1 Sample Preparation

For the majority of postglacial samples olivine and plagioclase phenocrysts were hand-picked from sieved non-magnetic fractions. Phenocrysts were picked preferentially picked from the 500µm- 1mm however often samples only contained crystals from the 250µm-500µm fraction. Only the freshest phenocrysts were analysed where inclusions and signs of alteration were minimal. 1.7 ±0.2mg of phenocrysts were weighed into each hole in a 16 hole nickel tray. Four internal standards of San Carlos II were run in each tray in positions, 3, 7, 11 and 15. The samples analysed in position 1 was sacrificial to remove any contamination from the extraction line.

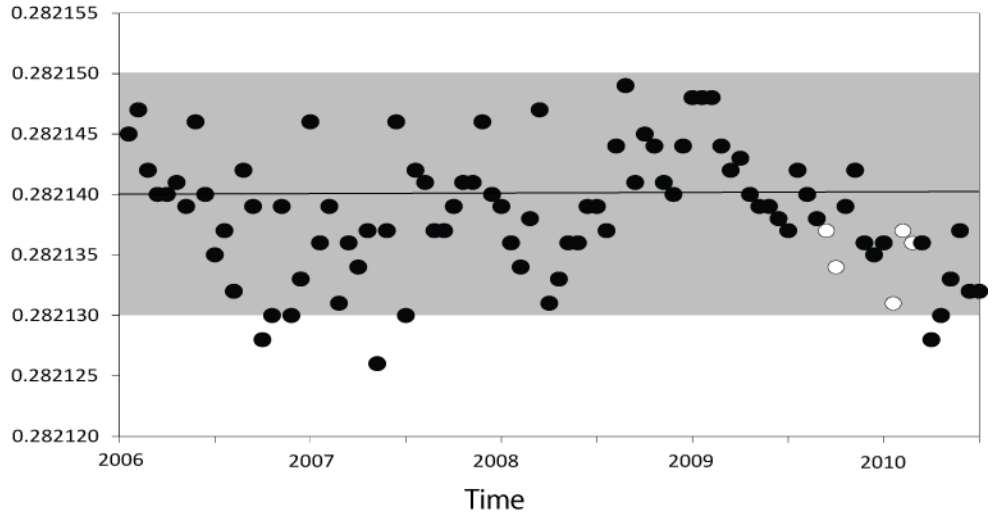

Figure A1.3: *Long term JMC475 mean*

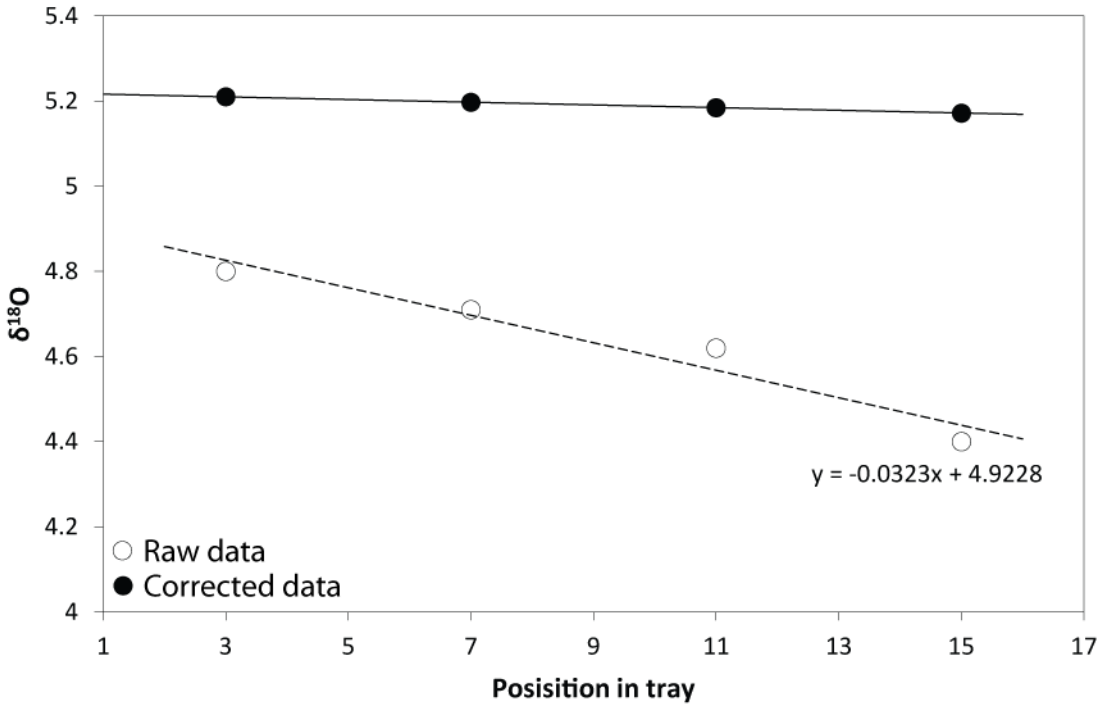

Figure A1.4: *Raw and drift corrected San Carlos II values. The same correction procedure was used on all oxygen isotope data.*

A1.7.2 Mass Spectrometry

Oxygen data was determined on the Royal Holloway Mark II laser fluorination system (LaserPrep) attached to a Micromass Optima mass spectrometer (Mattey and Macpherson 1993). The loaded tray was dried in an oven for a minimum of 2 hours prior to loading into the sample chamber to ensure no contamination from surface moisture. The chamber was then pumped to a high vacuum over night. The chamber was pre-fluorinated for 30 minutes before analysis to remove any oxygen contained in low temperature alteration products. The samples

were then reacted sequentially, the oxygen being released from the mineral through conversion to a fluoride by laser heating in the presence of BrFs reagent.

It was necessary to correct the standard data within each run for drift, this was done by placing a linear regression through the standard data on a plot of raw $\delta^{18}O$ San Carlos II vs hole number and using the gradient of this regression to correct the data within the run. Plots showing the raw and corrected San Carlos II data for each run are shown in figure A1.4. In addition to the correction for drift per hole there was an initial correction placed on the first hole to calibrate the data to the accepted value for San Carlos II of +5.23 ‰. This value was changed to generate a best fit line through the corrected San Carlos II data which lay at ~5.23‰.

APPENDIX 2: SAMPLE LOCALITIES AND AGES

All localities marked on the geological map of the NRZ (Appendix 2 included in the pocket) are listed below. Samples are divided by rift segment and are listed in age order.

Sample No.	Flow Name	Decimal W	Decimal N	Age
Krafla				
DL039	*Krafla Fires 1977-1984*	-16.789	65.723	1977-1984
DL040		-16.791	65.726	1977-1984
DL041		-16.792	65.727	1977-1984
DL042		-16.792	65.727	1977-1984
DL043		-16.794	65.724	1977-1984
DL045		-16.794	65.721	1977-1984
DL059		-16.792	65.723	1977-1984
DL038	*Myvatn Fires*	-16.859	65.672	1725 AD
DL062		-16.933	65.652	1725 AD
DL066		-16.778	65.683	1725 AD
DL010	*Dalseldar*	-16.856	65.623	850 AD
DL011		-16.850	65.623	850 AD
JPF0912		-16.765	65.723	850 AD
DL003	*Younger Laxárhraun*	-17.535	65.955	2000 BP
DL004		-17.522	65.943	2000 BP
DL060		-16.923	65.598	2000 BP
DL061		-17.113	65.600	2000 BP
JPF0901		-17.041	65.568	2000 BP
JPF0902		-16.923	65.598	2000 BP
JPF0902A		-16.923	65.598	2000 BP
JPF0902B		-16.923	65.598	2000 BP
JPF0907		-17.010	65.534	2000 BP
DL021B	*Bjarnarflagsstöð*	-16.853	65.638	2450 BP
DL022		-16.853	65.638	2450 BP
DL023		-16.852	65.634	2450 BP
DL035	*Krafla Caldera*	-16.807	65.660	~2400 BP
DL063		-16.738	65.721	~2400 BP
DL064		-16.732	65.723	~2400 BP
DL065		-16.737	65.720	~2400 BP
JPF0911		-16.773	65.700	~2400 BP
JPF0913		-16.761	65.720	~2400 BP
DL006		-16.874	65.615	~2600 BP
DL007		-16.867	65.618	~2600 BP
DL009		-16.863	65.622	~2600 BP
JPF0903	*Hverfjall*	-16.893	65.606	2800 BP
JPF0905		-16.875	65.613	2800 BP
JPF0953	*Asbyrgí*	-16.556	66.041	early holocene
JPF0954		-16.641	66.056	early holocene
JPF0956		-16.499	66.023	early holocene

DL067	*Heiðarsporður*	-16.782	65.646	~9350 BP
KK3		-16.802	65.590	~9350 BP
KK35		-16.805	65.619	~9350 BP
KR47		-16.799	65.604	~9350 BP
KR48		-16.807	65.606	~9350 BP
KK51		-16.846	65.573	~9350 BP
KK55		-16.813	65.525	~9350 BP
KR74		-16.807	65.573	~9350 BP
KR77		-16.785	65.645	~9350 BP
KR79		-16.795	65.652	~9350 BP
KR82		-16.846	65.595	~9350 BP
KR87		-16.800	65.609	~9350 BP
KR87A		-16.814	65.555	~9350 BP
KR88		-16.810	65.554	~9350 BP
JPF0914		-16.773	65.647	~9350 BP
DL013	*Vindbelgjarfjall*	-17.069	65.623	Intra-glacial
DL015		-17.070	65.622	Intra-glacial
DL033	*Namafjall Rigde*	-16.823	65.651	Intra-glacial
DL034		-16.808	65.659	Intra-glacial
DL046	*nr. Krafla Caldera*	-16.731	65.713	Intra-glacial
DL048		-16.730	65.714	Intra-glacial
JPF0971	*Grimsstadaheidi*	-17.000	65.669	Inter-glacial
DL053		-16.037	65.775	Inter-glacial
DL055	*Sandabotnafjall*	16.729	65.692	Inter-glacial
JPF1006	*Holasandur*	-17.128	65.744	Inter-glacial
JPF0909	*Grænavatnsoruni*	-17.039	65.502	Inter-glacial
JPF0910		-17.036	65.511	Inter-glacial
Fremri-Námur				
JPF0906	*Older Laxárhraun*	-16.986	65.544	2300 BP
JPF0908		-17.014	65.526	2300 BP
JPF0915	*Burfellshraun*	-16.703	65.645	2500-3000 BP
JPF0915A		-16.702	65.644	2500-3000 BP
JPF0916		-16.559	65.660	2500-3000 BP
	Main rifting event			
JPF0917	*Sveinahraun*	-16.469	65.660	6000-8000 BP
JPF0918		-16.443	65.654	6000-8000 BP
JPF0950	*Randarholar*	-16.387	65.854	6000-8000 BP
JPF0970		-16.443	66.108	6000-8000 BP
JPF0958	*Kerlingarhraun*	-16.413	66.262	6000-8000 BP
JPF0964		-15.921	66.411	6000-8000 BP
JPF0968		-16.132	66.154	6000-8000 BP
JPF0945	*Fosshraun*	-16.348	65.810	6000-8000 BP
JPF0919	*Basement*	-16.416	65.653	?early holocene
JPF0921		-16.357	65.646	?early holocene
JPF0922		-16.357	65.646	?early holocene
JPF0957	*Nupar*	-16.483	66.175	Intra-glacial
JPF0959	*Snartarstaðarúpur*	-16.453	66.354	Intra-glacial
JPF0960		-16.453	66.354	Intra-glacial
JPF0943	*Hrossaborg*	-16.192	65.621	Inter-glacial
JPF0944		-16.340	65.762	Inter-glacial

JPF0946	*Dettifoss*	-16.380	65.819	Inter-glacial
JPF0947		-16.381	65.818	Inter-glacial
JPF0948		-16.382	65.818	Inter-glacial
JPF0949		-16.383	65.819	Inter-glacial
JPF0951		-16.417	66.009	Inter-glacial
JPF0961	*Melrakkasletta*	-16.369	66.479	Inter-glacial
JPF0962		-16.236	66.486	Inter-glacial
JPF0969	*Axarfjaðrarheiði*	-16.317	66.141	Inter-glacial
Askja				
	Caldera fissure eruptions			
JPF0932		-16.565	65.054	1961 AD
JPF0933		-16.637	65.057	1961 AD
JPF0934		-16.730	65.060	1961 AD
JPF0938		-16.728	65.066	1961 AD
JPF0935		-16.715	65.045	AD 1920
JPF0920	*Nyjahraun*	-16.389	65.650	AD 1875
JPF0937		-16.730	65.052	1477 AD - 2900 BP
JPF0939		-16.662	65.058	1477 AD - 2900 BP
JPF0940		-16.587	65.042	2900-3500 BP
JPF0928	*Flatadyngja Sheild*	-16.214	65.166	*3500-4500 BP*
JPF0931	*Svartadyngja Sheild*	-16.398	65.067	*>4500 BP*
JPF0942	*Dyngjufjallahraun*	-16.650	64.945	~7000 BP
DL002	*Trölladyngja Sheild*	-17.555	65.701	*~7200 BP*
JPF0927	*Basement*	-16.177	65.237	?early holocene
JPF0926		-16.159	65.256	?early holocene
JPF0924		-16.186	65.501	?early holocene
JPF0941	*Vadalda*	-16.541	64.989	Inter-glacial
JPF0936	*Öskavatan*	-16.718	65.047	Inter-glacial
JPF0923		-16.227	65.592	Inter-glacial
JPF0925		-16.087	65.374	Inter-glacial
Kverkfjöll				
JPF1022	*Kverkfjallahraun*	-16.462	64.838	6950 BP
JPF1021		-16.522	64.811	6950 BP
JPF1019		-16.631	64.747	> 6950 BP
JPF1020		-16.599	64.771	> 6950 BP
JPF1017		-16.615	64.759	> 6950 BP
JPF1015		-16.384	64.903	> 6950 BP
JPF1018		-16.653	64.745	> 6950 BP
JPF1010	*Krepputunga*	-16.155	65.098	early holocene
JPF1011		-16.208	65.065	early holocene
JPF1012		-16.222	64.985	early holocene
JPF1013		-16.298	64.909	early holocene
JPF1014		-16.328	64.963	early holocene
JPF1016	*Lindafjöll*	-16.392	64.899	Intra-glacial
JPF1023		-16.453	64.866	Intra-glacial
JPF1007		-15.841	65.350	Inter-glacial
JPF1008		-15.883	65.304	Inter-glacial
JPF1009		-16.108	65.100	Inter-glacial

Fjallgarðar				
JPF0973	*Moðrudalur*	-15.685	65.467	Intra-glacial
JPF0974		-15.676	65.326	Intra-glacial
DL074	*Vegahnjukur*	-15.940	65.442	Intra-glacial

Ages are complied from personal field observations; Global Volcanism Program *www.volcano.si.edu*; Hjartarson, (2008); Tentler and Mazzoli, (2005); Jóhannesson and Sæmundsson (1998); Sigvaldason et al., (1992); Nicholson, (1990); Helgason, (1989); Sigbjarnarson et al., (1974); Sigurdsson and Sparks, (1981); Thorarinsson (1979); Sæmundsson, (1977).

APPENDIX 3: MINERAL ANALYSES

Table A3.1: Olivine mineral compositions. Minerals analysis by LA-ICP-MS except were noted.

	Fo%	Li ppm	MgO wt%	Al ppm	SiO2 wt%	CaO wt%	Sc ppm	TiO2 wt%	V ppm	Cr ppm	MnO wt%	FeO wt%	Ni ppm	Y ppm	Zr ppm	Total
JPF0958a	84.21	1.481	45.90	0.033	39.80	0.328	9.10	0.00589	6.42	236.2	0.219	15.34	1364	0.0831	0.0217	101.50
JPF0958b	85.25	1.315	47.17	0.038	39.97	0.345	9.53	0.00662	6.56	251.7	0.212	13.96	1395	0.0873	0.0187	102.25
JPF0958c	79.72	1.823	42.40	0.028	39.08	0.302	10.28	0.00884	7.90	56.1	0.279	19.23	1037	0.1332	0.0247	101.17
JPF0958d	85.35	1.310	46.78	10.243	39.99	0.415	9.64	0.00735	6.52	249.6	0.211	14.31	1387	0.0951	0.0187	111.91
JPP0958e	85.17	1.379	46.59	0.031	39.96	0.334	8.97	0.00694	5.70	231.2	0.211	14.47	1399	0.0747	0.0231	101.47
JPF0958f	85.32	1.344	46.84	0.030	39.98	0.337	9.20	0.00676	5.52	228.3	0.212	14.37	1387	0.0837	0.0199	101.77
JPF0958g	85.24	1.209	46.28	0.049	39.97	0.331	10.14	0.00727	7.14	285.9	0.211	14.28	1442	0.0904	0.0168	101.12
JPF0958h	85.25	1.372	46.78	0.033	39.97	0.336	9.14	0.00674	5.90	237.3	0.212	14.43	1433	0.0725	0.0171	101.73
JPF0958i	85.00	1.321	46.49	0.034	39.93	0.339	9.22	0.00639	6.22	231.1	0.212	14.62	1396	0.0770	0.0156	101.59
JPF0958j	85.40	1.341	46.89	0.032	39.99	0.343	9.11	0.00667	5.91	233.1	0.212	14.29	1396	0.0770	0.0198	101.73
JPF0958k	85.35	1.381	47.24	0.031	39.98	0.347	9.18	0.00594	5.79	236.8	0.212	14.46	1395	0.0817	0.0178	102.24
JPF0958l	85.32	1.300	46.49	0.037	39.98	0.338	9.31	0.00656	6.19	251.2	0.211	14.25	1405	0.0848	0.0158	101.28
JPF0958m	84.79	1.348	46.44	0.036	39.89	0.343	9.39	0.00641	6.65	232.1	0.214	14.86	1392	0.0803	0.0144	101.75
JPF0958n	84.99	1.304	46.22	0.037	39.93	0.339	9.35	0.00633	6.94	232.0	0.212	14.55	1386	0.0827	0.0175	101.25
JPF0958o	85.41	1.412	46.80	0.031	39.99	0.345	9.20	0.00655	5.68	233.1	0.210	14.25	1377	0.0801	0.0217	101.60
JPF0958p	79.72	1.827	42.73	0.027	39.08	0.313	10.09	0.00868	7.70	57.3	0.282	19.38	1045	0.1268	0.0276	101.65
JPF0958q	85.14	1.310	46.51	0.044	39.95	0.333	9.63	0.00700	6.99	264.5	0.211	14.47	1436	0.0846	0.0153	101.49
JPF0958r	85.20	1.307	46.61	0.037	39.96	0.355	9.24	0.00650	6.39	244.7	0.212	14.44	1406	0.0847	0.0226	101.54
DL009a	71.79	2.555	37.03	0.029	37.85	0.272	10.98	0.01258	11.67	49.4	0.360	25.94	840	0.1823	0.0397	101.00
DL009b	71.79	2.551	37.24	0.034	37.92	0.278	10.61	0.01054	11.98	78.2	0.353	25.48	993	0.1524	0.0561	101.03
DL009c	71.74	2.610	37.04	0.034	37.84	0.276	11.42	0.01178	12.47	76.9	0.362	26.00	839	0.2041	0.0384	101.25
DL009d	72.10	2.473	37.00	0.027	37.90	0.274	10.71	0.01252	11.09	52.5	0.355	25.53	850	0.1798	0.0353	100.92
DL009e	71.92	2.587	37.16	0.036	37.87	0.272	11.92	0.00888	13.83	55.4	0.360	25.87	844	0.2004	0.0363	101.30
DL009f	72.10	2.392	36.89	0.027	37.90	0.270	10.24	0.00983	10.94	54.6	0.357	25.45	871	0.1638	0.0280	100.63
DL009g	71.88	2.509	36.83	0.027	37.86	0.275	10.69	0.01200	11.11	48.5	0.359	25.68	838	0.1749	0.0329	100.77
DL009h	71.88	2.529	37.12	0.030	37.86	0.285	11.29	0.01251	12.06	50.3	0.365	25.88	824	0.1874	0.0349	101.18
DL009i	72.38	2.317	37.19	0.034	37.94	0.256	10.79	0.00954	12.48	77.4	0.342	25.30	991	0.1723	0.0282	100.82
DL009j	71.96	2.432	37.20	0.028	37.87	0.274	11.10	0.01254	11.78	50.0	0.358	25.84	842	0.1721	0.0333	101.33
DL009k	73.16	2.223	37.89	0.033	38.06	0.274	11.12	0.01095	12.59	71.0	0.339	24.79	959	0.1585	0.0364	101.15
DL009l	71.90	2.367	36.91	0.030	37.87	0.270	10.70	0.01177	11.78	62.1	0.355	25.71	888	0.1893	0.0365	100.88
DL009m	72.11	2.399	36.93	0.027	37.90	0.272	10.64	0.01126	11.20	50.4	0.354	25.47	843	0.1828	0.0326	100.69

	Fo%	Li ppm	MgO wt%	Al ppm	SiO2 wt%	CaO wt%	Sc ppm	TiO2 wt%	V ppm	Cr ppm	MnO wt%	FeO wt%	Ni ppm	Y ppm	Zr ppm	Total
DL009o	71.66	2.554	36.66	0.185	37.83	0.421	11.64		17.70	50.0	0.361	25.85	827			101.01
DL009p	75.28	2.479	37.98	0.035	38.38	0.276	11.38	0.00947	12.39	83.2	0.362	22.24	966	0.1927	0.0281	99.12
DL009 EMP	71.53		35.78		38.11	0.240					0.390	25.39				100.09
DL009 EMP	71.89		36.05		37.96	0.290					0.360	25.13				99.97
JPF0969a	80.82	1.763	41.99	0.031	39.25	0.308	9.95	0.01190	10.76	36.2	0.293	17.76	932	0.1552	0.0329	99.45
JPF0969b	82.38	1.687	43.22	0.031	39.50	0.330	9.81	0.01119	8.10	82.0	0.280	16.48	981	0.1318	0.0273	99.68
JPF0969c	82.25	1.700	43.39	0.031	39.48	0.326	9.66	0.01001	9.47	88.7	0.276	16.69	1041	0.1306	0.0273	100.06
JPF0969d	82.56	1.669	43.45	0.033	39.53	0.327	9.94	0.01135	8.38	99.7	0.273	16.36	1050	0.1340	0.0257	99.84
JPF0969e	81.01	1.600	43.58	0.032	39.28	0.315	9.53	0.01021	7.79	116.5	0.264	18.21	1096	0.1305	0.0235	101.55
JPF0969f	81.76	2.091	43.71	0.048	39.40	0.323	9.86	0.01119	9.13	97.0	0.289	17.38	1064	0.1721	0.2682	101.00
JPF0969g	83.18	1.688	44.22	0.031	39.63	0.325	9.56	0.01027	7.67	116.1	0.268	15.94	1105	0.1275	0.0299	100.29
JPF0969h	80.81	1.934	42.24	0.033	39.25	0.319	10.01	0.01125	9.93	77.7	0.291	17.88	1013	0.1654	0.0262	99.84
JPF0969i	88.07	1.247	47.65	0.042	40.44	0.322	8.47	0.00679	6.61	269.8	0.190	11.50	1853	0.0851	0.0177	100.19
JPF0969j	83.16	1.745	43.96	0.031	39.63	0.329	9.30	0.00961	7.19	131.7	0.264	15.86	1127	0.1194	0.0262	99.95
JPF0969k	81.61	1.868	43.26	0.036	39.38	0.325	10.25	0.01242	11.09	63.9	0.291	17.38	978	0.1623	0.0788	100.50
JPF0969l	82.88	1.783	43.84	0.030	39.58	0.327	9.44	0.00996	7.65	106.6	0.272	16.14	1083	0.1324	0.0268	100.06
JPF0969m	81.20	1.872	42.57	0.031	39.31	0.316	9.86	0.01179	8.71	51.0	0.294	17.55	963	0.1482	0.0297	99.90
JPF0969n	80.24	3.056	39.77	1.030	39.16	0.783	10.45		14.77	44.7	0.286	17.45	843			98.30
JPF0969o	82.38	1.974	42.80	0.309	39.50	0.534	10.15		12.75	100.3	0.273	16.32	1032			99.59
JPF0969p	81.66	2.030	43.17	0.036	39.39	0.323	10.71	0.01391	9.92	64.1	0.289	17.27	1002	0.1673	0.0387	100.32
JPF0969q	71.35	3.179	34.70	0.209	37.78	0.543	11.77	0.02339	24.82	24.1	0.394	24.73	666	0.6181	0.5361	98.05
JPF0908a	83.42	1.538	41.72	0.042	39.13	0.321	9.69	0.00942	12.74	219.5	0.264	18.51	1246	0.1258	0.0276	101.64
JPF0908b	82.45	1.504	40.83	0.039	38.95	0.328	10.40	0.00935	15.81	226.2	0.279	19.41	1212	0.1378	0.0249	101.34
JPF0908c	82.88	1.658	41.03	0.039	39.03	0.336	10.09	0.02321	17.89	221.0	0.268	18.93		0.1438	0.0434	101.16
JPF0908d	83.37	1.786	41.13	0.238	39.12	0.479	10.16	0.02748	17.31	214.1	0.263	18.31		0.4382	0.8913	100.83
JPF0908e	83.45	1.641	41.75	0.043	39.14	0.321	9.84	0.00950	12.72	221.0	0.265	18.48	1260	0.1258	0.0236	101.67
JPF0908f	82.48	1.529	40.49	0.035	38.97	0.320	9.87	0.00869	15.65	220.7	0.269	19.13	1215	0.1349	0.0317	101.18
JPF0908g	83.41	1.458	41.77	0.035	39.13	0.320	9.32	0.00808	12.90	205.5	0.263	18.55	1267	0.1241	0.0257	101.74
JPF0908h	82.39	1.612	40.46	0.036	38.94	0.322	10.16	0.01931	19.17	224.6	0.270	19.31	1179	0.1411	0.0261	100.92
JPF0908i	83.23	1.803	41.62	0.038	39.10	0.326	10.07	0.00859	14.59	223.1	0.265	18.72	1257	0.1294	0.0309	101.71
JPF0908j	83.09	1.459	41.32	0.036	39.07	0.323	9.66	0.00814	14.51	215.8	0.265	18.78	1253	0.1274	0.0220	101.41
JPF0908k	83.01	1.512	41.56	0.035	39.06	0.327	9.74	0.00814	15.19	218.1	0.267	19.00	1241	0.1284	0.0241	101.85
JPF0908l	83.34	1.565	41.63	0.036	39.12	0.321	9.34	0.00818	12.88	209.9	0.265	18.59	1271	0.1200	0.0235	101.61

	Fo%	Li ppm	MgO wt%	Al ppm	SiO2 wt%	CaO wt%	Sc ppm	TiO2 wt%	V ppm	Cr ppm	MnO wt%	FeO wt%	Ni ppm	Y ppm	Zr ppm	Total
JPF0908m	82.29	1.557	40.78	0.035	38.93	0.322	10.11	0.00821	16.47	237.7	0.277	19.59	1165	0.1310	0.0226	101.41
JPF0908n	83.29	1.585	41.85	0.037	39.11	0.328	9.60	0.00842	13.42	217.9	0.267	18.75	1254	0.1223	0.0267	101.99
JPF0908o	83.21	1.420	41.48	0.043	39.09	0.320	10.09	0.01006	14.69	228.8	0.264	18.69	1267	0.1183	0.0239	101.52
JPF0908p	83.49	1.616	41.96	0.041	39.14	0.316	9.53	0.00881	12.22	209.6	0.261	18.52	1296	0.1210	0.0255	101.93
JPF0908q	83.43	1.549	41.59	0.035	39.13	0.317	9.23	0.00784	12.49	204.3	0.263	18.44	1272	0.1217	0.0187	101.45
JPF0908r	81.92	1.552	40.33	0.036	38.86	0.322	10.43	0.00906	17.24	235.3	0.282	19.87	1134	0.1329	0.0228	101.12
JPF0908s	82.96	1.522	41.24	0.036	39.05	0.320	9.54	0.00855	14.41	221.5	0.267	18.92	1239	0.1226	0.0217	101.42
JPF1010a	86.62	1.552	47.68	0.031	40.20	0.338	8.74	0.00658	8.15	190.6	0.210	13.12	1326	0.0954	0.0213	101.50
JPF1010b	85.91	1.551	47.14	0.036	40.08	0.341	9.24	0.00703	11.16	191.8	0.217	13.78	1308	0.1006	0.0229	101.51
JPF1010c	86.60	1.415	47.49	0.033	40.19	0.340	9.09	0.00701	9.12	189.6	0.211	13.10	1329	0.1029	0.0251	101.30
JPF1010d	86.14	1.517	46.62	0.036	40.12	0.335	9.06	0.00687	10.73	198.8	0.211	13.37	1322	0.1037	0.0174	100.62
JPF1010e	86.94	1.426	47.36	0.032	40.25	0.337	8.65	0.00626	7.84	202.3	0.208	12.68	1359	0.0966	0.0170	100.79
JPF1010f	87.52	1.418	48.50	0.035	40.34	0.337	8.39	0.00621	8.16	246.1	0.193	12.33	1533	0.0805	0.0178	101.71
JPF1010g	84.19	1.752	45.92	0.032	39.80	0.336	9.39	0.00662	10.21	164.3	0.238	15.36	1226	0.1158	0.0163	101.57
JPF1010h	86.81	1.509	47.61	0.034	40.23	0.333	8.78	0.00606	7.52	208.3	0.208	12.89	1418	0.0965	0.0150	101.24
JPF1010i	86.99	1.617	48.22	0.032	40.26	0.336	8.60	0.00580	7.03	205.0	0.210	12.85	1438	0.0967	0.0175	101.84
JPF1010i	86.99	1.617	48.22	0.032	40.26	0.336	8.60	0.00580	7.03	205.0	0.210	12.85	1438	0.0967	0.0175	101.84
JPF1010j	86.06	1.126	47.32	0.033	40.10	0.344	10.14	0.00673	7.32	140.5	0.222	13.67	1328	0.1335	0.0173	101.60
JPF1010k	82.08	1.757	43.63	0.035	39.45	0.342	10.47	0.00853	13.98	109.9	0.265	16.98	1038	0.1525	0.0232	100.53
JPF1010l	84.15	1.618	45.41	0.031	39.79	0.324	9.45	0.00814	10.84	147.8	0.234	15.25	1256	0.1136	0.0261	100.93
JPF1010m	87.00	1.577	48.05	0.034	40.26	0.337	9.06	0.00661	8.56	204.5	0.209	12.79	1354	0.0900	0.0169	101.61
JPF1010n	80.49	1.835	43.53	0.035	39.20	0.353	11.02	0.01093	14.46	104.0	0.289	18.82	999	0.1672	0.0377	102.03
JPF1010o	86.86	1.557	48.25	0.034	40.24	0.345	9.01	0.00643	8.30	216.2	0.211	13.01	1364	0.1016	0.0223	102.02
JPF1010p	87.11	1.692	48.29	0.033	40.28	0.337	9.03	0.00662	8.08	216.4	0.207	12.74	1400	0.1018	0.0217	101.82
JPF1010q	86.41	1.425	47.53	0.034	40.16	0.334	9.23	0.00673	9.18	182.6	0.211	13.32	1376	0.0883	0.0208	101.53
JPF1010r	86.92	1.489	47.97	0.033	40.25	0.341	8.96	0.00666	7.79	206.3	0.208	12.86	1408	0.1027	0.0182	101.59
JPF1010s	87.17	1.514	47.93	0.032	40.29	0.340	9.15	0.00688	7.28	197.8	0.205	12.57	1347	0.0923	0.0192	101.30
JPF1010t	86.43	1.443	47.69	0.034	40.16	0.337	9.12	0.00705	9.89	192.8	0.211	13.35	1347	0.0967	0.0229	101.72
JPF0949a	65.32	5.539	29.09	0.021	36.90	0.332	12.78	0.02330	20.57	4.0	0.492	27.54	430	0.6506	0.1101	94.05
JPF0949b	67.78	3.206	33.55	0.024	37.25	0.303	11.75	0.01044	22.54	19.7	0.416	28.44	577	0.3626	0.0383	99.64
JPF0949c	64.28	4.134	31.21	0.017	36.72	0.315	11.40	0.01885	17.61	11.8	0.456	31.14	512	0.4799	0.0653	99.48
JPF0949d		4.799	28.44	0.018	36.61	0.313	11.62	0.01978	18.61	6.7	0.483	29.32	456	0.6880	0.0799	96.41
JPF0949e	75.63	3.305	38.75	0.025	38.43	0.294	10.60	0.01510	18.25	67.0	0.319	22.27	822	0.2398	0.0478	99.87

	Fo%	Li ppm	MgO wt%	Al ppm	SiO2 wt%	CaO wt%	Sc ppm	TiO2 wt%	V ppm	Cr ppm	MnO wt%	FeO wt%	Ni ppm	Y ppm	Zr ppm	Total
JPF0949f	66.57	3.994	32.53	0.021	37.08	0.311	11.53	0.01749	20.56	17.7	0.429	29.12	535	0.4359	0.0737	99.13
JPF0949g	68.64	3.437	33.60	0.146	37.35	0.436	12.44	0.03161	25.84	60.5	0.405	27.61		0.7483	1.0253	99.22
JPF0949h		3.939	32.03	0.019	37.55	0.312	11.72	0.01844	20.28	10.6	0.443	24.68	507	0.4485	0.0618	94.65
JPF0949i	75.28	2.583	38.47	0.027	38.38	0.302	10.69	0.01086	19.59	62.0	0.320	22.52	841	0.2252	0.0370	99.81
JPF0949j	70.50	3.260	35.32	0.024	37.66	0.299	11.23	0.01069	21.12	35.9	0.385	26.34	659	0.3163	0.0475	99.73
JPF0949k		5.848	23.44	2.787	36.24	1.635	10.80	0.04025	20.24	14.3	0.401	27.12		0.9831	4.5669	91.27
JPF0949l		5.919	29.02	1.681	37.18	1.091	10.49	0.03786	20.76	44.3	0.377	25.20		0.8098	1.9862	94.23
JPF0949m	70.04	4.411	34.83	0.085	37.59	0.307	11.04	0.01668	19.90	35.8	0.388	26.56		0.4146	1.6399	99.45
JPF0949n	58.65	4.747	27.52	0.016	35.90	0.329	12.21	0.02286	14.69	2.9	0.515	35.19	426	0.7679	0.1115	99.01
JPF0949o	61.62	4.572	29.50	0.018	36.37	0.331	12.19	0.02154	18.89	5.6	0.479	32.77	451	0.5702	0.1200	99.17
DL046a	86.27	1.378	46.83	0.044	40.14	0.285	8.05	0.00652	6.88	257.3	0.194	13.28	2049	0.0855	0.0204	100.80
DL046b	85.77	1.309	46.63	0.041	40.06	0.300	8.06	0.00655	7.74	251.4	0.198	13.06	1966	0.0896	0.0200	100.94
DL046c	86.51	1.386	47.39	0.055	40.18	0.279	8.11	0.00688	8.15	351.4	0.187	13.17	2405	0.0893	0.0196	101.24
DL046d	86.72	1.615	47.23	0.058	40.21	0.299	9.09	0.00759	10.09	353.0	0.184	12.89	2255	0.1016	0.0278	100.84
DL046e	86.89	1.302	47.57	0.048	40.24	0.295	8.22	0.00731	6.72	304.5	0.184	12.79	2262	0.0907	0.0244	101.11
DL046f	85.80	1.278	46.32	0.047	40.06	0.281	7.91	0.00683	9.09	290.6	0.193	13.67	2163	0.0859	0.0207	100.53
DL046g	86.83	1.220	47.29	0.052	40.23	0.282	7.94	0.00657	7.08	321.1	0.184	12.78	2402	0.0852	0.0203	100.81
DL046h	86.24	1.249	46.93	0.047	40.13	0.284	8.03	0.00689	8.75	292.0	0.192	13.34	2181	0.0893	0.0231	100.88
DL046i	86.45	1.291	47.35	0.054	40.17	0.276	7.92	0.00613	7.20	371.3	0.189	13.23	2516	0.0818	0.0231	101.26
DL046j	86.10	1.457	46.83	0.031	40.11	0.211	7.15	0.01045	7.59	229.7	0.200	13.48	1891	0.0612	0.0318	100.79
DL046k	86.25	1.276	47.18	0.047	40.13	0.282	7.87	0.00594	7.79	300.8	0.190	13.39	2271	0.0936	0.0241	101.20
DL046l	86.41	1.313	47.23	0.047	40.16	0.274	7.91	0.00615	9.45	329.4	0.190	13.24	2322	0.0878	0.0273	101.12
DL046m	87.40	1.263	48.05	0.050	40.32	0.276	7.66	0.00645	6.87	367.3	0.179	12.35	2512	0.0867	0.0221	101.24
DL046n	86.58	1.289	46.94	0.055	40.19	0.276	7.78	0.00657	8.58	334.4	0.182	12.97	2448	0.0823	0.0227	100.61
DL046p	86.45	1.355	46.74	0.048	40.17	0.279	7.60	0.00633	7.08	325.8	0.190	13.06	2366	0.0866	0.0216	100.47
DL046q	87.15		46.68		40.20	0.272				357.6	0.178	12.27	2202		0.0208	99.87
DL046r	86.62		46.31		40.12	0.277				293.5	0.188	12.75	2005		0.0191	99.99
DL046s	87.34		46.89		40.23	0.282				326.0	0.182	12.11	2035		0.0199	99.98
DL046t	85.64		45.53		39.97	0.286				246.4	0.202	13.61	1787		0.0411	99.83
DL046u	87.22		46.91		40.21	0.264				357.7	0.180	12.25	2242		0.0278	100.06
DL046v	87.86		47.40		40.31	0.280				379.3	0.174	11.67	2206		0.0177	100.10
DL046w	87.06		46.97		40.18	0.268				348.3	0.183	12.44	2152		0.0235	100.40
DL046x	86.91		46.40		40.16	0.279				291.7	0.185	12.46	1976		0.0203	99.80

	Fo%	Li ppm	MgO wt%	Al ppm	SiO2 wt%	CaO wt%	Sc ppm	TiO2 wt%	V ppm	Cr ppm	MnO wt%	FeO wt%	Ni ppm	Y ppm	Zr ppm	Total
DL046y	86.72		46.46		40.13	0.282				294.1	0.188	12.68	1969		0.0167	100.00
DL046z	86.41		46.00		40.08	0.269				326.0	0.190	12.90	2046		0.0294	99.72
DL046aa	86.38		46.12		40.08	0.279				295.2	0.191	12.96	1999		0.0146	99.81
DL046ab	87.66		46.95		40.28	0.274				430.6	0.174	11.78	2344		0.0248	99.84
DL046ac	87.38		46.86		40.23	0.277				320.0	0.179	12.07	2116		0.0264	99.89
DL046ad	87.11		46.74		40.19	0.285				274.4	0.181	12.33	2165		0.0165	100.09
DL046ae	85.96		45.93		40.02	0.288				261.9	0.197	13.37	1827		0.0249	100.00
DL046af	86.50		46.22		40.10	0.283				290.2	0.191	12.86	1999		0.0255	99.96
DL046ag	86.05		45.92		40.03	0.280				266.9	0.196	13.27	1895		0.0262	99.99
DL046ah	83.54		43.91		39.64	0.276				226.1	0.214	15.43	1691		0.0240	99.99
DL046ai	86.32		46.20		40.07	0.278				285.1	0.191	13.05	1953		0.0228	99.99
DL046-221	86.51	1.202	46.73	0.054	39.73	0.272	9.40	0.00884	7.82	319.9		13.04	2253	0.0831	0.0225	99.20
DL046 EMP	85.26		44.98		39.76	0.290					0.210	13.87				99.39
DL046 EMP	87.08		45.91		41.04	0.280					*0.210*	12.15				99.87
DL046 EMP	86.34		45.19		40.70	0.280					*0.210*	12.75				99.39
JPF0957a	83.86	1.564	45.05	0.059	39.74	0.304	9.47	0.01346	12.77	344.5	0.214	15.46	2027	0.1266	0.0348	100.71
JPF0957b	76.95	2.345	40.34	0.029	38.64	0.275	9.18	0.01442	9.91	100.7	0.305	21.55	1177	0.1842	0.0453	101.09
JPF0957c	85.37	1.445	46.77	0.054	39.99	0.322	9.39	0.01067	8.62	325.9	0.202	14.29	2172	0.1214	0.0247	101.74
JPF0957d	90.38	1.054	50.12	0.055	40.83	0.282	6.44	0.00497	6.43	441.8	0.133	9.51	3214	0.0849	0.0184	101.20
JPF0957e	89.25	0.997	49.56	0.076	40.63	0.273	7.58	0.00941	7.24	453.2	0.150	10.63	2794	0.1079	0.0296	101.54
JPF0957f	77.79	2.463	41.09	0.032	38.77	0.280	9.20	0.01409	10.43	145.1	0.297	20.90	1362	0.1799	0.0553	101.35
JPF0957g	75.86	2.189	39.26	0.031	38.47	0.274	9.30	0.01568	10.04	105.4	0.309	22.27	1091	0.1797	0.0438	100.56
JPF0957h	85.31	1.412	46.36	0.059	39.98	0.321	9.56	0.01298	9.35	343.3	0.202	14.23	2154	0.1192	0.0261	101.21
JPF0957i	90.52	0.916	50.73	0.087	40.85	0.286	7.17	0.00907	6.81	610.6	0.138	9.47	2904	0.1096	0.0294	101.77
JPF0957j	86.93	2.027	47.23	0.080	40.25	0.272	7.87	0.00839	13.21	490.9	0.163	12.66	2586	0.1300	0.0829	100.81
JPF0957k	77.67	2.385	40.55	0.032	38.75	0.273	9.32	0.01423	10.71	147.6	0.296	20.78	1395	0.1782	0.0386	100.68
JPF0957l	88.11	1.213	48.62	0.065	40.44	0.299	7.47	0.00935	6.99	411.8	0.165	11.69	2719	0.0980	0.0309	101.47
JPF0957m	90.57	1.116	50.51	0.060	40.86	0.295	6.41	0.00474	5.42	494.1	0.132	9.37	3281	0.0872	0.0222	101.50
JPF0957n	82.00	2.038	42.88	0.045	39.44	0.286	8.14	0.00455	13.15	297.6	0.217	16.78	2179	0.1140	0.0188	101.39
JPF0957o	88.21	1.370	48.73	0.064	40.46	0.300	7.57	0.00894	6.52	401.3	0.164	11.61	2746	0.0995	0.0280	101.52
JPF0957p	90.52	0.916	50.18	0.087	40.85	0.276	7.20	0.00890	6.57	584.2	0.136	9.37	2950	0.0981	0.0266	101.11
JPF0957q	78.69	2.246	41.34	0.029	38.91	0.283	9.12	0.01393	10.16	144.8	0.290	19.96	1185	0.1733	0.0475	100.78
JPF0957r	90.48	0.953	49.89	0.086	40.84	0.279	7.18	0.00881	6.59	588.9	0.136	9.36	2913	0.1051	0.0302	100.80

	Fo%	Li ppm	MgO wt%	Al ppm	SiO2 wt%	CaO wt%	Sc ppm	TiO2 wt%	V ppm	Cr ppm	MnO wt%	FeO wt%	Ni ppm	Y ppm	Zr ppm	Total
JPF0957s	85.21	1.429	45.90	0.051	39.96	0.321	9.21	0.01110	8.77	303.9	0.201	14.20	2166	0.1116	0.0282	100.74
JPF0957t	90.36	1.071	50.42	0.082	40.82	0.284	6.96	0.00892	6.76	576.3	0.136	9.59	2933	0.1029	0.0281	101.49
DL006a		3.114	31.46	1.542	37.73	1.284	13.80	0.20663	59.48	46.3	0.325	22.88	731	3.5130	11.4066	93.60
DL006b	75.24	2.244	39.21	0.029	38.37	0.289	10.41	0.00861	10.71	67.1	0.325	23.00	999	0.1434	0.0201	101.14
DL006c	71.97	2.598	36.88	0.027	37.88	0.277	10.65	0.01251	11.53	49.1	0.361	25.61	868	0.1954	0.0394	100.92
DL006d	72.60	2.446	37.11	0.031	37.97	0.276	10.53	0.01026	11.87	65.3	0.350	24.96	922	0.1694	0.0295	100.60
DL006e	74.73	2.025	38.74	0.029	38.30	0.286	11.53	0.01081	11.26	40.3	0.337	23.35	804	0.1556	0.0266	100.92
DL006f	72.15	2.650	36.71	0.029	37.90	0.272	10.80	0.01305	11.77	49.0	0.354	25.26	872	0.1785	0.0377	100.43
DL006g	72.08	2.644	36.98	0.028	37.89	0.281	10.82	0.01288	11.64	49.2	0.360	25.54	862	0.1819	0.0383	100.95
DL006h	72.31	2.672	36.91	0.036	37.93	0.266	11.07	0.00956	10.88	104.9	0.353	25.19	955	0.1921	0.0298	100.58
DL006i	72.88	2.358	37.22	0.032	38.01	0.277	10.45	0.01037	11.05	61.5	0.344	24.69	926	0.1638	0.0316	100.47
DL006j	72.07	2.581	36.90	0.031	37.89	0.277	10.94	0.01313	11.84	50.1	0.358	25.49	859	0.1918	0.0359	100.84
DL006k	72.53	2.538	37.39	0.031	37.96	0.306	11.07	0.00987	12.89	63.2	0.354	25.25	918	0.1790	0.0445	101.19
DL006l	72.17	2.557	36.58	0.029	37.91	0.273	10.69	0.01284	11.45	49.4	0.356	25.14	861	0.1821	0.0385	100.30
DL006m	72.06	2.600	36.95	0.030	37.89	0.275	10.78	0.01326	12.81	49.5	0.360	25.53	870	0.1985	0.0389	100.91
DL006n	72.38	2.648	37.05	0.029	37.94	0.276	10.93	0.01328	11.54	49.8	0.357	25.21	873	0.1847	0.0322	100.75
DL006o	72.43	2.596	36.88	0.033	37.95	0.276	10.82	0.01216	12.17	50.7	0.354	25.03	855	0.1889	0.0473	100.41
DL006p	75.33	1.983	39.40	0.033	38.39	0.292	11.86	0.01026	12.60	37.7	0.343	23.00	793	0.1676	0.0275	101.33
DL006q	72.15	2.561	36.83	0.029	37.90	0.272	10.69	0.01297	11.98	48.7	0.358	25.34	868	0.1886	0.0346	100.63
DL006r	72.16	2.531	36.88	0.035	37.91	0.273	11.38	0.01264	13.07	54.8	0.357	25.36	871	0.2080	0.0419	100.70
DL006s	72.13	2.525	38.27	0.037	37.90	0.285	12.06	0.01273	15.04	63.5	0.369	26.36	912	0.2110	0.0439	103.10
DL006 EMP	72.24		36.49		37.77	0.290					0.370	25.00				100.07
DL006 EMP	71.18		35.88		37.54	0.270					0.410	25.90				100.12
DL006 EMP	71.47		35.94		37.66	0.270					0.380	25.58				99.96
DL002a	86.52	1.364	45.68	0.042	40.08	0.358	8.58	0.00509	6.77	312.8	0.207	13.10	1442	0.0846	0.0227	100.73
DL002b	86.80	1.385	45.91	0.038	40.23	0.359	8.46	0.00501	6.48	298.2	0.205	12.35	1454	0.0790	0.0222	100.63
DL002c	86.05	1.435	45.58	0.040	40.10	0.368	8.76	0.00536	6.91	269.2	0.216	13.09	1383	0.0893	0.0197	100.92
DL002d	86.43	1.413	45.51	0.040	40.16	0.364	8.56	0.00491	6.56	280.7	0.210	12.68	1408	0.0845	0.0139	100.48
DL002e	86.64	1.337	45.20	0.036	40.20	0.359	8.38	0.00494	6.25	287.7	0.202	12.34	1436	0.0816	0.0142	99.85
DL002f	86.32	1.392	45.35	0.041	40.14	0.367	8.75	0.00523	6.99	288.2	0.208	12.75	1400	0.0918	0.0165	100.38
DL002g	86.42	1.430	45.17	0.034	40.14	0.355	8.07	0.00430	5.96	264.8	0.207	12.59	1419	0.0825	0.0219	100.02
DL002h	87.07	1.311	46.38	0.046	40.27	0.363	8.72	0.00523	6.81	326.0	0.201	12.19	1503	0.0804	0.0183	101.00
DL002i	86.60	1.403	45.10	0.039	40.19	0.359	8.41	0.00489	6.45	295.0	0.204	12.36	1434	0.0829	0.0155	99.77

	Fo%	Li ppm	MgO wt%	Al ppm	SiO2 wt%	CaO wt%	Sc ppm	TiO2 wt%	V ppm	Cr ppm	MnO wt%	FeO wt%	Ni ppm	Y ppm	Zr ppm	Total
DL002j	86.78	1.391	45.62	0.038	40.22	0.364	8.57	0.00492	6.17	288.8	0.203	12.31	1426	0.0820	0.0128	100.28
DL002k	86.96	1.288	45.80	0.050	40.25	0.358	9.11	0.00502	7.00	312.3	0.200	12.20	1507	0.0866	0.0115	100.38
DL002m	86.36	1.345	45.58	0.035	40.16	0.348	8.20	0.00489	6.59	301.0	0.210	12.67	1448	0.0750	0.0195	100.53
DL002n	86.73	1.361	45.56	0.040	40.21	0.358	8.54	0.00512	6.66	300.9	0.204	12.39	1438	0.0799	0.0136	100.28
DL002o	86.82	1.378	45.85	0.040	40.23	0.372	8.63	0.00498	6.54	297.2	0.202	12.33	1460	0.0769	0.0198	100.56
DL002p	87.06	1.245	45.52	0.054	40.26	0.358	9.36	0.00605	7.48	342.3	0.196	12.01	1467	0.0812	0.0153	99.91
DL002q	86.47	1.438	45.52	0.039	40.17	0.372	8.88	0.00554	6.28	281.0	0.207	12.60	1393	0.0777	0.0204	100.43
DL002r	86.51	1.463	45.20	0.037	40.18	0.358	8.57	0.00561	6.47	278.7	0.205	12.46	1396	0.0903	0.0190	99.96
DL002t	86.05	1.415	45.63	0.036	40.11	0.340	8.10	0.00511	6.49	290.4	0.210	13.02	1423	0.0729	0.0145	100.88
DL002 240	85.33	1.413	46.75	0.041	39.88	0.329	9.81	0.00690	6.91	307.8		14.40	1456	0.0828	0.0121	100.54
DL002 EMP	85.69		45.55		40.19	0.370					0.220	13.56				100.11
DL002 EMP	85.98		45.65		40.29	0.370					0.200	13.27				99.99
DL002 EMP	85.31		45.20		39.73	0.360					0.220	13.87				99.58
DL002 EMP	85.20		45.27		39.63	0.340					0.230	14.02				99.76
DL067a	80.39	1.956	41.54	0.038	39.19	0.294	10.60	0.00679	16.87	119.7	0.263	18.03	1237	0.1235	0.0187	99.21
DL067b	82.94	1.764	45.14	0.044	39.59	0.326	11.08	0.00737	13.53	172.9	0.249	16.55	1548	0.1472	0.0294	101.81
DL067c	83.26	2.003	44.73	0.039	39.64	0.296	10.17	0.00686	10.61	135.2	0.242	16.03	1585	0.1279	0.0352	100.89
DL067d	84.58	1.424	45.29	0.043	39.86	0.314	8.88	0.00569	9.31	146.7	0.223	14.72	1634	0.0939	0.0125	100.39
DL067e	81.81	2.084	42.27	0.045	39.44	0.495	11.64	0.00755	20.37	152.7	0.245	16.51	1305	0.1073	0.0301	98.88
DL067f	80.93	2.109	42.26	0.038	39.27	0.304	10.67	0.00661	14.29	144.1	0.264	17.75	1356	0.1362	0.0180	99.76
DL067g	83.34	1.915	44.04	0.041	39.66	0.302	10.39	0.00736	10.53	173.3	0.240	15.69	1500	0.1261	0.0249	99.88
DL067h	79.93	1.991	41.65	0.036	39.11	0.298	10.52	0.00634	16.10	132.3	0.271	18.64	1338	0.1397	0.0206	99.86
DL067i	82.07	1.801	44.45	0.039	39.45	0.318	10.95	0.00736	16.63	150.2	0.259	17.31	1433	0.1406	0.0305	101.72
DL067j	83.44	1.749	43.92	0.038	39.67	0.291	9.65	0.00646	9.76	163.5	0.239	15.53	1479	0.1062	0.0158	99.60
DL067k	82.19	1.770	43.59	0.034	39.47	0.313	9.56	0.00636	12.01	159.7	0.261	16.83	1320	0.1170	0.0157	100.38
DL067l	78.34	2.089	39.94	0.035	38.86	0.295	10.91	0.00742	17.89	100.1	0.287	19.69	1133	0.1375	0.0234	98.92
DL067m	79.61	2.151	41.33	0.034	39.06	0.303	10.67	0.00694	16.80	113.3	0.280	18.86	1191	0.1412	0.0477	99.71
DL067n	82.82	2.117	44.12	0.039	39.57	0.301	10.18	0.00726	12.08	175.1	0.250	16.31	1430	0.1209	0.0258	100.48
DL067o	82.77	1.877	43.77	0.037	39.56	0.297	9.53	0.00619	10.20	135.9	0.246	16.24	1455	0.1112	0.0201	100.05
DL067p	78.90	1.901	40.76	0.031	38.95	0.310	10.30	0.00645	17.54	104.7	0.289	19.42	1122	0.1347	0.0158	99.58
DL067q	81.47	1.872	42.84	0.038	39.36	0.292	10.30	0.00647	16.90	145.7	0.256	17.36	1431	0.1195	0.0191	100.03
DL067r	82.25	1.857	43.38	0.038	39.48	0.291	10.08	0.00651	13.60	150.0	0.250	16.68	1424	0.1092	0.0248	100.01
DL067s	83.10	1.943	44.45	0.041	39.62	0.293	10.22	0.00702	13.58	169.6	0.241	16.10	1541	0.1192	0.0238	100.66

	Fo%	Li ppm	MgO wt%	Al ppm	SiO2 wt%	CaO wt%	Sc ppm	TiO2 wt%	V ppm	Cr ppm	MnO wt%	FeO wt%	Ni ppm	Y ppm	Zr ppm	Total
DL067t	82.23	1.965	42.74	0.037	39.48	0.287	9.72	0.00689	14.06	154.3	0.250	16.46	1447	0.1241	0.0192	99.16
DL067u	77.48	2.288	40.24	0.042	38.72	0.312	11.54	0.00699	18.04	103.4	0.315	20.84	1110	0.1871	0.0380	100.26
DL067 EMP	82.40		43.31		39.32	0.300					0.250	16.49				99.85
DL067 EMP	80.93		42.22		38.99	0.260					0.270	17.74				99.66
DL067 EMP	81.68		42.54		39.50	0.310					0.250	17.01				99.83
DL062a	75.14	2.441	38.16	0.031	38.36	0.262	10.02	0.01250	11.06	109.8	0.332	22.50	1167	0.1727	0.0434	99.42
DL062b	75.27	2.545	38.11	0.040	38.38	0.259	9.52	0.01107	10.92	111.7	0.335	22.31	1180	0.1616	0.0343	99.21
DL062d		2.848	32.43	0.036	37.13	0.320	12.52	0.02051	32.04	104.3	0.418	28.56	777	0.3741	0.1293	98.54
DL062e	75.27	2.489	38.22	0.031	38.38	0.258	9.89	0.01157	11.06	119.4	0.336	22.39	1203	0.1806	0.0383	99.40
DL062f		3.264	34.30	0.035	37.29	0.335	13.57	0.02418	32.18	97.6	0.413	28.76	741	0.3007	0.0932	100.77
DL062g		2.933	34.09	0.029	37.21	0.347	13.68	0.02079	31.45	100.6	0.420	29.31	761	0.3545	0.0832	101.05
DL062i	66.66	3.144	32.20	0.027	37.09	0.303	12.21	0.02015	30.98	89.3	0.414	28.70	728	0.2955	0.0757	98.39
DL062j	74.83	2.432	38.44	0.029	38.31	0.258	9.84	0.01212	14.77	108.8	0.338	23.03	1146	0.1833	0.0445	100.18
DL062l		3.248	32.42	0.031	37.18	0.327	13.33	0.02235	30.33	85.9	0.406	28.06	711	0.3442	0.1353	98.08
DL062 EMP	73.76		37.31		38.09	0.280					0.340	23.66				99.83
DL062 EMP	73.25		37.13		37.60	0.270					0.360	24.17				99.67
DL062 EMP	73.79		37.42		38.06	0.270					0.370	23.70				99.98
DL075a	74.22	2.379	37.13	0.029	38.22	0.251	9.62	0.02470	9.71	35.9	0.338	22.99	698	0.1813	0.0681	98.68
DL075b	73.91	2.327	37.39	0.025	38.17	0.253	9.39	0.02057	9.34	29.5	0.341	23.53	700	0.1662	0.0642	99.43
DL075c	72.12	2.515	36.35	0.026	37.90	0.249	9.56	0.02250	9.76	18.9	0.362	25.06	591	0.1758	0.0976	99.64
DL075d	72.22	2.580	36.36	0.026	37.91	0.245	9.70	0.02376	10.12	19.3	0.359	24.93	609	0.1898	0.0607	99.52
DL075e	73.24	2.479	37.03	0.026	38.07	0.250	9.65	0.02290	10.01	29.0	0.351	24.11	660	0.1773	0.0631	99.54
DL075f	71.13	2.816	36.56	0.031	37.75	0.264	10.58	0.02656	10.91	5.9	0.393	26.44	473	0.2228	0.0814	101.07
JPF0962a	61.02	5.523	28.96	0.025	36.29	0.291	12.69	0.01647	23.76	38.9	0.456	32.98	689	0.8544	0.0533	98.60
JPF0962b		6.497	27.02	0.017	35.84	0.271	11.49	0.01398	19.66	23.3	0.470	35.11	611	1.6841	0.0506	98.32
JPF0962c	66.65	4.504	33.19	0.033	37.09	0.291	12.14	0.00979	21.35	44.3	0.406	29.61	889	0.3485	0.0892	100.29
JPF0962d	84.61	3.070	40.66	0.615	39.88	0.337	8.31	0.02528	16.91	284.3	0.223	13.43	1067	0.4851	6.7257	94.45
JPF0962e	75.70	2.392	38.66	0.533	38.45	0.402	11.09	0.10485	19.32	39.9	0.331	22.13	858	0.3744	2.4569	99.74
DL038a	74.47	2.542	39.26	0.030	38.26	0.270	9.92	0.01235	11.09	112.4	0.346	23.94	1164	0.1802	0.0331	101.94
DL038b	67.17	3.185	34.06	0.287	37.20	0.851	13.49	0.06639	43.88	114.7	0.411	29.35	713	0.4439	0.8831	101.55
DL038c	75.04	2.643	39.25	0.033	38.34	0.269	9.84	0.01252	10.71	112.5	0.337	23.27	1137	0.1714	0.0442	101.29
DL038d	74.39	2.512	38.41	0.030	38.24	0.262	9.64	0.01211	10.61	110.4	0.335	23.57	1145	0.1702	0.0371	100.63
DL038e	74.45	2.511	38.66	0.030	38.25	0.265	9.76	0.01201	11.31	107.8	0.337	23.65	1147	0.1749	0.0326	100.97

	Fo%	Li ppm	MgO wt%	Al ppm	SiO2 wt%	CaO wt%	Sc ppm	TiO2 wt%	V ppm	Cr ppm	MnO wt%	FeO wt%	Ni ppm	Y ppm	Zr ppm	Total
DL038 EMP	73.76		37.28		38.11	0.260					0.380	23.65				99.79
DL038 EMP	73.80		37.34		37.70	0.270					0.370	23.63				99.52
DL038 EMP	73.81		37.59		38.08	0.260					0.330	23.78				100.21
JPF0917a	79.98	1.821	42.77	0.028	39.12	0.311	9.60	0.00952	8.06	60.1	0.286	19.08	1045	0.1325	0.0234	101.40
JPF0917b	79.98	1.893	42.88	0.029	39.12	0.307	9.36	0.00934	8.16	57.9	0.287	19.13	1059	0.1382	0.0264	101.58
DL013a	87.23	1.450	48.41	0.060	40.30	0.318	8.13	0.00528	8.76	341.7	0.185	12.63	2413	0.1099	0.0159	101.96
DL013b	87.86	1.357	48.62	0.079	40.37	0.322	8.29	0.00501	8.11	381.2	0.178	12.18	2524	0.1248	0.0598	101.82
DL013c	85.24	1.606	47.23	0.057	39.97	0.326	9.24	0.00575	12.75	329.8	0.209	14.57	2136	0.1392	0.0223	102.37
DL013d	87.35	1.280	48.95	0.058	40.32	0.328	8.23	0.00493	7.68	326.5	0.186	12.63	2329	0.1144	0.0304	102.52
DL013 EMP	86.02		45.64		39.89	0.300					0.200	13.22				99.59
DL013 EMP	87.13		46.49		40.05	0.300					0.190	12.24				99.50
DL013 EMP	87.11		46.34		40.19	0.320					0.180	12.23				99.54
DL013 EMP	86.51		46.00		40.06	0.330					0.200	12.79				99.72
DL013 EMP	87.00		46.45		40.36	0.320					0.190	12.38				100.02
JPF1016a	75.75	2.178	39.71	0.027	38.45	0.274	9.11	0.01732	8.70	21.5	0.329	22.67	751	0.1781	0.0565	101.20
JPF1016b	76.44	2.083	40.11	0.028	38.56	0.277	9.39	0.01726	8.79	22.9	0.321	22.04	736	0.1527	0.0514	101.08
JPF1016c	75.59	1.994	39.78	0.025	38.43	0.272	8.81	0.01630	8.66	17.1	0.334	22.89	692	0.1631	0.0496	101.46
JPF1016d	75.77	1.916	40.11	0.028	38.46	0.285	9.58	0.01899	9.15	21.6	0.335	22.87	693	0.1742	0.0560	101.81
JPF1016e	74.07	2.107	37.78	0.413	38.50	0.478	9.91	0.09659	21.80	16.7	0.342	23.56	609	0.9840	5.2961	100.39
JPF1016f	76.77	2.060	39.54	0.548	38.61	0.651	10.29	0.09821	21.53	26.6	0.313	21.33	749	1.1367	5.6936	100.23
JPF0907a	82.45	1.498	43.98	0.031	39.51	0.323	8.91	0.00811	7.69	99.1	0.251	16.68	1251	0.1170	0.0309	100.66
JPF0907b	82.98	1.500	44.34	0.032	39.60	0.318	8.80	0.00823	7.61	103.4	0.245	16.20	1329	0.1079	0.0230	100.63
JPF0907c	83.16	1.454	45.87	0.032	39.63	0.342	9.15	0.00779	7.72	99.0	0.251	16.56	1307	0.1334	0.0458	102.57
JPF0907d	81.95	2.632	44.63	0.036	39.43	0.262	8.72	0.01275	7.36	137.0	0.266	17.51	1194	0.1490	0.1145	101.99
JPF0907e	82.50	1.512	44.74	0.031	39.52	0.329	8.89	0.00785	8.68	92.2	0.254	16.91	1303	0.1261	0.0407	101.67
JPF0907g	82.83	1.524	45.37	0.040	39.57	0.357	9.03	0.00870	8.01	102.5	0.253	16.76	1279	0.1662	0.1461	102.22
JPF0902a	82.94	1.455	44.49	0.032	39.59	0.320	8.90	0.00822	8.03	101.3	0.247	16.36	1335	0.1134	0.0250	100.92
JPF0902b	72.98	3.236	37.22	0.025	38.04	0.267	9.61	0.01096	11.02	21.4	0.348	24.51	1058	0.2780	0.0359	100.17
JPF0902c	82.88	1.452	44.44	0.032	39.58	0.325	8.98	0.00806	8.36	100.9	0.245	16.38	1349	0.1138	0.0243	100.90
JPF0902d	81.64	3.456	43.03	0.031	39.38	0.246	9.41	0.01242	8.81	111.2	0.266	17.25	1242	0.1266	0.0572	100.70
JPF0902e	82.55	1.513	44.44	0.030	39.53	0.326	8.84	0.00756	7.84	85.7	0.249	16.76	1319	0.1078	0.0267	101.23
JPF0902f		5.457	0.11	17.577	32.42	7.682	1.54	0.02280	1.90	0.5	0.003	0.48	0	0.0816	0.0083	40.69
JPF0902g	81.17	1.528	43.34	0.028	39.31	0.322	8.97	0.00854	7.83	67.8	0.273	17.91	1137	0.1222	0.0264	101.02

	Fo%	Li ppm	MgO wt%	Al ppm	SiO2 wt%	CaO wt%	Sc ppm	TiO2 wt%	V ppm	Cr ppm	MnO wt%	FeO wt%	Ni ppm	Y ppm	Zr ppm	Total
DL003a	82.60		43.96		39.51	0.319				99.2	0.245	16.41	1200		0.0254	100.69
DL003b	82.92		44.11		39.55	0.321				102.7	0.247	16.20	1226		0.0155	100.58
DL003c	80.25	1.466	42.83	0.028	39.16	0.320	9.68	0.00991	10.39	39.3	0.286	18.79	937	0.1459	0.0352	101.22
DL003d	82.48		43.82		39.48	0.310				98.8	0.250	16.60	1203		0.0192	100.61
DL003e	82.35		43.75		39.48	0.317				100.4	0.256	16.72	1122		0.0225	100.75
DL003f	82.35		40.47		39.39	0.284				95.0	0.237	15.90	1133		0.0168	96.51
DL003g	82.85		43.92		39.54	0.316				101.3	0.246	16.21	1224		0.0310	100.43
DL003h	82.91		44.13		39.54	0.306				102.4	0.246	16.22	1227		0.0254	100.60
DL003i	82.87		43.95		39.54	0.317				100.8	0.246	16.20	1219		0.0265	100.42
DL003j	82.81		43.86		39.53	0.316				102.4	0.245	16.19	1223		0.0307	100.32
DL003k	79.24	1.614	42.03	0.030	39.00	0.334	9.99	0.00945	15.01	69.7	0.282	19.63	1139	0.1533	0.0283	101.13
DL003l	82.76		43.34		39.24	0.317				97.8	0.242	16.08	1192		0.0271	99.42
DL003m	79.99	1.497	42.64	0.028	39.12	0.314	9.45	0.00959	9.63	33.0	0.287	19.02	908	0.1413	0.0302	101.21
DL003n	78.08	1.742	41.34	0.027	38.82	0.314	9.74	0.01152	11.64	40.3	0.313	20.69	840	0.1664	0.0398	101.27
DL003o	82.60		43.39		39.50	0.308				98.0	0.250	16.27	1153		0.0218	99.88
DL003p	82.90		43.57		39.54	0.313				99.4	0.242	16.02	1196		0.0236	99.83
DL003q	82.94		43.62		39.55	0.316				99.6	0.242	15.96	1207		0.0180	99.93
DL003r	82.54		43.23		39.49	0.312				97.7	0.243	16.31	1198		0.0242	99.84
DL003s	82.85		43.47		39.54	0.321				97.9	0.242	16.04	1200		0.0218	99.82
DL003t	82.81		43.11		39.53	0.302				99.7	0.244	15.95	1215		0.0273	99.38
DL003 EMP	82.40		43.20		39.33	0.310					0.260	16.45				99.73
DL003 EMP	82.46		43.14		39.27	0.320					0.270	16.36				99.56
DL003 EMP	82.24		43.22		39.24	0.320					0.270	16.64				99.89
DL053a	86.33		46.25		40.07	0.310				326.6	0.189	13.06	1867		0.0110	100.18
DL053b	86.58		46.29		40.11	0.303				319.4	0.186	12.79	1853		0.0134	99.92
DL053c	85.03		45.27		39.87	0.309				341.9	0.203	14.21	1641		0.0154	100.06
DL053d	85.15		45.39		39.89	0.302				332.5	0.201	14.11	1733		0.0180	100.13
DL053e	84.85		45.21		39.84	0.304				338.9	0.207	14.38	1636		0.0137	100.15
DL053f	86.73		46.33		40.13	0.306				321.7	0.185	12.63	1887		0.0095	99.82
DL053g	86.58		46.27		40.11	0.305				322.9	0.187	12.78	1852		0.0128	99.88
DL053h	84.22		44.52		39.75	0.332				333.8	0.213	14.87	1521		0.0131	99.88
DL053i	85.90		45.83		40.01	0.304				335.2	0.192	13.41	1800		0.0189	99.96
DL053j	86.68		46.04		40.13	0.303				347.3	0.184	12.61	1926		0.2902	99.52

	Fo%	Li ppm	MgO wt%	Al ppm	SiO2 wt%	CaO wt%	Sc ppm	TiO2 wt%	V ppm	Cr ppm	MnO wt%	FeO wt%	Ni ppm	Y ppm	Zr ppm	Total
DL053k	86.61		46.27		40.12	0.303				315.1	0.186	12.75	1851		0.0131	99.86
DL053l	86.37		46.05		40.08	0.308				313.8	0.188	12.95	1858		0.0157	99.82
DL053m	85.30		45.36		39.91	0.305				343.4	0.197	13.94	1703		0.0103	99.94
DL053n	85.01		45.34		39.87	0.312				349.8	0.204	14.26	1673		0.0141	100.19
DL053o	86.04		46.16		40.03	0.304				323.0	0.192	13.35	1843		0.0119	100.28
DL053p	86.14		45.92		40.04	0.309				309.1	0.193	13.17	1896		0.0086	99.86
DL053q	84.48		45.09		39.79	0.320				356.4	0.212	14.77	1643		0.0183	100.39
DL053r	86.46		46.27		40.09	0.302				335.4	0.187	12.92	1910		0.0103	100.02
DL053s	85.49		45.63		39.94	0.300				347.8	0.197	13.81	1844		0.0166	100.12
DL053t	86.39		46.09		40.08	0.302				330.2	0.188	12.95	1903		0.0138	99.87
JPF0925a			42.30		39.20	0.301				266.7	0.251	18.09	1373		0.0239	94.40
JPF0925b	83.20		44.04		39.59	0.282				1104.2	0.220	15.85	1676		0.0224	100.20
JPF0925c	84.22		44.94		39.75	0.287				243.0	0.212	15.02	1764		0.0248	100.42
JPF0925d	82.99		44.08		39.56	0.307				2474.3	0.221	16.10	1652		0.0312	100.47
JPF0925e	85.86		45.92		40.00	0.258				302.8	0.186	13.49	2136		0.0339	100.11
JPF0925f	83.95		44.57		39.70	0.278				249.6	0.213	15.19	1796		0.0154	100.18
JPF0925g	82.95		43.75		39.55	0.270				277.4	0.224	16.03	1804		0.0342	100.05
JPF0925h	84.58		45.13		39.80	0.279				240.4	0.210	14.66	1812		0.0227	100.32
JPF0925i	83.71		44.43		39.67	0.289				230.6	0.218	15.41	1789		0.0322	100.23
JPF0925j	80.30	1.573	42.91	0.039	39.17	0.322	9.67	0.01084	15.76	257.1	0.265	18.78	1519	0.1369	0.0314	101.37
JPF0925k	85.15		45.36		39.89	0.263				274.2	0.198	14.10	2022		0.0182	100.07
JPF0925l	84.72		45.05		39.82	0.267				262.1	0.205	14.48	1974		0.0271	100.08
JPF0925m	83.19		43.97		39.59	0.284				252.6	0.220	15.84	1722		0.0243	100.13
JPF0925n	84.09		44.84		39.73	0.274				256.7	0.214	15.13	1926		0.0276	100.43
JPF0925o	81.40	1.485	43.81	0.042	39.34	0.306	9.51	0.01014	15.63	256.9	0.246	17.84	1652	0.1248	0.0284	101.51
JPF0925p	85.21		45.95		39.90	0.264				299.2	0.198	14.22	2110		0.0240	100.82
JPF0925q	83.53		44.26		39.64	0.286				259.2	0.213	15.56	1823		0.0240	100.19
JPF0925r	82.79		44.02		39.53	0.291				1008.8	0.226	16.32	1753		0.0384	100.60
JPF0925s	84.87		45.43		39.85	0.281				263.1	0.203	14.44	1961		0.0172	100.45
JPF0925t	82.47	1.361	44.58	0.043	39.52	0.298	9.14	0.00962	13.44	257.5	0.237	16.90	1762	0.1173	0.0283	101.52
JPF0931a	83.73		44.83		39.67	0.255				220.2	0.212	15.55	1877		0.0357	100.65
JPF0931b	82.51		44.31		39.48	0.280				201.3	0.236	16.77	1521		0.0262	101.19
JPF0931c	82.58		44.27		39.49	0.267				208.1	0.235	16.69	1550		0.0391	101.15

	Fo%	Li ppm	MgO wt%	Al ppm	SiO2 wt%	CaO wt%	Sc ppm	TiO2 wt%	V ppm	Cr ppm	MnO wt%	FeO wt%	Ni ppm	Y ppm	Zr ppm	Total
JPF0931d	83.01		44.46		39.55	0.266				209.9	0.229	16.28	1620		0.0319	101.02
JPF0931e	82.76		44.22		39.52	0.270				201.4	0.232	16.45	1594		0.0396	100.97
JPF0931f	82.23		43.82		39.44	0.284				188.5	0.242	16.89	1455		0.0288	100.75
JPF0931g	81.71	1.472	43.83	0.047	39.40	0.266	9.17	0.00983	13.05	239.2	0.244	17.48	1683	0.1073	0.0412	101.19
JPF0931h	82.60		44.11		39.49	0.269				215.5	0.232	16.60	1592		0.0301	100.85
JPF0931i	83.76		45.07		39.67	0.267				216.8	0.218	15.58	1795		0.0261	100.99
JPF0931j	82.65		44.14		39.50	0.273				208.2	0.234	16.55	1538		0.0238	100.86
JPF0931k	83.10		44.44		39.57	0.267				229.7	0.224	16.12	1824		0.1024	100.82
JPF0931l	83.76		44.66		39.67	0.260				225.5	0.216	15.46	1851		0.0329	100.50
JPF0931m	82.52	1.458	44.38	0.039	39.53	0.281	8.13	0.00957	7.01	192.9	0.242	16.74	1625	0.1081	0.0426	101.14
JPF0931n	84.78		45.85		39.83	0.260				253.7	0.204	14.66	1988		0.0225	101.02
JPF0931o	83.94		45.11		39.70	0.264				227.5	0.215	15.40	1867		0.0234	100.97
JPF0931p	81.51	1.464	44.07	0.041	39.37	0.285	9.07	0.01016	11.81	198.2	0.255	17.79	1547	0.1219	0.0287	101.71
JPF0931q	83.45		44.96		39.63	0.261				220.3	0.223	15.88	1784		0.0308	101.09
JPF0931r	82.77		44.37		39.52	0.271				213.1	0.236	16.51	1705		0.0362	101.13
JPF0931s	80.23	1.549	42.83	0.064	39.16	0.282	11.06	0.01583	20.13	288.2	0.264	18.81	1420	0.1470	0.0516	101.26
JPF0931t	82.48		44.19		39.47	0.277				197.7	0.241	16.80	1547		0.0356	101.28
JPF0951a	82.14	1.611	43.81	0.032	39.46	0.324	9.15	0.00846	9.39	136.7	0.251	16.98	1090	0.1216	0.0273	100.72
JPF0951b	84.18	1.698	45.39	0.042	39.79	0.307	9.08	0.00886	11.49	199.7	0.225	15.21	1517	0.1813	0.0244	100.89
JPF0951c	82.08	1.549	43.75	0.033	39.45	0.325	8.93	0.00809	10.00	161.8	0.246	17.03	1125	0.1146	0.0165	100.70
JPF0951d	79.63	1.699	42.64	0.037	39.00	0.329	9.82	0.00834	12.69	157.7	0.283	19.94	1053	0.1533	0.0234	102.03
JPF0951e	79.71	1.692	41.84	0.030	39.07	0.317	9.26	0.00725	12.09	128.2	0.268	18.99	1046	0.1110	0.0158	100.36
JPF0951f	78.26	1.756	41.44	0.034	38.85	0.324	9.87	0.00910	12.33	119.9	0.293	20.52	951	0.1491	0.0214	101.25
JPF0951g	81.81	1.642	44.01	0.033	39.41	0.323	8.94	0.00795	8.94	165.1	0.256	17.45	1136	0.1221	0.0185	101.34
JPF0951h	83.22	1.561	44.75	0.033	39.64	0.327	8.75	0.00794	8.48	185.2	0.236	16.08	1211	0.0970	0.0183	100.94
JPF0951i	82.20	1.575	44.11	0.020	39.47	0.323	9.12	0.00785	7.68	164.4	0.247	17.02	1151	0.1125	0.0170	101.07
JPF0951j	82.89	1.437	44.31	0.034	39.58	0.324	8.98	0.00814	7.53	172.2	0.240	16.31	1155	0.1100	0.0210	100.67
JPF0951k	83.52	1.464	45.09	0.019	39.69	0.322	8.88	0.00811	6.99	202.5	0.229	15.85	1268	0.1027	0.0186	101.11
JPF0951l	84.53	1.439	45.62	0.036	39.85	0.300	7.65	0.00649	8.09	230.8	0.204	14.88	1617	0.0803	0.0162	100.85
JPF0951m	83.14	1.627	44.69	0.018	39.62	0.327	8.88	0.00809	7.31	185.1	0.235	16.16	1205	0.1005	0.0191	100.94
JPF0951n	85.00	1.377	46.46	0.040	39.93	0.321	8.13	0.00777	7.69	249.5	0.209	14.61	1602	0.0921	0.0192	101.52
JPF0951o	82.79	1.664	44.44	0.031	39.57	0.328	8.87	0.00727	7.73	180.8	0.239	16.47	1235	0.1187	0.0226	100.96
JPF0951p	76.83	1.761	40.22	0.036	38.62	0.326	10.51	0.01022	14.07	111.2	0.306	21.62	932	0.1616	0.0399	100.91

	Fo%	Li ppm	MgO wt%	Al ppm	SiO2 wt%	CaO wt%	Sc ppm	TiO2 wt%	V ppm	Cr ppm	MnO wt%	FeO wt%	Ni ppm	Y ppm	Zr ppm	Total
JPF0951q	83.44	1.432	44.86	0.036	39.67	0.327	8.78	0.00760	8.40	199.8	0.232	15.86	1341	0.1030	0.0169	100.90
JPF0951r	81.74	1.560	44.17	0.032	39.40	0.319	8.99	0.00736	8.38	171.8	0.254	17.58	1175	0.1227	0.0170	101.62
JPF0951s	85.01	1.331	46.14	0.040	39.93	0.317	7.96	0.00765	7.49	254.5	0.206	14.51	1571	0.0925	0.0187	101.09
JPF0951t	82.96	1.448	44.64	0.035	39.60	0.327	9.21	0.00790	8.22	186.5	0.241	16.34	1197	0.1026	0.0187	101.05
JPF0922b			38.40		39.46	0.749				266.0	0.208	14.64	1400		3.2944	93.66
JPF0922c	85.64		45.81		39.97	0.297				316.9	0.196	13.69	1883		0.0088	100.19
JPF0922d	86.92		46.71		40.16	0.317				293.8	0.180	12.53	1834		0.0081	100.13
JPF0922e	87.02		46.46		40.18	0.320				286.0	0.179	12.35	1837		0.0130	99.72
JPF0922f	86.68		45.95		40.13	0.418				297.5	0.181	12.59	1799		0.4175	99.48
JPF0922g	87.06		46.60		40.18	0.320				288.5	0.179	12.35	1831		0.0082	99.86
JPF0922h	86.95		46.30		40.17	0.316				309.0	0.179	12.39	1851		0.0139	99.58
JPF0922i	85.90		46.04		40.01	0.321				320.9	0.192	13.47	1662		0.0137	100.23
JPF0922j	87.10		46.73		40.19	0.314				295.0	0.178	12.34	1842		0.0104	99.97
JPF0922k	87.02		47.01		40.18	0.328				282.9	0.182	12.50	1806		0.0039	100.41
JPF0922l	87.02		46.64		40.18	0.316				298.2	0.178	12.41	1845		0.0066	99.95
JPF0922m	86.93		46.60		40.16	0.322				303.6	0.180	12.49	1789		0.0083	99.96
JPF0922n	86.91		45.89		40.16	0.307				290.3	0.177	12.33	1873		0.0310	99.08
JPF0922o	87.15		47.14		40.20	0.318				288.2	0.179	12.39	1829		0.0134	100.43
JPF0922p	87.02		46.73		40.18	0.328				281.4	0.181	12.43	1791		0.0123	100.07
JPF0922q	86.96		46.75		40.17	0.324				287.4	0.180	12.50	1803		0.0118	100.13
JPF0922r	86.71		46.35		40.13	0.325				278.7	0.182	12.67	1747		0.0098	99.86
JPF0922s	86.99		46.68		40.17	0.322				298.7	0.180	12.45	1791		0.0146	100.02
JPF0922t	86.52		46.28		40.10	0.325				287.0	0.185	12.85	1733		0.0099	99.96
JPF0922u	84.02		45.11		39.72	0.359				340.4	0.224	15.29	1545		0.0297	100.88
JPF0927a	20.00		45.40		39.85	0.275				243.7	0.206	14.37	1695		0.0174	100.31
JPF0927b	86.03		46.23		40.03	0.257				242.8	0.189	13.39	1845		0.0241	100.31
JPF0927c	84.77		45.15		39.83	0.275				169.5	0.199	14.46	1534		0.0208	100.09
JPF0927d	85.60		45.61		39.96	0.261				302.9	0.193	13.67	1871		0.0222	99.92
JPF0927e	85.79		46.03		39.99	0.267				296.4	0.194	13.60	1904		0.0268	100.30
JPF0927f	85.40		45.81		39.93	0.269				333.2	0.200	13.97	1923		0.0294	100.40
JPF0927g	84.26		45.00		39.75	0.276				251.8	0.215	14.99	1608		0.0229	100.41
JPF0927h	85.52		46.04		39.95	0.276				251.4	0.201	13.90	1766		0.0208	100.57
JPF0927i	85.08		45.57		39.88	0.277				239.4	0.206	14.25	1716		0.0387	100.38

	Fo%	Li ppm	MgO wt%	Al ppm	SiO2 wt%	CaO wt%	Sc ppm	TiO2 wt%	V ppm	Cr ppm	MnO wt%	FeO wt%	Ni ppm	Y ppm	Zr ppm	Total
JPF0927j	85.73		46.16		39.98	0.271				283.5	0.196	13.70	1880		0.0368	100.51
JPF0927k	85.75		46.11		39.98	0.268				301.2	0.195	13.66	1922		0.0161	100.42
JPF0927l	86.40		46.32		40.08	0.255				365.0	0.185	13.00	2096		0.0157	100.08
JPF0927m	86.43		46.64		40.09	0.265				272.5	0.184	13.06	1890		0.0229	100.46
JPF0927n	84.52		44.17		39.79	0.619				3289.9	0.207	14.42	1711		2.4672	99.37
JPF0927o	86.16		46.41		40.05	0.261				336.8	0.188	13.30	2050		0.0270	100.44
JPF0927p	85.69		46.06		39.97	0.269				268.3	0.197	13.72	1832		0.0204	100.43
JPF0927q	85.19		46.05		39.90	0.276				274.7	0.206	14.27	1795		0.0241	100.91
JPF0927r	87.27	1.019	47.69	0.053	40.30	0.333	8.16	0.00526	7.83	306.7	0.183	12.42	2114	0.0822	0.0199	101.01
JPF0927s	80.94		44.16		39.86	0.603				268.2	0.200	13.91	1718		1.9679	98.90
JPF0927t	85.46		46.03		39.94	0.270				291.3	0.202	13.96	1868		0.0227	100.61
DL040 EMP	72.97		36.84		37.85	0.260					0.350	24.33				99.77
DL040 EMP	72.91		36.82		37.62	0.270					0.360	24.39				99.61
DL040 EMP	73.00		37.00		37.99	0.270					0.360	24.40				100.17
DL066 EMP	73.82		37.41		37.87	0.270					0.350	23.66				99.72
DL059 EMP	73.53		37.15		38.16	0.260					0.340	23.84				99.93
DL059 EMP	73.41		36.89		38.45	0.260					0.360	23.82				99.97
DL023 EMP	75.30		37.85		38.63	0.270					0.350	22.14				99.46

Table A3.2: Plagioclase mineral compositions. Minerals analysis by LA-ICP-MS except where noted.

	An%	SiO2 wt%	Al2O3 wt%	FeO wt%	MgO wt%	CaO wt%	Na2O wt%	K2O wt%	TiO2 wt%	Sr ppm	Y ppm	Ba ppm	La ppm	Sm ppm	Eu ppm	Gd ppm	Pb ppm	total
0951PL1	85.32	46.59	33.37	0.528	0.186	16.67	1.57	0.016	0.026	255.8	0.100	5.59	0.209	0.063	0.172	0.055	0.040	98.79
0951PL2	87.00	46.17	33.64	0.507	0.179	17.07	1.40	0.013	0.025	266.4	0.116	5.26	0.190	0.037	0.192	0.035	0.044	98.79
0951PL3	86.90	46.20	33.63	0.573	0.156	17.16	1.42	0.015	0.026	256.0	0.147	5.25	0.201	0.040	0.166	0.044	0.053	98.94
0951PL4	85.82	46.47	33.45	0.521	0.190	16.92	1.53	0.015	0.025	253.1	0.105	5.23	0.207	0.053	0.163	0.038	0.032	98.91
0951PL5	87.96	45.93	33.80	0.503	0.167	17.31	1.30	0.012	0.024	262.8	0.098	4.68	0.214	0.044	0.159	0.026	0.039	98.81
0951PL6	87.67	46.01	33.75	0.540	0.162	17.26	1.33	0.012	0.022	256.2	0.113	5.09	0.198	0.031	0.171	0.021	0.044	98.88
0951pl7	86.11	46.39	33.50	0.516	0.188	16.97	1.50	0.014	0.024	249.7	0.115	4.85	0.198	0.034	0.145	0.042	0.042	98.90
0951pl8	86.03	46.41	33.49	0.523	0.183	16.87	1.50	0.015	0.026	255.8	0.090	5.37	0.217	0.074	0.184	0.035	0.064	98.75
0951pl9	86.62	46.27	33.58	0.504	0.179	17.02	1.44	0.014	0.024	254.2	0.092	4.59	0.190	0.051	0.153	0.019	0.039	98.79
0951pl10	87.38	46.08	33.71	0.473	0.195	16.94	1.34	0.014	0.025	254.7	0.114	4.99	0.199	0.054	0.149	0.014	0.042	98.57
0951pl11	86.24	46.36	33.52	0.530	0.184	16.81	1.47	0.014	0.023	263.7	0.092	5.38	0.206	0.054	0.161	0.029	0.038	98.70
0951pl12	85.58	46.53	33.41	0.525	0.190	16.78	1.55	0.015	0.025	253.4	0.103	5.43	0.196	0.069	0.171	0.029	0.032	98.74
0951pa	86.27	46.35	33.53	0.515	0.192	17.01	1.49	0.016	0.024	266.2	0.088	5.90	0.220	0.015	0.168	-0.010	0.033	99.12
0951pb	85.38	46.57	33.38	0.488	0.212	17.23	1.62	0.020	0.027	256.0	0.120	5.39	0.204	0.049	0.183	0.028	0.051	99.55
0951pc	86.62	46.27	33.58	0.505	0.180	17.12	1.45	0.015	0.025	250.9	0.123	4.44	0.188	0.057	0.181	0.035	0.029	99.15
0951pd	86.89	46.20	33.63	0.502	0.184	17.73	1.47	0.015	0.025	254.0	0.128	5.40	0.227	0.045	0.180	0.061	0.022	99.75
0951pe	86.36	46.33	33.54	0.505	0.188	17.26	1.50	0.016	0.025	249.4	0.100	4.72	0.202	0.059	0.176	0.033	0.049	99.36
0951pf	87.03	46.16	33.65	0.506	0.185	17.14	1.40	0.014	0.028	260.9	0.141	5.70	0.253	0.091	0.206	0.067	0.039	99.09
0951pg	86.61	46.27	33.58	0.503	0.182	17.17	1.46	0.015	0.028	253.9	0.121	5.28	0.210	0.013	0.187	0.062	0.023	99.21
0951ph	86.59	46.27	33.58	0.520	0.185	17.14	1.46	0.015	0.024	257.8	0.111	4.99	0.181	0.061	0.169	0.020	0.051	99.19
0951pi	87.40	46.07	33.71	0.439	0.205	17.48	1.38	0.016	0.025	269.3	0.107	4.47	0.186	0.051	0.167	0.060	0.039	99.33
0951pj	87.18	46.13	33.67	0.508	0.181	17.62	1.42	0.015	0.022	252.5	0.085	4.92	0.195	0.051	0.164	0.039	0.036	99.56
0951pk	87.19	46.13	33.67	0.486	0.182	17.97	1.45	0.015	0.025	263.9	0.118	5.79	0.187	0.028	0.199	0.022	0.031	99.93
0951pl	86.97	46.18	33.64	0.516	0.186	17.67	1.45	0.015	0.025	247.2	0.118	4.89	0.180	0.054	0.186	0.020	0.031	99.68
0951pm	88.66	45.76	33.91	0.475	0.166	17.61	1.24	0.012	0.030	271.3	0.113	5.79	0.323	0.010	0.164	0.037	0.009	99.21
0951pn	86.82	46.22	33.61	0.556	0.148	17.19	1.43	0.014	0.025	257.7	0.109	5.27	0.208	0.080	0.170	0.014	0.034	99.20
0951po	87.45	46.06	33.72	0.491	0.182	17.31	1.36	0.014	0.025	257.4	0.097	4.78	0.225	0.027	0.187	0.040	0.033	99.16
DL002pl1	87.85	45.96	33.78	0.645	0.308	17.19	1.30	0.013	0.023	220.4	0.109	4.19	0.183	0.066	0.142	0.024	0.033	99.45
DL002pl2	88.85	45.71	33.94	0.419	0.199	17.41	1.20	0.009	0.018	207.3	0.098	3.40	0.120	0.046	0.152	0.041	0.042	99.09
DL002pl3	90.44	45.32	34.20	0.398	0.196	17.69	1.03	0.006	0.015	195.7	0.061	2.69	0.124	0.009	0.116	0.016	0.026	99.04
DL002pl4	87.79	45.98	33.77	0.443	0.197	17.01	1.30	0.010	0.022	208.9	0.116	4.08	0.196	0.042	0.158	0.044	0.025	98.95

	An%	SiO2 wt%	Al2O3 wt%	FeO wt%	MgO wt%	CaO wt%	Na2O wt%	K2O wt%	TiO2 wt%	Sr ppm	Y ppm	Ba ppm	La ppm	Sm ppm	Eu ppm	Gd ppm	Pb ppm	total
DL002pl5	90.63	45.27	34.23	0.404	0.164	17.57	1.00	0.007	0.016	211.3	0.105	3.12	0.111	0.027	0.155	0.016	0.038	98.75
DL002pl6	89.08	45.66	33.98	0.419	0.217	17.42	1.17	0.007	0.017	178.9	0.091	2.27	0.089	0.016	0.112	0.020	0.021	98.92
0931pl1	83.79	46.97	33.12	0.526	0.178	16.46	1.73	0.035	0.035	388.0	0.124	14.97	0.387	0.072	0.210	0.046	0.080	99.20
0931pl2	83.56	47.03	33.09	0.709	0.299	16.38	1.75	0.042	0.068	387.5				0.114	0.233	0.120	0.096	99.59
0931pl3	83.05	47.15	33.00	0.533	0.194	16.45	1.82	0.043	0.041	388.1	0.195	16.96	0.440	0.084	0.233	0.068	0.191	99.44
0931pl4	83.00	47.17	33.00	1.247	0.492	16.36	1.81	0.062	0.145	382.9				0.358	0.298	0.257	0.147	100.61
0931pl5	84.36	46.83	33.22	0.746	0.174	16.77	1.68	0.050	0.059	400.1			0.589	0.156	0.230	0.091	0.220	99.77
0931pl6	83.65	47.00	33.10	0.514	0.173	16.42	1.75	0.037	0.037	386.4	0.174	16.15	0.395	0.061	0.225	0.056	0.095	99.19
DL009pl1	83.45	47.05	33.07	0.664	0.128	16.51	1.79	0.023	0.023	234.3	0.161	8.76	0.229	0.029	0.213	0.057	0.061	99.36
DL009pl2	81.21	47.61	32.71	0.654	0.175	15.94	2.02	0.025	0.030	250.9	0.146	12.08	0.277	0.060	0.225	0.049	0.053	99.31
DL009pl3	79.25	48.10	32.39	0.713	0.141	15.75	2.25	0.033	0.029	228.4	0.121	9.25	0.224	0.050	0.193	0.038	0.049	99.80
DL009pl4	88.53	45.79	33.89	0.481	0.177	17.55	1.25	0.012	0.013	164.3	0.087	4.74	0.116	0.026	0.108	0.023	0.042	99.32
DL009pl5	73.78	49.46	31.50	0.708	0.172	14.52	2.82	0.042	0.038	247.8	0.149	13.27	0.270	0.050	0.226	0.035	0.053	99.43
DL009pl6	88.87	45.71	33.95	0.457	0.168	17.56	1.20	0.011	0.014	162.1	0.067	4.24	0.115	0.013	0.104	0.038	0.033	99.30
0908pl1	86.74	46.24	33.60	0.498	0.176	16.90	1.42	0.012	0.019	222.3	0.105	5.04	0.159	0.053	0.130	0.018	0.031	98.91
0908pl2	87.97	45.93	33.80	0.973	0.442	17.23	1.29	0.015	0.040	213.8		5.65	0.183	0.097	0.173	0.085	0.051	99.77
0908pl3	83.75	46.98	33.12	0.518	0.191	16.23	1.73	0.017	0.019	229.4	0.109	5.89	0.140	0.052	0.146	0.043	0.069	98.94
0908pl4	83.16	47.13	33.02	0.511	0.195	16.37	1.82	0.018	0.019	229.8	0.095	5.90	0.123	0.023	0.143	0.026	0.025	99.15
0908pl5	83.93	46.94	33.15	0.506	0.196	16.46	1.73	0.016	0.018	229.7	0.096	5.55	0.136	0.037	0.139	0.046	0.051	99.15
0908pl6	84.87	46.70	33.30	0.516	0.192	16.53	1.61	0.018	0.019	239.4	0.106	6.05	0.164	0.045	0.155	0.031	0.040	99.04
0902pl1	84.54	46.78	33.25	0.563	0.175	16.67	1.66	0.022	0.024	237.8	0.090	5.51	0.166	0.045	0.155	0.034	0.055	99.31
0902pl2	88.94	45.69	33.96	0.429	0.193	17.36	1.18	0.011	0.019	221.9	0.088	3.94	0.146	0.017	0.121	0.029	0.018	99.31
0902pl3	87.21	46.12	33.68	0.559	0.138	17.04	1.37	0.019	0.023	246.0	0.108	4.75	0.186	0.040	0.165	0.033	0.062	98.99
0902pl4	89.22	45.62	34.00	0.407	0.202	17.48	1.16	0.010	0.018	233.6	0.067	4.21	0.163	0.024	0.146	0.035	0.029	98.95
0902pl5	86.64	46.26	33.59	0.524	0.168	17.07	1.44	0.016	0.031	236.1	0.297	5.68	0.259	0.054	0.204	0.108	0.048	99.27
0902pl6	87.35	46.08	33.70	0.456	0.191	17.04	1.35	0.013	0.022	237.0	0.081	4.32	0.170	0.039	0.155	0.018	0.033	98.94
0922pl1	88.25	45.81	33.88	0.378	0.231	16.64	1.22	0.010	0.024	208.1	0.253	5.52	0.338	0.097	0.208	0.103	0.115	98.73
0922pl2	86.23	46.36	33.52	0.359	0.246	16.63	1.46	0.011	0.019	179.1	0.103	2.81	0.091	0.014	0.135	0.028	0.011	98.72
0922pl3	86.26	46.36	33.52	0.366	0.257	16.79	1.47	0.010	0.019	176.3	0.101	2.73	0.097	0.043	0.155	0.026	0.025	98.94
0922pl4	88.67	45.76	33.91	0.352	0.223	17.35	1.22	0.008	0.017	182.5	0.085	2.59	0.088	0.014	0.135	0.014	0.019	99.16
0922pl5	87.65	46.01	33.75	0.348	0.232	17.10	1.32	0.009	0.017	174.0	0.095	2.46	0.080	0.019	0.157	0.008	0.021	99.17
0922pl6	87.90	45.95	33.79	0.357	0.235	17.45	1.32	0.009	0.017	174.6	0.089	2.60	0.096	0.041	0.146	0.029	0.022	99.37

	An%	SiO2 wt%	Al2O3 wt%	FeO wt%	MgO wt%	CaO wt%	Na2O wt%	K2O wt%	TiO2 wt%	Sr ppm	Y ppm	Ba ppm	La ppm	Sm ppm	Eu ppm	Gd ppm	Pb ppm	total
0969pl1	88.34	45.84	33.86	0.433	0.180	17.58	1.27	0.014	0.024	321.9	0.120	5.92	0.261	0.057	0.193	0.062	0.027	99.40
0969pl2	84.56	46.78	33.25	0.609	0.131	16.78	1.68	0.020	0.031	288.7	0.154	6.68	0.260	0.054	0.215	0.055	0.049	99.51
0969pl3	88.39	45.83	33.87	0.424	0.168	17.20	1.24	0.013	0.025	319.9	0.110	5.21	0.249	0.076	0.176	0.056	0.056	98.99
0969pl4	88.05	45.91	33.81	0.560	0.106	17.57	1.31	0.014	0.022	286.8	0.122	4.42	0.200	0.073	0.185	0.031	0.048	99.55
0969pl5	84.53	46.78	33.24	0.612	0.128	16.72	1.67	0.020	0.029	292.4	0.116	7.01	0.275	0.062	0.217	0.065	0.064	99.43
0969pl6	87.99	45.93	33.80	0.435	0.174	17.25	1.29	0.014	0.024	310.8	0.109	5.67	0.246	0.079	0.205	0.041	0.047	99.10
0949pl1	84.00	46.92	33.16	0.502	0.208	16.62	1.73	0.024	0.033	311.0	0.122	7.47	0.280	0.060	0.220	0.043	0.046	99.57
0949pl2	83.70	46.99	33.11	0.587	0.187	16.73	1.78	0.021	0.030	249.1	0.117	6.48	0.231	0.087	0.220	0.061	0.048	99.82
0949pl4	82.29	47.34	32.88	0.549	0.136	16.32	1.92	0.025	0.034	297.4	0.160	7.35	0.300	0.062	0.216	0.035	0.057	99.29
0949pl5	85.19	46.62	33.35	0.624	0.135	17.04	1.62	0.021	0.027	246.7	0.133	5.95	0.242	0.032	0.184	0.031	0.086	99.67
0949pl6	86.03	46.41	33.49	0.559	0.165	17.04	1.52	0.017	0.027	243.4	0.137	5.70	0.239	0.047	0.195	0.057	0.037	99.59
DL003pl1	89.00	45.67	33.97	0.469	0.171	17.54	1.19	0.011	0.022	220.0	0.075	4.26	0.178	0.047	0.129	0.032	0.030	99.03
DL003pl2	85.08	46.65	33.33	0.515	0.195	16.61	1.60	0.017	0.025	241.7	0.104	5.51	0.178	0.038	0.173	0.032	0.038	99.18
DL003pl3	87.89	45.95	33.79	0.449	0.194	17.32	1.31	0.013	0.023	240.3	0.091	4.87	0.192	0.042	0.145	0.018	0.034	99.11
DL003pl4	89.36	45.59	34.03	0.466	0.160	17.60	1.15	0.012	0.018	223.3	0.099	4.08	0.135	0.027	0.134	0.013	0.063	98.96
DL003pl5	87.09	46.15	33.66	0.484	0.193	17.01	1.38	0.014	0.023	236.9	0.107	4.77	0.184	0.050	0.142	0.042	0.041	99.04
DL003pl6	88.26	45.86	33.85	0.575	0.235	17.46	1.27	0.014	0.025	230.7	0.191	4.11	0.158	0.052	0.123	0.048	0.035	99.45
dl003pa	88.33	45.84	33.86	0.490	0.165	17.77	1.29	0.014	0.020	234.2	0.088	4.54	0.182	0.068	0.158	0.040	0.042	99.45
dl003pb	89.88	45.46	34.11	0.490	0.156	18.12	1.12	0.012	0.019	241.2	0.118	4.93	0.184	0.032	0.155	0.084	0.035	99.49
dl003pc	88.29	45.85	33.85	0.446	0.199	17.82	1.30	0.014	0.022	240.8	0.097	4.82	0.181	0.035	0.145	0.053	0.034	99.50
dl003pd	88.14	45.89	33.83	0.449	0.183	17.19	1.27	0.013	0.020	220.3	0.101	4.13	0.164	0.020	0.137	0.073	0.036	98.84
dl003pe	87.96	45.94	33.80	0.450	0.199	17.31	1.30	0.014	0.023	235.1	0.100	4.21	0.197	0.024	0.145	0.065	0.031	99.03
dl003pf	87.73	45.99	33.76	0.433	0.210	17.20	1.32	0.015	0.022	242.5	0.094	4.93	0.209	0.055	0.151	-0.008	0.022	98.95
dl003pg	89.95	45.44	34.12	0.462	0.159	17.93	1.10	0.011	0.017	228.0	0.084	4.03	0.146	0.091	0.134	0.018	0.051	99.23
dl003ph	87.35	46.08	33.70	0.450	0.194	17.24	1.37	0.015	0.024	233.0	0.118	4.45	0.176	0.051	0.171	0.074	0.028	99.07
dl003pi	88.28	45.85	33.85	0.451	0.188	17.49	1.27	0.014	0.024	245.2	0.105	5.07	0.204	0.052	0.182	0.073	0.032	99.14
dl003pj	89.32	45.60	34.02	0.483	0.254	17.58	1.15	0.011	0.020	221.9	0.151	4.42	0.150	0.078	0.124	0.084	0.033	99.11
dl003pk	87.98	45.93	33.80	0.438	0.206	17.27	1.29	0.013	0.021	224.6	0.062	4.07	0.146	0.044	0.149	0.035	0.038	98.97
dl003pl	88.29	45.85	33.85	0.465	0.159	17.08	1.24	0.013	0.017	216.5	0.088	3.85	0.124	0.022	0.103	-0.002	0.028	98.68
dl003pm	89.23	45.62	34.00	0.431	0.161	16.74	1.11	0.012	0.017	225.2	0.067	3.90	0.146	0.032	0.154	0.054	0.025	98.09
dl003pn	89.66	45.51	34.07	0.415	0.181	17.56	1.11	0.011	0.018	219.9	0.104	3.51	0.150	0.085	0.136	0.034	0.032	98.88
dl003po	86.18	46.37	33.51	0.513	0.194	16.95	1.49	0.017	0.027	239.1	0.116	5.06	0.217	0.015	0.164	0.048	0.055	99.08

	An%	SiO2 wt%	Al2O3 wt%	FeO wt%	MgO wt%	CaO wt%	Na2O wt%	K2O wt%	TiO2 wt%	Sr ppm	Y ppm	Ba ppm	La ppm	Sm ppm	Eu ppm	Gd ppm	Pb ppm	total
dl033pa	87.97	45.93	33.80	0.424	0.220	17.33	1.30	0.012	0.020	180.9	0.115	4.29	0.121	0.034	0.130	0.007	0.089	99.04
dl033pb	88.78	45.73	33.93	0.650	0.111	17.65	1.22	0.026	0.020	245.6	0.103	7.91	0.233	0.108	0.151	0.038	0.052	99.33
dl033pc	85.87	46.45	33.46	0.447	0.257	17.11	1.55	0.015	0.028	269.2	0.138	8.71	0.264	0.052	0.197	0.022	0.058	99.32
dl033pd	87.58	46.03	33.74	0.401	0.221	17.09	1.33	0.011	0.022	198.1	0.134	5.68	0.204	0.033	0.166	0.040	0.034	98.84
dl033pe	88.57	45.78	33.90	0.457	0.183	17.60	1.24	0.017	0.022	215.0	0.126	5.42	0.200	0.067	0.152	0.049	0.030	99.20
dl033pf	86.31	46.34	33.53	0.433	0.254	17.34	1.51	0.013	0.026	216.6	0.126	5.65	0.225	0.046	0.124	0.033	0.016	99.45
dl033pg	89.03	45.67	33.97	0.467	0.184	18.05	1.22	0.016	0.021	211.3	0.121	5.96	0.227	0.073	0.185	0.031	0.031	99.60
dl033ph	87.92	45.94	33.79	0.415	0.225	17.41	1.32	0.010	0.023	198.0	0.102	5.06	0.171	0.059	0.141	0.033	0.037	99.14
dl033pi	88.00	45.92	33.81	0.417	0.226	17.60	1.32	0.010	0.021	202.7	0.128	6.41	0.199	0.052	0.138	0.018	0.039	99.32
dl033pj	87.55	46.03	33.73	0.470	0.194	17.63	1.37	0.019	0.025	219.6	0.132	7.46	0.257	0.053	0.192	0.067	0.039	99.48
dl033pk	87.13	46.14	33.67	0.423	0.233	17.40	1.41	0.011	0.020	198.1	0.089	5.66	0.155	0.038	0.148	0.017	0.024	99.30
dl033pl	88.53	45.79	33.89	0.407	0.205	17.87	1.27	0.011	0.020	174.5	0.096	4.28	0.143	0.017	0.123	0.017	0.004	99.47
dl033pm	88.80	45.72	33.94	0.415	0.211	17.72	1.23	0.010	0.018	177.9	0.123	4.23	0.158	0.080	0.146	0.043	0.020	99.27
dl033pn	86.36	46.33	33.54	0.521	0.240	17.30	1.49	0.025	0.032	261.8	0.191	9.46	0.324	0.044	0.145	0.087	0.041	99.48
dl033po	88.37	45.83	33.87	0.464	0.189	17.43	1.26	0.014	0.020	239.1	0.128	7.69	0.173	0.029	0.181	0.023	0.030	99.07
EMP																		
DL066	68.71	51.06	30.36	0.710	0.162	14.12	3.52	0.050										99.98
DL066	67.82	51.07	30.27	0.800	0.142	13.97	3.61	0.080										99.94
DL074	65.00	51.82	29.71	0.780	0.132	13.35	3.90	0.110										99.80
DL074	61.57	52.75	28.88	0.860	0.162	12.59	4.25	0.140										99.64
DL062	76.77	48.85	31.75	0.770	0.172	15.73	2.61	0.030										99.91
DL062	66.71	51.27	30.04	0.790	0.132	13.78	3.74	0.090										99.84
DL007	89.78	45.52	34.24	0.430	0.192	18.23	1.14	0.010										99.76
DL007	87.50	46.06	33.56	0.460	0.223	17.82	1.40	0.010										99.54
DL038	73.49	49.70	31.07	0.760	0.172	14.95	2.94	0.060										99.66
DL038	86.81	46.28	33.73	0.480	0.202	17.74	1.49	0.000										99.92
DL040a	83.64	47.00	33.13	0.750	0.081	17.11	1.83	0.030										99.93
DL040	73.34	50.00	31.02	0.760	0.152	15.00	2.98	0.050										99.96
DL059	71.39	50.03	30.46	0.780	0.200	14.34	3.15	0.040										99.00
DL059	69.44	50.43	30.27	0.800	0.180	14.05	3.37	0.070										99.17
DL011	71.15	50.01	30.65	0.700	0.200	14.44	3.19	0.070										99.26
DL011	84.79	46.52	33.32	0.590	0.190	17.08	1.68	0.020										99.40

	An%	SiO2 wt%	Al2O3 wt%	FeO wt%	MgO wt%	CaO wt%	Na2O wt%	K2O wt%	TiO2 wt%	Sr ppm	Y ppm	Ba ppm	La ppm	Sm ppm	Eu ppm	Gd ppm	Pb ppm	total
DL003	87.86	46.00	33.83	0.500	0.152	17.89	1.36	0.010										
DL003	87.73	45.94	33.91	0.480	0.192	17.89	1.37	0.020										99.80
DL033	88.31	46.16	33.93	0.480	0.190	18.00	1.29	0.040										100.09
DL033	88.06	45.68	33.87	0.500	0.190	17.92	1.33	0.020										99.51
DL033	88.08	45.95	33.40	0.700	0.370	17.70	1.31	0.020										99.45
DL033	86.52	46.40	33.38	0.520	0.220	17.58	1.50	0.020										99.62
DL033	86.47	46.50	33.74	0.420	0.240	17.62	1.51	0.020										100.05

Table A3.3: Clinopyroxene mineral compositions. Minerals analysis by LA-ICP-MS except where noted.

	Mg#	Li ppm	Na2O wt%	MgO wt%	Al2O3 wt%	SiO2 wt%	CaO wt%	Sc ppm	TiO2 wt%	V ppm	Cr ppm	MnO wt%	FeO wt%	Ni ppm	Sr ppm	Y ppm	Zr ppm	Nb ppm	La ppm
DL003CPXA	86.04	0.98	0.199	17.02	2.94	52.80	20.94	100	0.393	256.9	4177	0.124	4.918	222.367	11.50	6.904	5.341	0.0125	0.194
DL003CPXB	84.72	0.66	0.212	16.99	2.76	52.95	20.62	103	0.425	276.4	2698	0.140	5.460	231.128	11.53	7.851	5.741	0.0153	0.237
DL003CPXC	87.63	1.03	0.206	16.96	3.68	52.30	20.94	96	0.346	236.7	8237	0.107	4.270	264.195	11.26	6.008	5.139	0.0135	0.178
DL003CPXD	85.70	1.04	0.196	17.26	2.78	53.05	20.58	105	0.435	280.0	2841	0.135	5.134	247.484	11.45	8.204	5.988	0.0166	0.234
DL003CPXE	86.54	1.37	0.200	16.96	3.48	52.30	20.91	103	0.381	252.6	6308	0.118	4.704	252.371	10.81	6.894	5.832	0.0334	0.182
DL003CPXF	84.81	1.16	0.203	16.79	3.76	52.40	20.31	119	0.541	333.1	3065	0.135	5.358	240.816	11.16	10.406	10.807	0.0290	0.290
DL003CPXG	87.45	1.24	0.206	16.78	3.68	52.45	20.92	97	0.355	240.3	8206	0.107	4.291	260.879	11.02	6.167	5.118	0.0131	0.182
0951CPXA	85.01	1.11	0.227	16.59	3.25	52.54	20.74	106	0.426	257.3	5690	0.129	5.211	189.154	12.38	7.395	6.045	0.0156	0.218
0951CPXB	84.70	1.25	0.231	16.61	3.36	52.25	20.78	109	0.445	267.2	5759	0.132	5.349	187.083	12.05	7.810	6.493	0.0181	0.236
0951CPXC	82.51	1.64	0.230	17.15	3.63	52.52	18.48	133	0.596	306.8	4652	0.172	6.478	190.627	9.87	11.534	13.194	0.0578	0.316
0951CPXD	84.76	1.04	0.224	16.74	2.99	52.72	20.66	103	0.416	250.9	4786	0.135	5.367	188.219	11.86	7.428	5.803	0.0160	0.215
0951CPXE	84.06	1.22	0.235	16.45	3.45	52.29	20.62	118	0.490	286.6	5139	0.138	5.558	183.195	12.13	9.191	7.841	0.0197	0.281
0951CPXF	84.94	1.22	0.238	16.72	3.16	52.50	20.65	109	0.424	254.4	6271	0.134	5.284	193.094	11.53	7.805	6.373	0.0164	0.236
0951CPXG	85.22	1.24	0.230	16.60	3.18	52.60	20.89	101	0.402	248.6	5876	0.128	5.132	197.236	12.09	7.094	5.647	0.0122	0.209
0951CPXH	85.15	1.25	0.232	16.63	3.34	52.50	20.66	103	0.416	257.7	6186	0.129	5.170	196.718	12.18	7.275	5.851	0.0138	0.193
0951CPXI	83.76	1.23	0.232	17.02	3.08	52.85	19.68	116	0.484	277.9	3851	0.155	5.881	186.755	10.48	9.383	8.342	0.0228	0.267
0969CPXA	79.84	0.81	0.243	16.24	2.54	52.55	20.20	116	0.613	317.1	562	0.182	7.308	122.796	13.65	10.865	8.810	0.0247	0.349
0969CPXB	80.01	0.84	0.240	16.30	2.47	52.60	20.30	113	0.595	310.9	456	0.182	7.258	121.889	13.69	10.606	8.655	0.0193	0.357
0969CPXC	80.11	0.73	0.241	16.21	2.63	52.50	20.28	118	0.628	322.3	617	0.180	7.174	125.205	13.83	11.372	9.511	0.0227	0.374
0969CPXD	79.51	0.98	0.246	16.20	2.49	52.50	20.27	115	0.617	319.3	442	0.184	7.442	123.406	13.93	10.843	9.274	0.0434	0.354
0969CPXE	79.95	0.66	0.244	16.26	2.55	52.37	20.43	118	0.617	321.7	577	0.182	7.266	122.919	13.83	10.973	9.082	0.0194	0.374
0969CPXF	80.79	1.64	0.258	15.99	4.14	51.35	20.06	138	0.713	384.9	3156	0.161	6.780	177.732	13.83	15.352	16.401	0.0427	0.564
0969CPXG	79.93	0.82	0.245	16.29	2.52	52.45	20.32	117	0.614	317.9	567	0.180	7.287	122.478	13.80	10.986	9.036	0.0211	0.377
0969CPXH	79.83	0.71	0.245	16.19	2.53	52.65	20.22	115	0.610	315.0	549	0.182	7.294	121.198	13.89	10.984	8.832	0.0186	0.363
0902CPXA	86.27	1.28	0.201	16.84	3.20	52.65	21.00	102	0.400	264.5	5189	0.120	4.774	236.247	11.51	6.818	5.563	0.0146	0.199
0902CPXB	85.40	1.55	0.202	17.04	2.65	53.05	20.85	103	0.409	273.4	2737	0.133	5.191	227.557	11.57	7.394	5.444	0.0103	0.220
0902CPXC	88.05	1.79	0.198	17.23	2.88	53.07	21.02	91	0.311	208.4	6809	0.109	4.167	256.081	9.96	5.078	4.043	0.0148	0.169
0902CPXD	87.68	1.50	0.198	17.14	3.00	52.85	21.09	93	0.333	225.7	6636	0.110	4.295	247.211	10.51	5.750	4.336	0.0113	0.168
0902CPXE	87.59	1.41	0.199	17.08	2.97	52.87	21.18	92	0.329	221.9	6414	0.110	4.312	247.719	10.68	5.466	4.223	0.0104	0.162
0902CPXF	86.32	1.04	0.201	17.16	2.76	53.05	20.93	99	0.369	249.4	3753	0.126	4.849	241.814	11.39	6.768	5.111	0.0119	0.196
0902CPXG	87.15	1.64	0.208	17.11	2.80	52.85	21.18	94	0.338	219.2	6233	0.114	4.496	247.617	11.14	5.466	4.427	0.0138	0.176
0902CPXH	87.65	1.62	0.199	17.22	2.95	52.88	20.99	94	0.325	219.4	6478	0.113	4.322	253.372	9.84	5.525	4.383	0.0145	0.153

Table A3.3: Clinopyroxene mineral compositions. Minerals analysis by LA-ICP-MS except where noted.

	Ce ppm	Nd ppm	Sm ppm	Eu ppm	Gd ppm	Dy ppm	Er ppm	Yb ppm	Hf ppm	total
DL003CPXA	0.970	1.533	0.736	0.294	1.082	1.382	0.762	0.661	0.293	99.98
DL003CPXB	1.047	1.699	0.898	0.325	1.176	1.545	0.928	0.838	0.321	100.00
DL003CPXC	0.804	1.315	0.686	0.255	0.968	1.324	0.668	0.603	0.303	100.06
DL003CPXD	1.105	1.807	0.880	0.322	1.328	1.631	0.967	0.784	0.332	100.04
DL003CPXE	0.885	1.455	0.701	0.279	1.066	1.402	0.797	0.718	0.317	100.02
DL003CPXF	1.461	2.208	1.128	0.376	1.613	2.040	1.160	1.003	0.644	99.99
DL003CPXG	0.829	1.341	0.694	**0.228**	0.982	1.260	0.704	0.638	0.283	100.04
0951CPXA	1.035	1.648	0.826	0.287	1.164	1.435	0.825	0.777	0.359	99.98
0951CPXB	1.106	1.770	0.805	0.313	1.256	1.685	0.877	0.826	0.340	100.04
0951CPXC	1.469	2.352	1.107	0.453	1.654	2.279	1.313	1.159	0.844	99.99
0951CPXD	0.967	1.600	0.711	0.308	1.261	1.477	0.792	0.680	0.338	100.00
0951CPXE	1.239	2.008	1.031	0.347	1.585	1.897	1.043	0.910	0.480	100.03
0951CPXF	1.074	1.697	0.743	0.311	1.135	1.614	0.837	0.791	0.384	100.06
0951CPXG	0.952	1.588	0.747	0.300	1.188	1.412	0.791	0.716	0.316	100.06
0951CPXH	0.937	1.545	0.748	0.294	1.315	1.403	0.758	0.637	0.331	100.03
0951CPXI	1.195	1.827	0.936	0.358	1.460	1.831	1.086	0.904	0.486	99.98
0969CPXA	1.695	2.643	1.417	0.474	1.738	2.185	1.131	1.052	0.466	100.00
0969CPXB	1.618	2.597	1.136	0.472	1.831	2.227	1.162	0.925	0.458	100.04
0969CPXC	1.830	2.544	1.293	0.485	1.890	2.318	1.263	0.971	0.511	99.97
0969CPXD	1.733	2.627	1.244	0.485	1.730	2.182	1.172	1.029	0.499	100.06
0969CPXE	1.742	2.594	1.117	0.442	1.648	2.245	1.247	0.924	0.477	100.04
0969CPXF	2.399	3.793	1.733	0.588	2.591	3.044	1.701	1.487	0.916	99.97
0969CPXG	1.707	2.594	1.301	0.455	1.855	2.347	1.266	1.032	0.493	100.02
0969CPXH	1.707	2.504	1.287	0.395	1.831	2.186	1.232	1.054	0.509	100.05
0902CPXA	0.925	1.492	0.809	0.285	1.147	1.393	0.743	0.689	0.301	99.99
0902CPXB	0.982	1.499	0.800	0.301	1.123	1.537	0.838	0.715	0.300	99.97
0902CPXC	0.669	1.207	0.497	0.221	0.772	1.052	0.553	0.566	0.227	100.02
0902CPXD	0.773	1.290	0.536	0.227	0.932	1.122	0.591	0.538	0.253	100.04
0902CPXE	0.814	1.195	0.610	0.240	0.897	1.165	0.596	0.508	0.263	100.03
0902CPXF	0.909	1.432	0.679	0.265	1.038	1.442	0.780	0.696	0.253	100.04
0902CPXG	0.809	1.158	0.562	0.236	0.974	1.138	0.645	0.589	0.235	100.05
0902CPXH	0.733	1.181	0.603	0.237	0.758	1.163	0.624	0.561	0.254	99.99

Table A3.3: Clinopyroxene mineral compositions. Minerals analysis by LA-ICP-MS except where noted.

	Mg#	Na2O wt%	MgO wt%	Al2O3 wt%	SiO2 wt%	CaO wt%	TiO2 wt%	Cr2O wt%	MnO wt%	FeO wt%
DL074 EMP	75.00	0.330	13.87	4.18	48.94	19.70	1.620	0.13	0.210	9.900
DL074 EMP	76.40	0.340	14.65	3.88	49.58	19.18	1.440	0.18	0.210	9.500

APPENDIX 4: MAJOR AND TRACE ELEMENT DATA WITH PRESSURE RESULTS

Table A4.1: Major and Trace element concentrations as well as calculated crystallisation pressures (GPa). Values in bold were analysed by ID. Sample numbers in italics were analysis on the PANalytical Axios spectrometer.

	Krafla						
	Krafla Fires 1977-1984						
	DL039	DL040	DL041	DL042	DL043	DL045	DL059
SiO_2	49.34	49.46	49.52	49.47	49.41	49.30	49.30
Al_2O_3	13.39	13.15	13.23	13.18	13.20	13.15	13.28
Fe_2O_3	16.02	15.96	16.05	16.05	16.07	16.05	15.91
MgO	5.88	5.83	5.86	5.88	5.85	5.84	5.95
CaO	10.22	10.03	10.04	10.03	10.09	10.15	10.14
Na_2O	2.400	2.340	2.260	2.180	2.350	2.360	2.410
K_2O	0.334	0.332	0.339	0.341	0.322	0.334	0.336
TiO_2	1.994	2.043	2.067	2.055	2.049	2.053	1.995
MnO	0.238	0.246	0.242	0.246	0.246	0.248	0.242
P_2O_5	0.211	0.220	0.213	0.219	0.210	0.210	0.209
Cr_2O_3							
Total	100.03	99.61	99.82	99.65	99.80	99.70	99.78
LOI	-0.8	-1.1	-1.2	-0.5	-1.2	-1.0	-1.1
Ni	54.90	55.80	58.10	57.00	56.00	55.90	58.20
Cr	117.90	118.60	115.50	114.60	116.50	113.90	118.50
V	454	456	470	469	466	457	423
Sc	47.4	48.5	50.5	49.3	49.5	47.4	44.2
Cu	139	140	136	135	142	136	138
Zn	125.8	123.5	128.6	127.1	127.1	125.5	119.0
Cl	65.00	54.00	83.00	34.00	80.00	79.00	54.00
Ga	18.70	19.00	18.70	19.20	18.50	19.30	19.30
Pb	1.400	0.400	1.700	1.900	1.600	1.900	**0.783**
Sr	150.2	148.1	147.5	146.2	148.7	150.6	151.9
Rb	6.640	6.800	6.890	6.430	6.700	6.700	6.930
Ba	79.20	81.30	79.70	83.40	82.50	84.40	**83.70**
Zr	118.80	118.50	120.70	119.30	118.90	118.30	**116.70**
Nb	11.40	11.90	11.80	11.70	11.70	11.50	11.60
Th	1.600	1.400	1.700	1.100	1.400	1.200	**0.740**
La	10.70	9.20	9.20	10.80	9.40	10.40	9.80
Ce	26.10	22.50	23.80	25.60	23.80	21.00	25.10
Nd	15.10	14.40	15.70	16.40	15.60	14.80	15.80
Y	36.10	36.10	35.80	36.10	36.30	36.30	36.10
Yb							
U							**0.230**
Ta							
Co							
Hf							
La ID							
Ce ID							
Nd ID							
Sm ID							
Eu ID							
Gd ID							
Dy ID							
Er ID							
Yb ID							
Lu ID							
P (GPa)	0.528	0.489	0.512	0.515	0.508	0.491	0.512

	Myvatn Fires			*Dalseldar*		
	DL038	DL062	DL066	DL010	DL011	JPF0912
SiO_2	49.44	49.34	49.39	50.13	50.11	49.39
Al_2O_3	13.43	13.40	13.38	13.31	13.17	13.13
Fe_2O_3	15.80	15.91	15.92	16.14	16.01	15.85
MgO	5.97	5.93	6.00	5.28	5.25	5.93
CaO	10.20	10.15	10.12	9.68	9.66	10.34
Na_2O	2.320	2.370	2.330	2.560	2.560	2.344
K_2O	0.334	0.332	0.337	0.425	0.419	0.308
TiO_2	1.996	1.993	2.011	2.008	1.997	1.877
MnO	0.239	0.240	0.239	0.252	0.243	0.240
P_2O_5	0.209	0.204	0.207	0.197	0.198	0.184
Cr_2O_3						
Total	99.94	99.86	99.93	99.99	99.62	99.60
LOI	-1.2	-1.1	-1.1	-0.7	-1.0	-0.9
Ni	57.40	58.50	58.80	37.70	38.10	50.80
Cr	122.20	118.80	115.80	27.70	26.70	82.40
V	431	409	441	433	438	441
Sc	44.6	43.5	47.2	45.9	47.5	48.6
Cu	139	143	136	169	146	155
Zn	119.7	115.0	124.3	123.5	125.5	121.5
Cl	70.00	64.00	60.00	109.00	101.00	-47.30
Ga	18.90	19.60	18.50	19.10	18.60	17.00
Pb	**0.784**	**0.762**	1.800	0.600	0.500	1.200
Sr	149.9	152.7	150.2	149.5	149.0	142.3
Rb	6.820	6.410	6.510	8.510	8.190	6.300
Ba	**81.60**	**83.00**	79.80	98.30	93.70	73.80
Zr	**114.08**	**114.49**	115.90	139.20	137.40	107.70
Nb	11.40	11.00	11.30	13.30	12.80	10.30
Th	**0.729**	**0.736**	0.900	1.200	1.200	1.500
La	9.80	9.60	11.30	12.60	12.00	6.80
Ce	22.30	23.30	21.80	26.40	28.60	24.20
Nd	15.40	14.70	15.00	17.60	18.60	13.90
Y	35.00	36.10	35.60	39.60	39.20	33.30
Yb						
U	**0.228**	**0.228**				
Ta						
Co						
Hf	**3.093**	**3.102**				
La ID	9.244	9.333				
Ce ID	22.682	22.740				
Nd ID	15.403	15.449				
Sm ID	4.383	4.394				
Eu ID	1.538	1.542				
Gd ID	5.482	5.498				
Dy ID	6.111	6.128				
Er ID	3.769	3.780				
Yb ID	3.606	3.616				
Lu ID						
P (GPa)	0.519	0.532	0.538	0.448	0.405	0.435

	Younger Laxárhraun						
	DL003	DL004	DL060	DL061	JPF0901	JPF0902	JPF0902A
SiO_2	48.72	48.65	48.80	48.80	48.94	48.70	49.01
Al_2O_3	15.12	14.84	14.54	14.32	14.96	14.76	14.93
Fe_2O_3	12.00	12.38	12.35	12.65	11.91	12.15	12.08
MgO	7.45	7.44	7.55	7.64	7.54	7.52	7.48
CaO	12.65	12.57	12.46	12.44	12.59	12.57	12.56
Na_2O	2.020	2.090	2.190	2.240	1.994	2.013	2.067
K_2O	0.162	0.166	0.163	0.172	0.160	0.156	0.168
TiO_2	1.453	1.489	1.518	1.586	1.481	1.478	1.495
MnO	0.192	0.196	0.198	0.204	0.196	0.189	0.197
P_2O_5	0.136	0.139	0.142	0.150	0.140	0.142	0.143
Cr_2O_3							
Total	99.90	99.96	99.91	100.20	99.92	99.68	100.13
LOI	-0.7	-0.6	-0.8	-0.4	-0.6	-0.7	-0.7
	4.66	5.77	6.1	7.14			
Ni	80.20	81.50	83.10	81.60	82.10	83.30	80.40
Cr	122.60	119.60	127.00	119.80	124.70	139.20	120.50
V	312	311	332	333	321	313	319
Sc	44.2	43.7	48.1	47.0	43.4	44.2	44.4
Cu	131	142	146	170	120	120	140
Zn	83.1	83.8	89.6	87.8	85.5	85.7	85.8
Cl	8.00	21.00	24.00	40.00	-78.50	-100.30	-94.30
Ga	16.40	16.70	17.10	17.90	15.90	15.40	17.20
Pb	**0.447**	0.800	1.200	0.500	2.400	**0.426**	0.600
Sr	154.8	155.5	152.0	152.6	153.6	155.0	154.0
Rb	2.880	3.030	3.050	3.090	3.300	3.300	2.200
Ba	**34.70**	37.70	34.90	36.80	36.10	**31.20**	30.60
Zr	**79.16**	82.70	84.00	87.40	83.60	**83.12**	83.10
Nb	7.50	7.90	7.80	8.10	7.80	7.90	7.50
Th	**0.445**	1.200	1.200	1.200	1.700	**0.463**	-0.100
La	5.70	7.20	6.00	6.90	7.40	8.20	13.80
Ce	14.10	16.00	18.00	15.60	16.50	15.00	17.80
Nd	10.00	10.50	9.90	10.90	10.20	10.00	10.20
Y	24.50	25.00	25.80	26.60	25.40	25.00	24.80
Yb							
U	**0.141**					**0.147**	
Ta							
Co							
Hf	**2.185**					**2.291**	
La ID	5.762					5.859	
Ce ID	14.555					14.810	
Nd ID	10.414					10.624	
Sm ID	3.071					3.132	
Eu ID	1.133					1.151	
Gd ID	3.874					3.953	
Dy ID	4.255					4.335	
Er ID	2.538					2.585	
Yb ID	2.339					2.379	
Lu ID	0.348					0.353	
P (GPa)	0.334	0.333	0.279	0.281	0.295	0.299	0.297

			Bjarnarflagsstöð			*Krafla Caldera*	
	JPF0902B	JPF0907	DL021B	DL022	DL023	DL035	DL063
SiO_2	48.89	48.79	49.07	49.24	49.35	50.06	49.36
Al_2O_3	15.02	14.86	13.56	13.68	13.62	13.30	13.39
Fe_2O_3	11.98	12.16	16.12	15.22	15.37	15.85	15.79
MgO	7.46	7.49	5.79	6.32	6.35	5.36	5.96
CaO	12.51	12.51	9.94	10.44	10.48	9.66	10.18
Na_2O	2.018	2.080	2.480	2.300	2.370	2.630	2.400
K_2O	0.156	0.162	0.346	0.278	0.299	0.411	0.329
TiO_2	1.493	1.517	2.021	1.810	1.821	2.018	1.990
MnO	0.192	0.197	0.248	0.239	0.240	0.246	0.246
P_2O_5	0.145	0.141	0.209	0.180	0.175	0.198	0.217
Cr_2O_3		0.021					
Total	99.86	99.91	99.78	99.70	100.07	99.73	99.86
LOI	-0.6	-0.6	-1.2	-0.6	-0.6	-1.0	-1.0
			0.13		0.65		
Ni	81.40	78.60	54.60	68.60	66.60	38.00	33.10
Cr	127.50	118.80	100.30	137.90	139.00	27.20	24.70
V	322	309	459	424	422	446	448
Sc	46.5	42.4	48.9	49.2	49.9	47.1	46.4
Cu	139	130	139	144	132	102	77
Zn	88.0	84.8	127.4	119.0	117.3	124.6	124.5
Cl	-89.70	-96.70	92.00	24.00	62.00	278.00	102.00
Ga	17.60	17.40	19.00	18.10	18.00	20.00	19.10
Pb	0.600	1.500	0.800	0.800	0.900	1.000	1.600
Sr	152.8	152.0	147.1	146.1	147.9	150.9	151.8
Rb	2.500	3.500	6.430	5.280	5.450	8.260	8.420
Ba	32.70	29.80	79.10	71.70	74.90	94.10	95.50
Zr	81.90	81.20	118.10	101.80	102.90	138.30	140.40
Nb	7.50	7.70	11.70	9.70	9.80	12.90	12.90
Th	-0.400	1.700	0.900	1.200	0.500	1.400	1.400
La	5.20	4.90	10.50	8.30	9.10	10.70	11.80
Ce	17.50	16.20	22.30	19.50	20.10	27.30	27.50
Nd	10.20	10.60	14.50	13.20	14.40	16.40	15.90
Y	25.50	24.30	35.70	33.00	33.00	38.90	38.70
Yb							
U							
Ta							
Co							
Hf							
La ID							
Ce ID							
Nd ID							
Sm ID							
Eu ID							
Gd ID							
Dy ID							
Er ID							
Yb ID							
Lu ID							
P (GPa)	0.322	0.316	0.624	0.527	0.511	0.428	0.519

	DL064	DL065	JPF0911	JPF0913	DL006	DL007	DL009
SiO_2	50.06	50.48	49.74	50.04	49.10	49.34	49.41
Al_2O_3	13.22	12.90	13.16	13.06	13.42	13.62	13.01
Fe_2O_3	16.37	16.20	16.38	16.18	16.60	15.43	16.69
MgO	5.24	5.16	5.70	5.34	5.63	6.23	5.64
CaO	9.32	9.30	9.94	9.52	9.91	10.45	9.92
Na_2O	2.630	2.520	2.361	2.470	2.440	2.310	2.440
K_2O	0.412	0.440	0.338	0.423	0.345	0.296	0.337
TiO_2	2.083	2.130	2.028	2.044	2.011	1.807	2.030
MnO	0.252	0.251	0.250	0.251	0.252	0.238	0.250
P_2O_5	0.213	0.216	0.212	0.206	0.210	0.175	0.207
Cr_2O_3							
Total	99.81	99.60	100.10	99.54	99.92	99.90	99.93
LOI	0.2	-0.9	-0.9	-0.7	-1.2	-0.7	-1.0
Ni	36.10	32.80	46.90	37.00	46.30	66.90	48.00
Cr	28.00	24.20	71.50	27.80	59.20	138.10	61.00
V	453	444	452	438	454	414	452
Sc	49.0	46.4	46.3	45.8	47.6	47.3	46.6
Cu	161	117	142	120	146	147	151
Zn	135.2	127.1	124.7	123.5	125.6	115.8	126.1
Cl	-11.00	68.00	-7.20	-23.00	12.00	59.00	92.00
Ga	18.90	20.20	20.00	18.50	18.90	18.90	19.30
Pb	1.800	1.600	2.800	1.600	0.600	0.700	**0.763**
Sr	149.2	152.3	149.4	148.6	148.1	149.0	149.1
Rb	8.400	9.240	6.900	9.700	6.820	5.740	6.940
Ba	95.80	103.30	78.80	96.00	84.00	75.40	**85.80**
Zr	144.00	148.20	115.80	141.90	117.00	102.00	**117.11**
Nb	13.30	13.80	10.80	12.70	11.40	10.00	11.70
Th	1.700	1.700	1.700	1.100	1.700	1.100	**0.689**
La	12.10	11.50	12.00	10.40	9.60	8.00	9.00
Ce	26.80	26.80	25.10	26.10	23.00	20.80	22.90
Nd	15.10	17.80	15.60	17.30	14.90	13.60	15.80
Y	39.60	39.70	35.90	38.50	36.30	32.60	36.80
Yb							
U							**0.232**
Ta							
Co							
Hf							**3.169**
La ID							9.362
Ce ID							22.865
Nd ID							15.503
Sm ID							4.421
Eu ID							1.552
Gd ID							5.542
Dy ID							6.214
Er ID							3.848
Yb ID							3.691
Lu ID							0.558
P (GPa)	0.511	0.390	0.509	0.441	0.637	0.513	0.532

	Hverfjall		*Asbyrgí*			*Heiðarsporður*	
	JPF0903	JPF0905	JPF0953	JPF0954	JPF0956	DL067	*KK3*
SiO_2	48.92	48.93	47.06	47.89	47.26	48.83	64.55
Al_2O_3	14.91	14.47	14.79	15.08	15.29	14.87	15.15
Fe_2O_3	12.12	12.44	13.18	12.60	12.99	12.16	6.65
MgO	7.50	7.60	8.35	8.31	8.95	8.28	1.43
CaO	12.54	12.48	11.78	11.90	11.65	12.29	4.81
Na_2O	2.098	1.990	2.010	2.007	1.940	1.900	4.130
K_2O	0.167	0.169	0.160	0.159	0.140	0.115	1.308
TiO_2	1.505	1.537	1.943	1.780	1.935	1.023	0.897
MnO	0.200	0.204	0.203	0.200	0.196	0.198	0.116
P_2O_5	0.131	0.153	0.195	0.178	0.175	0.091	0.208
Cr_2O_3	0.020		0.042				0.002
Total	100.16	99.97	99.73	100.10	100.52	99.76	99.26
LOI	-0.6	-0.8	-0.9	-0.7	0.0	-0.8	1.4
			10.23			5.7	
Ni	31.40	89.40	131.30	121.90	150.70	104.00	12.93
Cr	28.00	117.50	290.70	284.80	263.90	164.80	25.95
V	437	301	313	295	314	293	69
Sc	45.5	42.2	37.9	37.9	37.8	43.9	12.9
Cu	129	147	132	127	105	117	48
Zn	112.9	93.5	95.1	89.3	92.1	81.6	99.6
Cl	-18.70	-76.00	-57.70	-83.70	147.60	-12.00	64.25
Ga	18.00	19.80	17.30	17.80	15.60	15.90	24.96
Pb	1.600	1.400	1.800	2.000	-0.400	**0.358**	4.953
Sr	140.0	168.6	202.7	189.1	206.6	102.0	217.2
Rb	8.300	2.500	2.900	2.400	1.300	1.920	35.125
Ba	105.10	28.10	52.30	39.00	39.10	**26.00**	279.99
Zr	130.40	89.10	110.30	106.30	98.30	**56.47**	457.92
Nb		8.00	10.80	10.60	9.50	4.28	25.96
Th	0.600	0.400	0.400	1.200	-0.900	**0.248**	4.878
La	14.50	5.00	13.10	6.50	5.20	3.80	31.88
Ce	28.90	14.40	21.00	17.40	17.90	11.30	66.00
Nd	19.60	9.80	13.10	12.10	11.30	7.50	30.47
Y	37.20	27.00	27.90	26.10	25.90	22.60	56.89
Yb							5.18
U						**0.082**	0.948
Ta							0.32
Co							13.73
Hf						**1.580**	7.744
La ID						3.398	
Ce ID						8.619	
Nd ID						6.324	
Sm ID						2.025	
Eu ID						0.777	
Gd ID						2.814	
Dy ID						3.799	
Er ID						2.455	
Yb ID						2.401	
Lu ID							
P (GPa)		0.278		0.684	1.007		

	KK35	*KR47*	*KR48*	*KK51*	*KK55*	*KR74*	*KR77*
SiO_2	57.30	54.67	53.86	50.58	48.68	51.31	48.95
Al_2O_3	15.49	15.05	15.96	15.23	14.80	15.00	15.20
Fe_2O_3	10.41	12.20	12.11	12.10	12.13	11.88	12.22
MgO	3.32	3.82	4.69	6.71	7.39	6.23	8.28
CaO	7.29	7.85	8.70	10.67	12.48	10.16	12.34
Na_2O	3.530	3.240	2.960	2.550	2.110	2.480	1.910
K_2O	0.817	0.687	0.572	0.328	0.163	0.340	0.108
TiO_2	1.347	1.473	1.351	1.496	1.522	1.158	1.036
MnO	0.167	0.182	0.187	0.201	0.194	0.194	0.193
P_2O_5	0.280	0.241	0.213	0.262	0.142	0.174	0.089
Cr_2O_3	0.001	0.000	0.008	0.014	0.019	0.013	0.029
Total	99.97	99.43	100.66	100.16	99.65	98.95	100.38
LOI	0.8	0.9	0.6	0.5	0.4	0.8	1.2
Ni	26.31	33.95	44.85	84.99	75.62	65.70	100.83
Cr	41.87	35.64	56.13	115.91	140.22	96.94	212.52
V	193	295	283	257	300	238	303
Sc	23.8	28.7	31.5	39.3	40.5	36.0	44.0
Cu	111	128	129	164	136	101	129
Zn	99.6	104.7	102.0	98.4	80.7	89.6	77.4
Cl	71.42	86.97	81.22	47.88	52.00	42.72	39.62
Ga	19.77	19.95	18.61	18.23	17.06	16.95	15.85
Pb	1.753	1.588	1.155	0.972	0.761	0.957	0.990
Sr	161.5	151.4	141.7	147.6	152.6	122.3	104.1
Rb	15.239	12.560	10.541	5.439	2.871	5.831	1.531
Ba	174.30	147.03	124.39	75.53	36.95	79.93	29.26
Zr	286.42	247.07	211.54	160.87	78.62	146.88	55.06
Nb	20.52	17.89	15.22	15.42	7.59	10.65	4.12
Th	2.385	1.600	1.573	0.949	0.606	0.864	0.260
La	22.74	19.57	16.78	12.78	5.28	11.25	2.92
Ce	51.58	41.25	39.27	28.25	11.72	24.68	10.48
Nd	26.96	23.62	21.88	19.57	10.65	14.44	6.78
Y	44.83	41.58	37.80	37.66	23.84	33.02	22.47
Yb	4.35	5.19	4.20	5.27	2.31	4.41	2.52
U	1.179	1.043	1.319	0.694	0.409	0.374	-0.045
Ta	2.09	2.34	1.72	2.92	2.17	1.79	1.40
Co	31.51	37.59	40.39	45.75	46.29	42.42	49.35
Hf	6.564	6.323	5.196	6.587	2.811	3.762	1.390
La ID							
Ce ID							
Nd ID							
Sm ID							
Eu ID							
Gd ID							
Dy ID							
Er ID							
Yb ID							
Lu ID							
P (GPa)							

	KR79	*KR82*	*KR87*	*KR87A*	*KR88*	JPF0914
SiO_2	50.23	49.25	49.72	51.80	48.30	49.47
Al_2O_3	13.34	15.05	15.07	15.22	15.65	13.17
Fe_2O_3	15.71	11.71	11.86	12.37	11.23	16.36
MgO	5.46	8.24	7.01	5.68	8.83	5.70
CaO	9.82	12.44	11.88	9.49	12.76	9.83
Na_2O	2.410	1.850	2.010	2.770	1.820	2.244
K_2O	0.395	0.117	0.175	0.437	0.084	0.329
TiO_2	1.955	0.912	1.014	1.684	0.837	2.030
MnO	0.242	0.190	0.194	0.210	0.183	0.249
P_2O_5	0.204	0.086	0.110	0.340	0.083	0.211
Cr_2O_3	0.008	0.024	0.022	0.015	0.026	
Total	99.81	99.89	99.09	100.03	99.83	99.59
LOI	0.6	0.7	0.7	1.2	0.6	-1.0
Ni	45.41	89.76	87.57	65.88	135.10	48.30
Cr	71.54	166.39	161.27	81.11	187.74	78.50
V	433	238	265	251	238	459
Sc	45.5	37.8	38.4	35.0	40.5	47.4
Cu	151	111	132	174	129	148
Zn	121.4	71.1	81.8	111.2	75.7	126.3
Cl	112.30	34.32	32.60	88.23	27.08	-29.80
Ga	19.62	13.36	16.08	19.11	14.76	18.70
Pb	1.195	0.458	0.881	1.799	1.022	2.100
Sr	145.6	88.7	104.3	162.7	85.0	145.7
Rb	7.873	1.886	2.947	7.727	1.167	6.400
Ba	91.60	25.27	41.66	100.75	18.98	76.10
Zr	129.51	54.50	81.29	210.12	50.67	116.60
Nb	12.39	3.92	5.95	19.82	4.01	11.50
Th	0.824	0.294	0.752	1.039	0.582	0.500
La	10.96	3.37	5.87	16.44	3.56	8.40
Ce	25.12	9.41	10.11	36.90	7.44	25.40
Nd	15.91	6.82	7.47	23.04	5.52	16.30
Y	36.84	19.99	23.59	44.18	21.85	35.80
Yb	4.14	2.76	3.29	3.73	2.84	
U	0.389	0.395	0.342	0.358	0.029	
Ta	2.58	1.50	2.28	2.96	1.73	
Co	55.15	46.51	48.07	41.78	52.72	
Hf	3.515	1.615	3.312	5.509	2.865	
La ID						
Ce ID						
Nd ID						
Sm ID						
Eu ID						
Gd ID						
Dy ID						
Er ID						
Yb ID						
Lu ID						
P (GPa)						

	Intra glacial					
	Vindbelgjarfjall		*Namafjall Rigde*		*nr. Krafla Caldera*	
	DL013	DL015	DL033	DL034	DL046	DL048
SiO_2	48.35	50.18	48.72	57.09	48.35	74.33
Al_2O_3	15.78	15.85	15.31	11.25	14.93	12.19
Fe_2O_3	10.35	9.99	11.13	13.08	11.29	3.53
MgO	9.68	8.20	8.64	4.87	10.61	0.45
CaO	12.15	11.83	13.27	8.78	11.82	1.84
Na_2O	2.060	2.260	1.660	1.990	1.570	4.210
K_2O	0.132	0.292	0.069	0.275	0.145	2.740
TiO_2	0.857	1.011	1.058	1.887	1.224	0.460
MnO	0.167	0.178	0.181	0.201	0.171	0.080
P_2O_5	0.100	0.149	0.103	0.202	0.133	0.079
Cr_2O_3						
Total	99.63	99.93	100.13	99.63	100.03	99.90
LOI	-0.7	-0.5	-0.2	-0.4	1.4	0.1
	12.66	4.04	5.39		8.68	
Ni	191.70	136.50	111.70	42.30	215.70	3.20
Cr	457.50	365.50	351.10	98.10	529.50	2.80
V	221	234	279	377	280	7
Sc	37.5	39.5	44.7	40.9	37.3	7.4
Cu	68	102	136	112	100	12
Zn	70.6	80.9	76.8	101.9	75.0	46.2
Cl	-17.00	15.00	-25.00	81.00	-21.00	24.00
Ga	15.90	15.50	15.00	16.20	14.80	16.60
Pb	**0.358**	0.400	**0.276**	**0.695**	**0.403**	3.700
Sr	105.4	111.0	114.3	139.1	159.5	77.2
Rb	1.900	4.380	0.730	5.180	1.410	68.800
Ba	**29.50**	56.60	**15.10**	**65.70**	**71.30**	534.80
Zr	**63.31**	118.80	**49.87**	**106.47**	**63.37**	463.40
Nb	4.97	8.80	4.61	12.00	7.22	36.80
Th	**0.295**	1.000	**0.201**	**0.578**	**0.388**	7.700
La	5.00	9.60	3.60	8.80	6.40	42.20
Ce	11.90	21.00	12.80	22.00	13.80	85.40
Nd	8.80	13.00	8.00	14.80	8.30	40.30
Y	22.70	29.40	21.30	29.60	19.30	73.80
Yb						
U	**0.096**		**0.070**		**0.182**	**0.118**
Ta						
Co						
Hf	**1.708**		**1.394**	**2.809**	**1.680**	
La ID	4.416		3.397	8.446	6.319	
Ce ID	11.024		8.885	21.038	15.503	
Nd ID	7.564		6.816	14.411	10.525	
Sm ID	2.268		2.167	4.002	2.970	
Eu ID	0.847		0.843	1.409	1.067	
Gd ID	3.036		2.956	4.843	3.565	
Dy ID	3.588		3.492	5.162	3.803	
Er ID	2.258		2.188	3.074	2.254	
Yb ID	2.156		2.079	2.865	2.091	
Lu ID			0.519			
P (GPa)	0.607	0.308	0.336		0.706	

	Inter glacial					
	Grimsstadaheidi		*Sandabotnafjall*	*Holasandur*	*Grænavatnsoruni*	
	JPF0971	DL053	DL055	*JPF1006*	JPF0909	JPF0910
SiO_2	49.78	48.07	74.81	49.03	47.36	47.20
Al_2O_3	14.20	15.40	12.02	14.95	15.46	16.00
Fe_2O_3	11.82	10.86	3.61	11.01	11.82	11.09
MgO	8.12	9.70	0.16	8.02	9.80	10.24
CaO	12.95	12.64	1.71	12.97	12.12	12.06
Na_2O	1.895	1.740	4.480	1.881	1.729	1.775
K_2O	0.133	0.093	2.727	0.148	0.096	0.109
TiO_2	1.029	0.900	0.246	1.165	1.236	1.164
MnO	0.192	0.178	0.102	0.182	0.180	0.175
P_2O_5	0.084	0.075	0.032	0.111	0.107	0.109
Cr_2O_3	0.005		0.005	0.054		0.041
Total	100.20	99.66	99.90	99.54	99.90	99.98
LOI	-0.6	-0.7	0.1	-0.4	-0.4	-0.3
	5.77					
Ni	80.40	171.20	2.20	91.60	196.40	197.50
Cr	193.70	392.20	3.30	351.30	423.30	297.50
V	298	247	5	280	247	226
Sc	46.9	37.9	5.3	46.5	35.3	33.1
Cu	132	126	9	139	123	107
Zn	81.0	69.3	134.3	75.1	78.1	75.3
Cl	-90.00	-3.00	406.00	35.00	-123.30	-112.50
Ga	14.50	14.90	21.30	15.30	16.20	15.20
Pb	**0.357**	0.400	4.300	0.400	-0.300	0.600
Sr	104.2	106.2	94.7	138.2	141.6	152.2
Rb	2.800	1.340	63.200	2.500	1.300	0.700
Ba	**27.40**	26.00	533.10	41.00	23.60	27.20
Zr	**55.15**	29.60	555.20	60.00	57.70	59.60
Nb	4.60	3.14	61.20	5.60	5.00	6.90
Th	1.000	0.900	8.000	0.700	0.200	-0.500
La	2.80	2.30	60.10	6.20	3.00	13.00
Ce	8.20	8.10	123.20	13.30	12.60	13.00
Nd	6.60	6.20	64.60	8.90	7.90	8.00
Y	23.60	17.90	106.50	20.60	20.60	19.10
Yb				2.90		
U				0.200		
Ta				0.70		
Co				46.90		
Hf	**1.593**					
La ID	3.239					
Ce ID	8.115					
Nd ID	6.056					
Sm ID	1.958					
Eu ID	0.740					
Gd ID	2.719					
Dy ID	3.304					
Er ID	2.113					
Yb ID	2.043					
Lu ID	0.309					
P (GPa)	0.067			0.170	0.853	0.956

	Fremri Námur				*Main rifting event*		
	Older Laxárhraun		*Burfellshraun*		*Sveinahraun*		*Randarholar*
	JPF0906	JPF0908	JPF0915	JPF0916	JPF0917	JPF0918	JPF0950
SiO_2	48.19	48.42	48.70	48.77	49.35	49.42	49.36
Al_2O_3	15.40	15.25	14.91	14.68	13.74	13.82	13.68
Fe_2O_3	13.04	12.90	12.64	13.14	13.89	13.70	13.76
MgO	7.04	7.55	7.43	7.48	6.90	6.91	6.86
CaO	12.01	11.96	11.98	11.93	11.50	11.49	11.55
Na_2O	1.964	1.921	2.132	2.058	2.296	2.303	2.323
K_2O	0.155	0.151	0.198	0.199	0.249	0.244	0.246
TiO_2	1.620	1.527	1.601	1.604	1.758	1.709	1.722
MnO	0.206	0.198	0.204	0.204	0.219	0.224	0.215
P_2O_5	0.137	0.130	0.150	0.159	0.182	0.160	0.165
Cr_2O_3			0.022				
Total	99.76	100.00	100.00	100.21	100.08	99.97	99.88
LOI	-0.6	-0.7	1.7	-0.6	-0.3	-0.7	-0.7
Ni	83.00	88.70	83.50	87.10	60.70	60.90	58.70
Cr	218.10	242.00	153.20	159.70	68.20	70.70	70.80
V	324	312	325	335	363	370	376
Sc	42.9	41.3	43.3	45.3	46.8	46.6	47.4
Cu	155	130	147	151	157	161	164
Zn	97.5	92.8	93.2	95.0	100.6	97.6	100.1
Cl	-115.80	-101.40	-93.50	-81.20	-71.80	-70.70	-68.80
Ga	18.10	17.10	17.30	18.20	18.30	17.20	17.40
Pb	**0.376**	2.000	1.900	1.500	2.800	1.700	1.600
Sr	169.6	164.1	172.6	171.2	154.7	153.3	154.3
Rb	2.100	2.600	3.200	3.200	4.800	4.300	4.400
Ba	**34.20**	34.20	43.50	44.70	52.30	48.10	47.70
Zr	**69.62**	69.90	87.30	88.90	99.00	96.40	95.60
Nb	7.50	7.40	9.20	9.20	9.80	9.80	9.20
Th	0.400	0.400	1.100	1.000	0.900	-0.500	0.600
La	3.00	3.30	4.60	4.00	6.70	7.30	6.50
Ce	14.30	12.60	17.80	18.80	21.50	21.30	20.60
Nd	10.30	10.30	10.60	11.40	12.90	13.70	12.90
Y	23.90	23.30	25.10	25.80	30.30	29.30	29.40
Yb							
U							
Ta							
Co							
Hf		**1.953**					
La ID	4.861						
Ce ID	12.659						
Nd ID	9.604						
Sm ID	2.896						
Eu ID	1.116						
Gd ID	3.676						
Dy ID	4.051						
Er ID	2.434						
Yb ID	2.276						
Lu ID	0.341						
P (GPa)	0.611	0.604	0.450	0.470	0.300	0.286	0.254

		Kerlingarhraun			*Fosshraun*	*Basement*	
	JPF0970	JPF0958	JPF0964	JPF0968	JPF0945	JPF0919	JPF0921
SiO_2	49.25	49.60	49.46	49.41	50.16	47.99	48.25
Al_2O_3	13.72	13.88	13.72	13.77	13.60	14.96	16.42
Fe_2O_3	13.83	13.59	13.78	13.69	14.31	12.11	10.35
MgO	6.85	6.99	6.82	6.96	6.04	9.93	9.43
CaO	11.47	11.57	11.53	11.55	10.47	11.57	13.08
Na_2O	2.282	2.219	2.192	2.245	2.498	1.933	1.730
K_2O	0.247	0.240	0.237	0.235	0.383	0.150	0.080
TiO_2	1.722	1.693	1.734	1.699	1.957	1.226	0.912
MnO	0.215	0.219	0.219	0.223	0.225	0.190	0.169
P_2O_5	0.166	0.165	0.168	0.163	0.211	0.113	0.074
Cr_2O_3							
Total	99.76	100.17	99.86	99.96	99.85	100.18	100.49
LOI	-0.2	-0.6	-0.3	-0.6	-0.4	-0.7	-0.5
Ni	60.00	59.50	58.50	61.00	41.70	204.30	153.80
Cr	66.70	68.30	66.90	72.10	29.70	457.10	370.40
V	373	361	359	377	399	278	224
Sc	45.6	44.6	45.6	46.6	45.1	37.0	35.9
Cu	172	119	154	141	150	123	110
Zn	97.3	94.6	94.6	100.2	111.1	85.7	63.1
Cl	-70.30	-54.60	-85.30	14.20	-4.30	-106.20	-143.70
Ga	17.20	18.60	17.60	17.40	17.70	17.00	15.90
Pb	1.000	0.500	1.400	1.200	**0.854**	0.900	-0.200
Sr	154.0	155.2	154.2	151.9	181.2	154.3	134.7
Rb	4.900	4.600	4.100	4.400	7.900	2.700	0.800
Ba	52.80	52.60	54.20	45.10	**77.00**	36.10	19.30
Zr	97.60	95.10	96.90	94.50	**126.27**	60.50	42.60
Nb	10.00	9.50	9.60	9.20	12.90	5.50	3.10
Th	0.100	0.800	-0.200	0.100	**0.936**	-0.200	-0.600
La	6.00	7.20	6.10	6.20	9.80	2.80	1.70
Ce	17.20	18.70	21.30	17.00	28.50	11.80	7.90
Nd	12.30	12.70	13.80	12.90	14.90	8.10	5.30
Y	30.30	28.70	28.70	28.90	32.60	20.60	17.20
Yb							
U					**0.286**		
Ta							
Co							
Hf					**3.356**		
La ID					10.478		
Ce ID					25.312		
Nd ID					16.532		
Sm ID					4.505		
Eu ID					1.567		
Gd ID					5.357		
Dy ID					5.668		
Er ID					3.347		
Yb ID					3.108		
Lu ID							
P (GPa)	0.289	0.276	0.265	0.277	0.284	0.789	

		Intra glacial		Inter glacial		
		Nupar	*Snartarathanupur*	*Hrossaborg*		*Dettifoss*
	JPF0922	JPF0957	JPF0959	JPF0943	JPF0944	JPF0946
SiO_2	48.05	48.86	49.07	50.02	48.76	49.19
Al_2O_3	15.98	13.50	14.09	13.86	14.82	13.60
Fe_2O_3	10.43	14.61	13.43	13.87	12.73	14.46
MgO	9.96	6.38	6.81	5.77	6.94	6.38
CaO	12.84	10.56	11.82	10.27	11.78	10.97
Na_2O	1.712	2.407	2.325	2.752	2.281	2.519
K_2O	0.081	0.337	0.203	0.566	0.221	0.258
TiO_2	0.917	2.590	1.847	2.401	1.892	2.253
MnO	0.172	0.228	0.215	0.217	0.199	0.224
P_2O_5	0.070	0.280	0.183	0.280	0.181	0.220
Cr_2O_3					0.027	0.011
Total	100.20	99.75	99.99	100.01	99.85	100.10
LOI	-0.5	-0.6	-0.7	-0.6	-0.4	-0.7
					3.75	1.77
Ni	190.20	74.40	54.90	37.70	66.10	52.80
Cr	434.70	161.00	137.10	40.50	185.00	53.50
V	236	382	353	355	298	358
Sc	37.6	40.6	46.3	37.8	40.1	41.0
Cu	111	117	150	127	163	151
Zn	67.7	120.1	102.4	106.0	89.6	103.7
Cl	-126.10	99.10	-41.30	26.40	-66.20	-47.50
Ga	14.60	20.40	18.20	18.90	19.50	19.70
Pb	**0.270**	1.100	1.500	2.600	0.300	2.300
Sr	129.7	191.2	168.1	234.0	181.8	187.2
Rb	1.000	6.700	2.800	10.900	3.300	4.000
Ba	**15.80**	64.30	41.40	119.20	48.40	58.50
Zr	**42.34**	169.10	103.50	185.30	109.50	132.20
Nb	3.00	16.70	9.50	18.80	10.10	11.30
Th	**0.143**	-0.400	0.200	1.100	0.900	2.000
La	0.70	10.50	7.40	16.60	9.60	10.20
Ce	8.40	30.30	23.40	41.40	22.30	28.90
Nd	4.80	20.60	14.40	23.50	14.90	16.60
Y	17.10	39.70	28.50	33.90	29.20	34.50
Yb						
U	**0.048**					
Ta						
Co						
Hf	**1.221**					
La ID	2.619					
Ce ID	7.005					
Nd ID	5.667					
Sm ID	1.844					
Eu ID	0.748					
Gd ID	2.496					
Dy ID	2.891					
Er ID	1.782					
Yb ID	1.682					
Lu ID	0.464					
P (GPa)	0.636	0.458	0.300	0.276	0.370	0.370

					Melrakkasletta	
	JPF0947	JPF0948	JPF0949	JPF0951	JPF0961	JPF0962
SiO_2	49.45	49.24	49.05	48.92	48.99	48.74
Al_2O_3	13.93	13.54	14.10	15.98	14.06	14.51
Fe_2O_3	13.77	14.09	12.94	11.34	14.45	12.61
MgO	6.86	6.40	6.98	7.22	5.89	7.43
CaO	11.51	11.18	11.69	12.97	10.78	12.10
Na_2O	2.295	2.442	2.353	2.034	2.522	2.240
K_2O	0.239	0.311	0.269	0.136	0.286	0.178
TiO_2	1.742	2.196	1.857	1.373	2.428	1.685
MnO	0.215	0.222	0.204	0.185	0.227	0.204
P_2O_5	0.158	0.218	0.177	0.113	0.245	0.157
Cr_2O_3	0.009					
Total	100.21	99.83	99.62	100.27	99.88	99.85
LOI	-0.4	-0.6	-0.6	-0.4	-0.5	-0.7
	3.27	0.86	3.42	4.59	0.07	5.55
Ni	59.20	51.00	57.10	67.10	65.80	80.50
Cr	68.60	99.20	118.60	197.80	88.30	215.80
V	371	322	314	294	366	303
Sc	46.3	41.2	40.2	41.0	40.7	42.2
Cu	155	128	124	136	116	121
Zn	100.4	99.8	92.1	78.1	108.3	87.9
Cl	-63.30	-3.40	-46.50	-79.40	36.40	-60.10
Ga	17.70	19.50	20.50	16.90	20.70	19.20
Pb	-0.600	1.900	0.900	1.700	1.900	1.700
Sr	152.1	190.8	190.9	169.0	193.2	172.6
Rb	4.200	5.500	4.900	2.000	5.300	1.500
Ba	48.60	61.80	53.30	28.60	66.50	40.40
Zr	96.30	135.80	115.80	70.40	149.60	88.50
Nb	10.00	11.50	10.60	6.10	13.60	8.80
Th	-0.200	0.500	0.900	0.900	1.300	1.300
La	13.30	13.20	7.10	4.60	15.00	7.30
Ce	20.70	26.70	25.90	12.00	29.60	18.90
Nd	12.60	16.90	15.40	10.00	18.70	11.10
Y	29.00	34.00	29.30	22.60	37.00	27.30
Yb						
U						
Ta						
Co						
Hf						
La ID						
Ce ID						
Nd ID						
Sm ID						
Eu ID						
Gd ID						
Dy ID						
Er ID						
Yb ID						
Lu ID						
P (GPa)	0.306	0.275	0.263	0.350	0.461	0.345

		Askja	*Caldera fissure eruptions*			
	Axarfjaðrarheiði	*1961 AD*				*1920 AD*
	JPF0969	JPF0932	JPF0933	JPF0934	JPF0938	JPF0935
SiO_2	48.85	49.88	50.43	50.02	50.06	50.03
Al_2O_3	14.30	12.67	12.89	12.72	12.76	12.75
Fe_2O_3	12.90	16.63	16.84	16.67	16.70	16.77
MgO	7.10	4.89	4.74	4.66	4.70	4.70
CaO	12.20	8.92	9.01	8.92	8.95	8.95
Na_2O	2.214	2.750	2.900	2.825	2.769	2.787
K_2O	0.199	0.544	0.551	0.548	0.540	0.545
TiO_2	1.819	2.722	2.778	2.769	2.742	2.723
MnO	0.205	0.255	0.258	0.257	0.263	0.255
P_2O_5	0.180	0.320	0.317	0.308	0.322	0.310
Cr_2O_3						0.004
Total	99.96	99.58	100.71	99.70	99.81	99.90
LOI	-0.6	-0.9	-1.4	1.1	-0.9	-0.8
	3.84					
Ni	63.70	27.00	26.80	25.50	27.90	28.80
Cr	139.30	25.80	25.20	22.70	23.40	30.60
V	330	488	492	484	482	495
Sc	42.0	42.6	43.0	41.7	43.5	43.6
Cu	159	115	114	109	114	116
Zn	92.2	138.4	138.6	138.3	137.0	138.1
Cl	-86.00	79.10	68.00	44.40	93.80	90.20
Ga	17.20	18.70	20.80	22.50	21.30	21.00
Pb	2.000	1.200	2.800	3.700	1.200	**1.320**
Sr	177.9	180.2	183.4	180.9	182.8	180.3
Rb	3.200	11.300	12.100	12.000	11.400	10.700
Ba	45.90	108.30	115.00	111.40	115.60	**111.40**
Zr	101.00	182.70	184.80	184.40	184.90	**181.98**
Nb	9.10	20.70	20.80	20.30	20.50	20.30
Th	1.300	2.200	1.500	2.900	3.100	**1.510**
La	6.40	16.10	17.60	15.20	15.10	14.80
Ce	21.50	36.70	40.50	41.40	45.50	39.90
Nd	13.60	22.60	24.60	24.60	24.70	23.80
Y	27.90	44.30	45.20	44.00	45.10	44.30
Yb						
U						**0.497**
Ta						
Co						
Hf						**4.780**
La ID						14.447
Ce ID						34.802
Nd ID						22.244
Sm ID						5.926
Eu ID						1.979
Gd ID						7.471
Dy ID						7.942
Er ID						4.681
Yb ID						4.346
Lu ID						0.302
P (GPa)	0.282	0.463		0.437	0.456	

	1875 AD	*1477-2900 BP*		*2900-3500*	*Flatadyngja*	*Svartadyngja*
	JPF0920	JPF0937	JPF0939	*JPF0940*	JPF0928	JPF0931
SiO_2	49.93	50.69	49.87	49.39	49.34	47.64
Al_2O_3	12.75	12.91	12.76	13.96	14.51	15.08
Fe_2O_3	16.79	16.43	16.82	14.36	12.69	13.24
MgO	4.74	4.57	4.78	6.47	7.24	8.51
CaO	8.99	8.76	9.08	10.95	11.93	11.41
Na_2O	2.794	2.771	2.739	2.301	2.230	2.160
K_2O	0.534	0.555	0.498	0.295	0.259	0.294
TiO_2	2.731	2.652	2.699	1.870	1.607	1.703
MnO	0.253	0.259	0.257	0.225	0.210	0.193
P_2O_5	0.310	0.327	0.310	0.187	0.167	0.187
Cr_2O_3				0.006		0.055
Total	99.83	99.92	99.80	100.06	100.18	100.49
LOI	-1.1	-0.8	-0.9	0.0	-0.6	-1.2
Ni	26.40	23.80	27.40	48.40	69.10	138.50
Cr	21.20	9.60	25.80	92.00	211.80	371.20
V	486	463	508	401	336	308
Sc	41.7	42.7	45.0	47.6	44.0	38.0
Cu	120	136	125	142	145	119
Zn	136.8	135.8	140.9	106.3	88.0	90.6
Cl	60.50	13.60	31.10	97.00	-36.40	-14.00
Ga	19.80	19.80	21.10	18.80	18.00	17.30
Pb	1.900	**1.190**	1.600	0.500	-1.500	1.900
Sr	181.9	180.3	177.7	174.5	176.2	224.4
Rb	11.100	11.300	10.300	5.500	4.400	5.100
Ba	114.80	**116.30**	104.70	74.00	52.20	70.40
Zr	180.00	**183.24**	175.40	107.80	92.00	97.90
Nb	20.20	19.50	19.20	12.10	9.30	11.10
Th	2.100	**1.437**	1.600	0.800	-0.200	1.400
La	14.10	14.90	13.20	7.70	6.10	8.60
Ce	42.70	41.10	38.50	22.40	21.10	20.10
Nd	24.50	23.80	22.10	13.50	13.10	12.10
Y	44.10	44.30	44.20	29.70	25.50	23.50
Yb				4.00		
U				0.500		
Ta				0.50		
Co				51.90		
Hf		**4.846**				
La ID		16.013				
Ce ID		37.993				
Nd ID		23.951				
Sm ID		6.355				
Eu ID		2.115				
Gd ID		7.457				
Dy ID		7.780				
Er ID		4.592				
Yb ID		4.263				
Lu ID		0.647				
P (GPa)	0.467	0.426	0.478	0.418	0.298	0.849

						Inter glacial
	Dyngjufjallahraun	*Trölladyngja*	*Basement*			*Vadalda*
	JPF0942	DL002	JPF0927	JPF0926	*JPF0924*	JPF0941
SiO_2	50.03	48.67	47.94	48.18	48.81	48.09
Al_2O_3	13.09	16.22	14.92	15.55	14.97	16.65
Fe_2O_3	15.81	10.19	11.38	11.58	13.02	10.27
MgO	5.24	8.07	9.76	8.93	7.21	8.76
CaO	9.58	13.79	11.56	11.38	11.14	12.96
Na_2O	2.598	1.830	1.895	2.117	2.311	1.698
K_2O	0.469	0.079	0.256	0.320	0.346	0.077
TiO_2	2.471	0.922	1.365	1.511	1.797	0.967
MnO	0.244	0.172	0.182	0.182	0.200	0.168
P_2O_5	0.273	0.078	0.158	0.188	0.202	0.074
Cr_2O_3				0.045	0.029	0.065
Total	99.80	100.02	99.42	100.03	100.09	99.80
LOI	-0.8	-0.5	-0.7	-0.7	0.9	-0.1
		7.19				
Ni	41.20	91.90	197.30	156.30	89.40	154.30
Cr	70.80	307.50	522.70	335.50	214.50	403.70
V	462	259	266	264	350	223
Sc	43.5	44.3	36.9	35.5	40.6	35.1
Cu	132	117	107	100	128	92
Zn	127.4	67.5	81.3	83.4	94.4	64.8
Cl	3.30	-10.00	-14.10	-5.10	112.00	-151.60
Ga	19.30	15.20	19.00	22.50	18.30	15.70
Pb	1.700	**0.254**	**0.607**	-0.200	0.600	**0.240**
Sr	178.5	122.5	174.4	217.4	199.4	130.7
Rb	9.500	1.250	4.000	5.600	6.900	1.700
Ba	101.60	**14.50**	**57.10**	73.80	85.00	**22.30**
Zr	159.30	**44.78**	**86.05**	98.50	98.50	**43.22**
Nb	17.10	3.18	9.50	11.70	11.70	3.50
Th	0.500	**0.200**	-0.400	1.000	0.800	-0.200
La	13.20	3.50	6.50	7.40	7.70	1.90
Ce	33.20	7.60	20.90	20.40	21.80	8.20
Nd	21.00	6.20	11.50	13.10	13.60	5.70
Y	40.00	18.50	22.10	22.20	25.20	17.90
Yb					2.20	
U		**0.062**			0.200	
Ta					0.60	
Co					49.00	
Hf		**1.299**	**2.348**			**1.226**
La ID		2.607	7.361			2.861
Ce ID		7.006	17.682			7.560
Nd ID		5.733	11.551			5.888
Sm ID		1.903	3.102			1.859
Eu ID		0.757	1.120			0.747
Gd ID		2.615	3.648			2.509
Dy ID		3.072	3.789			2.962
Er ID		1.909	2.207			1.865
Yb ID		1.808	2.025			1.789
Lu ID		0.270	0.252			0.636
P (GPa)	0.397	0.272	0.671			

				Kverkfjöll			
	Oskavatan			*Kverkfjallahraun*			
	JPF0936	JPF0923	JPF0925	*JPF1022*	*JPF1021*	*JPF1019*	*JPF1020*
SiO_2	48.48	49.94	47.30	50.76	50.83	48.66	48.78
Al_2O_3	19.82	13.83	14.96	13.07	13.08	13.13	13.28
Fe_2O_3	8.27	13.90	12.25	15.78	15.73	16.37	16.22
MgO	6.07	5.79	9.31	3.92	3.93	4.85	4.82
CaO	14.19	10.33	11.67	8.05	8.04	9.22	9.27
Na_2O	1.745	2.712	1.980	3.120	3.116	2.840	2.838
K_2O	0.186	0.556	0.208	0.765	0.764	0.581	0.575
TiO_2	1.040	2.394	1.641	3.043	3.044	2.941	2.893
MnO	0.132	0.212	0.191	0.268	0.267	0.248	0.244
P_2O_5	0.106	0.274	0.152	0.504	0.504	0.374	0.367
Cr_2O_3					0.002	0.002	0.005
Total	100.05	99.94	99.67	99.36	99.39	99.25	99.32
LOI	1.2	-0.6	0.0	-1.0	-1.0	-1.2	-0.9
Ni	66.60	37.70	167.80	3.00	3.10	27.00	24.00
Cr	191.10	38.60	402.60	2.00	15.40	18.60	15.60
V	217	327	277	300	279	375.90	373
Sc	36.9	36.2	34.5	35.7	37.5	40.00	37.0
Cu	102	126	120	32	29	127.20	124
Zn	57.7	100.8	84.4	143.1	144.5	122.00	119.0
Cl	-108.80	26.70	-63.50	231.00	242.00	200.00	197.00
Ga	16.90	20.30	21.20	22.80	22.50	25.40	22.40
Pb	-0.900	0.300	1.400	1.200	0.900	3.50	0.500
Sr	194.4	240.4	194.3	247.3	246.8	247.30	244.3
Rb	3.200	10.800	3.400	14.100	14.800	14.00	11.000
Ba	37.70	117.00	51.60	157.00	156.00	133.00	130.00
Zr	59.50	185.30	81.60	242.50	252.10	197.90	194.90
Nb	6.90	18.50	8.60	26.10	26.90	22.80	19.80
Th	0.000	2.000	1.100	2.300	2.000	4.40	1.400
La	5.20	15.70	6.30	20.80	20.80	20.00	17.00
Ce	17.10	39.20	17.70	51.10	52.20	43.60	40.60
Nd	9.90	23.80	11.30	31.70	32.60	30.10	27.10
Y	16.20	34.90	22.50	45.30	46.90	41.00	38.00
Yb				5.00	4.20	7.10	4.10
U				1.000	0.900	3.500	0.500
Ta				1.80	1.30	4.10	1.10
Co				40.90	40.10	48.10	45.10
Hf							
La ID							
Ce ID							
Nd ID							
Sm ID							
Eu ID							
Gd ID							
Dy ID							
Er ID							
Yb ID							
Lu ID							
P (GPa)		0.275	0.792	0.430	0.424	0.569	0.585

			Krepputunga				
	JPF1015	*JPF1018*	*JPF1010*	*JPF1011*	*JPF1012*	*JPF1013*	*JPF1014*
SiO_2	49.29	49.65	48.80	48.51	48.60	48.76	48.73
Al_2O_3	13.09	13.94	16.39	16.98	16.89	15.49	15.40
Fe_2O_3	16.45	13.95	10.41	10.19	10.30	10.98	11.11
MgO	4.63	5.81	7.35	7.02	6.87	7.76	7.46
CaO	8.95	10.39	13.22	13.37	13.27	13.21	12.95
Na_2O	2.929	2.706	1.955	1.900	1.977	1.986	2.000
K_2O	0.637	0.543	0.130	0.129	0.131	0.135	0.141
TiO_2	3.030	2.444	1.232	1.201	1.241	1.301	1.328
MnO	0.250	0.212	0.170	0.164	0.168	0.180	0.181
P_2O_5	0.388	0.271	0.105	0.103	0.108	0.110	0.114
Cr_2O_3	0.005	0.005	0.031	0.033	0.029	0.036	0.029
Total	99.68	100.00	99.81	99.62	99.63	99.97	99.46
LOI	-1.0	-0.4	-0.5		-0.5	-0.8	-0.6
Ni	19.80	24.80	69.90	66.90	71.90	78.50	74.60
Cr	10.10	31.70	221.50	218.50	190.40	235.50	234.70
V	407	408	247	243.50	272	291	283
Sc	38.1	41.9	38.2	35.20	40.1	43.9	41.7
Cu	122	113	133	130.20	125	138	147
Zn	132.0	120.1	64.5	61.50	72.4	75.6	73.3
Cl	209.00	181.00	38.00	35.00	40.00	44.00	42.00
Ga	22.20	20.30	17.00	14.00	16.80	17.00	16.80
Pb	0.800	0.500	0.400	-2.60	0.300	0.300	0.100
Sr	240.5	225.9	158.2	155.20	157.7	153.5	154.0
Rb	12.100	10.000	2.300	-0.70	2.100	2.400	2.400
Ba	136.00	131.00	35.00	32.00	32.00	34.00	33.00
Zr	210.20	185.90	63.10	60.10	65.30	65.80	67.70
Nb	22.20	19.30	6.10	3.10	6.50	6.40	6.60
Th	1.700	1.400	0.700	-2.30	0.400	0.400	0.400
La	17.50	16.70	4.40	1.40	3.80	5.00	5.40
Ce	46.00	39.90	12.20	9.20	12.40	12.30	11.90
Nd	27.10	27.40	8.50	5.50	8.70	8.60	9.00
Y	39.80	35.60	19.90	16.90	20.10	20.90	21.40
Yb	4.30	3.20	2.60	-0.40	2.60	2.70	2.40
U	0.800	0.900	0.300	-2.700	0.000	0.500	0.500
Ta	1.40	1.50	0.20	-2.80	0.50	0.10	0.20
Co	47.30	49.10	44.40	41.40	43.20	46.90	45.70
Hf							
La ID							
Ce ID							
Nd ID							
Sm ID							
Eu ID							
Gd ID							
Dy ID							
Er ID							
Yb ID							
Lu ID							
P (GPa)	0.546	0.319	0.317	0.382			0.245

	Intra glacial		Inter glacial			***Fjallgarðpar***	
	Lindafjoll					*Modrudalur*	
	JPF1016	*JPF1023*	*JPF1007*	*JPF1008*	*JPF1009*	JPF0973	JPF0974
SiO_2	49.49	48.35	49.60	49.71	49.06	49.24	49.02
Al_2O_3	13.48	15.27	13.48	13.46	14.02	16.61	13.50
Fe_2O_3	16.13	13.57	16.14	15.97	15.19	11.96	14.61
MgO	4.98	5.53	4.98	5.03	5.07	5.47	6.41
CaO	9.33	10.54	9.46	9.48	9.87	11.69	11.07
Na_2O	2.737	2.575	2.825	2.765	2.662	2.388	2.481
K_2O	0.571	0.542	0.482	0.523	0.443	0.433	0.271
TiO_2	2.895	2.716	2.603	2.561	2.452	1.988	2.325
MnO	0.248	0.206	0.240	0.238	0.231	0.178	0.222
P_2O_5	0.373	0.349	0.291	0.288	0.266	0.229	0.233
Cr_2O_3		0.009		0.003	0.003		
Total	100.26	99.73	100.12	100.04	99.29	100.19	100.15
LOI	-0.6	-0.4	-0.8	-0.8	-0.7	-0.3	-0.5
Ni	39.00	37.30	25.10	26.10	27.50	62.20	60.00
Cr	43.00	80.60	22.40	26.60	24.20	25.40	23.60
V	368	356	432	415	384	434	435
Sc	38.3	33.5	42.5	40.9	41.0	38.9	40.0
Cu	146	80	125	120	168	138	140
Zn	113.8	108.3	127.5	120.3	115.5	123.5	122.4
Cl	218.00	215.00	92.00	110.00	88.00	92.30	94.50
Ga	21.30	21.10	20.70	20.70	21.00	20.30	18.90
Pb	0.500	0.900	0.900	0.600	0.800	1.000	2.400
Sr	265.1	263.3	217.2	217.9	222.4	267.2	180.4
Rb	10.200	9.400	7.800	9.700	7.700	8.700	5.400
Ba	116.00	122.00	128.00	124.00	119.00	62.30	60.00
Zr	174.80	170.90	176.70	176.20	163.50	140.50	131.90
Nb	18.50	19.40	18.70	18.50	17.00	15.40	12.60
Th	1.400	1.000	1.400	1.500	1.300	0.500	0.900
La	13.40	15.20	14.80	15.10	15.20	18.20	21.20
Ce	31.00	39.90	37.30	37.50	36.60	39.60	42.60
Nd	19.90	23.70	22.70	22.60	22.90	25.90	28.90
Y	32.00	32.30	36.30	36.20	34.30	37.30	40.30
Yb	2.70	3.00	4.30	4.10	3.70	6.70	9.70
U	0.400	0.500	0.400	0.700	0.500	3.500	6.500
Ta	0.70	1.00	0.80	0.70	1.20	4.20	7.20
Co	47.70	40.60	50.90	48.20	47.70	50.70	53.70
Hf							
La ID							
Ce ID							
Nd ID							
Sm ID							
Eu ID							
Gd ID							
Dy ID							
Er ID							
Yb ID							
Lu ID							
P (GPa)	0.579	0.652	0.533	0.497	0.541		0.374

	Vegahnjukur DL074
SiO_2	48.91
Al_2O_3	13.28
Fe_2O_3	15.70
MgO	5.16
CaO	9.59
Na_2O	2.770
K_2O	0.654
TiO_2	3.307
MnO	0.232
P_2O_5	0.346
Cr_2O_3	
Total	99.95
LOI	-0.3
Ni	30.30
Cr	34.10
V	469
Sc	38.6
Cu	106
Zn	122.8
Cl	175.00
Ga	20.30
Pb	1.100
Sr	232.4
Rb	12.270
Ba	132.40
Zr	213.80
Nb	22.80
Th	2.300
La	20.20
Ce	45.40
Nd	27.90
Y	38.30
Yb	
U	
Ta	
Co	
Hf	
La ID	
Ce ID	
Nd ID	
Sm ID	
Eu ID	
Gd ID	
Dy ID	
Er ID	
Yb ID	
Lu ID	
P (GPa)	0.483

APPENDIX 5: RADIOGENIC AND STABLE ISOTOPE DATA

Table A5.1: Radiogenic and Stable Isotope Data

	Krafla					
	DL040	DL059	DL038	DL062	DL010	DL011
87Sr/86Sr	0.703237	0.703234	0.703230	0.703230	0.703204	0.703196
2 se	0.000008	0.000009	0.000010	0.000010	0.000009	0.000010
144Nd/143Nd	0.513031	0.513035	0.513033	0.513038	0.513034	0.513049
2se	0.000005	0.000004	0.000003	0.000003	0.000004	0.000004
206Pb/204Pb		18.295	18.297			
2se		0.0019	0.0017			
207Pb/204Pb		15.461	15.462			
2se		0.0016	0.0015			
208Pb/204Pb		38.015	38.018			
2se		0.0042	0.0039			
Δ7/4		-1.33	-1.28			
Δ8/4		26.87	26.95			
177Hf/176Hf		0.283201	0.283201			
2se		0.000006	0.000007			
δ18O ol				3.89		
δ18O plag						

	JPF0901	JPF0902	DL003	JPF0907	DL022	DL006
87Sr/86Sr	0.703125	0.703126	0.703206		0.703220	0.703246
2 se	0.000008	0.000009	0.000011		0.000019	0.000010
144Nd/143Nd	0.513062	0.513063	0.513053	0.513061		0.513033
2se	0.000004	0.000004	0.000005	0.000004		0.000004
206Pb/204Pb		18.437	18.433			
2se		0.0023	0.0016			
207Pb/204Pb		15.463	15.457			
2se		0.0020	0.0014			
208Pb/204Pb		38.128	38.114			
2se		0.0053	0.0031			
Δ7/4		-2.67	-3.22			
Δ8/4		21.10	20.14			
177Hf/176Hf		0.283202	0.283204			
2se			0.000006			
δ18O ol			3.43			4.20
δ18O plag						

	Heiðarsporður					
	DL009	DL063	DL067	KK51	KR77	KR82
87Sr/86Sr	0.703231	0.703202	0.703170	0.703146	0.703144	0.703118
2 se	0.000025	0.000011	0.000009	0.000010	0.000008	0.000009
144Nd/143Nd	0.513033	0.513036	0.513062			
2se	0.000005	0.000004	0.000004			
206Pb/204Pb	18.289		18.326			
2se	0.0014		0.0015			
207Pb/204Pb	15.463		15.461			
2se	0.0011		0.0013			
208Pb/204Pb	38.012		38.023			
2se	0.0031		0.0034			
Δ7/4	-1.08		-1.71			
Δ8/4	27.42		23.94			
177Hf/176Hf	0.283194		0.283194			
2se	0.000010		0.000009			
δ18O ol			4.27			
δ18O plag			4.87			

	KR88	KR87	KR48	KK55	KR74	KR87A
87Sr/86Sr	0.703216	0.703144	0.703104	0.703174	0.703144	0.703138
2 se	0.000011	0.000010	0.000011	0.000010	0.000010	0.000010
144Nd/143Nd	0.513060		0.513039			
2se	0.000004		0.000004			
206Pb/204Pb						
2se						
207Pb/204Pb						
2se						
208Pb/204Pb						
2se						
Δ7/4 Δ8/4						
177Hf/176Hf						
2se						
δ18O ol δ18O plag			3.72	3.89		

	KK35	KK3	JPF0971	JPF1006	DL013	DL015
87Sr/86Sr	0.703223	0.703227	0.703154	0.703198	0.703147	0.703245
2 se	0.000012	0.000013	0.000012	0.000012	0.000010	0.000010
144Nd/143Nd		0.513042	0.513060	0.513029	0.513041	0.513031
2se		0.000006	0.000005	0.000004	0.000004	0.000004
206Pb/204Pb			18.307	18.331	18.433	
2se			0.0026	0.0015	0.0036	
207Pb/204Pb			15.461	15.467	15.466	
2se			0.0023	0.0012	0.0031	
208Pb/204Pb			38.018	38.064	38.106	
2se			0.0061	0.0030	0.0078	
Δ7/4			-1.41	-1.16	-2.33	
Δ8/4			25.76	27.47	19.43	
177Hf/176Hf			0.283201		0.283200	
2se			0.000008		0.000008	
δ18O ol					4.63	
δ18O plag						

					Fremri-Namur	
	DL033	DL034	DL046	DL048	JPF0908	JPF0916
87Sr/86Sr	0.703169	0.703268	0.703237	0.703249	0.703217	0.703225
2 se	0.000010	0.000009	0.000012	0.000039	0.000010	0.000008
144Nd/143Nd	0.513043	0.513019	0.513019	0.513026	0.513037	
2se	0.000004	0.000004	0.000004	0.000003	0.000004	
206Pb/204Pb	18.312		18.317		18.373	
2se	0.0026		0.0024		0.0014	
207Pb/204Pb	15.464		15.466		15.470	
2se	0.0023		0.0021		0.0013	
208Pb/204Pb	38.027		38.019		38.087	
2se	0.0059		0.0057		0.0035	
Δ7/4	-1.25		-1.10		-1.31	
Δ8/4	26.13		24.69		24.69	
177Hf/176Hf	0.283205	0.283157	0.283164		0.283191	
2se	0.000011	0.000011	0.000006		0.000008	
δ18O ol			3.99			
δ18O plag						

	JPF0917	JPF0950	JPF0958	JPF0945	JPF0922	JPF0944
87Sr/86Sr	0.703209	0.703203	0.703196	0.703226	0.703126	0.703213
2 se	0.000011	0.000011	0.000011	0.000012	0.000010	0.000010
144Nd/143Nd	0.513038		0.513043	0.513032	0.513020	
2se	0.000006		0.000004	0.000005	0.000004	
206Pb/204Pb			18.465	18.457	18.291	
2se			0.0018	0.0018	0.0034	
207Pb/204Pb			15.477	15.478	15.476	
2se			0.0011	0.0015	0.0030	
208Pb/204Pb			38.188	38.182	38.019	
2se			0.0031	0.0039	0.0078	
Δ7/4			-1.57	-1.42	0.24	
Δ8/4			23.64	24.02	27.88	
177Hf/176Hf				0.283179	0.283220	
2se				0.000006	0.000008	
δ18O ol						
δ18O plag						

	JPF0949	JPF0962	JPF0969	JPF0957	JPF0959	**Askja** JPF0938
87Sr/86Sr	0.703204	0.703199	0.703209	0.703183	0.703187	0.703239
2 se	0.000009	0.000009	0.000009	0.000010	0.000010	0.000009
144Nd/143Nd	0.515056	0.513050	0.513048	0.513050		0.513032
2se	0.000027	0.000004	0.000020	0.000005		0.000004
206Pb/204Pb	18.405	18.499	18.452	18.441		
2se	0.0017	0.0025	0.0018	0.0017		
207Pb/204Pb	15.453	15.460	15.467	15.460		
2se	0.0014	0.0017	0.0012	0.0014		
208Pb/204Pb	38.093	38.155	38.182	38.129		
2se	0.0042	0.0044	0.0032	0.0037		
Δ7/4	-3.29	-3.64	-2.41	-2.99		
Δ8/4	38.09	16.20	24.64	20.76		
177Hf/176Hf						
2se						
δ18O ol						
δ18O plag						

	JPF0935	JPF0937	JPF0940	JPF0927	JPF0924	DL002
87Sr/86Sr	0.703226	0.703255	0.703243	0.703264	0.703283	0.703041
2 se	0.000010	0.000010	0.000010	0.000009	0.000010	0.000009
144Nd/143Nd	0.513029	0.513038	0.513030	0.513019	0.513016	0.513102
2se	0.000004	0.000004	0.000004	0.000005	0.000005	0.000004
206Pb/204Pb	18.481	18.471		18.419		18.316
2se	0.0013	0.0018		0.0015		0.0028
207Pb/204Pb	15.479	15.477		15.478		15.446
2se	0.0012	0.0017		0.0013		0.0024
208Pb/204Pb	38.211	38.192		38.166		37.979
2se	0.0031	0.0049		0.0033		0.0061
Δ7/4	-1.50	-1.62		-0.97		-3.03
Δ8/4	24.08	23.38		26.94		20.88
177Hf/176Hf		0.283183		0.283180		0.283225
2se		0.000012		0.000008		0.000031
δ18O ol						3.70
δ18O plag						

					Kverkfjöll	
	JPF0941	JPF0936	JPF0925	JPF1018	JPF1010	JPF1012
87Sr/86Sr	0.703147	0.703242	0.703254	0.703324	0.703110	0.703121
2 se	0.000009	0.000010	0.000009	0.000011	0.000012	0.000009
144Nd/143Nd	0.513056	0.513013		0.513005	0.513074	0.513069
2se	0.000004	0.000004		0.000011	0.000013	0.000010
206Pb/204Pb	18.371	18.626		18.511	18.414	18.416
2se	0.0018	0.0031		0.0008	0.0017	0.0017
207Pb/204Pb	15.469	15.492		15.491	15.453	15.454
2se	0.0016	0.0026		0.0010	0.0014	0.0013
208Pb/204Pb	38.087	38.379		38.319	38.087	38.093
2se	0.0044	0.0071		0.0026	0.0036	0.0034
Δ7/4	-1.36	-1.81		-0.70	-3.45	-3.32
Δ8/4	24.96	23.33		31.17	19.72	20.06
177Hf/176Hf	0.283218					
2se	0.000006					
δ18O ol						
δ18O plag						

	JPF1007	JPF1009	JPF1023	DL074
87Sr/86Sr	0.703287	0.703280	0.703311	0.703320
2 se	0.000011	0.000010	0.000010	0.000009
144Nd/143Nd		0.513014	0.513007	0.513017
2se		0.000004	0.000005	0.000005
206Pb/204Pb				
2se				
207Pb/204Pb				
2se				
208Pb/204Pb				
2se				
Δ7/4				
Δ8/4				
177Hf/176Hf				
2se				
δ18O ol				4.07
δ18O plag				4.67

APPENDIX 6: GEOLOGICAL MAP

This map, which shows sample locations, was digitally compiled from the following sources:

Jónasson, 2005

Skovgaard et al., 2001

Jóhannesson and Sæmundsson, 1998

Sigvaldason et al., 1992

Sæmundsson, 1977

Sigbjarnarson et al., 1988

18° 00´ W
17° 00´ W
16° 00´ W
15° 00´ W
66° 00´ N
65°00´ N
18° 00´
17° 00´
16° 00´
15° 00´

APPENDIX 6:
GEOLOGICAL MAP OF THE NOTHERN RIFT ZONE

LEGEND

Bedrock:

Postglacial Basalts
- Younger than 1900 AD
- 1900 AD - ~2900 BP
- ~2900 BP - ~3500 BP
- > 3500 BP

- Hyaloclastite and tuffaceous sediment >0.7 Ma
- Basalts 0.7-3.3 Ma
- Basalts >3.3 Ma
- Rhyolite and dacite extrusives

Unconsolidated Deposits:
- Glaciers and ground moraine
- Alluvium
- Water

Symbols:
- Eruptive fissures, Holocene
- Lava flow boundary
- Sample Location

Dyngjufjallahraun - Name of lava flow

Þeitareykjabunga - Shield Volcano/ Hyaloclastite ridge

KISTUFELL - Central Volcano

Kræðuborgir - Crater row

SCALE 1:600 000

0 6 12 24 36 48 60

kilometers

Compiled as part of a thesis by J. F. Pernet-Fisher

ÖXARFJÖRÐUR
SKJÁLFANDI
Tjörnes
Melrakkaslétta
Snartarstaðarúpur
Valþjófsstaðafjall
Núpur
Axarfjarðarheiði
Ásbyrgi
Kerlingarhóll
Kerlingarhraun
Hvannstaðafjallgarður
Dimmifjallgarður
Hólssandur
Hrossaborg
ÞEISTAREYKIR
Þeitareykjabunga
Mælifell
Storaviti
Langaviti
Grjótháls
Borgarhraun
KRAFLA
Gæsafjöll
Krafla Fires
Dettifoss
Fosshraun
Jökulsá á Fjöllum
Randarhólar
Grímsstaðaheiði
Mývatn Fires
Sveinahraun
Gaðafoss
Vindbelgjarfjall
MÝVATN
Hverfjall
Younger Laxárhraun
Older Laxárhraun
Heiðarsporður
Kræðuborgir
Búfellshraun
Búfell
Rauðhólar
Nýjahraun
Skjálfandafljót
Bláfjall
Ketildyngja
Seffandafjall
FREMRI-NÁMUR
Kerlingardyngja
Herðubreiðarfjöll
Suðurárhraun
Utbruni
Eggert
Kollóttadyngja
Flatadyngja
Litladyngja
Svartadyngja
Herðubreið
Herðubreiðartögl
Arnaraalsada
Krepputunguhraun
Upptyppingar
Álftadalsdyngja
Þríhyrningsfjallgarður
FJALLGARÐUR
Frambruni
Dyngjufjöll ytri
ASKJA
ÖSKJUVATN
Dyngjufjöll
Dyngjufjallahraun
Vaðalda
Tröllադyngja
Urðarháls
KISTUFELL
Holuhraun
Kverkfjallahraun
Lindahraun
Lindafjöll
Dyngjujökull
Brúarjökull
VATNAJÖKULL
KVERKFJÖLL
Kverkjökull
SNÆFELL

Námafjall
Hverfjall
Hraunbunga
Lúdent
Dimmuborgir
Prengslaborgir
Bláfjallsfjallgarður
0 5 km 10

JPF0961 JPF0962 JPF0964 JPF0960 JPF0958 JPF0957 JPF0968 JPF0969 JPF0970 JPF0954 JPF0953 JPF0956 JPF0951 JPF0952 JPF0950 JPF0946 JPF0947 JPF0948 JPF0949 JPF0945 JPF0944 JPF0943 JPF0923 JPF0924 JPF0925 JPF0926 JPF0927 JPF0928 JPF0973 JPF1007 JPF0974 JPF1008 JPF1010 JPF1009 JPF1011 JPF0931 JPF0938 JPF0934 JPF0937 JPF0933 JPF0936 JPF0935 JPF0939 JPF0932 JPF0940 JPF0941 JPF1012 JPF1014 JPF0942 JPF1015 JPF1016 JPF1013 JPF1023 JPF1022 JPF1021 JPF1020 JPF1017 JPF1018 JPF1019 JPF1006 JPF0913 JPF0911 JPF0971 JPF0916 JPF0917 JPF0919 JPF0918 JPF0920 JPF0921 JPF0922 JPF0915 JPF0915a JPF0901 JPF0906 JPF0907 JPF0908 JPF0909 JPF0910

DL003 DL004 DL002 DL053 DL064 DL063 DL065 DL039 DL043 DL040 DL045 DL041 DL059 DL042 DL048 DL046 DL055 DL066 DL038 DL062 DL034 DL035 DL013 DL015 DL061 DL074

KK79 KR77 DL021b DL022 DL067 DL023 KK35 DL010 DL009 DL011 DL007 DL006 KR87 JPF0904 JPF0905 KR48 KR47 JPF0903 KR82 JPF0902 DL060 KK51 KK3 KR74 KR87a KR88 KK55 JPF0914

APPENDIX 7: COMPACT DISK

The CD in the sleeve at the back contains the following file:

A7.1.*avi*